GSI

GSI 2001-1
April 2001
ISSN 0174-0814

SCIENTIFIC REPORT 2000

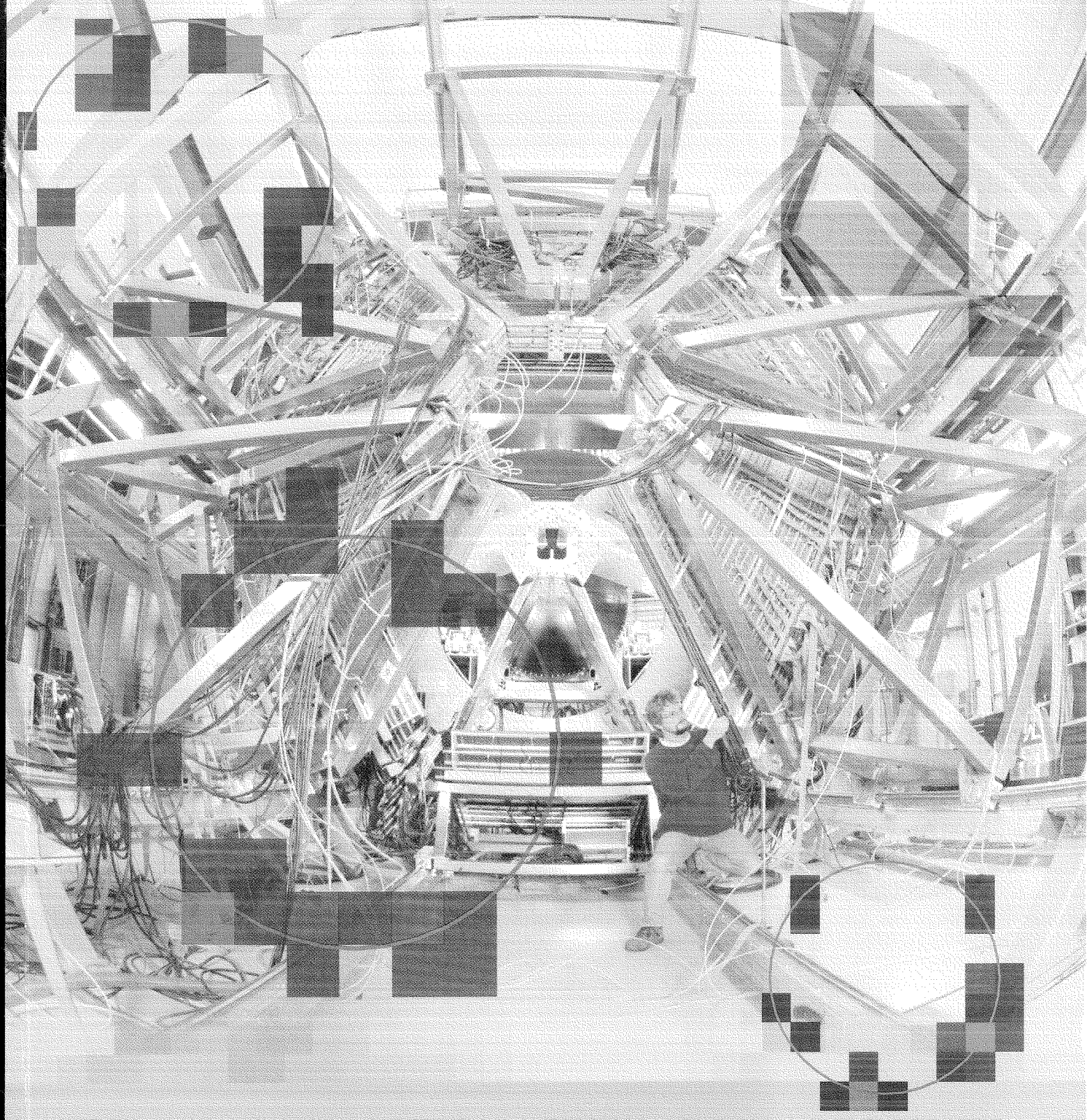

Gesellschaft für Schwerionenforschung mbH Darmstadt

Cover Picture:

The di-electron spectrometer HADES at GSI was put into operation at GSI early in 2000. An international collaboration with more than 130 scientists from 8 European countries participates in the project. The photograph is a view from upstream, showing the six symmetric sectors covering the complete azimuth. As a key feature, HADES has fast online electron recognition based on a ring-imaging Cherenkov (RICH) detector around the target, and a pre-shower detector as well as a time-of-flight wall at the outer shell of the spectrometer. Momentum measurement for charged particles is accomplished by a super-conducting toroid complemented with low-mass drift chambers. The photograph is speckled with "rings" detected in the first experiment by the RICH from traversing energetic electrons.

SCIENTIFIC REPORT
2000

(URL: http://www.gsi.de/annrep)

Publisher: **Gesellschaft für Schwerionenforschung (GSI)**

Address: GSI
Planckstr. 1
D-64291 Darmstadt
Germany

Editor: U. Grundinger, Scientific Information and Documentation
Tel.: 06159 71-2610
FAX: 06159 71-2785
E-mail address: U.Grundinger@GSI.de

Print: druckplus U. Bauer, Darmstadt

C O N T E N T S

ANNEX

Foreword

The past year provided several reasons for GSI to take a look back, far back in certain respects, but also into the future.

GSI celebrated a multiple anniversary: 30 years ago GSI was founded; in addition the last year saw the completion of 25 years of successful operation of the UNILAC accelerator and of 10 years of SIS/ESR. Someone with obviously good mathematics skills pointed out that the anniversaries added up to 65 years, the mandatory retirement age in Germany! So I will quickly add that the past year also saw a major effort to start developing the detailed proposal for the future facilities.

The anniversary event extended over 3 days, with an open house on the first and on the third day, and a celebration and summer party on the second. In wonderful weather everybody, guests and GSI staff, enjoyed the occasion. But perhaps the more significant consequence was that the open house, and more specifically the science exhibit, received such a response and attention that it has since – through word-of-mouth – been on the road as a traveling exhibit from high-school to high-school.

The work on a specific proposal for the future GSI facilities started in the past year. It is based on a range of discussions and workshops at and around GSI over many years that have explored various science opportunities and have provided a basis for the specific concept now under development. The proposal will be completed in 2001 and submitted to the Wissenschaftsrat, the highest scientific advisory committee to the German Federal Government, for evaluation.

After the high-intensity upgrade of the UNILAC over the previous years, the ongoing experimental program went back into full gear in 2000. The HADES di-lepton spectrometer took first data with good lepton identification through the ring imaging Cerenkov counter (see front cover). An experiment with the INDRA set-up from GANIL generated high quality data on nucleus-nucleus collisions, covering the full rapidity range with indications of strong dynamical effects. Analysis of the K-shell pionic atoms of heavy nuclei suggest the possibility to determine the s-wave pion-nucleus potential and the modification of the pion-nucleon coupling constant in the nuclear medium.

The fragment separator provided beams of short-lived nuclei for a range of measurements. Among them are novel studies of spectroscopy on neutron-rich heavy nuclei with gamma-rays, by tagging with K-isomers populated with rather high-spins in projectile fragmentation reactions at 1 GeV/u incident energy.

Elements 111 and 112 were confirmed through new measurements, a requirement set by IUPAC in order to assign discovery to the GSI group. The new even-even isotope $^{290}110$ was surprisingly strongly populated (8 events with α-decay chains in 7 days) using the odd-neutron target ^{207}Pb.

The bound beta-decay - capture of the emitted electron in beta-decay into an atomic orbit - which had been observed at GSI indirectly several years ago was now directly observed in the ESR by detecting the Schottky signals of both, mother and daughter nucleus circulating in the storage ring. In studies of short-lived nuclei with ion traps the highest precision Q-value was determined at ISOLTRAP through a mass measurement of the 65 msec nucleus ^{74}Kr.

In the biological research program accumulation of a specific (immunofluorescence-stained) protein at the sites of damaged DNA was observed and seen to persist for several hours, thus providing a new sensitive measure for radiation damage studies. The cancer therapy program with ^{12}C beams continued successfully for the full year and in parallel with the science program.

These are just a few selected examples. The total, much broader program generated by a large number of outside users and visitors together with GSI staff is described in this report. This is a good opportunity to thank all contributors for their past work and express best wishes for the successful continuation of an exciting research program.

NUCLEAR HEAVY ION PHYSICS

Results included here are progress reports of research projects and therefore should be considered as preliminary communications.

Several university projects were funded by the Federal Ministry of Education, Science, Research and Technology (BMBF); they are marked with a 'B' after the title. In addition GSI supported external groups with certain resources for development of methods and facilities which are of general interest, this is indicated by a 'G' in the title.

Nuclear Structure

Synthesis and Studies of Heavy and Superheavy Elements

Nuclei far off Stability

Secondary Beams and Nuclear Collective Modes

Theory

Nuclear Matter

Multifragmentation

Highly Excited Hadron Matter

Nucleus-Nucleus Collisions at Ultrarelativistic Energies

Theory

New Results on Element 111 and 112

S. Hofmann, F.P. Heßberger, D. Ackermann, B. Kindler, J. Kojouharova, B. Lommel,
R. Mann, G. Münzenberg, S. Reshitko, H.J. Schött, GSI Darmstadt
A.G. Popeko, A.V. Yeremin, JINR Dubna
S. Antalic, P. Cagarda, S. Śaro, University Bratislava
H. Kettunen, M. Leino, J. Uusitalo, University Jyväskylä

The elements 110, 111, and 112 were first identified in a series of experiments in 1994 and 1996 at the SHIP velocity filter [1]. A total of 4 decay chains was measured of the isotope ^{269}110 and 9 decay chains of ^{271}110. Cross-sections of 3.5 and 15 pb, respectively, were determined. The cross-sections for element 111 and 112 were 3.5 and 1.0 pb, deduced from a total of 3 and 2 decay chains.

The new isotopes were identified by position and time correlation analysis. The data were obtained by using position-sensitive Si detectors (details of the experimental set-up and the analysis procedure are given elsewhere [2]). In order to prepare a safe identification of the ^{269}110 nucleus, the decay chain of the daughter ^{265}Hs and its excitation function were measured in a preceding irradiation. In the case of the isotope ^{271}110, the granddaughter ^{263}Sg was known from literature. Therefore the identification of these nuclei was straightforward and without a doubt. The discovery of element 110 by this work was recognized recently by a IUPAC/IUPAP Joint Working Party (JWP) [3].

Concerning the discovery of elements 111 and 112, the JWP concluded that further experiments are needed in order to fulfill the previously worked out criteria for assigning priority of discovery for these elements.

In order to confirm our previous results, we performed two experiments in 2000 aiming at new data on the synthesis and the decay pattern of ^{272}111 and ^{277}112. The irradiation took place from October 16 – 29 and May 3 – 29, respectively. The reactions were the same as in our first experiments, ^{64}Ni + ^{209}Bi → ^{273}111* and ^{70}Zn + ^{208}Pb → ^{278}112*. First results from the Z = 112 experiment were already published in [2]. Subsequent to the irradiation of ^{209}Bi with ^{64}Ni we irradiated a ^{207}Pb target aiming at the synthesis of the even-even nucleus ^{270}110. The results are presented in a succeeding contribution to this report.

In completion of the set-up used in our previous experiments, an electronic circuit was installed in the Z = 111 run, which allowed for switching off the beam within 50 μs after an implanted residue was detected by coincidence of energy and time-of-flight signal. In a subsequent time window of 10 ms a preset number of α particles (in this experiment one) was counted which then prolonged the beam-off period up to the expected measurable end of the decay chain. In our experiment 10 min were chosen, thus making provision for the detection of a possible α decay of ^{252}Md, $T_{1/2}$ = 2.3 min. This improvement considerably reduced the background and allowed for the safe detection of signals from long lived decays. The circuit was prepared already in May for the Z = 112 experiment, however, the trigger conditions could not be set properly, mainly due to the energy shift by degrader foils used in front of the detector.

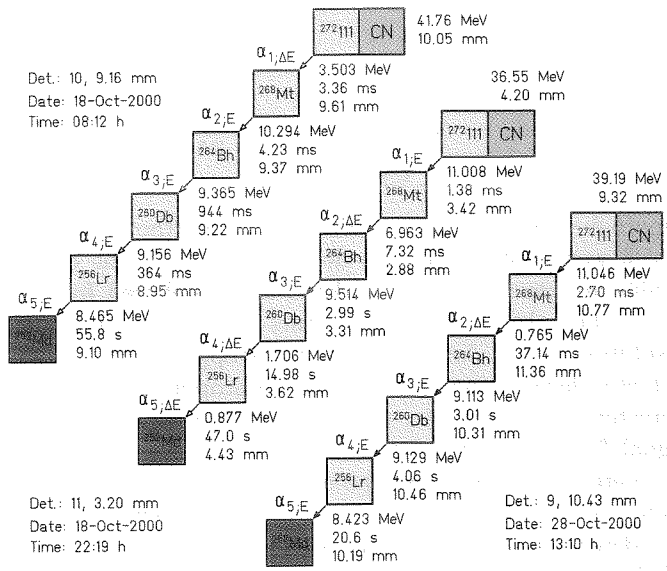

Figure 1: Decay chains and decay data measured during an experiment aiming at the confirmation of element 111.

The targets were prepared in the usual way, 450 μg/cm^2 lead or bismuth was evaporated on a 40 μg/cm^2 carbon foil. The targets were then covered by 10 μg/cm^2 carbon to protect the targets from sputtering and to improve radiative cooling.

The beam energy in the Z = 111 experiment was 320.0 MeV, the resulting excitation energy of the compound nucleus was 14.1 MeV using the mass tables of ref. [4]. At this energy we had measured 2 events in the first experiment during an irradiation time of 5.9 days (one chain was observed at 12.7 MeV excitation energy). A beam dose of 1.1×10^{18} had been collected from which a cross-section of $(3.5\ ^{+4.6}_{-2.3})$ pb resulted. In the new experiment the irradiation time was 13 days and the beam dose 2.2×10^{18} ions. A total of 3 decay chains was measured from which, in agreement with the first result, a cross-section of $(2.5\ ^{+2.5}_{-1.4})$ pb follows. The mean value from both experiments (5 events at 3.3 $\times10^{18}$ projectiles) is $(2.9\ ^{+1.9}_{-1.3})$ pb.

The decay data of the 3 chains measured in the October 2000 experiment are plotted in Fig. 1. A comparison with the 3 previously measured chains and with literature data is shown in Fig. 2. The most important results are summarized in the following: 1) The trigger for the switching off the beam worked properly. All three chains were measured in full length during beam-off periods. 2) In the case of two of the three new chains (chain 5 and 6) the full α energy was measured from the decay of ^{272}111. The two energy values agree, however, the mean value of 11.03

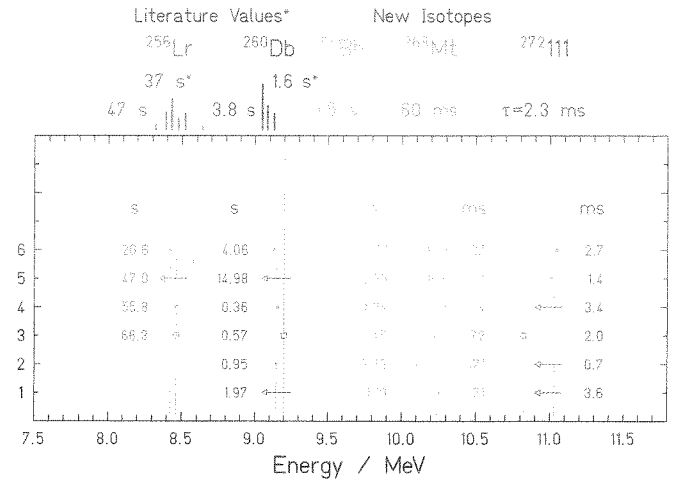

Figure 2: Comparison of α-decay data from the six events which were assigned to the decay of $^{272}111$. The event chains are chronologically ordered and numbered from 1 to 6. The size of the data points reflects the detector resolution, small dots stand for $\alpha's$ stopped in the main detector, larger squares for escape $\alpha's$ stopped in the back detectors and arrows for escape $\alpha's$ delivering only a ΔE signal from the main detector. Vertical lines are drawn at energies of single data points or at the mean energy values of transitions which have the same energy within the detector resolution. The single and mean values of lifetimes (not half-lives) are also given. Above the upper abscissa the α spectra deduced from literature are plotted for the decays of ^{256}Lr and ^{260}Db.

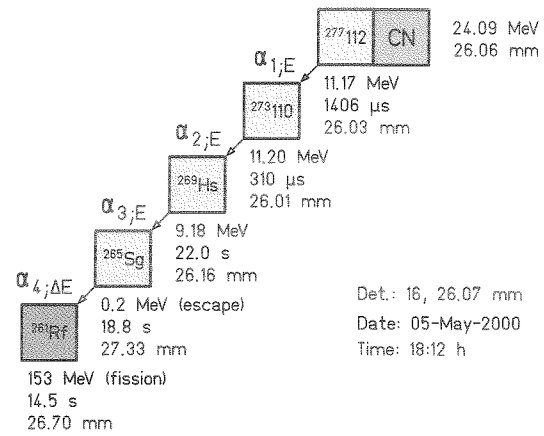

Figure 3: Decay chain of $^{277}112$ measured during a recent experiment aiming to confirm element 112.

MeV is 0.21 MeV higher than the energy obtained from chain 3 of the first experiment. 3) The energies of the α decay of the daughter, ^{268}Mt, and granddaughter, ^{264}Bh, are spread across a wide energy range. Similar, even wider energy distributions were measured from the decay of the neighboring odd-odd isotopes ^{266}Mt and ^{262}Bh [5]. 4) A total of four α-energies was measured from the ^{260}Db decay. Three of them agree within the detector resolution. The mean value of 9.14 MeV also agrees with one of the 3 lines given in the literature. For this line energies of 9.14 and 9.12 MeV were reported [6, 7]. A slightly different, 60 keV higher energy was measured from chain 3. However, the energy value of 9.20 MeV was determined from an escape event stopped in the back detectors. For such events the energy resolution is only 40 keV (FWHM). 5) Six α lines in the energy range from 8.30 to 8.65 MeV are known from the decay of ^{256}Lr [6, 7]. Our energies from chain 3, 4, and 6 agree with the literature values. 6) The measured lifetimes agree for each of the nuclei and in the case of ^{260}Db and ^{256}Lr also with the literature values. There is only one exception. The decays of ^{268}Mt are spread across a larger lifetime period. Although the distribution is still in agreement with statistical fluctuations, it could also be possible that the longest (171 ms) or shortest (4 and 7 ms) lifetimes are related to decays from isomeric states.

Our conclusion of the recent Z = 111 experiment is that our first results are confirmed and that the new data reveal considerably improved information on the decay pattern of the chains starting at $^{272}111$.

In the study of the reaction for the synthesis of element 112 we used a beam energy of 346.1 MeV. The resulting excitation energy of 12.0 MeV is 2.0 MeV higher than in our first experiment. During an irradiation time of 19 days we collected a total of 3.5×10^{18} projectiles. One decay chain was observed. The measured data and our assignment are given in Fig. 3. The first two α decays have energies of 11.17 and 11.20 MeV, respectively, which are succeeded by an α of only 9.18 MeV, an energy step by about 2 MeV. Correspondingly, the lifetime increases by about five orders of magnitude between the second and third α decay. This decay pattern is in agreement with the one observed for chain 2 in our first experiment. It was explained as the result of a local minimum of the shell correction energy at neutron number N = 162 which is crossed by the α decay of $^{273}110$.

The α energy of 9.18 MeV for the decay of ^{269}Hs is identical within the detector resolution with the value of 9.17 MeV obtained in chain 1 of our previous experiment. A new result is the occurrence of fission ending the chain at ^{261}Rf. Fission was not yet known from ^{261}Rf, but is likely to occur taking into account the high fission probabilities of the neighboring even isotopes.

A cross-section of $(0.5^{+1.1}_{-0.4})$ pb was measured for the new data point at 12.0 MeV excitation energy. This value fits well into the systematics of cross-sections. A cross-section increase with increasing beam energy as predicted by theoretical investigation [8] was not observed.

References

[1] Hofmann, S. et al., Z. Phys. A350 (1995) 277 and 281; Z. Phys. A354 (1996) 229

[2] Hofmann, S. and Münzenberg, G., Rev. Mod. Phys. 72 (2000) 733

[3] IUPAC/IUPAP, private communication (Jan. 2001)

[4] Myers, W.D. and Swiatecki, W.J., Nucl. Phys., A601(1996) 141

[5] Hofmann, S., et al., Z. Phys. A358 (1997) 377

[6] Ghiorso, A. et al., Phys. Rev. Lett. 24 (1970) 1498

[7] Bemis, C.E. et al., Phys. Rev. C16 (1977) 1146

[8] Denisov, V.Yu. and Hofmann, S., Phys. Rev. C61 (2000) 034606

The New Isotope $^{270}110$ and its Decay Products ^{266}Hs and ^{262}Sg

S. Hofmann, F.P. Heßberger, D. Ackermann, B. Kindler, J. Kojouharova,
B. Lommel, R. Mann, G. Münzenberg, H.J. Schött, GSI Darmstadt
A.G. Popeko, A.V. Yeremin, JINR Dubna
S. Antalic, P. Cagarda, S. Šaro, University Bratislava
S. Ćwiok, University Warsaw

Synthesis and investigation of heavy even-even nuclei provide especially clear data for comparison with theoretical predictions. The absence of unpaired nucleons results in unhindered α decay or spontaneous fission. Also the low-energy level scheme is expected to be relatively simple. However, the synthesis of even-even nuclei is more difficult by the fact, that in fusion reactions with ^{208}Pb and neutron rich projectiles 2 neutrons must be evaporated, or the target must be replaced by ^{207}Pb. In both cases the measured cross-sections for the synthesis of nuclei beyond rutherfordium revealed a stronger decrease than in 1n reactions using ^{208}Pb targets. Consequently, only few even-even nuclei are known beyond rutherfordium with ^{264}Hs being so far the heaviest one produced in reactions with ^{207}Pb targets [1]. Evidence of heavier even-even nuclei ($^{262}116$) was obtained from recent work in Dubna [2]. In this work we present results obtained in an experiment at the GSI SHIP aiming at the synthesis of the even-even nucleus $^{270}110$ using the reaction ^{64}Ni + ^{207}Pb. A more detailed discussion of the results will be published in [3].

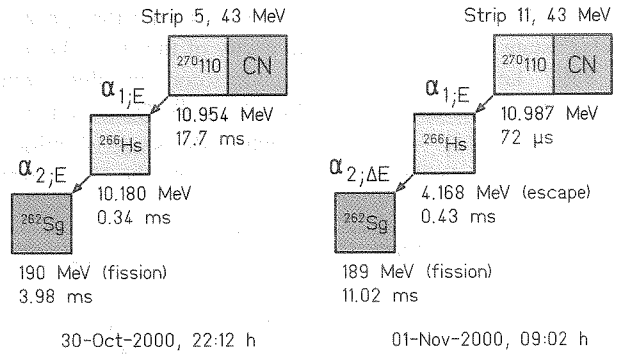

Figure 1: Two representative decay chains observed in irradiation of a ^{207}Pb target with ^{64}Ni projectiles. The chain on the left side starts with a relatively long lived α decay of $^{270}110$ which is attributed to a high spin K isomer. The chain on the right side represents the decay of the short lived ground-state.

A total of eight α-decay chains was measured during an irradiation time of seven days. Two representative chains are plotted in Fig. 1. The ground-state of $^{270}110$ decays by α emission with an energy of 11.03 MeV and a half-life of 100 μs. In addition we measured an isomeric level in $^{270}110$ which decays with a half-life of 6.0 ms. Alpha rays with energies of 10.95, 11.15, and 12.15 MeV were attributed to the decay of the isomer. A tentative assignment of the 12.15-MeV α particle to a transition into the ground-state of ^{266}Hs results in an energy of the isomer at 1.13 MeV. The spin of the isomer was estimated from retardation of the α-decay probability to be approximately (10 $\pm$ 2) $\hbar$. A γ/IC branching of $\approx$30 % to the ground-state seems possible, but could not be definitely established.

The decay properties of the ground-state of $^{270}110$ are in agreement with predictions of the macroscopic-microscopic model and with self-consistent Hartree-Fock-Bogoliubov calculations with Skyrme-Sly4 interaction. The HFB calculations resulted also in two quasiparticle excited levels, one of them could be the origin of the isomeric state. Their configuration and energy is $\{\nu[613]_{7/2+}\ \nu[725]_{11/2-}\}_{9-}$ at 1.31 MeV and $\{\nu[615]_{9/2+}\ \nu[725]_{11/2-}\}_{10-}$ at 1.34 MeV.

The new nuclei ^{266}Hs and ^{262}Sg were identified as members of the α-decay chain. The nucleus ^{266}Hs decays by α emission with an energy of 10.18 MeV and a half-life of 2.3 ms. However, it is also possible as indicated by the decay data, that the α decay has two components with half-lives of 0.35 and 6.3 ms. In that case an isomeric level would exist also in ^{266}Hs which could originate from states analogue as in the case of $^{270}110$. Their energies in ^{266}Hs are predicted to be at 0.90 and 0.94 MeV using HFB calculations. For both nuclei fission was not observed. Using calculated fission half-lives, we estimated fission branchings of 0.2 and 1.4 % for the nuclei $^{270}110$ and ^{266}Hs, respectively.

The nucleus ^{262}Sg decays by fission with a half-life of 6.9 ms and a total kinetic energy of the fission fragments of 222 MeV. Alpha decay was not measured, an upper limit for the α branching is 22 %. This value is in agreement with an estimate of 15 % α-branching, using a half-life deduced from a calculated value for the α energy of ^{262}Sg.

The measured cross-section of 13 pb was unexpectedly high. It is shared equally between ground-state and isomeric state.

Future experiments at longer irradiation time and higher beam dose will certainly provide a more detailed decay scheme and low-energy level scheme of $^{270}110$ and its daughter nuclei. Coincidence experiments using large Ge detectors are promising to search for transitions within the rotational band in ^{266}Hs after α decay of $^{270m}110$. The low-energy rotational levels can be studied via fine structure of the α decay. The measurement of the excitation function will provide data on the population of ground-state and isomeric state. The daughter nucleus ^{266}Hs could possibly be studied directly using the radiative capture reaction of ^{58}Fe and ^{208}Pb. An important next step using ^{207}Pb target is the investigation of $^{276}112$. The result will demonstrate if the synthesis of even-even nuclei in cold fusion reactions could be applied also for still heavier systems.

References

[1] G. Münzenberg et al., Z. Phys. A **328** (1987) 49
[2] Yu.Ts. Oganessian et al., PR C63 (2000) 011301
[3] Hofmann, S. et al., EPJ A, to be published (2001)

Fine Structure in the α - decay of ^{255}Rf

F.P.Heßberger[1], S. Hofmann[1], D.Ackermann[1,2], A. Lavrentev[3], M. Leino[4], G. Münzenberg[1], V.Ninov[1,5], A.G. Popeko[3], S. Saro[6], Ch. Stodel[1,7], A.V.Yeremin[3]

[1]GSI, Darmstadt, Germany, [2] also Johannes Gutenberg - Universität, Mainz, Germany, [3]FLNR JINR, Dubna, Russia, [4]University of Jyväskylä, Jyväskylä, Finland, [5]now at LBNL, Berkeley, USA, [6]Comenius University, Bratislava, Slovakia, [7]now at GANIL Caen, France

In a recent experiment ^{255}Rf was produced by the reactions ^{208}Pb(^{50}Ti,3n)^{255}Rf and ^{206}Pb(^{50}Ti,n)^{255}Rf. From an unusual low number of ^{255}Rf α-decays in the energy interval (8720-8730) keV followed by α - decays of ^{251}No, the existence of a low lying isomeric state with $T_{1/2} \approx 0.9$ s was suspected [1]. Since neither from theoretical predictions [2] nor from the known levels of the lighter N=151 isotones with even Z number [3], which have a similar nuclear structure, the existence of such an isomer could be expected, we decided to clarify this problem using the reaction ^{207}Pb(^{50}Ti,2n)^{255}Rf, for which a cross section $\sigma \approx 10$ nb was obtained. The result is shown in fig. 1a,b. On the basis of a twenty times higher number of observed counts, no ‚abnormally' low correlation rate for E_α = (8720-8730) keV was evident.

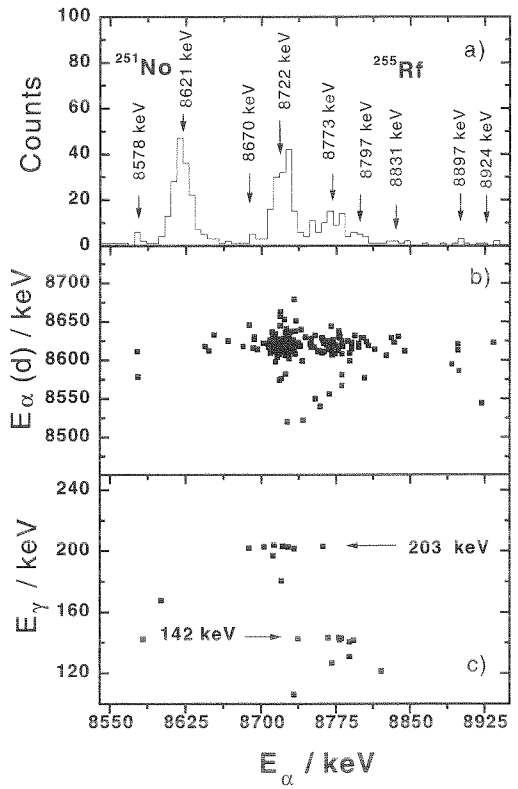

Fig. 1 Decay spectra of ^{255}Rf; a) spectrum of α - events following the implantation of a heavy residue within Δt = 20 s; b) α-α- correlation plot for ^{255}Rf → ^{251}No; c) α-γ - coincidences attributed to the decay of ^{255}Rf

In addition a few γ - events in coincidence to the α - decays of ^{255}Rf were observed (fig. 1c). Two different groups are indicated: a) γ - events of E_γ = (203±3) keV and α - decays of E_α = (8722±10) keV; b) γ - events of E_γ = (142±3) keV and E_α = (8773±10) keV. Since for a) the sum $E_\alpha + E_\gamma$ = 8924 keV, i.e. close to the transition with the highest energy correlated to ^{251}No, we conclude that this γ - transition leads to the ground state and due to the lowest hindrance factor of HF = 3 the 8722 keV - transition is assigned to the favored transition.

According to calculations of Cwiok et al. [2] and assignments for lighter N=151 and N=149 isotones, we tentatively set the ground - states of ^{255}Rf as 9/2$^-$[734] and ^{251}No as 7/2$^+$[624] (fig. 2). Due to the striking low hindrance factor HF = 7 the 8773 keV transition cannot be assigned to the decay into the level 5/2$^+$[622], which is the first excited Nilsson level in the lighter N = 149 isotones (^{247}Cf, ^{245}Cm, ^{243}Pu) [3], although theory predicts it above the 9/2$^-$[734]. Relative intensities of decays into this level are typically lower than 0.05. Therefore we interprete the 142 keV - line due to the transition 9/2$^-$[734] → 9/2$^+$, the first member of the ground state rotational band of ^{251}No (see fig. 2). The succeeding transition 9/2$^+$ → 7/2$^+$[624] is preferrably M1 and thus highly converted. So the 8773 keV - line is understood as due to energy summing of 8722 keV - α-particles with conversion electrons. So are the α - lines at 8797 keV and 8831 keV. In theses cases we assume that primarily the 11/2$^+$ state is populated by the decay of the 9/2$^-$[734] level. The 8897 keV-line finally is understood as due energy summing between α-particles and electrons from conversion processes 9/2$^-$[734] → 7/2$^+$[624], while the small shoulder at 8670 keV may be explained by transitions into the 11/2$^-$ - state.

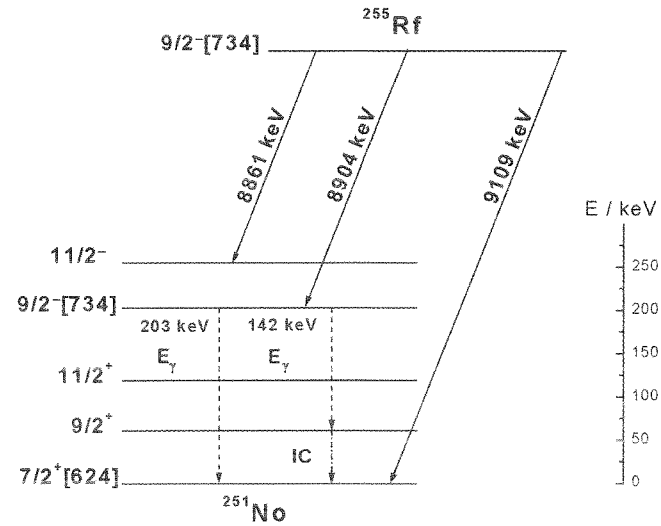

Fig. 2: Decay scheme suggested for ^{255}Rf; the energies denote the Q_α - values.

References:

[1] F.P. Heßberger et al. Z. Phys. A 359, 415 (1997)
[2] S. Cwiok et al. Nucl. Phys. A575, 356 (1994)
[3] R. Firestone et al. (eds.) Table of Isotopes (1996)

Beta Decay of ^{56}Cu

R. Borcea[1], J. Äystö[2], E. Caurier[3], P. Dendooven[2], J. Döring[1], M. Gierlik[4], M. Górska[1], H. Grawe[1], M. Hellström[1], Z. Janas[4], A. Jokinen[2], M. Karny[4], R. Kirchner[1], M. La Commara[1], K. Langanke[5], G. Martínez-Pinedo[5,6], P. Mayet[1], A. Nieminen[2], F. Nowacki[7], H. Penttilä[2], A. Płochocki[4], M. Rejmund[1], E. Roeckl[1], C. Schlegel[1], K. Schmidt[1], R. Schwengner[8], and M. Sawicka[4]

[1] *GSI, Darmstadt,* [2] *University of Jyväskylä, Finland,* [3] *Institut de Recherches Subatomiques, Strasbourg, France,* [4] *Institute of Experimental Physics, University of Warsaw, Poland,* [5] *Institut for Fysik og Astronomi, Århus Universitet Denmark,* [6] *Department für Physik und Astronomie, Universität Basel, Switzerland,* [7] *Laboratoire de Physique Théorique de Strasbourg, France,* [8] *Forschungszentrum Rossendorf e.V., Germany*

Beta-decay studies of proton-rich isotopes near the doubly closed-shell nucleus ^{56}Ni are of interest as (i) nuclei with a few nucleons outside a doubly-magic core are expected to represent comparatively simple configurations and thus be useful for testing nuclear shell-model predictions, and (ii) the large decay-energy window permits to experimentally access a sizeable fraction of the strength of the allowed β decay. Moreover, nuclear structure properties of proton-rich N $\sim$ Z isotopes are of astrophysical interest, e.g., concerning the EC cooling of supernovae and the astrophysical rp-process.

The β decay of ^{56}Cu was studied at the GSI On-line Mass Separator by using a 5.5 MeV/u ^{32}S beam from the UNILAC to induce ^{28}Si(^{32}S, p3n)^{56}Cu fusion-evaporation reactions. The reaction products were stopped in a catcher inside an ion source, released as singly-charged ions, accelerated to 55 kV and mass-separated in a magnetic field. The A=56 beam was implanted into a movable tape and investigated by means of a β-γ-γ detector array consisting of two composite high-resolution germanium (Ge) detectors and a plastic scintillator.

The ^{56}Cu decay to the doubly-magic nucleus ^{56}Ni has been investigated for the first time at the On-line Mass Separator in 1996 [1]. Four γ transitions have been observed, corresponding to the β-feedings of three excited ^{56}Ni states, and a half-life of (78 $\pm$ 15) ms has been determined. In the present experiment [2], due to the more efficient detection set-up and a longer measurement time, the quality of the data was considerably improved, and it was in particular possible to observe γ-γ coincidences. Six γ transitions were identified besides the four ones already known, three new states were added to the level scheme of ^{56}Ni, and the half-life ((92 $\pm$ 3) ms) was determined more accurately. By using the newly determined level scheme and halflife, β feedings and reduced Gamow-Teller (GT) transition probabilities (B(GT)) were deduced with higher accuracy. The experimental B(GT) values were confronted with predictions obtained from five shell-model calculations. Two of these theoretical predictions, one using the FPD6* [3] and the other the KB3G [4] interaction, are presented together with the experimental results in Fig. 1. The shell-model calculations include a 'quenching factor' of 0.74 [5]. It was found that the experimental GT-strength distribution over ^{56}Ni states between 3.9 and 6.6 MeV qualitatively agrees with the predictions (see [2]). We consider this to be a valuable test of shell-model calculations, including their ability to reliably predict the higher-lying GT strength. Moreover, the identification of hitherto unobserved low-spin states in ^{56}Ni is important for further improvement of data from in-beam spectroscopy as well as for further tests of nuclear models. Finally, it was shown [2] that the new experimental data do not imply a revision of the calculated stellar weak-interaction rates of A=56 nuclei [6].

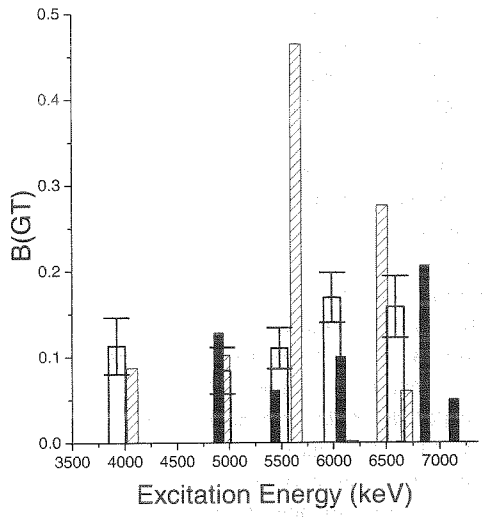

Figure 1: Experimental B(GT)values (empty bars) for the ^{56}Ni levels together with shell-model predictions obtained by using the FPD6* (dashed bars) and KB3G interactions (black bars).

[1] M. Ramdhane *et al.*, Phys. Lett. B 432 (1998) 22
[2] R. Borcea *et al.*, submitted to Nucl. Phys. A
[3] T. Otsuka *et al.*, Phys. Rev. Lett. 81 (1998) 1588
[4] A. Poves *et al.*, nucl-th/0012077, submitted to Nucl. Phys. A
[5] G. Martínez-Pinedo *et al.*, Phys. Rev C 53 (1996) 2602
[6] K. Langanke and G. Martínez-Pinedo, Nucl. Phys. A 673 (2000) 481

Beta-decay properties of ^{60}Ga

C. Mazzocchi[1,2], Z. Janas[1,3], M. Axiotis[4], L. Batist[5] , R. Borcea[1], D. Cano-Ott[6], G. de Angelis[4], J. Döring[1], E. Farnea[4,7], A. Faßbender[1], A. Gadea[4,7], H. Grawe[1], A. Jungclaus[8], M. Kapica[1], R. Kirchner[1], J. Kurcewicz[1], S. M. Lenzi[9], T. Martínez[4,7], I. Mukha[1], E. Nácher[7], D. R. Napoli[4], E. Roeckl[1], B. Rubio[7], R. Schwengner[10], J.L. Tain[7], and C.A. Ur[9]

[1]GSI D-64291 Darmstadt, [2]University of Milan, I-20133 Milan, [3]University of Warsaw, PL-00681 Warsaw,
[4]LNL- INFN, I-35020 Legnaro, [5]St. Petersburg Nuclear Physics Institute, RU-188-350 Gatchina,
[6]Dept. of Nuclear Fission, CIEMAT, E-28040 Madrid, [7]CSIC-University of Valencia, E-46100 Burjassot-Valencia,
[8]University of Göttingen, D-37073 Göttingen, [9]University of Padova and INFN, I-35131 Padova,
[10]FZ Rossendorf, D-01314 Dresden

The recent progress in experimental and theoretical investigations of N~Z nuclei has been motivated by a rather unique multidisciplinary interest spanning from nuclear-structure physics to fundamental physics, with e.g. tests of the standard model of weak interaction by precision measurements of superallowed $0^+ \rightarrow 0^+$ β decays, and to astrophysics, concerning the EC cooling of supernovae or the astrophysical rp-process. A particularly interesting sample of N~Z nuclei is the series of N=Z - 2 (T_Z= -1) odd-odd nuclei in the fp shell. The isotope ^{60}Ga, which is part of this series, was identified in fragmentation reactions [1,2]. These experiments provided evidence that the ground state is probably bound, but did not yield any decay information. In this contribution we report on preliminary results obtained in the first spectroscopic investigation of the β-decay properties of ^{60}Ga performed at the GSI On-line Mass Separator.

The nucleus ^{60}Ga was produced in the ^{28}Si(^{36}Ar,p3n) fusion-evaporation reaction, induced by a 4.71 MeV/u, 85 particle-nA ^{36}Ar beam. The reaction products were stopped and ionized inside the ion source in two separate experiments:

1. A FEBIAD-E [3] ion source was used. The A=60 beam contained, however, strong isobaric long-lived contaminants of ^{60}Cu and ^{60}Zn.
2. A TIS [3,4] ion source was employed to strongly suppress the A=60 contaminants compared to the values obtained during experiment 1. A suppression factor of 700 for the strongest contaminant ^{60}Cu was reached, while the release efficiency for ^{60}Ga was only reduced by a factor of 6 due to the lower efficiency of thermoionization.

The mass-separated A=60 beam was implanted during consecutive time intervals in two carbon foils each viewed by a ΔE-E silicon telescope for detection of β-delayed protons (βp) in experiment 1 and 2. A total of 613 βp events were collected. By comparing the number of events occurring during the beam-on and beam-off periods in one of the two telescopes (288 events), we determined the half-life of ^{60}Ga to be (70±15) ms.

The investigation of β-delayed γ–rays was also performed in both experiments. Another beam line was used and the detector array consisted of a plastic scintillator surrounded by 13 germanium detectors. Figure 1 shows part of the γ-ray data accumulated as the sum of β-coincident single-hit events. Three γ-lines can clearly be observed, i.e. the known 1004 keV line corresponding to the $2^+ \rightarrow 0^+$ transition in the daughter nucleus ^{60}Zn, the 826 keV line of ^{60}Cu, and the 834 keV line of ^{72}As. The latter one is due to a long-lived contamination from a previous A=72 measurement. Moreover, a 3848(2) keV γ-ray has been identified, which shows an unambiguous coincidence relationship with the 1004 keV line (see Figure 1). On the basis of these experimental data, we assign the 3848 - 1004keV cascade to the deexcitation of the isobaric analogue state (IAS) in ^{60}Zn. This consideration positions the IAS at 4852(2) keV. By combining this result with Coulomb-energy systematics [5], we deduced a semi-empirical Q_{EC} value of 14176(3) keV for ^{60}Ga. This finding, together with the known [6] mass excess values of ^{60}Zn and ^{59}Zn, yields a mass-excess of –40007(11) keV and a proton separation energy of 36(41) keV for the proton-dripline nucleus ^{60}Ga.

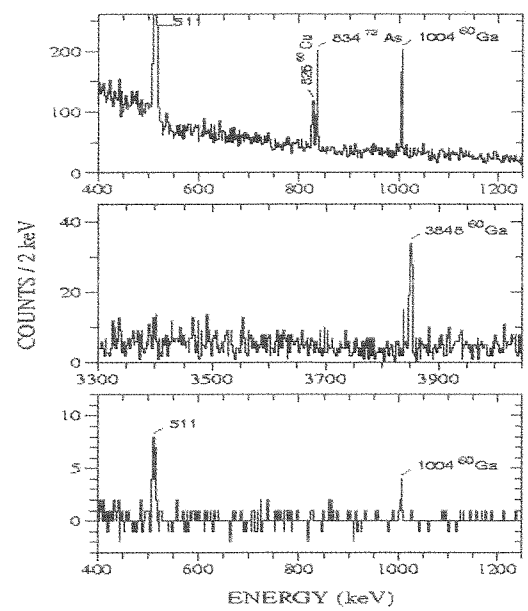

Figure 1. Energy spectrum of β-delayed γ-rays recorded at mass 60. The upper and central panels show parts of the β-coincident γ spectrum, while the lower one displays a background corrected part of the γ spectrum acquired in coincidence with positrons and the 3848 keV γ-ray.

References

[1] B. Blank *et al*, Phys. Rev. Lett. **74**, 4611 (1995)

[2] R. Pfaff *et al.*, Phys. Rev. C **53**,1753 (1996)

[3] R. Kirchner *et al.*, Nucl. Instr. and Meth. **186**, 295 (1981)

[4] R. Kirchner, Nucl. Instr. and Meth. in Phys. Res. **A** 292, 203 (1990)

[5] M. S. Antony *et al.*, At. Data Nucl. Data Tab. **66**, 1 (1997)

[6] G. Audi *et al.*, Nucl. Phys. A **624**, 1 (1997)

Beta-decay study of the self-conjugate odd-odd nuclei ^{62}Ga and ^{70}Br

J. Döring[1], C. Plettner[2], M. Axiotis[3], R. Borcea[1], J. Eberth[4], A. Gadea[3], M. Górska[1], H. Grawe[1], Z. Janas[1,5], R. Kirchner[1], M. La Commara[1], C. Mazzocchi[1,6], E. Nácher González[1], A. Płochocki[5], E. Roeckl[1], K. Schmidt[1], R. Schwengner[2], T. Steinhardt[4], J. Żylicz[5]
[1]GSI Darmstadt, [2]Forschungszentrum Rossendorf, [3]INFN-LNL Legnaro,
[4]Univ. Köln, [5]Warsaw University, [6]Universitá degli Studi di Milano

Nuclei in the mass 70 region exhibit a variety of nuclear structure effects such as rapid shape changes and shape coexistence. Whereas the nuclei around the doubly-magic nucleus ^{56}Ni are considered to be spherical in shape, oblate-deformed ground states have been found in a region around ^{69}Se ($Z = 34$) [1], and prolate-deformed ground states in the proton-rich Sr ($Z = 38$) isotopes [2]. The deformed shapes are well-stabilized by the competing $Z = 34$, 36, and 38 gaps in the single-particle energies. To explore the evolution of the nuclear shape along the $N = Z$ line and their influence on the competition of $T = 0$ and $T = 1$ isospins in odd-odd nuclei, the β-delayed γ-ray emission of the self-conjugate nuclei ^{62}Ga and ^{70}Br has been investigated. The measurements were performed at the on-line mass separator of GSI Darmstadt. Experimental details were reported earlier [3], and preliminary results of the data analysis have been communicated at several conferences [4, 5].

In the experiment on the β^+ decay of ^{62}Ga, an intense 511 keV annihilation peak originating from the $0^+ \rightarrow 0^+$ Fermi ground-state decay [6] and the much weaker 954 keV $2^+ \rightarrow 0^+$ yrast transition in ^{62}Zn have been identified. If a coincidence gate is set on this 954 keV line, weak γ transitions at 1388 and 2225 keV show up. Thus, the transitions may depopulate levels at 2342 and 3179 keV in ^{62}Zn. From a previous (p,t) reaction study [7], levels at 2330 (0^+) and 3160 keV (2^+) are known in ^{62}Zn which are close in energy to the levels populated in β decay. However, due to limited statistics, no reliable half-life for the β-delayed 954 keV γ ray could be deduced.

The occurrence of the 954, 1388, and 2225 keV transitions can result from two different scenarios: (i) from the β decay of a low-lying isomeric state in ^{62}Ga or (ii) from a non-analog decay branch of the 0^+ ground state in ^{62}Ga to higher-lying 0^+ and/or 1^+ states in ^{62}Zn which are deexcited by the emission of γ rays. If we assume that the observed 954 keV line intensity results from a non-analog decay branch, then a branching ratio of $(0.106 \pm 0.017)\%$ can be estimated. This ratio agrees quite well with a previously reported value of $(0.120 \pm 0.021)\%$ [8]. Since almost the same ratio has been obtained in two very different measurements, the interpretation as a non-analog branch is favoured.

In the study of the lightest proton-bound bromine isotope, ^{70}Br, extensive β-γ-γ coincidences have been measured for the decay of the known $T_{1/2} = 2.2(2)$ s isomer [9]. The analysis reveals a complex decay scheme with about 74% of the β feeding populating the 4606 keV level in ^{70}Se which is known as a $(8,9^+)$ state from previous in-beam work [10]. This level was found to be depopulated by transitions of 569.0 and 690.2 keV. However, we observe additional γ rays of 958 and 1604 keV which link this level further to the yrast 6^+ and the 6_2^+ states in ^{70}Se, and thus restrict spin and parity to $I^\pi = 8^+$. Furthermore, the yrast sequence in ^{70}Se has been observed up to the 10^+ state at 5207 keV for the first time in β decay. The deduced β feeding of the 10^+ level is about 1.2(2)%. The spectrum of γ rays in coincidence with the 1169 keV $10^+ \rightarrow 8^+$ transition is displayed in Fig. 1 which clearly shows all lower-lying transitions of the yrast sequence in ^{70}Se. Thus, the β-decaying isomeric state in ^{70}Br must

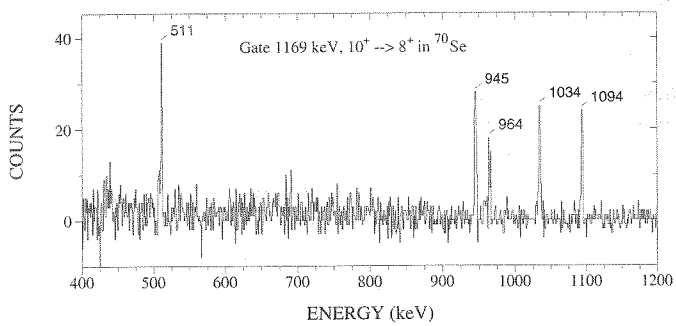

Figure 1: Background-corrected γ-ray spectrum in coincidence with β rays and the $10^+ \rightarrow 8^+$ γ transition in ^{70}Se.

have a high spin, and we propose spin and parity of 9^+, the only assignment being consistent with all experimental results. The high spin of the isomer is interpreted as arising from the Nilsson configuration ($\pi 9/2^+[404]$, $\nu 9/2^+[404]$)) at an oblate deformation of $\beta_2 \approx -0.3$. Our findings are in agreement with very recently reported conclusions from another experiment [11] where also a 9^+ assignment is proposed. However, this is at variance with the earlier assignment of 5^+ given by the same group [12].

The authors appreciate technical support from the GSI mass-separator group, the GSI VEGA group, and from the FZ Rossendorf.

References

[1] M. Wiosna et al., Phys. Lett. B **200** (1988) 255.
[2] C.J. Lister et al., Phys. Rev. Lett. **49** (1982) 308.
[3] J. Döring et al., GSI Scientific Report 2000, p. 14.
[4] E. Roeckl et al., Nucl. Phys. A (in press).
[5] J. Döring et al., Proc. Pingst2000, Report of Lund Uni., p. 131.
[6] C.N. Davids et al., Phys. Rev. C **19** (1979) 1463.
[7] R.A. Hinrichs et al., Phys. Rev. C **10** (1974) 1381.
[8] B.C. Hyman et al., Cyclotrone Inst., Texas A&M Univ., Progress in Research 1999, p. I-28.
[9] B. Vosicki et al., Nucl. Instrum. Meth. **186** (1981) 307.
[10] T. Mylaeus et al., J. Phys. G **15** (1989) L135.
[11] A. Piechaczek et al., Phys. Rev. C **62** (2000) 054317.
[12] A. Piechaczek et al., Proc. Conf. on Perspectives in Nucl. Phys., World Scientific, Singapore, 1999, p. 201.

Beta decay of ^{96}Ag isomers and delayed proton emission to ^{95}Rh levels

L. Batist [1], C.R. Bingham [2], R. Borcea [3], J. Döring [3], M. Gierlik [4], H. Grawe [3], K. Hauschild [5], Z. Janas [3,4] M. Karny [2,4], R. Kirchner [3], M. La Commara [3,6], C. Mazzocchi [3], F. Moroz [1], E. Roeckl [3], K. Schmidt [3,7]
[1] PNPI Gatchina, [2] University of Tennessee, [3] GSI Darmstadt, [4] University of Warsaw, [5] DAPNIA/SPhN CEA Saclay, [6] University Frederico II Naples, [7] University of Edinburgh

The decay of ^{96}Ag was first investigated by Kurcewicz et al. [1], who measured a half-life of 5.1(4) s and observed the emission of β-delayed γ rays (βγ) and β-delayed protons (βp). Later on, Schmidt et al. [2] inferred a half-life of 5.22(15) s from βp data, and found it to be different from the weighted mean (4.50(6) s) of the half-lives of the βγ transitions, indicating the existence of two decaying states in ^{96}Ag. This result is in agreement with shell-model calculations, which predict two closely spaced 2^+ and 8^+ states to occur at low ^{96}Ag excitation-energy. However, the previous works [1,2] did not draw definite conclusions concerning the two ^{96}Ag states. The aim of the present study was to clarify the decay characteristics of these isomers by reinvestigating their βγ and βp properties. We used a total absorption γ-ray spectrometer (TAS) [3]. TAS was expected to be more suitable for this purpose as it is capable of detecting the whole γ cascade following the β decay rather than individual γ transitions. Concerning the βp decay, a coincidence condition between a proton detector and TAS was used. This condition was expected to select the cascades of γ rays de-exciting the ^{95}Rh levels populated by proton emission.

The neutron-deficient isotope ^{96}Ag was produced by fusion-evaporation reactions of a ^{40}Ca beam from the heavy-ion accelerator UNILAC with a ^{60}Ni target. The reaction products were separated at the GSI on-line mass separator by using a chemically selective FEBIAD ion source. The mass-separated A=96 beam was implanted into a transport tape, with the resulting radioactive sources being periodically moved from the collection position to the centre of the TAS, where it was viewed by two 0.5 mm thick silicon detectors. One of them, placed at the side of the tape where the ions had been implanted, was used to detect positrons and protons. The other detector placed at the opposite side of the tape served to record positrons and thus distinguish the protons emitted after β^+ decay from those related to EC decay.

The ^{96}Pd levels populated via ^{96}Ag β-decay are shown in Fig. 1. The analysis of TAS spectra yields evidence for β feeding of both the 2^+ and 8^+ levels in ^{96}Pd. This result indicates β-decaying isomers in ^{96}Ag with low and high spin, respectively. The ^{95}Rh levels populated via βp emission are also displayed in Fig. 1. The strongly populated ^{95}Rh level at 1350 keV can be unambiguously related to the $13/2^+$ level established by in-beam spectroscopy [4]. Besides the agreement in energy, this assignment is supported by the observation that the decay curve for this level is similar to that for the 8^+ ^{96}Pd level. Several new ^{95}Rh levels have been found in addition to those established earlier by in–beam spectroscopy and β decay of ^{95}Pd. One of them, the strongly populated 680 keV level shows the same decay characteristics as that observed for the β feeding to the 2^+ ^{96}Pd level. The evident shell-model counterpart to this level is that with a spin-parity assignment of $7/2^+$ and calculated energy of 650 keV [5], which corresponds to the first excited state built on the proton $g_{9/2}$ single-particle ground state. Tentative spin assignments of $5/2^+$ and $11/2^+$ can be deduced for the other new ^{95}Rh levels on the basis of the comparison with shell-model predictions [5], and by taking into account that they are not populated by the yrast cascade identified by in-beam spectroscopy.

The half-life of the high-spin isomer was determined by evaluating the time characteristics of the β^+ feeding to the ^{96}Pd 8^+ level. The half-life of the low-spin isomer was deduced by using the decay curves of the TAS peak corresponding to the 2^+ ^{96}Pd level and the 680 keV $(7/2^+)$ ^{95}Rh state. The βp branching ratios, indicated in Fig.1 for both isomers of ^{96}Ag, were determined on the basis of a decomposition of the decay curves for βp events and positron-coincident γ rays detected by TAS. The additional uncertainties, which are due to the non-observation of EC-delayed γ rays, were estimated not to exceed 10% of the presented values. Making use of the new half-lives and branching ratios, one can estimate that the summed βp Gamow-Teller strengths for the two isomers are remarkably different. This result probably points to the effect of proton-γ competition for highly excited ^{96}Pd levels.

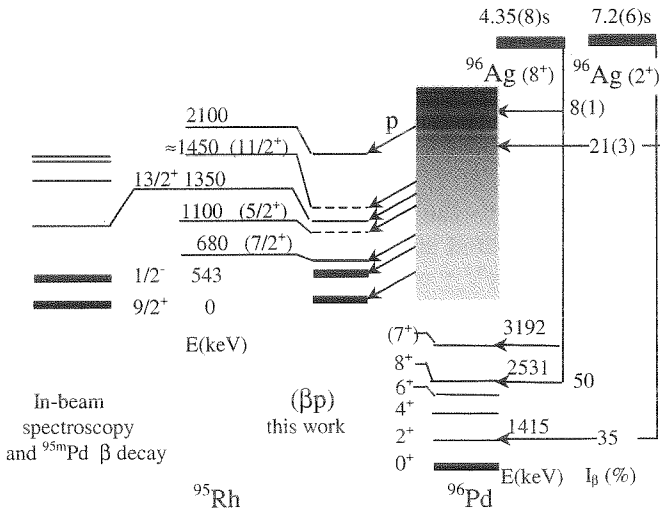

Fig. 1. Excited states in ^{96}Pd and ^{95}Rh populated by the ^{96}Ag β decay and β-delayed proton emission. For unbound ^{96}Pd levels, only βp-intensities are presented.

[1] W. Kurcewicz et al., Z. Phys. A 308 (1982) 21.
[2] K. Schmidt et al., Nucl. Phys. A 624 (1997) 185.
[3] M. Karny et al., Nucl. Instr. and Meth. Phys. Res., B 126 (1997) 320.
[4] H.A. Roth, Phys. Rev., C50 (1994) 1330.
[5] I.P. Johnstone and L.D. Skouras. Phys. Rev, C55 (1997) 1227.

The β^+/EC decay of ^{100}In and the ^{100}Sn shell model

J. Döring[1], C. Plettner[1,2], V. Belleguic[3], H. Grawe[1], L. Batist[4], R. Borcea[1], M. Górska[5], N. Harrington[6], Z. Janas[1,7], R. Kirchner[1], C. Mazzocchi[1,8], P. Monroe[6], E. Roeckl[1], Ch. Schlegel[1], K. Schmidt[1,6], R. Schwengner[2]

[1]GSI, D-64291 Darmstadt, [2]FZ Rossendorf, D-01314 Dresden, [3]Université de Paris-Sud, F-91405 Orsay, [4]PNPI, RU-188-350 Gatchina, [5]IKS KU Leuven, B-3001 Leuven, [6]University of Edinburgh, Edinburgh EH9 3JZ, UK, [7]University of Warsaw, PL-00681 Warsaw, [8]University of Milan, I-20133 Milan

The nucleus ^{100}In, the neutron-proton particle-hole (*ph*) neighbour of the doubly magic ^{100}Sn, is the closest lying neighbour which can be studied today in β^+/EC decay with rates allowing detailed $\beta\gamma\gamma$ spectroscopy, while still having a simple *ph* shell-model structure. Its ground state is expected to be the $I_{max} - 1 = 6^+$ respectively 7^+ member of the $[\pi g_{9/2}^{-1}\nu d_{5/2}]_{2-7}$ or $[\pi g_{9/2}^{-1}\nu g_{7/2}]_{1-8}$ multiplets (Fig. 1). Their centroids are predicted to be nearly degenerate [1, 2]. The Gamow-Teller (GT) decay of a $\pi g_{9/2}$ proton in ^{100}In to a $\nu g_{7/2}$ neutron in ^{100}Cd will preferably populate either the $I^\pi = (5-7)^+$ members of the two-quasiparticle configurations $\nu d_{5/2} g_{7/2}$ or $\nu g_{7/2}^2$ or the four-quasiparticle GT resonance, where these configurations are coupled to an unpaired $\pi g_{9/2}^{-2}$ proton state. The two-quasiparticle $I^\pi = (5-7)^+$ states in the daughter nucleus ^{100}Cd have simple configurations, which are easily accessible to shell-model interpretation [3, 4]. They are lying well below the GT resonance in a region of low level density, so that their GT feeding and γ decay can be used to assign configurations to parent and daughter states.

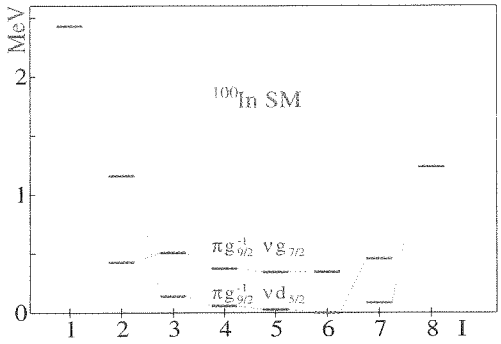

Figure 1: States from the $\pi g_{9/2}^{-1}$ $\nu g_{7/2}$ and $\pi g_{9/2}^{-1}$ $\nu d_{5/2}$ multiplets as predicted by the shell model

We have performed a study of the ^{100}In β^+/EC decay at the GSI on-line mass separator. The reaction ^{50}Cr(^{58}Ni,αp3n) at 6.15·A MeV energy and 45 particle-nA intensity of the ^{58}Ni beam was used to produce mass separated ^{100}In at an average rate of 5 atoms/s from a TIS ion source [5]. The ^{100}In samples were collected and measured in grow-in mode in cycles of 16 s on a movable tape and then removed to suppress long-lived daughter activity. The collection point was surrounded by a plastic scintillator to detect positrons with 70 % efficiency. Two composite HPGe detectors, a cluster of the EUROBALL type and a superclover from the VEGA array, a large volume single HPGe and a LEPS detector served for γ-ray detection with a total detection efficiency of 3.7 % for a 1.33 MeV γ ray.

A γ-coincidence spectrum gated by positrons and the $2^+ \rightarrow 0^+$ γ transition in the daughter ^{100}Cd is shown in Fig. 2. This nucleus has been well studied in in-beam spectroscopy up to high spin [3, 4]. A strong apparent GT feeding of the known $I^\pi = 6^+$ and 8^+ states is clearly observed. From the preliminary analysis of the feeding pattern a spin and parity assignment of $I^\pi = (7^+)$ is inferred for the parent state in ^{100}In. A halflife analysis of the strong 297, 795 and 1005 keV γ lines yields a value of 5.1(5) s in agreement with the adopted average of previous results 6.1(7) s [6].

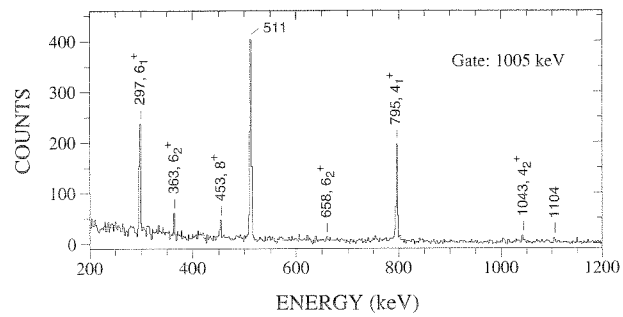

Figure 2: Partial β-gated $\gamma\gamma$ spectrum of the ^{100}In decay gated on the $2^+ \rightarrow 0^+$ transition in the daughter ^{100}Cd

The spin and parity assigned to the parent state, which could be the ground state or an isomer, is clearly at variance with the shell-model prediction shown in Fig. 1 [1]. The residual interactions used in shell-model calculations favour $I^\pi = 6^+$ [1, 7, 8] in agreement with tentative assignments to the odd-odd In isotopes and N=51 isotones. The *ph* nature of the interaction requires that the two assignments belong to different configurations (Fig. 1). This excludes a trivial solution to the problem by shifting the centroids of the multiplets, as the configuration mixing would counteract, and would rather indicate a revision of the realistic interaction used in the shell model.

References

[1] M. Górska et al., Proc. ENPE 99, eds. B. Rubio, M. Lozano, W. Gelletly, AIP Conf. Proc. **495** (1999) 217

[2] H. Grawe et al., Proc. SM2K, RIKEN, ed. T. Otsuka, Nucl. Phys. A, in print

[3] M. Górska et al., Z. Phys. **A350** (1994) 181

[4] R.M. Clark et al., Phys. Rev. **C61** (2000) 044311

[5] R. Kirchner, Nucl. Instr. and Meth. **A292** (1990) 203

[6] G. Audi et al., Nucl. Phys **A624** (1997) 1

[7] H. Grawe et al., Physica Scripta **T56** (1995) 71

[8] B.A. Brown and K. Rykaczewski, Phys. Rev. **C50** (1994) R2270

Halflives of neutron deficient nuclei near ^{100}Sn

E. Wefers[1], T. Faestermann[1], R. Schneider[1], A. Stolz[1], K. Sümmerer[2], J. Friese[1], H. Geissel[2], M. Hellström[3], P. Kienle[1], H.-J. Körner[1], M. Münch[1], G. Münzenberg[2], P. Thirolf[4] and H. Weick[2]

[1]TU München, [2]GSI, [3] University of Lund, [4] LMU München

Neutron deficient nuclei near ^{100}Sn have been produced by fragmentation of a 1 A·GeV ^{112}Sn beam in a beryllium target, separated in the FRS and identified with a new detector system [1]. The unambiguously identified ions were stopped in a highly segmented silicon detector stack [2]. We determined the halflives for each implanted isotope using a maximum likelihood method [3].

Fig. 1 shows the measured isotopic yields for fragments from strontium to indium. The cross sections extracted from these yields are in good agreement with empirical predictions (EPAX). The spectra show the previously unobserved $N = Z - 2$ nuclei ^{76}Y (2 events) and ^{78}Zr (one event). Due to the excellent resolution of our identification detectors we can assign a 3σ confidence level to these observations. In addition fig. 1 demonstrates the absence of the $N = Z - 1$ nuclei ^{81}Nb, ^{85}Tc and ^{89}Rh, which are probably unstable against proton emission.

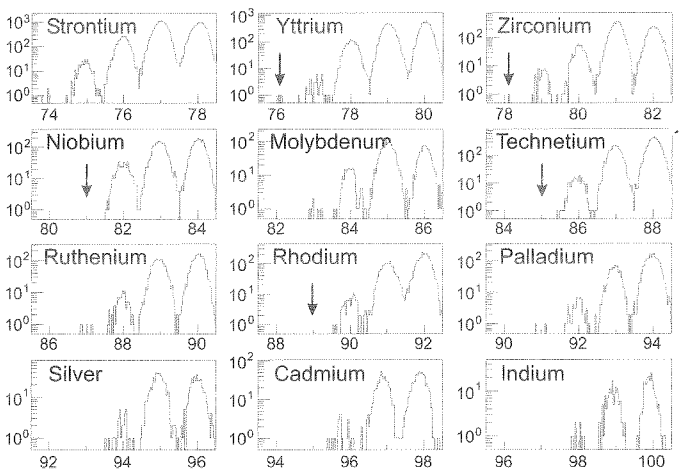

Figure 1: Mass spectra of the observed ions between Sr and In. The arrows indicate the identification of ^{76}Y and ^{78}Zr and the absence of ^{81}Nb, ^{85}Tc and ^{89}Rh.

The identification of ^{76}Y and ^{77}Y coincides with recent predictions of the relativistic Hartree-Bogoliubov model for the proton dripline [4], whereas ^{81}Nb and ^{85}Tc are not predicted to be dominantly proton emitters.

For the identified nuclides as well as for the unobserved ones we determined limits for their halflives resulting from their flight time through the FRS (table 1). Note that the failure to observe ^{89}Rh could also be due to the small cross section expected (50 pb) just at our detection limit. In order to improve our knowledge on the proton dripline we implanted the $N = Z - 1$ nuclei ^{75}Sr, ^{77}Y, ^{79}Zr and ^{83}Mo into the Si detector stack. The measured halflives, which are as short as expected for β-decays between mirror nuclei, are also listed in table 1. For ^{77}Y we collected 12 nuclei which decay all via β-decay, setting an upper limit

	$T_{1/2}$		$T_{1/2}$		$T_{1/2}$
^{75}Sr	80^{+400}_{-40} ms	^{76}Y	> 170 ns	^{77}Y	57^{+22}_{-12} ms
^{78}Zr	> 170 ns	^{79}Zr	80^{+400}_{-40} ms	^{81}Nb	< 44 ns
^{83}Mo	6^{+30}_{-3} ms	^{85}Tc	< 110 ns		

Table 1: Halflives of $N < Z$ nuclei. For details see text.

to a possible proton branch of 10% (1σ c.l.).

An important nuclear physics input quantity for network calculations modelling the astrophysical rp-process are the halflives of the so-called waiting point nuclei. We measured the halflives of all these nuclei from ^{80}Zr up to ^{92,93}Pd. In addition we were able to determine halflives of several unknown indium, rhodium and technetium isotopes near the $N = Z$-line with the same magnet settings of the FRS. These results are listed in table 2.

	$T_{1/2}$ [s]		$T_{1/2}$ [s]		$T_{1/2}$ [s]
^{80}Zr	$5.3^{+1.1}_{-0.9}$	^{84}Mo	$3.7^{+1.0}_{-0.8}$	^{87}Tc	2.18 ± 0.16
^{88}Ru	$1.2^{+0.3}_{-0.2}$	^{89}Ru	1.45 ± 0.13	^{91}Rh	1.74 ± 0.14
^{92}Rh	5.6 ± 0.5	^{93}Rh	13.9 ± 1.6	^{92}Pd	$1.0^{+0.3}_{-0.2}$
^{93}Pd	1.0 ± 0.2	^{99}In	$3.0^{+0.8}_{-0.7}$		

Table 2: Halflives of nuclei near the $N = Z$ line.

In an earlier report of preliminary results [5], an erroneous value for the ^{93}Pd and ^{92,93}Rh halflife was given because some daughter decays were included and the background suppression was insufficient in the first analysis.

To investigate superallowed Fermi-β-decays we studied the six heaviest candidates of $N = Z$ odd-odd nuclei between ^{78}Y and ^{98}In. For the first time we observed fast transitions, compatible with superallowed Fermi transitions for ^{90}Rh, ^{94}Ag and ^{98}In. In addition to these fast transitions, we have observed a few long-lived isomeric states. The measured halflives are listed in table 3.

	$T_{1/2}$[ms]	$T^{iso}_{1/2}$[s]		$T_{1/2}$[ms]	$T^{iso}_{1/2}$[s]
^{78}Y	55^{+9}_{-6}	$5.7^{+0.7}_{-0.6}$	^{82}Nb	48^{+8}_{-6}	
^{86}Tc	59^{+8}_{-7}		^{90}Rh	12^{+9}_{-4}	$1.0^{+0.3}_{-0.2}$
^{94}Ag	26^{+26}_{-9}	$0.45^{+0.20}_{-0.13}$	^{98}In	32^{+32}_{-11}	$1.2^{+1.2}_{-0.4}$

Table 3: Halflives of $N = Z$ odd-odd nuclei.

This work was supported by BMBF (06TM872 TPI) and SFB 375.

References

[1] A. Stolz et al., GSI Scientific Report 1998, p.174
[2] E. Wefers et al., GSI Scientific Report 1998, p.173
[3] A. Stolz, PhD thesis, TU München (2001)
[4] G.A. Lalazissis et al., Nucl. Phys. A679 (2001) 481
[5] E. Wefers et al., AIP Conference Proc. 495 (1999) 375

Alpha decay of ^{114}Ba

C. Mazzocchi[1,2], Z. Janas[1,3], L. Batist[4], V. Belleguic[2], J. Döring[2], M. Gierlik[1], M. Kapica[1], R. Kirchner[1], H. Mahmud[5], E. Roeckl[1], K. Schmidt[5], P.J. Woods[5], and J. Żylicz[1]

[1]GSI D-64291 Darmstadt, Germany,[2]University of Milan, I-20133 Milan, Italy, [3]University of Warsaw, PL-00681 Warsaw, Poland, [4]St. Petersburg Nuclear Physics Institute, RU-188-350 Gatchina, Russia, [5]University of Edinburgh, Edinburgh EH9 3JZ, UK

In recent years, intense experimental and theoretical research has been devoted to investigate nuclei near the doubly magic nucleus ^{100}Sn (Z=N=50). In this region of the nuclear chart, an island of α emission occurs, covering neutron-deficient isotopes of tellurium (Z=52) through cesium (Z=55). Alpha emission is a rich source of nuclear structure information [1]. The α-particle energy E_α, corrected for the recoil effect, yields the difference between the masses of mother and daughter nucleus. Above ^{100}Sn, this quantity directly relates to the Z=N=50 shell-strength. Moreover, the information on energy, half-life and α-decay branching ratio (b_α) yields the reduced widths for this disintegration mode (W_α). Measurements of W_α values may shed light on the question whether superallowed α decay occurs for nuclei beyond ^{100}Sn, with protons and neutrons occupying identical $d_{5/2}$, $d_{3/2}$ and $g_{7/2}$ orbitals. Moreover, these nuclei, and in particular ^{114}Ba, are predicted to be promising candidates for the observation of cluster (^{12}C) radioactivity. The decay of ^{114}Ba had already been investigated in previous experiments [2-4], but only lower limits for α and ^{12}C partial half-lives could be established [2]. In this contribution we report on preliminary results obtained in a reinvestigation of the α-decay properties of ^{114}Ba.

The experiment was performed at the GSI On-line Mass Separator. ^{114}Ba was produced in fusion-evaporation reactions induced by a 284 MeV ^{58}Ni beam on 2.0-3.8 mg/cm^2 thick ^{58}Ni targets. The reaction products were stopped inside a high-temperature cavity ion source in two tantalum catcher foils, from which most recoils – at the ion source temperature of about 2400 K – are swiftly released as thermalized atoms. Chemical selectivity for barium isotopes was achieved by adding CF_4 and thus using on-line fluorination. The ionization takes place selectively in the fluorination sideband of BaF, all contaminants including CsF being reduced to levels well below 10^{-5} [5]. The BaF^+ ions were accelerated to 55 keV, mass-separated and focused alternately onto two carbon foils, each one being viewed by a ΔE-E silicon telescope.

The search for α emission was performed using the ΔE spectrum registered in anticoincidence with the E detector. Figure 1 shows the corresponding spectrum obtained from both telescopes during a measurement time of 55.6 hours. Three α lines were observed at the energies 3410±40, 3740±30 and 4160±30 keV, containing 38, 21 and 22 events, respectively. We assign the lowest-energy line to the α decay of ^{114}Ba. This assignment is based on the Z and A selectivity that was reached combining the fluorination ion source with mass-separation. The higher-energy members of this triplet are assigned to the known [6] α lines from the decay of ^{110}Xe and ^{106}Te. Taking into account the recoil correction, we obtained a Q_α value of 3540±40 keV for ^{114}Ba. This result, together with the known [6] Q_α values of ^{110}Xe and ^{106}Te, yields a Q value of 19000±60 keV for ^{12}C decay of ^{114}Ba, which is important to obtain experimentally relevant predictions for this decay mode.

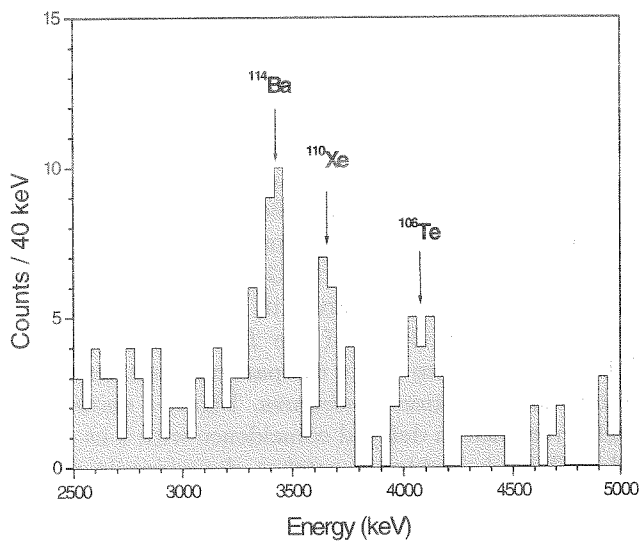

Figure 1. Section of the ΔE spectrum from both telescopes, taken in anticoincidence with the related E detectors.

By comparing the 38 α events observed with the 980 β-delayed protons (βp) detected simultaneously in ΔE-E coincidence, the b_α value of ^{114}Ba was determined to be $(9\pm3)\cdot10^{-3}$. This result takes into account the detection efficiencies of the telescopes and the known βp branching ratios for ^{114}Ba [4] and its daughter ^{114}Cs [7]. The new b_α value is somewhat larger but still compatible with the previously obtained upper limit of $3.7\cdot10^{-3}$ (68% c.l.) [2]. Moreover, the analysis of time correlations will allow us to deduce the half-life of ^{110}Xe and the b_α values for ^{110}Xe and ^{106}Te.

References

[1] E. Roeckl, Alpha decay, in: *Nuclear Decay Modes*, ed. D.N. Poenaru, IOP, 1996, pp. 237

[2] A. Guglielmetti et al., Phys. Rev. C **52** (1995) 740

[3] A. Guglielmetti et al., Phys. Rev. C **56** (1997) R2912

[4] Z. Janas et al., Nucl. Phys. A **627** (1997) 119

[5] R. Kirchner, Nucl. Instr. Meth. B **126**, 135 (1997)

[6] D. Schardt et al., Nucl. Phys. A **368**, 153 (1981)

[7] E. Roeckl et al., Z. Phys. A **294** (1980), 221

A new micro-second isomer in neutron-rich ^{136}Sb

M.N. Mineva[1], M. Hellström[1,2], M. Bernas[3], J. Gerl[2], H. Grawe[2], M. Pfützner[4], P.H. Regan[5], D. Rudolph[1], J. Genevey[6], Z. Janas[4], J. Kurcewicz[4], P. Mayet[2], J.A. Pinston[6], Zs. Podolyàk[5], M. Rejmund[7], Ch. Schlegel[2], K. Sümmerer[2]
[1]Lund University, [2]GSI-Darmstadt, [3]IPN Orsay, [4]Warsaw University, [5]University of Surrey, [6]ISN Grenoble, [7]CEA Saclay

By studying the properties and decay patterns of isomeric states resulting from the coupling of valence particles in high-j orbitals at the $Z = 50$ and $N = 126$ shell closures, valuable information on nuclear structure and nucleon-nucleon interaction in very neutron-rich systems can be obtained. In December 1999, we therefore performed an experiment at GSI to search for new, relatively long-lived (100ns - 100μs) isomeric states in the region around the neutron-rich doubly magic nucleus ^{132}Sn. The nuclei of interest were produced by projectile fission of ^{238}U at 750 MeV/u in a 1.0 g/cm^2 ^{9}Be target, separated using the Fragment Separator (FRS) and implanted in a catcher at the final focus surrounded by Ge detectors. More details about the experiment are given in [1, 2].

The well-known decay of the $I^\pi = 19/2^-$ isomer in ^{135}Te [3] was used to verify the particle identification and lifetime determination procedures. Figure 1 shows the γ-spectra recorded in delayed coincidence with ions of ^{135}Te and ^{136}Sb implanted in the catcher. A previously unknown delayed γ-transition at 173 keV is clearly seen in the ^{136}Sb-gated spectrum.

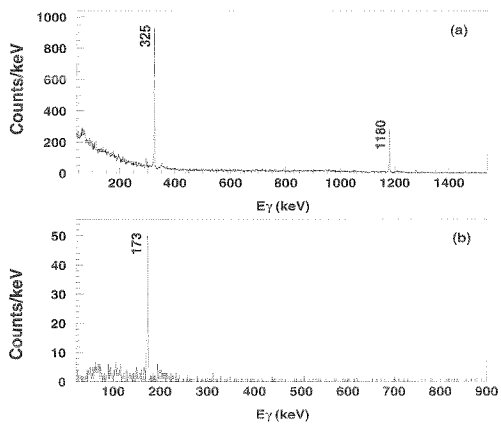

Figure 1: Delayed γ-ray spectra measured in coincidence with implanted ^{135}Te (a), and ^{136}Sb (b) ions. The time-delay is 250 ns, and 500 ns, respectively. The energy labels are in keV.

The decay curves of ^{135}Te and ^{136}Sb are presented in figure 2. The distributions were fitted to obtain the corresponding half-lives of the isomeric decays, and the results are summarized in Table 1. The half-life of the proposed new isomeric state in ^{136}Sb is $T_{1/2}$=566±46 ns [2].

The β-decay of the ^{136}Sb ground state was studied by Hoff et al. [4], who suggest it is the $I^\pi = 1^-$ member of the $\pi g_{7/2}\nu f^3_{7/2}$ multiplet. Previous to our experiment, however, no excited states were known. The energy (173 keV) and half-life (566 ns) of the single delayed γ-ray we observe

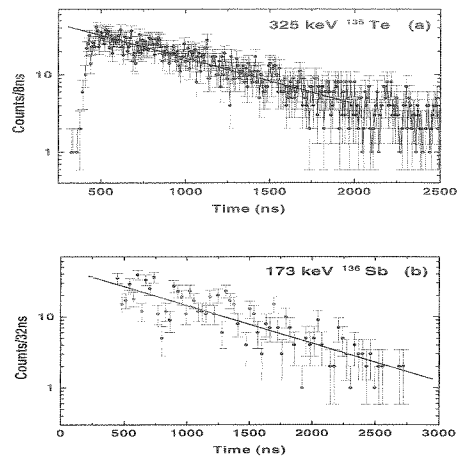

Figure 2: Time distribution curves of a) the 325 keV line from the decay of the $I^\pi = 19/2^-$ isomer in ^{135}Te and b) the 173 keV line identified in ^{136}Sb.

Table 1: Determined isomer half-lives

Isotope	I^π	$T_{1/2}$ (ns) (this work)	$T_{1/2}$ (ns) (previous)
^{135}Te	$19/2^-$	512±22	510±20 [3]
^{136}Sb	-	566±46	-

make it an unlikely candidate for the transition deexciting the isomeric state. More likely, the primary isomeric transition has low energy (<50 keV) and escapes detection in our setup due to internal conversion or absorption.

To help in interpreting the experimental observations we have performed spherical shell model calculations, using two different sets of interactions, to calculate the excitation energies for the $\pi g_{7/2}\nu f^3_{7/2}$ multiplet members. The calculations indicate that the isomer may have $I^\pi = 6^-$, and the observed 173 keV γ-ray could be the $4^- \rightarrow 2^-$ transition. However, although ^{136}Sb has only one proton and three neutrons outside the doubly magic ^{132}Sn core, the gradual onset of collectivity as more valence particles are added could influence the level ordering and spacing. More experimental studies of ^{136}Sb are clearly needed.

References

[1] M.N. Mineva *et al.*, *Proc. 2nd International Balkan School on Nuclear Physics*, Bodrum, Turkey, September 2000, Balkan Physics Letters, in press.
[2] M.N. Mineva *et al.*, to be submitted to EPJ A.
[3] K. Kawade *et al.*, Z. Phys. A **298**, (1980) 273.
[4] P. Hoff *et al.*, Phys. Rev. C **56**, (1997) 2865.

High Spin States Populated via Projectile Fragmentation in Very Neutron-Rich Nuclei Around Mass 180

P. Mayet[1], J. Gerl[1], Ch. Schlegel[1], Zs. Podolyák[2], P.H. Regan[2], M. Caamaño[2], M. Pfützner[3], M. Hellström[1], M. Mineva[4] for the GSI ISOMER collaboration

K-isomers can be found mainly in the A∼180 region. The best examples of K-isomerism are predicted to occur on the neutron-rich side of the valley of stability and are thus barely reachable by standard nuclear reactions like deep inelastic reactions. Up to now, only projectile fragmentation has proven to be an efficient method in populating heavy neutron-rich isotopes with cross-sections sufficient to perform γ-ray spectroscopy. Thus, the FRagment Separator [1] (FRS) associated with γ-ray spectroscopy techniques has been successfully used at GSI to search for K-isomers with lifetimes ranging from nano- to milliseconds in the mass region around A∼180.

These isomers were produced following the fragmentation of a 1 GeV/nucleon ^{208}Pb beam impinging on a 1.6 g/cm^2 Be target. The fragments were separated through the FRS working in achromatic mode and identified using the Bρ-ΔE-TOF method. Ions were stopped in a 5 mm thick Al catcher covering an implantation area of 16 cm on horizontal position. Prompt and delayed γ-rays in coincidence with implanted ions of interest were measured using a Segmented Clover Array whose efficiency was about 6% at 1.33 MeV for the central position of the catcher.

Several new isomers were observed in neutron-rich A=180-200 nuclei, as shown in the following figure, providing the first nuclear structure information from the successive γ-decay cascade. In particular, the rotational band of ^{190}W [2] has been observed for the first time.

Moreover, the ability of this novel method to reach high spin states has been demonstrated by populating K=$\frac{35}{2}^-$ isomeric state in ^{175}Hf [3], ^{179}W [4] and ^{181}Re [5]. This spin represents the highest value observed so far in projectile fragmentation.

Institutes :

[1] *GSI, Planckstrasse 1, D-64291 Darmstadt, Germany, contact person: P.Mayet@gsi.de*

[2] *Dept. of Physics, University of Surrey, Guildford, GU2 5XH, UK*

[3] *Institute of Experimental Physics, Warsaw University, Pl-00861 Warsaw, Poland*

[4] *Div. of Cosmic and Subatomic Physics, Lund University, SE-22100, Sweden*

References:

[1] H. Geissel *et al.*, Nucl. Inst. Meth. B **70**, 286 (1992).

[2] Z. Podolyák *et al.*, Phys. Lett. **B491**, 225 (2000).

[3] G.D. Dracoulis and P.M. Walker, Nucl. Phys. A **342**, 335 (1980).

[4] P.M. Walker *et al.*, Nucl. Phys. A **568**, 397 (1994).

[5] C.J. Pearson *et al.*, Phys. Rev. Lett. **79**, 605 (1997).

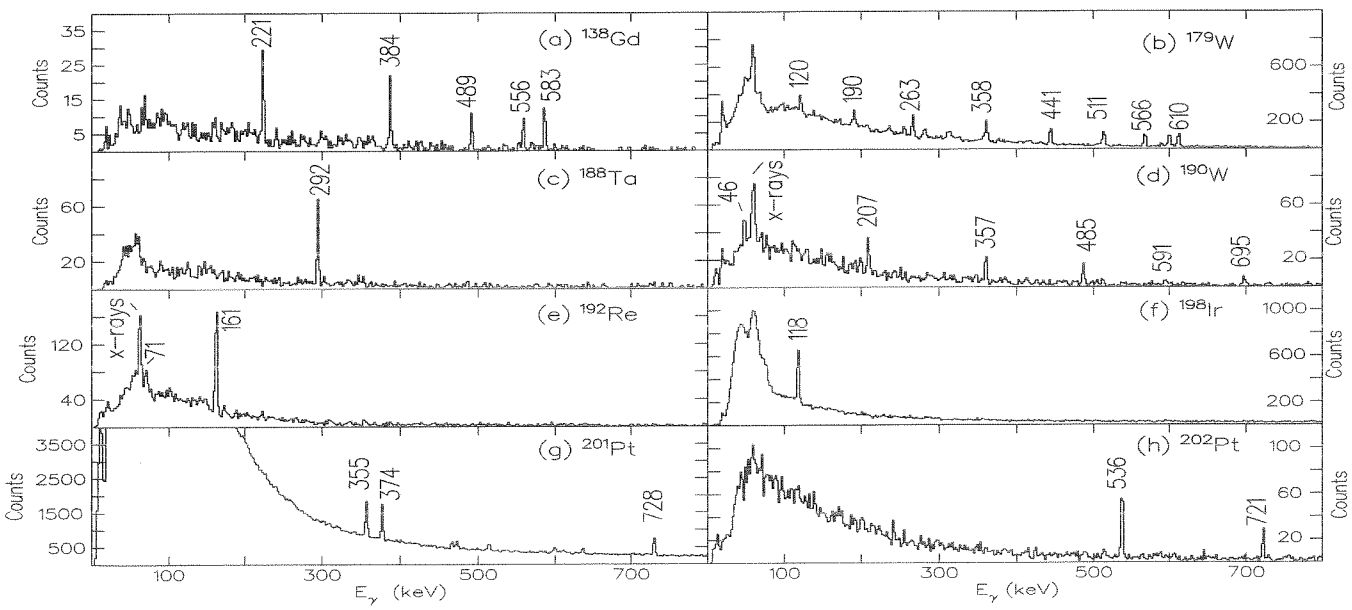

New microsecond isomers in ^{189,190}Bi

A.N. Andreyev[1,5], D. Ackermann[2], P. Cagarda[3], J. Gerl[2], F. P. Heßberger[2], S. Hofmann[2], K. Heyde[4], M. Huyse[1], A. Keenan[5], H. Kettunen[6], A.Kleinböhl[2], A. Lavrentiev[7], M. Leino[6], B. Lommel[2], M. Matos[3], G.Münzenberg[2], C. Moore[5], C. D. O'Leary[5], R. D. Page[5], S. Reshitko[2], S. Śaro[3], C. Schlegel[2], H. Schaffner[2], M. Taylor[5], P.Van Duppen[1], L. Weissman[1], R. Wyss[8]

[1]Instituut voor Kern- en Stralingsfysica, University of Leuven, Belgium; [2]GSI Darmstadt, Germany; [3]Comenius University of Bratislava, Slovakia; [4]Institute for Theoretical Physics, Gent, Belgium, [5]Oliver Lodge Laboratory, University of Liverpool, United Kingdom; [6]University of Jyväskylä, Finland; [7]JINR, Dubna, Russia; [8]Royal Institute of Technology, Stockholm, Sweden

New microsecond isomers in the neutron-deficient isotopes ^{189,190}Bi have been identified at the velocity filter SHIP in the p4n and p3n evaporation channels, respectively, of the complete fusion reaction of ^{52}Cr ions with a ^{142}Nd target. After in-flight separation the evaporation residues (EVRs) were implanted into a position-sensitive silicon detector (PSSD), where their subsequent α-decays were measured. Behind the PSSD a four-fold segmented Ge-clover detector was installed for prompt and delayed (up to 5 ms) α-γ and α-X ray coincidence measurements allowing for the investigation of long-lived isomeric states. EVRs were identified by excitation-function measurements and by using the Recoil-Decay-Tagging method on the basis of delayed recoil-γ, recoil-X ray, and recoil-γ-α coincidences. A detailed description of the experimental set-up used and of the results for ^{188,189,190}Po and their daughter products was given in [1].

Fig.1a shows the γ-ray spectrum measured by the clover detector in coincidence with recoils registered in the PSSD. The γ-transition observed at 357(1) keV has an excitation function similar in shape and position to the 6672-keV α-decay of the $9/2^-$ ground state of ^{189}Bi ($T_{1/2}$ = 680 ms) and of the 7298 keV α-decay of the $1/2^+$ isomeric state (^{189m1}Bi) of ^{189}Bi. On this basis we assign this transition to ^{189}Bi. Fig.1b shows the same spectrum as in Fig.1a, but with an additional condition that the EVR-γ pair is correlated within the time interval of 2 s with an α decay of E_α = 6672 keV. The procedure to take into account the background of possible random correlations is described in detail in [2]. In Fig.1b, besides a peak at E_γ = 357(1) keV coincidences with the K-X rays of Bi are also observed. Thus, the excitation function behaviour, coincidence with the Bi K-X rays and the condition of correlation with the α decay of ^{189g}Bi establishes the origin of the 357 keV γ-line as an isomeric state (^{189m2}Bi) built on top of the $9/2^-$ ground state in ^{189}Bi.

By comparing the number of the K-X rays and γ-rays in Fig.1b, corrected for the corresponding efficiencies [1], a conversion coefficient of α_K = 0.9(1) was deduced, which is consistent with the theoretical value of α_K(357 keV, M2) = 0.77. This establishes the spin and the parity of the 357-keV isomeric state ^{189m2}Bi as $13/2^+$. We assume that this state decays by the M2 transition directly to the $9/2^-$ ground state of ^{189}Bi, as in the cases of ^{191,193,195}Bi [3]. Applying a procedure described in [2] , we deduced a lower limit of $T_{1/2}$ > 360(120) ns for the half-life value of the 357-keV transition.

By using the same method as described above for ^{189m2}Bi and by analysing the recoil-γ (Fig.1c) and recoil-γ-α(6450 keV) (Fig.1d) correlations a previously unknown isomeric γ-decay with the energy of E_γ = 273(1) keV and a lower half-life limit of $T_{1/2}$ > 500(100) ns was observed on top of the α-decaying (E_α = 6450 keV) 10^- isomeric state in ^{190}Bi. The detailed discussion of the observed results is given in [2].

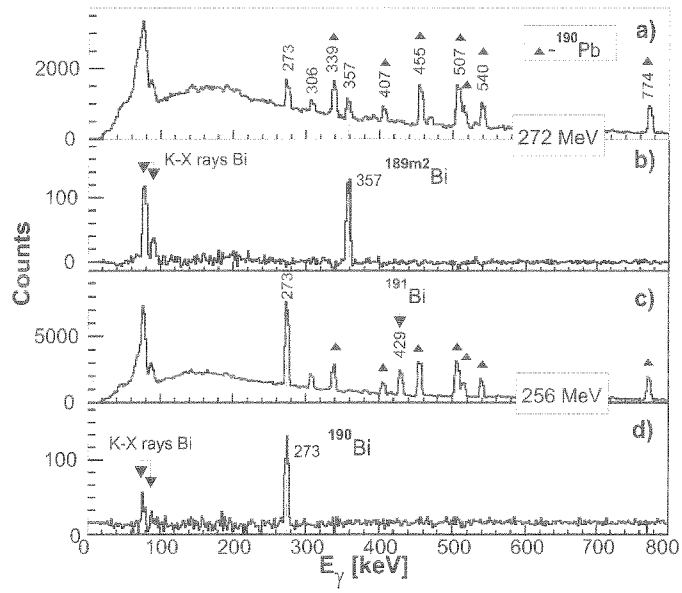

Figure 1. a) Recoil-γ coincidence spectra (time interval ΔT(EVR-γ) < 5 μs and b) background-subtracted recoil-γ-α(6672 keV) spectra for ^{189}Bi collected at the beam energy of 272.0(5) MeV; c) and d) the same as a) and b), but for ^{190}Bi, collected at the beam energy of 256.0(5) MeV. Known γ-decays of the microsecond isomeric states in ^{190}Pb [4] are marked by filled triangles.

References

[1] A.N. Andreyev et al., Eur. Phys. J. A6, 381 (1999).
[2] A.N. Andreyev et al., submitted to Eur. Phys. J. A, (2001).
[3] P. Nieminen et al., Proc. XXXV Zakopane School of Physics, Zakopane, Poland, Sep. 5-13, 2000. To be published in Acta Physica Polonica B (2001).
[4] G.D. Dracoulis, A.P. et al. Phys. Lett. B432, 37 (1998).

Direct observation of bound beta decay of bare ^{206,207}Tl at FRS-ESR

T. Ohtsubo[1,2], F. Bosch[1], H. Geissel[1,3], C. Scheidenberger[1], F. Attallah[1], K. Beckert[1], P. Beller[1], T. Faestermann[4], B. Franzke[1], M. Hausmann[1], M. Hellström[1], P. Kienle[4], O. Klepper[1], C. Kozhuharov[1], Yu. Litvinov[1,5], L. Maier[4], G. Münzenberg[1], F. Nolden[1], Yu. Novikov[5], T. Radon[1], V. Shishkin[1], J. Stadlmann[3], M. Steck[1], T. Stöhlker[1], K. Sümmerer[1], H. Weick[1], M. Winkler[3]

[1] *GSI Darmstadt,* [2] *Niigata University,* [3] *JLU Gießen,* [4] *TU München,* [5] *St. Petersburg NPI*

Bound beta decay (β_b decay), the time-mirrored orbital electron capture, is a special form of β^- decay, where the electron becomes bound in an inner atomic shell (predominantly the 1s-shell) of the daughter atom. For neutral atoms the capture of an electron into an unoccupied shell has a small probabiliy because of the small overlap of the wavefunction with the nucleus. Therefore, β_b decay remains there a spurious effect only. However, when atoms get highly ionized, as, e. g., in a stellar plasma, β_b decay can become a significant decay branch. Then β^- lifetimes may alter by many orders of magnitude with respect to those of the corresponding neutral atoms, as has been proven by several experiments performed at the ESR over the last years [1,2]. The exploration of β_b decay is important for a comprehensive understanding of the creation of matter in hot stellar plasmas.

An experiment was carried out at the FRS-ESR facilities, where the β_b decay of ^{206}Tl and ^{207}Tl was *directly* observed for the first time. The mass difference between mother- and β_b daughter-atom amounts in either case to about 1.6 MeV, and the β_b decay-branch to 10-20%[3]. The ^{206}Tl and ^{207}Tl-atoms were produced by fragmentation of a ^{208}Pb primary beam in a Be target at the FRS and separated using the Bρ-ΔE-Bρ method. This technique ensured that bare Tl ions, but no hydrogen-like Pb ions were injected into the ESR. In the ESR, the ions were stored, electron-cooled, and detected via time-resolved Schottky spectroscopy. The beam noise, which is induced in pick-up electrodes, is recorded and frequency-analyzed. At the revolution frequency of each stored ion species the frequency spectrum shows lines with an area being proportional to the ion number.

Figure 1 presents the first direct observation of β_b decay. It shows time-resolved frequency spectra of the Schottky lines of stored and cooled bare $^{207}Tl^{81+}$ ions, together with their β_b-daughters $^{207}Pb^{81+}$. The mass resolving power $m/\Delta m$ exceeds $7*10^5$, which is by far sufficient to resolve both peaks clearly. The spectra have been determined from summing-up one hundred subsequent, 64.8 milliseconds lasting measurements and covered an observation time of up to 40 minutes after injection.

Figure 2 shows the number of ions in both peaks as a function of observation time. The initial number of bare ^{207}Tl ions in the ESR was about 2000. After the cooling phase of approximately 100 seconds the intensity of the $^{207}Tl^{81+}$ mother nuclei decreases exponentially due to beta decay to the continuum ($^{207}Pb^{82+}$, not shown here), β_b decay to $^{207}Pb^{81+}$, and due to charge-changing processes in the residual gas and in the electron cooler of the ESR. These unavoidable 'storage ring losses' also lead, finally, to a slow decrease of the stable $^{207}Pb^{81+}$ ions, whose intensity increases at the beginning due to the feeding from the decaying $^{207}Tl^{81+}$.

From those spectra, together with the measured β^- decay to the continuum (β_c), a wealth of unique information will result: total and partial β_b lifetimes, the β_b Q-value and, moreover, the ratio of bound- and continuum electron wave function, which yields the 'Fermi function'. For β^- decay, the latter has never before been probed by experiments (in contrast to β^+- and orbital electron-capture decay).

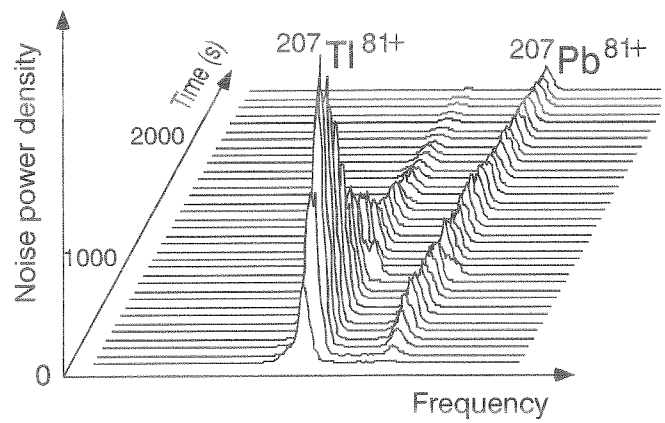

Figure 1: Time-resolved frequency spectra of bare $^{207}Tl^{81+}$ mother and hydrogen-like $^{207}Pb^{81+}$ β_b-daughter ions. The noise-power is a direct measure for the number of ions.

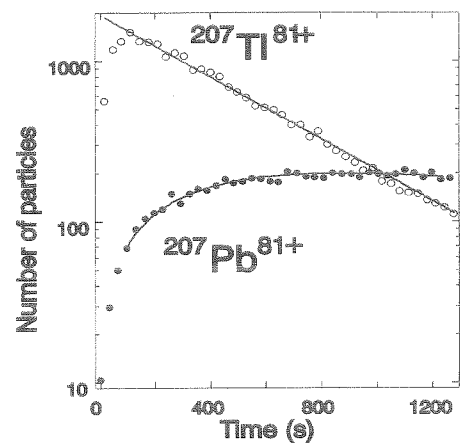

Figure 2: Number of mother ($^{207}Tl^{81+}$) and β_b-daughter ions ($^{207}Pb^{81+}$) as a function of time after injection. The first 100 seconds are needed for electron cooling of the hot fragment beams (first three data points, which have been excluded from the fit). Each data point is obtained from 32.4 seconds of observation time.

References

[1] M. Jung et al., Phys. Rev. Lett. 69, 2164 (1992).

[2] F. Bosch et al., Phys. Rev. Lett. 77, 5190 (1996).

[3] K. Takahashi et al., At. Data Nucl. Data Tables 36, 375 (1987).

Mass Measurements of Stored Exotic Nuclei

Yu.A. Litvinov[1,2], J. Stadlman[3], F. Attallah[1], K. Beckert[1], F. Bosch[1], M. Falch[4], B. Franczak[1], B. Franzke[1], H. Geissel[1,3], M. Hausmann[1], Th. Kerscher[4], O. Klepper[1], H.-J. Kluge[1], C. Kozhuharov[1], K.E.G. Löbner[4], G. Münzenberg[1], N. Nankov[1,3], F. Nolden[1], Yu.N. Novikov[2,5], Z. Patyk[1], T. Radon[1], H. Schatz[1], C. Scheidenberger[1], M. Steck[1], Z. Sun[1], H. Weick[1], H. Wollnik[3]

[1] GSI, Darmstadt, Germany, [2] State University, St. Petersburg, Russia,
[3] JLU, Giessen, Germany, [4] LMU, München, Germany, [5] PNPI, St. Petersburg, Russia

Exotic nuclei are produced via projectile fragmentation of different primary beams in beryllium targets placed at the entrance of the Fragment Separator (FRS). The fragments are spatially separated by the FRS, injected and stored in the Experimental Storage Ring (ESR) for direct mass measurements. Two complementary methods have been applied:

1 Schottky Mass Spectrometry (SMS)

Masses of more than 100 neutron-deficient heavy nuclides in the lead region were directly measured for the first time with a precision of roughly 100 keV in our first run with ^{209}Bi projectiles [1]. The combination of these measurements with experimental Q_α values allowed the determination of more than 60 new masses in addition [2]. The measured masses in this experiment cover a large area of proton-rich heavy nuclei up to the proton dripline.

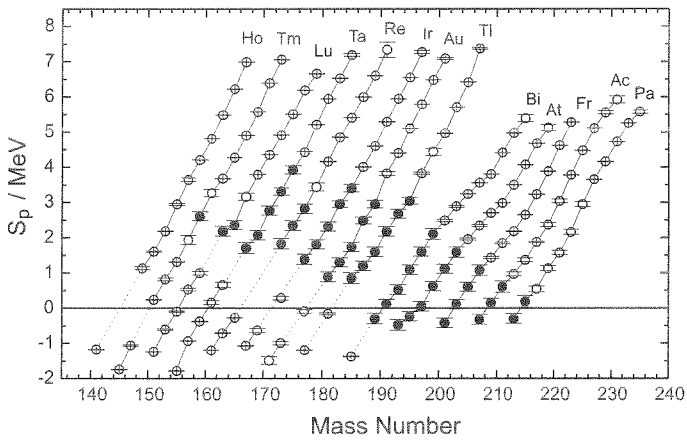

Figure 1: One-proton separation energies for odd-Z and odd-A nuclides. The full circles represent masses determined in this experiment [2].

Fig. 1 shows the one-proton separation energies for odd-Z and odd-A isotopes in the measured region. These data allowed to determine the experimental one-proton dripline for elements from bismuth to protactinium. For even-Z elements from tungsten to radium our data allow to predict reliably the two-proton dripline.
The single particle gap G_p is defined as $2G_p \equiv S_{2p}(Z,N) - S_{2p}(Z+2,N)$, where S_{2p} is the correspondig two-proton separation energy. The G_p values for the Z=82 shell region are shown in Fig. 2. Moving away from the doubly magic ^{208}Pb nucleus towards the proton dripline the shell gap is drastically reduced, which has not been observed for other

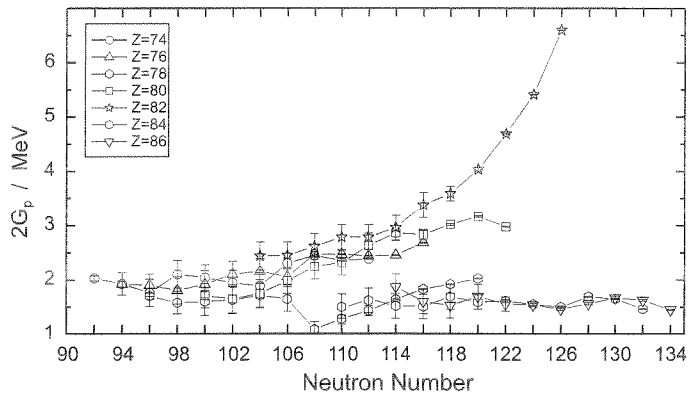

Figure 2: Experimental shell gaps G_p for different elements (see insert) in the vicinity of the Z=82 shell [2].

magic numbers. This can be explained, for example, by nuclear shape changes along the isotopic chains.
Our second experiment with ^{209}Bi projectiles contained several improvements. The better cooler performance, stabilization of power supplies and a new data aquisition system [3] increased the resolving power by a factor of two to $m/\Delta m \approx 700000$. This allows to resolve peaks with close mass-to-charge ratios as demonstrated in Fig. 3 for

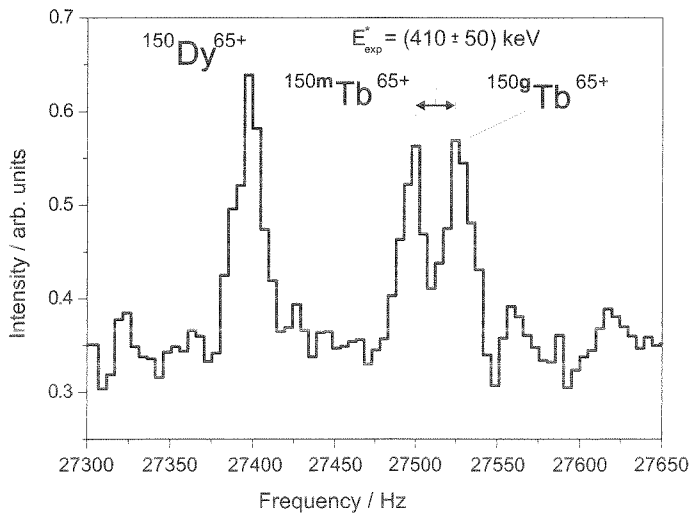

Figure 3: Schottky spectrum representing the ground state of ^{150}Dy^{65+} ions and bare ^{150}Tb^{65+} ions in the ground and isomeric state respectively. Note that the peaks of the ground and the isomeric state of ^{150}Tb correspond to only one particle each.

the frequency peaks of the ground and isomeric states of ^{150}Tb. The excitation energy deduced from our mass measurements is in good agreement with the literature [4]. The measured mass surface of the recent experiment covers our previous measurement and adds roughly 50 new proton-rich unknown masses. Although the data analysis is still in progress we can expect a precision of the mass values of about 50 keV. Schottky Mass Spectrometry was successfully applied to nuclides with half-lives longer than 10 sec, which is needed for cooling and spectrum recording.

2 Isochronous Time of Flight Mass Spectrometry (IMS)

To extend the study to shorter half-lives the ESR was operated in an isochronous mode where the inherent velocity spread of the hot fragments is compensated by different orbit lengths [5], i.e., the revolution time is independent on the velocity spread. Therefore, precise mass measurements can be performed without beam cooling. A time-of-flight detector was used to measure the revolution times of the stored fragments within a few hundred turns in the ESR (approx. 500 ns/turn). The stored ions penetrate a thin carbon foil (17 μg/cm^2) covered with CsJ [6] (approx. 10 μg/cm^2) on each side and release secondary electrons at each turn. These electrons are detected by micro channel plates (MCPs) and the signals are recorded by a digital sampling oscilloscope. The time differences between different occurences of a particle were used to deduce its revolution time. Spectra of the revolution times were generated using the data from several injections with an identical setting. The example of such a spectrum in Fig. 4 shows only a part of the m/q - acceptance of about $\pm$ 7.5%. The mass values of ^{70,71}Se therein were unknown according to ref. [4] and the uncertainities given for ^{68}As and ^{73}Br were large. Therefore, we measured masses for these nuclides.

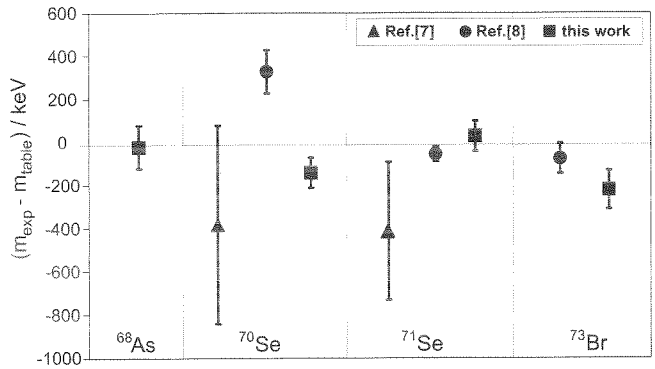

Figure 5: Comparison of mass values obtained from the isochronous TOF-measurements and other experiments [7, 8] with the table values of ref. [4]. Uncertainties of the table values are not included.

Fig. 5 shows the comparison of our results and recent measurements of ref. [7, 8] with the table values of ref. [4].

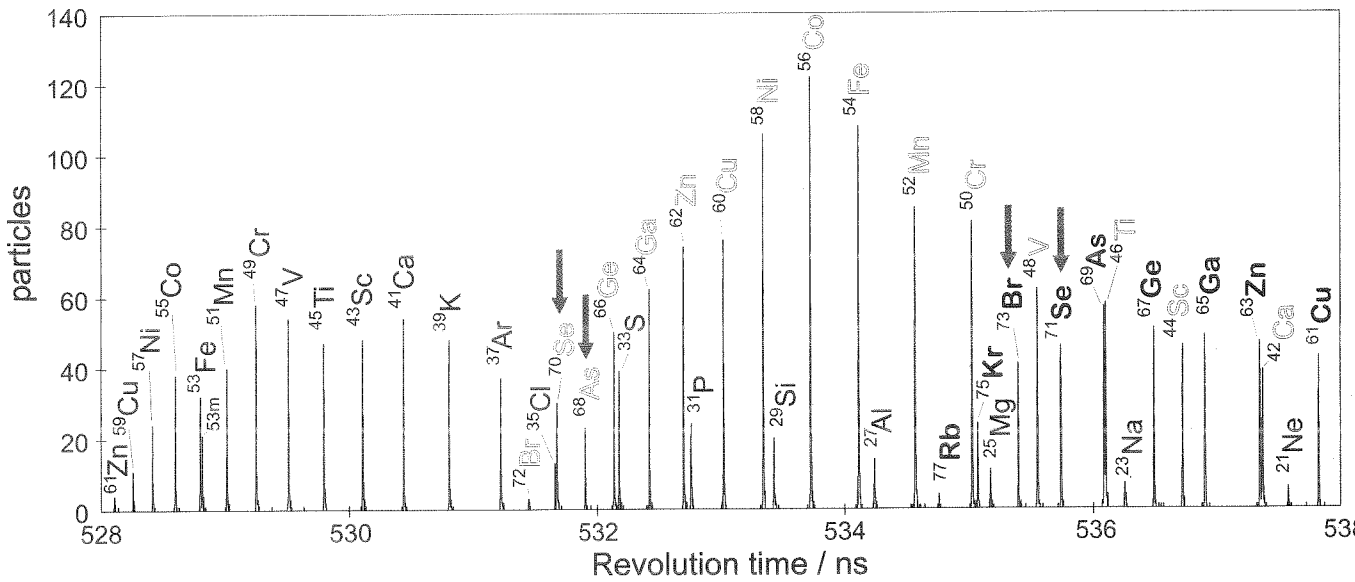

Figure 4: Revolution time spectrum of uncooled projectile fragments from a ^{84}Kr beam with an incident energy of 445.3 $A\cdot$ MeV. Groups of ions with the same isospin are marked with the same font. The arrows indicate those species which are shown in Fig. 5.

A mass resolving power of $m/\Delta m$ = 110000 and a precision of δm $\approx$ 100 keV have been obtained. IMS is especially suited for direct mass measurements of nuclides with short half-lifes down to a few 10 μs.

References

[1] T. Radon *et al.*, Nucl. Phys. **A 677** (2000) 75
[2] Yu. N. Novikov *et al.*, submitted to Nucl. Phys. A
[3] M. Falch, Thesis, LMU München (2000)
[4] G. Audi *et al.*, Nucl. Phys. **A624** (1997) 1
[5] M. Hausmann *et al.*, NIM **A446** (2000) 569
[6] W. Thalheimer *et al.*, Cryst. Res. Technol. Vol.**34** **2** (1999) 175
[7] M. Chartier *et al.*, Nucl. Phys. **A 637** (1998) 3
[8] D. Brenner, Proc. of APAC2000 to be published in Hyperfine Interaction

Fine structure in the α - decay of radium isotopes $^{212\text{-}209}$Ra

F.P. Heßberger, S. Hofmann, D. Ackermann[1]

GSI, Darmstadt, Germany, [1] also Johannes Gutenberg - Universität, Mainz, Germany

Although Ra - isotopes with mass numbers 207≤ A ≤212 had been synthesized first by Valli et al. more than thirty years ago [1] little knowledge on their decay properties has been added since then. The successful application of α-γ-coincidence measurements to detect α-decay branches with low intensity in ^{214}Ra and $^{214\text{-}216}$Ac [2] motivated us also to investigate Ra-isotopes with A ≤212. We therefore chose the reaction ^{204}Pb(^{12}C,xn)$^{216\text{-}x}$Ra at incident beam energies of E_{lab}= (78-137) MeV. New decay data were obtained for ^{212,211,210,209}Ra. The results are listed in table 1.

For the even - even nuclei ^{212}Ra and ^{210}Ra we observed α-decay into the first excited 2^+ - levels of the daughter nuclides. Our γ - energies of E_γ = (635.1 ± 0.2) keV for ^{212}Ra and E_γ = (574.9 ± 0.2) keV for ^{210}Ra fit well to the excitation energies of the first 2^+ - levels of ^{208}Rn (635.8 keV) and ^{206}Rn (575.3 keV) reported in literature [3].

Two weak γ - lines of E_γ = (387.0 ± 0.5) keV and E_γ = (633.7 ± 1.1) keV were attributed to the decay of ^{209}Ra. Unlike the case of the N=119 isotone ^{207}Rn, whose α-decay populates low lying states at E^* = 62.54 keV and E^* = 133 keV with relative intensities of 0.007 and 0.001, respectively, we did not observe α-γ - coincidences with E_γ < 200 keV that could be attributed to the decay of ^{209}Ra.

Altogether, six γ - lines were assigned to the decay of ^{211}Ra. While five of them fulfilled the relation $Q_\alpha + E_\gamma \approx Q_\alpha$ (gs), where Q_α and Q_α(gs) denote the Q-values for the observed transition and the ground - state transition, respectively, the 162.9 keV line delivered a considerably lower Q - value. It is, therefore, interpreted to be the transition between the E^* = 283.0 keV and E^* = 120.0 keV - levels, since it perfectly fits to the energy difference. The energy of coincident α-particles, however, is shifted by ≈20 keV as compared to α-particles coincident with E_γ = 283.0 keV. This we attribute to energy summing with conversion electrons from the transition 120 keV → 0 keV (g.s.). From the intensities of the 120 keV - line and the K_α - and K_β -lines of Rn we obtained a conversion coefficient of α = 4.5 ± 0.5 which agrees best with the value α = 6.5 expected for an M1 - transition [4]. Taking $5/2^-$ as the ground state configuration of ^{207}Rn [3], we obtain $3/2^-$ as spin and parity for the 120 keV - level. Due to the high background of x-rays from the decay by internal conversion of the 110 keV - level in ^{213}Ra, which are coincident to α - particles with energies very similar to that of α - particles coincident with the 283 keV - level in ^{211}Ra, we were not able to determine the conversion coefficient and to make a spin and parity assignment.

In the lighter N = 117 isotones ^{203}Pb and ^{205}Po two low lying levels with spins and parities $1/2^-$ and $3/2^-$ are known. While $3/2^-$ was assigned to the 120 keV level in our experiment, we did not observe a γ - line that could be attributed to the decay of a $1/2^-$ level. It should be remarked, that in our experiment we observed γ -decays from the $3/2^-$ (142.7 ± 0.5 keV) - as well as from the $1/2^-$ - level (154.5±0.5 keV) in ^{205}Po, both being populated by (^{213}Ra – α →) ^{209}Rn – α → ^{205}Po.

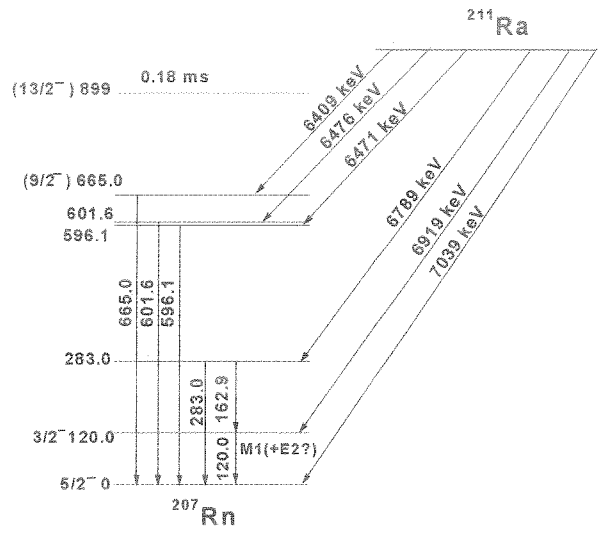

Fig. 1: Experimental decay scheme of ^{211}Ra; the energies denote the Q_α - values

Table 1: Results of α-γ - coincidence measurements for radium isotopes.

Isotope	E_α / keV	E_γ / keV
^{212}Ra	6902 ± 5	(gs)
	6269 ± 5	635.1 ± 0.2
^{211}Ra	6907 ± 5	(gs)
	6788 ± 5	120.0 ± 0.2
	(6648 ± 5)	162.9 ± 0.2
	6627 ± 5	283.0 ± 0.2
	6320 ± 10	596.1 ± 0.4
	6315 ± 10	601.6 ± 0.4
	6255 ± 5	665.0 ± 0.2
^{210}Ra	7003 ± 10	(gs)
	6447 ± 5	574.9 ± 0.2
^{209}Ra	7003 ± 10	(gs)
	6625 ± 5	387.0 ± 0.6
	6376 ± 10	633.7 ± 1.1

References:

[1] K. Valli et al. Phys. Rev 161, 1284 (1968)
[2] F.P. Heßberger et al. EPJ A 8, 521 (2000)
[3] R. Firestone et al (eds.) Table of Isotopes, 1996
[4] R.S. Hager, E.C. Seltzer Nucl. Data A4 (1968)

Fine structure in the α - decay of ^{213,214}Ac

F.P. Heßberger, S. Hofmann, D. Ackermann[1]
GSI, Darmstadt, Germany, [1] also Johannes Gutenberg - Universität, Mainz, Germany

The isotopes ^{213}Ac and ^{214}Ac were first identified in 1968 by Valli et al. [1], who reported $T_{1/2}$ = 0.8±0.2 s and E_α = (7362 ±8) keV for ^{213}Ac, and $T_{1/2}$ = (8.2±0.2) s and three α-lines of E_α = 7212±5 keV (i_{rel} = 0.52±0.02), 7080 ±5 keV (i_{rel} = 0.44 ± 0.02), and 7000±15 keV (i_{rel} = 0.04±0.01) for ^{214}Ac. In a recent experiment [2] new results on the decay of ^{214}Ac were obtained by means of α-γ- coincidence measurements, but due to low count rates some of the assignments had to be regarded as tentative. To study its decay in more detail and also to search for fine structure in the α-decay of ^{213}Ac we produced them by the reaction ^{209}Bi(^{12}C, xn)^{213,214}Ac (x=8,7). The nuclides were separated from the projectile beam in-flight by SHIP and implanted into a 16-strip-Si-detector, where their α-decay was measured in coincidence with γ-rays registered with a high purity Ge-detector mounted closely behind the Si- detector.

Two γ - lines of E_γ = (341.6 ± 0.4) keV and E_γ = (608.8 ± 0.5) keV were assigned to the decay of ^{213}Ac; the energies of the coincident α-particles are (7022±10) keV and (6767±10) keV.

The result for ^{214}Ac was more complex; besides coincidences characterized by $E_\gamma + Q_\alpha = Q_\alpha(gs) \pm 10$ keV (Q_α , $Q_\alpha(gs)$ are the Q-values of the observed and of the ground-state (gs) transition, resp.) and $\Delta E_\alpha(FWHM) < 30$ keV, we also observed those having $E_\gamma + Q_\alpha < Q_\alpha(gs)$ and/or $\Delta E_\alpha(FWHM) > 30$ keV. The first group is assigned to γ-dcays into the gs or low lying levels. (Summing with conversion electrons (CE) from those states will shift the α-energy close to the value of the gs transition, while the line width is not effected significantly, as shown for ^{212}Fr α-γ decays into the 23.5 keV - level in ^{208}At, followed by L - conversion to the gs.)

The second group is interpreted as transitions between excited states. A preliminary decay scheme based on these results is shown in fig 1. The tentative assignment of the γ-lines reported in [2] was confirmed and some weaker transitions, not indicated so far, were observed. However, these results led to new questions: especially the assignment of two strong γ-transitions E_γ = 224.8 keV and E_γ = 162.5 keV still causes some problems. Since ΔE = (363.8-139.0) keV = 224.8 keV the first line may be attributed to the transition between these two levels, which is supported by the energy distribution of the coincident α-particles. About 62% have a mean energy E_α = 6868 keV (i.e. close to that coincident to E_γ = 363.8 keV) and 18% E_α = 6909 keV, which can be understood as due to summing with K - CE from decay of the 139.0 keV - level. Yet, 20% have E_α = 6989 keV. The intensity is too high for summing with L - CE since for an M1 - transition at ΔE = 139 keV, i(K)/i(L) ≈ 2.4 is expected. We thus tentatively assume a level at E = 224.8 keV, having accidentially (within our experimental accuracy) the same energy as the 363.8 keV → 139.0 keV - transition. This assumption is corrobated by the 162.5 keV - line, which is close to ΔE = (224.8-62.6) keV. The energy distribution of the α -particles coincident to this line does not support a transition to the ground state, but is very similar to that of those coincident to the E = 146.5 keV - line, which is interpreted as the transition 209.3 keV → 62.6 keV.

References:

[1] K. Valli et al. Phys. Rev. 167, 1094 (1968)
[2] F.P.Heßberger et al. EPJ A 8, 521 (2000)

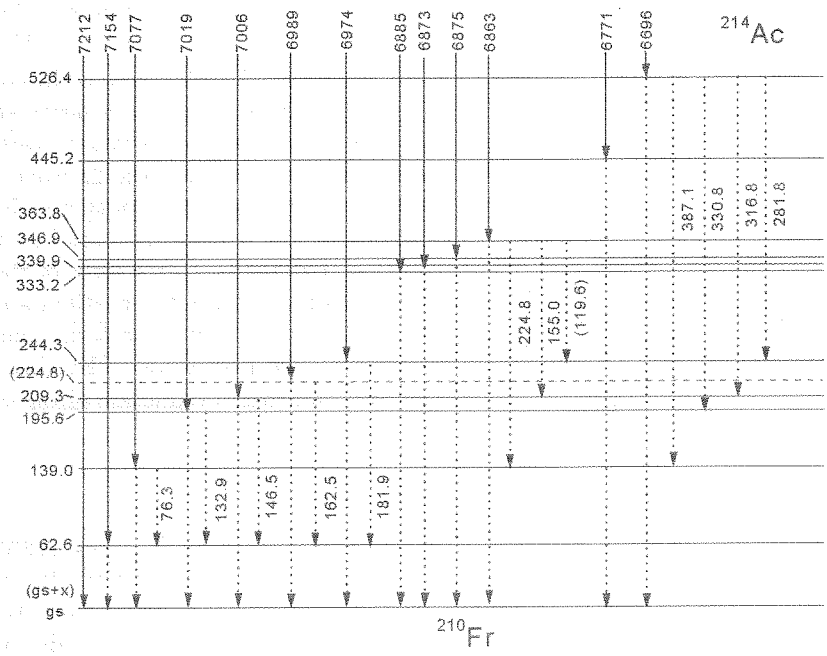

Fig. 1: Decay scheme suggested for ^{214}Ac; full lines: α-decay; dashed lines: observed γ-decays (energies for gs transitions are omitted)

Deeply Bound $1s$ and $2p$ Pionic States and the s-Wave Part of the Pion-Nucleus Interaction

H. Geissel[1], H. Gilg[2], A. Gillitzer[3], R. S. Hayano[4], S. Hirenzaki[5], K. Itahashi[6], M. Iwasaki[6], P. Kienle[2], M. Münch[2], G. Münzenberg[1], K. Suzuki[4], W. Schott[2], D. Tomono[6], H. Weick[1], T. Yoneyama[6], T. Yamazaki[7]

[1]GSI Darmstadt, [2]Technische Universität München, [3]Forschungszentrum Jülich, [4]University of Tokyo, [5]Nara Women's University, [6]Tokyo Institute of Technology, [7]RIKEN

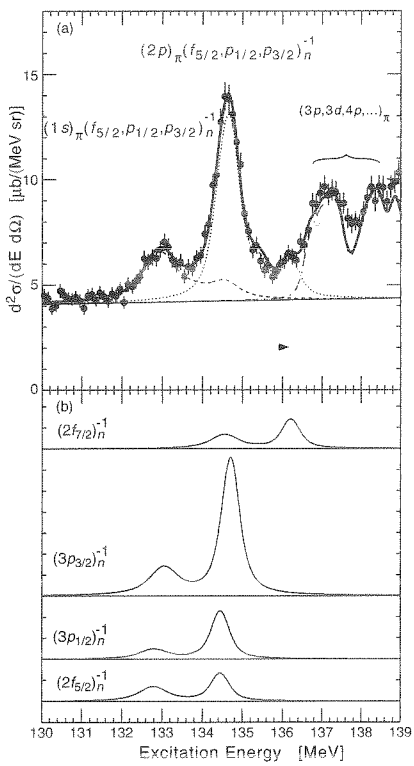

Figure 1: Measured excitation energy spectrum for the ^{206}Pb(d,^{3}He) reaction (T_d = 600 MeV) in the region of the bound pionic states. In a fit (fitting region indicated by the arrow) $(1s)_\pi$ and $(2p)_\pi$ peak are decomposed into the contributing neutron hole configurations of which the most important are $2f_{5/2}$, $3p_{1/2}$ and $3p_{3/2}$.

After the discovery of the deeply bound $(1s)_\pi$ and $(2p)_\pi$ states in ^{207}Pb in the ^{208}Pb(d,^{3}He) reaction [1] and the determination of the real and imaginary s-wave-potential parameters b_0 and ImB_0 from the $(2p)_\pi$ binding energy and width [2, 3], a new experiment on the ^{206}Pb(d,^{3}He) reaction was performed at the Fragment Separator (FRS). The better suited neutron shell structure of ^{206}Pb compared to ^{208}Pb and an improved energy resolution allowed for a clear separation of the $(1s)_\pi$ component from the dominant $(2p)_\pi$ peak in the excitation spectrum [4], which was not achieved in the ^{208}Pb(d,^{3}He) experiment. Accordingly the binding energy and width of the $(2p)_\pi$ state (B_{2p}, Γ_{2p}) and especially of the $(1s)_\pi$ state (B_{1s}, Γ_{1s}) can be determined with significantly higher precision.

Decomposing the excitation energy spectrum into $(1s)_\pi$ and $(2p)_\pi$ components coupled to different neutron hole contributions (Figure 1) the values B_{1s} = 6.768 ± 0.044 (stat.) ± 0.041 (syst.) MeV, $\Gamma_{1s} = 0.778^{+150}_{-130}$ (stat.) ± 0.055 (syst.) MeV, B_{2p} = 5.110 ± 0.015 (stat.) ± 0.042 (syst.) MeV and Γ_{2p} = 0.371 ± 0.037 (stat.) ± 0.048 (syst.) MeV were obtained.

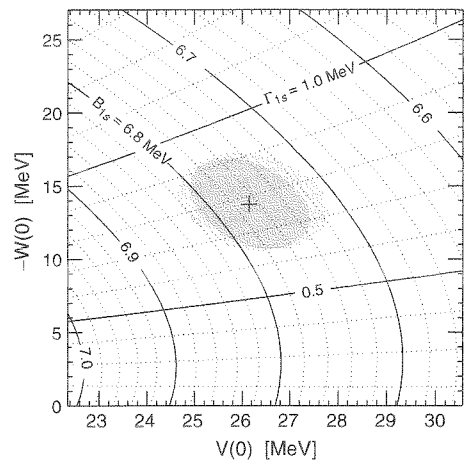

Figure 2: Binding energy and width of the $(1s)_\pi$ state in ^{205}Pb related to the real ($V(0)$) and imaginary ($W(0)$) part of the s - wave potential in the center of the nucleus. The p - wave potential is taken from a parameter set given by Seki and Masutani [5]

These quantities were used to determine the pion-nucleus s - wave optical potential. The most precise values for the real and imaginary part ($V(0) = 26.1^{+1.7}_{-1.5}$ MeV, $W(0) = -13.8^{+3.4}_{-3.5}$ MeV) were deduced from B_{1s} and Γ_{1s} (Figure 2). The $1s$ state has a larger sensitivity, since the pionic $1s$ wave function has larger overlap with the nuclear density distribution than the $2p$ wave function, and since the $1s$ binding energy and width are almost exclusively determined by the s -wave potential parameters. With the assertion that the isovector term of the π^--nucleus interaction $b_1^\star$ is modified in the medium and that the isoscalar part is induced by double scattering mainly, one can derive from $V(0)$ = 26.1 MeV for ^{205}Pb that $b_1^\star \simeq -0.125 m_\pi^{-1}$. This also indicates a reduction of the quark condensate to 72%.

References

[1] T. Yamazaki *et al.*, Z. Phys. **A355** (1996) 219, H. Gilg *et al.*, GSI Scientific Report 1996, p. 40
[2] T. Yamazaki *et al.*, Phys. Lett. B **418** (1998) 246
[3] H. Gilg *et al.*, Phys. Rev. C **62**, 025201 (2000) K. Itahashi *et al.*, Phys. Rev. C **62**, 025202 (2000)
[4] H. Geissel *et al.*, GSI Scientific Report 1999, p. 31
[5] R. Seki, K. Masutani, Phys. Rev. C **27** (1983) 2799

Excitation and Fragment-Neutron Correlations of Halo Nuclei [B,G]

D. Aleksandrov[1], T. Aumann[2], L. Axelsson[3], T. Baumann[2], M.J.G. Borge[4], D. Cortina-Gil[2], L.V. Chulkov[1,2], W. Dostal[5], B. Eberlein[5,2], Th.W. Elze[6], H. Emling[2], C. Forssén[3], H. Geissel[2], A. Grünschloß[6], M. Hellström[2], B. Jonson[3], J.V. Kratz[5], R. Kulessa[7], Y. Leifels[2], A. Leistenschneider[6], K. Markenroth[3], M. Meister[3,8], I. Mukha[1,8], G. Münzenberg[2], T. Nilsson[3], G. Nyman[3], M. Pfützner[2], A. Richter[8], K. Riisager[9], C. Scheidenberger[2], G. Schrieder[8], H. Simon[8], O. Tengblad[4], M.V. Zhukov[3]

[1]Kurchatov Institute, Moscow, [2]GSI Darmstadt, [3]CTH Göteborg, [4]CSIC Madrid, [5]Univ. Mainz, [6]Univ. Frankfurt, [7]Univ. Kraków, [8]TU Darmstadt, [9]Univ. Aarhus,

Dissociation of ^{8}He and ^{14}Be in carbon and lead targets has been studied in kinematically complete experiments. The data allow to deduce invariant mass spectra, angular distributions in the one neutron knock-out channel as well as inelastic scattering in the 2n decay channels.

The invariant mass spectrum in the inelastic channel ^{6}He+n+n shows a broad distribution extending up to about 3.5 MeV. This may be interpreted either (i) as a single broad 1^- resonance or (ii) as a relatively narrow 2^+ state and a broad peak from higher excited 1^- state.

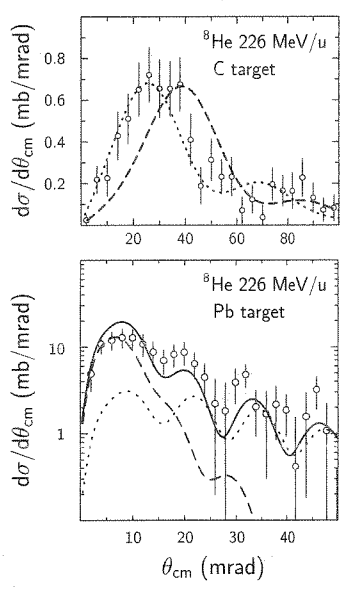

Figure 1: Differential cross section for inelastic scattering of ^{8}He on two different targets. C target (top): experimental data are compared with DWBA calculations for dipole (dotted line) and quadrupole (dashed line) excitations. Pb target (bottom): the contribution from the electromagnetic dissociation is shown as dashed line while the nuclear diffractive dissociation is displayed as dotted lines. The calculations where performed in eikonal DWBA and result in the solid line as sum of the two processes.

The dominance of dipole transitions can be seen in Figure 1 (top) where the experimental angular distribution for ^{8}He inelastic scattering on a carbon target [1] is shown in comparison with DWBA calculations. The differential cross section obtained for ^{8}He inelastic scattering from a lead target shown in Fig. 1 (bottom) exhibits Coulomb-nuclear interferences, thus confirming the $J^\pi = 1^-$ assignment to a broad peak in the ^{8}He invariant-mass spectrum.

Table 1 presents partial cross sections for the ^{8}He fragmentation on carbon and lead targets. In both cases, neutron knock-out is the dominating reaction channel. It becomes comparable in magnitude with the inelastic scattering in case of the ^{208}Pb target. For the carbon target, the difference of the ^{8}He and ^{4}He interaction cross sections exceeds the sum $\sigma_{in} + \sigma_{-1n} + \sigma_{-2n}$ in ^{8}He by about 100 mb. This excess is due to the breakup into α+4n and is likely a sign of the five-body character of ^{8}He.

For the lead target, the difference of the ^{8}He and ^{4}He interaction cross sections is smaller than the sum $\sigma_{in} + \sigma_{-1n} + \sigma_{-2n}$. The Coulomb dissociation cross section can be calculated from this difference by taking into account the missing contribution of about 250 mb from the breakup into α+4n. An independent method based on DWBA calculations and a normalisation to the experimental angular distribution at forward angles gave the same result. The contribution of electromagnetic dissociation is then 160 mb which leads to a B(E1) value equal to 0.46 e^2fm^2 below 7 MeV excitation energy.

Table 1: Extracted contributions of nuclear (N) and electromagnetic (C) processes to the fragmentation cross sections of ^{8}He on lead and on carbon targets. Here σ_{in} denotes cross sections for inelastic scattering, whereas σ_{-1n} corresponds to one-neutron knock-out.

Target	σ^N_{in} (mb)	σ^C_{in} (mb)	σ^N_{-1n} (mb)	σ^C_{-1n} (mb)
Lead	80 ± 12	160 ± 25	322 ± 37	6 ± 97
Carbon	32 ± 5		129 ± 15	

The structure of the unbound ^{13}Be is currently poorly understood. The ^{12}Be-n relative energy spectrum shown in Figure 2 and obtained in a one-neutron knockout reaction of ^{14}Be on a carbon target, reveals interesting structures. The angular distributions analysed as explained in [2], but gated on different bins in the relative energy spectrum show isotropy (bottom,left) and asymmetry (bottom,right) as expected for adopted s- and p- wave resonances at about 250 keV and 1.2 MeV, respectively.

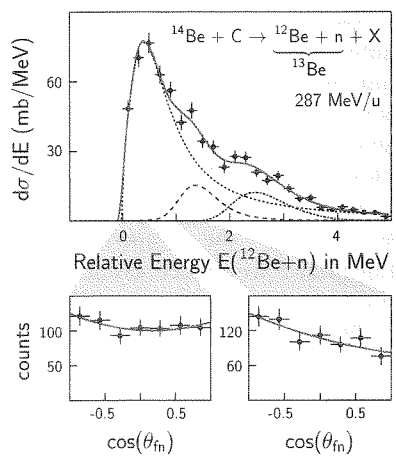

Figure 2: (Top) The relative energy spectrum between ^{12}Be fragments and neutrons. The solid line represents a fit to the data taking s (dotted), p (dashed) and d (dashed dotted) contributions into account. (Bottom) angular distributions gated on the relative energy as indicated by the shaded areas. The solid lines are fits with 2nd order polynomials to guide the eye.

The asymmetric distribution stems hereby from the interference of two overlapping states with different parity. As the groundstate shows the typical behaviour of an s-intruder state, the interfering first excited state should be a p-state. This allows a tentative assignment of $(1s_{1/2})$, $(0p_{1/2})$ and $(0d_{5/2})$ for the groundstate and the first two excited states of ^{13}Be.

References

[1] K. Markenroth et al., Nucl. Phys. **A679** (2001) 462
[2] H. Simon et al., Phys. Rev. Lett. **83** (1999) 469

Nuclear Matter Distributions of Neutron-Rich Li-Isotopes from Elastic Proton Scattering in Inverse Kinematics

A.V. Dobrovolsky[1,2], G.D. Alkhazov[2], M.N. Andronenko[2], A. Bauchet[1], P. Egelhof[1], S. Fritz[1], G.E. Gavrilov[2], H. Geissel[1], C. Gross[1], A.V. Khanzadeev[2], G.A. Korolev[2], G. Kraus[1], A.A. Lobodenko[2], G. Münzenberg[1], M. Mutterer[3], S.R. Neumaier[1], T. Schäfer[1], C. Scheidenberger[1], D.M. Seliverstov[2], T. Suzuki[1], N.A. Timofeev[2], A.A. Vorobyov[2] and V.I. Yatsoura[2]

[1] GSI Darmstadt, [2] PNPI Gatchina, [3] TU Darmstadt

The method of proton elastic scattering at intermediate energies, which was already proven for the neutron-rich helium isotopes ^{6,8}He [1],[2] to be well suited for obtaining accurate and detailed information on nuclear matter distributions of halo nuclei, was recently applied for the investigation of the lithium isotopes ^{6,8,9,11}Li. Absolute differential cross sections $d\sigma/dt$ for small-angle Li-p elastic scattering were determined by an inverse-kinematics measurement using secondary Li-beams with E ≈ 0.7 GeV/u from the SIS-FRS, and gaseous hydrogen as the proton target. The hydrogen filled ionization chamber IKAR served simultaneously as target and detector for recoil protons. Projectile scattering angles were measured precisely with multi-wire tracking detectors. Furthermore, a magnetic-rigidity analysis of the scattered particles was performed with the aid of the ALADIN magnet and a position sensitive scintillator wall behind for the separation of neutron break-up channels. For this purpose the entire experimental setup was installed at the Cave B.

The data analysis has fairly progressed within the year 2000. The (still preliminary) differential cross sections $d\sigma/dt$ for p^{9,11}Li scattering are displayed in Fig. 1 together with the cross section for p^{6}Li scattering, the results of which were discussed already in the previous GSI annual report 1999.

For establishing the nuclear density distributions from the measured cross sections, the Glauber multiple scattering theory was applied. Calculations were performed using the basic Glauber formalism for proton-nucleus elastic scattering, and taking experimental data on the elementary proton-proton and proton-neutron scattering amplitudes as input. In the present analysis two different parametrizations for modelling the nuclear density distribution were used for the Glauber calculations, and the parameters were varied in order to obtain a best fit to the experimental cross sections. Both parametrizations applied assume the nuclei involved to consist of a core and two valence neutrons. A Gaussian distribution for the core, and either a Gaussian (GG) or a 1p-shell harmonic

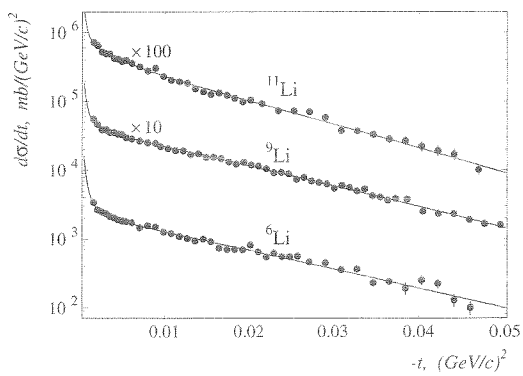

Figure 1. Absolute differential cross sections $d\sigma/dt$ versus the four momentum transfer squared t for p^{6,9,11}Li elastic scattering obtained from the present experiment. Full lines are the result of fits to the data performed on the basis of the Glauber multiple scattering theory.

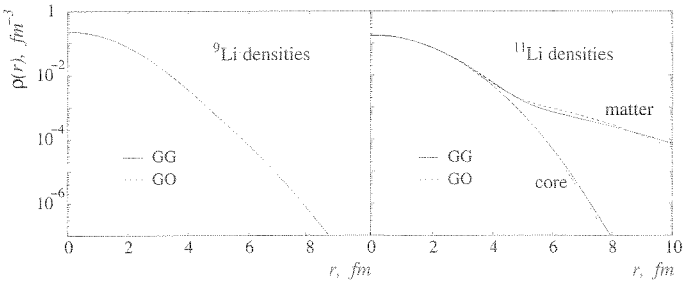

Figure 2. The nuclear matter and nuclear core density distributions ρ(r) of ^{11}Li deduced from the present experimental data are compared with the nuclear matter density distribution of ^{9}Li. Labels denote different parametrizations of phenomenological density distributions used in the analysis (see text).

oscillator-type density (GO) for the valence neutrons were used (for details see ref.[1]). The experimental data are comparably well described with both density parametrizations, with a reduced χ^2 around unity. Solid lines in Fig. 1 show the GG case as an example.

The nuclear matter distributions of ^{11}Li and ^{9}Li deduced from the present data are displayed in Fig. 2. The radii obtained for the total matter, the core, and the halo distributions for ^{9,11}Li are given in Table 1 in comparison with those of ^{6,8}He from the previous experiment [1],[2]. It is obvious from the data that the matter distribution of ^{11}Li exhibits the by far most pronounced halo structure compared to all the other nuclei investigated, including ^{6}He and ^{8}He. This is also reflected in the deduced nuclear matter radius R_m= 3.62 (14) fm and the halo radius R_h= 6.54 (38) fm, the latter being more than twice as large as in ^{6}He and ^{8}He. A comparison of the nuclear matter and core distributions of ^{11}Li with the matter distribution deduced for ^{9}Li, and the corresponding radii (Table 1), supports the generally accepted picture of ^{11}Li to consist of a ^{9}Li core and a two-neutron halo.

Table 1: Summary of nuclear matter radii deduced for the helium isotopes ^{6,8}He [1],[2] and for the lithium isotopes ^{9,11}Li from the present experiment (please note that the results on the lithium isotopes are still preliminary). R_m denotes the total rms matter radius, R_c the core radius, and R_h the halo radius. The errors given include statistical and systematical uncertainties.

nucleus	R_m	R_c	R_h
^{6}He	2.30 (7)	1.88 (12)	2.97 (26)
^{8}He	2.45 (7)	1.55 (15)	3.08 (10)
^{9}Li	2.43 (7)	2.21 (10)	3.10 (28)
^{11}Li	3.62 (14)	2.55 (12)	6.54 (38)

References

[1] G.D. Alkhazov et al., Phys. Rev. Lett. 78 (1997) 2313

[2] S.R. Neumaier et al., Nucl.Phys. A (2001), to be published

Coulomb Breakup of ^{15}C and ^{17}C [B,G]

U. Datta Pramanik[1], T. Aumann[1], K. Boretzky[2], D. Cortina-Gil[1], Th.W. Elze[3], H. Emling[1], H. Geissel[1], A. Grünschloß[3], M. Hellström[1], S. Ilievski[3], N. Iwasa[1], J.V. Kratz[2], R. Kulessa[4], Y. Leifels[1], A. Leistenschneider[3], E. Lubkiewicz[4], G. Münzenberg[1], P. Reiter[5], C. Scheidenberger[2], Ch. Schlegel[1], H. Simon[6], K. Sümmerer[1], E. Wajda[4], W. Walus[4]

(LAND-FRS Collaboration)

[1]GSI Darmstadt, [2]Univ. Mainz, [3]Univ. Frankfurt, [4]Univ. Kraków, [5]LMU München, [6]TU Darmstadt

Coulomb breakup of secondary beams of unstable nuclei at intermediate energies has developed into a standard spectroscopic tool in exploring properties of weakly bound nuclei. Here, this method has been applied to a study of ^{15}C and ^{17}C isotopes which have very small neutron separation energies of 1.2 and 0.73 MeV, respectively.

Radioactive beams of ^{15,17}C were produced in a fragmentation reaction of a primary ^{40}Ar beam, delivered by the synchrotron SIS at GSI, Darmstadt, and were subsequently separated in flight by the FRS. The incoming beam and fragments were identified utilizing energy-loss and time-of-flight measurements together with the known magnetic rigidity. Neutrons and γ-rays were detected by the LAND and Crystal Ball spectrometers, respectively. From the measured momenta of all decay products of the projectile after inelastic scattering followed by breakup, the excitation energy of the nucleus was determined. The Coulomb dissociation cross sections with the Pb (1.8 g/cm^2) target were obtained after subtracting nuclear contributions determined from the data with a C (0.573 g/cm^2) target.

By comparing measured differential cross sections $d\sigma/dE^*$ (excitation energy E^*) for electromagnetic excitation with calculated cross sections (see below) one can deduce information on the ground state structure. The Coulomb breakup cross section can be written [1]:

$$\frac{d\sigma}{dE^*} = (\frac{16\pi^3}{9\hbar c})N_{E1}(E^*)\sum_m |< q \mid (Ze/A)rY_m^1 \mid \psi(r) >|^2 .$$

$N_{E1}(E^*)$ represents the number of equivalent dipole photons of the target Coulomb field, computed in a semiclassical approximation, ψ(r) represents the ground state single particle wave function of the neutron and $< q \mid$ describes the wavefunction of the neutron in the continuum.

In the case of ^{15}C with the known g.s. spin $I^\pi = 1/2^+$, the experimental data show that Coulomb breakup populates predominatly the ground state of ^{14}C, a small branch of about 10 % feeding excited states at 6 - 7 MeV is observed in addition. A comparision between our measured $d\sigma/dE^*$ for this isotope with the fragments in its ground state and the calculated one, delivers a spectroscopic factor (0.72) for a ℓ=0 neutron which is consistent with an earlier reported value [2].

The ground state spin of ^{17}C is not fully established experimentally. Our experimental data for Coulomb break up of ^{17}C show that most of the cross section yields the ^{16}C core in its first excited state, $I^\pi = 2^+$, and an excited state at an excitation energy around 3 MeV. Only a small part of the cross section leaves the core in its ground state. Fig. 1 (top) shows the sum energy spectra of the γ decay from ^{16}C fragments and indicates the relative

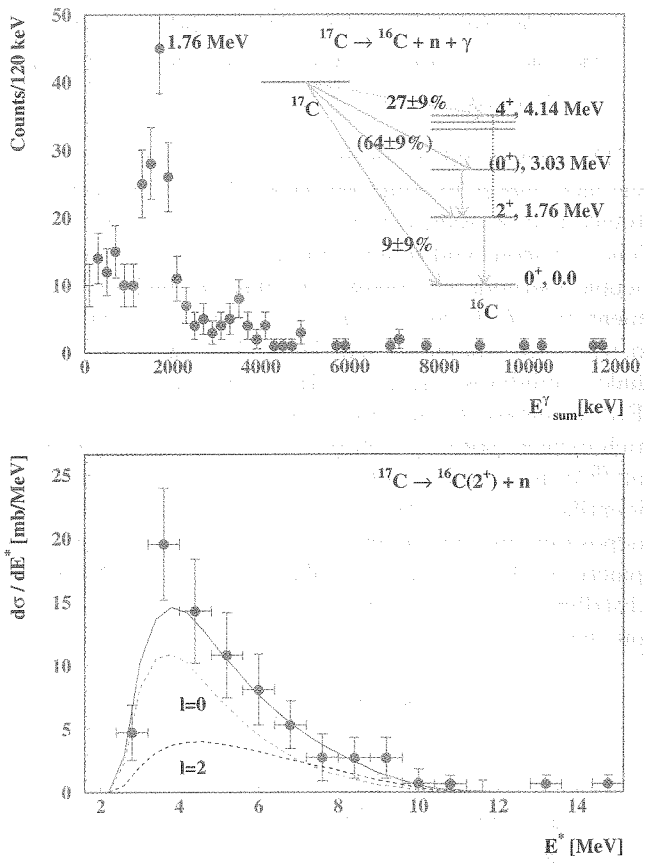

Fig. 1: Sum energy of γ decay transitions (top). Differential Coulomb dissociation cross section (bottom).

partial cross sections for the population of different core states. The lower part of the Fig. 1 shows $d\sigma/dE^*$ for electromagnetic excitation of ^{17}C in coincidence with the 1.766 MeV γ transition ^{16}C($2^+ \rightarrow 0^+$) without acceptance and efficiency corrections for the neutron detector. These corrections, however, are taken into account in the cross sections calculated according to equ. (1). A proper choice of relative contributions from $\ell = 0$ and $\ell = 2$ neutrons forming the ^{17}C g.s. wave function, as shown Fig 1, can reproduce well the data. Thus, ^{16}C(2^+) $\bigotimes \nu_{s,d}$ is the predominant g.s. configuration and one can rule out a $1/2^+$ ground state spin of ^{17}C. The major part of our results is in agreement with those from a different method, i.e. obtained from a knockout reaction [3].

References

[1] T. Nakamura *et al.*, *Phys. Rev. Lett.* **83** (1999) 1112.

[2] J.D. Goss *et al.*, *Phys. Rev.* C **8** (1973) 514.

[3] V. Maddalena *et. al.*, *Phys. Rev.* C **63** (2001) 024613.

Nuclear Halo Structure Studies via High-Energy Break-up Reactions

D. Cortina-Gil[1,2], J. Fernandez-Vazquez[1], K. Markenroth[3], T. Aumann[2], T. Baumann[4], J. Benlliure[1], K. Boretzky[2], M.J.G. Borge[5], L. Chulkov[2,6], U. Datta-Pramanik[2], Ch. Forssen[3], Luis M. Fraile[5], H. Geissel[2], J. Gerl[2], F. Hammache[2], V. Hansper[7], K. Ithashi[8], M. Ivanov[2], R. Janik[9], B. Jonson[3], T. Kato[10], K. Kimura[11], S. Mandal[2], M. Meister[3], M. Mocko[9], G. Münzenberg[2], T. Ohtsubo[2,10], S. Ohya[10] T. Okuda[12], A. Ozawa[13], Y. Prezado[5], V. Pribora[6], K. Riisager[7], G. Schneider[14], H. Scheit[15], G. Schrieder[16], M. Sekiguchi[12], B. Sitar[9], A. Stolz[14], P. Strmen[9], K. Sümmerer[2], T. Suzuki[9], X. Szarka[9], I. Tanihata[13], S. Wan[2], H. Weick[2], Y. Yamaguchi[10]

[1]Universidad de Santiago de Compostela, [2]GSI, [3]CTH Göteborg, [4]MSU, [5]Instituto de Estructura de la Materia, [6]Kurchatov Institute, [7]Aarhus Universitet, [8]Tokyo Institute of Technology, [9]Comenius University, [10]Niigata University, [11]Nagasaki Institute of Applied Science, [12]Tohoku University, [13]RIKEN, [14]TU München, [15]MPI, [16]TU Darmstadt

The nuclear halo structure can be efficiently investigated via high-energy breakup reactions. Partial and differential break-up cross section measurements for the removal of valence nucleons and momentum measurements are spectroscopic methods successfully applied at high-energy fragmentation facilities. A narrow momentum distribution of the core fragments can be a clear signature for new halo candidates [1, 2, 3]. In recent experiments at the FRS we measured the momentum distributions of neutron-rich oxygen isotopes isotopes produced via fragmentation of ^{40}Ar projectiles. The fragments were unambiguously identified by magnetic rigidity, time-of-flight and energy-deposition measurements in front of the breakup target placed at the central focal plane of the FRS. Momentum distributions of the secondary fragments after removal of one neutron are shown in fig. 1.

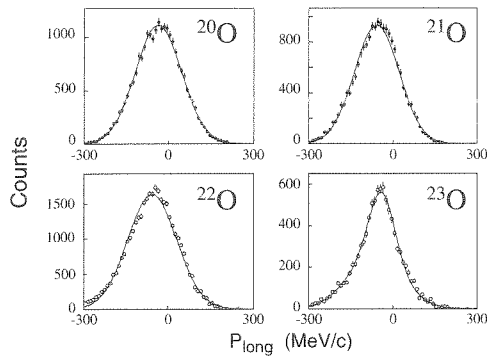

Figure 1: Measured momentum distributions of oxygen isotopes after one-neutron removal reaction in a carbon breakup target placed at the central focal plane of the FRS. The preliminary fwhm values of the distributions are ^{20}O (192 ± 5 MeV/c), ^{21}O (187 ± 9 MeV/c), ^{22}O (203 ± 14 MeV/c) ^{23}O (130 ± 8 MeV/c).

The narrow momentum distribution of the valence neutron in ^{23}O reflects a clear shell structure in accordance to the observation in ref.[4]. From the shape of the measured longitudinal momentum distribution the orbital angular momentum of the removed nucleon can be determined and from the removal cross section the spectroscopic factors. These powerful spectroscopic tools were extended by γ-ray detection to identify the final states of the core fragments after the removal reaction. The gamma detector consisted of an array of 32 NaI units located 80 cm behind of the breakup target (total efficiency (ϵ)= 3 % and energy resolution (ΔE/E)= 12% for E_γ=429 keV).

The method is illustrated by a test measurement of ^{8}B, performed in the beginning of this experimental campaign. In this part, the ^{8}B beam was produced by fragmentation of a primary beam of ^{12}C at 1 GeV/nucleon. The nuclear structure of ^{8}B was studied via one-proton removal reaction in lead and carbon breakup targets and the measured momentum distributions were recorded in coincidence with γ-ray spectroscopy. The corresponding one-proton removal cross section are: σ_{-1p}(C) = (94 ± 9) mb and σ_{-1p}(Pb) = (662 ± 60) mb both in excellent agreement with our earlier measurements [5].
The contributions from the ground and excited state to the ^{7}Be momentum distribution after the p-removal in the carbon target are shown in fig.2. It is clearly seen that the ground-state transition dominates the measured momentum distribution.

The data analysis for the oxygen isotopes is still in progress, however, the preliminary results show that we can extract the above mentioned spectroscopic information. In future, we will extend the measurements to heavier elements and will also use a hydrogen breakup target in combination with an improved γ-setup.

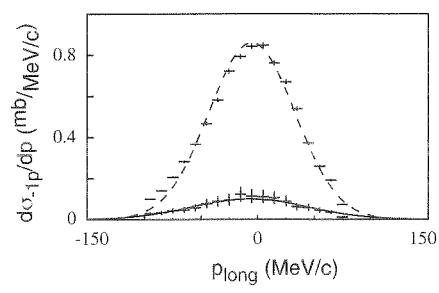

Figure 2: The measured momentum distribution of ^{7}Be. The separate contributions for the transition in the ground-state (dashed line) and first excited state (full line) after the p-removal in the lead target are shown.

References

[1] W. Schwab et al., Z. Phys. A 350 (1995) 283.
[2] T. Baumann et al., Phys. Lett. B 439 (1998) 256.
[3] M.H. Smedberg et al., Phys. Lett. B 452 (1999) 1.
[4] A. Ozawa et al., Phys. Rev. Lett. 84 (2000) 5493
[5] D. Cortina-Gil et al, Eur. Phys. J. A 10 (2001)49

Model calculations of a two-step reaction scheme for the production of the neutron-rich secondary beams

J. Benlliure, K. Helariutta, M.V. Ricciardi, K.-H. Schmidt

Actually, the design of more powerful next-generation secondary-beam facilities is being intensively discussed. The main challenge is the production of neutron-rich isotopes, because the neutron-drip line has only been reached for the lightest elements. The traditional way for producing neutron-rich nuclei is fission of actinides. Another approach introduced recently, based on cold fragmentation [1], has successfully been used to produce a number of new neutron-rich isotopes. A new idea is to combine these two methods in a two-step reaction scheme. Medium-mass neutron-rich isotopes are produced with high intensities as fission fragments. They are used as projectiles in a second step to produce even more neutron-rich nuclei by cold fragmentation. This idea might be realised in an-flight facility by consecutive reactions in a thick target, while the application in an ISOL-based facility needs post acceleration to sufficiently high energies to allow for fragmentation in a second target.

In our recent work [2], we studied the feasibility of this two-step reaction scheme by calculating the relevant cross sections and the beam intensities to be obtained. We concentrated our studies on the second step of this approach, cold fragmentation of projectiles far from stability, since there are no experimental data available for the fragmentation of exotic, very neutron-rich projectiles. Two types of codes were used, EPAX [3], the semi-empirical parameterisation of fragmentation cross sections and COFRA [4,1], a modern analytical version of the abrasion-ablation nuclear reaction model. In figure 1, the cross sections from fragmentation of ^{132}Sn as predicted by the two codes are compared. While the EPAX code extrapolates the production cross sections, measured in fragmentation of the available stable projectiles, the nuclear-reaction code takes into account the variation of the nuclear properties as a function of neutron excess. Most important is an enhanced neutron evaporation caused by the low neutron-separation energies of the extremely neutron-rich fragments. This leads to considerably lower cross sections if compared to EPAX.

According to the COFRA calculations, the direct production by fission of ^{238}U prevail in most cases. The two-step scenario might only become advantageous in the production of extremely neutron-rich isotopes. The situation changes appreciably if we consider the available secondary-beam intensities including extraction, ionisation and re-acceleration in an ISOL-type facility. Here, the two-step reaction scenario can be useful by profiting from very high secondary-beam intensities to be obtained for specific neutron-rich nuclides. Extracting an abundant and long-lived neutron-rich nuclide like ^{132}Sn from the ISOL source and fragmenting it, one can reach those isotopes that have low ISOL efficiencies due to their short half lives or difficulties in the extraction from the source [5].

We conclude that the predictions of EPAX for the production of very neutron-rich nuclides by fragmentation of non-stable neutron-rich projectiles seem to be far too optimistic. The two-step reaction scheme studied might be advantageous in specific cases.

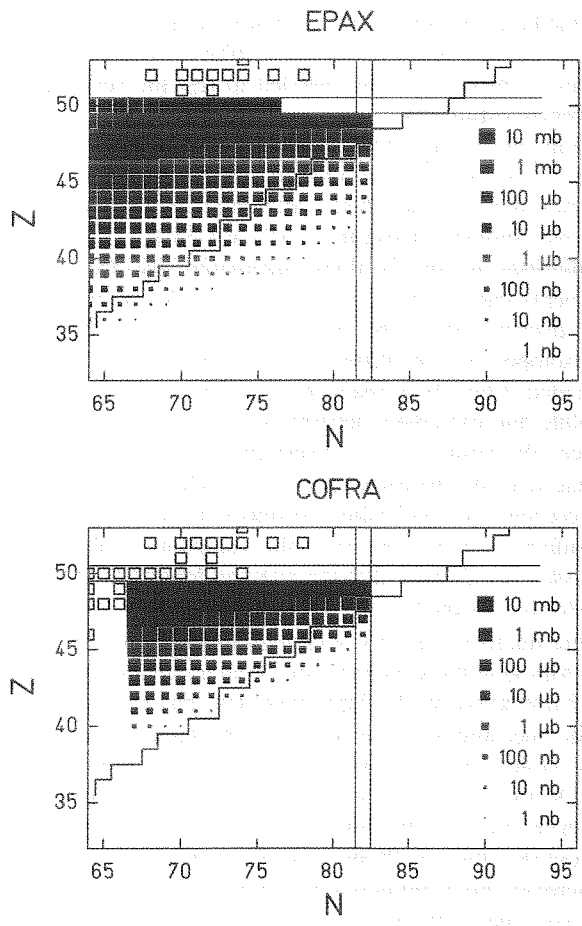

Figure 1. Predicted cross sections for the cold-fragmentation of ^{132}Sn in beryllium target from the empirical systematics EPAX and the nuclear-reaction code COFRA on a chart of the nuclides.

References

[1] J. Benlliure , K.-H. Schmidt, D. Cortina-Gil, T. Enqvist, F. Farget, A. Heinz, A. R. Junghans, J. Pereira, J. Taieb, Nucl. Phys. **A 660** (1999) 87.

[2] J. Benlliure, K. Helariutta, M.V. Ricciardi, K.-H. Schmidt, GSI-Preprint-00-41, November 2000.

[3] K. Sümmerer and B. Blank, Phys. Rev. **C 61** (2000) 034607.

[4] J.-J. Gaimard and K.-H. Schmidt, Nucl. Phys. **A 531** (1991) 709.

[5] H. L. Ravn, P. Bricault, G. Ciavola, P. Drumm, B. Fogelberg, E. Hagebo, M. Huyse, R. Kirchner, W. Mittig, A. Mueller, H. Nifenecker, E. Roeckl, Nucl. Instrum. Methods **B 88** (1994) 441.

Properties of light nuclides produced in the fragmentation of ^{238}U

M. V. Ricciardi[(1)], K. -H. Schmidt[(1)], P. Armbruster[(1)], J. Benlliure[(2)], M. Bernas[(3)], T. Enqvist[(1)], F. Rejmund[(1)]
(1) GSI – Planckstr. 1 – 64291 Darmstadt - Germany
(2) Univ. Santiago de Compostella – E-15706 Santiago de Compostella - Spain
(3) IPN Orsay – IN2P3, F-91406 Orsay - France

In the last years, motivated by the plans for the construction of ADS and RIB facilities, fragmentation and fission reactions at intermediate energies have acquired a greater interest. The physics of such reactions is still a subject of research, and precise experimental data are needed to test the reliability of the theoretical estimations.

Experiments on the formation of residual nuclei from ^{238}U, ^{208}Pb, ^{197}Au, and ^{56}Fe beams on several targets at relativistic energies have already been performed in inverse kinematics with the fragment separator (FRS) at GSI [1]. Some attractive peculiarities of the in-flight separation are that radioactive fragments can be measured before they decay, the whole isotopic distribution can be obtained for every element, and, once the isotopes are identified, their velocities can precisely be evaluated from their magnetic rigidities. This method yields absolute and extremely accurate velocity values. Here, we will present the result of our investigations on the light residues produced in the fragmentation of 1·A GeV ^{238}U + Ti, and we will compare our preliminary results to previous knowledge.

An important result concerns the velocities of these residues. Morissey [2] showed that the average longitudinal momentum transfer for residual nuclei with masses close to the mass of the mother nucleus ($\Delta A<50$) increases linearly with the mass loss ΔA. Although the validity of this systematic dependence on ΔA could not be proved for large mass loss due to the uncertainties of the measurements, it seemed reasonable to expect that a more violent collision will produce a larger momentum transfer. On the contrary, Lindenstruth [3], analysing the residual nuclei produced in the interaction of gold with several targets, showed that for $\Delta A>70$ the momentum transfer stops definitely to increase and eventually starts slowly to decrease. In the present experiments, the velocities of the reaction products could be determined with high precision, and this allows us to check the finding of Lindenstruth. In figure 1 (left) the mean values of the velocity-spectra of fragmentation residues are collected for several elements. Our preliminary data (·) are compared with those obtained in the reaction 1·A GeV ^{238}U + Pb [7] (-), where the acceleration of light elements is even more enhanced. Our results confirm the finding of Lindenstruth in the sense that the momentum transfer does not increase further when the mass loss becomes very important. In addition, we find a clear inversion of the trend for the very light products which are found to be even slightly faster than the projectiles. The reason for this acceleration is not obvious. A possible explanation could be the interaction between the surviving part of the projectile and the expanding fire streak behind it in the later stage of the collision.

Another interesting peculiarity of the fragmentation of ^{238}U is the mean N/Z of the produced elements. In figure 1 (right) the EPAX systematics [4] for a ^{197}Au projectile (---) and the stability line are reported (—). These two reference lines are compared with several experimental data. Results from the reactions 800·A MeV ^{197}Au + p [5] (□) and 414·A MeV ^{56}Fe + p [6] (△) follow the EPAX systematics. In these cases, the produced fragments are not far from the mother nucleus. However the reactions 1·A GeV ^{238}U + Pb [7] (-), 750·A MeV ^{238}U + Pb [8] (-) and 1·A GeV ^{238}U + Ti (our data) (-) leave the EPAX evaporation corridor, and the more the produced light-nuclides are far from the mother nucleus, the more neutron-rich they are, up to the point that they even cross the stability line. A possible explanation could be found in the predictions of statistical multi-fragmentation models (see [9]). In these models, the light products emerge from the freeze-out of a low-density configuration. Since most of the excitation energy was spent for the disintegration of the system, their secondary deexcitation starts from rather low temperature. Thus these products have larger N/Z-ratios than the fragments produced as a result of evaporation from the mother nucleus.

Properties of light projectile fragments from collisions of massive nuclei have been measured with a high-precision spectrometer. Unexpectedly high velocities and deviations of the N/Z ratio from the evaporation corridor have been found. While the N/Z ratio seems to scale with the mass loss, the velocities also strongly depend on the target nucleus. These features, which seem to be related to multifragmentation, give important information on the dynamics of relativistic nuclear collision.

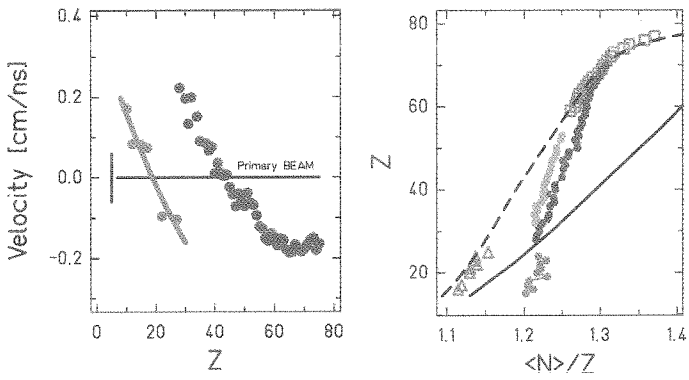

Figure 1: Left: Mean velocities of the fragmentation residues (see text for symbols). Right: Mean N/Z-ratio of the isotopic distributions of the produced elements (see text for symbols).

[1] http://www-wnt.gsi.de/kschmidt/activiti.htm
[2] D. J. Morrissey, *Phys. Rev.* **C 39** (1989) 460
[3] V. Lindenstruth, *GSI-93-18* (1993)
[4] K. Sümmer, B. Blank, *Phys. Rev.* **C 61** (2000) 034607
[5] F. Rejmund et al., *Nucl. Phys.* **A 683** (2001) 540
[6] W. R. Webber et al., *Astr. Jour.* **508** (1998) 949
[7] T. Enqvist et al., Nucl. Phys. **A 658** (1999) 47
[8] J. Benlliure et al., *Eur. Phys. J.* **A 2** (1998) 193
[9] A. S. Botvina et al., *Nucl. Phys.* **A 531** (1991) 709

Critical analysis of dissipative effects in fission

B. Jurado, A. Heinz, A. Junghans, K.-H. Schmidt, GSI Darmstadt, Germany
J. Benlliure, Univ. Santiago de Compostela, Spain
T. Enqvist, Univ. Jyväskylä, Finland
F. Rejmund, IPN Orsay, France

According to Grangé and Weidenmüller [1], dissipation effects in the fission process of a hot heavy-nucleus lead to a time-dependent fission-decay width Γ_f (t) that is first suppressed, then increases gradually and finally reaches a stationary value Γ_{stat}. see full line in figure 1.

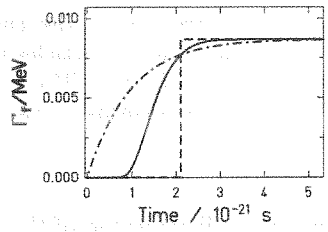

Figure 1: $\Gamma_f(t)$ obtained from the solution of the Fokker-Planck eq. [2] (full line) in comparison with two approximations. The dashed-dotted line corresponds to the approximation (a) and the dashed line to the approximation (b)

However, the implementation of this function in a nuclear-reaction code is rather complicated, and thus most codes use one of the following approximations: (a) an exponential in-grow function of the form $\Gamma_f(t) = \Gamma_{stat}(1-\exp(-2.3 \cdot t/\tau_f))$ and (b) a step function that switches from zero to the stationary value Γ_{stat} at the transient time τ_f, where the Fokker-Planck solution raises up to 90% of its stationary value. Both approximations are depicted in figure 1. Compared to the exact solution, the description (a) overestimates the fission width, while description (b) underestimates the fission width up to the transient time. We implemented both approximations in our Abrasion-Ablation Monte-Carlo code ABRABLA [3].

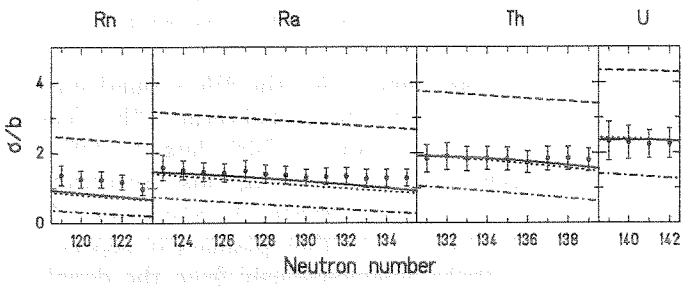

Figure 2: Experimental total nuclear-induced fission cross sections (black dots) as a function of the neutron number for different Rn, Ra, Th and U isotopes at 420 A MeV on a lead target. The data are compared with four calculations, see text

Model calculations are compared to measured total nuclear fission cross sections of different projectiles in figure 2. The full line represents a calculation with the description (b) and a value of the dissipation coefficient, $\beta = 2 \cdot 10^{21} s^{-1}$. This combination shows a very good agreement with the data. However, the combination $\beta = 2 \cdot 10^{21} s^{-1}$ and description (a) clearly overestimates the cross sections, dashed line in figure 2. Nevertheless, the reproduction of the total fission cross sections with description (a) is also possible if we increase the transient time by increasing β up to $9 \cdot 10^{21} s^{-1}$, this is represented in figure 2 by the dotted line. The dashed-dotted line shows that the combination $\Gamma_f(t)$ according to (b) and $\beta = 9 \cdot 10^{21} s^{-1}$ underestimates the cross sections.

The experiment also allowed to determine the nuclear charges of the fission fragments. In figure 3 we compare the two combinations of β and $\Gamma_f(t)$ that reproduce the total fission cross sections of figure 2 with experimental partial fission cross sections. We observe that only the step-function with $\beta = 2 \cdot 10^{21} s^{-1}$ fits the data, while description (b) leads to important deviations from the data.

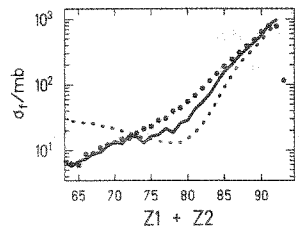

Figure 3: Fission cross sections for ^{238}U on CH_2 at 1 A GeV (full dots) as a function of the sum of the charges of the two fission fragments. The data are shown in comparison with two calculations. The full line is a calculation done with description (b) and $\beta = 2 \cdot 10^{21} s^{-1}$, and the dotted line is a calculation with description (a) and $\beta = 9 \cdot 10^{21} s^{-1}$

Our analysis is based on both a new experimental information from fission induced by relativistic nuclear collisions and the implementation of different in-grow functions in the same code. We conclude that the deduced dissipation coefficient β depends strongly on the function which is used to describe $\Gamma_f(t)$. We have found that all our data are well reproduced with a step function for $\Gamma_f(t)$ (option (b)) and $\beta = 2 \cdot 10^{21} s^{-1}$ and that the most widely used description of $\Gamma_f(t)$, an exponential in-grow function, does not reproduce our data, because it fails to describe the essential feature of the solution of the Fokker-Planck equation, namely the practically complete suppression of fission during most part of the transient time. Our result sheds severe doubts on part of the previous work on nuclear dissipation.

References

1 P. Grangé et al., Phys. Rev. C 27 (1983) 2063

2 S. Chandrasekhar, Rev. Mod. Phys. 15 (1943) 1

3 A. Heinz et al., GSI Ann. Rep.(1999)30 and references within

Quaternary Fission of ^{252}Cf [B,G]

Yu.N. Kopatch[1], M. Mutterer[2], J. von Kalben[2], H.-J. Wollersheim[1], E. Lubkiewicz[3], and P. Adrich[3]

[1] *GSI Darmstadt,* [2] *TU Darmstadt,* [3] *Cracow University, Poland*

The rare ternary fission process ($\simeq 1/260$ relative to binary fission, for ^{252}Cf) is of particular interest not only for the understanding of the fission process itself, but also as a source of various neutron-rich light nuclei [1]. The study of "exotic" light nuclei is a major topic in modern nuclear structure physics with radioactive beams. The even rarer quaternary fission (QF) mode [2], when two light charged particles (LCP) are emitted simultaneously in addition to the main fission fragments, can originate either from a break-up of unstable species among the LCPs, e.g. ^{7}Li*, ^{8}Be, ^{9}Be* ("pseudo" quaternary fission), or from the independent emission of two LCPs ("true" quaternary fission).

The QF processes were studied at GSI using a spontaneous ^{252}Cf fission source ($\sim$ 5000 fissions/sec). The LCPs were identified by a set of eight ΔE-E telescopes (12 μm + 380 μm Si detectors of 1 cm^2 each) subtending a total solid angle of $\sim$ 20%. Fission fragments and the 6.1 MeV α-particles from the ^{252}Cf radioactivity were stopped in suitable absorbers placed between source and detectors. The telescopes allowed for a clean separation of the LCP nuclear charges. A total of 255 α-α coincidences were detected, within a time window of 10 nsec. Simultaneously, single LCP events with the emission of ternary α, Li and Be particles were registered and could be used as a reference.

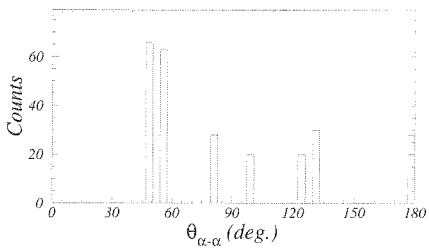

Figure 1: Measured relative angles for α-α coincidences.

Figure 1 shows the number of α-α coincidences as a function of the relative angle between the centers of the telescope surfaces. There is a clear enhancement of the quaternary fission yield at the smaller angles which is attributed to the break-up of ^{8}Be LCPs, while the homogeneous distribution at the larger angles signals the true QF events. Simple estimates based on the kinematics of the ternary ^{8}Be decay in flight show that the largest possible angle between the two α-particles from the ^{8}Be ground-state decay ($T_{1/2}$ = 0.07 fs, Q = 0.092 MeV) equals 8°, while the smallest distance between neighbouring telescopes corresponds to an opening angle of 16°. Thus, the observed enhancement in the angular distribution is presumably due to the decay from the first excited level in ^{8}Be ($T_{1/2} = 3 \times 10^{-22}$ s, Q = 3.13 MeV). In that case the distribution of the relative angles is expected to be significantly broader [2].

The energy spectra of the true and pseudo QF components are presented in Fig. 2. The yield for the true

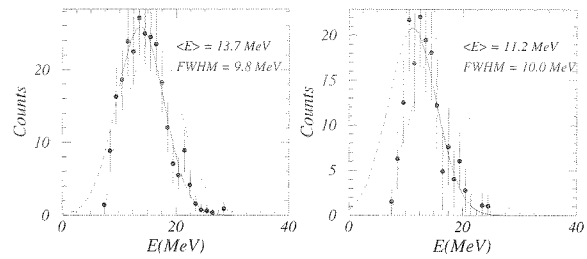

Figure 2: Energy spectra (corrected for the energy loss in the absorbers) of the true quaternary α-particles (left) and α-particles mediated by ^{8}Be* LCPs (right). The solid lines are Gaussian fits, the dotted line is the measured ternary α-particle spectrum ($< E >= 15.9$ MeV).

α-α QF, assuming isotropic distribution of the relative angles, is estimated as $(3 \pm 1) \times 10^{-4}$ relative to the yield of ternary ^{4}He. The two quaternary α-particles mediated by the ground-state decay of ^{8}Be are registered in our set-up as an admixture to the Li spectrum, as they fall into the same range in the ΔE-E patterns. An attempt was made to disentangle these two contributions by fitting the known Li energy spectrum [3] and the sum spectrum of the two α-particles from the ^{8}Be decay, considering the energy loss in the absorbers and ΔE detectors, to the measured E_{rest} spectrum (Fig. 3).

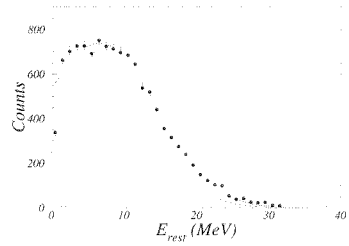

Figure 3: Decomposition of the E_{rest} spectrum gated on the ΔE-E patterns for Li (points): Dashed line - ternary Li spectrum, dotted line - sum spectrum of two α's hitting a telescope, solid line - sum of both components.

The result (still preliminary) for the ^{8}Be ground-state yield is $\simeq 1 \times 10^{-3}$ relative to the yield of ternary ^{4}He. The systematic error in this procedure is fairly large ($\geq 50\%$), because of the uncertainty in the energy loss corrections and the not precisely known ternary Li spectrum. In a forthcoming experiment it is thus planned to separate the Li ternary particles unambiguously from the double α-particle hits in each telescope by applying pulse-shape discrimination in suitable E_{rest} detectors.

References

[1] M. Mutterer *et al.*, Proc. 2nd Int. Conf. on Fission and Properties of Neutron-Rich Nuclei, St.Andrews, 1999, (World Scientific) (2000), p. 316.

[2] F. Gönnenwein *et al.*, Proc. Int. Workshop Fission Dynamics of Atomic Clusters and Nuclei, Luso, 2000, (World Scientific), in press.

[3] P. Singer, Dissertation, TU Darmstadt (1996).

Mean field and beyond in α-decay chains of superheavy elements[B+G]

P.–G. Reinhard[1], P. Fleischer[1], M. Bender[2],

[1] Institut für Theoretische Physik, Universität Erlangen, Staudtstr. 7, D–91058 Erlangen
[2] Gesellschaft für Schwerionenforschung, Planckstr. 1, D–64291 Darmstadt

Recent experiments at GSI [1] and JINIR Dubna [2] brought evidence for the synthesis of new superheavy elements. One of the key observable in these experiments is the Q_α value along the α-decay chains. In this contribution, we want to investigate this observable within self-consistent mean-field models.

We consider two different models, the Skyrme-Hartree-Fock approach (SHF) and the relativistic mean-field model (RMF), for a most recent review see [3]. From the world of different parametrisations we confine the discussion to a few well adjusted, typical and recent sets. For SHF we consider the parametrisations SkP, SkI3, SkI4, and SLy6. The force SkP uses effective mass $m^*/m = 1$ and is designed to allow a self-consistent treatment of pairing. The other forces all have smaller effective masses around $m^*/m = 0.7-0.8$. The force SLy6 stem from an attempt to cover properties of pure neutron matter together with normal nuclear ground-state properties. The forces SkI3/4 employ a spin-orbit force with isovector freedom to simulate the relativistic spin-orbit structure. SkI3 contains a fixed isovector part exactly analogous to the RMF, whereas SkI4 is adjusted allowing free variation of the isovector spin-orbit force. The modified spin-orbit force has a strong effect on the spectral distribution in heavy nuclei and thus for the predictions of superheavy elements. For the RMF we consider the parametrisations NL-Z2 and NL3. The force NL-Z2 comes from fits much similar to those of SkI3 and SkI4. NL3 is fitted without looking at the electron-scattering formfactor but with taking more care about the isovector trends. We ought to remind here that these different parametrisations produce much different predictions for the magic shell closure in SHE [4, 5].

Fig. 1 compares calculated and experimental α energies for the new isotopes. Most models make similar predictions at the lower end of the chains and these agree very nicely with the available new data for both chains. Larger differences among the forces show up when going to heavier systems. This is mainly due to differently pronounced shell closures which produce these curious kinks. Having a closer look on the deformation energies shows that one comes into a regime of very soft nuclei with pronounced shape isomerism. The mean-field state represents the one configuration at the absolute minimum of energy. But many other configurations are energetically competitive in soft nuclei. Thus one needs to consider a correlated ground state built from an appropriate coherent mixture of configurations. In practice, we superpose the states along the quadrupole deformation path using the generator-coordinate method [6]. The effect of such correlations is shown in Fig. 2. They wipe out the kinks and produce a smooth trend throughout. There is little correlation effect at the lower end of the chain such that the orginally given good agreement with data is maintained. Moreover, correlations bring the predictions from the the various forces closer together again. The then remaining difference is a clear signal of different bulk properties deep within the models, yet to be worked out in detail.

To conclude, mean-field models provide a pertinent description for the Q_α values along the recently measured decay chains of superheavy elements. Correlations effects beyond mean field need to be taken into account for the heavier isotopes.

References

[1] S. Hofmann *et al.*, GSI preprint 2000–52.
[2] Yu. Oganessian *et al.*, Phys. Rev. C **62**, 41604 (2000).
[3] P.-G. Reinhard *et al.*, Comm. Nucl. Part. Sci. (2001).
[4] K. Rutz *et al.*, Phys. Rev. C **56**, 238 (1997).
[5] M. Bender *et al.*, Phys. Rev. C **60**, 034304 (1999).
[6] P.–G. Reinhard, *et al.*, RIKEN Review **26**, 23 (2000)

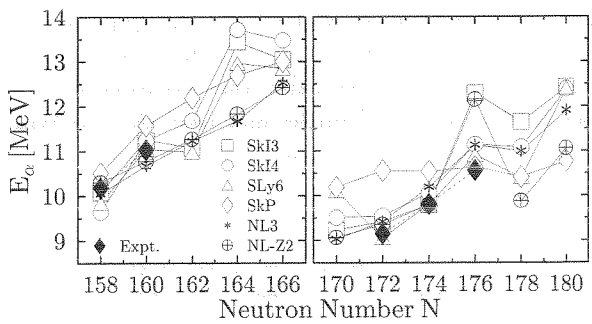

Figure 1: Ground-state-to-ground-state α energies for the α-decay chains containing $^{270}_{160}110$ (left panel) and $^{282}_{176}116$ (right panel) from mean-field calculations with the forces as indicated. Filled diamonds denote the experimental values.

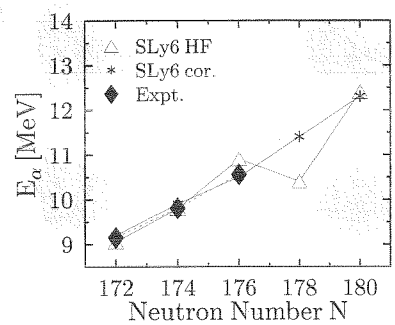

Figure 2: Ground-state-to-ground-state α energies for the decay chain containing $^{282}_{176}116$ computed with the force SLy6. Compared are calculations with and without taking ground-state correlations into account.

Shell stabilization in superheavy elements[B+G]

M. Bender,[1] P.–G. Reinhard[2]

[1] Gesellschaft für Schwerionenforschung, Planckstr. 1, D–64291 Darmstadt
[2] Institut für Theoretische Physik, Universität Erlangen, Staudtstr. 7, D–91058 Erlangen

Superheavy elements (SHE) are by definition those very heavy nuclei which have a negligible liquid-drop fission barrier. Quantum mechanical shell effects create one or several minima in the potential energy surface which stabilize the nucleus against fission. This additional binding from shell effects is quantified by the shell correction energy which is thus a first hint on the fission stability.

The shell correction energy can be computed by comparing the actual discrete distribution of single-particle energies with a smoothened level density. The weakly–bound SHE require a careful treatment of the continuum which we perform according to the recipe of [1]. Fig. 1 shows the shell correction energies from fully self-consistent calculations with the Skyrme interactions SkI3 and SLy6 and the relativistic mean-field interactions NL3 and NL–Z2. Remind that the shell correction is always sharply peaked at shell closures for nuclei up to Pb. This changes when going to SHE. There emerges a broad island of shell stabilization which spreads around the shell closures predicted by the various forces. Similar pattern are found in macroscopic-microscopic models. As a consequence, the significant differences seen in the prediction of magic numbers when looking at the δ_{2q} [2] are much mellowed by the generally softer pattern of the shell energy which looks similar for all models investigated in [3]. The reason for this behaviour is an accumulation of states with low angular momentum at the Fermi surface for these SHE. On one hand, this causes the fast changes of the various shell closures by small shifts of individual levels [4]. On the other hand, this turns the shell effect of individual levels into the shell effect of a bunch of levels more independent on the subtle details of actual shell closures.

Spherical shell corrections are, of course, a first indicator only for the stability of SHE. What finally counts is the fission barrier. And fission can go unusual paths in SHE.

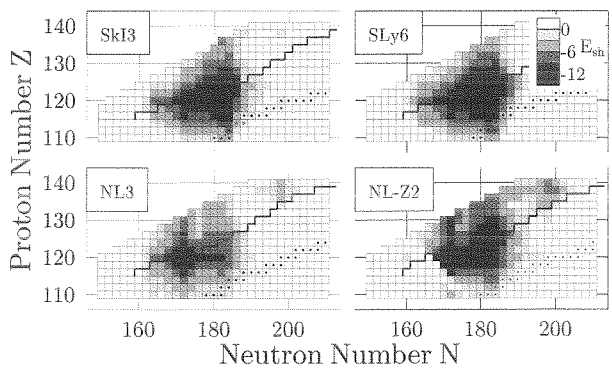

Figure 1: Total shell correction for spherical configurations of superheavy nuclei extracted from self–consistent calculations with the effective interactions as indicated. The (calculated) two–proton drip line and the valley of stability are emphasized. Data taken from [3].

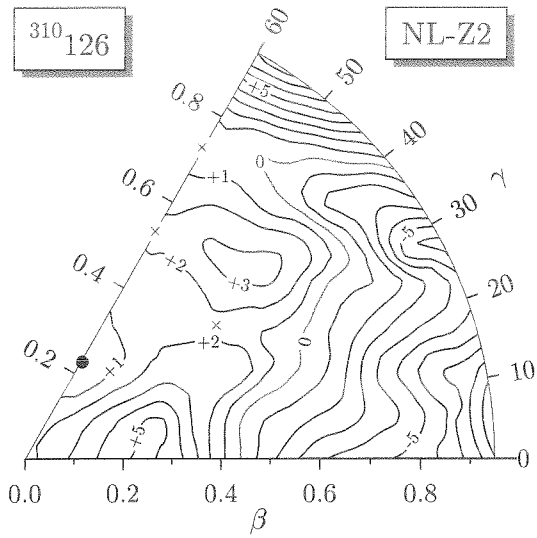

Figure 2: Potential energy surface of $^{310}_{184}126$ in the β–γ plane calculated with the relativistic mean-field interaction NL–Z2. The filled circle denotes the oblate minimum, while crosses denote the various saddle points. Deformation energies in MeV are with respect to the oblate ground state.

Fig. 2 shows as an example the potential energy landscape of $^{310}_{184}126$ in the full triaxial plane. In spite of the huge shell correction of more than -12 MeV at spherical shape the actual ground state of $^{310}_{184}126$ is oblate when calculated with NL–Z2. Triaxial configurations reduce the axial prolate barrier of more than 5 MeV to 1.8 MeV. The result has to be taken with precaution because these detailed fission pattern seem to depend sensitively on the actual nucleus and force used. $^{292}_{172}120$ has spherical shape and a triaxial barrier of nearly 6 MeV when calculated with the same force. Skyrme interactions give a similar potential landscape in $^{310}_{184}126$ but with a spherical ground state and substantially higher barriers around 9 MeV, see [5]. This systematic difference in fission barrier heights when comparing Skyrme interactions and relativistic mean field has already been seen in [6] and still needs to be understood. Fig. 2 demonstrates, however, that one has to be aware of surprises in this region of nuclei and that there is still a bulk of work ahead to uncover all these features.

References

[1] A. T. Kruppa *et al.*, Phys. Rev. C **61**, 034313 (2000).
[2] K. Rutz *et al.*, Phys. Rev. C **56**, 238 (1997).
[3] M. Bender, W. Nazarewicz, P.–G. Reinhard, in preparation.
[4] M. Bender *et al.*, Phys. Rev. C **60**, 034304 (1999).
[5] S. Ćwiok *et al.*, Nucl. Phys. **A611**, 211 (1996).
[6] M. Bender *et al.*, Phys. Rev. C **58**, 2126 (1998).

Proton shell closures in proton–rich heavy nuclei

T. Cornelius[1], M. Bender[2], T. Bürvenich[1], L. Kudling[1], A. Sulaksono[1], P.–G. Reinhard[3], J. A. Maruhn[1], W. Greiner[1]

[1] Institut für Theoretische Physik, Universität Frankfurt, Robert-Mayer-Str. 8–10, D–60325 Frankfurt am Main
[2] Gesellschaft für Schwerionenforschung, Planckstr. 1, D–64291 Darmstadt
[3] Institut für Theoretische Physik, Universität Erlangen, Staudtstr. 7, D–91058 Erlangen

Magic numbers are a key feature of any finite Fermion system as they provide crucial clues on the underlying mean field. The study of shell closures is thus very interesting in exotic nuclei. One wants to know how the shell closures develop when moving towards the driplines. It is now well–established for neutron–rich $N=20$ and $N=28$ isotones that the neutron shells fade away. This gives rise to a transient regime of pronounced low-lying collecive states and finally to stable ground-state deformation [1]. There are hints from the systematics of 2^+ and 4^+ excitation energies in Cd and Pd isotopes that also the $N=50$ and $N=82$ shells are weakened when going towards neutron–rich nuclei [2]. All these examples concern a weakening of neutron shells. The situation seems to be different for protons. For light nuclei there is no indication that the proton shell closures fade away towards the proton drip line. But the analysis of recent mass measurements [3] shows a substantial weakening of the two–proton shell gap

$$\delta_{2\mathrm{p}}(Z,N) = E(Z-2,N) - 2E(Z,N) + E(Z+2,N)$$

for very proton-rich Pb isotopes. It is speculated whether this is related to a weakening of the $Z=82$ shell [4]. This contribution looks at this problem from a theoretical perspective.

As tool we take self-consistent mean-field models which are nowadays well developed and provide a pertinent picture of the nuclear properties throughout the whole mass table. We consider two different models, the Skyrme-Hartree-Fock approach (SHF) and the relativistic mean-field model (RMF). We take one typical parametrisation for each model, SkI3 for the SHF and NL3 for the RMF, see e.g. [5]. SHF as well as RMF produce single–proton spectra in Pb with a well developed magic gap at $Z=82$ for all isotopes up to the dripline. This is confirmed by the systematics of the shell-correction energies extracted from self-consistent calculations [6]. The $\delta_{2\mathrm{p}}$ are presented in Fig. 1. The upper panel shows $\delta_{2\mathrm{p}}$ for spherical calculations in Pb as well as in its $Z\pm2$ neighbours Po and Hg. The theoretical results give an almost constantly large $\delta_{2\mathrm{p}}$ along the whole isotopic chain, in compliance with the large spectral gap and shell-correction energy. But the results for $\delta_{2\mathrm{p}}$ are clearly at variance with the data. This changes dramatically when allowing for ground–state deformation, see the lower panel. While the ground states of Pb isotopes stay spherical, the ground states of proton-rich Hg and Po isotopes become deformed. They thus gain energy which significantly reduces the extremely sensitive double difference $\delta_{2\mathrm{p}}$. The findings are consistent with the currently available data which confirm deformation softness in these heavy proton-rich isotopes, see e.g. [7] and references therein. Important for our purpose is: (i) $^{180-190}$Hg have oblate deformed ground states, (ii) data on excitation spectra and charge radii for Pb isotopes are consistent with spherical ground states, and (iii) proton-rich Po isotopes show an increased collectivity.

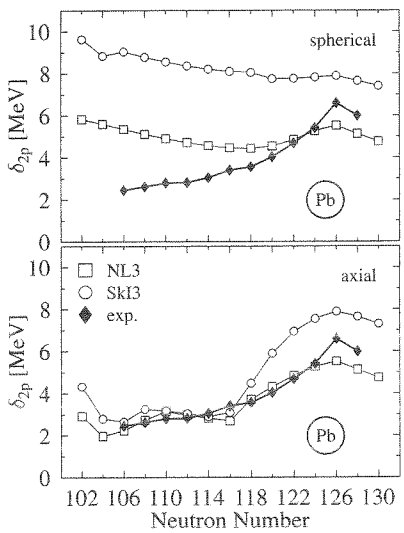

Figure 1: Two–proton shell gap δ_{2p} for Pb isotopes calculated with SHF (force SkI3) and RMF (force NL3) and compared with experimental data. Upper panel: from spherical configurations of all nuclei. Lower panel: allowing for ground-state deformations.

In summary the observed weakening of $\delta_{2\mathrm{p}}$ around $Z=82$ is caused by the increased collectivity of the Hg and Po isotopes, and not by a quenching of the $Z=82$ shell. Large values of $\delta_{2\mathrm{p}}$ are a sufficient, but not a necessary indicator for a shell closure. This example shows that a thorough analysis of magic shells requires a simultanous consideration of various signals, e.g. the $\delta_{2\mathrm{p}}$ together with energy and strength of low-lying 2^+ and 4^+ states, possibly complemented by α-decay hindrance factors [8]. True proton-shell quenching, however, is expected for the next magic proton number in the realm of superheavy elements [9].

References

[1] S. Pèru *et al.*, Eur. Phys. J. **A9**, 35 (2000).
[2] T. Kautzsch *et al.*, Eur. Phys. J. **A9**, 201 (2000).
[3] T. Radon *et al.*, Nucl. Phys. **A677**, 75 (2000).
[4] Yu. N. Novikov *et al.*, submitted to Nucl. Phys. A.
[5] P.–G. Reinhard *et al.*, Comm. Nuc. Part. Sci. (2001)
[6] M. Bender *et al.*, in preparation.
[7] K. Heyde *et al.*, Phys. Rev. **C53**, 1035 (1996).
[8] J. Wauters *et al.*, Phys. Rev. Lett. **72**, 1329 (1994).
[9] M. Bender *et al.*, Phys. Rev. C **60**, 034304 (1999).

Microscopic Description of Charge and Matter Distributions of Long-Tailed and Halo Nuclei

M. Tomaselli[a,b], T. Kühl[b,c], P. Egelhof[b,c], C. Kozhuharov[b], D. Marx[b], A. Dax[b], S.R. Neumaier[b], W. Nörtershäuser[b,d], M. Mutterer[a], H. Wang[b,e], H.-J. Kluge[b], and S. Fritzsche[f]

[a] Darmstadt University, [b] GSI Darmstadt, [c] Mainz University, [d] Tübingen University, [e] Tokyo University, [f] Kassel University

Elastic proton scattering experiments in inverse kinematics recently performed at GSI [1] have reopened important, partially unresolved questions concerning the physics of the halo nucleus ^{11}Li. In order to obtain a deeper insight into the halo structure of light exotic nuclei and to understand the difference between the matter and the charge distributions, microscopic calculations for the ground states of the ^{6,7,9,11}Li and ^{7,9}Be isotopes have been performed within the Dynamic-Correlation Model (DCM) [2].

The DCM describes the ground states of nuclei in terms of interacting clusters: valence particles and intrinsic vacuum states. The amplitudes of the mixed-mode wave-functions are derived in the framework of non-perturbative solutions of the Equation of Motion. Theoretically, the model spaces for the ground states of the ^{6,7,9,11}Li and the ^{7,9}Be isotopes are constructed by allowing valence particles to be scattered to higher configuration states ($2\,\hbar\omega$) and to interact with the core intrinsic states formed by exciting particles from the s,p-shell. The single-particle states used as input in the DCM have been approximated by harmonic oscillators with a state-dependent range introduced to reproduce the single-particle radii as calculated in a Wood-Saxon potential well. The single-particle energies are also obtained in this procedure. The two-body matrix elements are the same as used in Ref. [2].

The matter and charge distributions calculated with this microscopic approach can be used to predict experimentally accessible quantities. In this report we present and discuss the matter distributions for the lithium isotopes ^{7,9,11}Li. Root-mean-square matter and charge radii obtained for the above mentioned beryllium isotopes are also given.

The DCM matter distributions for the lithium isotopes are presented in Fig. 1. The oscillations in the theoretical matter distribution result from the interferences of the valence and the intrinsic states. For ^{11}Li two matter distributions are shown. The dotted line has been obtained by taking the three neutrons in the p-shell into account, while the solid line considers the effect of the neutons moving in the p, s, and d shells and interacting with the vacuum states. It is obvious that the s and d neutrons as well as the core excitations have a profound influence on the halo structure [4]. While there are experimental values for the matter radii of all accessible lithium and beryllium isotopes [5], the charge radii are only known for the stable isotopes [5, 6]. Experimental and theoretical values are in good agreement. However, for a better understanding of the neutron halos influence on the core nucleus, it is desirable to determine the charge radii of the radioactive lithium isotopes experimentally, particularly for ^{11}Li. For this purpose an experiment is being prepared at GSI and ISOLDE, CERN [7] to determine this value by means of an optical isotope-shift measurement. The agreement of the calculated (rms) charge and matter radii for the lithium isotopes with experimental data [5] is good in all cases with the exception of the matter radius of ^{11}Li, which is considerably larger than the experimental value. For ^{7}Be and ^{9}Be the calculated radii (Tab.1) are close to the values of Ref. [5]. It should be mentioned that the experimental values for the matter distribution are model-dependent and that new proton-scattering data from GSI [3] indicate a larger matter radius than the one given previously in Ref. [5]. The matter distribution of ^{11}Li (solid line) and the calculated matter radius of 3.64 fm agree with the phenomenological distribution and with the radius of 3.65 fm given in Ref. [3].

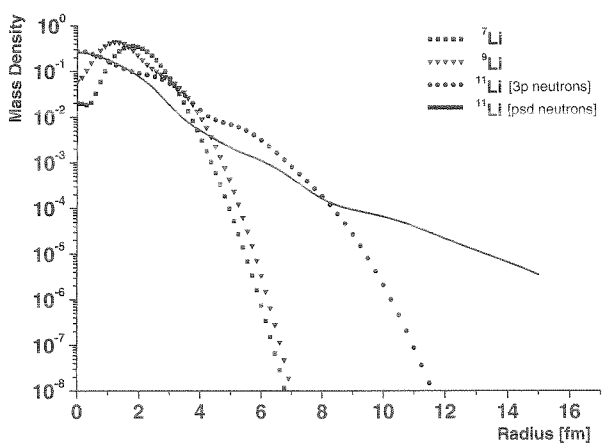

Fig. 1: Calculated mass distribution for ^{7,9,11}Li. The halo structure of ^{11}Li is mainly associated to sd neutrons and to core excitations.

Table 1: Rms-mass and -charge radii for beryllium isotopes

	$R^{calc.}_{matter}$	$R^{calc.}_{charge}$	$R^{exp.}_{matter}$[5]	$R^{exp.}_{charge}$[5]
^{7}Be	2.38 fm	2.39 fm	2.31(2) fm	? fm
^{9}Be	2.46 fm	2.62 fm	2.38(1) fm	2.47(1) fm

References

[1] S.R. Neumaier et al., submitted to Nucl. Phys. A (2001); G.D. Alkhazov et al., Phys. Rev. Lett. 78, 2313 (1997)

[2] M. Tomaselli et al., APAC 1999, Hyperfine Interactions 127, 95 (2000); Phys. Rev. C62 (2000), 67305

[3] A.V. Dobrowolsky et al., GSI Report (1999) and Verhdlg. DPG 35, 5 (2000)

[4] M. Tomaselli, C. Kozhuharov, and T. Kühl, 2001 in preparation

[5] I. Tanihata et al., Phys. Lett. B 206, 592 (1988)

[6] C.W. de Jaeger et al., At. Data, Nucl. Data Tables 14, 479 (1974)

[7] A. Dax et al., CERN/INTC 2000-006 INTC/P118

Ground-State Structure based on Realistic NN-Potentials

H. Feldmeier, P. Krafft, T. Neff and R. Roth (GSI)

A long standing goal of theoretical nuclear physics is the description of nuclear structure starting from a realistic nucleon-nucleon potential. All realistic NN-interactions show however two characteristics that inhibit a treatment of the many-body problem in a mean-field model. Firstly, the local part of the interaction shows a strong short-range repulsion (the so called *core*) and, secondly, there is a strong tensor part. Both properties give rise to special correlations in the many-body state, which cannot be described by Slater determinants or a superposition of shell model states from a few major shells.

In the framework of the Unitary Correlation Operator Method (UCOM) [1] we describe both types of correlations explicitly by unitary transformations of shell model type many-body states. Thus we obtain states that contain the relevant correlations induced by the interaction between the nucleons.

To describe the short-range correlations caused by the repulsive core of the interaction the unitary correlation operator generates a radial distance-dependent shift in the relative coordinate of each pair of particles. By that the particles are shifted out of the repulsive region of the interaction. Alternatively the correlation operator can be used to transform the Hamilton operator with the bare interaction.

For the correlations induced by the tensor part of the interaction a similar procedure is applied. The new aspect is that tensor interactions correlate coordinate and spin space in a complex way. The unitary transformation, which describes these correlations, acts on the angular part of the relative coordinates in dependence on the spin orientation of the two particles.

As a preliminary step towards a full ab initio calculation on the basis of the central and tensor correlated Bonn-A potential [2] we use a parameterized correction to account for tensor correlations. The core-induced central correlations are fully included by a spin- and isospin-dependent correlation operator [1]. In order to account for tensor correlations we add to the Bonn-A potential a correction in the $S = 1, T = 0$ channel. According to the structure expected for the tensor correlated interaction the correction consists of an additional attractive central potential and a repulsive momentum-dependent part. Three parameters (strength of local correction, and strength and range of momentum part) are adjusted to reproduce the experimental binding energies and charge radii of ^{4}He, ^{16}O, and ^{40}Ca.

Based on this correlated Bonn-A potential the many-body problem is treated in the framework of Fermionic Molecular Dynamics (FMD) [3]. The uncorrelated many-body state is described by a Slater determinant of gaussian one-body states, which contain the mean position, mean momentum, complex width and spin orientation as variational parameters. The ground-state wave function is determined by energy minimization with the correlated interaction.

The Figure shows the ground state one-body density distributions of ^{16}O, ^{20}Ne, and ^{24}Mg obtained with this method. For ^{16}O we find a spherical shell-model like distribution with a characteristic depletion of the central density. ^{20}Ne shows a prolate axially symmetric density distribution with α-like structures at the ends and a toroidal distribution in the central plane. Finally ^{24}Mg exhibits a complicated triaxial deformation with some remnants of α-clustering.

These calculations demonstrate the flexibility of the FMD basis as well as the possibility to perform nuclear structure calculations based on realistic NN-interactions in a nearly ab initio way. Our next step will be the inclusion of tensor correlations in a stringent way by calculating the appropriate unitary correlation operator explicitly.

[1] H. Feldmeier, T. Neff, R. Roth, J. Schnack; Nucl Phys. A632 (1998) 61.

[2] R. Machleidt; Adv. Nucl. Phys. 19 (1989) 189.

[3] H. Feldmeier, J. Schnack; Rev. Mod. Phys. 72 (2000) 655.

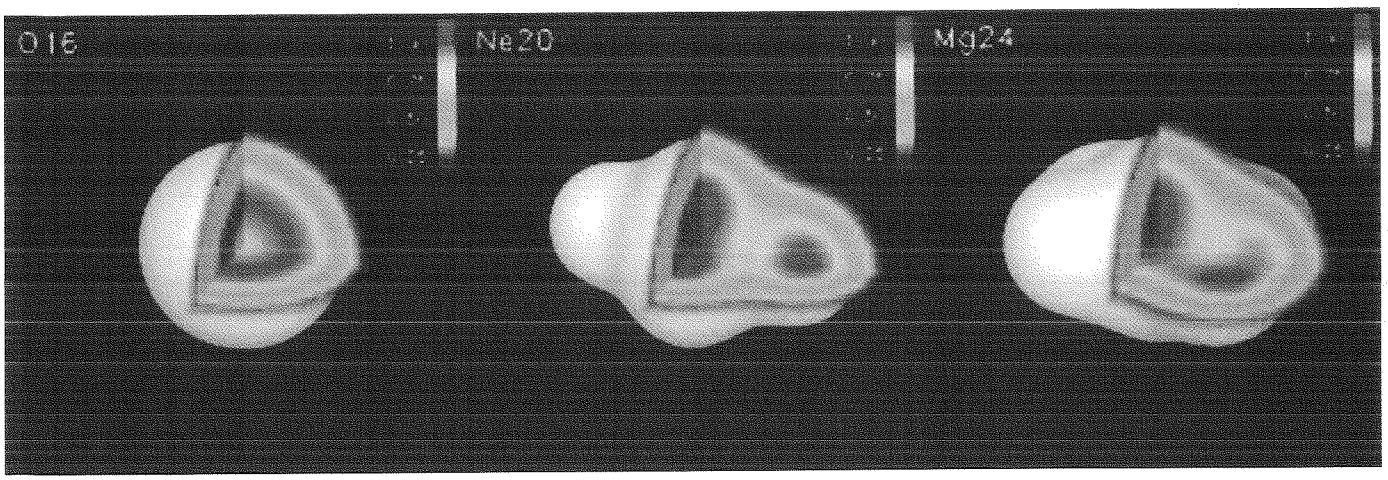

Figure 1: One-body density distributions (3-dimensional) of ^{16}O, ^{20}Ne, and ^{24}Mg. The white body shows the iso-density surface corresponding to half nuclear matter density ($\rho_0 = 0.17\text{fm}^{-3}$). The embedded planar cuts show the interior density distribution with color coding according to the color bar (in units of ρ_0). The mesh size of the background grid is 1fm $\times$ 1fm. Visit the FMD-Gallery at http://www.gsi.de/~fmd/.

Midrapidity emissions, can they be thermal? First results of the INDRA@GSI Campaign

J. Łukasik and A.S. Botvina for the INDRA-ALADIN Collaboration

High quality experimental data obtained with the 4π multi-detector system INDRA set up on the beam delivered by SIS offer now an unique opportunity to perform a detailed study, including the isospin degree of freedom, of the collisions of both symmetric (Au+Au, Xe+Sn) and asymmetric (C+Au, C+Sn) systems in a broad energy range. It covers the interesting transition region from around the Fermi energy up to relativistic energies, approaching the participant-spectator domain.

Non-central collisions of symmetric heavy systems turn out to be essentially of binary character with pronounced projectile and target like sources. Nevertheless, a sizable amount of detected particles and fragments have parallel velocities intermediate between those of the projectile and of the target [1]-[3] and their importance increases with the increasing centrality of the collision. They are often referred to as midrapidity (-velocity) emissions.

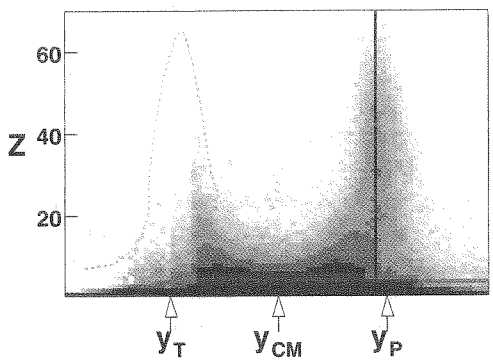

Figure 1: Z vs rapidity distribution of fragments from peripheral collisions Au+Au at 80 MeV/n. The dashed line marks the target-side region which is affected by detection thresholds. The arrows denote the target, CM and projectile rapidities, respectively.

These emissions seem to be strongly influenced by dynamical effects and are thought to proceed on a relatively short time scale. One can imagine various scenarios of formation of those midrapidity fragments following the predictions of various dynamical or hydrodynamical models. These scenarios include fast pre-equilibrium particles, neck emitted particles and fragments, as well as light fission fragments preferentially aligned in between the two main reaction partners. The importance of these midrapidity emissions can be viewed from Fig. 1, which presents the rapidity distribution of fragments emitted from the reaction Au+Au at 80 MeV/n at large impact parameters. The vertical line corresponding to the projectile-like source rapidity is drawn to emphasize a strong forward-backward asymmetry with respect to it.

Numerous analyses assume the existence of a well defined statistically equilibrated source. Can midrapidity emissions be regarded as those originating from such a source? Certainly not all of them, however at least a fraction of these emissions, in the vicinity of the Coulomb ring, can be interpreted in the framework of the statistical multifragmentation model (SMM) [4] provided, the Coulomb influence of the heavy partner on the (multi)fragmenting excited nucleus is taken into account. Inclusion of, preferentially elliptical, flow and angular momentum effects also seems to be important.

Fig. 2 presents the predictions of the SMM (left panels) and of a hybrid, the molecular dynamics model CHIMERA [5] plus the statistical sequential decay model GEMINI [6] used as an afterburner (right panels). These predictions are compared with the experimentally measured (middle panels) invariant cross sections of lithium ions emitted in peripheral Au+Au reaction at 80 MeV/n.

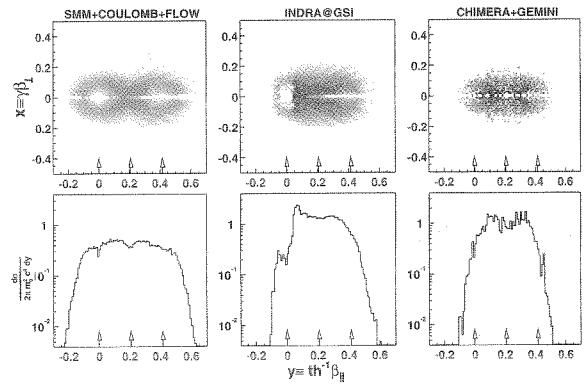

Figure 2: Invariant cross sections of lithium fragments emitted in peripheral reaction of Au+Au @ 80 MeV/n (upper row) and their projections (lower row). The central column gives the experimental results.

The above figure shows that, at least qualitatively, both models: statistical and dynamical, can account for midrapidity emissions. For a clear separation of the equilibrated and the dynamical components further studies are required, including consistent statistical treatment and careful adjustment of flow, and possibly inclusion of angular momentum and deformation effects in SMM, for a range of impact parameters and energies. Dynamical models should be traced more carefully in terms of emission and equilibration times.

References

[1] J.F. Dempsey *et al.* Phys. Rev. C **54**, 1710 (1996).
[2] J. Łukasik *et al.* Phys. Rev. C **55**, 1906 (1997).
[3] E. Plagnol *et al.* Phys. Rev. C **61**, 014606 (2000).
[4] J.P. Bondorf *et al.* Phys. Rep. **257**, 133 (1995), A.S. Botvina *et al.* GSI Preprint 2000-50.
[5] J. Łukasik *et al.* Acta Phys. Pol. B **24**, 1959 (1993).
[6] R.J. Charity *et al.*, Nuc. Phys. **A483**, 371 (1988).

SPECTATOR FRAGMENTATION INDUCED BY RELATIVISTIC ^{12}C PROJECTILES

Ketel TURZÓ for the INDRA-ALADIN Collaboration

In 1998 and 1999, a series of experiments[1] was conducted at the GSI with the INDRA multidetector [2], using high-energy beams from the heavy-ion synchrotron SIS. A part of them was devoted to asymmetric systems like ^{12}C+^{197}Au and ^{12}C+^{112,124}Sn at bombarding energies ranging from 95 to 1800 AMeV. High resolution at backward angles, dominated by emissions from the target spectator, was achieved with the Si-Si-CsI(Tl) calibration telescopes of INDRA. The physics goals in this study of spectator fragmentation are the principal question of thermal and/or dynamical breakup of the source, and, with the isotopically pure tin targets, the role of the isospin degree of freedom in the fragmentation process.

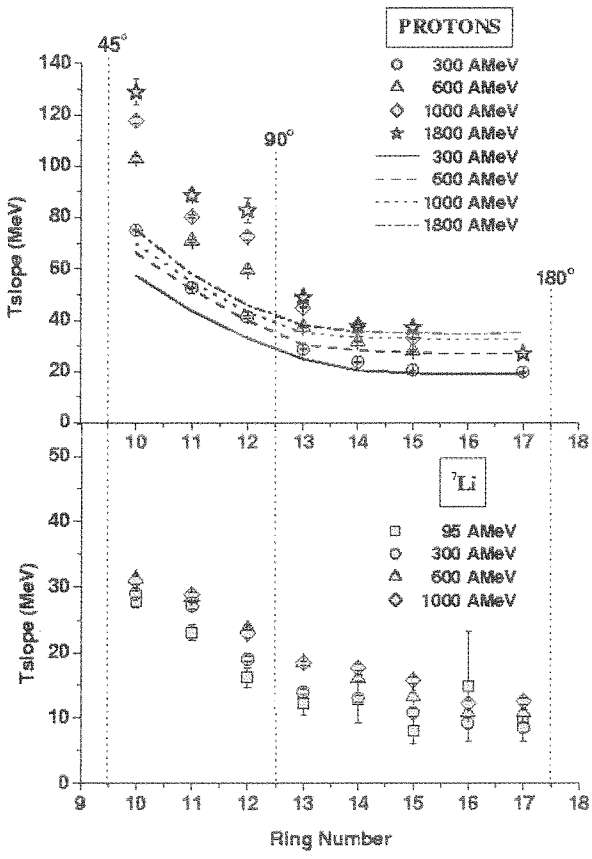

Figure 1: Slope temperatures $T_{\rm slope}$ of protons (top) and ^{7}Li (bottom) as a function of the ring number for ^{12}C+^{197}Au at the indicated bombarding energies. For the protons, the high-temperature values are given and compared with the results of the Gudima-Toneev cascade model (lines).

Inclusive energy spectra measured with the calibration telescopes were fitted, as a first approach, with two-parameter Maxwell-Boltzmann functions. A superposition of two such sources was required for the proton spectra which exhibit a low-energy component, probably containing the contributions of evaporation, and breakup at different time scales, superimposed on the hard component that extends to rather high energies. The temperatures given by the slopes of these Maxwellians show different behaviors. For the low-temperature component of protons and for the ^{7}Li ions, they increase very slowly with the incident energy. The lithium temperatures even seem to reach some saturation near 600 AMeV, consistent with the invariance of the fragment kinetic energies, observed for $3 \leq Z \leq 20$ in the ^{12}C+^{197}Au reaction for 600 to 1000 AMeV [3]. The evolution of the slope temperatures with the polar angle is shown in Fig. 1. A forward peaking is observed for the high-temperature component of protons and for the ^{7}Li ions. But, while the lithium spectra are only weakly dependent on the beam energy, pointing to a source equilibration, the high-temperature component of the protons is much more sensitive to the beam energy, in particular at forward angles. This is consistent with its presumable origin in the initial cascading stages of the reaction.

A comparison with the results obtained with the Gudima-Toneev intra-nuclear cascade model [4] is also shown in the figure. The calculated proton yields were sorted into spectra according to the ring structure of the INDRA geometry and fitted with one-source maxwellians. Between 90° and 180°, the experimental and theoretical slope temperatures are in good agreement, confirming that the primary nucleon yields extend into the spectator rapidity regime. However, the model fails to describe quantitatively the rise of the slope temperatures at polar angles smaller than 90°. Whether this discrepancy is due to the particular model used or a more general feature of the approximations made in the intra-nuclear cascade is not clear at present.

With the calibration part of the data analysis mostly completed, the physics analysis of the INDRA@GSI experiments has started. First results, so far derived from inclusive particle and fragment yields, demonstrate the usefulness of this detector for fragmentation studies up to the relativistic energy regime. The preliminary data for light particles and fragments from the ^{12}C+^{197}Au reaction show a gross behavior in agreement with previous ALADIN [3] and EOS [5] results. From the continuing analysis exclusive data are to be expected, complementing the existing data on this asymmetric collision system obtained in inverse kinematics.

References

[1] INDRA-ALADIN collaboration, Scientific Report 1999, report GSI-2000-1, p. 39 (2000)
[2] J. Pouthas et al., Nucl. Inst. and Meth. A 357(1995)418
[3] A. Schüttauf et al., Nucl. Phys. A 607(1996)457
[4] V.D. Toneev and K.K. Gudima, Nucl. Phys. A 400(1983)173c
[5] J.A. Hauger et al., Phys. Rev. C 62(2000) 024616

Source Shape Parameters in Central Ru + Ru Collisions at 400 AMeV

N. Bastid, J.P. Alard, V. Barret, A. Bendarag, P. Crochet, P. Dupieux, FOPI Collaboration
LPC Clermont-Ferrand, France

Collective flow effects in heavy ion collisions are of interest since they are expected to provide insight into the properties of hot and dense nuclear matter and its Equation of State (EoS). They are not uniquely sensitive to the stiffness of the EoS but also to other effects such as the momentum dependent interaction (MDI) and the in-medium modification of the nucleon-nucleon cross section (σ_{nn}).

In this context a complete study of the nuclear collective flow has been performed with a method which can be used in a restricted region of momentum space where the spectator contribution is believed to be negligible. In this procedure, applied successfully to DIOGENE data [1], the two-dimensional momentum distributions (p_z^{cm}/m, p_x/m), (p_z^{cm}/m, p_y/m) are fitted with anisotropic Gaussian distributions in and out of the reaction plane, respectively. The emission pattern is then approximated by an ellipsoid whose orientation and shape are defined by the flow angle, θ_F, and the in-plane and out-of-plane aspect ratios, $\lambda_{31} = \sigma_3/\sigma_1$ and $\lambda_{21} = \sigma_2/\sigma_1$, respectively. σ_i are the standard deviations, σ_3 is oriented along the flow axis.

Studied were Ru + Ru collisions at 400 AMeV measured with the FOPI detector. We focus on central events ($< b_{geo} > = 1.1$ fm) selected by means of the energy ratio criterion Erat [2]. The reaction plane is reconstructed according to the transverse momentum analysis method [3]. The observables are corrected for autocorrelation and momentum conservation effects [4] and for reaction plane fluctuations as described in [5, 1]. The shape parameters are determined with the data measured in the central part of FOPI and they are shown for proton-like fragments. We emphasise on the possibility to constrain σ_{nn} on the basis of the present data. In this purpose the shape parameters are compared in fig.1 to the predictions of the Isospin Quantum Molecular (IQMD) model [7] for a hard EoS including MDI (HM parametrisation) and different values of σ_{nn}. The shape parameters exhibit important sensitivities to this quantity. Both the flow angle and the aspect ratios rise strongly as σ_{nn} increases from $0.5\sigma_{nn}^{free}$ to $2\sigma_{nn}^{free}$ and a saturation of the shape parameters seems to be reached for $\sigma_{nn} > 2\sigma_{nn}^{free}$. It is obvious that the data cannot be reproduced by the IQMD model for $\sigma_{nn} \geq 2\sigma_{nn}^{free}$. A significant reduction of σ_{nn} seems to be excluded as well. This is consistent with results on the nuclear stopping obtained from isospin tracer observables [6].

The present work shows that the source shape parameters extracted from gaussian fits to double differential momentum distributions offer the possibility to constrain the range of the nucleon-nucleon cross section in the nuclear medium. This constitutes an important step towards the determination of the Equation of State.

References

[1] J. Gosset et al., Phys. Lett. B 247 (1990) 233 and references therein
[2] W. Reisdorf et al., Nucl. Phys. A 612 (1997) 493
[3] P. Danielewicz and G. Odyniec, Phys. Lett. B157 (1985) 146
[4] C.A. Ogilvie et al., Phys. Rev. C40 (1989) 2592
[5] J.Y. Ollitrault, Nucl-ex/9711003 (1997)
[6] F. Rami et al., Phys. Rev. Lett. 84 (2000) 1120
[7] C. Hartnack et al., Eur. Phys. J. A 1 (1998) 151

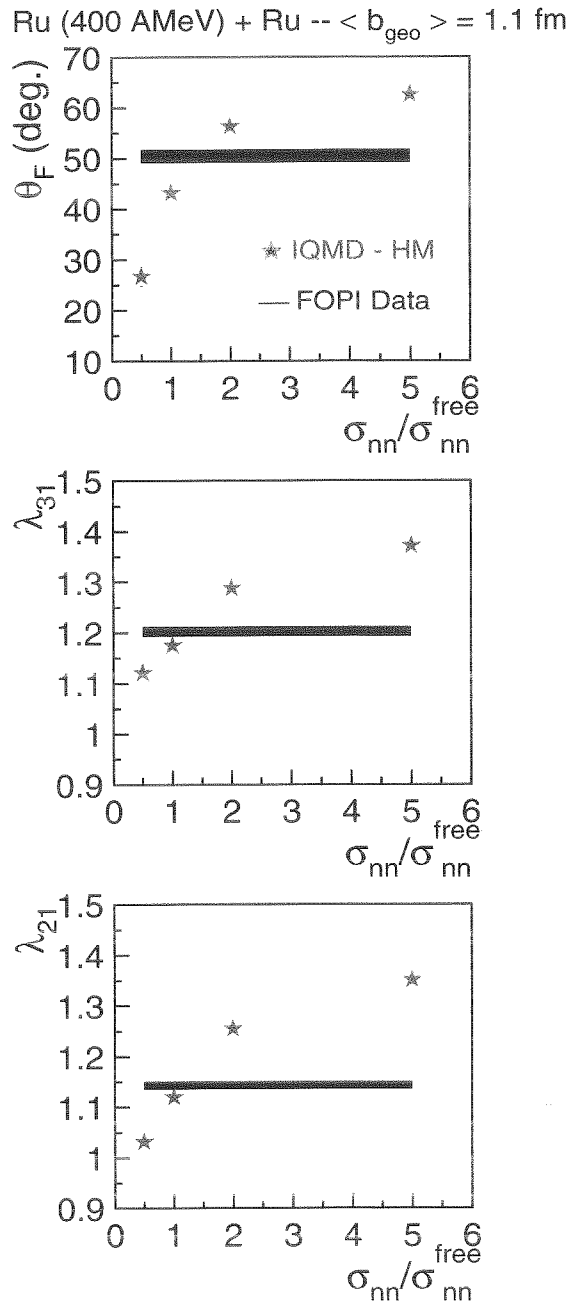

Figure 1: Flow angle and aspect ratios of proton-likes measured in central Ru + Ru reactions at 400 AMeV. The data are compared to the IQMD predictions (HM version) for different values of σ_{nn}. The stars correspond to the model calculations. The solid line represents the experimental data and includes the statistical uncertainties.

The Isospin Influence on Squeeze-out Phenomena in Heavy Ion Collisions

M. Petrovici[1,2], G. Stoicea[1,2], Y. Leifels[3,2], A. Andronic[1], N. Herrmann[3], K. Hildenbrand[2], and the FOPI Collaboration
[1]NIPNE-Bucharest, [2]GSI-Darmstadt, [3]Univ. of Heidelberg

Equilibration of the isospin degree of freedom, the isospin dependence of the sidewards flow, balance energy, preequilibrium nucleon emission and subthreshold pion production are phenomena proven to be sensitive to the isospin-dependent nuclear equation of state and in-medium nucleon-nucleon cross section [1]. In this contribution we will report on preliminary experimental evidence on the influence of the N/Z content of the spectator matter on the azimuthal distributions. We used the experimental data obtained with the Phase II of the FOPI detector at GSI - Darmstadt for Ru + Zr and Zr + Ru collisions at 400 A·MeV [2]. The charge multiplicity in the central drift chamber was used in order to select the collision geometry. The impact parameter value was extracted from a standard geometrical sharp cut-off approximation for the reaction cross section. The reaction plane reconstruction is based on the transverse momentum method. For an impact parameter of 5 fm, a geometrical estimate based on straight trajectory approximation gives for the fireball three times lower left-right N/Z asymmetry relative to 1.18 : 1.4 corresponding to the spectators for Ru + Zr combination. In such a situation, even if the chemical equilibrium of the fireball is not completely reached the remaining asymmetry can be neglected in a first approximation and we have to do with an expanding object in the presence of spectator matter asymmetric in N/Z.

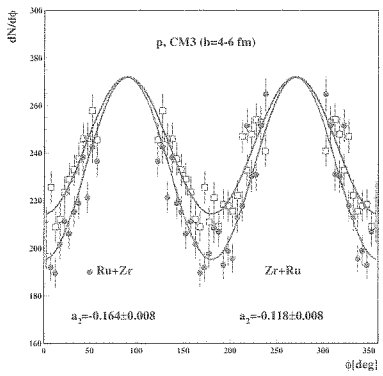

Figure 1: Azimuthal proton distributions for Ru + Zr (dots) and Zr + Ru (squares) measured between 0^o-60^o and 300^o-360^o and reflected relative to 90^o and 270^o, respectively

In the nuclear medium isospin dependent nucleon-nucleon interaction will influence the azimuthal distribution of different particles emitted by the fireball and interacting with the spectator matter. The left - right asymmetry being small, the effect on the azimuthal distributions cannot be expected to be very large. For this reason, our studies are performed in a system of coordinates rotated by the sidewards flow angle [3]. Breaking in this way the azimuthal symmetry of the experimental device we have to symmetrise the experimental distributions obtained in the azimuthal range 0^o-60^o and 300^o-360^o relative to 90^o and 270^o respectively in order to obtain the complete azimuthal distribution. Although, the azimuthal distributions obtained using this recipe do not correspond to the real situation (they correspond to a situation where the fireball has on both sides Ru-like spectators in the case of Ru + Zr or Zr-like spectators for the Zr on Ru combination, respectively) we prefer such representations in order to show also the results of the fits with a standard-second order Fourier expansion in azimuth.

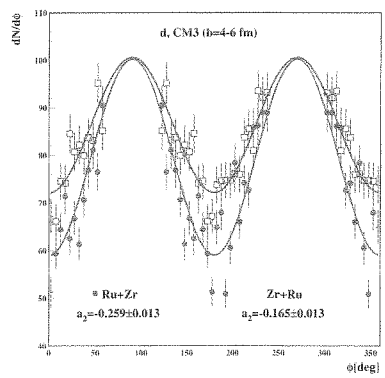

Figure 2: The same as Fig.1 but for deuterons

The results for impact parameters between 4 and 6 fm and a range in the scaled transverse momentum $p_t^{(0)} = (p_t/A)/(p_P^{cm}/A_P)$ of 0.8-1.2 are presented in Fig. 1 for protons and Fig. 2 for deuterons. The distributions are normalised at 90^o. Although quite preliminary, the result seem to indicate an influence of the N/Z value of the spectator matter on the observed azimuthal distributions of the order of 30% for p and about 45 % for deuterons in a_2 coefficients. Detailed analysis will confirm in which extend they are sensitive probes for studying the isospin dependence of the in-medium nucleon-nucleon interaction used in microscopic transport codes.

References

[1] Bao-An Li *et al.*, Int. J. Mod. Phys. **E7**, 147 (1998) and references therein
[2] F. Rami *et al.*, Phys. Rev. Lett. **84**, 1120 (2000)
[3] A. Andronic *et al.*, Nucl. Phys. **A679**, 765 (2001)

^{3}H/^{3}He Squeeze-Out - A Signature of the Fireball's Isospin Distribution?

M. Petrovici[1,2], G. Stoicea[1,2], Y. Leifels[3,2], A. Andronic[1,2], N. Herrmann[3], K. Hildenbrand[2], and the FOPI Collaboration

[1]NIPNE-Bucharest, [2]GSI-Darmstadt, [3]Univ. of Heidelberg

The Phase I FOPI data evidence for highly central Au + Au collisions at 100, 150 and 250 A·MeV systematically larger mean kinetic energies for ^{3}He fragments relative to the ^{3}H values [1]. The EOS Collaboration find the same trend with somewhat larger size [2]. Microscopic transport models [3] and hybrid hydrodynamical models, including pure Coulomb repulsion at the freeze-out moment [4] do not succeed to explain quantitatively this difference. Similar findings are recently reported by the INDRA Collaboration [5] for ^{129}Xe + ^{119}Sn at 50 A·MeV. At a higher incident energy 1.15 A·GeV it seems that this difference disappears. Both types of fragments have the same mean kinetic energy, following a trend as a function of the fragment mass only, which is specific for the emission from an expanding source.

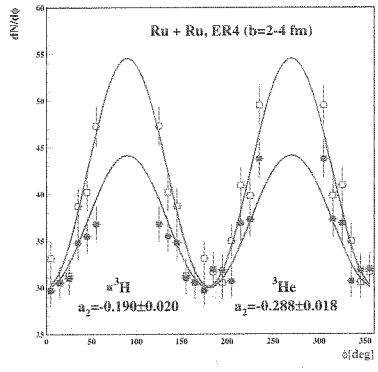

Figure 1: ^{3}He and ^{3}H azimuthal distributions for Ru + Ru collision at b=2-4 fm and $p_t^{(0)} = (p_t/A)/(p_P^{cm}/A_P)$ range of 0.8-1.2

Corroborating these facts, based on the dynamics of the expansion suggested by hydrodynamical models, one could imagine that due to the Coulomb repulsion, the outer layers of the initial fireball are to some extend more proton rich than the inner zones. If this is the case, then one expects ^{3}He fragments originating with higher probability from these regions of the fireball and consequently having larger expansion velocities as far as the expansion has an almost linear dependence as a function of the distance from the the center of the fireball [3, 4]. Within such a scenario, the ^{3}He fragments are supposed to be emitted preferentially in earlier phases of the expansion than the ^{3}H fragments, and feel a larger shadowing from the spectators passing by. For mid-central collisions this may lead to a difference in the squeeze-out signal. In order to check this, we analysed data of Ru + Ru collision at 400 A·MeV obtained with the Phase II - FOPI experimental configuration.

The mass and charge identification of A=3 fragments is achieved using the combined information from the central drift chamber (CDC) and the time-of-flight Barrel surrounding the CDC. The low momentum range cannot be used due to the geometrical gap between the CDC and HELITRON. However, the kinetic energy distribution of ^{3}He and ^{3}H, for highly central collisions (1% cross section), show similar trends as those observed in Au + Au collision [1]. The selection of the collision geometry and reaction plane determination are explained in a different contribution to this report. The azimuthal distributions are obtained in the reference frame rotated by the sideward flow angle relative to the collision axis. Due to geometrical cuts the experimental data are analysed in the angular range 0^o-60^o and 300^o-360^o. The angular distributions presented in Fig.1 are obtained by symmetrising these results relative to 90^o and 270^o, respectively. For an impact parameter range of b = 2-4 fm one observes a much larger squeeze-out signal for ^{3}He relative to ^{3}H. The two azimuthal distributions are normalised at 0^o. A second order Fourier expansion ($f(\Phi) = a_o(1 + a_2 cos(2\Phi))$) is used to fit the azimuthal distributions. The resulting a_2 coefficients for all fragments from A=1 to A=4 are presented in Fig.2. While p,d and ^{4}He show the well known enhancement of the squeeze-out signal as a function of mass, larger a_2 values for ^{3}He relative to ^{3}H can be observed. Different cross-checks and comparisons with microscopic model predictions are in progress. However, this preliminary result seem to indicate that the relative value of the squeeze-out signal of ^{3}H and ^{3}He could be related to the isospin distribution in the fireball at the freeze-out moment. Obviously, other contributions (like Coulomb focusing) to the observed effect are not excluded.

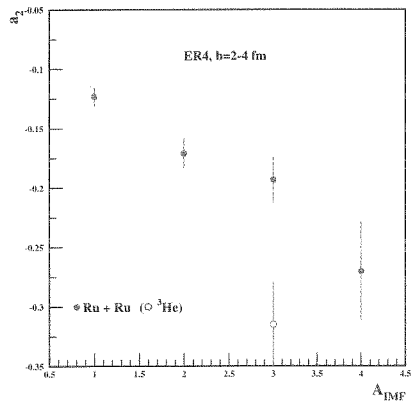

Figure 2: a_2 values as a function of mass of the reaction products for Ru + Ru collision for the same geometry and $p_t^{(0)}$ values as for Fig. 1

References

[1] G. Poggi et al., Nucl. Phys. **A586**, 755 (1995)
[2] M. Lisa et al., Phys. Rev. Lett. 7526621995
[3] P. Danielewicz, et al., Phys. Rep. 517161995
[4] M. Petrovici, FOPI Collaboration, "Heavy Ion Physics at Low Intermediate and Relativistic Energies",World Scientific, 1997, p. 216
[5] D. Gorio et al., Eur. Phys. J. A7,245(2000)
[6] A. Andronic et al., Nucl. Phys. **A679**, 765 (2001)

Incident Energy and A_{part} Dependence of the Fireball Expansion in Au+Au Collisions

G. Stoicea[1,2], M. Petrovici[1,2], A. Andronic[1,2], A. Gobbi[2], N. Herrmann[3], K. Hildenbrand[2], Y. Leifels[3,2], W. Reisdorf[2], and the FOPI Collaboration
[1]NIPNE-Bucharest, [2]GSI-Darmstadt, [3]Univ. of Heidelberg

A unified representation of the squeeze-out trends can be done in terms of the azimuthal distribution of the kinetic energy [1, 2]. A comprehensive description of the squeeze-out phenomena in the energy range 0.25 - 1.15 A·GeV is based on the parametrisation of the transverse mass spectra with an expression describing a radially symmetric expanding shell [1]. As far as such a situation can hardly be encountered in heavy ion collisions and is not specific at all for mid-central collisions, a presentation of the experimental information free of any model is preferred.

In this contribution we present results on azimuthal distributions of the collective flow β (=v/c) which is extracted from the rise of the experimental mean kinetic energy $< E_{kin}^{cm} >$ with the mass of the reaction products. We use the full coverage of the FOPI experimental device in order to extract as precise as possible this experimental information. Therefore, we have to combine the information from the forward plastic wall detector where the reaction products are identified only by their charge with the one from the central drift chamber (CDC) where the reaction products are identified by their mass. This is achieved by using the information obtained during earlier Phase I experiments when Si-CsI telescopes delivered a very good mass and charge separation of the light products within the acceptance of the plastic wall [3]. The collision geometry definition is based on CDC charged particle multiplicity and the ratio of transversal to longitudinal energies [4]. The analysis is performed in a reference frame with the z axis along the sidewards flow direction and within $80^o \leq \Theta_{cm} \leq 100^o$ polar angular range. The azimuthal distributions are symmetric with respect to 90^o and 270^o, hence, we overlap 0^o-90^o and 270^o-360^o azimuthal ranges to decrease the statistical errors, make five bins in azimuth and reflect the results in order to cover the full angular range 0^o-360^o. The average flow value, β_o, and the out-of-plane - in-plane difference, $\Delta\beta$, are taken from a fit to the flow (β=v/c) azimuthal distributions using the following expression:

$$\beta(\Phi)=\beta_o - \Delta\beta \cdot cos2\Phi$$

The elliptic flow characterised by the major axis perpendicular to the reaction plane rises continuously from 90 to 400 A·MeV for mid-central collisions (Fig. 1). At 90 A·MeV the in-plane and out-of-plane flow values are very similar, specific for the E_{tran} region [4]. At all energies the flow β_o increases with the centrality, namely with increasing the baryonic content of the fireball (A_{part}), while $\Delta\beta$, the difference between out-of-plane and in-plane flow, decreases showing the shadowing effect of the spectator matter. At lower centralities, i.e. larger impact parameters, the spectator matter being more compact, the bulk of products detected in the reaction plane emitted by the fireball and not hindered by the spectators correspond to the late phase of the expansion when the flow is weaker and the spectators moved apart from the collision zone.

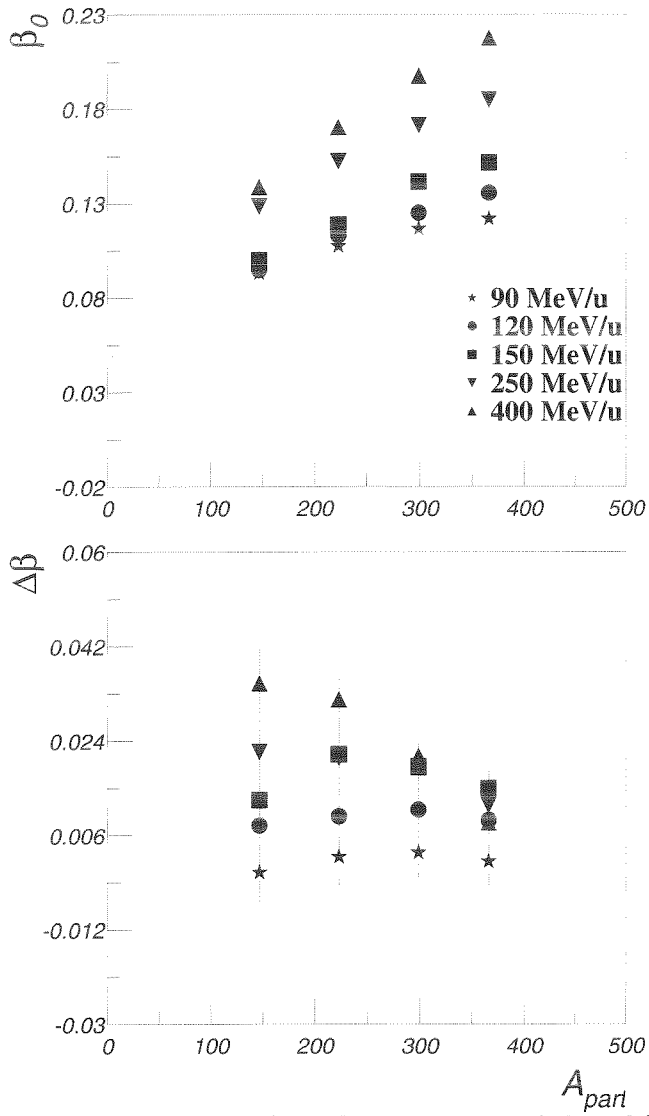

Figure 1: The average, β_o, and in-plane - out-of-plane difference, $\Delta\beta$, of the flow value as a function of centrality, for 90, 120, 150, 250, 400 A·MeV

These experimental trends can be followed in Fig.1. The continuation of these studies at higher energies and detailed comparisons with microscopic transport model predictions are in progress.

References

[1] S. Wang et al., Phys. Rev. Lett. 76 (1996) 3911
[2] M. Petrovici, FOPI Collaboration, Proc. of International Research Workshop on Heavy Ion Physics at Low, Intermediate and Relativistic Energies using 4π Detectors, ed. M. Petrovici et al., World Scientific, 1997, p. 216
[3] G. Poggi et al., Nucl. Phys. **A586**, 755 (1955)
[4] A. Andronic et al., Nucl. Phys. **A679**, 765 (2001)

Kaon and Antikaon Production in Proton-Nucleus Collisions[B,C]

W. Scheinast (FZ Rossendorf) and the KaoS Collaboration

Recent experiments on K-meson production in nucleus-nucleus at SIS energies found that the K^-/K^+ ratio is enhanced by about 2 orders of magnitude as compared to proton-proton collisions at proton beam energies close to threshold [1]. Within transport calculations, this enhancement is explained by (i) a reduced in-medium mass of K^- mesons and (ii) multiple step processes like strangeness exchange reactions $\pi Y \rightarrow K^- N$ with $Y = \Lambda, \Sigma$ [2]. The investigation of K^- mesons in proton-nucleus collisions will help to disentangle these two effects because (i) the effective K^- mass is expected to be reduced by about 25% in nuclear matter at saturation density whereas (ii) strangeness exchange reactions are negligible.

Using the Kaon Spectrometer at SIS/GSI we have performed the first measurements of K^- production yields in proton-nucleus collisions at proton energies below 4 GeV. The heavy ion synchrotron delivered protons beam with energies of 1.6, 2.5 and 3.5 GeV with intensities up to 10^{10} protons/sec impinging on C and Au targets of 7 and 2 mm thickness, respectively. A trigger based on the kaon time-on-flight and tracking reduced the data rates to about 5 kHz. The K meson momentum distributions were measured at laboratory angles between Θ_{lab}=32-64 degrees.

Figure 1 presents preliminary double differential production cross sections of K^+ and K^- mesons measured in p+C and p+Au collisions at 2.5 and 3.5 GeV at $\Theta_{lab}=40^o$ as function of the laboratory momentum. The data taken at 3.5 GeV beam energy are not yet corrected for the tracking trigger efficiency. This might be the reason for the structure in the spectra around p_{lab}=700 MeV/c. The smooth spectra measured at 2.5 GeV proton energy were taken at reduced beam intensities without tracking trigger.

Figure 2 shows the K^-/K^+ ratio for p+C and p+Au collisions at a beam energy of 3.5 GeV obtained from the spectra as presented in figure 1. The maximum values of the ratio are about 0.04 and 0.03 for p+C and p+Au, respectively. The corresponding value calculated from inclusive cross sections measured in p+p collisions at 3.5 GeV is about 0.033. Before drawing conclusions on in-medium effects from these values, inclusive K meson production yields have to be extracted from the proton-nucleus data by analyzing the measured polar angle distributions. Moreover, in-medium effects should be more visible in the data measured at 2.5 GeV which is the threshold energy for antikaon production in proton-proton collisions.

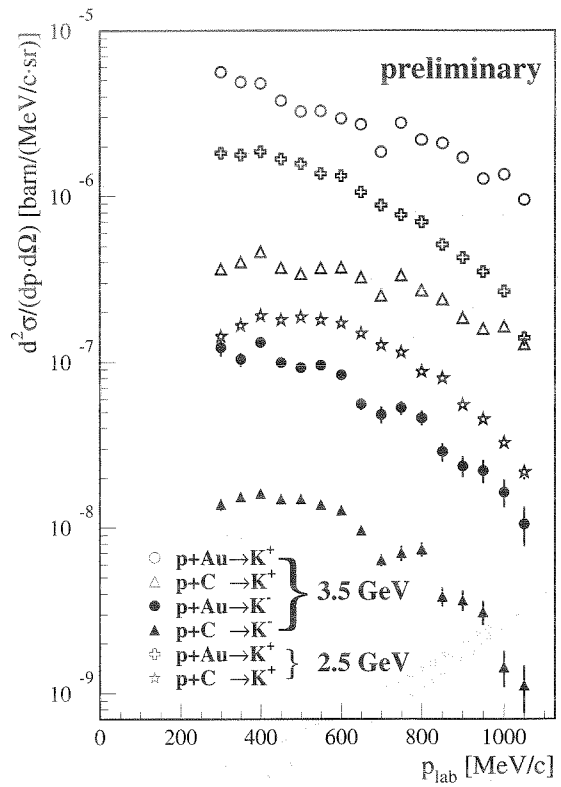

Figure 1: Double differential K^+ and K^- production cross sections measured in p+C and p+Au collisions at 2.5 and 3.5 GeV bombarding energy at a laboratory angle of $\Theta_{lab}=40^o$ as function of laboratory momentum.

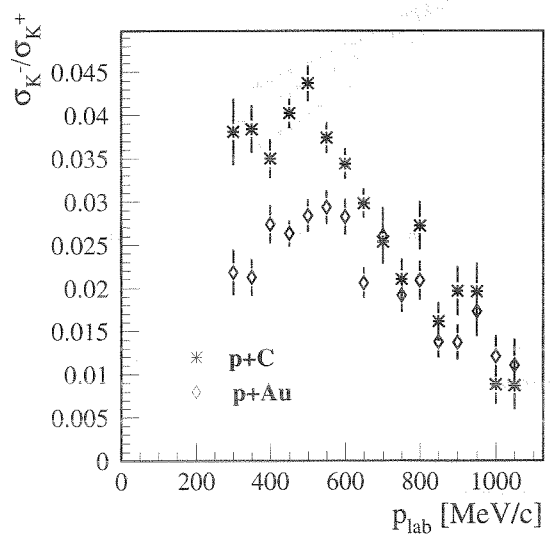

Figure 2: Preliminary K^-/K^+ ratio measured in p+C and p+Au collisions at 3.5 GeV bombarding energy at a laboratory angle of $\Theta_{lab}=40^o$ as function of laboratory momentum.

References

[1] F. Laue, C. Sturm et al., Phys. Rev. Lett. 82 (1999) 1640

[2] W. Cassing and E. Bratkovskaya, Phys. Rep. 308 (1999) 65

Kaon and Pion Production in Nucleus-Nucleus Collisions from 0.6 to 2 AGeV[B,G]

C.Sturm[2], I.Böttcher[4], M.Dębowski[5], A.Förster[2], E.Grosse[6], P.Koczoń[1], B.Kohlmeyer[4], F.Laue[1], M.Mang[1], M.Menzel[4], L.Naumann[6], H.Oeschler[2], F.Pühlhofer[4], E.Schwab[1], W.Scheinast[6], Y.Shin[3], P.Senger[1], J.Speer[2], H.Ströbele[3], G.Surowka[1,5], F.Uhlig[2], A.Wagner[2,6], W.Waluś[5]
[1]GSI, [2]TU Darmstadt, [3]Univ. Frankfurt, [4]Univ. Marburg, [5] Univ. Cracow (Poland), [6]FZ Rossendorf
KaoS Collaboration

During the past years the KaoS collaboration has provided for various collision systems a rather detailed set of data on meson production at SIS energies from 0.6 to 2 A·GeV. Inclusive spectra of K^+ mesons are published in [1]. A selection of π^+ spectra is shown in Fig. 1 for C+C and Au+Au collisions at various energies around midrapidity. All spectra exhibit the typical concave shapes, interpreted as due to decaying Δ resonances and free pions [2]. The slope parameters of the high-energy parts agree well with those of the K^+ spectra.

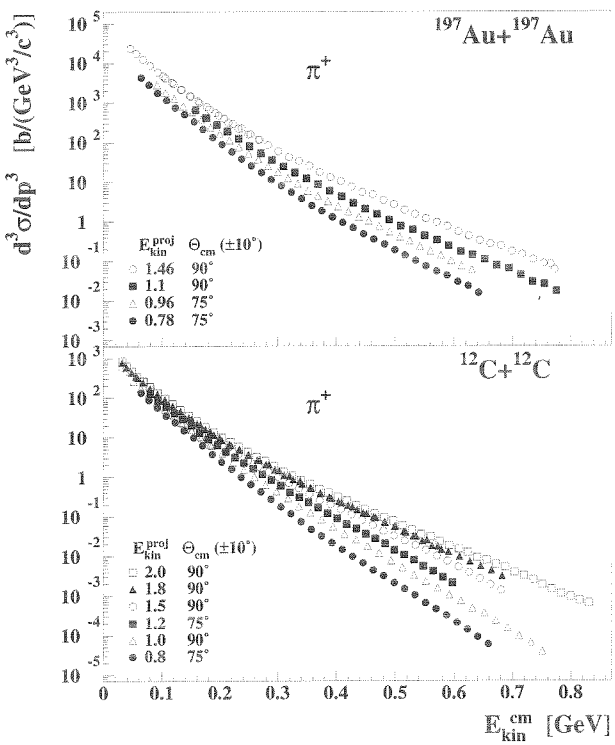

Figure 1: *Spectra of positively charged pions around midrapidity at various incident energies.*

Microscopic transport calculations indicate that the yield of kaons created in collisions between heavy nuclei at subthreshold beam energies (E_{beam} ¡ 1.58 GeV) is sensitive to the compressibility of nuclear matter at high baryon densities [3, 4]. This sensitivity is due to the production mechanism of K^+ mesons at subthreshold beam energies requiring multiple nucleon-nucleon or meson-nucleon collisions. These processes are expected to be enhanced at high baryon densities, and the densities reached in the fireball depend on the nuclear equation of state [5]. Pions are rather insensitive to this parameter of the nuclear equation of state. Their spectra and yields can be used to gauge phase-space effects [1].

Two effects influence the K^+ yield, the compressibility of the nuclear matter as mentioned and possibly a modification of the kaon properties in the dense nuclear medium. Our idea is to disentangle these two competing effects by studying K^+ production in a very light (^{12}C+^{12}C) and a heavy collision system (^{197}Au+^{197}Au) at different beam energies near threshold. The maximum baryonic density reached in Au+Au collisions depends on the nuclear compressibility [4, 6] whereas in the small C+C system this dependence is very weak [7]. The repulsive K^+N potential is assumed to depend nearly (or less than) linearly on the baryonic density [8] and thus reduces the kaon yield accordingly.

Our concept is summarized in Fig. 2. It shows in the upper part the pion and K^+ multiplicity per nucleon for C+C and Au+Au collisions as a function of the beam energy. The pion data points are scaled by a factor of 1/100; they represent the sum of charged and neutral pions as calculated from the measured π^+ multiplicities according to the isobar model [9]. This model explains very well the π^+/π^- ratios measured in Au+Au collisions [10]. The pion multiplicity per nucleon is smaller in Au+Au than in C+C collisions whereas the K^+ multiplicity per nucleon is larger. This observation demonstrates a key difference between pion and kaon emission. In order to illustrate the different behaviour of pions and kaons in nuclear matter we plot the ratio of the pion and kaon excitation functions $(M/A)_{\mathrm{Au+Au}}/(M/A)_{\mathrm{C+C}}$ in the lower panel of Fig. 2. The error bars of the kaon multiplicities include systematic uncertainties due to the extrapolation procedure. The experimental uncertainties due to efficiencies, acceptances and beam normalization, however, cancel in the ratio and therefore have not been taken into account.

The pion ratio $(M/A)_{\mathrm{Au+Au}}/(M/A)_{\mathrm{C+C}}$ (full triangles) is smaller than unity and decreases with decreasing beam energy. A ratio smaller than unity might be caused by the reabsorption of pions which is more effective in the larger system or by decompressional flow of nuclear matter which is expected to be more important in Au+Au than in C+C collisions. In a thermal picture both arguments are equivalent.

In contrast to the pion data, the kaon ratio $(M/A)_{\mathrm{Au+Au}}/(M/A)_{\mathrm{C+C}}$ increases by a factor of almost 3 with decreasing beam energy. An increase of the K^+ yield with decreasing beam energy is found by a transport model calculation in central Au+Au collisions if a soft instead of a hard equation of state is used [4]. The sensitivity

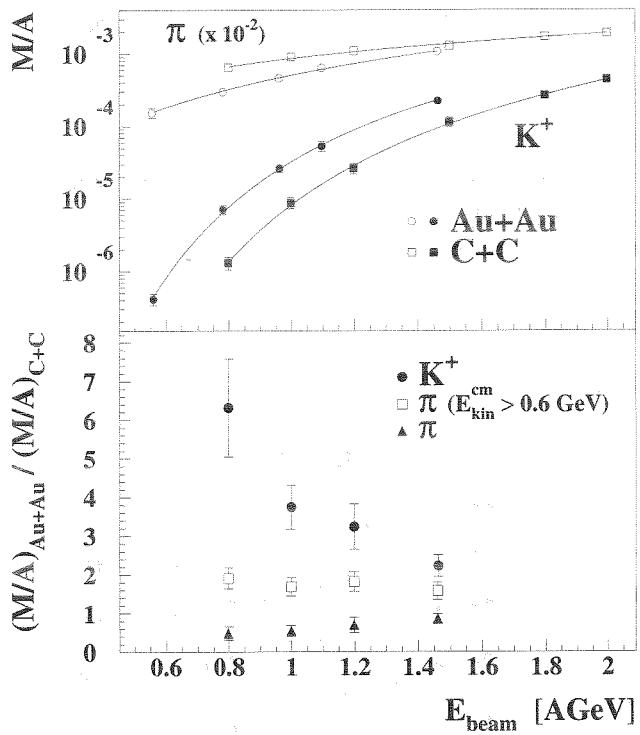

Figure 2: *Upper panel: Pion and K^+ multiplicity per A for the two collision systems as a function of E_{beam}. The pion multiplicities represent all pions species. The lines are to guide the eye. Lower panel: Ratio of the multiplicities per nucleon (Au+Au over C+C collisions) for K^+ mesons (full circles), pions (full triangles) and high-energy pions (E^{cm}_{kin} > 0.6 GeV, open squares) as a function of E_{beam}.*

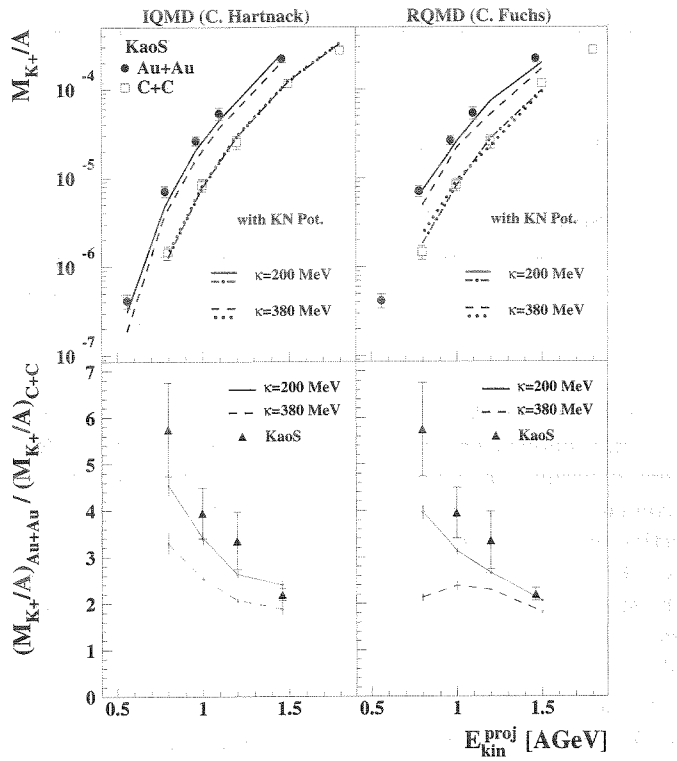

Figure 3: *The upper parts show the inclusive K^+ multiplicities per A together with model calculations for two values of the nuclear compressibility. The lower parts display the ratio $(M/A)_{Au+Au}/(M/A)_{C+C}$ as in fig. 2 together with the model predictions.*

of the kaon multiplicity on the nuclear compressibility is enhanced at beam energies well below the kaon production threshold because the energy required to create a K^+ meson has to be accumulated by multiple collisions of participating nucleons.

In order to exclude trivial phase-space effects as the reason for the observed behaviour we present in the lower panel of Figure 2 the ratio $(M/A)_{\mathrm{Au+Au}}/(M/A)_{\mathrm{C+C}}$ for pions with kinetic energies above $\mathrm{E}^{cm}_{kin} = 0.6$ GeV. The production of these pions is equivalent – in terms of available energy – to the production of K^+ mesons with a kinetic energy above 70 MeV. At this energy the kaon spectra have reached their maximum yields.

Figure 3 shows a comparison of the experimental results with two transport model calculations (lhs: IQMD [11], rhs: RQMD [7]). Both calculations have been performed with KN potential and a compressibilty of 200 MeV and 380 MeV. In the upper part the K^+ multiplicity per A is shown as a function of the beam energy both for Au+Au and C+C collisions. As expected the calculations with κ = 200 MeV yields higher multiplicities than those with κ = 380 MeV for Au+Au collisions, while for C+C no sensitivity is seen. The data are best described with κ = 200 MeV, yet the data are still slightly higher.

The lower part of Fig. 3 shows the ratio of the $(M/A)_{\mathrm{Au+Au}}/(M/A)_{\mathrm{C+C}}$ as measured and as calculated. In both calculations the ratio rises towards lower incident energies using a κ of 200 MeV in agreement with the data. For the stiffer equation of state the two calculation differ somewhat, but clearly deviate strongly from the data. These trends are rather independent whether a KN potential is used or not [7]. This evidences that the used ratio is a very sensitive quantity in extracting the compressibility of nuclear matter and that this ratio does depend little on less known input quantities.

References

[1] C. Sturm et al., Phys. Rev. Lett. **86** (2001) 39
[2] C. Müntz et al., Z. Phys. A **357** (1997) 399.
[3] J. Aichelin and C.M. Ko, Phys. Rev. Lett. **55** (1985) 2661
[4] G.Q. Li and C.M. Ko, Phys.Lett. **B 349** (1995) 405
[5] C. Fuchs et al., Phys. Rev. **C 56** (1997) R606
[6] J. Aichelin, Phys. Rep. **202** (1991) 233
[7] C. Fuchs, et al., Phys. Rev. Lett. (in print)
[8] J. Schaffner-Bielich, J. Bondorf, I. Mishustin, Nucl. Phys. **A 625** (1997) 325
[9] B. J. Ver West and R. A. Arndt, Phys. Rev. **C 25** (1982) 1979
[10] A. Wagner et al., Phys. Lett. **B 420** (1998) 20
[11] C. Hartnack, J. Aichelin, private communication

Centrality Dependence of Kaon and Antikaon Production in Ni+Ni Collisions at SIS Energies [B,G]

M. Menzel[4], I.M. Böttcher[4], M. Dębowski[5,6], F. Dohrmann[6], A. Förster[2], E. Grosse[6,7], P. Koczoń[1], B. Kohlmeyer[4], F. Laue[1,*], L. Naumann[6], H. Oeschler[2], F. Pühlhofer[4], W. Scheinast[6], E. Schwab[1], P. Senger[1], Y. Shin[3], H. Ströbele[3], C. Sturm[2], G. Surówka[5], F. Uhlig[2], A. Wagner[6], W. Waluś[5]
[1]GSI Darmstadt, [2]TU Darmstadt, [3]Univ. Frankfurt, [4]Univ. Marburg, [5]Univ. Kraków,
[6]FZ Rossendorf, [7]TU Dresden
The KaoS Collaboration

Kaons and antikaons are regarded as a promising probe to study hadron properties in dense nuclear matter. Recent experimental results obtained with the Kaon Spectrometer indicate modifications of the in-medium properties of K^+ and K^-. Remarkable results are that the K^-/K^+ ratio is enhanced compared to pp collisions [1,2,3], the spectral slope for the antikaons is steeper than for the kaons [2] and a preferential out-of-plane emission of K^+ is observed [4].

In order to study the kaon production as a function of the reaction centrality and the beam energy, we have measured K^+ and K^- mesons around midrapidity ($\theta_{lab} = 40° \pm 4°$) in Ni+Ni reactions at beam energies of 1.1 (K^+ only), 1.5 and 1.93 AGeV. The multiplicity of charged particles measured by a target hodoscope is used to determine the centrality. The data set is subdivided in five centrality bins MUL1 to MUL5 for each beam energy. From a measurement under minimum bias conditions the reaction cross section is determined. For all beam energies we find a reaction cross section of $\sigma_R = 2.9 \pm 0.3$ barn, which agrees with the geometric model. The relative reaction cross section for each centrality class $\sigma_{R,MUL}/\sigma_R$ is given in Table 1 for 1.5 and 1.93 AGeV. Errors of about 10 % have to be added to the ratio $\sigma_{R,MUL}/\sigma_R$.

Figure 1 shows the invariant cross sections of K^+ (full circles) and K^- (open circles) for central to peripheral collisions (see middle panel: MUL 5 to MUL 1) as a function of the center-of-mass kinetic energy at beam energies of 1.1, 1.5 and 1.93 AGeV. The K^- mesons are scaled by a factor of 20 (see lower panel) and the yields in the bins are scaled by factors of 10 (see upper panel). The error bars shown are due to statistics only and a systematic error of 10% has to be added, caused by beam normalization, acceptance determination and trigger efficiency. The lines represent Boltzmann distributions $d^3\sigma/dp^3 \propto exp(-E_{CM}/T)$ fitted to the spectra individually for each multiplicity bin. The integrated kaon cross sections $4\pi(d\sigma_K/d\Omega_{CM})$ and the inverse slope parameters T as a function of the centrality are given in Table 1 for 1.5 and 1.93 AGeV. The errors of both quantities include the systematic effects. For all beam energies the spectral slopes decrease (Figure 1) and the inverse slope parameters T increase (Table 1) with increasing centrality of the reaction for both, kaons and antikaons.

We determined the average multiplicity per number of participating nucleons M_K/A_{part} as a function of the number of participating nucleons. M_K is calculated via $M_K =$

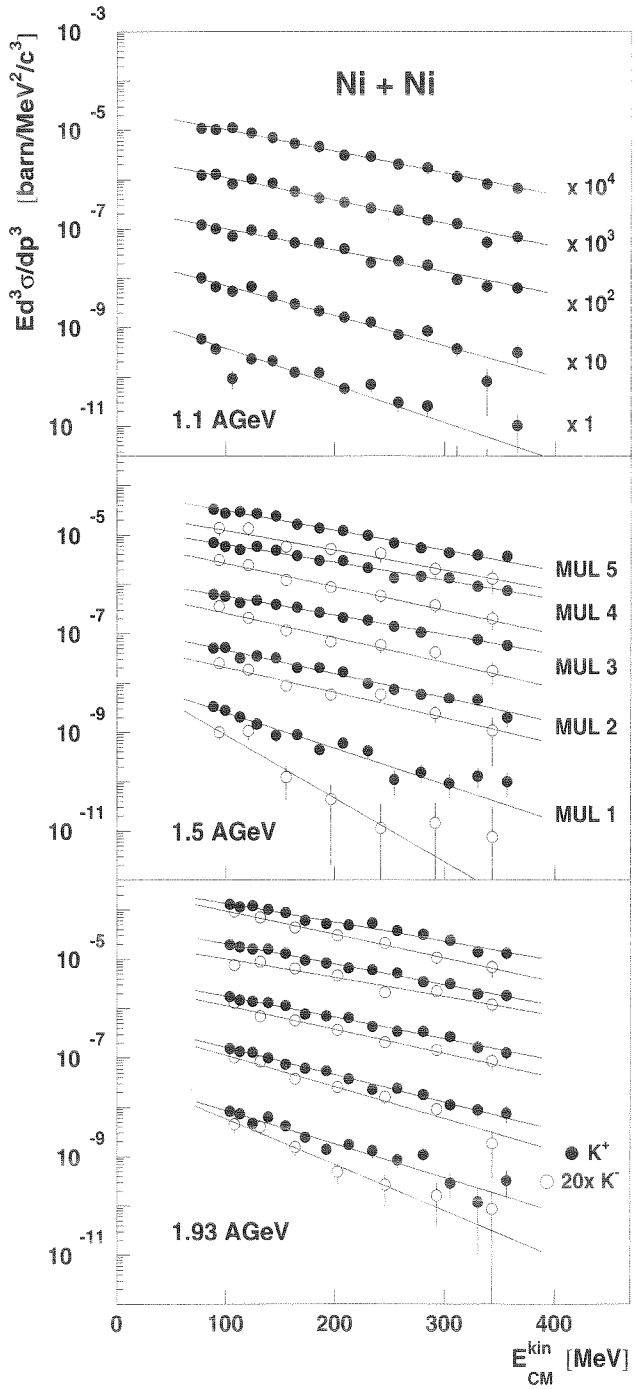

Figure 1: *K^+ and K^- invariant cross sections as a function of the kinetic energy and the centrality of the reaction measured around midrapidity ($\theta_{lab} = 40° \pm 4°$) for Ni+Ni collisions at different beam energies (preliminary).*

Energy	MUL	$\frac{\sigma_{R,MUL}}{\sigma_R}$	$4\pi\frac{d\sigma_K}{d\Omega_{CM}}$ [mb]	T [MeV]
	1	0.41	2.2 ± 0.2	55 ± 4
1.5	2	0.23	4.5 ± 0.4	79 ± 6
AGeV	3	0.18	6.2 ± 0.5	96 ± 7
K^+	4	0.14	7.2 ± 0.5	101 ± 8
	5	0.05	3.3 ± 0.3	93 ± 7
	1	0.44	7.6 ± 0.7	58 ± 5
1.93	2	0.23	14.8 ± 1.2	70 ± 6
AGeV	3	0.16	18.1 ± 1.4	88 ± 7
K^+	4	0.11	21.4 ± 1.6	91 ± 7
	5	0.06	14.8 ± 1.2	97 ± 7
	1	0.41	0.06 ± 0.011	33 ± 3
1.5	2	0.23	0.10 ± 0.012	74 ± 6
AGeV	3	0.18	0.12 ± 0.013	78 ± 7
K^-	4	0.14	0.13 ± 0.014	80 ± 7
	5	0.05	0.07 ± 0.011	90 ± 10
	1	0.44	0.30 ± 0.06	43 ± 3
1.93	2	0.23	0.51 ± 0.07	63 ± 7
AGeV	3	0.16	0.56 ± 0.06	79 ± 10
K^-	4	0.11	0.57 ± 0.07	96 ± 8
	5	0.06	0.46 ± 0.05	81 ± 7

Table 1: Relative reaction cross sections, K^+ and K^- production cross sections and inverse slope parameters as a function of the centrality for Ni+Ni collisions at beam energies of 1.5 and 1.93 AGeV (preliminary).

$\sigma_K/\sigma_{R,MUL}$ with $\sigma_K = 4\pi(d\sigma_K/d\Omega_{CM})$ and with the reaction cross section for each multiplicity class $\sigma_{R,MUL}$. A_{part} is calculated from the number of nucleons in the overlap of the colliding nuclei. The impact parameter b is determined for the center of each multiplicity bin. The kaon and antikaon multiplicity per A_{part} (full circles: K^+, open: K^-) is shown in Figure 2 (different scaling factors) with a parameterization according to $M_K \propto A_{part}^{\alpha}$ (lines).

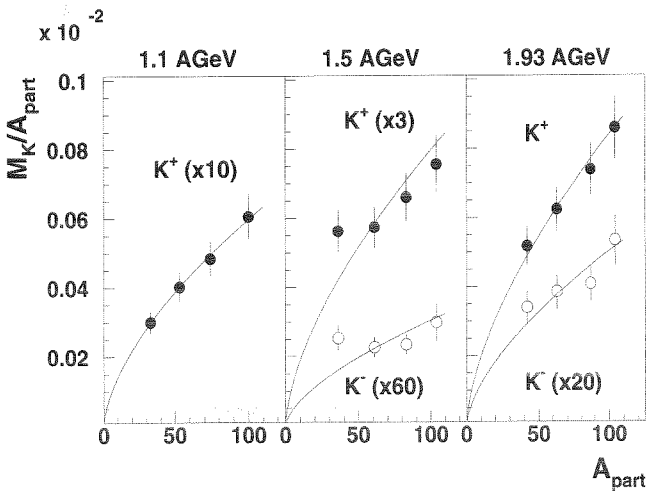

Figure 2: Kaon and antikaon multiplicity per A_{Part} *as a function of* A_{Part} *for Ni+Ni collisions at beam energies of 1.1, 1.5 and 1.93 AGeV (preliminary).*

The multiplicities for MUL 1 are not shown because the errors in integrating the cross sections are larger compared to the other bins. Within the uncertainties of A_{part} we get a common $\alpha = 1.62 \pm 0.21$ for K^+ and K^- and for all beam energies. Values of α larger than unity indicate that the nucleons participate more than once in the kaon production.

In Figure 3 we present the K^-/K^+ ratio as a function of the impact parameter b for the beam energy 1.5 AGeV (full triangles) and 1.93 AGeV (full squares). Within the error bars the values are constant between 1.8 fm and 6 fm and the averaged ratios are 0.020 ± 0.004 for 1.5 AGeV and 0.031 ± 0.004 for 1.93 AGeV. The ratio for 1.93 AGeV

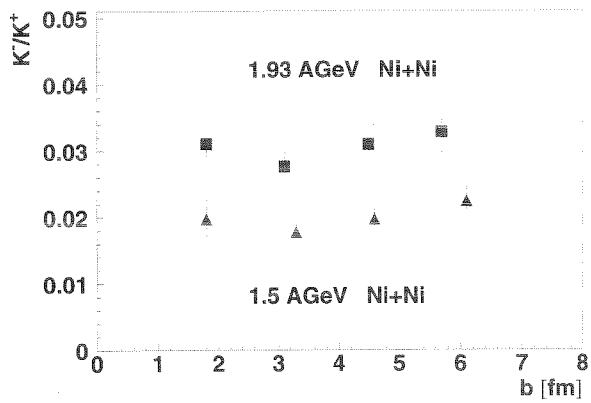

Figure 3: K^-/K^+ *ratio as a function of the impact parameter b for Ni+Ni collisions at beam energies of 1.5 and 1.93 AGeV (preliminary).*

agrees with the value of 0.031 ± 0.005 for non-central and near-central collisions in Ni+Ni measured for the full rapidity range (θ_{lab} = 28° to 64°) at the same beam energy [3]. All measured K^-/K^+ ratios for Ni+Ni can be compared with the smaller system C+C [2] and the corresponding inclusive values of 0.025 ± 0.007 for the beam energy 1.8 AGeV and 0.038 ± 0.013 for 2.0 AGeV.

In conclusion, the K^-/K^+ ratio at a given bombarding energy is constant as a function of the centrality of the reaction and the size of the collision system. This indicates, that the antikaon yield is coupled to the kaon yield via the strangeness exchange reaction $Y\pi \rightarrow K^-N$ (with $Y = \Lambda, \Sigma$).

* now at Ohio State Univ., Columbus, USA

References

[1] R. Barth et al., Phys. Rev. Lett. **78** (1997) 4007
[2] F. Laue et al., Phys. Rev. Lett. **82** (1999) 1640
[3] M. Menzel et al., Phys. Lett. **B 495** (2000) 26
[4] Y. Shin et al., Phys. Rev. Lett. **81** (1998) 1576

Dependence of K^+ Production on the System Size at 1.5 AGeV

A. Devismes[1], N. Herrmann[2], P. Crochet[3], K. Wiśniewski[2], A. Andronic[1], C. Finck[1], A. Gobbi[1], O. Hartmann[1], K.D. Hildenbrand[1], T. Kress[1], Y. Leifels[1] and, W. Reisdorf[1], FOPI Collaboration
GSI Darmstadt[1], University of Heidelberg[2], LPC Clermont-Ferrand[3]

The FOPI collaboration has recently measured K^+ production in Ca+Ca, Ru+Ru and Au+Au collisions at 1.5 AGeV [1] to investigate the dependence on system size and to learn more about modification of kaon properties in dense hadronic matter which is eventually connected to the partial restoration of chiral symmetry. Several theoretical models predict that the K^+ mass increases slightly with baryon density whereas the K^- mass should decrease [2, 3, 4, 5, 6]. These medium modifications of the kaon masses lead to a lower probability for K^+ production since it becomes energetically more difficult to produce them and to a higher probability for K^-.
Previous results from FOPI on kaon flow [7] and K^-/K^+ ratio [8] seem to favor the existence of in-medium potentials for kaons derived from the comparison to transport model calculations [9, 10].

The K^+ mesons are identified in the central part of the FOPI detector by a drift chamber (CDC) surrounded by a barrel of plastic scintillators for the measurement of the time of flight. The TOF subsystem covers the polar angular range between 40° and 130°. For a clean identification of K^+ in the Au+Au system a laboratory momentum cut of $p < 0.4$GeV/c is required. This cut is also applied to the other systems in order to select the same region of the phase space although K^+ can be identified in the lighter collision systems up to p=0.5 GeV/c. A simulation of the FOPI detector response based on the GEANT package is used to estimate the tracking efficiency in each system. The results vary between 87% for the Au system and 99% for the Ca system. The data are further corrected for the matching efficiency between the CDC and the TOF barrel that is estimated from proton tracks and for the kaon lifetime.

Figure 1 shows the number of K^+ per participant as function of the number of participants for Ca+Ca, Ru+Ru and Au+Au at 1.5 AGeV. The charged particle multiplicity measured in the forward plastic wall of the FOPI detector has been used to select central collisions corresponding to 10% of the total cross section. The data are shown by the circles, the error bars include statistical and systematical errors. The experimental results are compared to the predictions of transport models, RBUU [10] (upper panel) and IQMD [11] (lower panel). These calculations are available in two versions: the first one employs the free kaon mass (triangles), the other one includes modified masses (squares), i.e. the K^+ mass depends linearly on density with an increase of 5% at normal nuclear matter density. Within errors the data do not show any dependence on the system size whereas both models consistently predict an increase of the kaon production with the system size. This increase is slightly more pronounced in the absence of medium effects. In both cases, in addition the absolute yields are better described by the versions including the in-medium modification of the K^+ mass.

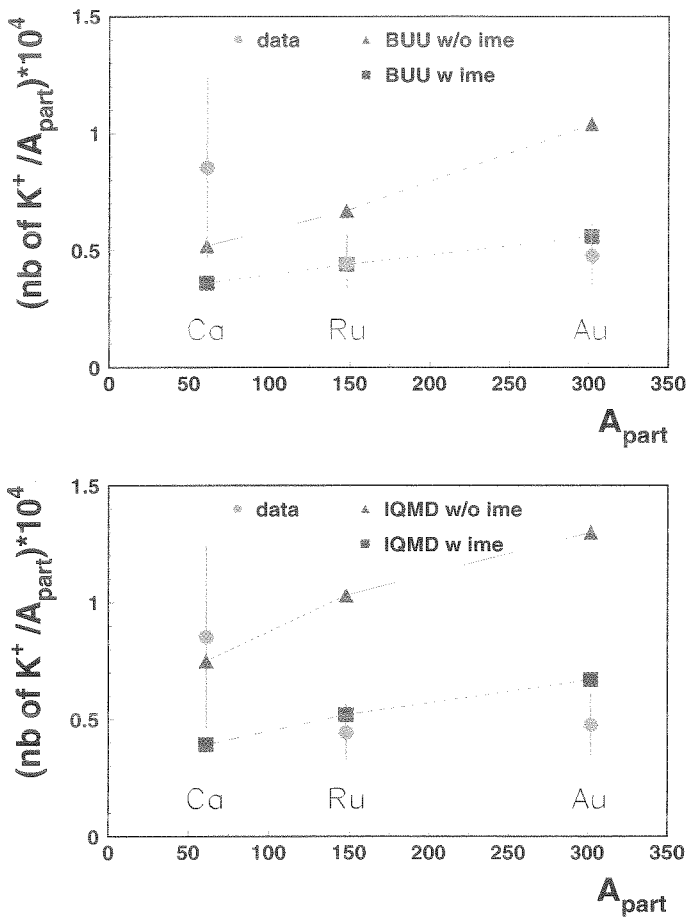

Figure 1: *Number of K^+ per participant as function of the number of participant in Ca+Ca, Ru+Ru and Au+Au collisions at 1.5 AGeV. The data (circles) are compared to the predictions of RBUU (upper) panel and IQMD (lower panel) with in-medium modification of kaon mass (squares) and without (triangles).*

References

[1] A. Devismes, PhD. thesis, Univ. Darmstadt, Feb. 2001
[2] G.E. Brown et al., Nucl.Phys. A567 (1994) 937
[3] M.Lutz et al., Nucl.Phys. A574 (1994) 755
[4] G.Q.Li et al., Phys.Rev.Lett. 79 (1997) 5214
[5] J. Schaffner *et al.*, Nucl. Phys. A625 (1997) 325
[6] G. Mao *et al.*, Phys. Rev. C59 (1999) 3381
[7] P. Crochet *et al.*, Phys. Lett. 486 (2000) 6
[8] K. Wiśniewski, Eur. Phys. J. A9 (2001) 515
[9] C.M.Ko, G.Q.Li, J.Phys.G22 (1996) 1673
[10] W. Cassing, E.L. Bratkovskaya, Phys.Rep. 308 (1999) 65 and private communication
[11] C. Hartnack, private communication

Commissioning Results from the Dielectron Spectrometer HADES[B,G,EC]

The HADES Collaboration

Status overview

During the year 2000 most of the detector modules were installed and equipped with readout electronics. All 6 sectors of the Pre-Shower detector, the outer Time-Of-Flight (TOF) wall, the forward Time-of-Flight paddles (Tofino), two complete planes of Multiwire Drift Chambers (MDC, 12 modules) in front of the superconducting magnet as well as the Ring-Imaging-Cherenkov detector (RICH) surrounding the target were installed. Due to the delayed delivery of a few readout modules and since only 4 RICH sectors were equipped with mirrors, common readout was performed for 4 out of the 6 sectors during a commissioning beam-time in November 2000. Since only one out of the altogether 12 outer MDC's was installed, the momentum resolution of the setup was restricted to about 10%. The current setup is shown in Figure 1.
In the following part, first results regarding the performance of this setup are reported.

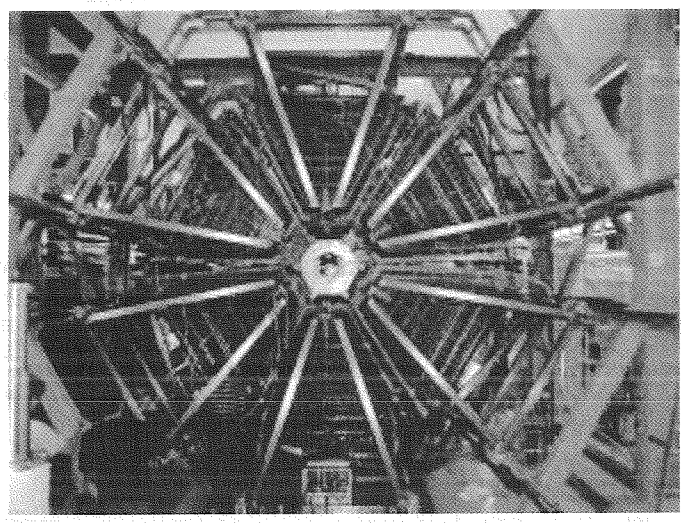

Figure 1: Upstream view of the Hades setup. Only the support structure and outermost detector layer (Pre-Shower detector, part of TOF) are visible.

Electron Identification in the RICH

The readout electronics of the ring imaging Cherenkov detector (RICH) was completed and extensively tested. The refined gas supply system went into routine operation. In order to allow for commissioning measurements with beam a preliminary RICH mirror was equipped with 4 segments of float glass coated with Al / MgF_2. The photon detector was operated during the beam times under stable conditions with an anode voltage of 2550 V at negligible leakage currents. The VUV transmission of the gas (CH_4 at 1000 hPa) at the detector exhaust was measured to be essentially free of impurities down to the absorption cut-off at λ = 146 nm. This was not yet the case for the standard radiator gas C_4F_{10} due to so far unknown contaminations.
In order to verify the performance of the detector and especially its CsI photon converter a series of measurements were performed with light and medium heavy ions radiating Cherenkov light in a stack of two solid radiator discs (SiO_2 and MgF_2) located close to the regular target station inside the RICH. Since the amount of light can be calculated precisely this configuration is a calibrated and pulsed (τ ~10 ps) light source. Due to the different refraction indexes two 'super ring' patterns with different radii are generated and the optical dispersion results in a well defined broadening of their radial distributions. A typical ring pattern accumulated for 600 projectiles and a 600 AMeV C beam is shown in Figure 2 and exhibits the high photon statistics expected for $Z > 1$ particles.

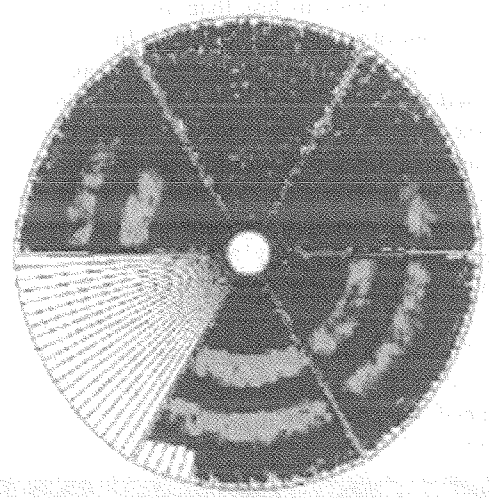

Figure 2: Superposition of ~600 Cherenkov rings from C ions (E = 600 AMeV, β = 0.794) impinging on a MgF_2 and a SiO_2 radiator. The upper sectors are in the shadow of the beam pipe; one lower sector was not equipped with mirrors.

Proper choice of radiator thickness (5mm for SiO_2, 1mm for MgF_2) allowed for a clear spatial separation of single photon hits on the pad plane. The measured shape of the radial distribution of individual photons agrees well with results of a full GEANT simulation using optimum detector parameters. These parameters would translate to a figure of merit N_0 = 110 when the solid radiators are replaced by the C_4F_{10} gas radiator. From a comparison of the amplitudes we deduce for the two lower sectors in Figure 2 values N_0 = 90 and N_0 = 105, the reduction being probably due to a slight deterioration of the CsI quantum efficiency.
Taking pulse height spectra for single photo electrons fitted with a Polya function an effective gas gain of ~$1.5 \cdot 10^5$ slightly above the design value was obtained. With the noise level reduced to about 3500 e^- (3σ) a detection efficiency of ~94% for single photo electrons was extracted.

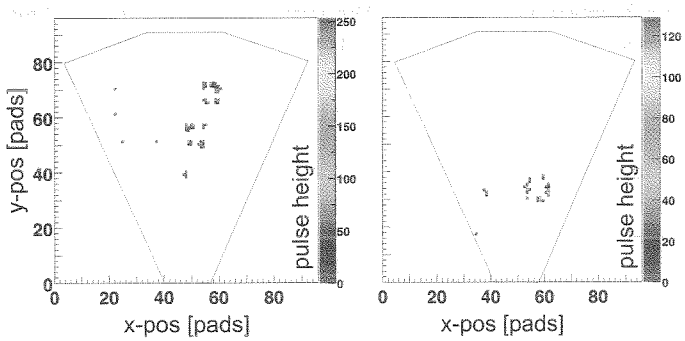

Figure 3: Double and single ring patterns observed in the RICH for electrons from C + C at E = 1.5 AGeV.

From 2 · 10^6 events recorded for C+C collisions at 1.5 AGeV about 10k events were found showing clear Cherenkov ring patterns as shown in Figure 3. First results from the analysis of the combined detector setup are presented in the following chapters.

Multiwire Drift Chambers

During the past year the inner section of the tracking system was completed and tested in two beam times. It comprises 12 chambers in two different geometries covering an area of 5 m^2. About 13.000 individual drift cells are read out by customised front-end electronics in less than 10 µs. Data is transferred to read-out controllers located close to the detector units. These units were developed in the electronic department of GSI and were used for the first time in the November beam time.
The assembly of the outer tracking system was started with the installation of the first plane III module built at FZ Rossendorf. A second plane III and the first plane IV module (constructed at IPN Orsay) are currently commissioned and will be available in the spring beam time 2001. The completion of the outer tracking system, which will finally cover 28 m^2, is scheduled for 2002. Figure 4 shows the plane IV module being lifted to the service table for commissioning. In particular the size of the plane IV module, with maximum wire length of 280 cm, demanded for customised infrastructure and a thorough construction.

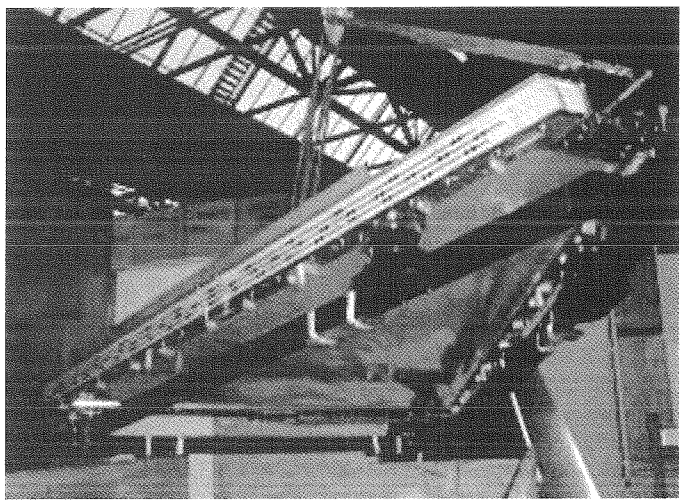

Figure 4: Picture showing the first plane IV module arriving at GSI. For transportation the chamber is mounted on a support structure via surge dampers. It has a height of 3 m and weighs about 200 kg.

During commissioning with beam a stable operation of all chambers was observed. The detectors perform well within the specifications. Operated with a gas mixture of Helium/i-butane (60/40) the chambers reach efficiencies of single cells above 98%. The intrinsic resolution lies around 120 µm. Composed of 6 individual drift cell layers per module, the tracking chambers provide sufficient redundancy to identify tracks even at the highest multiplicities. Due to the optimised wire orientations and multiple measurement of positions, the resolution in the direction of the magnetic kick is about a factor two smaller than the intrinsic resolution. Figure 5 visualises the operation principle of the tracking chamber. The crossing area of the cells being hit by the particle identifies impact positions. The information shown in the Figure 5 is used in the tracking software (version developed by the Dubna group) to search for track candidates.

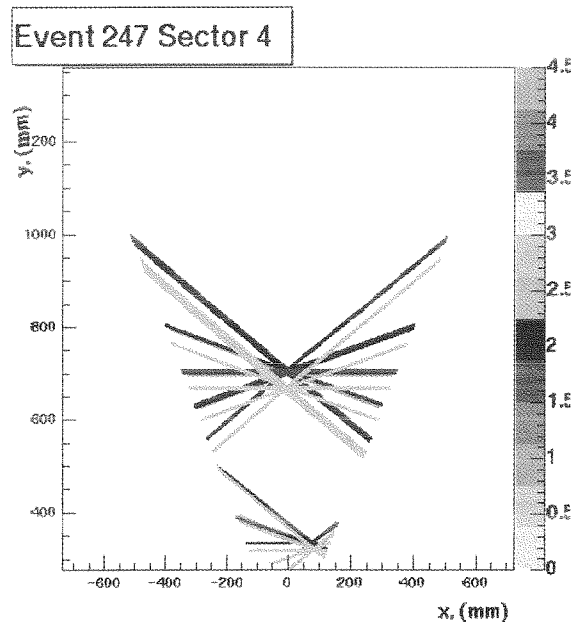

Figure 5: Projection of fired drift cells of three detectors in one sector. Black and dark grey refer to the inner tracking detectors, cyan to the cells of plane III. The shift of the crossing point of plane III with respect to the other two detectors is the result of the momentum kick in the magnetic field.

Start/Veto Detector

A pair of segmented diamond detectors located 75 cm upstream and downstream of the target is used to determine the start time for TOF measurements. The downstream detector vetos ions which were not reacting in the target. For 1 AGeV C+C a veto efficiency of ~90% was obtained. For an optimised beam focussing the veto efficiency should be significantly higher.

Time-Of-Flight Detector

The Time-of-Flight detector consists of an inner part (TOFino, 24 scintillators) in front of the Pre-Shower detector and an outer TOF wall. As of December 2000 both detectors were complete and fully assembled. The 384 scintillating rods of the outer wall, made from BC408 and each one equipped with two photomultipliers, produce fast signals handled by means of 48 constant fraction discriminator modules (16-fold C808 by CAEN). The logical outputs are delayed using 24 32-fold active delay units developed by the collaboration along with the 32-fold TDC units used to digitise the signals. These latter modules, in VME standard, are read-out via the fast Chained Block Transfer (CBT) protocol, allowing to sustain high event rates. The final tests on the amplitude measuring electronics (CAMAC shapers and VME ADCs) have been successful and their mass production is in progress. The forthcoming installation of this electronics, during the first half of 2001, will further improve the TOF performance.
The laser calibration system is complete and allows to evaluate the needed calibration constants for all the detector channels. An extension of this system is already in progress, in order to accommodate for the calibration of the TOFINO as well.
A newly developed slow control software using the EPICS framework allows to initialise and operate the TOF electronics, the high voltage system and the laser calibration system. An

online analysis package and a Graphical User Interface (GUI) have been developed within the HYDRA environment that allow a quick and easy monitoring of detector data throughout a beam time. A sample online plot for the TOF detector is shown in Figure 6.

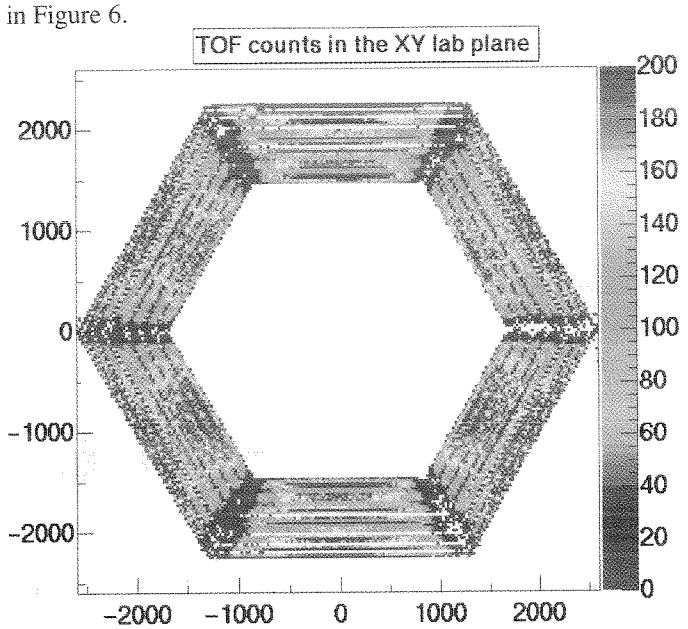

Figure 6: The TOF detector inclusive count distribution in the XY laboratory frame (units are in mm), as seen by means of the online GUI for monitoring.

A preliminary analysis of the collected data shows that the calibration procedure is reliable, and that a few levels of iteration on the related data may further improve the results. Correlated data from TOF and RICH prove that HADES can really identify leptons, as can be seen in Figure 7.

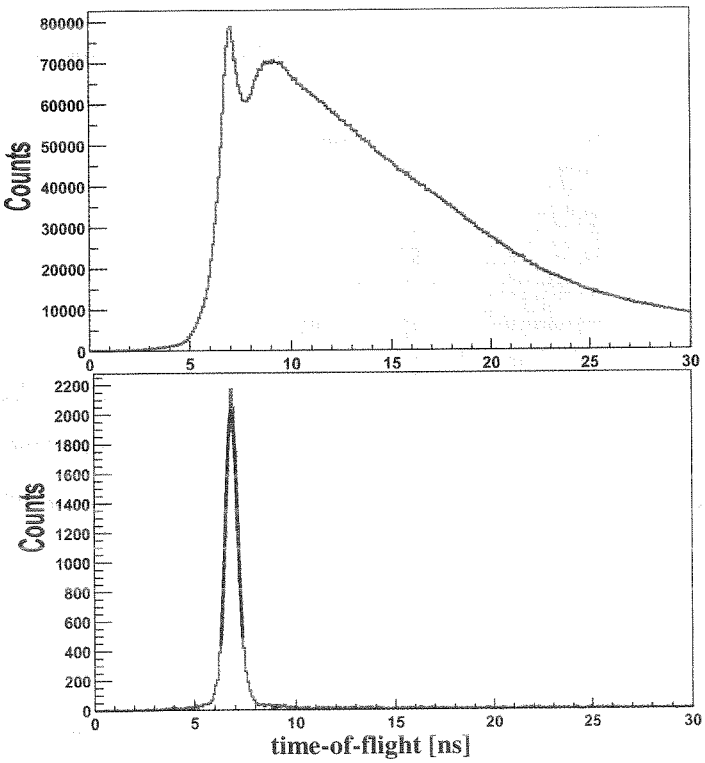

Figure 7: Upper plot: TOF spectrum of all particles detected. Lower plot: TOF spectrum for electron candidates, as selected by means of a position correlation between RICH and TOF hits. Data were taken without magnetic field.

The measured times in the TOF detector have been re-normalised to equal flight path (2.1 m). The lepton peak in the upper part of Figure 7 is due to knockon electrons with energies well below the Rich threshold of 10 MeV.

Pre-Shower Detector

The whole Pre-Shower detector has been finally mounted on the HADES spectrometer mainframe. All detector channels are connected to the read-out electronics consisting of 32 channels Front-End cards and fast digital Read-out Boards located directly on the detector. The main goal of this detector is electron identification at forward polar angles (smaller than 45 degree). This should be achieved measuring electromagnetic showering in two lead converters placed between 3 gas chambers with pad readout. As has been shown in simulations, full electron identification can only be achieved when electron candidate hits are matched with rings in the RICH and fast particle hits in the TOFino detector. The Pre-Shower detector can also be used as a tracking device since it provides a hit position of a particle track after bending in the magnetic field and thus allows for a rough momentum determination.
The whole system has been successfully tested in C+C collisions. Charged particle tracks have been reconstructed from Pre-Shower and TOFino hits and from positions in the MDC (plane 2). Figure 8 (upper row) shows the resulting time of flight spectrum and TOF versus momentum correlations. The plots in the lower row present similar distributions with the additional condition on spatially correlated rings found in the RICH and electromagnetic shower candidates found in the Pre-Shower detector. The discrimination of the electron signal in the time of flight spectra is clearly visible. A gaussian fit to the electron peak gives σ=0.67ns, however a TOF correction due to the track length in the magnetic field has not yet been applied. The intrinsic time resolution of TOFino amounts to 0.25-0.3 ns.

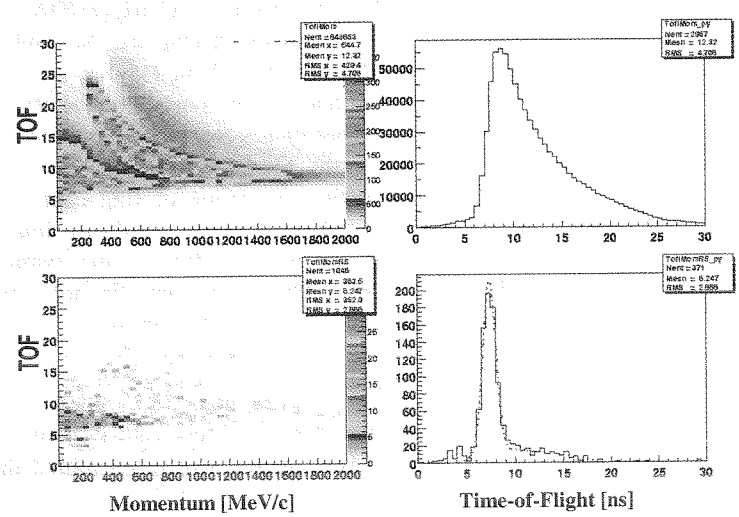

Figure 8: TOF versus Momentum (left) and TOF distributions (right). Upper part: All charged particles. Lower part: Spatial correlation with RICH rings required.

Trigger and Data Acquisition

In order to facilitate the handling of the various detector subsystems during commissioning, the trigger distribution system was enhanced by adding a trigger hub featuring flexible configuration and diagnostics options. In particular, it is now

possible under software control to run with any combination of subsystems without recabeling of the trigger bus.

Readout for the Pre-Shower and TOF subsystems

The Pre-Shower readout hardware was completed and integrated into the setup. Zero suppression and calibration were successfully tested.

Readout of the TOF/TOFino-subsystem in Chained Block Transfer Mode (CBLT) was successfully implemented using modified versions of the CAEN TDC/ADC-modules and the new combined TOF readout/trigger modules. Here, a scheme with one SHARC-DSP-based readout/trigger module per VME crate connected to a common concentrator board was used.

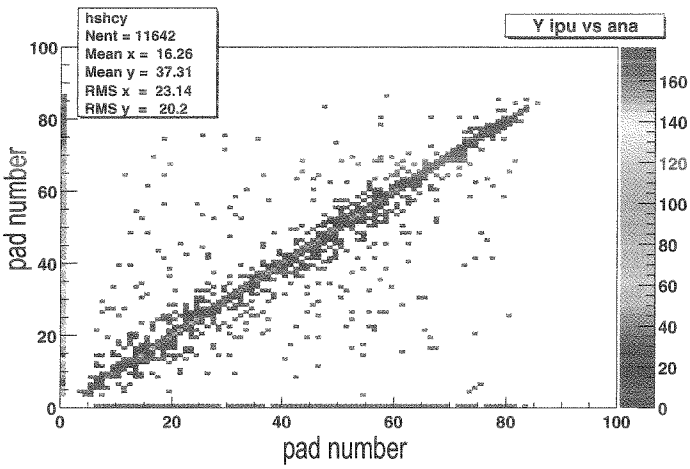

Figure 9: Correlation of x-coordinates of ring candidates found by hardware and by software. Events above and below the diagonal are due to different threshold settings in both algorithms.

RICH Trigger Hardware and Matching Unit

A first successful test of the first/second level trigger/DAQ – scheme with pipelining was conducted during the November commissioning run. Here, the Matching Unit (MU) was connected to the TOF subsystem and to one module of the RICH Image Processor. RICH ring coordinates were transmitted to the MU and recorded event-by-event. Figure 9 shows the result of an off-line analysis showing the correlation of ring center x-coordinates on the RICH padplane found by hardware image processing and by applying the RICH software ring finding algorithm. Additional events, which are non-diagonal are resulting from different thresholds in both algorithms.

Common Event Building

Based on a dedicated ATM network data from the various detector subsystems are transferred asynchronously from 7 VME-CPU's to a common event builder which assembled the full events. A data taping speed of up to 5 MB/s could be achieved, corresponding to up to 2000 events/s for the system C+C.

First Results

The combined analysis of detector signals from one MDC plane and the outer TOF wall allows to identify charged particles. As the outer drift chambers were not yet included, this analysis could be done in a low momentum resolution mode only. The result is shown in Figure 10 for the system C+C at 1.5 AGeV beam energy. Pions, protons and deuterons are clearly separated. The data were taken at 72% of the maximum magnetic field. The calibration of the detector alignment is still in progress and an improved resolution is expected.

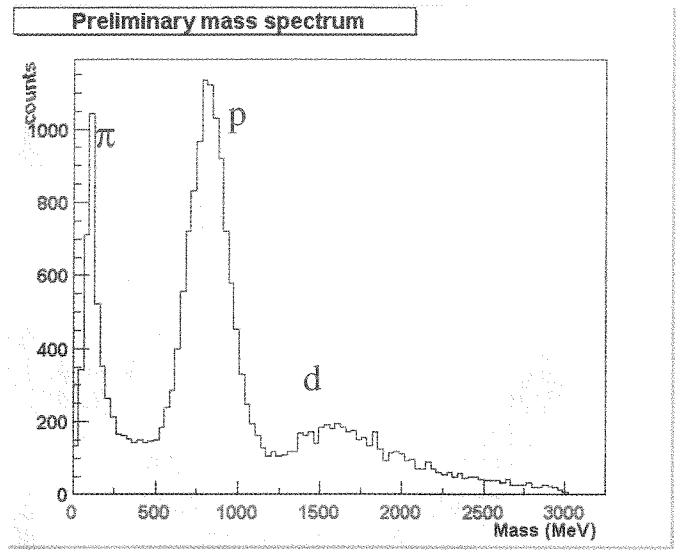

Figure 10: Mass spectrum obtained by analysing the transverse momentum kick within the magnetic field using position and angle information from one inner drift chamber and position measured with the outer TOF wall. Calibration is preliminary.

From a first preliminary analysis of the RICH data an opening angle distribution for lepton pairs was obtained for about 800.000 events C+C at 1.5 AGeV (Figure 11). As expected, the distribution is dominated by small opening angles due to pairs from Dalitz decays of π^0 and conversion of photons in the target and radiator. Besides ring recognition in the Rich no further lepton identification or track matching was required.

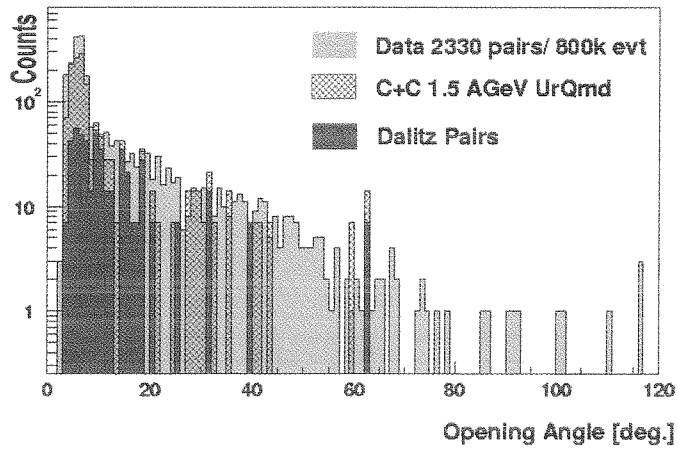

Figure 11: Opening angle distribution of lepton pairs obtained for about 800000 C+C collisions at 1.5 AGeV(blue) as compared to a simulation which includes only Conversion and Dalitz decays of the π^0. Preliminary result.

Summary and Outlook

The setup has proven its capability to measure lepton pairs. With the installation of outer drift chambers during 2001 and spring 2002 the momentum resolution should be significantly improved. Physics runs providing lepton pair spectroscopy with good statistics are expected for this year.

Quenching of resonance production in nuclear collisions around 1 AGeV

A.B. Larionov*, W. Cassing, S. Leupold, U. Mosel
University of Giessen

Pion production in heavy-ion collisions is relatively well studied both theoretically and experimentally. There is still, however, a longstanding open question: Why pion multiplicities produced by transport models like BUU and QMD overestimate the experimental data? The largest discrepancy is observed for central Au+Au collisions at 1 AGeV [1]. In this system pions are mostly produced through the Δ-resonance excitations in a two-step process: $NN \to N\Delta$, $\Delta \to N\pi$. Since this process happens in nuclear matter, in-medium effects (besides evident Pauli blocking of the nucleons in final states) cannot be excluded.

We have studied the effect of possible in-medium modification of the cross sections for the processes $NN \leftrightarrow NR$ on the pion observables. The calculations have been done within the BUU model [2] employing the SM mean field (K=220 MeV). The in-medium spin-averaged matrix element squared for the resonance R production/absorption was parametrized as $\overline{|\mathcal{M}_{NN\leftrightarrow NR}|^2} = \kappa(\rho)\overline{|\mathcal{M}^{vac}_{NN\leftrightarrow NR}|^2}$, where $\overline{|\mathcal{M}^{vac}_{NN\leftrightarrow NR}|^2}$ is the vacuum matrix element squared and $\kappa(\rho)$ is a density-dependent function to be determined from a fit of the experimental data. The function $\kappa(\rho)$ is for simplicity supposed to be the same for all baryon resonances. Fig. 1 shows the π^- multiplicity vs time for a central Au+Au collision at 1.06 AGeV for the three choices of $\kappa(\rho)$: $\kappa(\rho) = 1$ – standard (dashed line), $\kappa(\rho) = 1 + 3\rho/\rho_0$ – amplified (dotted line) and $\kappa(\rho) = \min(1, \max(0, 1 - 2(\rho/\rho_0 - 1)))$ – quenched (solid line). There is a reduction of the pion yield in both

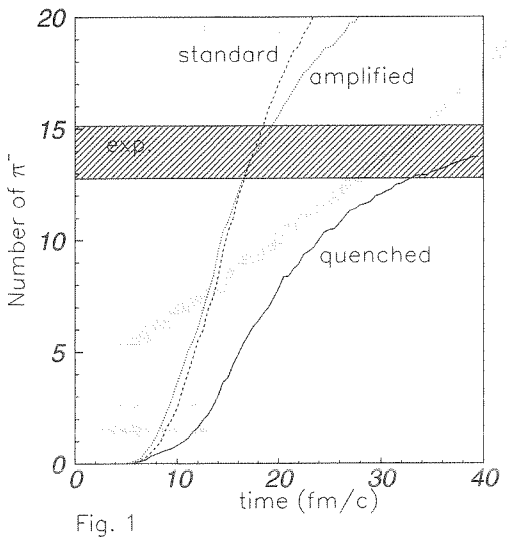

Fig. 1

cases, but the experimental data are only well fitted for the quenched choice of $\kappa(\rho)$. We checked that a further increase of the amplification factor will not modify the pion multiplicity essentially: it always overpredicts the data at least by 30% [3]. The quenching scenario assumes that at $\rho \le \rho_0$ the in-medium modifications are absent,

*On leave of absence from RRC "I.V. Kurchatov Institute", 123182 Moscow, Russia

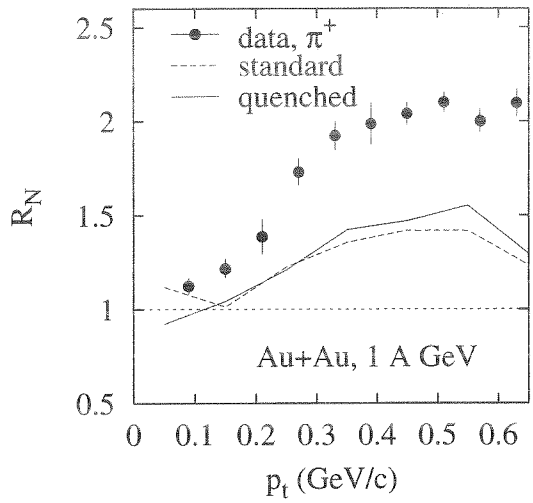

Fig. 2

at $\rho_0 < \rho \le 1.5\rho_0$ the resonance production/absorption matrix elements decrease linearly with density and at $\rho \ge 1.5\rho_0$ the matrix elements become zero, i.e. at high density resonances do not experience any elastic or inelastic scatterings with nucleons. They can, however, decay or be produced in processes $R \leftrightarrow N\pi$.

We show in [3] that for Au+Au at 1 AGeV the quenching results in a vertical downward shift of the pion p_t-spectra, thus improving the agreement with the data [1, 4]. For the light system C+C at 0.8÷2 AGeV, both standard and quenched calculations produce practically the same m_t-spectra of π^o's [3], since in the lighter system medium modifications are weaker.

Both, transverse in-plane and out-of-plane pion flows are weakly influenced by the quenching. There is a good agreement of our calculations with the data on the in-plane $\pi^\pm$ flow [5] (see [3] for details). However, we underpredict the high-p_t π^+ squeeze-out ratio $R_N := (N_{\pi^+}(90^o) + N_{\pi^+}(270^o))/(N_{\pi^+}(0^o) + N_{\pi^+}(180^o))$ [6] as shown in Fig. 2. Therefore, in order to describe the pion squeeze-out some additional effects have to be taken into account. We expect, that the introduction of a momentum-dependent pion potential as well as further modifications of the resonance life time will improve the agreement with data on pion squeeze-out in analogy to the case of nucleon squeeze-out [7].

References

[1] D. Pelte et al., Z. Phys. A **357**, 215 (1997).
[2] M. Effenberger, E.L. Bratkovskaya, and U. Mosel, Phys. Rev. C **60**, 044614 (1999).
[3] A.B. Larionov et al., in preparation.
[4] O. Schwalb et al., Phys. Lett. B **321**, 20 (1994).
[5] J.C. Kintner et al., Phys. Rev. Lett. **78**, 4165 (1997).
[6] Y. Shin et al., Phys. Rev. Lett. **98**, 1576 (1998).
[7] A.B. Larionov et al., Phys. Rev. C **62**, 064611 (2000).

Pion and Kaon Production in central Pb+Pb Collisions at 40 GeV per Nucleon from the NA49 Experiment[G,B]

A.Billmeier[1], C.Blume[2], R.Bramm[1], P.Buncic[1], P.Dinkelaker[1], M.Gaździcki[1], T.Kollegger[1], I.Kraus[1], C.Markert[2], A.Mischke[2], R.Renfordt[1], A.Sandoval[2], H.Sann[2], R.Stock[1], H.Ströbele[1], M.Wensveen[2], A.Wetzler[1], J.Zaranek[1] for the NA49 Collaboration.
[1]Universität Frankfurt, [2]GSI Darmstadt

The creation of new particles is the most important process in high energy nuclear collisions and its excitation function may allow to detect threshold effects and non-monotonic behavior. The NA49 experiment at the CERN SPS has complemented its 158 GeV per nucleon data by recording 1.8 million Pb+Pb events at 40 GeV per nucleon in fall 1999 and 400.000 central events at 80 GeV per nucleon in fall 2000. Results on pion and kaon production in central (7%) 40 GeV per nucleon events are presented here.

The experiment NA49 was designed for Pb-beams at top SPS energy. The effects of a four times lower Lorentz boost at 40 GeV/nucleon was compensated by lowering the magnetic field strength accordingly. This kept all the essential features of the NA49 detector [1] intact. The identification procedures based on the specific enery loss (dE/dx) were supplemented by time-of-flight identified particles in the TOF acceptance regions. In order to get pion rapidity spectra, one had to identify pions in momentum intervals where their energy loss is the same as for kaons or protons. Therefore we first analysed negatively charged particles [2]. To get the π^- spectrum, we subtracted the kaons and antiprotons as identified by dE/dx (at different laboratory momenta!) and then constructed from the resulting π^- the π^+ spectra using dE/dx determined π^+ to π^- ratios in regions where identification was possible. Those parts of the spectra for which the ratios were not measured have been obtained from extrapolation.

Acceptance losses, tracking inefficiencies and losses due to particle identification procedures were corrected for in bins of rapidity and p_T. The systematic errors on the multiplicity of pions and kaons are estimated to be less then 10%. Since the NA49 acceptance covers only the forward hemisphere, the measured spectra were mirrored at midrapidity to calculate the total multiplicities.

Fig.1 shows the rapidity distribution of negatively charged pions. The rapidity density at mid-rapidity is 110 $\pm$ 5 and the FWHM of the distribution comes out to be 2.45 $\pm$ 0.1. This is to be compared to 3.4 $\pm$ 0.15 at 158 GeV per nucleon. The respective fractions relativ to the full rapidity gap are very similar. The integral over the full rapidity distribution yields an average of 313 $\pm$ 15 π^- per central event. Fig.2 displays the transverse mass distribution of the pions. Its form is obviously not an exponential. We therefore refrain from giving a slope parameter but rather caluct the mean $p_T = 0.36 \pm 0.2$, which is slighly lower than the value found at 158 GeV per nucleon.

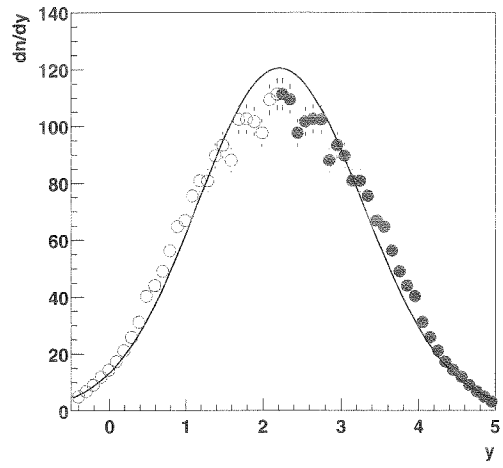

Figure 1: Rapidity distribution of negatively charged pions in central Pb+Pb collisions at 40 GeV per nucleon.

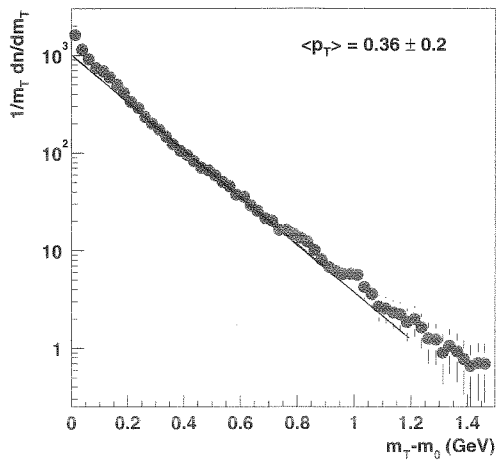

Figure 2: Transverse mass distribution of negatively charged pions in central Pb+Pb collisions at 40 GeV per nucleon.

In Fig.3 we present the rapidity distributions of charged kaons. The integrals over the full rapidity distributions yield 17.8 $\pm$ 0.9 K^- and 56.3 $\pm$ 3 K^+ per central event [3]. The total yields and the multiplicities at midrapidity are summarized in table 1.

	total yield	midrapidity yield
π^-	313 ± 15	110 ± 5
π^+	282 ± 15	99 ± 7
K^-	17.8 ± 0.9	8.18 ± 0.4
K^+	56.3 ± 3	20.52 ± 1

Table 1: Pion and kaon multiplicities in central 40 A·GeV Pb+Pb collisions, the midrapidity yields are calculated for $|\frac{y-y_{cm}}{y_{cm}}| < 0.125$.

These measurements allow together with previous NA49 measurements at 158 GeV per nucleon [4], measurements at the AGS [5] and RHIC [6] to plot the energy dependence of the $K^+/\pi+$-ratio. It shows a non monotonic behavior in the SPS energy range (figure 4). To further study this structure, the 80 GeV per nucleon data is currently being analysed and NA49 will take additional Pb+Pb data at 20 and 30 GeV per nucleon.

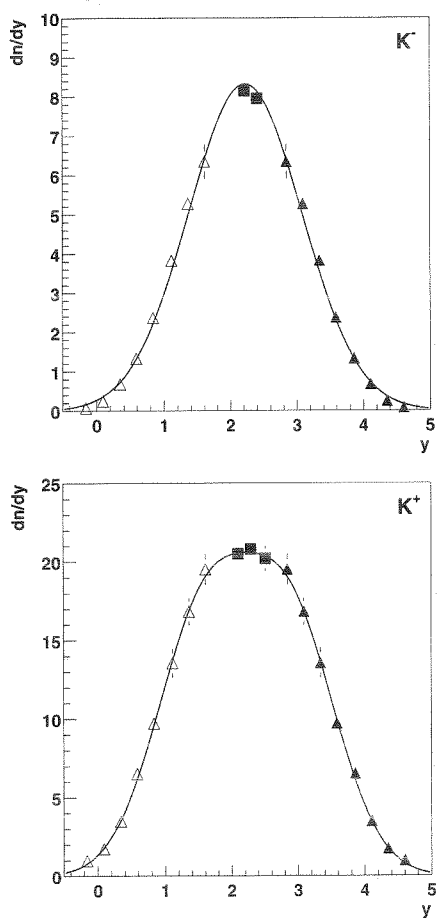

Figure 3: Rapidity distribution of charged kaons in central Pb+Pb collisions at 40 GeV per nucleon. Squares are from TOF-dE/dx analysis, triangels from dE/dx-only analysis. Open symbols are reflected at midrapidity.

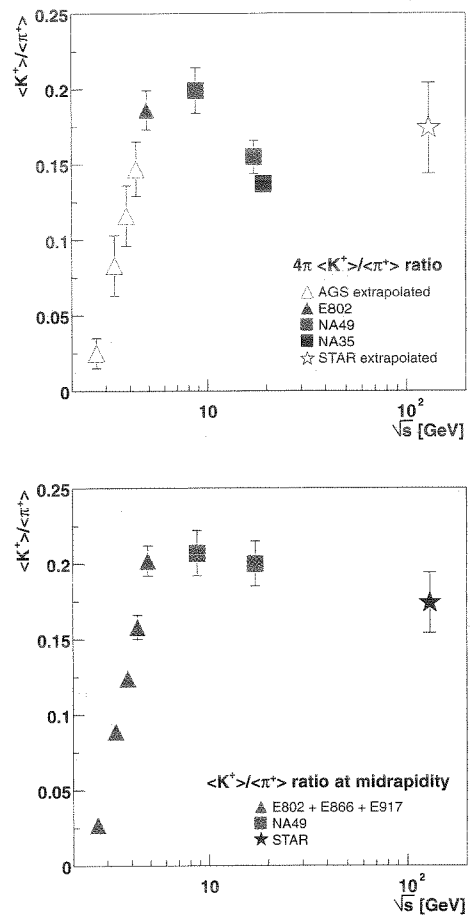

Figure 4: $K^+/\pi+$-ratio as function of collision energy for central Au+Au and Pb+Pb collisions. Figure a) shows the 4π-ratios, b) the midrapidity ratios

References

[1] S. Afanasiev *et al.* [NA49 Collaboration], Nucl. Instrum. Meth. **A430** (1999) 210.

[2] R. Bramm, diploma thesis, Universität Frankfurt, 2001.

[3] T. Kollegger, diploma thesis, Universität Frankfurt, 2001.

[4] J. Bachler *et al.* [NA49 Collaboration], Nucl. Phys. A **661** (1999) 45.

[5] L. Ahle *et al.* [E866 Collaboration and E917 Collaboration], Phys. Lett. **B476** (2000) 1.

[6] H. Caines for the STAR collaboration, QM2001, to appear in the proceedings.

Λ Hyperons Produced in 158 A GeV Pb+Pb Collisions[G,B]

A.Billmeier[1], C.Blume[2], R.Bramm[1], P.Buncic[1], P.Dinkelaker[1], M.Gaździcki[1], T.Kollegger[1], I.Kraus[1], C.Markert[2], A.Mischke[3], R.Renfordt[1], A.Sandoval[2], H.Sann[2], R.Stock[1], H.Ströbele[1], M.Wensveen[2], A.Wetzler[1], J.Zaranek[1] for the NA49 Collaboration.
[1]Universität Frankfurt, [2]GSI Darmstadt

Most of the Λ hyperons observed in the final state of nucleus-nucleus collisions at SPS energies are truly participating baryons and their rapidity distribution is an appropriate measure of baryon stopping. In addition correlations between Λs probe the Λ-Λ interaction which is the decisive parameter for a possible six-quark bound state, the H-Dibaryon. Finally, the relativ yield of Λ resonances may be compared in p+p and Pb+Pb collisions in order to learn about the differences between in-medium effects of baryons and baryonic resonances. In the past, reconstruction of Λ hyperons proved to be difficult in central Pb+Pb collisions due to the high track density and the resulting confusion when searching for the characteristic V^0 decay topology. Similarily the identification of the $\Lambda(1520)$ excited state by a signal in the (K^-p) invariant mass was hampered by the large combinatorial background. New software improvements in V^0 detection and in particle identification have led to reliable Λ and $\Lambda(1520)$ signals. In this contribution we present new preliminary results on the Λ rapidity distribution in $1.5< y <4.5$, on Λ-Λ correlations and on the comparison of the $\Lambda(1520)$ signal in p+p and central Pb+Pb collisions.

Fig. 1 shows the rapidity distribution of Λs in the 5% most central Pb+Pb collisions. The data are not corrected for feed down from Ξ and Ω decays. Also shown is the published result from experiment WA97 [1] again not corrected for feed down and derived from the 3% most central collisions. It should be noted that the feed down corrections need not to be the same for the NA49 and WA97 analysis. For a comparison of the data to p+p measurements see [2].

In Fig. 2 the Λ-Λ correlation is plotted as a function of the invariant momentum difference (q_{inv}). At low q_{inv} a significant dip signals the Pauli principle for fermions. The absence of a positive correlation at small q_{inv} suggests that the s-wave interaction is rather weak. A fit to the correlation function yields a radius parameter of approximately 2 fm assuming the absence of final state interactions.

Fig. 3 shows the invariant (K^-p) invariant mass distributions after background subtraction for inelastic p+p (upper) and central Pb+Pb (lower) collisions[3]. The $\Lambda(1520)$ resonance is clearly visible in both data samples; their positions are within errors the same and agree with the PDG value. It seems that the width of the $\Lambda(1520)$ from Pb+Pb is slightly broader than from p+p. The yield per participating nucleon pair is slightly lower in the nuclear reaction, although the Λ yield per nucleon pair shows a strong enhancement in A+A over p+p.

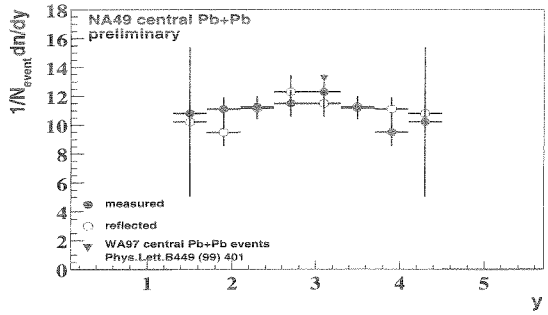

Figure 1: Rapidity distribution of Λ hyperons in central Pb+Pb collisons at 160 GeV per nucleon)

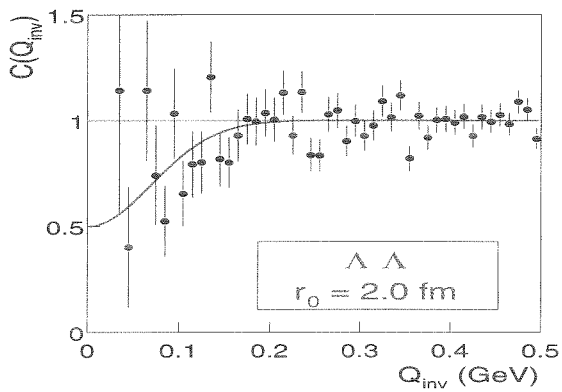

Figure 2: Λ-Λ correlation function from central Pb+Pb collisions.

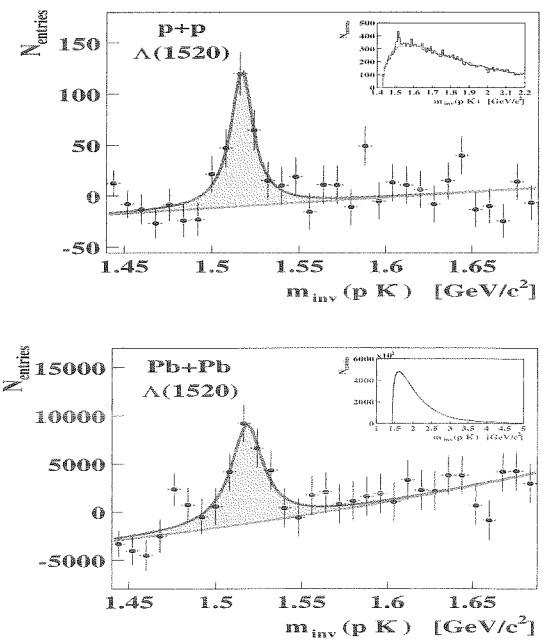

Figure 3: Invariant mass distribution of K^-p pairs in p+p (upper) and central Pb+Pb(lower) collisions at 158 A GeV. The widths of the $\Lambda(1520)$ signals are 15±4 MeV and 23±6 MeV.

References

[1] E. Andersen et al., Phys. Lett B449(99)401
[2] A. Billmeier et al., this GSI Annual Report
[3] C. Markert, PhD Thesis, Universität Frankfurt, 2000

Strangeness Production in ultrarelativistic p+p Collisions at 158 GeV from the NA49 Experiment[G,B]

A.Billmeier[1], C.Blume[2], R.Bramm[1], P.Bunčić[1], P.Dinkelaker[1], M.Gaździcki[1], T.Kollegger[1], I.Kraus[2], C.Markert[2], A.Mischke[2], R.Renfordt[1], A.Sandoval[2], H.Sann[2], R.Stock[1], H.Ströbele[1], M.Wensveen[2], A.Wetzler[1], J.Zaranek[1] for the NA49 Collaboration

[1]Universität Frankfurt, [2]GSI Darmstadt

The interpretation of results from high energy nuclear collision experiments requires accurate knowledge about the corresponding reaction characteristics in elementary hadron-hadron interactions. This information is not always available with the wanted precision, as early particle physics experiments either did not cover full phase space or suffered from low statistics. The SPS experiment NA49 [1] has therefore started a program to study hadron production in p+p interactions at 158 GeV/c beam momentum. An important part of this program is the measurement of strangeness production in full phase space [2].

The NA49 experiment has recorded a total of 2.26 million p+p interactions at 158 GeV. After event selection cuts, which ensure that the interaction occurs in the liquid hydrogen target, 83 % of the total inelastic cross section remain for the analysis. The detection of the measured strange hadrons is based on the recognition of the characteristic V^0 topology, which arises from the decay of long lived neutral particles into two charged decay products. Λ and K^0_S decays are searched for by intersecting tracks from oppositely charged particles and by studying the resulting invariant mass distribution of those pairs which have a valid secondary vertex. Cuts on its position, the distance of the daughter particles in the target plane as well as the cm-decay angles are used to maximise the signal to noise ratio in these distributions. The double strange hyperon Ξ^- and its antiparticle $\overline{\Xi}^+$ were identified by combining the trajectories of all Λ and $\overline{\Lambda}$ candidates with those of negatively (Ξ^-) and positively ($\overline{\Xi}^+$) charged particles. The whole procedure is applied to equal-sized, non-overlapping intervals in rapidity and transverse momentum, which have been chosen according to signal statistics in these two variables. Detection efficiencies and acceptance corrections were determined in the same $y - p_T$ bins by processing simulated strange particle decay topologies using the complete analysis chain.

Figs. 1a,b and 2 show the rapidity distributions of K^0_S, Λ, and Ξ-hyperons in inelastic p+p interactions. Also shown for the neutral strange hadrons are previously measured data [3] at similar energies. The transverse momentum distributions (not shown) follow within experimental errors an exponential function with slope parameters of $\simeq$ 138, 142, 174 MeV for K^0_S, Λ, and Ξ hyperons respectively.

The scaling of the p+p spectra by the number of participants in Pb+Pb collisions at the same energy allows a direct comparison of both systems. Fig. 3 shows the rapidity distributions of K^0_S for both – central Pb+Pb data as well as the scaled p+p results together with a fit to the identified charged kaons [4]. A strangeness enhancement of a factor ≈ 2 in the Pb+Pb compared to p+p reactions is clearly visible.

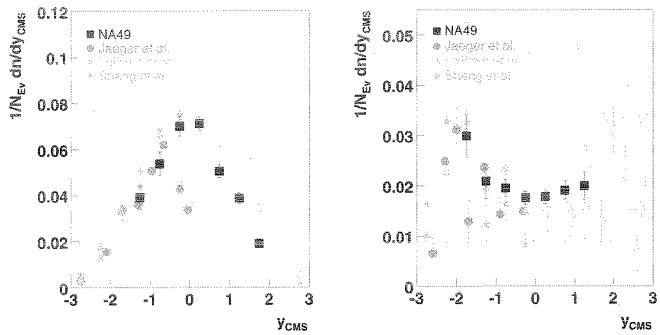

Figure 1: Rapidity distributions for K^0_S (left) and Λ (right) compared to reference data at similar energies [3]. The shape of the distributions is reproduced, the dip around midrapidity in the K^0_S spectra cannot be verified.

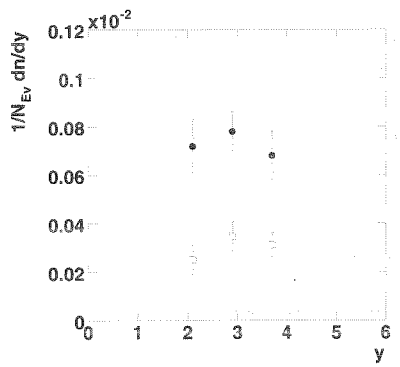

Figure 2: Rapidity distributions for Ξ^- (•) and $\overline{\Xi}^+$ (□).

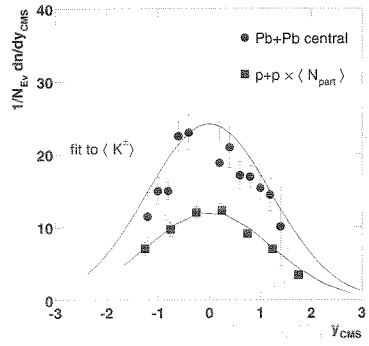

Figure 3: Comparison of the rapidity distribution for K^0_S in central Pb+Pb collisions with the scaled p+p results.

References

[1] S. Afanasiev *et al.*, NIM A430 (1999), 210–244.

[2] A. Billmeier, Ph.D. Thesis, Universität Frankfurt (2001).

[3] Data compiled in: M. Gaździcki, O. Hansen, Nuclear Physics **A528** (1991) 754–770.

[4] J. Bächler *et al.*, Nucl. Phys. **A661** (1999) 45–54.

[G,B] supported by GSI and BMBF

Stability and instability of a hot and dilute nuclear droplet: adiabatic isoscalar modes

W. Nörenberg, G. Papp*and P. Rozmej†

The diabatic approach to dissipative large-amplitude collective motion [1] is reformulated in a local energy-density approximation. We consider a general displacement field, which is defined by an expansion of the displacement potential in terms of multipoles, and include Coulomb interactions. This expansion allows the analytical evaluation of collective mass and stiffness tensors within a consistent harmonic approximation. The set of eigenvalue equations couple modes with different number of nodes in the radial function of the displacement field. The orthogonal eigenmodes of the droplet are determined as function of the relaxation time τ for the decay of deformations of the local Fermi sphere, *i.e.* continuously from the adiabatic to the diabatic limit. Furthermore we consider also pure surface modes and compare the instability properties for soft and stiff equations of state.

In a first application the adiabatic ($\tau = 0$) isoscalar modes are studied and results for the eigenvalues of compressional (bulk) and pure surface modes are presented as function of density and temperature inside the droplet, as well as for different mass numbers and for soft and stiff equations of state [2]. We have studied these adiabatic isoscalar modes in detail, because they are related to thermodynamics and to many studies performed in the past.

The results on adiabatic isoscalar bulk instabilities are summarized as follows.

- As compared to infinite nuclear matter the spinodal region for compressional (bulk) instabilities shrinks to smaller densities and temperatures with $T_{\rm crit} = 6$ MeV (8 MeV) for a soft (stiff) EOS. The observed fragmentation temperatures of about 5 MeV are consistent with spinodal decomposition after expansion. Typical values for the growth rates are $\gamma \approx 5$ MeV (10 MeV for a stiff EOS) corresponding to growth times $\hbar/\gamma \approx 40$ fm/c (20 fm/c).
- Effects from Coulomb interactions on the bulk instabilities are negligible.
- With decreasing density and temperature the modes with the lowest multipolarities and no radial node become unstable first.
- At densities below $0.3\varrho_0$ (with $\varrho_0 = 0.16$ fm^{-3}) the instability growth rates for different multipolarities ($l = 2, 3, 4, 5$) and number of nodes ($n = 0, 1, 2, 3$) are practically equal. This property can yield a power-law behavior $A^{-\sigma}$ with $\sigma \approx 2.0$ of the fragment-mass distribution in agreement with experimental observations and is not related to the critical point.

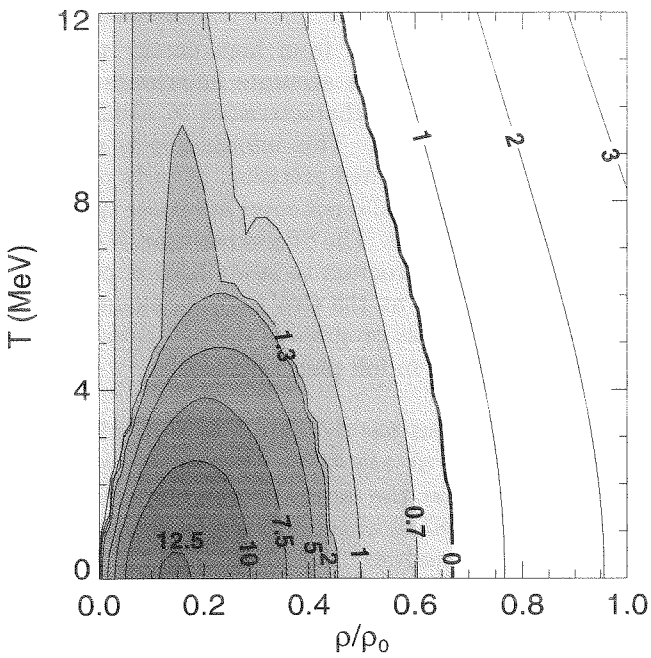

Figure 1: Combined bulk (below $T_{crit} = 6$ MeV) and surface instabilities for a gold-like droplet and a soft EOS. Shown are the largest growth rates (shaded areas) and the lowest vibrational energies (surface modes).

For finite nuclear droplets surface modes are important in addition to the compressional modes. Indeed, pure surface modes show some interesting features.

- The instability region of pure surface modes extends to larger densities up to about the spinodal line of infinite nuclear matter and to large temperatures.
- In general the growth times are smaller by half an order of magnitude as compared to the typical values for bulk instabilities.
- In the stable region surface modes are slow, such that deformations initiated in the excitation process will persist during expansion and clustering.
- The surface instability is dominated by quadrupole deformation.

References

[1] W. Nörenberg, *New Vistas in Nuclear Dynamics*, ed. P.J. Brussard and J.H. Koch (Plenum Press, New York 1986) p. 91; W. Nörenberg, *Heavy Ion Reaction Theory*, ed. by W.Q. Shen, J.Y. Liu and L.X. Ge (World Scientific, Singapore 1989) p. 1.

[2] P. Rozmej, W. Nörenberg and G. Papp, Eur.Phys.J. A **9**, 327 (2000)

* *Permanent address:* HAS Research Group for Theoretical Physics, Eötvös University, Budapest, Pázmány P. s. 1/A, H-1117 Budapest, Hungary

† *Permanent address:* Institute of Mathematics, Technical University of Zielona Góra, ul. Podgórna 50, Pl-65246 Zielona Góra, Poland

Statistical evolution of fragment isospin in nuclear multifragmentation.

A.S. Botvina, *GSI Darmstadt and INR Moscow.*

The knowledge of the isotope composition of fragments produced in nuclear multifragmentation can help in resolving important problems: Do the fragments keep the memory of the initial dynamical stage or are they produced statistically? How does the isospin influence the disintegration of finite nuclei and what is the difference to the case of nuclear matter? What is the isospin dependence of the nuclear equation of state? Generally, this study addresses an intriguing interdisciplinary problem of the phase transition in a finite-size two-component system (i.e. in a nucleus consisting of neutrons and protons), that is instructive for all fields dealing with finite systems. The problem was investigated within the statistical multifragmentation model (SMM) [1], which is successfully used for explanation of experimental data. A new Markov chain method of partition generation was incorporated in the model [2], that allows for considering the multifragmentation process on a solid microcanonical basis. The reported results reflect statistical properties of the fragment production and can be used for identification of the phenomenon.

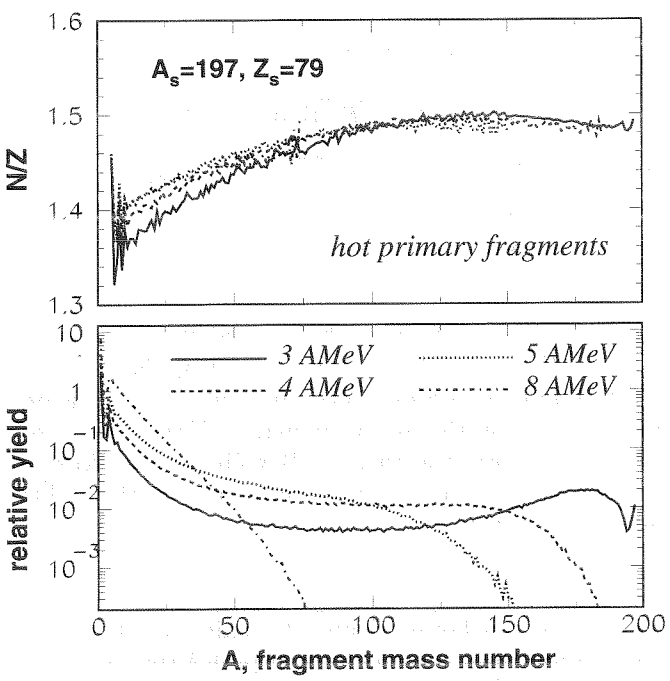

Figure 1: The neutron-to-proton ratio N/Z (top) and relative yield (bottom) of hot primary fragments produced after break-up of Au nuclei at different excitation energies: 3 (solid lines), 4 (dashed lines), 5 (dotted lines) and 8 (dot-dashed lines) MeV per nucleon.

The mass distributions and neutron-to-proton ratios (N/Z) of hot primary fragments produced after multifragmentation of a Au source (mass number A_s=197, charge Z_s=79) are shown in Fig. 1. One can see a general statistical trend: the N/Z ratio of the fragments increases with their mass numbers. This is a consequence of the interplay between the Coulomb and symmetry energy contributions to the binding energy of fragments [1]. This trend persists up to $A \leq A_s/2$, while at larger A the finite-size effects due to the mass and charge conservation prevail. In Fig. 1 one can also see the evolution of the N/Z ratio in the excitation energy range E_s^*=3–8 MeV/nucleon, where the fragment mass distribution evolves from the U–shape, at the multifragmentation threshold $E_s^* \sim 3$ MeV/nucleon, to an exponential fall at the highest energy. This energy range is usually associated with a liquid-gas type phase transition in finite nuclei: During this evolution the temperature reaches a "plateau" and is nearly constant [1, 3]. As the energy increases the N/Z ratio of primary intermediate mass fragments (IMF, charges Z=3–20) increases, too. The reason is that the heaviest neutron-rich fragments are destroyed at increasing excitation energy, and some of their neutrons are bound in the IMFs, since the number of free neutrons is still small at this stage. Simultaneously, the N/Z ratio of the heaviest fragments decreases slightly. At very high excitation energy ($E_s^* > 8$ MeV/nucleon) the N/Z ratio of IMFs does not rise anymore but drops because no heavier fragments are left and the number of free neutrons increases rapidly, together with the temperature. This isospin evolution shows how the isospin fractionation phenomenon predicted for nuclear matter [4] actually shows up in finite nuclear systems. Such a mechanism is consistent with recent experimental data [5]. New experiments for studying mass and isospin effects in multifragmentation are planned at GSI [6].

Interesting phenomena are also predicted for peripheral nucleus–nucleus collisions [2]: 1) The neutron content of IMF increases if a considerable angular momentum is transfered to the source, because of an interplay of the rotational and Coulomb energy. 2) There is a break of the symmetry of the phase space population, including the space isospin distribution, because of the external Coulomb field of the partner nucleus. The space asymmetry leads to predominant population of the midrapidity kinematic region by neutron-rich IMFs, that should be considered as purely statistical alternative to a dynamical explanation of the midrapidity emission [7]. Such processes are examples of a new kind of statistical emission influenced by an inhomogeneous long–range field.

References

[1] J.P.Bondorf et al., *Phys. Rep.* **257**, 133 (1995).
[2] A.S.Botvina and I.N.Mishustin. GSI preprint 2000-50, Darmstadt, 2000; nucl-th/0011072, 2000.
[3] J. Pochodzalla et al., *Phys.Rev.Lett.* **75**, 1040 (1995).
[4] H.Müller and B.D.Serot, *Phys.Rev.* **C52**, 2072 (1995).
[5] P.M.Milazzo et al., *Phys.Rev.* **C62**, 041602(R) (2000).
[6] K.Kezzar et al., Proposal-S254, GSI, 2000.
[7] J.Lukasik et al., Contrib. to this Scientific Report.

Thermal Boson Expansion

Z. Aouissat and J. Wambach
Institut für Kernphysik, Technische Universität Darmstadt.

Based on recent progress in the application of thermo field dynamics (TFD) [1] to thermal many-body systems, several authors [2, 3, 4] have considered a consistent thermal boson expansion (TBE). In this regard two points of view have been taken [2]. The first (path I) consists of a bosonization of the original degrees of freedom of the system, substituting for these ideal boson images. The thermalization is then achieved by doubling those newly introduced bosons as according to TDF prescription. The second possibility (path II) proceeds on the other hand via a thermalization of the system by doubling the original degrees of freedom and a subsequent bosonization of the entire new system. The two paths do not lead to the same results. Moreover, when applied to the Lipkin model, a closer look shows that the choice of path I implies that the thermal density of states are of bosonic type although the original system is purely fermionic.
To circumvent this problem one may choose path II where the thermal density of states is of fermionic type, since the thermalization is performed on the original fermions. However, inconsistencies related to the quasi-particle energies defining the thermal density of states, emerge. The latter are usually taken as solutions of a Hartree-Fock-Bogoliubov (HFB) approximation which, in most cases, leads to a dynamical mass generation. For massless modes, such as Goldstone modes, this gives the wrong solution. On the other hand, a mean-field description that is compliant with the symmetry requirements, is the Hartree-Bogoliubov (HB) approximation which can be obtained after a bosonization à la Holstein-Primakoff (HP). Therefore, when considering the symmetry constraints, it is rather path I that is favored. Amendments are, however, needed in order to reconcile it with the requirements of the statistics as explained earlier.
It was shown in [5] that a Boson expansion approach that treats on equal footing pair- as well as single-particle mapping offers a simple solution to the problems outlined above. For that matter the extended form of the bosonic HP mapping has been proposed in [6] which accommodates single-boson and boson-pair mappings:

$$\begin{aligned}
(\vec{a}\vec{a})_I &= \mathcal{G}_N(n,m)A\ , \qquad (\vec{a}^+\vec{a})_I = 2n+m\ ,\\
(a_i)_I &= \mathcal{G}_N(n,m)\Gamma_N(m)\alpha_i + 2\alpha_i^+ A\Gamma_N(m)\ ,\\
(\vec{a}^+\vec{a}^+)_I &= (\vec{a}\vec{a})_I^+\ , \qquad (a_i^+)_I = (a_i)_I^+\ , \qquad (1)
\end{aligned}$$

where N is an integer, $n = A^+A$, $m = \sum_i \alpha_i^+\alpha_i$, and Γ_N is given by

$$\mathcal{G}_N(n,m) = \sqrt{2N+4(n+m)}\ , \qquad (2)$$

$$\Gamma_N(m) = \left[\frac{m+N-2}{2(2m+N)(2m+N-2)}\right]^{\frac{1}{2}}\ . \qquad (3)$$

Thus, instead of the original bosons a_i, one has an ideal boson α_i which, as was shown in ref. [6], can accommodate the symmetry requirements. This is at the expense of introducing a power series in an auxiliary boson A. The thermalization of the system is then undertaken in a consistent way by using the TFD formalism. The time-translation operator, $\mathcal{H} = H - \tilde{H}$, of the system is obtained as usual by considering the tilde conjugate of all operators such as A and α_i among others. However, the independent thermal quasiparticle representation is obtained by rotating only the ideal bosons α_i, α_i^+ and their tilde conjugate (t.c.), via a unitary thermal Bogoliubov transformation

$$\alpha_i^+ = u(T)\gamma_i^+ + v(T)\tilde{\gamma}_i\ , \qquad (4)$$

into the thermal quasiboson operators γ_i, γ_i^+, and their t.c. We insist here on the fact that the bosons $A, \tilde{A}$ need not be transformed since they are only auxiliary modes. This point of view is different from those adopted in all earlier works [2, 3, 4].
For fermionic systems, the situation is rather similar to the bosonic case. The extended form for the fermionic HP mapping proposed by Marshalek [7] is given by

$$\begin{aligned}
(J_z)_I &= \frac{1}{2}n_f + B^+B\ ,\\
(J_+)_I &= B^+\sqrt{N-(B^+B+n_f)}\ ; \quad (J_-)_I = (J_+)_I^+\\
(c_{2p})_I &= N^{-1}\left(\sqrt{N-(B^+B)}\,a_{2p} + B\,a_{1p}\right) \qquad (5)\\
(c_{1p})_I &= N^{-1}\left(\sqrt{N-(B^+B)}\,a_{1p} - B\,a_{2p}\right)\\
n_f &= \sum_{p=1}^{N}(a_{2p}^+a_{2p} - a_{1p}^+a_{1p})\,.
\end{aligned}$$

where B^+ and a_{ip}^+ are ideal boson and fermion operators, respectively. It allows a consistent mapping of pairs and single-fermion states. The thermalization is again obtained following the amended path I. Thus one introduces as previously the thermal Bogoliubov transformation which rotates only the ideal fermions and their tilde transform, such that

$$a_{ip}^+ = x_i\beta_{ip}^+ + y_i\tilde{\beta}_{ip}\ , \qquad (6)$$

while the auxiliary bosons B are left unaltered. Obviously our procedure cures the problems of path I that were encountered in ref. [2] regarding the fermion statistics [5].

References

[1] Y. Takahasi, H. Umezawa, Coll. Pheno., 2 (1975) 55.
[2] T. Hatsuda, Nucl. Phys. A492 (1989) 187.
[3] N. R. Walet, A. Klein, Nucl. Phys. A510 (1990) 261.
[4] O. Civitarese et al., Phys. Rev. C60 (1999) 34302.
[5] Z. Aouissat, A. Storozhenko, A. Vdovin, J. Wambach, Submitted to Phys. Rev. C.
[6] Z. Aouissat, Phys. Rev. C62 (2000) 012201(R)
[7] E.R. Marshalek, Nucl. Phys. A224 (1974) 221.

Chiral Phase Transition in the scaled $O(4)$-Model

O. Bohr, B.-J. Schaefer, J. Wambach
Institut für Kernphysik, Technische Universität Darmstadt.

Due to the non-Abelian character of QCD gluons self-interact and form bound states, so-called glueballs. Such glueballs have been seen in recent lattice simulations and are actively searched for in experiment. Glueballs can be used to construct effective models of QCD which respect the symmetries and anomaly structure of the theory.
At the classical level and in the limit of vanishing quark masses QCD for n flavors exhibits a global chiral $U(n)_L \times U(n)_R$ symmetry and is in addition invariant under scale transformations. Due to anomalies not all of the associated currents are conserved and the symmetry is broken down to $SU(n)_L \times SU(n)_R$ which, in the case of two flavors, is isomorphic to $O(4)$. This symmetry is spontaneously broken to $SU(n)_{L+R}$. The divergence of the anomalous scale current is given by the trace of the energy-momentum tensor which, in the limit of massless quarks, is given by

$$\langle \theta^\mu_\mu \rangle = \langle \frac{\beta(g)}{2g} G^a_{\mu\nu}(x) G^{a\mu\nu}(x) \rangle \ , \qquad (1)$$

where $G^a_{\mu\nu}(x)$ denotes the gluonic field-strength tensor and $\beta(g)$ is the usual QCD beta function. An effective realization of the scale anomaly can be achieved by adding to the classical Lagrangian a scalar color singlet dilaton field χ with an interaction potential of the form

$$V(\chi) = h \left(\frac{\chi}{\chi_0} \right)^4 \left(\ln \frac{\chi}{\chi_0} - \frac{1}{4} \right) \ , \qquad (2)$$

where h is a constant that is related to the vacuum energy density ε_{vac} via $h = -4\varepsilon_{vac}$, when there are no quarks. The potential has a minimum at $\chi = \chi_0$.
In a previous work [?] we have tested a novel renormalization group approach to investigate chiral symmetry restoration at finite temperature and could analyze the critical behavior at the chiral phase transition of the $O(N)$-model. In this work we investigate the influence of the additional dilaton field on the chiral phase transition and the critical behavior. Therefore we couple a massive scalar dilaton field, which breaks the scale invariance, to the $O(4)$-model. Here we follow here the work in [?] and consider the following Lagrangian

$$\begin{aligned} \mathcal{L} \ = \ & \frac{1}{2}\partial_\mu\sigma\partial^\mu\sigma + \frac{1}{2}\partial_\mu\vec{\pi}\partial^\mu\vec{\pi} + \frac{1}{2}\partial_\mu\chi\partial^\mu\chi \qquad (3) \\ & - \frac{\lambda}{4}\left(\sigma^2 + \vec{\pi}^2 - \frac{\chi^2}{\zeta^2}\right)^2 - V(\chi) \ , \end{aligned}$$

where σ, $\vec{\pi}$ denote the sigma- and the pion fields respectively.
Lattice calculations hint that the lightest glueball has a mass of 1.3 - 1.6 GeV. We use this mass as a constraint to fix the parameters of the model at $T = 0$. We then perform a finite-temperature calculation, where we calculate the vacuum expectation value (VEV) of the meson fields and the critical exponents of the chiral phase transition. From a comparison with the $O(4)$-model calculation without the dilaton field we can then estimate the influence of the dilaton field on the chiral phase transition.

The temperature dependence of the scalar mesonic VEV $\langle\phi\rangle$ (cf. Fig. 1) is very similar to the temperature dependence in the pure $O(4)$-model calculation without the dilaton field. Around T_c we again obtain a scaling behavior of the VEV $\langle\phi\rangle$ and of the mesonic coupling constant λ with critical exponents $\beta = 0.39$ and $\nu = 0.79$.

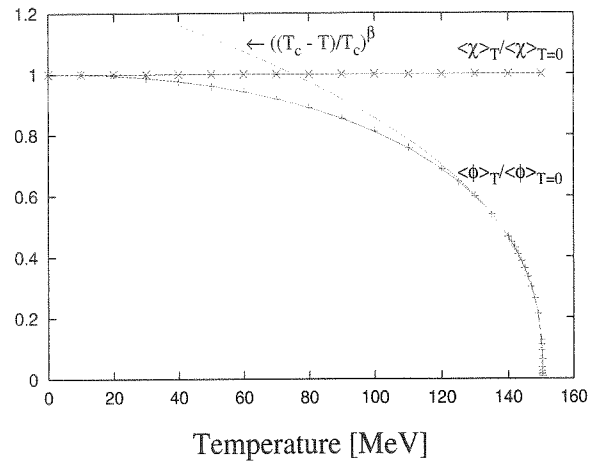

Figure 1: The temperature evolution of the vacuum expectation values of the dilaton field $\langle\chi\rangle$ and the scalar meson field $\langle\phi\rangle$ in the chiral limit.

These values of the exponents coincide within the estimated numerical error bars with the pure $O(4)$-model values.
On the other hand the glueballs themselves change very little in the temperature region up to the chiral phase transition. The change of the mass as well as of the VEV of the dilaton field (cf. Fig. 1) is less then 0.1% in this region. Calculations within the framework of a pure dilaton model show that the glueballs begin to be modified considerably at temperatures around 250 MeV.

In summary we can conclude that the glueballs, due to their high mass of ≈ 1.5 GeV, have very little influence on the temperature evolution in the mesonic sector where we still find a second order chiral phase transition with $O(4)$ critical exponents.

References

[1] O. Bohr, B.-J. Schaefer and J. Wambach, eprint: hep-ph/0007098
[2] H. Gomm, J. Schechter, Phys. Lett **B158** (1985) 449; E. K. Heide, S. Rudaz, P. J. Ellis, Phys. Lett. **B293** (1992) 259.

Chiral Fluctuations in Nuclei

Z. Aouissat, C. Isselhorst and J. Wambach
Institut für Kernphysik, Technische Universität Darmstadt.

The near-threshold enhancement in the $\pi^+\pi^-$ invariant mass distribution in nuclei, observed by CHAOS collaboration [1] and for $\pi^0\pi^0$ pairs by the Crystal Ball collaboration [2], offers the interesting possibility of directly observing a signal for partial restoration of chiral symmetry in a dense medium. There seems to be theoretical consensus on a strong in-medium reshaping of the s-wave isoscalar pion-pair correlations as a direct consequence of increased fluctuations of the chiral order parameter. This translates into a significant downward shift of the strength in the $\pi\pi$ T-matrix in the scalar-isoscalar channel as seen in Fig. 1.

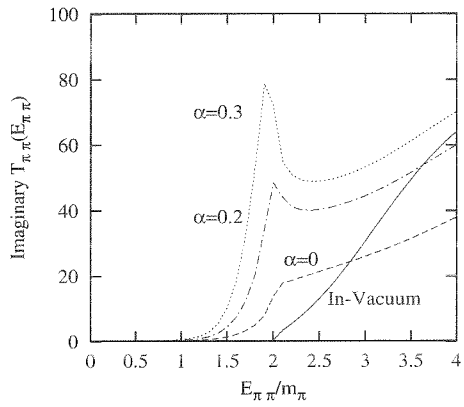

Figure 1: The imaginary part of the in-medium $\pi\pi$ T-matrix at normal nuclear density. The parameter α represents the medium effects on the mean field sigma-mass. See ref. [3] for details.

The reaction theory for the $A(\pi, 2\pi)$ knockout process has been thoroughly studied in the past [4], but only recently has the in-medium $\pi\pi$ final-state interaction (FSI) been seriously considered [5]. Taking into account the elementary $\pi\pi$ production process on the nucleon, the experimental acceptance, the Pauli constrained phase-space, and the nuclear absorption of the incoming and outgoing pions, the total cross-section for the $A(\pi, 2\pi)$ process in local density approximation reads

$$\begin{aligned}\sigma &= \frac{\pi}{q}\int d^2b dz A_{in}(\rho(\vec{r}))A^+_{out}(\rho(\vec{r}_1))A^-_{out}(\rho(\vec{r}_2)) \\ &\int \frac{d^3k}{(2\pi)^3}\frac{d^3q_1}{(2\pi)^3}\frac{d^3q_2}{(2\pi)^3}n(\vec{k})[1-n(\vec{q}+\vec{q}-\vec{q}_1-\vec{q}_2)] \\ &\delta(q_0+\varepsilon_{\vec{k}}-\omega_{\vec{q}_1}-\omega_{\vec{q}_2}-\varepsilon_{\vec{k}+\vec{q}-\vec{q}_1-\vec{q}_2})\frac{1}{2\omega_{\vec{q}_1}}\frac{1}{2\omega_{\vec{q}_2}} \\ &|T_{(\pi N\to\pi\pi N)}|^2\left|\frac{T_{\pi\pi}}{V_{\pi\pi}}\right|^2_{FSI}\times Acceptance\,. \qquad (1)\end{aligned}$$

To remove both experimental and theoretical uncertainties in the reaction dynamics, the CHAOS collaboration has considered the composite ratio, $C^A_{\pi\pi} = \frac{\sigma^A(M_{\pi\pi})}{\sigma^A_T}/\frac{\sigma^N(M_{\pi\pi})}{\sigma^N_T}$, where $\sigma^A(M_{\pi\pi})$ ($\sigma^N(M_{\pi\pi})$) denotes the invariant mass distribution in the nucleus (nucleon), while σ^A_T (σ^N_T) is the corresponding total cross section for the $A(\pi, 2\pi)$ process [6]. Comparing this ratio for both $\pi^+\pi^-$ and $\pi^+\pi^+$ final states, one can argue that the observed near-threshold enhancement must be an $I = 0$ effect. The theoretical predictions shown on Fig. 2 assume the effect of the FSI as appearing in Fig. 1. The various curves reflect the current state-of-the-art calculations by different groups (see [7] for details). The dashed curve uses the model in [3].

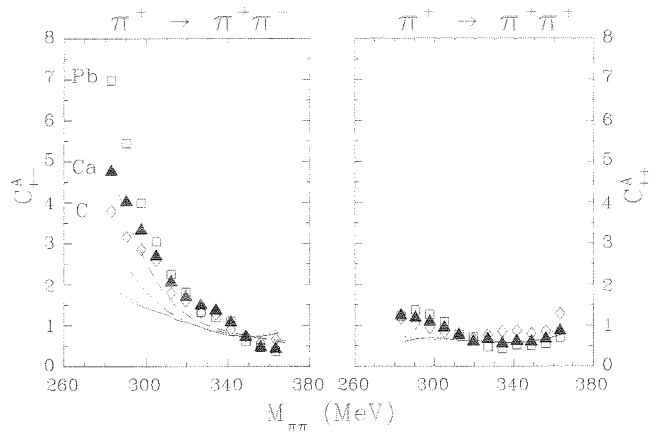

Figure 2: The ratio $C^A_{\pi\pi}$ for various nuclear targets [6].

However, improvements in the reaction calculations are needed. The kinematical analysis of the 3-body final state, for instance, reveals that the average momentum of the pion-pair is about 200 MeV/c. Therefore the back-to-back kinematics assumption used in all previous calculations needs to be revised [8].

On the experimental side, a very exciting possibility which circumvents the strong absorption in the initial state is the photoproduction $A(\gamma, 2\pi^0)$. Such experiments have been conducted at MAMI in Mainz and are currently analyzed [9]. A theoretical description is also in progress [8].

References

[1] F. Bonutti et al., Phys. Rev. Lett. 77 (1996) 603.
[2] A. B. Starostin et al., submitted to Phys. Rev. Lett.
[3] Z. Aouissat, G. Chanfray, P. Schuck, J. Wambach, Phys. Rev. C 61, (2000) 12202
[4] M. J. Vicente Vacas, E. Oset, nucl-th/9907008
[5] P. Schuck, Z. Aouissat, F. Bonutti, G. Chanfray, E. Fragiacomo, N. Grion, J.Wambach, Proceedings of the XXXVI, international Winter Meeting on Nuclear Physics, Ed. I. Iori, Bormio (Italy), January 1998.
[6] F. Bonutti et al., Nucl. Phys. A677 (2000) 213.
[7] J. Wambach, Z. Aouissat, P. Schuck, to appear in Nucl. Phys. A.
[8] Z. Aouissat, C. Isselhorst, J. Wambach, in progress.
[9] V. Metag, to appear in Nucl. Phys. A.

Nonpertubative renormalization flow and infrared physics

J. Meyer, K. Schwenzer, T. Spitzenberg and H.J. Pirner,
Institut für Theoretische Physik der Universität Heidelberg

Renormalization group flow equations have proved to be a good tool to analyze the dynamics of strong interaction in the nonperturbative region. They have been successfully applied to effective mesonic models in a thermal environment and revealed detailed insight into the chiral phase transition [1]. The basic aim of the renormalization group treatment is to systematically integrate out quantum and/or thermal fluctuations with momenta above a certain cutoff scale k and include them into the couplings of an effective action.

We are interested in the low energy theory of strong interaction resulting from the integration of high momentum modes. Assuming a dominant one gluon exchange or a instanton vacuum, gluonic degrees of freedom can be absorbed into an instantaneous four fermion interaction described by the NJL-model. Our analysis shows that the standard solution of the NJL-model and the flow of the linear σ-model, which we are using, coincide in the large N_C-limit, where the dynamics is dominated by fermion loops. In the full solution though, the additional dynamics of the mesonic degrees of freedom becomes important and yields an improved low energy behaviour compared to the NJL-model. The linear σ-model describes a massless two flavour quark field q interacting with chiral fields $\Phi = (\sigma, \vec{\pi})$ and is believed to give a valid description of chiral dynamics at scales $\leq$ 1GeV. It has the action

$$S_{UV} = \int d^4x \left[\bar{q} \left(i\partial\!\!\!/ - g \left(\sigma + i\vec{\tau}\vec{\pi}\gamma_5 \right) \right) q + \frac{1}{2} \left(\partial\Phi \right)^2 - U(\Phi^2) \right],$$

with a general O(4) symmetric potential $U(\Phi^2)$. From this, we compute the effective action in a one loop approximation using Schwinger proper time regularization [2]. The resulting expression is truncated to second order derivative in order to include the relevant terms for the flow. This inclusion of higher order terms, results in a splitting in the dynamics of the massive σ-mode and the massless Goldstone-bosons. By a renormalization group improvement the one loop expressions are turned into nonperturbative flow equations. The resulting flow for the most important parameters is plotted below. An interesting feature is, that like the four boson coupling λ also the Yukawa coupling g_σ vanishes in the infrared. Therefore, aside from providing a broken vacuum, the σ decouples from the dynamics and leaves the pions as the only dynamic particles. We obtain the resulting infrared effective action

$$\Gamma_{IR} = \int d^4x \Big[\bar{q} \left(i\partial\!\!\!/ - m_q - i g_\pi \vec{\tau}\vec{\pi}\gamma_5 + \frac{g_\pi}{f_\pi}\pi^2 \right) q - \frac{1}{2} \left(\partial\vec{\pi} \right)^2 + \text{derivative couplings} \Big].$$

Our approximation obeys the chiral Ward identities and ensures that the $\pi\pi$-scattering amplitude vanishes at tree level due to a $\bar{q}q\pi^2$-contact term that cancels the 1π-contributions in the IR.

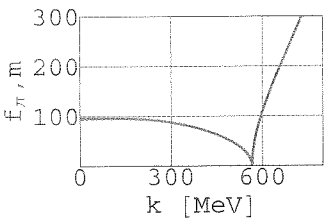

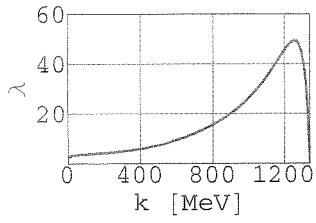

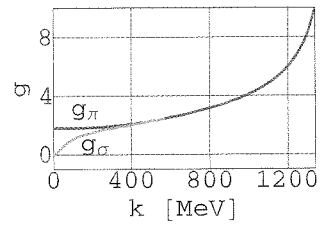

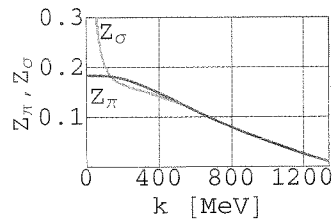

Once the flow equations for the linear σ-model are written down, the chiral order parameter $\langle \bar{q}q \rangle$ can be calculated from the partition function. Using the same cutoff function as for the flow equations one obtains in the local potential approximation

$$\partial_k \langle \bar{q}q \rangle = -\frac{N_c g k^5 \phi_k}{2\pi^2 \left(k^2 + g^2 \phi_k^2 \right)^2} .$$

Starting in the symmetric regime where the order parameter is zero, we find a value of $\langle \bar{q}q \rangle = -(194\text{Mev})^3$, as shown below.

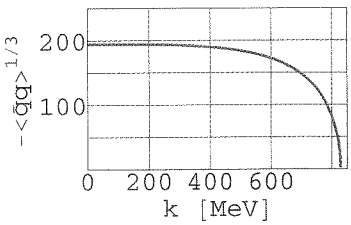

It is now tempting to derive a flow equation for the spectral density $\rho(\lambda)$ of the Dirac operator. This may be done by establishing a relation between $\langle \bar{q}q \rangle$ (λ) and $\rho(\lambda)$ similar to the Banks-Casher relation. It would be interesting to compare the results with recent data available from lattice QCD.

Another promising idea is to connect our cutoff parameter to a physical momentum scale and continue our Euklidian flows to the full complex plane. By this, it would be possible to compute spectral functions of mesonic resonances and make a direct connection to low energy hadron phenomenology.

References

[1] J. Berges, N. Tetradis and C. Wetterich,
to appear in Phys. Rep., hep-ph/0005122

[2] B.-J. Schaefer and H.-J. Pirner,
Nucl. Phys. **A660** (1999) 439, nucl-th/9903003

e^+e^--pair production in π^-p reactions

Matthias Lutz, Bengt Friman (GSI) and Madeleine Soyeur (CE Saclay)

The cross section for the reaction $\pi^- p \to e^+e^-$ is computed, using vector-meson dominance and the amplitudes for the processes $\pi^- p \to \rho^0 n$ and $\pi^- p \to \omega n$, obtained in a coupled channel analysis of meson-nucleon scattering at energies near the threshold for vector-meson production [1]. These amplitudes are sensitive to the coupling of the vector mesons to baryon resonances below the vector meson production threshold. Data that directly reflect these amplitudes would provide very useful constraints on the dynamics of vector mesons propagation in nuclear matter and e^+e^- pair production in heavy-ion collisions. The $\pi^- p \to e^+e^- n$ reaction offers the possibility to experimentally test the pion induced vector meson production amplitudes below threshold. The interference of the two light vector mesons in the e^+e^- channel is sensitive to the magnitudes and the relative phase of the ρ^0 and ω production amplitudes (see Fig. 1). An experimental test of the N*Nρ^0 and N*Nω vertices through the $\pi^- p \to e^+e^- n$ reaction below the vector meson production threshold would be a most valuable constraint on the in-medium propagation of ρ^0- and ω-mesons.

We shall restrict our discussion to e^+e^- pairs of invariant masses ranging from 0.5 to 0.8 GeV. The exclusive measurement of the $e^+e^- n$ outgoing channel ensures that the e^+e^- pairs come from vector meson decays (pseudoscalar mesons decay into an e^+e^- pair and an additional photon). We note however that only s- and d-wave pion-nucleon resonances are at present included in the model of Ref. [1]. To be complete, the description of the $\pi^- p \to e^+e^- n$ reaction in the energy range discussed in this work ($1.2 < \sqrt{s} < 1.8$ GeV) should include also the effect of other partial waves.

The magnitude of the $\rho^0 - \omega$ interference in the $\pi^- p \to e^+e^- n$ is illustrated in Fig. 2, where we show the cross section for this reaction as function of the total center of mass energy. We have selected e^+e^- pairs of invariant mass m=0.55 GeV. This figure elucidates the role of baryon resonances with masses in the range of 1.5 to 1.6 GeV in generating strong interference effects.

Above the vector meson threshold, the $\rho^0 - \omega$ interference in the $\pi^- p \to e^+e^- n$ cross section is particularly interesting for e^+e^- pair invariant masses close to the ω mass. This effect is manifested in the invariant mass spectrum shown in Fig. 3 ($\sqrt{s}$=1.8 GeV). The model of Ref. [1] for the $\mathcal{M}_{\pi^- p \to \rho^0 n}$ and $\mathcal{M}_{\pi^- p \to \omega n}$ amplitudes predicts a constructive interference at this energy. This feature appears to be a very sensitive test of the model.

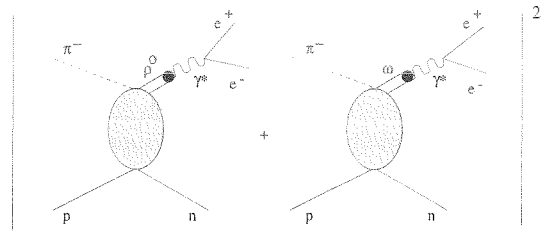

Figure 1: Squared amplitude for the $\pi^- p \to e^+e^- n$ reaction with intermediate ρ^0- and ω-mesons.

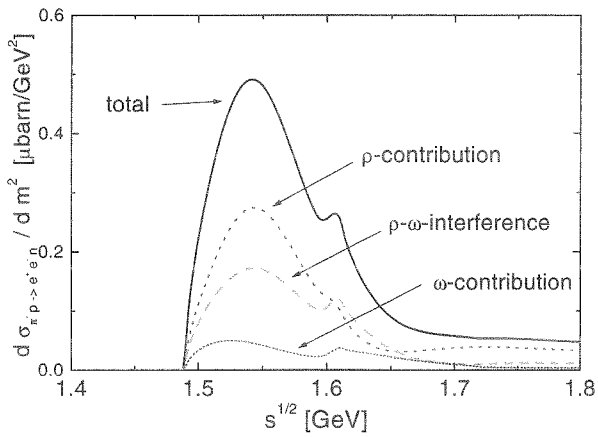

Figure 2: Differential cross section $d\sigma/dm^2$ for the $\pi^- p \to e^+e^- n$ reaction as function of $\sqrt{s}$ for a fixed e^+e^- pair invariant mass m=0.55 GeV.

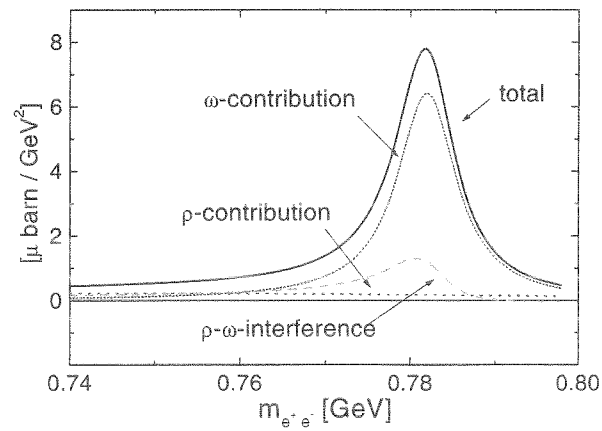

Figure 3: Differential cross section $d\sigma/dm^2$ as function of the e^+e^- pair invariant mass for a fixed total center of mass energy $\sqrt{s}$=1.8 GeV.

References

[1] M. Lutz, G. Wolf and B. Friman, Nucl. Phys. **A 661** (1999) 526c and Proc. of Hirschegg 2000.

[2] M. Lutz, B. Friman and M. Soyeur, in preparation.

e^+e^- production in pp, pd and pA reactions at SIS energies

E.L. Bratkovskaya, W. Cassing, and U. Mosel
University of Giessen

The modification of hadron properties in the nuclear matter is of fundamental interest. The dilepton data from heavy-ion experiments at SPS energies have provided first experimental evidence for a change of the vector meson properties, however, the heavy-ion data can be interpreted within different scenarios of in-medium modifications, i.e. by the dropping mass scenario or the collisional broadening approach. Since in heavy-ion experiments the nuclear matter is probed at different densities and temperatures within the complex dynamical evolution, it will be very useful to have independent experimental information from photon-nucleus, pion-nucleus or proton-nucleus reactions, where the properties of vector mesons are probed at normal nuclear density or below. This question becomes very actual with respect to the HADES experiments coming up at GSI soon [1].

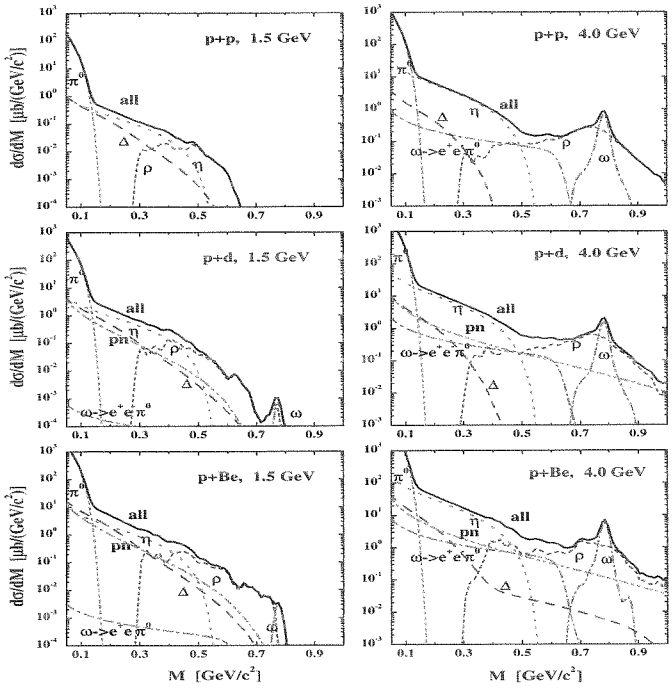

Figure 1: The dilepton invariant mass spectra $d\sigma/dM$ for pp (upper part), pd (middle part) and pBe collisions (lower part) at 1.5 GeV (left panel) and 4.0 GeV (right panel) including a 10 MeV mass resolution [2].

Dilepton production in from pp, pd and pBe collisions from 1 – 5 GeV has been studied in Ref. [2] within the framework of the combined resonance-string approach [3]. here, it has been found that the DLS data for pp and pd collisions can be reasonably well described whereas for pBe systems (especially at 4.9 GeV) our calculations give slightly higher dilepton yield. We have demonstrated, futhermore, the importance to measure dileptons from pp and pd (or even pBe) collisions simultaneously since such data provide constraints on the isospin dependence of pp and pn interactions, which is important for an understanding of heavy-ion data.

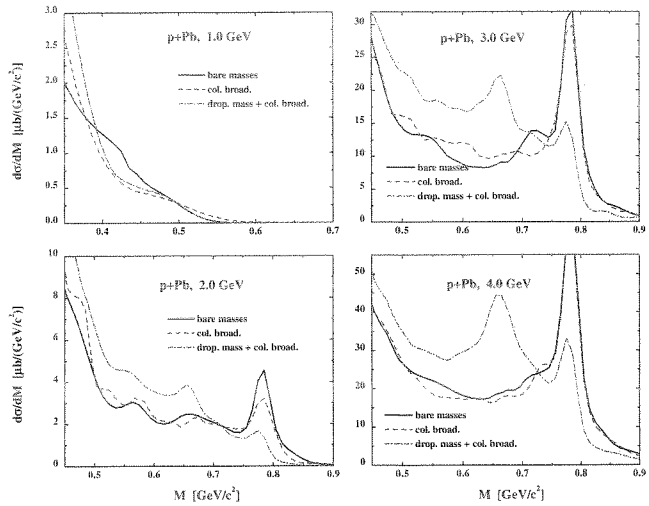

Figure 2: The comparison of different in-medium modification scenarios, i.e. collisional broadening (dashed lines) and collisional broadening + dropping vector meson masses (dash-dotted lines), with respect to the bare mass case (solid lines) for $p + Pb$ from 1–4 GeV [4].

In Fig. 1 we show our detailed predictions for the differential dilepton spectra from pp, pd and pBe collisions at 1.5 and 4.0 GeV energy with a 10 MeV mass resolution that can be controlled experimentally by the HADES Collaboration in near future.

A comparison of the different in-medium modification scenarios is shown in Fig. 2, i.e. collisional broadening (dashed lines) and collisional broadening + dropping vector meson masses (dash-dotted lines), with respect to the bare mass case (solid lines) on a linear scale for $p+Pb$ collisions from 1–4 GeV. The collisional broadening + 'dropping mass' scenario leads to an enhancement of the dilepton yield in the range $0.5 \leq M \leq 0.75$ GeV and to a reduction of the ω-peak, which is more pronounced for heavy systems (up to a factor 2 for $p + Pb$ at 3–4 GeV), since most of the ρ's and ω's now decay in the medium approximately at density ρ_0. This leads to a pronounced peak around $M \approx 0.65$ GeV, which can be attributed to the in-medium ω decay since the ρ spectral strength is distributed over a wide low mass regime. Especially when comparing dilepton spectra from C and Pb targets, it should be experimentally possible to distinguish an in-medium mass shift of the ω meson by taking the ratio of both spectra.

References

[1] The HADES Collaboration, Proposal, GSI 1994.
[2] E.L. Bratkovskaya et al., Nucl. Phys. A 686 (2001) 476.
[3] M. Effenberger et al., Phys. Rev. C 60 (1999) 044614.
[4] E.L. Bratkovskaya, nucl-th/0101067.

Renormalisation of Self-consistent Resummation Schemes[G]

H. van Hees, J. Knoll (GSI)

For the description of physical systems with strong interactions generally perturbative methods are insufficient. Rather on the basis of effective field theories non-perturbative methods such as partial resummation schemes have to be applied. There are a couple central questions connected with such methods which concern symmetries and conservation laws as well as thermodynamic consistency and detailed balance. While the question of conserving approximations was addressed by Baym's Φ-functional method [1, 2, 3], in field theoretical descriptions a further complication arises, namely that of renormalization. Loop integrals generally diverge and renormalization concepts were developed in perturbation theory. In the context of resummation schemes the question arises under which conditions they are still renormalizable with temperature and density independent counter terms. In the past only a few specific examples were investigated.

Our purpose was to analyze self consistent partial Dyson resummation schemes defined by a set of basic generating self energy diagrams with dressed propagators. In terms of perturbative diagrams this leads to an infinite iterative insertion of all basic diagrams. The sum of all these perturbative diagrams defines the self consistent self energy which determines the dressed propagator, cf. (1). All diagram subpieces with the topology of a single loop which are connected to the rest of the diagram at most via two vertices, are divergent and have to be renormalized. These structures, however, appear in a nested way such that first the most inner ones have to be renormalized through counter-terms given by the reduced diagrams where the divergent sub-pieces are contracted to a point. The so obtained reduced diagrams themselves are to be subjected to the same procedure. This iterative process is formalized as the BPHZ-renormalization scheme. For the self consistent scheme under consideration the key issue is to find a compact iteration scheme that generates all the required counter terms at once.

For an initial study we choose a simple scalar field theory model, the ϕ^4-model. For the Hartree approximation given by the tadpole self-energy diagram the subtraction scheme can be formulated as a gap equation. As a new part we included a genuine two-point contribution, namely the sunset diagram. The latter gives rise to an imaginary part in the self-energy, i.e., a finite width for the particles in the medium. In terms of perturbative diagrams the self consistent scheme then leads to all kinds of "super-daisy", "super-sunset" diagrams and all possible mixtures of them, cf. (1).

It could be shown that also this approximation can be renormalized in a BPHZ-type procedure (for details see [4]). The considerations show that one first has to solve the problem in the vacuum where subtracted dispersion relations can be used to renormalize the self-energy. In the same way one obtains the renormalized vertex functions which are needed to replace the corresponding divergent vacuum sub-diagrams in the finite temperature case. This means that for the renormalization of the finite temperature case one needs only *local temperature independent vacuum counter-terms* in perfect analogy to the well known theorem for perturbative finite-temperature quantum field theory.

We argue that the Φ-functional properties of the self energies indeed enforces the consistency of the counter-terms and symmetry factors for the explicit as well as the hidden nested and overlapping divergences since the divergent sub-diagrams are given by higher derivatives of the Φ-functional with respect to the dressed Green's function.

This substitution of divergent sub-diagrams together with direct subtractions of counter-terms on the level of the integrands provides a scheme where one has to deal only with convergent integrals without any explicite beforehand regularization which opened the possibility to calculate the self–energy and thermodynamic quantities such as the entropy in full self–consistency.

The results are important, e.g., for the description of hadrons in dense matter, e.g. [5] or for an effective description of gauge fields such as QCD in cases where the damping width of the particles is of considerable importance. Supplementary to the renormalization question functional methods have been developed on the basis of the Φ-functional concept, which permit to investigate and cure possible violations of symmetries and conservation laws at the level of higher order correlation functions [4]. This is of particular importance for gauge theories[5].

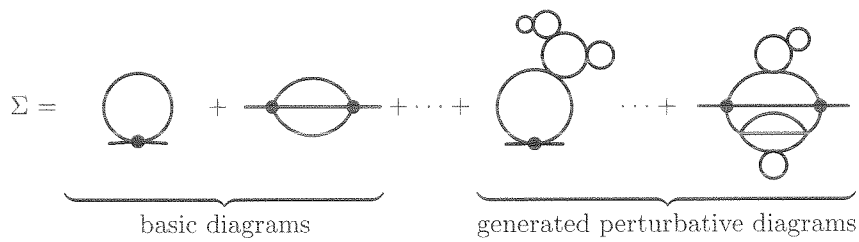

(1)

References

[1] G. Baym, Phys. Rev. **127** 1391 (1962).
[2] Y. B. Ivanov, J. Knoll, D. N. Voskresensky, Nucl. Phys. **A657** 413 (1999), hep-ph/9807351.
[3] Y. B. Ivanov, J. Knoll, D. N. Voskresensky, Nucl. Phys. **A672** 313 (2000), nucl-th/9905028.
[4] H. van Hees, Renormierung selbstkonsistenter Näherungen in der Quantenfeldtheorie bei endlichen Temperaturen, Ph.D. thesis, TU Darmstadt (2000), http://elib.tu-darmstadt.de/diss/000082/.
[5] H. van Hees, J. Knoll, Nucl. Phys. **A683** 369 (2001), hep-ph/0007070.

Vector mesons within a conserving self-consistent approximation[G]

H. van Hees, J. Knoll (GSI)

The experimental results on di-lepton production in heavy ion collisions by the CERES and DLS collaborations has shown an enhancement of the di-lepton production rate in the invariant pair mass region between 300-600 MeV compared to the rate to be expected from proton-proton collisions. Since dileptons are direct signals from the decay of vector mesons within the hot reaction zone this enhancement points towards in-medium modifications of vector-mesons in dense hadronic matter.

From the theoretical point of view a consistent description of such phenomena within effective quantum field theoretical models needs a treatment of particles which considers the finite spectral width. This concerns not only the widths of resonances but also the width due to collisions of the particles within the hot and dense medium. For such questions a perturbative approach is generally insufficient and a self-consistent treatment is at place.

There is a class of self-consistent approximations derived from a generating functional which leads to a closed set of conserving equations of motion for the mean fields and the Dyson resummed dressed propagators [1]. They posses exact conservation laws for the expectation values for conserved Noether-currents (including those from space-time symmetry, i.e., energy, momentum and angular momentum).

A detailed symmetry analysis nevertheless shows that on the level of higher order correlation functions such as propagators the Ward-Takahashi identities (WTI) of the underlying symmetries are not fulfilled [2]. In the case of vector or gauge fields this has serious consequences: The WTI are necessary to ensure the physicality of states. A violation of this symmetry causes the excitation of unphysical degrees of freedom and violates unitarity and causality within the dressed propagators and currents are no longer conserved at the correlator level.

On the other hand corrections which restore current conservation on the correlator level have been studied within a diffusion equation approximation of the according kinetic equation (Fokker-Planck-equation) [3]. The study shows that the space components of the polarization tensor suffer only small corrections, if the scattering of a particle is isotropic on the average. The self consistent time component, however has a completely wrong behavior as it also exponentially decay in time within this approximation, while it should stay constant in time due to charge conservation.

In order to cure this defect we have invented a particular projection method. It discards the wrong time components of the polarization tensor and solely uses the space components. This way a 4-dimensionally transverse polarization tensor for the vector field can be constructed. The two independent components of the thermal polarization tensor, the longitudinal and transverse components, $\Pi_T(q)$ and $\Pi_L(q)$, can be obtained from

$$2\Pi_T + g_{ik}\Pi^{ik} = -\frac{q_i q_k}{\vec{q}^{\,2}}\Pi^{ik} = -\frac{(q^0)^2}{q^2}\Pi_L.$$

Here the indices (i,k) run over the spatial components from 1 to 3. We have numerically solved the coupled self-consistent equations of motion for this projected self-energies. For details see [2, 4].

The results show a significant enhancement of the spectral width in the low energy mass region and all thresholds, present in the perturbative quantities, are gone due to collision broadening of the self-consistently treated pions.

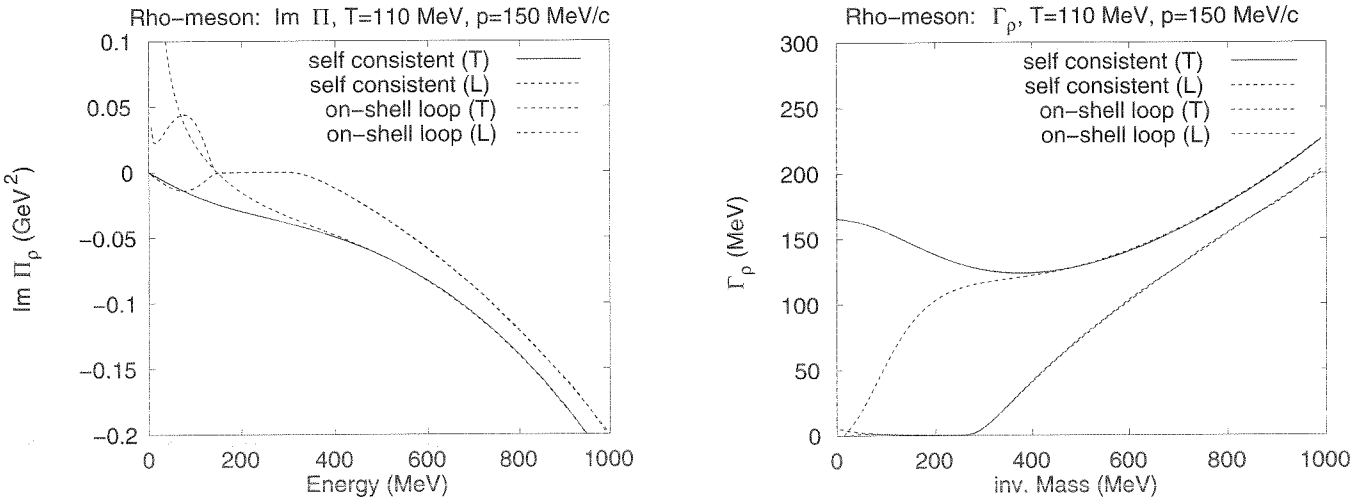

The transverse components of the imaginary part of the self-consistent ρ–meson self-energy (left) and the corresponding spectral width (right).

References

[1] G. Baym, Phys. Rev. **127** 1391 (1962).
[2] H. van Hees, Renormierung selbstkonsistenter Näherungen in der Quantenfeldtheorie bei endlichen Temperaturen, Ph.D. thesis, TU Darmstadt (2000), http://elib.tu-darmstadt.de/diss/000082/.
[3] J. Knoll, D. Voskresensky, Annals of Physics **249** 532 (1996).
[4] H. van Hees, J. Knoll, Nucl. Phys. **A683** 369 (2001), http://de.arXiv.org/abs/hep-ph/0007070.

Exact Conservation Laws in the Gradient Expanded Kadanoff–Baym Equations[G]

Jörn Knoll, Yuri B. Ivanov, and Dmitri N. Voskresensky
GSI Darmstadt

One of the challenging problems in quantum many-body physics is the appropriate inclusion of resonances or particles with broad damping width into a self-consistent non-equilibrium dynamics. Such kind of description can be constructed on the basis of the so called Kadanoff–Baym equations (KBE) derived within the non-equilibrium Green function technique [1]. While the KBE are exact, in actual calculations one has to rely on further approximations. They provide (a) a truncated self-consistent scheme and (b) through the gradient approximation they lead to transport type of equations of motion. Interested in the dynamics of particles with broad mass width one has to avoid the quasi-particle approximation, and solely rests on the first-order gradient approximation of the KBE. This concept was first addressed by Kadanoff and Baym [1] and recently reconsidered in the context of hadronic matter and heavy ion collisions [2–7]. As for any such approximation, however, symmetries and conservation laws as well as detailed balance and thermodynamic consistency may no longer a priori be guaranteed.

In ref. [8] we re-investigated a generalization of the Φ derivable method of Baym [9] to the real-time Green function technique which provides truncated self-consistent approximations which are conserving and thermodynamically consistent at the level of KBE. In particular a conserved energy-momentum tensor could be derived for local field couplings. The subsequent gradient approximation leads to two coupled equations: a quantum transport equation, which governs the four-phase distribution functions $f(\vec{x},t,p)$, and a retarded equation, which determines the time evolution of the spectral function $A(\vec{x},t,p)$. For this approximate set of equations the conservation laws generally are expected to become only *approximate*. Such approximate nature of conservation laws may be well acceptable theoretically as its accuracy precisely corresponds to that of the approximation. Nevertheless, both from a principle perspective and also from a practical point of view this situation is less satisfactory.

In this work [10] we investigated the quantum kinetic equations in the form originally derived by Kadanoff and Baym. The key point is to do a systematic first-order gradient expansion of all gradient terms even those internally present in the self-energies. Through a careful investigation of all gradient terms we could in fact prove that the quantum kinetic equations possess the generic feature of exact conservation laws at the expectation value level.

The conserved currents and the energy-momentum tensor take the original Noether form [8] ($X=(\vec{x},t)$)

$$J^{\mu}(X) = \int \frac{\mathrm{d}^4p}{(2\pi)^4} p^{\mu} f(X,p) A(X,p), \qquad (1)$$

$$\Theta^{\mu\nu}_{\rm loc}(X) = \int \frac{\mathrm{d}^4p}{(2\pi)^4} v^{\mu}p^{\nu} f(X,p) A(X,p) + g^{\mu\nu}\left(\mathcal{E}^{\rm int}_{\rm loc}(X) - \mathcal{E}^{\rm pot}_{\rm loc}(X)\right) \qquad (2)$$

now however in the so called local form, i.e. void of any gradient corrections. For the energy–momentum tensor the first term accounts for the single particle part which by itself overcounts the interaction energy. This is compensated by gradient terms which assemble to the difference between interaction energy density and single-particle potential energy density, $\mathcal{E}^{\rm int}_{\rm loc}(X) - \mathcal{E}^{\rm pot}_{\rm loc}(X)$, both obtained from the same Φ-functional in the local approximation as the self-energies driving the gradient expanded KBE.

In order to preserve the exact conserving property, a few conditions have to be met. First, the original KBE should be based on a Φ-derivable approximation scheme that guarantees that the KBE themselves are conserving [8, 9]. Second, all possible memory effects due to internal vertices within the self-energy diagrams are also consistently expanded to first-order gradients. Finally it is important that after the gradient expansion no further approximations are applied that violate the balance between different first-order gradient terms.

The presence of exact conservations puts the Kadanoff–Baym formulation of quantum transport on the level of generic phenomenological equations. They offer a phenomenological approach to the dynamical description of particles with broad damping widths, such as resonances, with built-in consistency and exact conservation laws. For practical simulations of complex dynamical systems this approach may even be applied in cases, where the smallness of the gradients can not always be guaranteed.

References

[1] L.P. Kadanoff and G. Baym, *Quantum Statistical Mechanics*, Benjamin, 1962.

[2] Yu.B. Ivanov, J. Knoll, and D.N. Voskresensky, Nucl. Phys. **A672** (2000) 313.

[3] M. Effenberger, U. Mosel, *Phys. Rev. C* **60** (1999), 51901.

[4] W. Cassing and S. Juchem, *Nucl. Phys. A* **665** (2000), 377; **672** (2000), 417.

[5] S. Leupold,*Nucl. Phys. A* **672** (2000), 475.

[6] Yu. B. Ivanov, J. Knoll, H. van Hees and D. N. Voskresensky, e-Print Archive: nucl-th/0005075; *Yad. Fiz.* **64** (2001).

[7] H. van Hees, and J. Knoll, *Nucl. Phys. A* **A683** (2001), 369.

[8] Yu.B. Ivanov, J. Knoll, and D.N. Voskresensky, Nucl. Phys. **A657** (1999) 413.

[9] G. Baym, Phys. Rev. **127** (1962) 1391.

[10] J. Knoll, Yu.B. Ivanov, and D.N. Voskresensky, nucl-th/0102044, submitted to Ann. Phys. (NY)

Production of vector mesons in pion nucleus reactions[B,G]

W.Schön, R.Schneider, W.Weise
Physik-Department TU-München

Model independent constraints from QCD sum rules connect the vector meson mass with the gap Δ between the nπ continuum and the $< q\bar{q} >$ vacuum state. At normal nuclear density, Δ is expected to be reduced by about 15% as a consequence of the restauration of chiral symmetry [1, 2]. In this work, the spectral functions of the vector mesons calculated in infinite matter are combined with a Monte Carlo simulation of π^- induced production and propagation of vector mesons inside nuclei.

The self-energy of the vector mesons in matter Π_v is based on the low density approximation which connects the vacuum self-energy Π_0 with the meson nucleon scattering matrix T_{vN}: $\Pi_v(\omega,\vec{q},\rho) = \Pi_0(\omega,\vec{q}) - \rho T_{vN}(\omega,\vec{q})$. The potential (and therefore the mass shift) depends to leading order linearly on the baryon density ρ: $2\omega U = \Pi_v(\omega,\vec{q},\rho) - \Pi_0 = \rho T_{vN}(\omega,\vec{q})$. The resulting spectral functions for infinite matter at $\rho = \rho_0$ show a different behavior for the ω- and the ρ meson. While the pole mass of the ρ meson is shifted only slightly, its width is heavily influenced by $\rho N \to \pi N$, $\rho N \to \pi\Delta \to \pi\pi N$ and $\rho N \to \omega N \to \pi\pi\pi N$ scattering. Effectively the ρ-meson is dissolved in the nuclear medium. The ω-meson pole mass is shifted by about -80 MeV/c^2 and the width is broadened from 8 to 40 MeV/c^2. However at $\rho = \rho_0$ the ω-meson still keeps its quasi-particle character. The MC-simulation is based on measured cross sections for $\pi^- + p \to \rho,\omega,\phi + n$ reactions. The absorption channels are calculated via detailed balance. The baryon density distribution of the Pb nucleus is based on measured charge distributions. The fermi motion of the nucleons is taken into account. With an elementary ω-meson cross section of 2.5 mb ($p_{\pi^-} = 1.3$ GeV/c) one could expect Z_{Pb}*2.5≈200 mb for a Pb nucleus. However the effective cross section results in only 33 mb. Because of the strong interaction of π^- with nuclear matter, only the hemisphere of the nucleus facing the beam takes part in the reaction (shadowing, Fig. 1). The mesons are produced with vacuum pole mass. In case of decay the mass of the meson is sampled according to the local baryon density at this "freezeout" point based on the spectral functions for infinite matter. The sampling is done in accordance with energy conservation. The spectral functions in the finite system (Fig. 2) are obtained by integration over the probability distribution of the meson decays. The majority of the ω-mesons decay outside the Pb nucleus and produce a narrow structure. The contributions from the inner part of the nucleus (full shift of the ω-meson mass) and the surface (reduced shift) increase the broadening of ω-mesons from 40 to about 80 MeV/c^2. This additional broadening is a consequence of the finite size of the system. The reaction $\pi^- Pb$ seems to be a promising experiment to probe the in-medium spectral distribion of vector mesons. The predicted dilepton spectra could be measured with the HADES spectrometer [3]. In Fig. 2 the HADES resolution is taken into account.

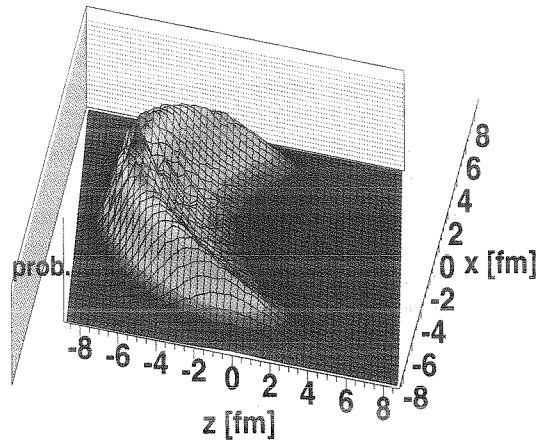

Figure 1: Spatial probability distribution of meson creation for $\pi^- Pb$ at p_π=1.3 [GeV/c].

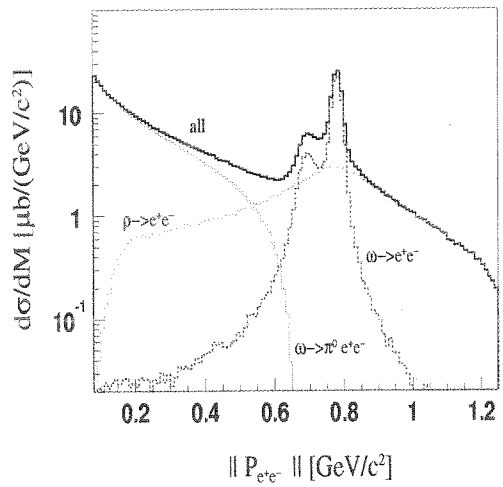

Figure 2: ρ- and ω-meson contributions to the dilepton specta for $\pi^- Pb$ at p_π=1.3 [GeV/c].

Below the η mass strong contributions from η Dalitz and other channels are expected. In the mass region of the (shifted) ω peak both πN Bremsstrahlung [4] and combinatorial background from π Dalitz decay [5] contribute still below the ρ-meson contribution.

References

[1] F.Klingl and W.Weise EPJ A4 (1999) 225
[2] E.Marco and W.Weise Phys. Lett. B482 (2000) 87
[3] J.Friese et.al. Nucl. Phys A654,(1999) 268
[4] W.Cassing et.al. Phys. Rep. 308, 65 (1999)
[5] W.Schön et.al. Act. Phys. Pol B27 Number 11 (1996)

Modifications in resonance life times and cross sections in a test-particle description of off-shell processes in transport theory

A.B. Larionov*, S. Leupold, U. Mosel
University of Giessen

For the understanding of heavy-ion collisions semi-classical transport theory has become an indispensable tool. While former works have focused their attention more or less on the quasi-particle regime the extension of the formalism to off-shell phenomena has become a topic of growing interest in the last few years since it has been realized that the collision rates present in high energetic nucleus-nucleus collisions typically are so large that an on-shell approximation seems to be inappropriate. In addition, the resonances excited during the reaction may have large decay widths. Therefore, a representation of these states by stable particles may not be a proper approximation. The usual approach to solve a transport equation is the representation of the phase-space density by test-particles. If not only asymptotically stable states but also resonances are simulated by test-particles, one has to attribute to those 'resonance test-particles' finite life times and arbitrary invariant masses (chosen according to their spectral distribution), i.e. the generalized test-particle representation is given by $\sum_i \delta^{(3)}(\vec{x}-\vec{x}_i(t))\,\delta(p_0^2 - E_i^2(t))\,\delta^{(3)}(\vec{p}-\vec{p}_i(t))$. Note that here in contrast to the quasi-particle approximation the test-particles are allowed to have arbitrary energies. The question which (in general energy- or mass-dependent) life time has to be attributed to the resonance test-particles is under present discussion. The commonly used recipe is to take the inverse of the decay width Γ of the resonance, evaluated for the respective invariant mass. Near threshold the width becomes small due to the available phase-space. Hence the life time — if identified with the inverse width — becomes large. In [1] it was suggested to rather calculate the life time from the time delay that the particles suffer which form the resonance. This time delay is given by the energy derivative of the scattering phase shift of these particles: $\tau = \partial\delta/\partial p_0$. This quantity vanishes near threshold. Hence the two expressions for the life time show a completely different behavior as functions of the invariant mass of the resonance as shown in Fig. 1 for the $\Delta(1232)$ resonance. Recently a novel approach to solve these questions has been presented [2, 3]. It has been shown there that the life time of an off-shell test-particle is indeed given by $\tau = \partial\delta/\partial p_0$. In addition, the cross section for any collision which involves an off-shell test-particle in the incoming channel is subject to an in-medium modification: the cross section has to be divided by $r = 2\sqrt{s}\Gamma\,\mathcal{A}\,(1-K)$ where Γ is the total width of the particle, $\mathcal{A}$ its spectral function and $1-K$ a renormalization factor (cf. [2, 3] for details).

To test the ideas above, we applied the BUU model in version [4] with the resonance production/absorption quenching [5]. The most sensitive observable for the Δ-resonance life time modifications turns out to be the invariant mass spectrum of the correlated proton-pion pairs.

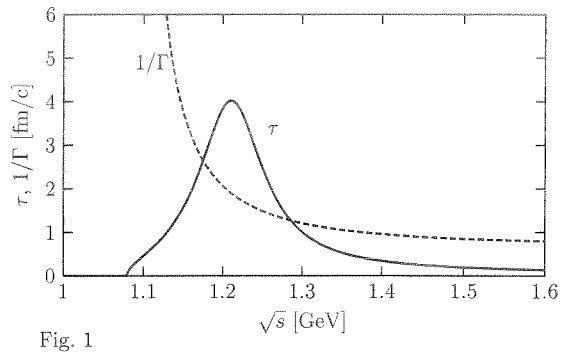

Fig. 1

Fig. 2 shows the invariant mass (p,π^+) spectra for a central Au+Au collision at 1.06 AGeV calculated without life time modifications (solid line), with modified Δ-resonance life time only (dashed line) and with both modified Δ-resonance life and $N\Delta \to NN$ cross section (dotted line). The life time modification leads to a sharper peaked spectrum at $M \simeq 1.2$ GeV due to longer life time of the Δ-resonances near the pole mass (Fig. 1). An additional modification of the $N\Delta \to NN$ cross section produces an even more sharp spectrum, since the absorption of the Δ-resonances near the pole mass gets reduced. Thus we conclude that the resonance life time modifications somewhat increase the deviation of the BUU calculation with the data [6] on the spectrum of the (p,π^+) pairs. Further studies will show if this effect could be counterbalanced by the off-shellness of the produced pions (work in progress).

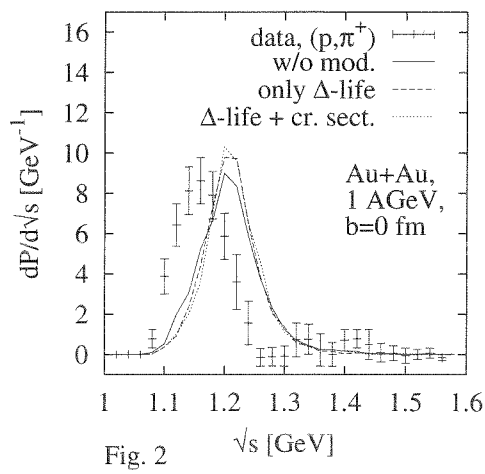

Fig. 2

References

[1] P. Danielewicz, S. Pratt, Phys. Rev. **C53**, 249 (1996).
[2] S. Leupold, Nucl. Phys. **A672**, 475 (2000).
[3] S. Leupold, nucl-th/0008036, subm. to Nucl. Phys. A.
[4] M. Effenberger, E.L. Bratkovskaya, U. Mosel, Phys. Rev. **C60**, 044614 (1999).
[5] A.B. Larionov, W. Cassing, S. Leupold, U. Mosel, contr. to this Annual Report.
[6] M. Eskef et al., Eur. Phys. J. **A3**, 335 (1998).

*On leave of absence from RRC "I.V. Kurchatov Institute", 123182 Moscow, Russia

Strange Particle Production and Equilibration at SIS energies within a Semiclassical Off-shell Transport Approach

W. Cassing, S. Juchem
University of Giessen

Recently we have formulated a novel transport approach that incorporates the propagation of particles off the mass-shell [1]. It goes beyond the conventional transport description within the on-shell quasiparticle limit to propagate particles with a finite lifetime by means of a dynamical spectral function. This spectral function is directly determined by the spacetime and momentum-dependent imaginary part of the particle self-energy. By this procedure it is guaranteed, that the actual spectral function is consistently adjusted to the scatterings and decays of the particle in the nuclear medium as well as in vacuum.

Within this off-shell transport approach we have studied strange meson production in the SIS energy regime. When treating baryons as well as antikaons off-shell we obtain an increase by a factor of about two for the production of K^- mesons in comparison to the on-shell calculation for $Ni + Ni$ at 1.8 A GeV (Fig. 1). This enhancement arises since antikaons couple strongly to nucleons such that they achieve a considerable collision width in the nuclear medium which leads to an effective lowering of their production threshold. So the antikaons might be produced at subtreshold energies and enhance the final K^--yield when becoming asymptotically on-shell. The inclusion of the off-shell propagation therefore gives a (partial) explanation for the high K^- abundancy that has been measured by the FRS, KaoS and FOPI Collaborations [2,3]. The data are still underestimated by the off-shell calculations that have been performed without any potentials for the strange mesons. Thus antikaon potenials will still be necessary to get a full description of the experimental results. We have also investigated the production of K^+ mesons in

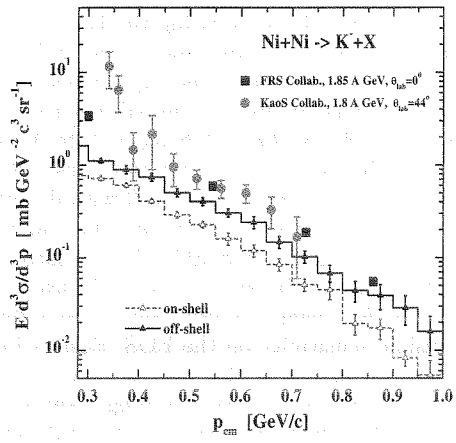

Figure 1: The inclusive spectra of K^- for $Ni + Ni$ at 1.8 A GeV within the off-shell transport approach (solid histogram, full triangles) and in the on-shell limit (dashed histogram, open triangles). The data are from [2] for $\theta_{lab} = 0^o$ (squares) and from [3] for $\theta_{lab} = 44^o$ (circles).

the same reaction, however, find only a small enhancement within the off-shell treatment relative to the on-shell limit which should be attributed to the weak coupling of kaons to nucleons [1b].

Furthermore, we have studied equilibration phenomena in the off-shell transport approach. For this aim we have confined the system to a box in coordinate space with periodic boundary conditions (using a density of $\rho = \rho_0$). We find that the off-shell generalization has practically no influence on the equilibration time of the nuclear system for various bombarding energies up to 1 A GeV [1c].

In order to study the equilibrium properties we compare the results of our transport (box) calculations with a simple statistical model for an ideal hadron gas . All hadron species that are propagated in the transport calculation (N,Δ,π) are also taken into account in the statistical model within the grand canonical ensemble. In Fig. 2 we

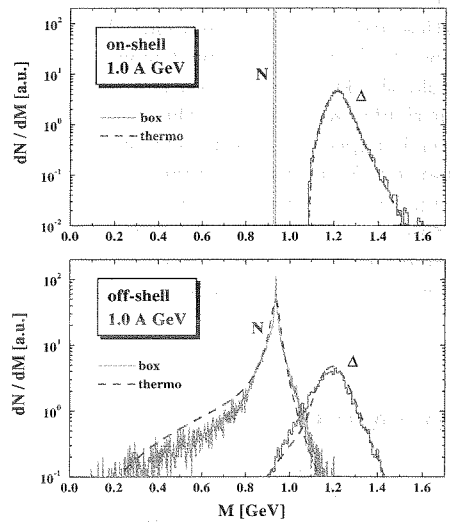

Figure 2: Differential distribution in mass for nucleons and Δ resonances for a bombarding energy 1 A GeV at $\rho = \rho_0$.

show the differential distributions in mass for nucleons and Δ resonances in the long time limit of the transport (box) calculations in comparison to the statistical model (dashed lines) for a bombarding energy of 1 A GeV. We find that the transport theoretical treatment yields nearly the same distributions in mass as the thermodynamical model, when for the latter the same spectral functions as in the transport calculation are employed. A temperature of 97 MeV (deduced from a transverse mass analysis of the particle spectra) has been used here. This result indicates that the actual realization of the off-shell dynamics guarantees the correct stationary solution in the long time limit.

References

[1] W. Cassing, S. Juchem, Nucl. Phys. A 665 (2000) 385; Nucl. Phys. A 672 (2000) 417; Nucl. Phys. A 677 (2000) 445.
[2] A. Schröter et al., Z. Phys. A 350 (1994) 101.
[3] P. Senger et al., Acta Phys. Pol. B27 (1996) 2993.

Probing the nuclear equation of state by K^+ production in heavy ion collisions

C. Fuchs, Amand Faessler, E. Zabrodin, Yu-Ming Zheng
Institut für Theoretische Physik, Universität Tübingen

From the very beginning kaons have been considered as one of the best probes to study dense and hot nuclear matter formed in relativistic heavy ion collisions. In particular at incident energies below the corresponding production thresholds in free space K^+ mesons are created in the early and high density phase of such reactions and – due to strangeness conservation – are not reabsorbed by the nuclear environment. Furthermore, there exist strong evidences that kaons change their properties inside the nuclear medium as predicted by effective chiral models. The aim of the present work is to study if decisive information on the nuclear EOS can be extracted from subthreshold kaon production by new high precision data [1]. The KaoS Collaboration has performed systematic measurements of the K^+ production far below threshold in heavy ($Au + Au$) and light ($C + C$) systems [2]. Looking at the ratios built from heavy and light systems possible uncertainties which might still exist in the theoretical calculations should cancel out to a large extent which allows to draw reliable conclusions. Furthermore, far below threshold the kaon production is a highly collective process and a particular sensitivity to the compression of the participant matter is expected. The present investigations are based on the Quantum Molecular Dynamics (QMD) transport model. For the nuclear EOS we adopt soft and hard Skyrme forces corresponding to a compression modulus of K=200 MeV and 380 MeV, respectively, and with a momentum dependence adjusted to the empirical optical nucleon-nucleus potential.

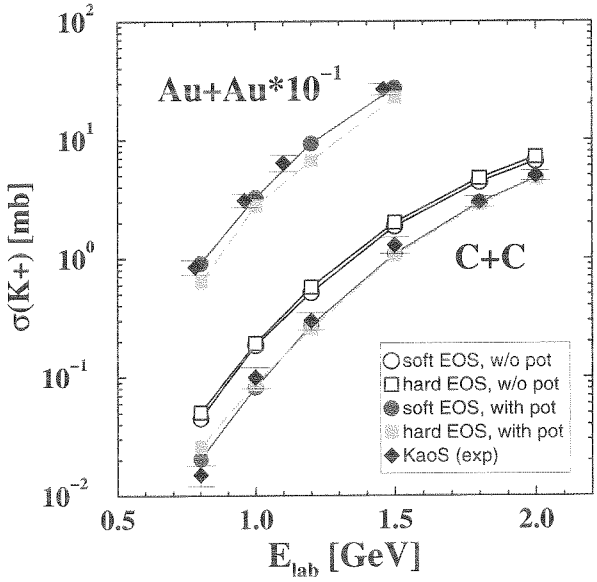

Figure 1: Excitation function of the K^+ cross section in $C+C$ and $Au + Au$ reactions. The calculations are performed with in-medium kaon potential and using a hard/soft nuclear EOS. For $C + C$ also results without in-medium kaon potential are shown.

In Fig. 1 the K^+ excitation function for $Au + Au$ and $C + C$ reactions starting from 0.8 A·GeV which is far below threshold ($E_{thr} = 1.58$ GeV) are shown. The calculations are performed for a soft/hard EOS including the in-medium kaon potential. For both systems the agreement with the KaoS data [3, 2] is very good when a soft EOS is used. In the large system there is a visible EOS effect which is absent in the light system. To estimate the influence of the in-medium kaon potential for $C + C$ also calculations without potential are shown. Already in the light system the K^+ yield is reduced by about **50%** by the influence of the potential which is essential to reproduce the yields [3]. The comparison to the new KaoS data [2] is made

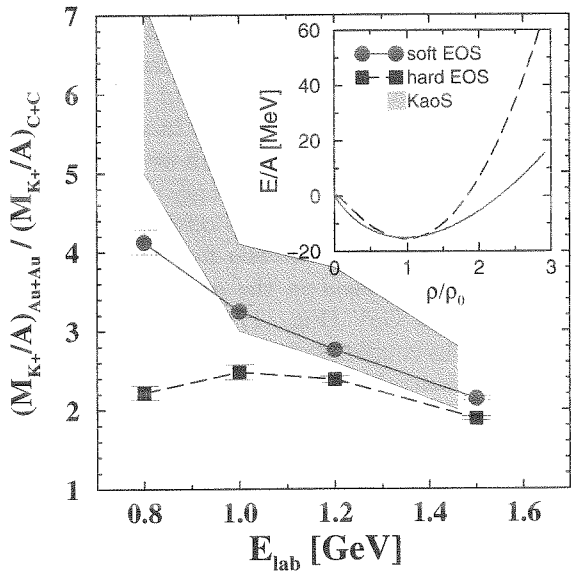

Figure 2: Excitation function of the ratio R of K^+ multiplicities obtained in inclusive $Au + Au$ over $C + C$ reactions. The calculations are performed with in-medium kaon potential and using a hard/soft nuclear EOS and compared to the experimental range of R (shaded area) given by the data from the KaoS Collaboration [2].

in Fig. 2. Here only calculations including the kaon potential are shown since it is already clear from Fig. 1 that without the potential one is not able to reproduce the experimental yields. The calculations are performed under minimal bias conditions with $b_{max} = 11$ fm for $Au + Au$ and $b_{max} = 5$ fm for $C + C$ and normalised to the experimental reaction cross sections [3, 2]. Both calculations show an increase of R with decreasing incident energy down to 1.0 A·GeV. However, this increase is much less pronounced using the stiff EOS. In the latter case R even drops for 0.8 A·GeV whereas the soft EOS leads to an unrelieved increase of R. Using the light system as reference frame there is a visible sensitivity on the EOS. Results for the K^+ excitation function in $Au + Au$ over $C + C$ reactions as measured by the KaoS Collaboration, strongly support the scenario with a soft EOS. The ratio itself is rather independent on the existance of the in-medium potential, but the potential is necessary to reproduce the total yields.

References

[1] C. Fuchs, A. Faessler, E. Zabrodin, Y.-M. Zheng, Phys. Rev. Lett. (2001) in press.

[2] C. Sturm *et al.*, Phys. Rev. Lett. **86**, 39 (2001).

[3] F. Laue et al., Phys. Rev. Lett. **82**, 1640 (1998).

Kaon Production via High Mass Resonances in UrQMD[B,G]

H. Weber, S.A. Bass[‡] , S. Soff[§] , H. Stöcker and W. Greiner
Institut für Theoretische Physik, Universität Frankfurt am Main, Germany

The investigation of strange matter in heavy ion collisions is of great interest, as the s and $\bar{s}$-quarks are not present in the initial projectile and target matter. Therefore the measurement of strange particles might yield deep insight into the reaction dynamics during the high density phase.

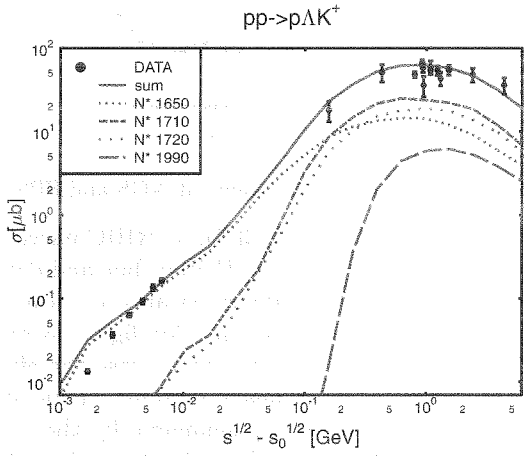

Figure 1: $pp \to p\Lambda K^+$ cross section in UrQMD compared to data.

For our investigation, we use the Ultrarelativistic Quantum Molecular Dynamics model (UrQMD) [1]. UrQMD provides a good description of NN and A+A collisions over a wide range of energies from a few hundred MeV/A up to hundreds of GeV/A. The production threshold for the lightest strange particle (K^+) via the process $NN \to N\Lambda K^+$ is 1.58 GeV. Particularly for SIS energies, the correct description of the production cross section near the threshold is very important. In contrast to most other models, UrQMD treats the elementary K^+ production via two-step processes

$$pp \to pB^* \to p\Lambda K^+, \qquad pp \to pB^* \to p\Sigma K$$

B^* are the high mass resonances N^*_{1650}, N^*_{1710}, N^*_{1720}, N^*_{1990} and Δ^*_{1920}. For the decay into the hyperon-kaon channel we use the experimental branching ratios, where available.

Figure 1 shows the cross section for the reaction $pp \to p\Lambda K^+$ as a function of energy above threshold. The dotted lines are contributions of the five resonances to the total cross section (solid line). With this approach we are able to describe the experimental data (dots) reasonably well, even a few MeV above the threshold (COSY data [2])

The $pp \to p\Sigma^0 K^+$ and the $pp \to p\Sigma^+ K^0$ channel can be described as well with this approach. Figure 2 shows these channels in UrQMD compared to data.

For higher collision energies, kaon production via string fragmentation becomes important. Figure 3 shows an excitation function of the K^+ to K^- ratio for central Pb+Pb

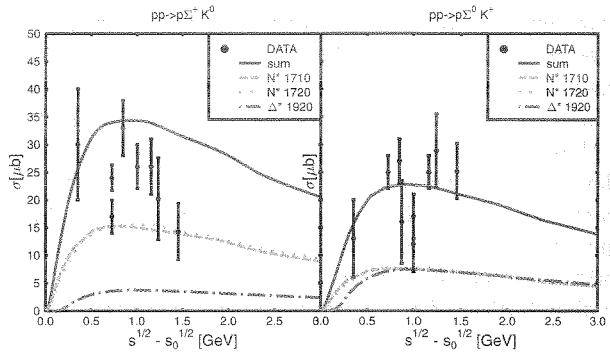

Figure 2: $pp \to p\Sigma^+ K^0$ and $pp \to p\Sigma^0 K^+$ cross section in UrQMD compared to data.

events calculated with the UrQMD model. The dots are experimental data from E802, E866/E917 [3] and NA49 [4, 5]. The model shows a good overall agreement with the experiments, except for the preliminary 40 GeV measurement from NA49 [5] which is slightly underestimated. Interestingly this good agreement for the K^+ to K^- ratio with the data can be obtained without invoking any medium dependent effects, such as in-medium masses.

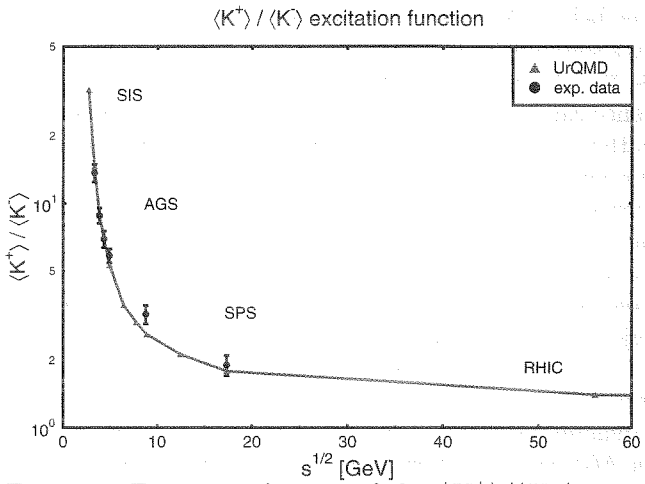

Figure 3: Excitation funtion of the $\langle K^+\rangle/\langle K^-\rangle$ ratio in central Pb+Pb or Au+Au collisions compared to data from E802, E866, E917 and NA49

References

[1] S. A. Bass *et al.*, Prog. Part. Nucl. Phys. **41**, 225 (1998)
[2] J. T. Balewski *et al.*, Phys. Lett. B **420**, 211 (1998)
[3] L. Ahle *et al.* [E866 Collaboration], Phys. Lett. B **490**, 53 (2000) [nucl-ex/0008010].
[4] J. Bachler *et al.* [NA49 Collaboration], Nucl. Phys. A **661**, 45 (1999).
[5] C. Blume *for the NA49 collaboration*, QM2001, to appear in the proceedings.

‡ Duke University and RIKEN BNL Research Institute, USA
§ LBL Berkeley, USA (Lynen-Fellow of the Humboldt-Foundation)

Collective flow in heavy ion collisions from SIS to SPS energies

E. Zabrodin, C. Fuchs, L. Bravina, and Amand Faessler, University of Tübingen

Collective effects, such as the transverse flow of particles produced in ultrarelativistic heavy ion collisions, are very important for the study of the nuclear equation of state (EOS) and for the search of a predicted transition to the quark-gluon plasma (QGP). At present the transverse flow is believed to be one of the most clear signals to detect the creation of the QGP in heavy-ion experiments. This explains the great interest of both experimentalists and theoreticians in the collective flow phenomenon [1].

The distribution of the particles in the azimuthal plane can be presented as [2]

$$\frac{dN}{d\phi} = a_0 \left[1 + 2 \sum_{n=1}^{\infty} v_n cos(n\phi) \right], \qquad (1)$$

where ϕ is the azimuthal angle between the momentum of the particle and the reaction plane. The first two coefficients, v_1 and v_2, colloquially known as directed and elliptic flow, are the amplitudes of the first and second harmonics in the Fourier expansion of the azimuthal distribution, respectively. The directed and elliptic flow of hadrons in heavy-ion collisions is very sensitive to the EOS of the nuclear medium. The formation of small domains of a QGP phase might happen already at the SPS energies or even below. Accompanied by the hadronization this enforces a softening of the EOS due to the dropping pressure. Thus, the disappearance of the directed flow in midrapidity range can be considered as an indication of a new state of matter. This conclusion is supported by hydrodynamic simulations with and without the QGP phase.

Microscopic models, which do not imply the QGP formation, describe the dynamics of nuclear collisions at energies up to $\sqrt{s} \approx 2A$ GeV in terms of reactions between hadrons and their excited states, resonances. At higher energies additional degrees of freedom, strings, should be taken into account to describe correctly the processes of multiparticle production. We employ the quantum molecular dynamics (QMD) model [3] at the SIS energies, while at the AGS and SPS energies the quark-gluon string model (QGSM) [4] is applied. For the simulations at $1A$ GeV, $11.6A$ GeV, and $160A$ GeV, we choose light (S+S) and heavy (Au+Au and Pb+Pb) symmetric systems [5].

The deviations of the nucleon directed flow from the straight line behavior start to develop already at AGS energies (Fig. 1) due to the shadowing effect, which plays a decisive role in the competition between normal flow and antiflow in (semi)peripheral heavy-ion collisions. Hadrons, emitted with small rapidities at the onset of the collision in the antiflow area can propagate freely, while their counterparts will be absorbed by the flying massive spectators. The signal becomes stronger with the rise of the impact parameter and with the rise of the incident energy. In the latter case the spectators are more Lorentz-contracted and more hadrons can be emitted unscreened with small rapidities in the direction of antiflow. This effect should appear

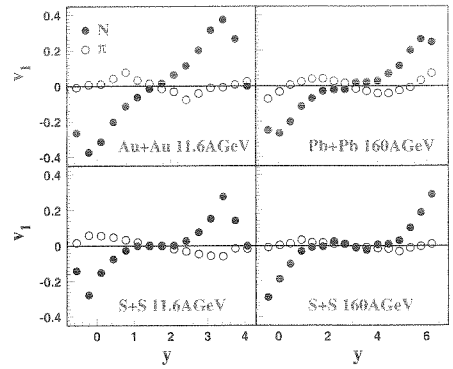

Figure 1: $v_1^{N,\pi}(y)$ in min. bias events at AGS and SPS.

in semicentral collisions with $b \leq 3$ fm at RHIC energies, and can mimic the softening of the EOS of hot and dense nuclear matter. However, the disappearance of directed flow due to shadowing is more distinct for light systems, such as S+S or Ca+Ca, while in the QGP case the effect should be more pronounced in heavy systems. Thus, one can distinguish between the two phenomena by the comparison of the directed flow of nucleons in the midrapidity range in light and heavy-ion collisions.

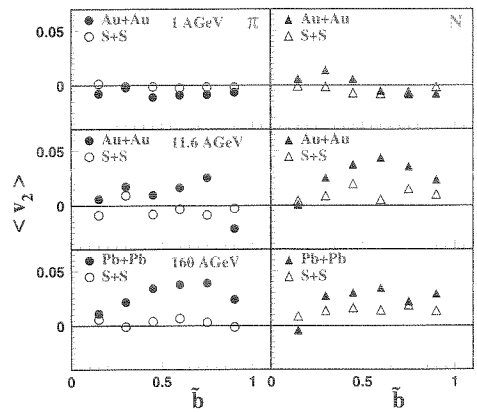

Figure 2: The mean elliptic flow of N's and π's in light and heavy system colliding at SIS, AGS, and SPS energies.

The elliptic flow of nucleons and pions is found to change its orientation from out-of-plane at $1A$ GeV to in-plane at $11.6A$ GeV (Fig. 2). The effect can be explained by stronger Lorentz-contraction of colliding nuclei. Also, at higher colliding energies the contracted spectators leave the reaction zone faster, thus giving space for the growth of elliptic flow in the reaction plane [5].

References

[1] Proc. of the QM'2001 conf.: Nucl. Phys. A (in press).

[2] S. Voloshin, Y. Zhang: Z. Phys. C 70 (1996) 665

[3] J. Aichelin: Phys. Rep. 202 (1991) 233;
C. Fuchs et al: J. Phys. G 22 (1996) 131

[4] N.S. Amelin et al: Phys. Rev. C 47 (1993) 2299

[5] L. Bravina, E. Zabrodin, C. Fuchs, Amand Faessler: Phys. Lett. B 470 (1999) 27; Phys. Rev. C 61 (2000) 064902; Phys. Rev. C 62 (2001) (in press).

Microscopic Interactions and Flow in Heavy Ion Collisions[B]

T. Gaitanos[1], C. Fuchs[2], H. H. Wolter[1], Amand Faessler[2]
[1]Sektion Physik, Universität München, [2]Inst. für Theor. Physik, Universität Tübingen

Relativistic heavy ion collisions have been extensively investigated to determine the equation-of-state (eos) of nuclear matter using phenomenological effective fields of the non-relativistic Skyrme or the relativistic Walecka type. It is found generally that a soft eos with momentum dependence can decribe much of the data in the SIS energy range. It is, however, of fundamental interest to test also microscopic fields derived from NN- interactions by many-body theory. We have previously used self energies from relativistic Brueckner calculations (DB) and have shown that these satisfactorily explain the data for flow observables [1], however, only if non-equlibrium effects are considered, i.e. taking into account that the momentum distribution is not equilibrated during a large part of an energetic heavy ion collision, which changes the effective fields. The non-equlibrium effects effectively soften the eos.

However, different approximations have been used in DB calculations, which may lead to similar saturation properties and results for finite nuclei but to different behaviours for higher density and momentum. It may thus be possible to distinguish different DB models in heavy ion collisions. Here we have tested two particular DB models: one from the Groningen group (DBHM)[2], and a more recent one from the Tübingen group (DBT) [3]. The latter takes care to eliminate spurious contributions from negative energy states, and leads to a softer eos at higher densities and to less repulsion at higher momenta.

We have performed a detailed study of flow observables in $Au + Au$ collisions [4], which have been investigated extensively by the FOPI collaboration [5]. We discuss differential flow observables: stopping or longitudinal flow and transverse in-plane and out-of-plane flow. We have used the common description in terms of the Fourier coefficients of the azimuthal distributions: v_1 (flow) and v_2 (elliptic flow), as functions of the normalized rapidity $Y^{(0)}$ and the total transverse momentum $p_t^{(0)}$. As an example in fig.1 we show for forward rapidities and different fragments the flow as a function of the transverse momentum. It is seen that the two DB models yield different results and that the DBT model reproduces preliminary FOPI data [5] better, which was not so clearly seen in global observables, like the directed flow (not shown here [4]). Similar in fig.2 we show an excitation function of the elliptic flow compared to data from different sources. We see that the DBT model reproduced the data considerably better, in particular the recent FOPI data between 400 Mev and 1 GeV. Similar results are found for other flow observables: above 400 MeV the softer and less repulsive DBT model seems to be preferred, below in some cases the DBHM model has advantages.

Thus we generally find that microscopic fields succeed also to reproduce more exclusive flow variables, thus leading to a rather unified picture of nuclear fields for nuclear matter, finite nuclei and heavy ion collisions. In the more detailed comparisons it was shown that different DB approximations can indeed be distinguished by looking at differential flow observables.

References

[1] T. Gaitanos, C. Fuchs, H.H. Wolter, Nucl. Phys. **A650** (1999) 97.
[2] B. ter Haar, R. Malfliet, Phys. Rep. **149** (1987) 207.
[3] C. Fuchs, T. Waindzoch, A. Faessler, D.S. Kosov, Phys. Rev. **C58** (1998) 2022; T. Gross-Boelting, C. Fuchs, A. Faessler, Nucl. Phys. **A648** (1999) 105.
[4] T. Gaitanos, C. Fuchs, H.H. Wolter, A. Faessler, EPJ submitted, nucl-th/0102010.
[5] A. Andronic, FOPI collaboration, Nucl. Phys. **A661** (1999) 333c, and refences cited there.

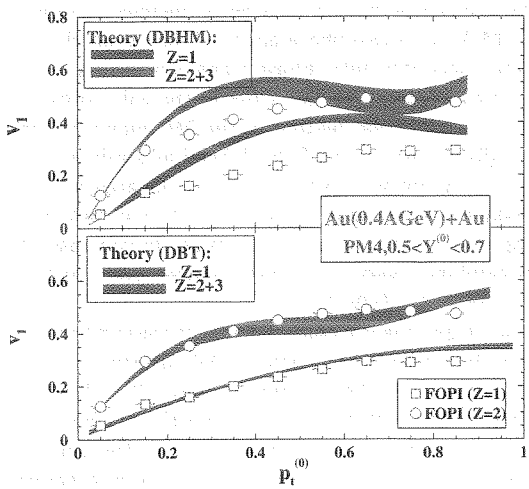

Figure 1: In-plane flow for semi-central Au+Au collisions at 400 AMeV for protons and light fragments [5] in comparisons to calculations using different DB fields. Statistical errors of the calculation are indicated by bands.

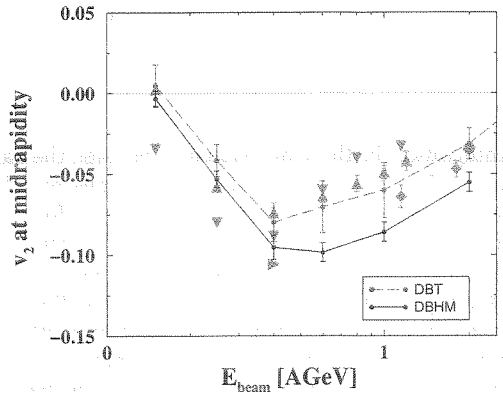

Figure 2: Energy dependence of the elliptic flow v_2 at midrapidity. The data denoted by upright triangles are taken from the FOPI collaboration [5], the others from others sources [4].

Directed Flow of Baryons in Heavy-Ion Collisions[G]

Yu.B. Ivanov, E.G. Nikonov, W. Nörenberg, A.A. Shanenko and V.D. Toneev
GSI Darmstadt

The collective motion of nuclear matter observed in heavy-ion interactions is essentially caused by the pressure gradients arising during the time evolution in the collision, and hence opens a promising way for obtaining information on the equation of state (EoS) and, in particular, on a possible phase transition. We analyze the collective motion of nucleons from high-energy heavy-ion collisions within a relativistic two-fluid model for different equations of state [1].

Our consideration is essentially based on the recently proposed Mixed-Phase (MP) model [2]. The underlying assumption of the MP model is that unbound quarks and gluons *may coexist* with hadrons forming a *homogeneous* quark/gluon–hadron phase. Since the mean distance between hadrons and quarks/gluons in this mixed phase may be of the same order as that between hadrons, the interaction between all these constituents (unbound quarks/gluons and hadrons) plays an important role and defines the order of the phase transition. For the case of quarks of two light flavors at zero baryon density ($n_B = 0$), the MP model is consistent with lattice QCD data providing a continuous phase transition of the cross-over type with a deconfinement temperature $T_{dec} = 153$ MeV. In a two-phase approach based on the bag model a first-order deconfinement phase transition occurs with a sharp jump in energy density ε at T_{dec} close to the value obtained from lattice QCD. A particular feature of the MP model is that, for $n_B = 0$ the *softest point* of the EoS, defined as a minimum of the function $p(\varepsilon)/\varepsilon$, is not very pronounced and located at comparatively low values of the energy density: $\varepsilon_{SP} \approx 0.45$ GeV/fm^3, which roughly agrees with the lattice QCD value. In contrast, the bag-model EoS exhibits a very pronounced softest point at large energy densities $\varepsilon_{SP} \approx 1.5$ GeV/fm^3.

We have studied experimental consequences of these differences in EoS within the hydrodynamic approach. We use the 3D relativistic two-fluid model with a finite stopping power [3]. These two fluids, initially associated with target and projectile nucleons, are described by a set of hydrodynamic equations with the coupling term, which characterizes friction between the counter-streaming fluids. The friction term originates from both elastic and inelastic NN collisions and gives rise to a direct emission of mesons in addition to the thermal mesons in the fluids [3].

The average directed flow is defined by

$$\langle P_x \rangle = \frac{\int dp_x dp_y dy \; p_x \left(E \frac{d^3N}{dp^3} \right)}{\int dp_x dp_y dy \left(E \frac{d^3N}{dp^3} \right)} ,$$

where the integration in the c.m. system runs over the rapidity region $[0, y_{cm}]$. The calculated excitation functions for $\langle P_x \rangle$ of baryons within different models are shown in the figure for $Au+Au$ collisions at the impact parameter $b = 3$ fm. As shown in the upper panel, conventional one-fluid (1F) hydrodynamics for pure hadronic matter [4] results in a very large directed flow due to the inherent instantaneous stopping of the colliding matter. This instantaneous stopping is unrealistic at high beam energies. If the deconfinement phase transition (PT), based on the bag-model EoS [4], is included, the excitation function of $\langle P_x \rangle$ exhibits a deep minimum near $E_{lab} \approx 6$ A·GeV, which is a manifestation of the strong softest-point effect in the bag-model EoS.

The result of two-fluid (2F) hydrodynamics with the MP EoS noticeably differs from the one-fluid calculations. After a maximum around 1 A·GeV, the average directed flow decreases slowly and smoothly. This difference is caused by the fact that the softest point of the MP EoS is washed out for $n_B \gtrsim 0.4$ and also by dynamical reasons, i.e. the finite stopping power and direct

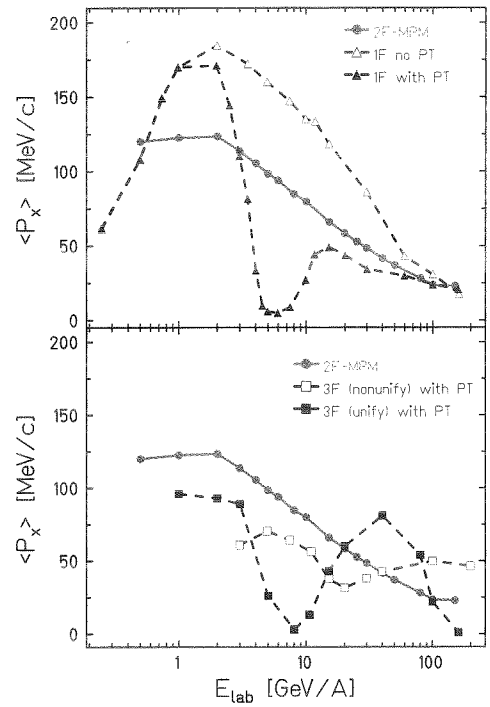

pion emission change the evolution pattern. The latter point is confirmed by comparison to three-fluid calculations with the bag EoS [5] plotted in the lower panel of the figure. As seen, the minimum of the directed flow excitation function, predicted by the one-fluid hydrodynamics with the bag EoS, survives in the three-fluid (nonunified) regime, but its value decreases and its position shifts to higher energies. If one applies the *unification procedure* of [5], which favors fusion of two fluids into a single one, and thus making stopping larger, three-fluid hydrodynamics gives results, which are very similar to those of the one-fluid model, and predicts in addition a bump at $E_{lab} \approx 40$ A·GeV.

Recent experimental results confirm that the excitation function of the directed baryonic flow is a smooth function in the 2-8 A·GeV energy range [6], which is in agreement with our MP EoS.

[1] Yu.B. Ivanov, E.G. Nikonov, W. Nörenberg, A.A. Shanenko and V.D. Toneev, GSI Preprint 2000-39; nucl-th/0011004.

[2] E.G. Nikonov, A.A. Shanenko, and V.D. Toneev, Heavy Ion Phys. **8** (1998) 89; nucl-th/9802018. V.D. Toneev, E.G. Nikonov, and A.A. Shanenko, Preprint GSI 98-30, Darmstadt, 1998.

[3] I.N. Mishustin, V.N. Russkikh, and L.M. Satarov, Nucl. Phys. **A494** (1989) 595; Yad. Fiz. **54** (1991) 429.

[4] D.H. Rischke, Y. Pürsün *et al.*, Heavy Ion Phys. **1** (1996) 309; D.H. Rischke, Nucl. Phys. **A610** (1996) 88c.

[5] J. Brachmann *et al.*, Phys. Rev. C **61** (2000) 024909.

[6] E895 Collaboration, H. Liu *et al.*, Phys. Rev. Lett. **84** (2000) 5488.

Maximum Strangeness Content in Heavy Ion Collisions Around 30 A·GeV[B,G]

J. Cleymans, University of Cape Town, South Africa
H. Oeschler, Technische Universität Darmstadt
K. Redlich, University of Wrocław, Poland and GSI, Darmstadt

Strangeness production in heavy ion collisions at relativistic energies provides one of the key information about the reaction mechanism and could indicate the onset of new phenomena.

The attempts to describe the measured particle ratios including strange hadrons at AGS and SPS and recently also at RHIC using a strangeness fugacity are very successful [1, 2, 3, 4, 5]. However, the usual grand-canonical treatment of strangeness conservation is not sufficient, if the number of strange particles is small [6]. This requires local strangeness conservation which is done in the statistical model using the canonical formulation of strangeness conservation [7].

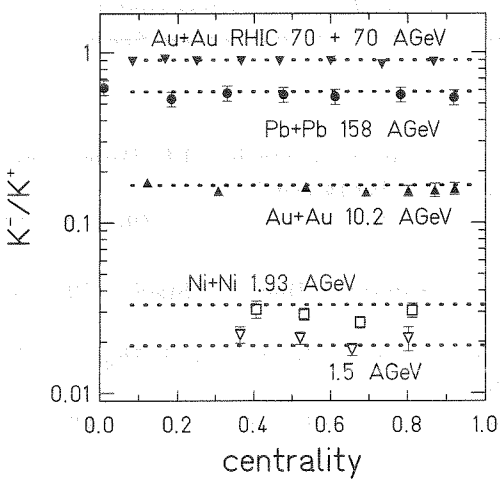

Figure 1: *K^+/K^- ratio is independent of the number of participating nucleons at incident energies from 1.5 A·GeV up to RHIC energies. The dashed lines show the values of the statistical model.*

The canonical approach describes the measured particle ratios at SIS energies and is able to explain the different excitation functions of K^+ and K^- in heavy ion collisions which – when plotted as a function of $\sqrt{s} - \sqrt{s}_{threshold}$ – cross around 1 A·GeV [8]. The canonical description also explains that $M(K^+)/A_{part}$ rises linearly with A_{part} as observed in Au+Au collisions at 1 A·GeV [7, 9] which is in contrast to the behavior of $M(\pi)/A_{part}$ which is independent of A_{part}. This difference is due to the volume term in the canonical description [7]

$$n_{K^+} \sim \exp\left(-\frac{E_{K^+}}{T}\right)\left[g_\Lambda V \int \frac{d^3p}{(2\pi)^3} \exp\left(-\frac{(E_\Lambda - \mu_B)}{T}\right)\right]$$

which takes care of the fact that strange particles are produced associately with another strange particle (e.g. a K^+ together with a Λ). The volume term V, however, drops out when studying the ratio of K^-/K^+ as for the production of K^- an analoguous formula holds

$$n_{K^-} \sim \exp\left(-\frac{E_{K^-}}{T}\right)\left[g_{K^+} V \int \frac{d^3p}{(2\pi)^3} \exp\left(-\frac{E_{K^+}}{T}\right)\right].$$

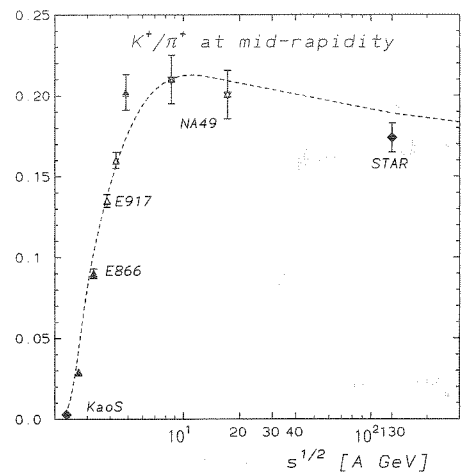

Figure 2: *K^+/π^+ ratio obtained around midrapidity as a function of $\sqrt{s}$ from the various experiments. The dashed line shows the calculation with the statistical model.*

Indeed, the measured ratios do not vary with the number of participating nucleons in Ni+Ni collisions [10]. This feature is found at all incident energies from 1.5 A·GeV up to RHIC energies as shown in fig. 1 [11, 12, 13]. The above result is especially interesting since between 1.5 and 2.5 A·GeV K^+ production is above while K^- production is below the corresponding NN thresholds.

The enhancement of multi-strange baryons from p+A to $A+A$ collisions might be explainable by a transition from canonical to grand-canonical description as demonstrated in [14].

Recently, the evolution of the K^+/π^+ ratio as a function of $\sqrt{s}$ has attracted great interest as a maximum seemed to appear around 40 A·GeV. Figure 2 shows this ratio obtained at midrapidity from SIS energies up to RHIC [12, 13, 15]. Indeed, a maximum around the data point obtained at 40 A·GeV is seen. In general, statistical-model calculations should be compared with 4π integrated results. Then the maximum is even more pronounced. The extrapolation to 4π is, however, in some cases not well established.

The fact that the statistical model based on the general freeze-out curve [16] (dashed line in Fig. 2 exhibits a maximum, too, might appear surprising. Intuitively, one expects that the fraction of strange particles increases with increasing incident energy. So, the question arises whether the maximum is caused by the distribution of strange quarks among the hadrons at freeze out or whether

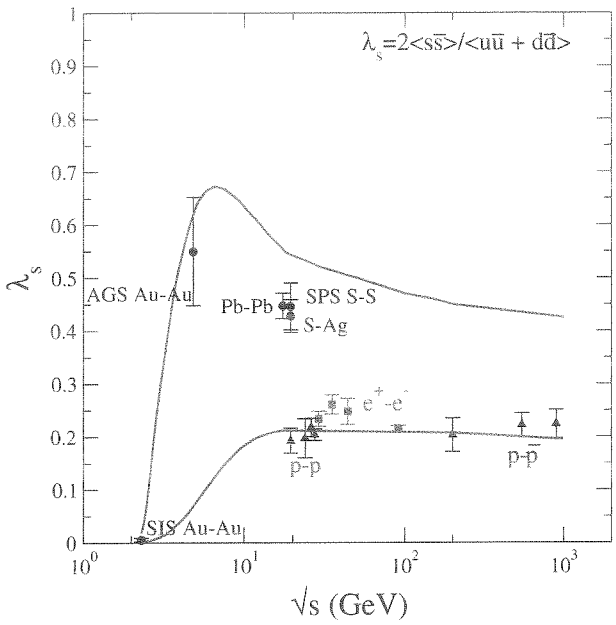

Figure 3: *The Wroblewski ratio λ_S as a function of $\sqrt{s}$. The points refer to measured values (not measured particles species with generally rather small cross sections are added according to the statistical model). The solid lines shows the statistical model results for PbPb and pp collisions.*

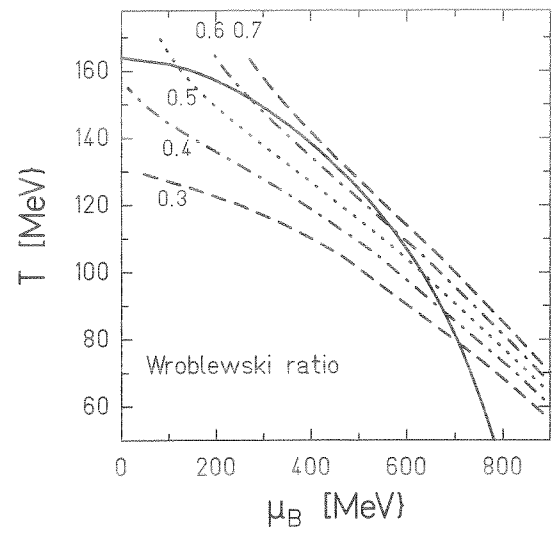

Figure 4: *Lines of constant strangeness content λ_S in the $T - \mu_B$ plane together with the general freeze-out curve (full line) [16].*

less strange quarks are produced in total above a certain incident energy.

To clarify this point, we study next the Wroblewski ratio [17], which is a measure of the strangeness content produced in the collisions. It is defined as

$$\lambda_S = \frac{2N(s\bar{s})}{N(u\bar{u}) + N(d\bar{d})}$$

where $N(q\bar{q})$ is the number of produced quark-antiquark pairs of the given species. The Wroblewski ratio varies from 0 at low incident energies, where no strange particle are produced to a upper limit of 1 for infinite temperature where the difference in masses can be neglected.

Figure 3 shows the values of λ_S extracted from the experimental data. The solid lines in Fig. 3 are the results of the statistical model based on the general freeze-out curve [16]. The results for pp, $p\bar{p}$, e^+e^- are also included. The lower values of λ_S in elementary compared to AA collisions are due to canonical suppression [18]. From Fig. 3 we conclude that around 30 A·GeV the strangeness content in heavy ion collisions reaches a maximum and decreases slightly towards higher incident energies. This is evidenced in Fig. 4 which shows contour lines of constant λ_S in the $T - \mu_B$ plane. As expected λ_S rises with increasing T. With decreasing μ_B, μ_S decreases and hence λ_S. Following the general freeze-out curve, shown as full line in Fig. 4, λ_S rises quickly at SIS and AGS energies, reaches then a maximum around 30 A·GeV.

References

[1] J. Cleymans and H. Satz, Z. Phys. **C57** (1993) 135.

[2] P. Braun-Munzinger, J. Stachel, J.P. Wessels and N. Xu, Phys. Lett. **B344** (1995) 43.

[3] J. Sollfrank, J. Phys. G: Nucl. Part. Phys. **23** (1997) 1903.

[4] P. Braun-Munzinger, I. Heppe, J. Stachel, Phys. Lett. **B465** (1999) 15.

[5] V.D. Toneev et al., submitted to J. Phys. G: Nucl. Part. Phys.

[6] R. Hagedorn and K. Redlich, Z. Phys. **A27** (1985) 541.

[7] J. Cleymans, H. Oeschler and K. Redlich, Phys. Rev. **C59** (1999) 1663.

[8] J. Cleymans, H. Oeschler and K. Redlich, Phys. Lett. **B485** (2000) 27.

[9] M. Mang, Dissertation, University of Frankfurt, (KaoS Collaboration), 1997.

[10] M. Menzel, Dissertation, U. Marburg, (KaoS Collaboration), 2000.

[11] L. Ahle et al., (E802 Collaboration), Phys. Rev. **C60** (1999) 044904.

[12] C. Blume, (NA49 Collaboration), Conference on "Quark Matter 2001", Stony Brook, Jan. 2001....

[13] J. Harris, (STAR Collaboration), idem.

[14] S. Hamieh, K. Redlich, A. Tounsi, Phys.Lett. **B486** (2000) 61.

[15] L. Ahle et al., (E866/E917 Collaboration), Phys. Lett. B476 (2000) 1.

[16] J. Cleymans and K. Redlich, Phys. Rev. Lett. **81** (1998) 5284; Phys. Rev. **C60** (1999) 054908.

[17] A. Wroblewski, Acta Physica Polonica **B16** (1985) 379.

[18] F. Becattini et al., hep-ph/0002267.

A model for dilepton production from an expanding fireball

R.A. Schneider, T.Renk and W. Weise, TU München

The search for the quark-gluon plasma (QGP) at CERN and RHIC requires a detailed understanding of the properties of hot QCD. It has become clear over the last years that a perturbative approach to thermal QCD is insufficient to calculate properties of the QGP because of the occurrence of infrared divergences and gauge dependencies of physical quantities. Even the Hard Thermal Loop resummation is likely to be applicable only for very large temperatures far outside the scope of present and future experiments. Clearly, nonperturbative input, e.g. from lattice simulations of QCD is needed to improve the situation.

Lattice results indicate that the equation of state (EOS) of a QGP can be fit with a relatively simple quasiparticle model, where quarks and gluons acquire thermal masses. For these quasiparticle masses, the ansatz $m_{th} \sim g(T)T$ is used, where the coupling $g(T)$ is fit to the lattice data. One finds effective quark masses of ~ 300 MeV.

Figure 1: Different quasiparticle scenarios [2] in comparison to the CERES Pb-Au data

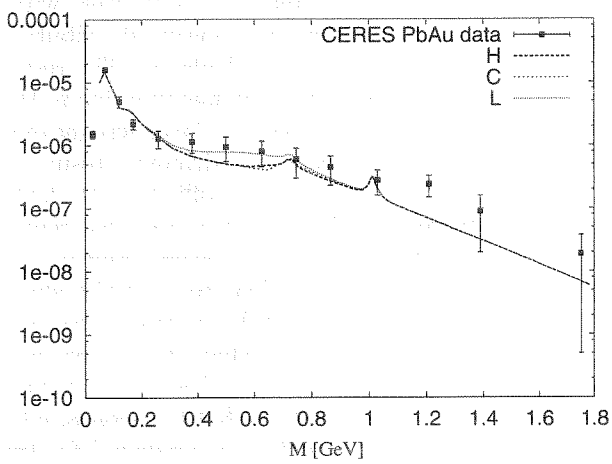

We employ this model for the calculation of the dilepton production in a fireball produced by a heavy ion collision and compare to data taken by the CERES collaboration at the SPS. The relevant degrees of freedom in the model above the phase transition temperature T_C are now quarks and antiquarks as thermal quasiparticles which couple to the photon with the standard quark charge, whereas all QCD corrections are already incorporated in the quasiparticle masses. Several scenarios are discussed for the quasiparticle masses close to T_C. In some models, these thermal masses appear to become heavy near T_C. On the other hand, chiral restoration at T_C would imply that the quark masses drop close to the transition. We therefore investigate three cases as to their influence on the spectra of the produced dileptons: a 'heavy' mass scenario (H), a 'light' one (L) which simulates the dropping of effective quark masses near T_C and a 'constant' one (C) in which the quasiparticle mass is kept at ~ 300 MeV at all temperatures.

Figure 2: Time evolution of the dilepton production yield under CERES conditions in the 'light' quasiparticle scenario, as function of the e^+e^- invariant mass M.

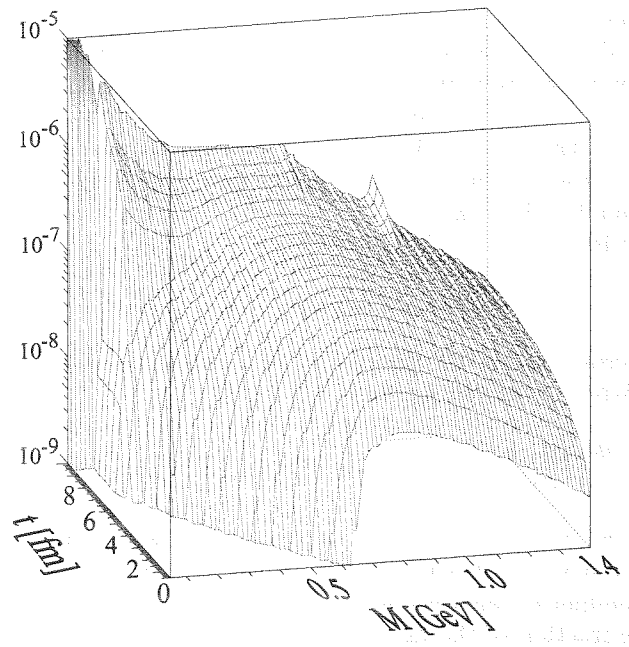

We use a model specified in [1] for the expansion of the fireball. For the hadronic phase below T_C, we use an improved Vector Meson Dominance model with ρ, ϕ and ω as the dominant degrees of freedom, combined with pionic excitations carrying the same quantum numbers. We assume factorization of finite baryon density effects and thermal effects and calculate the spectral function using perturbative methods.

The result describes the CERES data nicely (Fig. 1). The simple model for the fireball allows detailed insight into the expansion including its time evolution, this is shown for the 'light' scenario in Fig. 2. The low-mass region between 0.3 - 0.7 GeV is quite insensitive to the detailed parametrization of the thermal quark masses.

In conclusion, we have shown that a quasiparticle model of the QGP phase and, at $T < T_C$, a hadronic theory with finite density and temperature effects lead to a successful description of the CERES data, whereas a purely hadronic description fails in the low invariant mass region as well as in the high mass region.

References

[1] R.A. Schneider, and W. Weise, Eur. Phys. J. **A9** (2000) 357

[2] R.A. Schneider, T. Renk and W. Weise; in preparation

Work supported in part by BMBF and GSI.

The color dipole approach to the Drell-Yan process

B.Z. Kopeliovich[1], J. Raufeisen[2], A.V. Tarasov[1,3]
[1]MPI K Heidelberg, [2]LANL, [3]University of Heidelberg

The high center of mass energies at RHIC and LHC will allow one to study the Drell-Yan(DY) process in a kinematical region, where the dilepton mass M is much smaller than the center of mass energy $\sqrt{s}$. This region is the DY analog to small Bjorken-x_{Bj} DIS. In addition, coherence effects due to multiple scattering in proton-nucleus (pA) collisions can also be studied.

We developed an approach [1, 2], in which the DY cross section is expressed in terms of the same color dipole cross section as DIS. Our approach is formulated in the rest frame of the target, where DY dilepton production looks like bremsstrahlung of massive photons, rather than parton annihilation, fig. 1. The projectile quark is decomposed into a series of Fock states,

$$|q\rangle = \sqrt{Z_2}|q_{bare}\rangle + \Psi_{\gamma^* q}|\gamma^* q\rangle + \dots . \qquad (1)$$

The cross section for production of a virtual photon in quark-proton scattering reads then [1, 3]

$$\frac{d\sigma(qp \to \gamma^* X)}{d\ln\alpha} = \int d^2\rho\, |\Psi_{\gamma^* q}(\alpha,\rho)|^2 \sigma_{q\bar{q}}(\alpha\rho). \qquad (2)$$

Here, $\sigma_{q\bar{q}}$ is the cross section for scattering a $q\bar{q}$-dipole off a proton which depends on the $q\bar{q}$ separation $\alpha\rho$. The photon-quark transverse separation is denoted by ρ and α is the fraction of the light-cone momentum of the initial quark taken away by the photon.

This approach is especially suitable to describe nuclear effects, since it allows one to apply Glauber multiple scattering theory. At very high energy, the transverse separation between γ^* and q in the $|\gamma^* q\rangle$ state is frozen during propagation through the nucleus, due to Lorentz time dilatation. Therefore, partonic configurations with fixed separations in impact parameter space are eigenstates of the interaction and one can generalize (2) to nuclear targets by replacing $\sigma_{q\bar{q}}(\alpha\rho)$ with

$$\sigma^A_{q\bar{q}}(\alpha\rho) = 2\int d^2b \left\{1 - \exp\left(-\frac{\sigma_{q\bar{q}}(\alpha\rho)}{2}T(b)\right)\right\}. \qquad (3)$$

Here $T(b)$ is the nuclear thickness at impact parameter b.

The frozen approximation (3) is however not well justified at presently achievable fixed target energies, where the size of the $|\gamma^* q\rangle$-state may fluctuate on length scales of the order of the nuclear radius. In pA scattering, this leads to transitions between states which are eigenstates in proton-proton (pp) scattering. We go beyond the frozen approximation by summing over all possible trajectories of the quark in the $|\gamma^* q\rangle$-state. This summation can be formulated in terms of the Green function for a two dimensional Schrödinger equation with an imaginary potential proportional to $\sigma_{q\bar{q}}(\alpha\rho)$ [3, 4]. In the limit of very high energy of the projectile quark, one recovers the frozen approximation (3). The formulae are however too complicated to be displayed here.

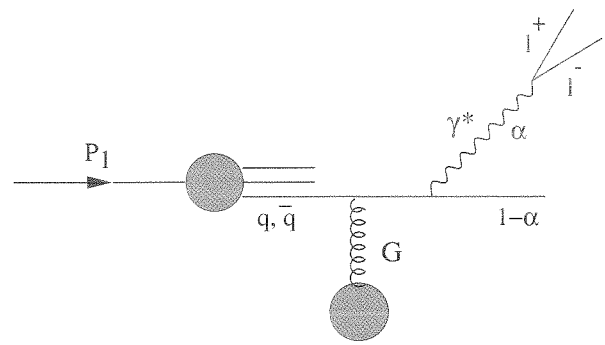

Figure 1: In the target rest frame, DY dilepton production looks like bremsstrahlung. A quark or an antiquark inside the projectile hadron scatters off the target color field and radiates a massive photon, which subsequently decays into the lepton pair. The photon can also be radiated before the quark hits the target.

Before calculating nuclear effects, we checked that the dipole approach is in agreement with DY data from pp collisions. We are able to reproduce E772 data well, without K factor [5]. The transverse momentum distribution of DY pairs in pp collisions is also calculated. The result does not diverge at zero transverse momentum due to the saturation of the dipole cross section at large separations. Note that first order pQCD leads to a divergent result.

The shadowing for DY in pA collisions at large Feynman-x_F measured at FNAL is then also well reproduced [4]. Nuclear effects on the transverse momentum distribution of the pairs are studied, too. While shadowing is predicted for dileptons with low transverse momenta, an enhancement at intermediate transverse momentum $q_\perp \sim 2$ GeV is expected. Nuclear effects vanish at very large $q_\perp$ For pA collisions at RHIC energies, considerable shadowing of DY dileptons is predicted for the whole x_F-range.

References

[1] B.Z. Kopeliovich, proc. of the workshop Hirschegg '95: Dynamical Properties of Hadrons in Nuclear Matter, Hirschegg January 16-21, 1995, ed. by H. Feldmeyer und W. Nörenberg, Darmstadt, 1995, p. 102 (hep-ph/9609385).

[2] S. J. Brodsky, A. Hebecker, and E. Quack, Phys. Rev. **D55** (1997) 2584.

[3] B.Z. Kopeliovich, A. Schäfer and A.V. Tarasov, Phys. Rev. **C59** (1999) 1609, extended version in hep-ph/9808378.

[4] J. Raufeisen, Ph.D. thesis, hep-ph/0009358.

[5] B.Z. Kopeliovich, J. Raufeisen and A.V. Tarasov, hep-ph/0012035, submitted to Phys. Lett. B.

Particle ratios in Pb+Pb at SPS in a chiral $SU(3) \times SU(3)$ model[B,G]

D. Zschiesche[a], C. Beckmann[a], K. Balazs[a], S. Schramm[a], J. Schaffner-Bielich[b]
H. Stöcker[a], W. Greiner[a]
[a] *Institut für Theoretische Physik J.W. Goethe Universität, D-60054 Frankfurt am Main*
[b] *Riken BNL Research Center, Brookhaven National Lab, Upton, New York 11973*

Ideal gas model calculations have been used for a long time to calculate particle production in relativistic heavy ion collisions, (see e.g. [1, 2] and references therein). Fitting the particle ratios as obtained from those noninteracting gas calculations to the experimental measured ratios at SIS, AGS and SPS for different energies and different colliding systems yields a curve of chemical freeze-out in the $T - \mu$ plane. Now the question arises, how much the deduced temperatures and chemical potentials depend on the model employed. Especially the influence of changing hadron masses and effective potentials should be investigated, as has been done for example in [3, 4, 5, 6]. This is of special importance for the quest of a signal of the formation of a deconfined phase, i.e. the quark-gluon plasma. As deduced from lattice data [7], the critical temperature for the onset of a deconfined phase coincides with that of a chirally restored phase. Chiral effective models of QCD therefore can be utilized to give important insights on signals from a quark-gluon plasma formed in heavy-ion collisions.

We compare experimental measurements for Pb+Pb collisions at SPS with the results obtained from a chiral $SU(3) \times SU(3)$ model [6, 8]. This effective hadronic model predicts a chiral phase transition at $T \approx 150\,\mathrm{MeV}$. Furthermore the model predicts changing hadronic masses and effective chemical potentials, due to strong scalar and vector fields in hot and dense hadronic matter, which are constrained by chiral symmetry.
In [2] the noninteracting gas model was fitted to particle ratios measured in Pb+Pb collisions at SPS. The lowest χ^2 is obtained for $T = 168\,\mathrm{MeV}$ and $\mu_q = 88.67\,\mathrm{MeV}$. Using these values as input for the chiral model leads to dramatic changes due to the changing hadronic masses in hot and dense matter [6] and therefore the freeze-out temperature and chemical potential have to be readjusted to account for the in-medium effects of the hadrons in the chiral model. We call the best fit the parameter set that gives a minimum in the value of χ^2, with $\chi^2 = \sum_i \frac{\left(r_i^{exp} - r_i^{model}\right)^2}{\sigma_i^2}$. Here r_i^{exp} is the experimental ratio, r_i^{model} is the ratio calculated in the model and σ_i represents the error in the experimental data points as quoted in [2]. In all calculations μ_s was chosen such that the overall net strangeness f_s is zero. The best values for the parameters are $T = 144\,\mathrm{MeV}$ and $\mu_q \approx 95\,\mathrm{MeV}$. While the value of the chemical potential does not change much compared to the noninteracting gas calculation, the value of the temperature is lowered by more than 20 MeV. Using the best fit parameters a reasonable description of the particle ratios used in the fit procedure can be obtained (see fig.1, data from [2]).

This shows, that in spite of the strong assumption of thermal and chemical equilibrium the obtained values for T and μ differ significantly depending on the underlying model, i.e. whether and how effective masses and effective chemical potentials are accounted for. Note that we assume implicitly, that the particle ratios are determined by the medium effects and freeze out during the late stage expansion - no flavor changing collisions occur anymore, but the hadrons can take the necessary energy to get onto their mass shall by drawing energy from the fields. Rescattering effects will alter our conclusion but are presumably small when the chemical potentials are frozen.

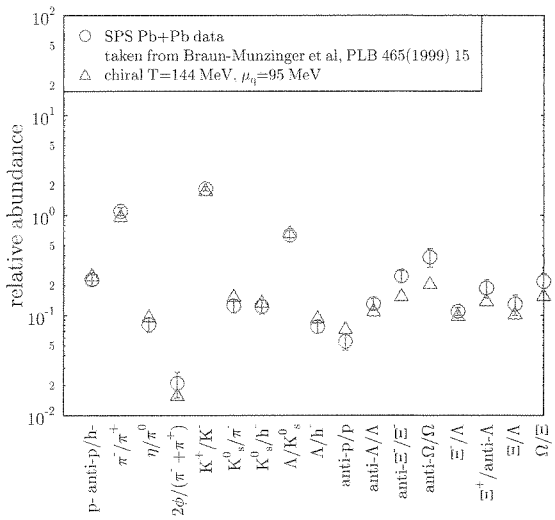

Figure 1: Particle ratios as predicted by the chiral $SU(3) \times SU(3)$ model ($T = 144\,\mathrm{MeV}$ and $\mu_q \approx 95\,\mathrm{MeV}, \mathrm{f_s} = 0$) compared to SPS Pb+Pb data (taken from [2]).

References

[1] D. Hahn and H. Stöcker, Nucl. Phys. **A452**, 723 (1986).
[2] P. Braun-Munzinger, J. Heppe, and J. Stachel, Phys. Lett. B **465**, 15 (1999).
[3] H. Stöcker, W. Greiner, and W. Scheid, Z. Phys. A **286**, 121 (1978).
[4] J. Theis *et al.*, Phys. Rev. D **28**, 2286 (1983).
[5] J. Schaffner, I. N. Mishustin, L. M. Satarov, H. Stöcker, and W. Greiner, Z. Phys. **A341**, 47 (1991).
[6] D. Zschiesche *et al.*, Springer Tracts in Modern Physics **163**, 129 (2000).
[7] F. Karsch, hep-lat/9903031 (1998).
[8] P. Papazoglou *et al.*, Phys. Rev. C **59**, 411 (1999).

Effects of coherence in nuclear and hadronic collisions

J.Hüfner[1,2], B.Z. Kopeliovich[2,3], J. Raufeisen[4], A.V. Tarasov[2,3]
[1]University of Heidelberg, [2]MPI-K Heidelberg, [3]University of Regensburg, [4]LANL

The light-cone QCD approach incorporating the effects of the nonperturbative interaction between produced quarks and gluons suggested in [1] is applied in [2] to calculation of nuclear shadowing for longitudinal and transverse photons. This work was motivated by the results of the HERMES experiment observed unusual shadowing at small Q^2 where perturbative methods cannot be used. Although an exciting effect of strong dependence of the coherence length on the photon polarization was discovered in [2], data of HERMES remain unexplained.

The strong nonperturbative interaction of radiated gluons leads not only to a substantially weaker shadowing in heavy ion collisions, but also for the first time explains the observed smallness of large mass diffraction and allows to explain in a parameter free way the energy dependence of elastic scattering of hadrons [3, 4] in a good agreement with data.

The phenomena related to propagation of fast partons through medium are important for prediction of the initial condition in heavy ion collisions and also for the so called jet quenching probe for the produced matter. Broadening of the transverse momentum of a quark propagating through nuclear medium is calculated in [5]. It is found to be a color filtering effect and expressed in terms of the universal color dipole cross section which is fitted to data for the proton structure function. The calculated broadening of p_T for a quark propagating through a nucleus is somewhat larger than what was measured in Drell-Yan reaction on nuclei.

Energy loss of a quark propagating through nuclear matter can be also measured in Drell-Yan reaction. The main problem is to discriminate between this effect and nuclear shadowing. This is done in [6] employing our experience in parameter free calculation of shadowing. The analysis of data for Drell-Yan reaction from the E772 and E866 experiments at Fermilab resulted in a rather large rate of energy loss $dE/dz \approx -2\,GeV/fm$. This is the first observation of a nonzero energy loss effect.

It is usually believed that energy loss leads to baryon stopping in heavy ion collisions. A different point of view is presented in [7] where it is shown that the dominant mechanism of stopping is baryon number transfer by gluons. Nearly the same stopping is expected at RHIC as at SPS, as is confirmed by the preliminary data from RHIC.

Charmonium suppression is considered as one of the main probes for creation of a hot deconfined matter in relativistic heavy ion collisions. The conventional base line for search of new physics relates charmonium suppression to simple absorption in cold nuclear matter. First of all, one needs to know the charmonium-nucleon cross section. It is predicted in [8] quite reliably employing the light-cone dipole formalism with the realistic charmonium wave functions and phenomenological dipole cross section fitted to DIS data. This method is tested comparing to data on charmonium photoproduction. The important effect missed in previous calculations is the relativistic spin rotation which increases the production rate of Ψ' by factor of 2-3. The cross sections are predicted for J/Ψ, Ψ' and χ, and with a proper mixture of these states the effective absorption cross section in cold nuclear matter is found.

In heavy ion collisions all nucleons which the produced charmonium interacts with, have already had a chance to interact with other nucleons and are in color-excited states. It is found in [9] that the colored 3-quark system interacts up to about 60% stronger than colorless one. Although this effect is not sufficiently strong to explain the observed anomalous E_T dependence of J/Ψ absorption, it must be included together with other missed effects in the interpretation of the experimental results. In particular, fluctuations of transverse energy should be taken into account, especially for most central collisions. It is demonstrated in [10] that they strongly correlate with fluctuation of charmonium suppression by interaction with the produced medium.

Coherent effects in elastic proton-nucleus scattering are proved to keep unchanged compared to pp scattering the ratio of spin-flip to non-flip amplitudes. This allows to use coulomb-nuclear interference in polarimetry as a basis for polarimetry. This method suggested in [11, 12] is accepted for polarimetery at RHIC.

References

[1] B.Z. Kopeliovich, A. Schaefer, A.V. Tarasov, Phys. Rev. D62 (2000) 054022
[2] B.Z. Kopeliovich, J. Raufeisen, A.V. Tarasov, Phys. Rev. C62 (2000) 035204
[3] B.Z. Kopeliovich, I.K. Potashnikova, B. Povh, E. Predazzi, Phys. Rev. Lett. 85 (2000) 507
[4] B.Z. Kopeliovich, I.K. Potashnikova, B. Povh, E. Predazzi, Phys. Rev. D63 (2001) 054001
[5] M.B. Johnson, B.Z. Kopeliovich, A.V. Tarasov, Phys. Rev. C63 (2001) 035203
[6] M.B. Johnson, B.Z. Kopeliovich, I.K. Potashnikova and the E772 Collaboration, hep-ex/0010051, submitted to Phys. Rev. Lett.
[7] G.T. Garvey, B.Z. Kopeliovich, B. Povh, hep-ph/0006325, accepted in Comments Nucl. Part. Phys.
[8] J. Hüfner, Yu.P. Ivanov, B.Z. Kopeliovich, A.V. Tarasov, Phys. Rev. D62 (2000) 094022
[9] J. Hüfner, B.Z. Kopeliovich, A. Polleri, hep-ph/0010282, accepted in Eur. Phys. J. A.
[10] J. Hüfner, B.Z. Kopeliovich, A. Polleri, nucl-th/0012003, submitted to Phys. Lett.
[11] B.Z. Kopeliovich, T.L. Trueman, hep-ph/0012091, submitted to Phys. Rev. D
[12] B.Z. Kopeliovich, A.V. Tarasov, Phys. Lett. B497 (2001) 44

Production of hard partons from soft gluonic fields^{B+G}

Dennis D. Dietrich, Gouranga C. Nayak, Walter Greiner, Johann Wolfgang Goethe Universität

We study parton-pair production from a space-time dependent chromofield via vacuum polarization by using the background field method of QCD. The processes we consider are both leading and higher order in gA but first order in the action. We derive general expressions for the corresponding probabilities. Parton production from a space-time dependent chromofield will play a crucial role in the production and equilibration of the quark-gluon plasma in ultra relativistic heavy-ion collisions at RHIC and LHC. In ultra relativistic heavy-ion collisions, when two highly Lorentz contracted nuclei pass through each other a chromofield is formed between them due to the exchange of soft gluons [1]. The chromofield so formed polarizes the QCD vacuum and produces $q\bar{q}$-pairs and gluons via a Schwinger-like mechanism [2]. As seen in numerical studies [3], the chromofield acquires a strong space-time dependence due to a combination of such effects as expansion, background acceleration, color rotation, collision and parton production. In situations like this, the parton production from a constant chromofield is not justified and one has to find the corresponding expression for a general space-time dependent chromofield.

The e^+e^- pair production from a weak space-time dependent classical field is studied by Schwinger [2]. Because of the same structure of the interaction lagrangian density the production of a $q\bar{q}$ pair is similar to the e^+e^- case except for color factors [5]. (*N.B.*: Only the real parts of the following expressions are to be taken.) Details are given in [6]:

$$\frac{dW_{q\bar{q}}}{d^4x d^3k} = \frac{g^2 m}{(2\pi)^5 k^0}\; A^a_\mu(x)\; e^{ik\cdot x} \int d^4x_2\; A^a_\nu(x_2)\; e^{-ik\cdot x_2}$$
$$(i[k^\mu (x-x_2)^\nu + (x-x_2)^\mu k^\nu + k\cdot(x-x_2) g^{\mu\nu}]$$
$$\Big(\frac{K_0(m\sqrt{-(x-x_2)^2})\, m\sqrt{-(x-x_2)^2} + 2K_1(m\sqrt{-(x-x_2)^2})}{[\sqrt{-(x-x_2)^2}]^3}$$
$$- m^2 g^{\mu\nu}\, \frac{K_1(m\sqrt{-(x-x_2)^2})}{\sqrt{-(x-x_2)^2}}\Big).$$

The computation of the probability for the production of gluons is not straight forward and there is no counter part to this in QED. The processes which in leading order of the action contribute to gluon pair production are evaluated following the background field method of QCD [7] which, in a gauge invariant manner incorporates a classical background field and a quantum gluonic field simultanously. The probability is obtained by spin-summing the phase-space integral over the absolute square of the amplitudes. The Feynman rules for the production of two gluons by coupling to the A-field once or twice can be read from the Lagrangian density and are given in [8, 6]. To obtain the correct physical gluon polarizations in the final state we put the sums over the polarizations of the outgoing gluons equal to the negative of the metric tensor and afterwards deduct the corresponding ghost contributions. The vertices involving two ghosts and one classical field and two ghosts and two classical fields respectively can again be read from the lagrangian density and are also found in [8, 6]. We obtain the probability per unit time and unit volume of the phase space for the production of a real gg pair from a space-time dependent classical chromofield A [6]:

$$\frac{dW_{gg}}{d^4x d^3k} = \frac{1}{(2\pi)^5 k^0} \int d^4x' e^{ik\cdot(x-x')} \frac{1}{(x-x')^2}$$
$$\{\frac{3}{4} g^2 A^{a\mu}(x) A^{a\mu'}(x')[3k_\mu k_{\mu'} - 8 g_{\mu\mu'} k^\nu i \frac{(x-x')_\nu}{(x-x')^2} + 6\frac{g_{\mu\mu'}}{(x-x')^2}$$
$$+5(k_\mu i\frac{(x-x')_{\mu'}}{(x-x')^2} + k_{\mu'} i\frac{(x-x')_\mu}{(x-x')^2}) - 12\frac{(x-x')_\mu (x-x')_{\mu'}}{(x-x')^4}]$$
$$-3ig^3 A^{a\mu}(x') A^{c\lambda}(x') A^{a'\mu'}(x) f^{a'ac} K_\lambda g_{\mu\mu'}$$
$$-\frac{1}{16} g^4 A^{a\mu}(x) A^{c\lambda}(x) A^{a'\mu'}(x') A^{c'\lambda'}(x')[24 g_{\mu\mu'} g_{\lambda\lambda'} f^{acx} f^{a'c'x}$$
$$+g_{\mu\lambda} g_{\mu'\lambda'}(f^{abx} f^{xcd} + f^{adx} f^{xcb})(f^{a'bx'} f^{x'c'd} + f^{a'dx'} f^{x'c'b})]\}.$$

As a simple example we choose the field to be

$$A^{a3}(t) = A_{in} e^{-|t|/t_0},\; t_0 > 0,\; a = 1, ..., 8.$$

The exponential decay of the source terms originates from the decay of the model-field. Their oscillatory behavior is due to the exponential factor,already present in the general formula.

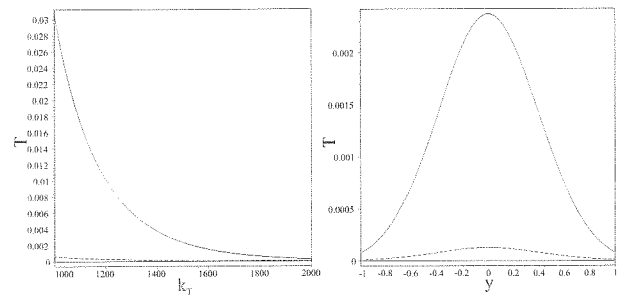

Fig. 1 Dimensionless time-integrated source terms for quarks (dash) and gluons (solid) versus transverse momentum kT in MeV and rapidity y for the parameters $\alpha_S = 0.15$, $A_{in} = 1.5GeV$, $t_0 = 0.5fm$, $k_T = 1.5GeV$, $y = 0$.

The decay behavior with the transverse momentum k_T in MeV is mostly due to the choice of the field. Only in the second contribution to the gluon source term there is already a factor $1/(k^0)^2$ present in the general formula. As the momentum structure of the general equations is mostly based on the k^0-component, the origin for the typical rapidity y behavior is mainly linked to the behavior for changing transverse momentum. For this model field, a stronger coupling, a stronger chromofield and/or a slowlier varying field emphasize dominance of the gluon-pair production over the production of $q\bar{q}$ pairs even more.

References

[1] F. E. Low, Phys. Rev. **D12** (1975) 163; S. Nussinov, Phys. Rev. Lett. **34** (1975) 1286; K. Kajantie and T. Matsui, Phys. Lett. **B164** (1985) 373; A. Karman, T. Matsui and B. Svetitsky, Phys. Rev. Lett. **56**, 219 (1986); G. Gatoff, A. K. Kerman and T. Matsui, Phys. Rev. **D36** (1987) 114; A. Bialas, W. Czyz, A. Dyrek and W. Florkowski, Nucl. Phys. **B296** (1988) 611; B. Banerjee, R. S. Bhalerao and V. Ravishankar, Phys. Lett. **B224** (1989) 16; M. Asakawa and T. Matsui, Phys. Rev. **D43** (1991) 2871; K. J. Eskola and M. Gyulassy, Phys. Rev. **C47** (1993) 2329; J. M. Eisenberg, Found. Phys. **27** (1997) 1213.

[2] J. Schwinger, Phys. Rev. **82**, 664 (1951).

[3] G. C. Nayak and V. Ravishankar, Phys. Rev. **D55** (1997) 6877; Phys. Rev. **C58** (1998) 356; R. S. Bhalerao and G. C. Nayak, Phys. Rev. **C61**, 054907 (2000).

[4] C. Itzykson and J. Zuber, *Quantum Field Theory* (McGraw-Hill Inc., 1980), R. S. Bhalerao and V. Ravishankar, Phys. Lett. **B409**, 38 (1997).

[5] G. C. Nayak and W. Greiner, *hep-th/0001009*

[6] D. D. Dietrich, G. C. Nayak and W. Greiner, hep-ph/0009178; hep-th/0007139.

[7] B. S. DeWitt, Phys. Rev. **162**, 1195 and 1239 (1967); *in* Dynamic theory of groups and fields (Gordon and Breach, 1965); G. 't Hooft, Nucl. Phys. **B62**, 444 (1973).

[8] L. F. Abbott, Nucl. Phys. **B185**, 189 (1981).

Nonequilibrium quark dynamics in ultrarelativistic heavy ion collisions[B,G]

S. Scherer[1], M. Hofmann[1], M. Bleicher[2], L. Neise[1], H. Stöcker[1], W. Greiner[1]
[1] Institut für Theoretische Physik, J. W. Goethe-Universität Frankfurt am Main, Germany,
[2] Nuclear Science Division, Lawrence Berkeley Laboratory, Berkeley, U.S.A.

Heavy ion collisions at the CERN-SPS are supposed to reach the transition form hadronic matter to the quark-gluon plasma. The analysis of collective observables such as flow allows to speculate that this transition may show up even down to AGS energies. The description of such a collision by microscopic models thus must treat properly the degrees of freedom emerging from soft QCD.

Such a model can be realized by treating quarks as classical particles interacting according to a two-body color potential [1]. The Hamiltonian of this quark molecular dynamics (qMD) reads

$$\mathcal{H} = \sum_{i=1}^{N} \sqrt{\mathbf{p}_i^2 + m_i^2} - \frac{1}{2} \sum_{i,j} C_{ij}^{\mathrm{c}} \left(\frac{3}{4} \frac{\alpha_s}{|\mathbf{r}_i - \mathbf{r}_j|} + \kappa \, |\mathbf{r}_i - \mathbf{r}_j| \right)$$

where the well known Cornell-potential is used to describe the quark interaction. Sign and relative strength of the interaction are described by the color factor C_{ij}^{c}, depending on the color combination of each pair. Confining properties are ensured by the linear increase of $V(r)$ at large distances. The time evolution of such a system yields colorless quark clusters which are mapped to hadrons.

When coupled to a hadronic transport model such as UrQMD[2] to create the initial quark distribution, the qMD can provide us with detailed information about the dynamics of the quark system and the parton-hadron conversion. Correlations between the quarks clustering to build new hadrons can be studied [3].

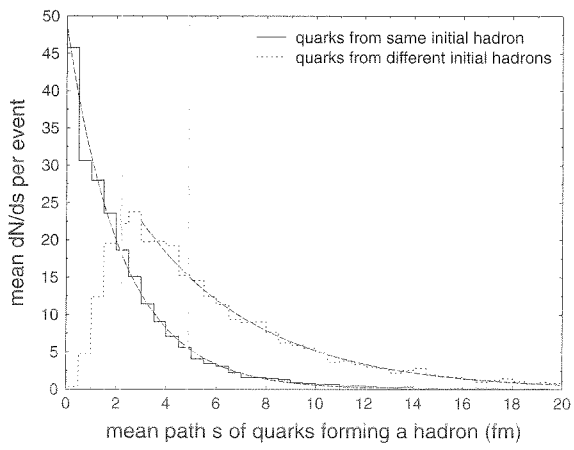

Figure 1: Hadronization in S+Au collisions at 200 GeV/N: Mean diffusion path of quarks forming a hadron from the same initial hadron (solid line) and from different initial hadrons (dashed line) within qMD. Fitting the decay profiles yields diffusion lengths of 2.2 fm and 4.8 fm.

Hadrons of the colliding nuclei are propagated in UrQMD, producing new hadrons in inelastic collisions and preformed hadrons in string excitations. Once complete overlap of the impinging nuclei is reached, all hadrons with at least one collision or within their formation time are broken up in their (valence) quark content. These quarks are then propagated in qMD, finally hadronizing again.

Figure 1 shows (for S+Au collisions at SPS energies of 200 GeV/N) the distribution for the mean path travelled by quarks forming a hadron (a) from the same initial hadron (solid line) and (b) from different initial hadrons (dotted line).

A measure of the relative mixing within the quark system and thus for thermalization is the relative number of hadrons formed by quarks from the same initial hadron versus hadrons formed by quarks from different initial hadrons. This ratio is $r = 0.574 \pm 0.008$ for the S+Au collision (spectators are not included). Since a value of $r = 1$ indicates complete rearrangement of quarks and thus complete loss of correlations in the quark system, one would expect a much larger value of r, considering the presumed transition to the quark-gluon plasma in Pb+Pb collisions at 160 GeV/N,

First results for the excitation function of this ratio in Pb+Pb collisions, however, shows a different picture (Figure 2): a nearly constant value of about 0.3 is obtained for energies in the range from 20 to 160 GeV/N, nearly independent of the impact parameter. This surprising behavior needs clarification by further investigations.

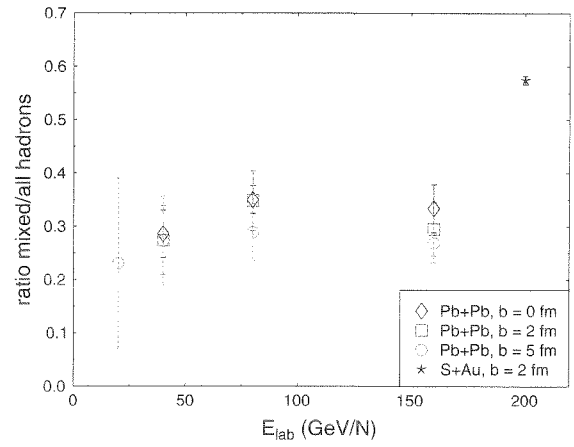

Figure 2: Excitation function of ratio of mixed to total hadrons for Pb+Pb collisions. The value for S+Au collision at 200 GeV/N is also shown.

References

[1] M. Hofmann et al., Phys. Lett. **B478** (200) 161 (nucl-th/9908030); nucl-th/9908031.
[2] S. A. Bass et al., Phys. Rev. C **60** (1999) 021902 [nucl-th/9902062].
[3] S. Scherer et al., N. Journ. Phys. *to be publ.*

Deconfinement, Color Screening and Quarkonium Suppression

S. Digal, M. Nardi, P. Petreczky and H. Satz, Universität Bielefeld

The study of color deconfinement in strongly interacting matter leads to challenging problems of theoretical as well as of more phenomenological nature. How does the transition from hadronic matter to a quark-gluon plasma take place - is it a genuine phase transition or some less 'singular' cross-over, and what are the basic properties of the new deconfined medium? In the chiral limit ($m_q = 0$) and in the limit of pure gauge theory ($m_q = \infty$) we do have critical behavior in the classical sense, with well-defined order parameters and singularities in the partition function and hence in thermodynamic observables. Is there some way to really 'define' the transition in full QCD with light but not massless quarks? On the other hand, the aim of high energy nuclear collisions is to investigate the transition and the predicted new deconfined state of matter in the laboratory. What probes exist for these tasks? Is there an experimentally accessible deconfinement order parameter, and how can the temperature dependence of the hot deconfined medium be tested?

The role of the effective quark mass in QCD is similar to that of an ordering external field H in spin theories [1]. For $H = 0$, spin systems show at $T = T_c$ the familiar order-disorder transition, which disappears for $H \neq 0$. The critical behavior at $T = T_c$ can be described either in terms of singularities of thermal observables, or equivalently, as singular behavior of suitably defined geometric cluster variables. Such singular cluster percolation features persist, however, even for $H \neq 0$. It is thus of particular interest to see if the deconfinement transition can in some way be associated to the onset of percolation of clusters of deconfined medium. The answer to this question requires a systematic study of percolation in QCD. First steps had indicated that in the strong coupling limit Polyakov loop percolation indeed led to the correct deconfinement transition in pure Gauge theory [2]. In recent work it was shown that this conclusion can in fact be extended to $SU(2)$ gauge theory in general [3]. Studies of full QCD with dynamical quarks are under way. They could eventually check if the cross-over line between confined and deconfined matter in the $m_q - T$ plane coincides with the line of singular behavior defined through cluster percolation [1].

The behavior of a deconfined medium can be tested by studying the dissociation of quarkonium states through color screening [4]. A prerequisite for this is an understanding of the heavy quark potential in a hot medium, which can in principle be obtained through finite temperature lattice studies. Such studies, however, require extensive computational efforts which have become possible only recently; hence the past year has led to pioneering work in this field [5, 6]. The results of this work will certainly have an impact on the application of quarkonium dissociation as deconfinement probe in nuclear collisions.

The results of experimental studies of J/ψ production in nuclear collisions at the CERN-SPS have made this a particularly interesting as well as challenging probe [7]. While peripheral $Pb-Pb$ collisions lead only to the pre-resonance absorption, already seen in pA and light ion interactions, there appears at a certain centrality a rather sudden onset of an additional 'anomalous' suppression, and for very central collisions a second further drop of the production rate occurs (see Fig. 1). Such a pattern is in fact expected from sequential charmonium suppression, leading first to the dissociation of the χ_c state and of its J/ψ decay products, then to the dissociation of the directly produced J/ψ [8]. More detailed recent investigations have led to a behavior which is qualitatively in accord with data [9, 10]; in particular, however, the central second drop appears to be much stronger than predicted by an onset of direct J/ψ suppression. The possible effects of fluctuations must therefore be taken into account in more detail [9, 11]. Such work is under way.

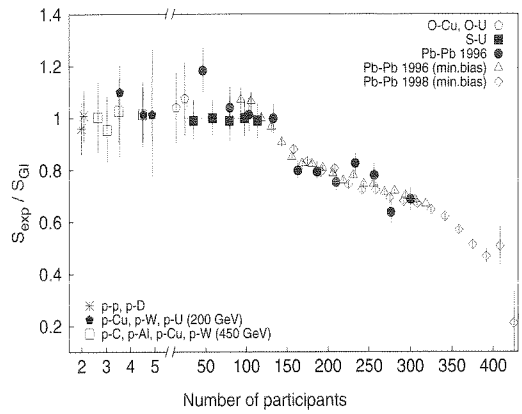

Figure 1: J/ψ production in different interactions

References

[1] H. Satz, Nucl. Phys. A642 (1998) 130.
[2] H. Satz and S. Fortunato, Phys. Lett. B475 (2000) 311.
[3] S. Fortunato, F. Karsch, P. Petreczky, H. Satz, hep-lat/0011084, to appear in Nucl. Phys. B.
[4] T. Matsui and H. Satz, Phys. Lett. 178 B (1986) 416.
[5] A. Cucchieri, F. Karsch and P. Petreczky, Phys. Lett. B497 (2001) 80.
[6] F. Karsch, E. Laermann and A. Peikert, hep-lat/0012023.
[7] see M. Abreu et al. (NA50), Nucl. Phys. A663 (2000) 721.
[8] S. Gupta and H. Satz, Phys. Lett. B383 (1992) 439.
[9] H. Satz, Nucl. Phys. A 661 (1999) 104c.
[10] M. Nardi and H. Satz, Phys. Lett. B442 (1998) 14.
[11] J.-P. Blaizot M. Dinh and J.-Y. Ollitrault, Phys. Rev. Lett. 85 (2000) 4012.

Quarkonium at Collider Energies^{B+G}

L. Gerland, H. Stöcker, W. Greiner
J.W.G. Universität, D-60054 Frankfurt a. M., Germany

There are different time scales relevant for the production of quarkonium states:
1) the time needed to produce a heavy quark pair in a hard collision,
2) the time needed for a $Q\bar{Q}$ pair to form a bound state.

The production time of a $Q\bar{Q}$ pair in its rest frame is given by $\tau_p = \frac{1}{m_Q}$. This is 0.13 fm/c for $c\bar{c}$ and 0.05 fm/c for $b\bar{b}$. The Lorentz factor of the pair at midrapidity in the rest frame of the target is $\gamma \approx 10$, 100 and 3000 for a Quarkonium state at SPS, RHIC and LHC energies. At SPS fixed target energies $\gamma c\tau_p$ is smaller than the average internucleon distance in nuclei $r_{NN} \approx 1.8$ fm. Thus, the production of heavy quark pairs is incoherent. At RHIC the production distance of $c\bar{c}$ pairs is already as large as the diameter of a gold nucleus, and for $b\bar{b}$ pairs $c\tau_p > 1.8$ fm, but this is still small as compared to the nuclear radius. At LHC both production distances exceed the diameter of a lead nucleus by an order of magnitude. The hadronisation time t_H resp. the coherence length l_c of heavy Quarkonium is $l_c = c \cdot t_H = \frac{1}{\Delta E} \approx \frac{\gamma}{\Delta M}$ with:

$$\Delta E = \sqrt{p^2 + (M_{Q\bar{Q}} + \Delta M)^2} - \sqrt{p^2 + M_{Q\bar{Q}}^2} \approx \frac{(M_{Q\bar{Q}}+\Delta M)^2 - M_{Q\bar{Q}}^2}{2p} \approx \frac{M_{Q\bar{Q}}\Delta M}{p} = \frac{\Delta M}{\gamma}.$$

p is the momentum of the Quarkonium in the rest frame of the target, $M_{Q\bar{Q}}$ is the mass of the $Q\bar{Q}$-pair and $\Delta M = \int \psi^2(k)\frac{k^2}{M_Q}\mathrm{d}^3k / \int \psi^2(k)\mathrm{d}^3k$, $\psi(k)$ is the wavefunction of the Quarkonium state in momentum space, we use here the wave functions from the refs. [1, 2]. ΔM is the average kinetic energy of the $Q\bar{Q}$-pair in the bound state and $l_c/\gamma = 0.44(0.34)$ fm for the J/Ψ (Υ).

Thus, for charm and bottom production at RHIC and LHC $l_c > 2 \cdot R_A$ (R_A is the nuclear radius), $l_c < 2 \cdot R_A$ for fixed target SPS energies. The applicability of the approach developed in this paper requires that $l_c > 2 \cdot R_A$ which is fulfilled at RHIC and LHC.

We assume here that $Q\bar{Q}$ pairs are produced in AB collisions predominantly in hard collisions. The basic quantity is the cross section of production of $Q\bar{Q}$ pairs with light cone momenta z_i, k_i, which we parametrize as $\frac{d\sigma(AB\to Q\bar{Q}+X)}{\mathrm{d}^2k_1\mathrm{d}z_1\mathrm{d}z_2\mathrm{d}^2k_2} = D_{AB}(z_1,z_2)\cdot\exp(-B(AB)(k_1^2+k_2^2))$. Here k_i $\{i=1,2\}$ are the transverse momenta of the Q and the $\bar{Q}$ quark and z_i $\{i=1,2\}$ are the fractions of their longitudinal momenta. Such a factorization does not contradict the data in pp collisions [3].

To evaluate the suppression of hidden heavy flavour production resulting from the broadening of the transverse momentum distributions of Q quarks due to final state interaction, we deduce first a relationship between the slopes for the various processes of heavy quark production. In the following we use the relative transverse momentum $k_t = \frac{k_1-k_2}{2}$ and the total transverse momentum $p_t = k_1 + k_2$ of the pair, writing $\frac{d\sigma(AB\to Q\bar{Q}+X)}{\mathrm{d}^2k_t\mathrm{d}^2p_t\mathrm{d}z_1\mathrm{d}z_2} = D_{AB}(z_1,z_2)\exp\left(-B(AB)\left(-\frac{p_t^2}{2} - 2k_t^2\right)\right)$.

To take into account possible nuclear effects on the longitudinal momentum distribution we make the ansatz $D_{AB}(z_1,z_2) = D(AB)\cdot f_{AB}(p_z)\cdot\exp\left(-\frac{k_z^2}{C_{AB}^2}\right)$, where p_z and k_z are the total and relative longitudinal momentum. We further assume that $f_{AB}(p_z) = f_{pp}(p_z)$, which means that we neglect parton energy losses of the pair, this effect will be discussed later on. The normalization condition follows from the QCD factorization theorem [4] for the total cross section: $\frac{D(AB)}{B(AB)^2\cdot C_{AB}} = \frac{AB\cdot D(pp)}{B(pp)^2\cdot C_{pp}}$ The differential cross sections are proportional to the square of the two body wave functions ϕ.

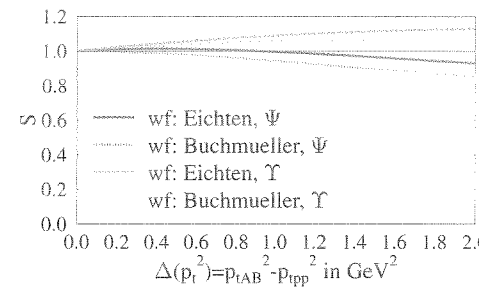

Figure 1: The righthandside of eq.(1) vs. the transverse momentum broadening for the J/Ψ and the Υ is plotted.

The production cross section of bound states of heavy quarks is proportional to the overlap integral of the two-body wave function and the wave function of the bound $\psi(k_t)$ state to get $\frac{\mathrm{d}^3\sigma(AB\to Quarkonium+X)}{\mathrm{d}^2p_t\mathrm{d}p_z} \propto |\langle\psi(k_t,k_z)|\phi_{AB}(k_t,p_t,k_z,p_z)\rangle|^2$. Here we neglected the difference between the current quark mass in the two body wave function and the constituent quark mass in the wave function of the bound state. With this one can evaluate the survival probability: $S \equiv \frac{\sigma(A+B\to Quarkonium+X)}{AB\cdot\sigma(p+p\to Quarkonium+X)}$. Our final result is then

$$S = \frac{B(AB)C_{AB}}{B(pp)C_{pp}}\left|\frac{\int \mathrm{d}^3k\psi(k)\exp(-B(AB)k_t^2)\exp\left(-\frac{k_z^2}{2C_{AB}^2}\right)}{\int \mathrm{d}^3k\psi(k)\exp(-B(pp)k_t^2)\exp\left(-\frac{k_z^2}{2C_{pp}^2}\right)}\right|^2 \quad (1)$$

up to nuclear effects in the parton distribution functions.

Note that if one defines the survival probability as the ratio of the differential cross section $\frac{\mathrm{d}^2\sigma}{\mathrm{d}^2p_t}$ for nuclear and nucleon targets their p_t dependence would be a factor $\exp\left(-\frac{B(AB)-B(pp)}{2}p_t^2\right)$. That means that the p_t dependence of J/Ψ suppression is due to the broadening of the transverse momentum distribution as a result of the final state interactions of the Q quarks in the nuclear medium.

In fig. 1 the result of eq. (1) is plotted versus the transverse momentum broadening of the J/Ψ's: $\Delta p_t^2 = 2/B(pp) - 2/B(AB)$. E.g. $\Delta p_t^2 = 0.48$ GeV^2 was found at Fermilab energies in pAu. $C_{AB}^2 = C_{pp}^2$ is used as a first approximation. $S \approx 1$ for the J/Ψ. That means there is practically no change due to the broadening of the transverse momentum distribution. The parameters used for the calculation are explained in ref. [5]. As one can see we obtain even a slight enhancement for the Υ meson production. This model neglects a lot of effects that might occur in AB-collisions, but predicts that the J/Ψ is less suppressed in pA collisions at collider energies than at fixed target energies.

References

[1] E. Eichten et al., Phys. Rev. **D21** (1980), 203
[2] W. Buchmüller and S. Tye Phys. Rev. **D24** (1981) 132
[3] M.J. Leitch et al., Phys. Rev. Lett. **72** (1994) 2542
[4] G.T. Bodwin, Phys. Rev. **D31**(1985) 2616
[5] L. Gerland et al., J. Phys. G in Print and eprint nucl-th/0009008

Shadowing Effects on Vector Boson Production*

R. Vogt (LBNL and UC Davis)

The Z^0 was proposed as an alternative reference process for quarkonium suppression at the LHC. There are two difficulties with using the Z^0 as a baseline for quarkonium suppression: the large mass differences, $m_{Z^0} \gg m_\Upsilon, m_{J/\psi}$, and the difference in production mechanisms, predominantly $q\bar{q}$ for the Z^0 and gg for quarkonium. Both these differences are important as far as nuclear effects are concerned. However, the differences that reduce the value of the Z^0 as a baseline process are the same that make it an interesting object of study itself—the Z^0 provides a unique opportunity to study quark shadowing at high Q^2. Therefore, we examine the possible effects of shadowing on Z^0 production as well as W^+ and W^- production which are also quark dominated. The impact parameter dependence of the shadowing effect will also be shown.

The electroweak production and decay channels of the massive vector bosons make them excellent candidates for shadowing studies since no hadronic final-state rescattering is possible. The Z^0 itself, with a 3.37% branching ratio to lepton pairs, will be easily observable by reconstructing the peak. Full reconstruction of the leptonic $W^\pm$ decays, $W^\pm \to l^\pm \nu$, is not possible due to the missing energy given to the undetected neutrino but charged leptons with momenta greater than 40 GeV should be prominent. This technique has been used at the Tevatron to measure the asymmetry between W^+ and W^- production through their lepton decays since this asymmetry is sensitive to the ratio f_d^p/f_u^p at intermediate values of x and high Q^2. If the charged leptons from $W^\pm$ decays can be identified in heavy ion collisions, such asymmetry measurements may also be employed at the LHC to reduce systematics and obtain a more meaningful determination of the Q^2 dependence of quark shadowing in the nucleus.

The table gives the total cross sections in the CMS and ALICE central acceptances $|y| < 2.4$ and $|y| < 1$ respectively for no shadowing and with three shadowing parameterizations. The cross sections are larger than the virtual photon mediated Drell-Yan cross sections at lower masses. The results, given for Pb+Pb collisions, are integrated over impact parameter in units of nb/nucleon pair.

Detector	σ_1 (nb)	σ_{S_1} (nb)	σ_{S_2} (nb)	σ_{S_3} (nb)
		Z^0		
CMS	15.41	10.87	10.96	14.26
ALICE	6.22	4.35	4.49	5.86
		W^+		
CMS	20.85	14.39	14.54	18.93
ALICE	8.13	5.52	5.73	7.44
		W^-		
CMS	21.84	15.08	15.26	19.83
ALICE	8.35	5.66	5.89	7.64

The figure compares the ratios of Z^0 production in Pb+Pb collisions with three shadowing parameterizations to Pb+Pb collisions with no shadowing as a function of rapidity. The isospin effects wash out the differences between the W^+ and W^- distributions in the ratios so that the results are essentially identical for the two charged vector bosons. Therefore the ratios are shown only for the W^+. The results are shown for several impact parameter bins, the most central bin, $b < 0.2R_A$, an intermediate impact parameter bin around $b \sim R_A$, and a peripheral bin around $b \sim 2R_A$. It is clear that by neglecting the impact parameter dependence of shadowing, one may make an overestimate of the effect in peripheral collisions, an important point if using the Z^0 as a baseline in different transverse energy bins. Note also that the integration over all impact parameters is equivalent to the average shadowing.

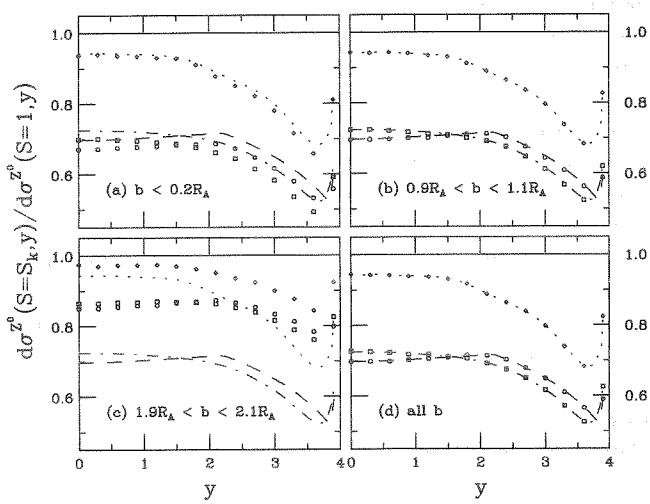

Once the basic nuclear shadowing effects on vector boson production have been understood, they can perhaps be used to study other medium effects in heavy ion collisions by comparing the leptonic and hadronic decay channels. The hadronic decays of the vector bosons, $\sim 70\%$ of all decays of each boson, may be more difficult to interpret. While the width of the Z^0 decay to l^+l^- is not expected to be modified in the quark-gluon plasma, the Z^0 has a 2.49 GeV total width and will decay in any quark-gluon plasma to two jets through $Z^0 \to q\bar{q} \to$ jet + jet in ~ 0.1 fm. Therefore, the decay jets could be modified in the medium which may still be progressing toward thermalization and will be subject to rescattering and jet quenching. Thus a comparison of a reconstructed Z^0 in the dilepton channel where no nuclear effects are expected since leptons do not interact strongly and medium-modified jets should result in a broader width for the $q\bar{q}$ channel than the l^+l^- channel. In addition, the Z^0 could be used to tag jets through the $q\bar{q} \to Z^0 g$ and $gq \to Z^0 q$ channels to study the jet properties in the quark-gluon plasma.

*Condensed from GSI-Preprint 2000-49, hep-ph/0011242.

Probing chiral dynamics by charged-pion correlations*

Jørgen Randrup (LBNL)

High-energy nuclear collisions are expected to produce transient systems within which chiral symmetry is approximately restored and the matter is partially deconfined. The identification and exploration of such a novel matter phase is a major experimental goal and the efforts have intensified with the recent commisioning of the Relativistic Heavy Ion Collider at BNL.

Through the past decade, it has been speculated that the rapid expansion of the collision zone, after an approximate restoration of chiral symmetry has occurred, may produce long-wavelength isospin-polarized agitations of the pionic field, commonly referred to as disoriented chiral condensates (DCC), which in turn should lead to anomalies in the resulting pion multiplicity distribution. However, the experimental search for the phenomenon has been hampered by the lack of signatures that are practically observable.

The present work identifies a novel observable that may be particularly suitable as an indicator of the DCC phenomenon, namely the approximate back-to-back correlation between oppositely charged soft pions.

The pionic degrees of freedom experience a rapidly changing environment that can be approximately accounted for by an in-medium effective mass depending both on the degree of agitation and on the chiral order parameter. Since the system is steadily cooling down while the order parameter reverts from its initial small value to its large vacuum value in a non-equilibrium fashion, the effective pion mass has then a correspondingly intricate evolution, displaying an overall decay towards the free mass overlaid by the effect of the rather regular oscillations by the relaxing order parameter. This time modulation of the effective mass may lead to parametric amplification those soft pionic modes with an energy near half the σ mass.

The effect is brought out most clearly in the simple case where the environment, and hence the effective mass, is spatially uniform, as is approximately the case in the interior of the collision zone. It is then obvious that although the time dependence of the mass may generate considerable agitation, this agency cannot add any net momentum. Thus the any pions produced by the mechanism must be formed pairwise and moving in opposite directions. Furthermore, by a similar reasoning, the time dependence of the mass does not add any change, so the produced pairs must be oppositely charged. Thus, the particles generated by an arbitrary time dependence in a uniform medium are charge-conjugate back-to-back pairs. This basic feature may be exploited as a probe of the chiral dynamcis.

When the environment has a spatial dependence, as is more realistic, the pions experience forces that tend to erode the clear back-to-back correlation pattern. We have examined this effect with a quantum-field treatment of a one-dimensional scenario, using a mass function that emulates the profiles obtained in more elaborate numerical simulations with the linear σ model. The resulting two-body correlation function for charge-conjugate pions is shown in the figure. The characteristic correlation structure is seen to be rather robust and so there is reason to hope that this signature may be experimentally observable.

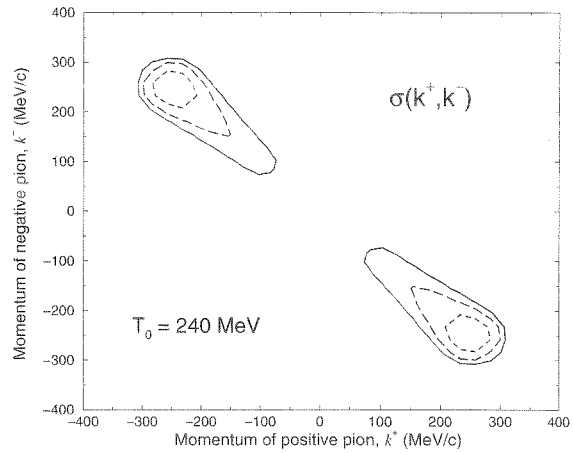

Of course, this "signal" is partially obscured or eroded by a number of other processes and thus any attempt to extract it from the experimental data must take careful account of such "background" contributions.

One important issue concerns the possible presence of other agencies that may lead to a similar signal and thus forge the DCC signature. While there are many physically different sources of charge-conjugate pion pairs, fortunately only few lead to strong back-to-back correlations. Particularly important is the decay $\rho(770) \to \pi^+\pi^-$ but due to the high ρ mass, at least one of the pions has a momentum above 360 MeV/c which is somewhat above the upper limit of the expected effect ($k_{\max} \approx 300$ MeV/c). Moreover, although $\eta(550)$ and $\omega(780)$ may both contribute soft $\pi^+\pi^-$ pairs, these all arise in three-body decays and thus they are only rather weakly correlated and so they should not pose a serious problem.

In conclusion, then, we suggest that the data now being taken at RHIC be analyzed for indications of the described signature in the large-angle correlation of soft charge-conjugate pion pairs. It may also be worthwhile to scrutinize existing SPS data for this signal. If indeed identified, this signal may offer a means for probing the degree of chiral restoration achieved and the subsequent DCC dynamics.

* Condensed from nucl-th/0012020.

ATOMIC HEAVY ION PHYSICS

Experiments

Theory

Lifetime Measurement of the Metastable 2^3P_0 state in He-like Au^{77+}

S. Toleikis[1], B. Manil[2], E. Berdermann[1], H.F. Beyer[1], B. Birkett[4], F. Bosch[1], M. Czanta[1], R.W. Dunford[6], P. Indelicato[2], C. Kozhuharov[1], D. Liesen[1], X. Ma[1], R. Marrus[4], P.H. Mokler[1], D. Schneider[5], A. Simionovici[3], Th. Stöhlker[1], Y. Zou[7]

[1]*GSI, Darmstadt, Germany,* [2]*Université P. et M. Curie, Lab. Kastler Brossel, Paris, France,*

[3]*European Synchrotron Radiation Facility (ESRF), Grenoble, France,* [4]*University of California, Berkeley, U.S.A.,*

[5]*Lawrence Livermore National Laboratory, Livermore, U.S.A.,* [6]*Argonne National Laboratory, Argonne, U.S.A.,*

[7]*Jiaotong University, Shanghai, China*

The $2^3P_1 - 2^3P_0$ fine-structure splitting has been and still is a subject of experimental and theoretical interest in atomic physics. While in low-Z systems for neutral helium and Li^+ very accurate calculations have been carried out in the 70´s, for helium-like high-Z ions new methods were needed to determine this fine structure splitting. Meanwhile, different theoretical approaches exist [1, 2, 3] and one aim of the experiment is to test which approach can give the correct values for the fine structure. For the high-Z region, only few measurements are available so far [4, 5]. Although this fine structure splitting is not directly measurable presently, it has been shown that this splitting can be determined indirectly by measuring the hyperfine-quenched lifetime of the 2^3P_0 state [6]. Due to the hyperfine interaction, the metastable 2^3P_0 state couples to the prompt 2^3P_1 state and the coupling strength depends on the $2^3P_1 - 2^3P_0$ fine-structure splitting. Thereby, the lifetime of the pure 2^3P_0 state is reduced and the fine-structure splitting can be determined.

The basic method to measure the lifetime of the hyperfine quenched 2^3P_0 state is beam foil spectroscopy. This rather simple method is illustrated in Figure 1, where the setup of the experiment performed at Cave A in August 2000 is shown. A hydrogen-like gold beam with an energy of 194.8 MeV/u ($\beta = 0.5621$) passes through a target foil (1.5 mg/cm^2 Ni) and hereby produces excited helium-like ions by electron capture. The radiation of the subsequent decay of the excited states is detected downstream of the foil by two Ge(i) detectors, located on opposite sides of the beam. The position of one detector is fixed while the other detector is moveable. By varying the distance between the target foil and the moveable detector and by measuring the ratio of counts of the $2^3P_0 - 1^1S_0$−transition in the moveable detector relative to the fixed detector, a decay curve can be traced out. Measuring the ratio allows normalization to the ion population in the excited state of interest and has the additional advantage that most systematic errors are eliminated.

In contrast to the old experiment performed in 1994 [7], now for the first time, it was possible to measure the x-rays in coincidence with the down-charged helium-like ions, because recently a charge state spectrometer consisting of a quadropole doublet and a bending magnet has been installed in Cave A. An experiment to determine projectile ionization cross setcions, performed one year ago, has served as a comissioning test and has shown the ability of the spectrometer to separate the different charge states [8]. In order to benefit from the charge state separation one also needs a position sensitve particle detector. Therefore a newly developed 32-fold strip diamond detector with a detection area of 60*40 mm^2 has been installed after the bending magnet. The advantages of this new type of particle detector are its time resolution below 50 ps and especially its single-particle count-rate capability of up to 10^8 ions/s [9].

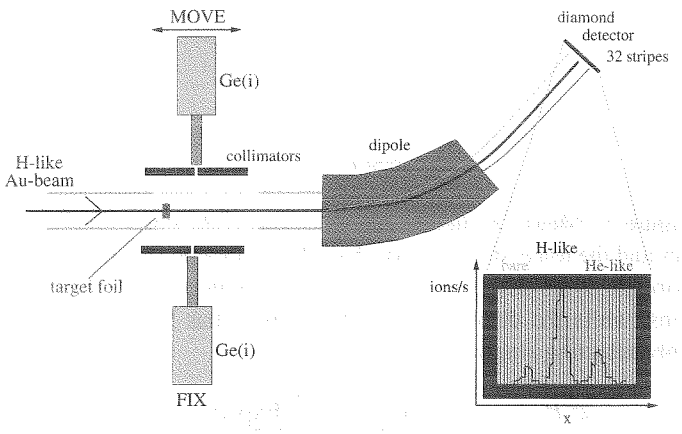

Figure 1: Experimental setup in Cave A.

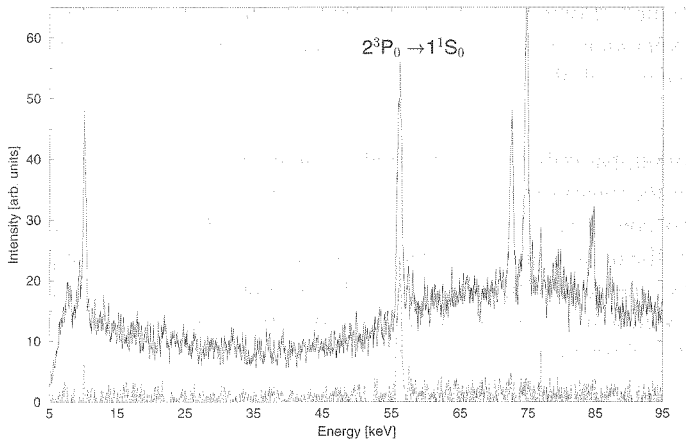

Figure 2: A raw and a coincidence spectrum obtained with the moveable Ge(i) detector.

Figure 2 now shows two sample energy spectra of the moveable x-ray detector. The upper spectrum shows a raw energy spectrum without coincidence condition while the lower one shows an energy spectrum obtained in coincidence with helium-like ions. The advantage of the coincidence technique is obvious.

The results of a prelimimary analysis of the obtained data can be seen in Figure 3. Decay curves at two different positions of the fixed detector resulting in different normalisations have been traced out, covering almost three decay lengths. In addition, to have a comparison with the old experiment also a decay curve without concidence requirement has been mea-

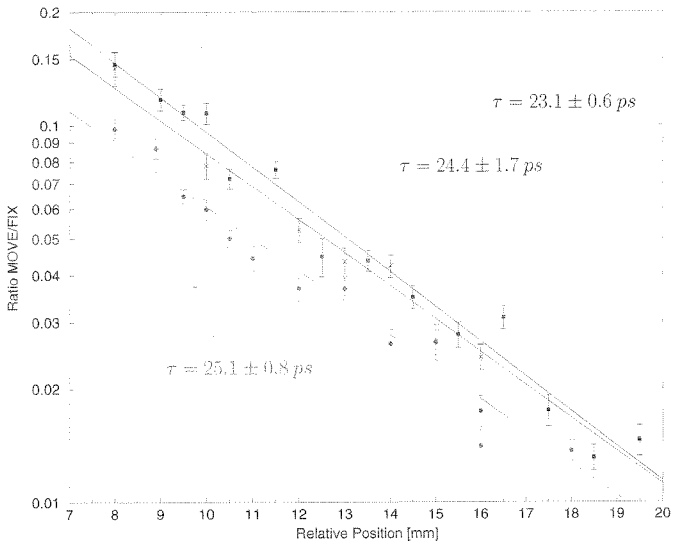

Figure 3: Measured decay curves of the 2^3P_0 state. The upper and the lower decay curves have been obtained for different normalizations detecting the x-rays in coincidence with He-like ions, while the decay curve in the middle has been obtained only detecting single x-rays.

2^3P_0	Theory		Experiment	
	[3]	[2]	this work	[7]
τ [ps]	24.66	23.66	23.9±0.5	32±4

Table 1: Comparison of the lifetime τ of the 2^3P_0 state between experiment and theory. Our experimental value is the weighted mean of all three decay curves.

sured, but only for one normalisation position. The error bars of the measured ratios are due to the statistical uncertainty at a 1σ confidence level. In order to extract the decay length l out of the decay curves, the data points have been fitted to a single exponential. With the extracted decay length l, the value for the speed of light c and the velocity of the ions β one can determine the lifetime in the laboratory frame:

$$\tau_{Lab} = \frac{1}{l\beta c}$$

This has to be transformed into the emitter frame, resulting in

$$\tau_{c.m.} = \frac{\tau_{Lab}}{\gamma}$$

for the lifetime of the 2^3P_0 state. The determined lifetimes of the different decay curves are also printed in Figure 3.

The given errors for the lifetimes are associated with the fitting procedure and are assumed to be the sole major contribution to the total experimental error. As one value overlaps with another value within the error bars, we took the weighted mean of all three values as a final result for the lifetime. The experimental results and the theoretical expectations are summarized in Table 1. Our final value agrees very well within the theoretical predictions. The results are only preliminary as the evaluation of the fine-structure splitting is still in progress.

One reason for the disagreement between the old and the new experiment may be the fact that the beam quality in the old experiment was very poor. As a consequence, the signal to background ratio was to low to get a reasonable result for the lifetime. In the new experiment the signal to background ratio has been enhanced roughly by a factor of four due to the improved beam quality. And now, even from detecting single x-rays one obtains a value for the lifetime, which agrees very well with the values that one obtains if one is using the coincidence technique.

Nevertheless, the reached accuracy of 2% looks promising concerning the planned experiment to measure the unqenched lifetime of the 2^3P_0 state in helium-like ^{238}U in the nuclear ground state from which the n=2 Lamb shift can be determined. Here the aim is to study the QED effects for the 2s-levels in a high-Z system with high accuracy.

References

[1] G.W.F. Drake, Can. J. Phys. 66, 586 (1988)

[2] P. Indelicato, F. Parente, R. Marrus, Phys. Rev. A40, 3505 (1989)

[3] W.R. Johnson, D.R. Plante, J. Sapirstein, Adv. At. Mol. Phys. 35, 255 (1995)

[4] P. Indelicato, B.B. Birkett, J.P. Briand, P. Charles, D.D. Dietrich, R. Marrus, A. Simionovici, Phys. Rev. Lett. 68, 1307 (1992)

[5] B.B. Birkett, J.P. Briand, P. Charles, D.D. Dietrich, K. Finlayson, P. Indelicato, D. Liesen, R. Marrus, A. Simionovici, Phys. Rev. A47, R2454 (1993)

[6] R. Marrus, A. Simionovici, P. Indelicato, D.D. Dietrich, P. Charles, J.P. Briand, K. Finlayson, F. Bosch, D. Liesen, F. Parente, Phys. Rev. Lett. 63, 502 (1989)

[7] R. Marrus et al., GSI-95-1, 136 (1995)

[8] H. Bräuning et al., GSI-2000-1, 91 (2000)

[9] E. Berdermann, B.E. Fischer, M. Schlögl, H. Stelzer, B. Voss, GSI-Preprint-2000-09

Spectroscopy of Ly-α Lines at Storage Rings by Absorption-Edge Technique

M. Czanta[1], C. Strietzel[2], S. Toleikis[1], H.J. Besch[2], H.F. Beyer[1], F. Bosch[1], R. Deslattes[5], A. Gumberidze[1], P. Indelicato[3], O. Klepper[1], C. Kozhuharov[1], A. Krämer[1], J. Lawall[5], D. Liesen[1], X. Ma[1], B. Manil[3], N. Pavel[2], A. Simionovici[4], M. Steck[1], T. Stöhlker[1], A.H. Walenta[2]
[1] GSI Darmstadt, Germany; [2] Universität Siegen, Germany;
[3] Université de Paris, France; [4] ESRF Grenoble, France; [5] NIST Gaithersburg, USA.

QED is very well tested in the case of light atoms. However, a test in the strong-field domain of highly charged heavy atoms with strongly pronounced higher order effects in $\alpha \cdot Z$ is still missing.

Sophisticated experiments have been devised to test QED in the high-Z region by the accurate determination of the ground-state Lambshift in hydrogenlike ions which recently has been calculated with an accuracy of the order of 10^{-5} of the ground-state binding energy of typically ($60 - 130$) keV [1]. The experiments are aimed to measure the Ly-α energies with comparable accuracy and therefore require instruments with high spectral resolution in the hard x-ray region. The absorption-edge technique fulfills this condition as has been demonstrated by a preliminary experiment [2, 3]. The experimental uncertainties of that "one-detector experiment" introduced by the Doppler-effect can be reduced by a measurement at several ion velocities β, x-ray observation angles Θ and absorbers.

The Doppler shift continuously depends on the ion velocity β and the angle of observation Θ while the energies of the K-edges discretely vary with the atomic number of the absorber. Since only a few fixed angles of observation at the gasjet target of the ESR are accessible, the number of suitable combinations of β, Θ and absorbers for a measurement on a certain ion is strictly limited.

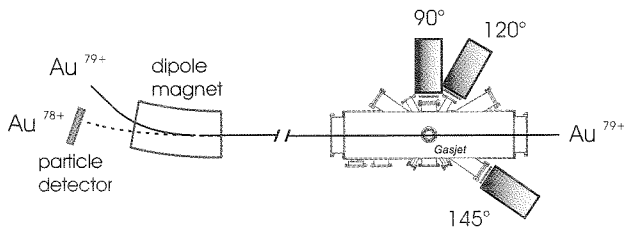

Figure 1: Experimental setup for the absorption-edge technique. Three position-sensitive drift chambers measure - in coincidence with downcharged ions - the intensity variations resulting from the shift of x-ray energies of H-like Au^{78+} which are due to the angle-dependent Doppler-effect over the absorption edges of heavy absorbers.

In the case of hydrogenlike gold such a combination could be found for $\beta = 0.253$ and 0.4196, $\Theta = 90°$, $120°$ and $145°$, and Sm, Tb, Ho, Tm, Lu and Ta as absorbers. The setup of an experiment performed in August 2000 is shown in Fig. 1. In this experiment, three position-sensitive drift-chambers [3, 4] were used for the measurement of the intensity variation of the Ly-α2 line across the K-edges of the absorbers due to the angle-dependent Doppler shift. The line with the sharp peak at the right in

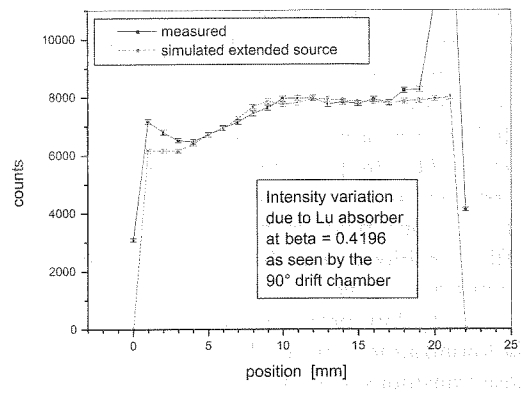

Figure 2: Measured and simulated intensity variation of the Ly-α2 line along the Lu absorption edge at 90° emitted by H-like Au ions at $\beta = 0.4196$. The sharp peak results from the inner geometry of the drift chambers. The calculation corresponds to an extended source.

Fig. 2 shows the experimental result for $\beta = 0.4196$ and $\Theta = 90°$ with Lu as absorber. Plotted is the observed intensity along the horizontal coordinate in the central plane of the detector, integrated over height and depth. The peak results from geometrical effects of the detector.

In order to analyse the experimental data, a program has been written which simulates the intensity variation of the detected photons. Here, the energies, widths and steps of the K-edges are fixed and the only free parameters are the observation angle Θ, the size of the emitting volume and the photon energy in the rest frame.

The line without sharp peaks in Fig. 2 shows preliminary results of the simulations for a 2 mm in diameter and 5 mm long emitting volume assuming $\Theta = 90°$ and the theoretical energy of the Ly-α2 transition [1] in comparison with the experimental data. Since the width of the observed absorption edge is sensitive to the spatial distribution of the emitting volume, it turns out that the extended source is close to the chosen values. The final results will be obtained from a combined fit of the simulations to the experimental data for all K-edges observed.

References

[1] Th. Beier et al., Phys. Lett. A 236, 329 (1997)
[2] C. Strietzel et al., GSI Scient. Rep. 1999, p.208
[3] C. Strietzel, Thesis, Universität Siegen, 2000
[4] M. Czanta et al., GSI Scient. Rep. 1999, p.207

Radiative Electron Capture into the K- and L-shell of H-, He-, and Li-Like Uranium Ions at Relativistic Energies

G. Bednarz[1], A. Warczak[1], D. Sierpowski[1], Th. Stöhlker [2], F. Bosch[2], A. Gumberidze[2] , S. Hagmann[2], C. Kozhuharov[2], D. Liesen[2], X. Ma [2], P.H. Mokler[2], T. Ludziejewski[3], Z. Stachura[4]

[1] *IFUJ-Cracow (Poland),* [2] *GSI-Darmstadt (Germany),* [3] *INS-Swierk (Poland),* [4] *INP-Cracow (Poland)*

Radiative electron capture (REC) is the most important channel for charge exchange in collisions of highly charged ions with light target atoms. As, in addition, the process is the time reversal of photoionization, its investigation opened new possibilities for advanced studies of radiation-matter interaction [1]. In particular, angular distribution of REC photons is a very sensitive probe of relativistic effects in strong fields of heavy ions. Here, magnetic spin-flip transitions were observed, for the first time, in fast collisions of bare U-ions [2] with low Z-ions. Even, at very low projectile velocities, corresponding to photoionization close to the threshold, the presence of these transitions was confirmed as well [3].

We report the experimental study of the angular distributions of photons for REC into the K-shell of H-like and into the L-shell of H-, He- and Li-like uranium ions. The main goal was to observe the role of spectator electrons in the heavy projectile in order to reveal possible electron-electron correlations.

The experiment was performed at the ESR storage ring at GSI-Darmstadt. The U^{91+}- , U^{90+}- and U^{89+}-ions at an energy of 216 MeV/u colliding with N_2-target were used. X-rays emitted from the active target area were detected simultaneously at 13°, 35°, 60°, 90°, 120° and 150° with respect to the beam axis. At all the angles Ge(i) detectors equipped with x-ray collimator slits (except for 13°) were used. The collimator dimensions allowed us to resolve the splitting of the $K\alpha$ transitions into the $K\alpha_1$ and $K\alpha_2$ components. At 13°, a Ge(i) detector with four independent segments, each furnished with an individual readout, was installed on a moveable support. After passing through the target the beam was charge state analysed in the next dipole magnet. Down- and up-charged U-ions were registered (for the study of capture and ionisation processes) with position-sensitive particle detectors located in the inner and outer part of the storage ring. In the following, preliminary results concerning electron capture are presented and discussed only.

Fig.1 shows a typical x-ray spectrum observed at 90° for U^{91+}-ions associated with capture of one electron. The broad structures arise from REC into the projectile K-, L- and M-shells. The line-widths are dominated by the Compton profile of the target electrons. Electron capture into excited states (L, M and higher shells) leads, via cascades, to the characteristic $K\alpha$- and $K\beta$ -transitions, clearly seen in the spectra.

All the x-ray spectra were first energy calibrated and corrected for random events and for detection efficiency. Then, the yields of K- and L-REC photons were determined via special fits to the experimental spectra. Simultaneously, the intensities of $K\alpha_2$-lines ($U^{91+} \rightarrow N_2$) were extracted. Assuming, that the $K\alpha_2$-line (similar to the $Ly\alpha_2$-line) is isotropic in the emitter system, all the angular distributions (U^{91+}, U^{90+}, $U^{89+} \rightarrow N_2$) for K- and L-REC were normalised relative to its intensity pattern in the laboratory frame.

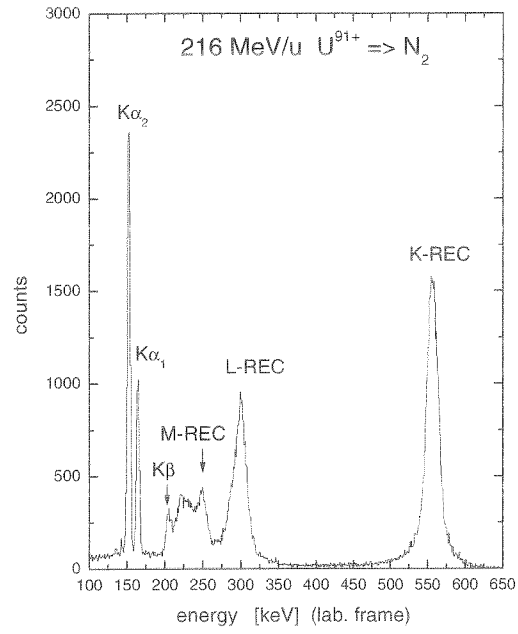

Fig.1 X-ray spectrum associated with one-electron capture (corrected for random events and detection efficiency) observed at an observation angle of 90°.

In Fig.2, the measured differential cross section for REC into the K-shell of 216 MeV/u U^{91+}-ions (present experiment) and 310 MeV/u U^{92+}-ions [2] are plotted as a function of the laboratory observation angle and compared with predictions (for $U^{92+} \rightarrow N_2$) based on rigorous relativistic calculations [4]. (The data obtained in the present experiment for 120° are still under evaluation and are therefore not displayed.)

All the experimental and theoretical cross sections were normalised to an arbitrary value at 90°. Fig.2 shows that the shape of the angular distribution is almost unchanged when comparing the results for bare and H-like U-ions. The experimental data are in accordance with a fully relativistic theoretical description (solid line). The REC emission pattern deviates considerably from symmetry around 90° (compare dashed-line displaying a $sin^2\theta_{lab}$ distribution). Nonvanishing cross sections close to 0° point to the occurrence of magnetic (spin-flip) transitions for REC into high-Z projectiles.

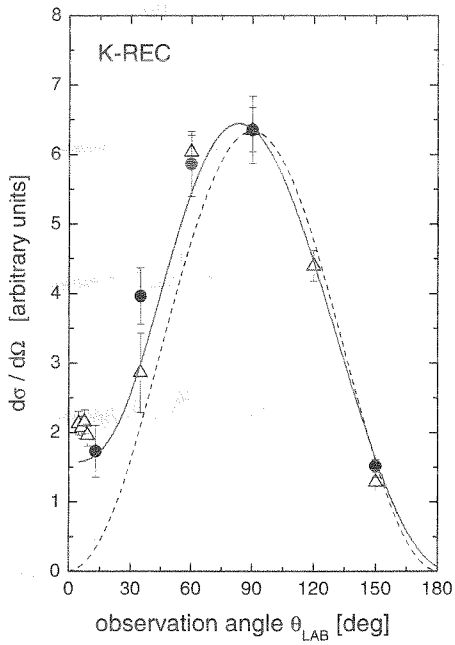

Fig.2 K-REC differential cross sections for 216 MeV/u $U^{91+} \rightarrow N_2$ (circles) and for 310 MeV/u $U^{92+} \rightarrow N_2$ (triangles); dashed-line – $sin^2\theta_{lab}$ distribution, solid-line – relativistic predictions for bare U-ions [4].

The differential cross sections for L-REC into U^{91+}-, U^{90+}- and U^{89+}-ions are presented in Fig.3a, 3b, 3c, respectively, along with theoretical calculations for the different subshells [4]. Similar to the K-REC, the photons observed at 0° and 180° angles present a clear signature of magnetic transitions. A basic feature of all the angular distributions displayed in Fig.3 is the asymmetry between the forward and the backward photon emission. The main contribution for H-like (Fig.3a) and He-like U-ions (Fig.3b) arises from the capture into the 2s-shell (dotted-line in Fig.3a) which has a pronounced maximum at the forward direction. Contributions from the 2p-shells (dashed-line: $2p_{1/2}$, dashed-dotted line: $2p_{3/2}$) reach their maximum at backward angles and do not compensate this forward peaking. In the case of $U^{89+} \rightarrow N_2$ system (Fig.3c) the emission pattern is shifted into backward direction due to the partially blocked contribution from the 2s-shell. Here, again the experimental data agree well with theoretical predictions taking into account only one electron present initially in the 2s-shell of U^{89+} (compare dashed-line in Fig. 3c. for one initial 2s vacancy and the full line for two initial 2s vacancies). In summary, we measured the angular distributions of K- and L-REC into H-, He-, and Li-like U-ions at an energy of 216 MeV/u. They are found to be asymmetric and more pronounced at forward directions. The emission pattern for K-REC stays unchanged for bare and H-like U-ions. One electron present in the L-shell of the projectile (U^{89+}) shifts the photon emission into backward direction. The experimental data provide an excellent agreement with rigorous relativistic predictions.

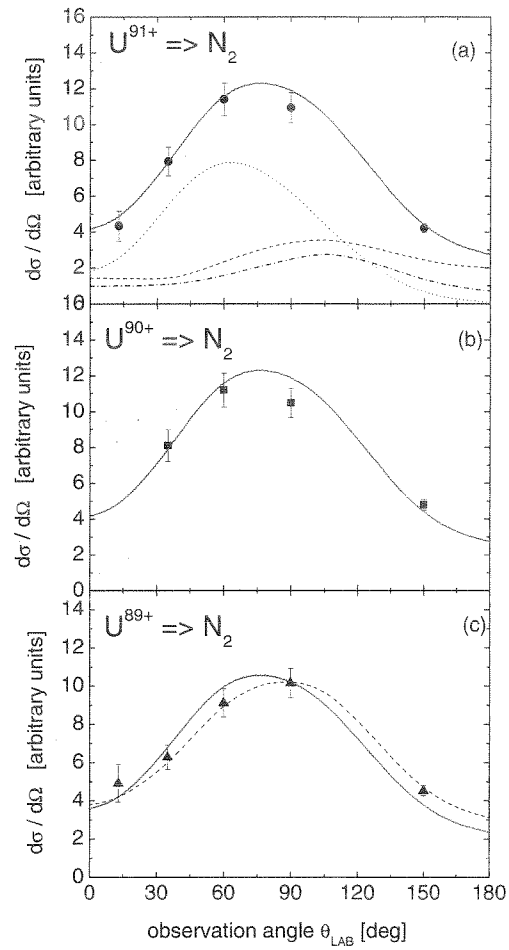

Fig.3 Differential cross sections for capture into the L-shell of U^{91+} (a) , U^{90+} (b) , U^{89+}(c) . (a) dotted-line: capture into the $2s_{1/2}$-shell, dashed-line: $2p_{1/2}$-shell, dot-dashed-line: $2p_{3/2}$-shell; (c) dashed-line – see text. All solid lines refer to the summed contributions for completely empty $2s_{1/2}$-, $2p_{1/2}$-, and $2p_{3/2}$-subshells (relativistic predictions [4]).

References

[1] Th. Stöhlker et al., Com. At. Mol. Phys. **33**, 271 (1997).
[2] Th. Stöhlker et al., Phys. Rev. Lett. **82**, 3232 (1999).
[3] Th. Stöhlker et al., Phys. Rev. Lett. **86**, 983 (2001).
[4] A. Ichihara at al., Phys. Rev. A **49**, 1875 (1994).

State-Selective Electron Capture Studied for U^{90+} Ions in Collisions with Gaseous Targets

X. Ma[1,2], Th. Stöhlker[1,3], F. Bosch[1], O. Brinzanescu[1], S. Fritzsche[4], C. Kozhuharov[1], P.H. Mokler[1] T. Ludziejewski[5], A. Warczak[6]

[1]GSI-Darmstadt, Germany; [2]IMP, Lanzhou, China; [3]IKF, Univ. of Frankfurt, Germany; [4]Univ. Kassel, Germany

[5]INS, Świerk, Poland; [6]Institute of Physics and Jagiellonian University, Cracow, Poland.

In relativistic collisions involving high-Z projectiles and heavy target atoms, non-radiative electron capture (NRC) is a very important charge exchange process [1], a process mediated by three-body interaction. In general, a precise theoretical treatment of this process is very difficult to achieve since the Coulomb field of the fast moving projectile leads to distortions of the atomic target wave functions even at infinite distances. For high-Z ions and relativistic energies the experimental information about NRC is restricted to total cross sections which are quite insensitive to the details of this process. An experiment aiming at a study of state-selective electron capture was conducted at the gas-jet area of the ESR, by utilizing the spectroscopy of projectile x-ray transitions following electron capture into excited projectile states. This method benefits in particular from the large fine structure splitting present in such heavy ion systems. In the experiment, the Balmer radiation produced by electron capture in collisions of 223 MeV/u U^{90+} ions on N_2, Ar, Kr, and Xe targets have been measured in coincidence with the down-charged uranium ions (here *Balmer* transition refers to the transitions from higher levels to n=2 states). The recorded x-ray spectra are shown in figure 1. As the target varies from light to heavy atoms, the relative intensities of the *Balmer* lines exhibit a significant change. This feature already indicates a strong influence of the target charge on the relative population of the various (n, l, j) projectile sublevels by electron capture.

The intensity pattern of the multitude of well-resolved *Balmer* transitions was used to obtain the j-selective cross section data as a function of target Z_T. For this goal a spectrum analysis and simulation code has been developed where electron cascades originating from states up to n=40 are considered. The latter was accomplished by using the individual decay rates and transition energies of all states involved. In the spectra simulation, both the NRC and the radiative electron capture (REC) were taken into account. The CDW theory was used to calculate the NRC cross sections. To obtain experimental information on the j-sensitive population for electron capture, a fit to the measured spectra was carried out by setting the relative cross sections as fitting parameters. From this procedure, the information on relative populations to the different j-sublevels has been deduced [2]. For N_2, where the cross sections for REC are a factor of 10 larger than for NRC, good agreement with theory is obtained. Here, the captured electrons mainly populate the s and p states where the $s_{1/2}$ levels are more favored which is in agreement with REC theory and the j-substate distribution behaves non-statistically. For the heavier targets (Ar, Kr, and Xe), NRC is the most important capture process. This process leads to a n, l, j-distribution which differs markedly from the one observed in the case of the N_2-target (REC). Here, our data analysis shows that NRC seems to favor the population of states with angular momentum l=1 which appears to be only in rough agreement with the CDW approach applied. The discrepancies between our data and the latter approach are in particular evident with respect to the j-dependency. For CDW a statistical j-distribution had to be assumed since we are dealing with a non-relativistic theory. For the case of high-Z projectiles, however, this assumption is questionable (see e.g Ichihara[3]). The systematic deviations between the experimental data and the theoretical calculations for the j-subshell cross sections indicate that a relativistic approach is needed for an appropriate description of NRC in the high-Z domain.

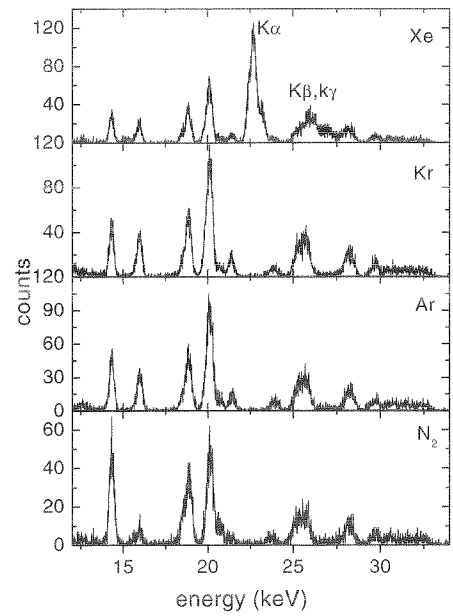

Figure 1: *Balmer* spectra measured in 223 MeV/u U^{90+} impinging on N_2, Ar, Kr, and Xe targets. For the case of Xe, also characteristic target transitions (Kα,Kβ,Kγ) are observed.

References

[1] J. Eichler and W. E. Meyerhof, Relativistic Atomic Collisions (Academic press, San Diego, 1995).

[2] X. Ma et al., Physica Scripta (in print).

[3] A. Ichihara, T. Shirai, and J. Eichler, At. Data and Nucl. Data Tab. 55 63 (1993).

Magnetic Sublevel Population Studied for H- and He-Like Uranium in Relativistic Collisions with Low-Z Targets

A. Gumberidze[1], Th. Stöhlker[1,2], G. Bednarz[3], F. Bosch[1], S. Fritzsche[4], S. Hagmann[5], D.C. Ionescu[1,6], C. Kozhuharov[1], O. Klepper[1], A. Krämer[1,2], D. Liesen[1], X. Ma[1,7], R. Mann[1], P.H. Mokler[1], D. Sierpowski[3], Z. Stachura[3], M. Steck[1] and A. Warczak[3]

[1]GSI-Darmstadt, Germany; [2]IKF, Univ. of Frankfurt, Germany; [3]Institute of Physics, Cracow University, Poland; [4]Univ. of Kassel, Germany; [5]Kansas State University, Kansas, USA; [6]TU Dresden, Germany; [7]IMP, Lanzhou, China.

In contrast to ionization, the experimental information about Coulomb excitation of one- and few-electron projectiles occurring in relativistic atomic collisions is very scarce. The lack of data must be attributed to the experimental difficulties which arise from the fact that excitation is not accompanied by projectile charge exchange. As a consequence, this process can only be studied in single pass experiments by measuring the photon production in coincidence with primary beams of low intensity. Indeed, this technique was applied in the first experimental study of projectile K-shell excitation for high-Z ions [1, 2]. Although this experimental study already elucidated the sensitive dependence of the excitation process on the details of the relativistic bound state wave-functions in the theoretical description, the experimental results suffered from counting statistics. Very recently, an alternative experimental approach has been introduced at the storage ring ESR. Here, the formation of excited states in Au^{78+} in relativistic collisions with an Ar target by Coulomb excitation has been studied by detecting the projectile x-ray emission in anti-coincidence with charge exchange [3]. By using this technique we now started to extent our earlier investigations to a more detailed angular differential study for the collision systems U^{91+}, $U^{90+} \rightarrow N_2$ at 217 MeV/u. For x-ray detection, observation angles in the range between $\approx 10^o$ and 150^o were used at the atomic physics photon detection chamber of the internal target of the ESR (for details see Ref. [4]).

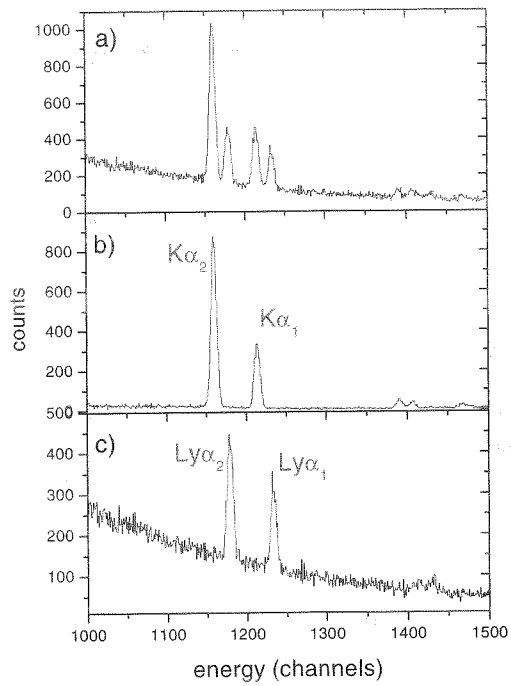

Figure 1: X-ray spectra recorded for 217 MeV/u $U^{91+} \rightarrow N_2$ collisions at the forward angle of close to 10 deg (a: total emission spectrum without coincidence requirement; b: photons in coincidence with electron capture; c: photons in anti-coincidence with electron capture).

In the experiment, the projectile x-ray emission was measured in coincidence with down-charged ions as well as in a single mode, i.e. without any coincidence requirement. As a representative example we depict in Fig. 1 x-ray spectra recorded for $U^{91+} \rightarrow N_2$ collisions at the forward angle of close to 10°. In the spectra, the transitions arising from electron capture (Kα transitions in He-like uranium) and these from excitation (Lyα transitions in H-like uranium) can clearly be distinguished by both the transition energies as well as by the coincidence requirement. Indeed, no Kα transitions are observed in the anti-coincidence spectrum. This also proves that the MWPC detector used for particle detection operates with a detection efficiency very close to 100%.

In the following we concentrate on the formation of magnetic-sublevels by Coulomb excitation as well as by electron capture. Information about this topic can be obtained from the study of the angular distribution of the photons associated with these processes. For the particular case of **E1** transitions, the photon angular correlation has the form:

$$W(\theta) = A_0 + A_2 P_2(\cos\theta) \propto 1 + \beta_{20}(1 - \frac{3}{2}\sin^2\theta). \quad (1)$$

Here θ is the angle between the de-excitation photon and the axis defined by the projectile motion (projectile frame) while P_2 is the second-order Legendre polynomial. The angular correlation is completely determined by the anisotropy coefficient β_{20}. In general, $W(\theta)$ is symmetric about 90° in the projectile frame and isotropic if the intermediate state has $j_n = \frac{1}{2}$ as it is the case for the Lyα_2 ($2p_{1/2} \rightarrow 1s_{1/2}$) transition. For the particular case of the $2p_{3/2}$ transition, however, one may also determine β_{20} from the alignment $\mathcal{A}_2$ of the state which is defined as

$$\mathcal{A}_2 = \frac{\sigma(\frac{3}{2},\pm\frac{3}{2}) - \sigma(\frac{3}{2},\pm\frac{1}{2})}{\sigma(\frac{3}{2},\pm\frac{3}{2}) + \sigma(\frac{3}{2},\pm\frac{1}{2})} = \frac{1}{\alpha}\beta_{20}, \quad (2)$$

where $\sigma(j = \frac{3}{2}, \mu)$ is the population of the magnetic substate with $\mu = \pm\frac{1}{2}, \pm\frac{3}{2}$. For the $2p_{3/2} \rightarrow 1s_{1/2}$ transition, $\alpha = \frac{1}{2}$. Quite similar expressions can be found

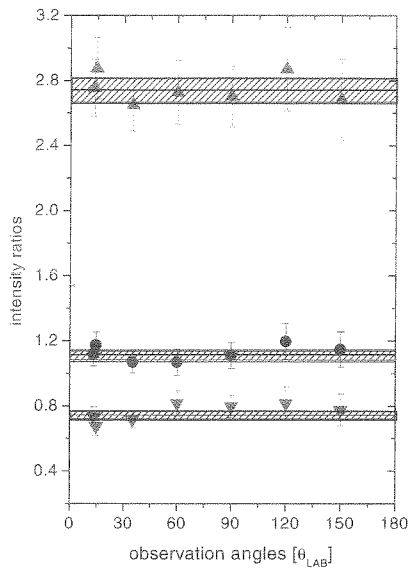

Figure 2: The intensities of Kα2- (up-triangles), Kα1- (solid circles), Lyα1-transitions (down-triangles) normalized to the Lyα2 line as function of observation angle. The experimental data were recorded for U^{91+}→N_2 collisions at the energy of 217 MeV/u. The full lines refer to the corresponding mean values and the shaded areas give the associated uncertainties.

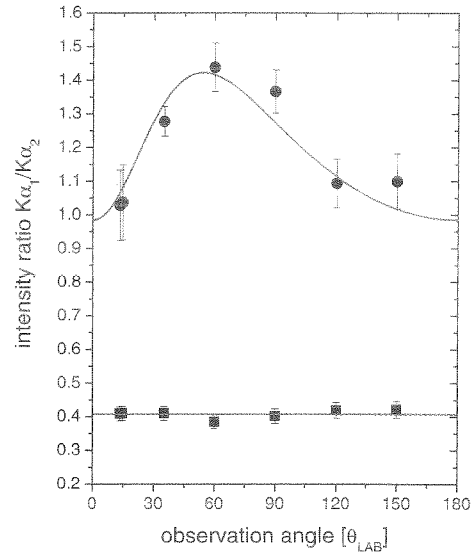

Figure 3: $K\alpha_1/K\alpha_2$ intensity ratio (solid circles) as observed for K-shell excitation of He-like uranium in collisions with N_2 at 217 MeV/u. The solid line refers to a least square fit of Eq. (1) to the experimental data including all required relativistic transformations. For comparison the corresponding intensity ratio (solid squares) as measured for capture into H-like uranium is shown.

for the case of the **E1** decay of the $[1s_{1/2}, 2p_{1/2}]^3P_1$ and the $[1s_{1/2}, 2p_{3/2}]^1P_1$ states in the He-like systems. Here, however, magnetic sublevels with the quantum numbers of $\mu_{J=1} = 0, \pm 1$ must be considered.

In our current experiment we strongly profited from the fact that the Lyα2 transition arising from the decay of the $2s_{1/2}$,$2p_{1/2}$ levels is known to be precisely isotropic. Consequently, it provides an ideal tool to measure a possible anisotropy of the close spaced Lyα1 or Kα transitions. In Fig. 2 the preliminary results for the emission pattern of the Lyα1 and the Kα transitions are shown, normalized to the Lyα2 intensity. In all cases no alignment is observed and the magnetic sublevels are therefore populated statistically. In the case of the Lyα1 transition ($2p_{3/2} \rightarrow 1s_{1/2}$) induced by excitation this finding seems to be in agreement with theoretical predictions [5]. However, the isotropy of the Kα1 emission $[1s_{1/2}, 2p_{3/2}]^1P_1$,$^3P_2$, which is caused by electron capture, is in contradiction to former observations and theoretical predictions for capture into bare uranium where a strong alignment of the $2p_{3/2}$ state was observed [6]. This surprising result may point to the importance of electron-electron interaction for the emission characteristic of excited levels in high-Z He-like ions. But we have also to emphasize that the decay of two levels (**E1** decay for $^1P_1$, **M2** decay for $^3P_2$) contribute to the Kα1 transition which cannot get resolved in our experiment. Since both transitions exhibit different angular distributions this may wipe out a distinctive anisotropy of the Kα1 emission. Currently this topic is subject of detailed theoretical investigations.

Also for K-shell excitation we observed a markedly difference between the H- and the He-like species. In Fig. 3, the $K\alpha_1/K\alpha_2$ intensity ratio, as measured for K-shell excitation of He-like uranium in 217 MeV/u U^{91+}→N_2 collisions, is plotted as a function of the observation angle. For comparison the corresponding intensity ratio (solid squares) as measured for capture into H-like uranium is shown in addition. In contrast to electron capture, the data for excitation exhibit a pronounced deviation from a constant intensity ratio. Note, that for the case of K-shell excitation of high-Z He-like ions, only the $[1s_{1/2}, 2p_{3/2}]^1P_1$ contributes to the Kα1 transition whereas the Kα2 intensity arises from the decay of the $[1s_{1/2}, 2p_{1/2}]^3P_1$ level only. In both cases an alignment of the different sublevels is possible. At present, it has not been clarified which of both states causes the observed anisotropic intensity ratio. However, at the current state of data analysis there are strong indications of a positive alignment of the $[1s_{1/2}, 2p_{1/2}]^3P_1$ level. This means that the magnetic sublevels with $\mu = \pm 1$ are preferably populated in the collision.

References

[1] Th. Stöhlker et al., Phys. Rev. A **57**, 845 (1998); Phys. Lett. A **238**, 43 (1998).

[2] T. Ludziejewski et al., Phys. Rev. A **61**, 052706-1 (2000).

[3] A. Krämer et al., Physica Scripta T80, 424 (1999).

[4] Th. Stöhlker et al., in:"X-Ray and Inner Shell Processes", AIP Conference Proc. 506, 389 (2000).

[5] D.C. Ionescu and Th. Stöhlker, contribution to this report.

[6] Th. Stöhlker et al., Phys. Rev. Lett. 79, 3270 (1997).

Projectile K-Shell Vacancy Production in $U^{89+} \rightarrow N_2$ Collisions: Selective Population of the 2s-States in He-Like Uranium

Th. Stöhlker[1,2], A. Gumberidze[1], G. Bednarz[3], F. Bosch[1], S. Fritzsche[4], S. Hagmann[5], D.C. Ionescu[1,6], C. Kozhuharov[1], A. Krämer[1,2], D. Liesen[1], X. Ma[1,7], R. Mann[1], P.H. Mokler[1], D. Sierpowski[3], Z. Stachura[3], M. Steck[1], and A. Warczak[3]

[1]GSI-Darmstadt, Germany; [2]IKF, Univ. of Frankfurt, Germany; [3]Institute of Physics, Cracow University, Poland; [4]Univ. of Kassel, Germany; [5]Kansas State University, Kansas, USA; [6]TU Dresden, Germany; [7]IMP, Lanzhou, China.

Until now, atomic physics experiments at the ESR storage ring focused on initially bare and hydrogen-like ions. However, there is an increasing demand to extend the range of possible structure and collision studies to heavy high-Z multi-electron systems such as helium-, lithium-, or beryllium-like ions. To accomplish the storage of intense heavy few-electron systems even at the highest beam energies possible at the ESR, thin carbon stripper foils are now available in the beam transfer line between SIS and ESR. In contrast to the commonly used copper stripper targets, carbon foils guarantee a strong yield enhancement for heavy multi-electron ions (see. Fig. 1). Very recently, this new possibility for atomic physics experiments has been exploited by injecting intense SIS beams of lithium-like uranium into the ESR at an energy of 217 MeV/u. In this experiment, projectile x-ray emission arising from collisions with a N_2 target was measured by intrinsic germanium detectors in coincidence with down-charged or up-charged ions, i.e. ions having captured (U^{88+}) or lost (U^{90+}) one-electron in the collision. For a detailed description of this set-up we refer to Ref. [1]. In the following we concentrate on the process of K-shell ionization. In Fig. 2 the x-ray spectrum observed at an forward angle of $\approx 10^o$ in coincidence with electron-loss is depicted. The spectrum is entirely governed by an intense single L→K ($K\alpha_2$) transition and a broad continuum distribution. Since we are dealing with He-like uranium produced by K-shell vacancy production of the Li-like species, the broad continuum can be explained by the two-photon decay (**2E1**) of the $[1s_{1/2}, 2s_{1/2}]^1S_0$ level. Consequently, the single $K\alpha$ transition observed arises exclusively from the **M1** decay of the $[1s_{1/2}, 2s_{1/2}]^3S_1$ state. To the best of our knowledge, no other process occurring in ion-atom collisions is known with such a high state selectivity. This also means that the 2s-electron stays passive during a collision leading to K-shell ionization because no decay from the neighouring excited p-states is observed (see level scheme inserted in Fig. 2). This unexpected and surprising finding is currently subject of theoretical studies.

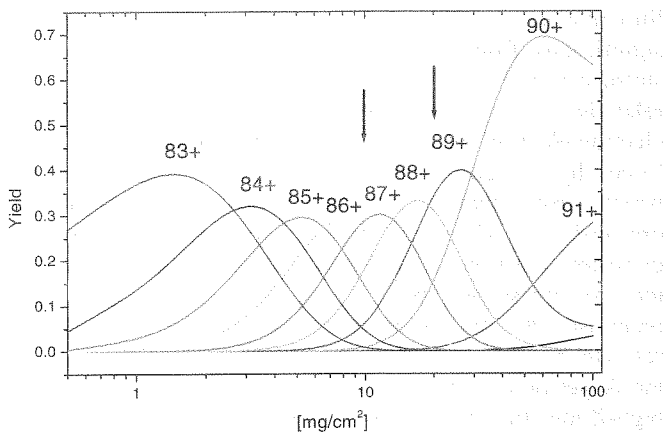

Figure 1: Calculated charge state evolution as function of target thickness for uranium ions traversing through a carbon foil at an energy of 300 MeV/u. For the calculation the program GLOBAL has been used [2]. The arrows mark the target thickness of the stripper targets installed.

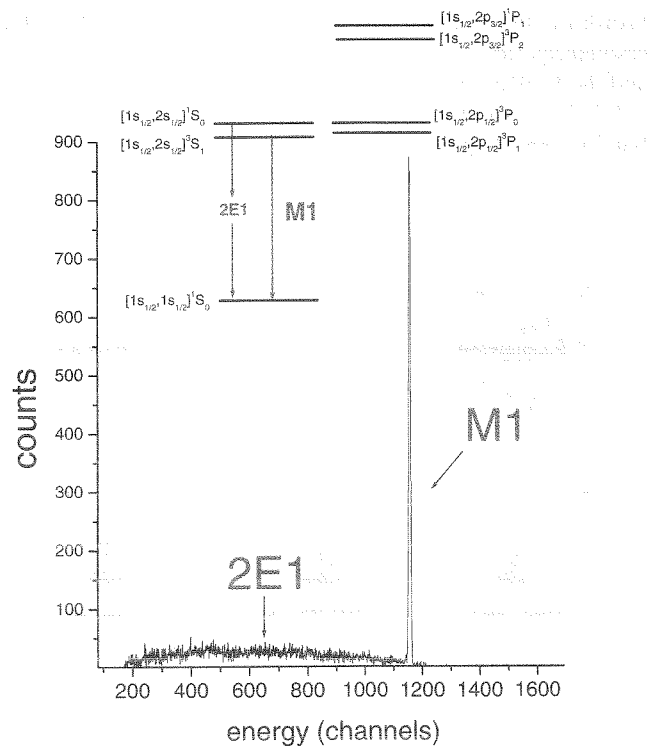

Figure 2: X-ray spectrum measured in coincidence with electron loss for $U^{89+} \rightarrow N_2$ collisions at 217 MeV/u. In the upper part, the level scheme of He-like uranium illustrates the origin of the observed photon emission.

References

[1] Th. Stöhlker et al., in:"X-Ray and Inner Shell Processes", AIP Conference Proc. 506, 389 (2000).

[2] C. Scheidenberger et al., Nuclear Instr. and Methods B **142**, 441 (1998).

Resonant Transfer and Excitation for H-like U Ions: A Case Study for Electron-Electron Interaction at Strong Central Fields

X. Ma[1,2], P.H. Mokler[1], G. Bednarz[3], F. Bosch[1], A. Gumberidze[1], S. Hagmann[1], C. Kozhuharov[1], D. Liesen[1], U. Popp[1], D. Sierpowski[3], Z. Stachura[4], Th. Stöhlker[1], S. Tashenov[5], S. Toleikis[1], A. Warczak[3], Y. Zou[6]
[1]GSI, Darmstadt, Germany; [2]IMP, Lanzhou; China; [3]Jagiellonian University, Cracow, Poland; [4]IFJ, Cracow, Poland;
[5]State University Moscow, Russia; [6]Jiaotong University, Shanghai, China.

Structure and dynamics for the heaviest atomic systems differ significantly from those of lighter ions due to the extremely strong central fields at the high atomic numbers Z. In particular relativistic effects are essential. There, for instance, the electron-electron interaction is governed beyond the Coulomb forces by the current or magnetic interactions (Breit term) which may change the corresponding Auger emission drastically [1]. Collisions of highly-charged heavy ions with quasi-free electrons from light target atoms provide a unique tool to investigate the electron-electron interaction in the relativistic domain via resonant capture and excitation. This resonant transfer and excitation (RTE) is the time reversal of the Auger process and leads first to a doubly excited state. For high-Z ions the intermediate doubly excited state stabilizes by x-ray emission due to the high radiative rates, cf. [2] [3].

The electron-electron interaction can by studied in an unperturbed manner for incoming H-like ions interacting with one target electron. Therefore, we have investigated this pure case at the ESR gas target for the heaviest possible system, for H-like U^{91+} projectiles colliding with hydrogen. For hydrogen as gas target the momentum distribution of the quasi-free electron determining the RTE resonance width (Compton profile) is the smallest possible. Fig. 1 shows the three $KL_jL_{j'}$ resonances (top) where one electron is captured into a L_j level and the K electron is excited resonantly to a $L_{j'}$ level – with j, j' = 1/2, 3/2 – and the following radiative decay modes (bottom). Satellite and hypersatellite x-ray lines (one and two initial K vacancies) can be separated by the Ge(i) x-ray detectors used.

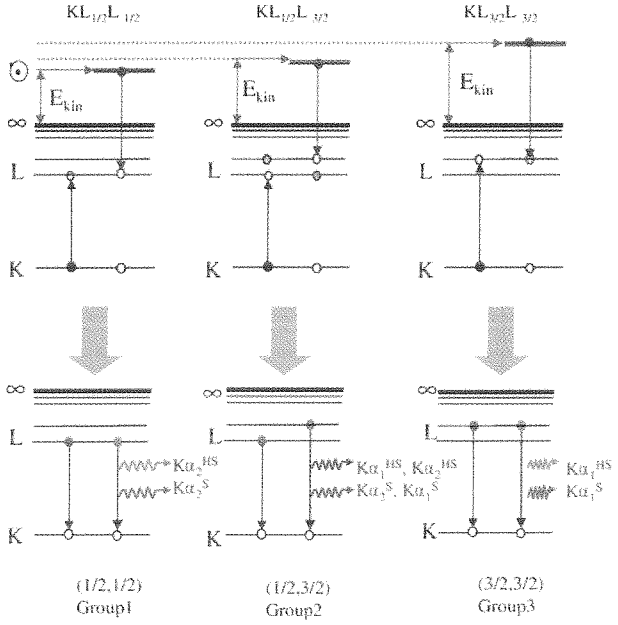

Fig.1: $KL_jL_{j'}$ RTE resonances and their radiative decays for incoming H-like U^{91+} ions.

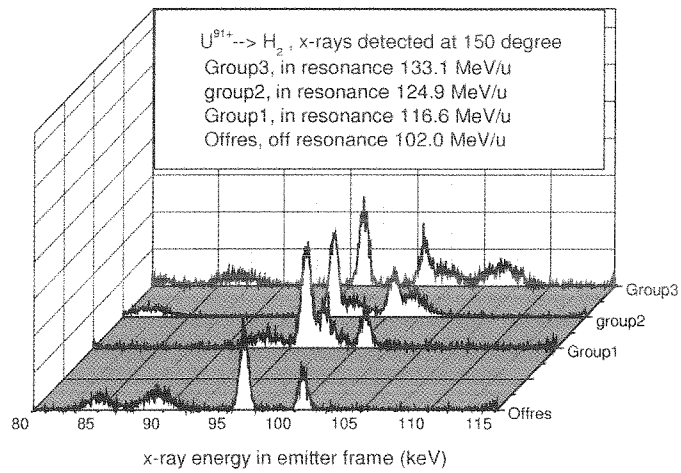

Fig. 2: X-ray spectra observed at 150^0 for U^{91+} - H collisions.

We have determined the x-ray emission pattern induced by U^{91+} - H collisions using six different observation angles (from ≈ 12^0 to 150^0) for the three RTE resonance maxima and for one off-resonance ion energy, cf. Fig. 2. For the off-resonance data at 102 MeV/u ion energy we find in the x-ray spectrum the L_j - REC lines with j = 3/2 and 1/2 (at ≈ 85 and 89 keV) and the subsequent $K\alpha_2$ and $K\alpha_1$ cascade lines (at ≈ 96 and 100 keV). With higher ion energies the REC lines shift correspondingly to higher x-ray energies. At the $KL_{1/2}L_{1/2}$ resonance – group 1 at 116.6 MeV/u in Fig. 2 – the $L_{1/2}$-REC line coincides with the $K\alpha_2^H$ hypersatellite line caused totally by RTE (at ≈ 97 keV). At 124.9 MeV/u, the $KL_{1/2}L_{3/2}$ -RTE resonance (group 2), both L_j-REC lines coincides with both the $K\alpha_i^H$ hypersatellites each. Finally, for the $KL_{3/2}L_{3/2}$ resonance at 133.1 MeV/u (group 3) the $L_{3/2}$ -REC line (at ≈ 102 keV) coincides with the $K\alpha_1^H$ hypersatellite line; the $L_{1/2}$ -REC line (at ≈ 106 keV) is here already beyond the region of interest.

The data are presently being evaluated in order to extract both total rate coefficients for the electron-electron interaction at strong fields and to get the angular distributions of the x-ray emission. From the emission patterns the j dependent level population of the doubly excited intermediate states can be deduced giving detailed insight into the electron-electron interaction mechanism in the relativistic domain. Calculations for this system are presently being performed by the theory group in Giessen, cf. [4].

References

[1] P. Zimmerer et al., Phys. Lett. A148 (1990) 457
[2] T. Kandler et al., Phys. Lett. A204 (1995) 274
[3] P.H. Mokler et al., Physica Scripta T73 (1997) 247
[4] M. Gail et al., J. Phys. B31 (1998) 4645

Measurement of Photorecombination of Highly Charged Ions at Low Relative Energies

C. Brandau[a], T. Bartsch[a], K. Beckert[b], S. Böhm[a], C. Böhme[a], F. Bosch[b], B. Franzke[b], N. Grün[c], A. Hoffknecht[a], H. Knopp[a], S. Kieslich[a], C. Kozhuharov[b], A. Krämer[b], P.H. Mokler[b], A. Müller[a], F. Nolden[b], W. Scheid[c], S. Schippers[a], W. Shi[a], Z. Stachura[d], M. Steck[b], T. Steih[c] T. Stöhlker[b],

[a]Institut für Kernphysik, Justus-Liebig-Universität, 35392 Gießen
[b] Gesellschaft für Schwerionenforschung (GSI), 64291 Darmstadt
[c]Institut für Theoretische Physik, Justus-Liebig-Universität, 35392 Gießen
[d]Instytut Fizyki Jądrowej, 31-342 Kraków, Poland

In the ongoing work on photorecombination (PR) measurements at the electron cooler of the ESR new results have been obtained during the last year. PR is the capture of a free electron under emission of one or more photons. It is usually described as two different processes, radiative recombination (RR) and dielectronic recombination (DR).
The interest in RR, which is the direct path of PR (time-inverse photoeffect), is mainly driven by the puzzling "rate enhancement phenomenon" at very low relative energies between electrons and ions. On the other hand in resonant DR, the free electron is captured radiationless by the ion (inverse to autoionisation), and a doubly excited compound system is formed. If the intermediate state decays under emission of a photon DR is completed. Therefore, investigations of DR provide insight into the atomic structure of the very heavy highly charged ions under study at the GSI.

RR measurements of U^{92+}

For relative energies between electrons and ions above 0.01-0.1 eV up to very high energies the measured rate coefficient for RR can be described by the dipole approximation within a non-relativistic treatment. However, at very low energies recombination rates exceed the predictions by factors of 1.6 for light ions and up to a factor of 5.2 for heavier bare species. For multicharged complex ions even higher enhancement factors have been found, which could partly be explained by low energy DR-resonances. Of course, for bare ions recombination can not proceed via DR. As a measure for the enhancement an excess rate $\Delta\alpha = \alpha_{exp} - \alpha_{theo}$ is defined. While the enhancement turns out not to be influenced by the electron target density, $\Delta\alpha$ is found to scale with the temperatures of the electron beam like $T_{\perp}^{-1/2}$ and $T_{||}^{-1/2}$. The dependence of the rate enhancement on the strength of the magnetic field used to guide the electron beam inside the cooler is even more puzzling than the enhancement itself: An increase of the enhancement with increasing magnetic field is commonly found at all storage rings. In addition, for very heavy ions at high ion energies, and hence at high electron energies, nearly periodic oscillations of the RR rate coefficient in dependence of the magnetic field strength have been observed at the ESR [1, 2]. So far, for very heavy bare ions ($Z > 18$) detailed investigations of the enhancement have only been performed with Bi^{83+} [2]. Recently, measurements with 297.1 MeV/u U^{92+} ions have been carried out at the ESR. The recombined ions have been detected with a position sensitive counter. This additional diagnostics allows one to monitor the ion beam properties during the measurement. It turned out that the size of the ion beam changes in the horizontal (x-) direction while for the size in the vertical direction no changes under variation of the guiding field could be observed. This decrease of ion beam quality is in accordance with previous findings at the ESR, where the transversal temperature $T_{\perp}$ has been found to vary with magnetic field strength [2]. Hence, the oscillations in the recombination rate seem to be closely connected with changes of the ion beam properties in the transversal direction, which are introduced by small variations of the guiding field. However, the reason for this peculiar behaviour is not known yet. Apart from the oscillations an overall increase of the rate enhancement with increasing magnetic field is found.
For less heavy bare ions ($Z < 18$) a $Z^{2.8}$ scaling of the scaled excess rate $kT_{\perp}^{0.5} kT_{||}^{0.5} \Delta\alpha$ has been reported [3]. When the two measurements for Bi^{83+} and U^{92+} are included this behaviour slightly changes to a $Z^{2.6}$ scaling.

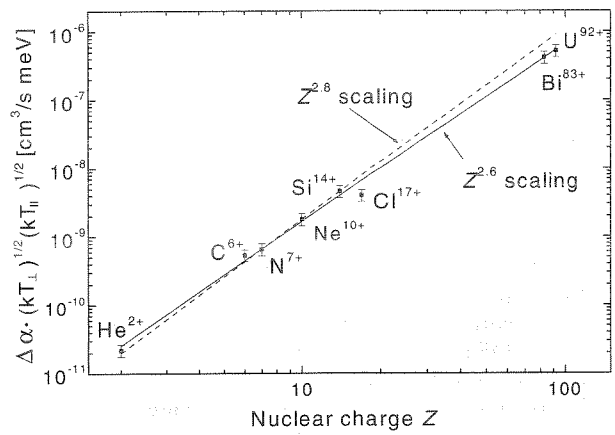

Figure 1: Dependence of the scaled excess rate $kT_{\perp}^{0.5} \cdot kT_{||}^{0.5} \cdot \Delta\alpha$ at 0 eV on the nuclear charge Z. The measurements have been performed at different storage rings (TSR, CRYRING, ESR). The excess rates have not been normalized to the same magnetic field strength. The dashed line is a $Z^{2.8}$ scaling according to [3]. The full line is the new $Z^{2.6}$ scaling with inclusion of the Bi^{83+} and U^{92+} data.

Determination of $2s_{1/2} - 2p_{1/2}$ energy splitting of Li-like heavy-ions by means of DR

Li-like ions are the simplest ions in which $\Delta n = 0$ excitations ($2s_{1/2} \rightarrow 2p_{1/2}$ and $2s_{1/2} \rightarrow 2p_{3/2}$) are possible from the ground-state, thus providing $1s^2 2p_{1/2,3/2} n\ell_j$-DR-resonances in the low-energy domain. For a comprehensive theoretical description of the measured DR features of the heavy ions under investigation (Au^{76+}, Pb^{79+}, Bi^{80+} and U^{89+}) a fully relativistic treatment is needed. In addition, radiative (QED) corrections scale approximately with Z^4 and therefore become increasingly important. The same is true for corrections caused by the finite size of the atomic nucleus and by relativis-

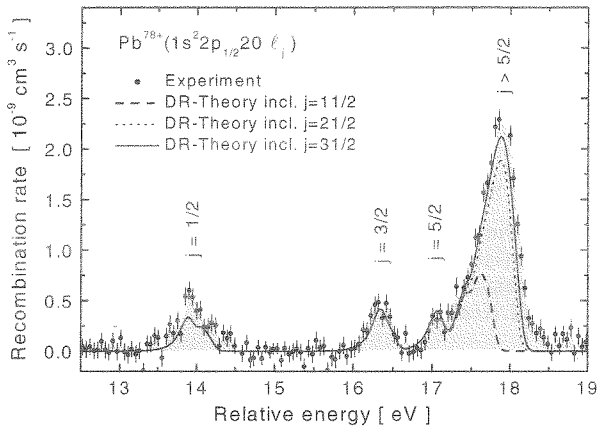

Figure 2: Measured Pb^{79+} recombination rate coefficient compared with our fully relativistic theoretical calculation (full line). The theory has been shifted by -0.65 eV (see text) .

tic effects. Up to now for DR in Li-like very heavy ions there are no strict QED calculations which allow for a direct comparison with the experiment and hence a testing of QED in strong fields. On the other hand a large number of QED calculations for the $2s-2p$ splitting in Li-like ions are available, mainly triggered by the accurate measurements of Schweppe et al. for U^{89+} [4]. We have developed a novel method which allows to extract excitation energies of the projectile ions from the DR resonance positions of the doubly excited recombined ion. For every excitation channel of the dielectronic capture an infinite number of dielectronic resonances converging to the associated series limit may be observed. The main idea is to extrapolate the energies of individual Rydberg resonances to the associated series limit. For increasing values of n and there especially for high angular momenta j the mutual influence of core and Rydberg electrons can be neglected and the excitation energy E_∞ can be described by

$$E_\infty(Z) = E_{Res}(Z,n,j) + E_B(Z,n,j), \qquad (1)$$

where $E_{Res}(Z,n,j)$ is the resonance energy and $E_B(Z,n,j)$ the binding energy of the Rydberg electron, e.g. in a H-like approximation (Dirac energies). Therewith, one deals with a multitude of resonances the energy dependence of which is well known. Beside the series limit as one fitting parameter, additonal free parameters can be introduced to improve the energy calibration.

In particular, for very heavy Li-like ions all $1s^22p_{1/2}n\ell_j$ resonance manifolds with $n \geq 20$ can be found within the energy range (0-400 eV) which is accessible by our present experimental set-up. Individual Rydberg states up to $n \approx 45$ have been observed. For Rydberg states with $n = 20-25$ detailed information about the fine-structure and resonance strengths could be obtained (see Fig. 2). As can be seen from the figure a very good agreement between the experiment and fully relativistic calculation (GRASP code) is found as long as the *shapes* and the *resonance strengths* of the DR-resonances are concerned. This agreement is even more striking as the experimental rate coefficient has been measured on an absolute scale, and hence theory and experiment are not normalized with respect to each other. It should be noted that the inclusion of very high angular momentum components ($j_{max} \gtrsim 23/2$) is needed. On the other hand it is known that uncertainties in absolute energies produced by the GRASP code are ≈ 1 eV or even more, which are mainly caused by the approximations used to include QED in the MCDF code. But the additional theory-based knowledge about the shape and the fine-structure of the doubly excited Rydberg states can be used to improve the accuracy of the extrapolation significantly.

With the method described above the following values for the $2s_{1/2}-2p_{1/2}$ splitting have been obtained: $E_\infty(Au^{76+}) = 216.11(20)$ eV, $E_\infty(Pb^{79+}) = 230.62(20)$ eV and $E_\infty(U^{89+}) = 280.56(20)$ eV. These results are sensitive to QED contributions of the order α^2. A further reduction of the error by a factor of ≈ 5 can be expected in the near future as the main source of errors is the available knowledge of the velocity distribution of the cooler electrons. This distribution can be probed with high accuracy with an ion of lower nuclear charge Z. In contrast to the very heavy ions, isolated resonances with small natural linewidth ("δ-like") are expected, so that a measured spectrum reflects the velocity distribution of the target electrons. Details can be found in [5].

Scaling behaviour of DR Rydberg states

As mentioned above, one strength of DR investigations utilizing storage ring coolers is the measurement of *absolute* rate coefficients. This allowed us to determine the scaling behaviour of the resonance strength $S = \int \sigma(E)\mathrm{d}E$ of the Rydberg series of Pb^{79+} (Fig. 3). For the doubly excited Rydberg states a $E^{-1}n^{-3}$ scaling can be expected as $S_{Res} \propto A_a \cdot \omega$, the autoionisation rate $A_a \propto n^{-3}$ and the flourescence yield $\omega \approx const.$ for sufficiently high n. A comparison (Fig. 3) between experimental resonance strengths for the DR of Pb^{79+}, reveals a n^{-3} scaling law and DR/MCDF calculations for $n = 20-25$ confirm these predictions.

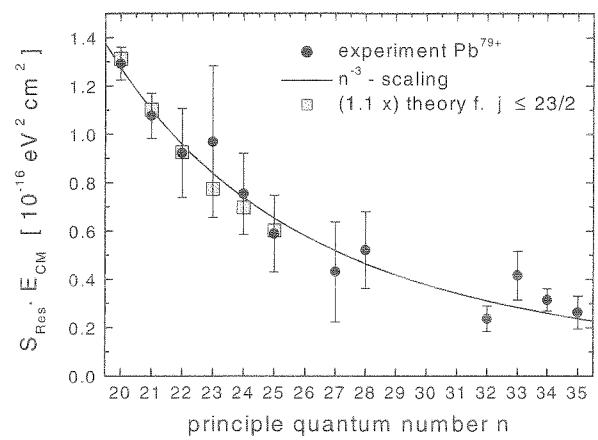

Figure 3: $E^{-1}n^{-3}$ scaling of the DR resonance strength S_{Res} of $Pb^{78+}(1s^22p_{1/2}n\ell_j)$-resonances (DR of Pb^{79+}). The full circles are experimental data, the full line is a scaling according to $E \cdot S_n = E \cdot S_{n=20} \cdot 20^3/n^3$. The grey squares are DR/MCDF calculations (GRASP). Theory has been multiplied by a factor 1.1 in order to take states into account with $j > 23/2$.

References

[1] M. Steck, GSI Workshop, June 21, 1997.
[2] A. Hoffknecht et al. , PRA **63**, 012702 (2000)
and: A. Hoffknecht et al. , GSI Sci. Rep. 1999, p. 88.
[3] H. Gao et al., JPB **30**, L499 (1997).
[4] J. Schweppe et al., PRL **66**, 1434 (1991).
[5] C. Brandau, Dissertation (Uni Giessen),
http://bibd.uni-giessen.de/ghtm/2001/uni/d01008.htm

Fragmentation of Atoms in Strong Fields viewed with Reaction-Microscopes

R. Moshammer[1,2], H. Kollmus[1,2], S. Hagmann[2,3,4], M. Schulz[5], B. Feuerstein[2], R. Mann[3], A. Dorn[2], D. Fischer[2], A. N. Perumal[2], C. Höhr[2], C.D. Schröter[1,2], J.R. Crespo Lopez-Urrutia[2], H. Rottke[6], C.Trump[6], W. Sandner[6], R.E. Olson[5], J. Ullrich[1,2]

[1]MPI-Heidelberg, [2]Uni Freiburg, [3]GSI Darmstadt, [4]KSU Manhattan, [5]UMR Missouri, [6]MBI Berlin

The interaction of both, highly charged ions and intense lasers fields, with matter or atoms attract increasing interest because of fundamental questions to be addressed and because of the long term perspectives of potential applications. Such applications cover a wide range from inertial fusion driven by heavy ion or intense laser beams to new techniques in material science and medical treatments. These developments rely on a profound knowledge about the interaction of radiation with single atoms and about the dynamical correlation of electrons in ultra-short and strong fields. In this context ionization of atoms in intense fields plays a key role because the coupling between radiation and matter is mediated by the electrons.

Theoretically, in particular the regime of large perturbations is of interest, where the radiation field strongly modifies the atomic states, where it interacts simultaneously with several electrons and where non-linear effects prevail. This puts severe constraints on theoretical descriptions revealing substantial problems in the treatment of the correlated motion of mutually interacting particles under the action of a time dependent force. In spite of these difficulties, successful theoretical approaches have been developed so far for single ionization of atoms by charged heavy-ion impact as well as by intense laser pulses. But, the extension to more complicated situations like e.g. double or multiple ionization has been identified as a key challenge for many-body Coulomb theories.

Experimentally, the recent developments of advanced many-particle coincidence techniques to study atomic fragmentation allow to identify simultaneously the momenta of all reaction products emerging from a single collision with high resolution. These so called reaction microscopes consist of recoil-ion momentum spectrometers combined with an electron analyzer with 4π efficiency and high momentum resolution. They enable experiments on single and multiple ionization reactions of atoms and molecules with unprecedented completeness and momentum resolution (for a review see [1]). Such kinematically complete experiments provide benchmark data for theories and allow for the first time the separation of different mechanisms involved in the ionization process.

In this report we discuss three topics concerning the fragmentation of atoms in the strong fields generated by fast passing highly-charged ions and intense low-frequency laser pulses. The experiments have been performed at the UNILAC of GSI and at the high power laser facility of the Max-Born-Institute in Berlin.

Ultimate Tests of Single Ionization Theories at Strong Perturbations

In a kinematically complete experiment the emission of low energy electrons (E_e < 150 eV) in single ionization of He-atoms induced by 3.6 MeV/u Au^{53+} ion impact has been studied. Using a reaction-microscope [1] the momenta of the recoiling target-ions and of the ejected electrons have been measured in coincidence. In a previous work the electron energy and angular distribution was studied irrespective of the projectile scattering [2]. These double differential electron emission cross sections have been shown to be in very good agreement with continuum distorted wave eikonal initial state (CDW-EIS) calculations. Because of the large perturbation of the projectile ion with q/v = 4.4 (the projectile charge to velocity ratio in atomic units is a measure of the perturbation strength. Perturbation theory usually can be applied for q/v < 1.), a strong postcollision effect has been observed even at very low electron energies. The receding projectile drags the electrons into the forward direction. As a next step in testing theory in more detail, we investigated the electron emission characteristics as a function of the momentum transferred from the projectile to the target atom. In almost all cases the longitudinal momentum transfer (i.e. the component along the beam direction) is very small compared to the transverse direction. This quantity is deduced from the measured vector momenta of the electron and the recoiling target ion using momentum conservation. In this way projectile scattering angles as small as 20 nrad became accessible, enabling for the complete determination of the three particle dynamics in singly ionizing heavy-ion atom collisions.

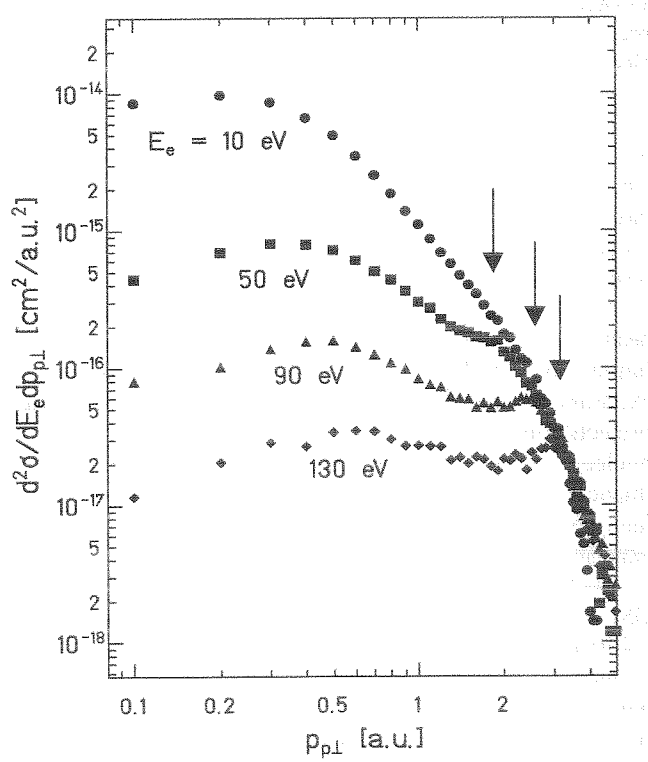

Figure 1: *The projectile momentum transfer in the transverse direction for given electron energies in single ionization of He by 3.6MeV/u Au^{53+} impact. A transverse momentum transfer of $p_{p\perp}$ = 1 a.u. corresponds to a scattering angle of 250 nrad.*

In fig. 1 the distribution of the transverse momentum transfer is shown for fixed ejected electron energies. Low energy electron emission is dominated by small transverse momentum transfers indicating that mainly dipol-transitions from the initially bound to the continuum state contribute [3]. In this so called soft collision regime the fast passing projectile acts much like a source of virtual photons which get absorbed by the target atom revealing similarities with photoionization [4]. With increasing electron energy more violent encounters contribute. Then, the momentum transfer exhibits a peak at a value which is equal to the momentum of the ejected electron (arrows in fig. 1) clearly demonstrating the transition to the binary-encounter regime: the target electron is knocked out in a binary collision with the projectile.

In addition, triple differential cross sections (TDCS) for these highly non-perturbative collisions have been measured. There the angular distribution of the ejected electron in the plane defined by the incoming and the scattered projectile (i.e. in coplanar geometry) is plotted for a given electron energy and for fixed momentum transfer. Such TDCS data are known to be very sensitive on the collision dynamics and they can be considered as the ultimate test of single ionization theories in the non-perturbative regime.

Electron-Electron Interaction in Projectile Ionization: A New Way to Explore (e,2e) on Ions ?

Measurements of differential cross sections for ionization of ions in collisions with high-energy electrons are extremely difficult to perform by applying conventional crossed beams techniques. In essence, due to the low luminosity, such experiments have not been possible up to now, not even in storage rings. If feasible, they would allow for instance high precision momentum spectroscopy of bound states in few-electron heavy-ions.

On the other hand, in a fast collision of a non-bare projectile-ion with a target atom the projectile can be ionized via an interaction with one of the target electrons (electron-electron (e-e) interaction). In those collisions both, the active target electron and the projectile electron, get ionized [5]. This process is equivalent to electron impact ionization of the projectile if the initially bound target electron can be treated as a quasi free electron. In such a scenario, using a dense atomic beam, one would circumvent the above mentioned low luminosity problem of conventional crossed beams experiments. But, there is a second mechanism contributing to projectile ionization: Interaction of the electron with the target nucleus (nucleus-electron (n-e) interaction). Thus, electron impact ionization of ions may be studied in very detail, if the many-particle dynamics is completely controlled experimentally.

Such a measurement has been performed at the UNILAC of GSI studying ionization of 3.6 MeV/u C^{2+} projectiles in collisions with He atoms. In the experiment the final state momentum vectors of all particles emerging from the collision have been mapped. In the following we will demonstrate that a separation of the two competing mechanisms contributing to projectile ionization is indeed possible, because different mechanisms populate kinematically different regions in the final state. If a (n-e) interaction takes place the target nucleus has to deliver the momentum transfer required to ionize the projectile. Thus, one expects a recoiling He^{1+} target ion with large momentum, whereas the target electron acts as a spectator. In contrast, in a (e-e) interaction the target electron plays the active role and the He-nucleus takes part as a spectator [6]. Therefore the two processes ((n-e) and (e-e)) can be separated event by event by putting a condition on the values of the momenta of the target electron p_{ele} and the He^{1+} ion p_{ion}. Selecting only those events, for which $p_{ele} > p_{ion}$ is fulfilled, implies that mainly the (e-e) interaction is left in the resulting subset of the experimental data. The validity of this approach is demonstrated in the fig. 2. There, the momentum distributions of the projectile electron, the target electron and the He^{1+} recoil-ion are projected onto the collision plane. This plane is defined by the incoming projectile momentum and the momentum transfer. As expected for (e-e) interaction, the ionized projectile electrons and the target electrons are preferentially emitted into opposite directions. The target ion behaves as a spectator and therefore exhibits no angular correlation with the emitted electrons.

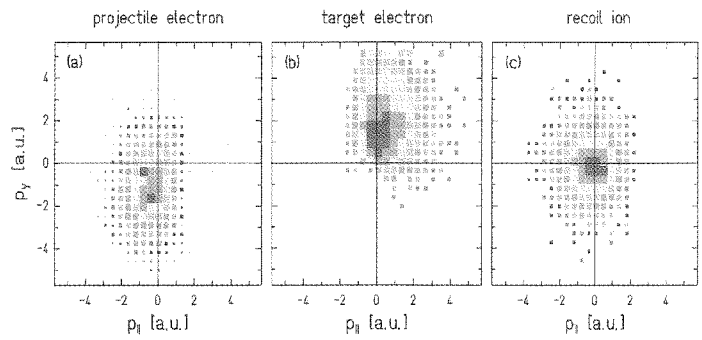

Figure 2: *The momentum distributions of the projectile electron (in the projectile frame), the target electron and the He^{1+} recoil-ion projected onto the collision plane.*

The experimental data are in very good agreement with classical trajectory Monte-Carlo (CTMC) calculations. According to these theoretical results more asymmetric collision partners with respect to the binding energies of the active electrons are required to fulfill the equivalence to electron impact ionization. Such experiments are in preparation and will be performed in near future in the storage ring ESR at GSI using one-electron heavy-ions and light or even excited targets as a dense electron target. Then, as a long term perspective, fully differential cross sections for electron impact ionization of few-electron heavy-ions will become accessible.

Double Ionization of Neon by Intense Laser Pulses

It is almost 20 years ago, that unexpected large yields for the creation of doubly charged ions were observed when atoms are exposed to intense laser fields [7]. This enhancement, termed non-sequential ionization, which can amount to several orders of magnitude, is a consequence of the electron-electron correlation, but the underlying mechanism remained unclear over many years (for a review see [8]). Among many others a classical rescattering model was proposed by Corkum [9] to explain double ionization. In this model the first ionized

electron is driven by the electric field of the laser pulse and thrown back to its parent ion knocking out a second electron in an (e,2e)-like collision. Many experimental findings, and in particular recent ion momentum measurements [10,11], favor the rescattering model. But, to ultimately unravel the many-particle dynamics of double ionization in intense laser fields a complete determination of the final state is required, i.e. the determination of the momentum vectors of all atomic fragments. Up to now, such a measurement was beyond experimental capabilities.

We succeeded in performing a first kinematically complete experiment on double ionization of Ne by ultra-short (25 fs) laser pulses (λ = 800 nm) at an intensity of 10^{15} W/cm^2. The created ion and up to two electrons were detected in coincidence using a reaction microscope. In the experiment the momentum vectors of all three particles (electrons and ion) and the charge state of the ion were determined.

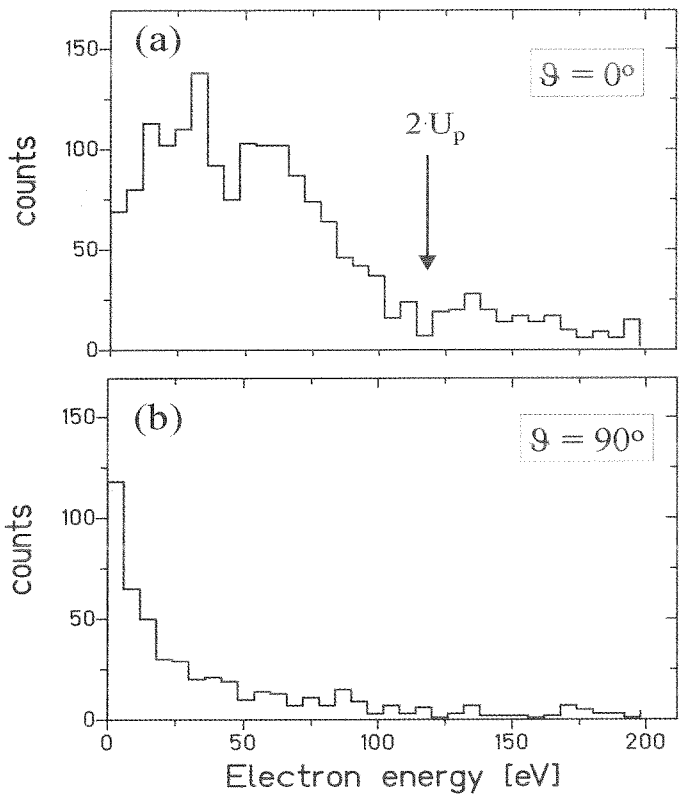

Figure 3: *The electron energy distributions for emission along ($\vartheta = 0^o$) and perpendicular ($\vartheta = 90^o$) to the light polarization axis in double ionization of Ne by 10^{15} W/cm^2 laser pulses.*

In contrast to single ionization, which is dominated by the emission of low energy electrons (E_e < 20 eV), for double ionization high energetic electrons with energies of more than 120 eV have been observed (fig. 3). In both cases electrons are preferentially emitted along the light polarization axis (i.e. along the electric field direction of the laser field). In fact, after being released from the atom the electrons perform a quiver motion in the external laser field. They are driven by the ponderomotive force mediated by the electric field in the light pulse. The final kinetic drift energy of the ionized electron after the end of the laser pulse depends on the phase of the oscillating electric field at which the electron was set free. This energy, which can be as large as 2·U_P (U_P is the mean quiver energy), maximizes if the electron is born at a time when the electric field goes through zero. In the rescattering model for double ionization the (e,2e)-like collision with the returning electron occurs very close to such a zero crossing. Hence, electron energies up to 2·U_P are expected in agreement with our experimental finding. Even though the electron motion is dominated by the ponderomotive force the signature of the (e,2e) collision dynamics is still preserved in the final state. In particular the analysis of correlated two electron spectra, which are not discussed here, yield more detailed information about the fragmentation in strong laser fields.

For the future, experimental studies of electron correlation in strong laser fields will be feasible using a large variety of targets, like e.g. atoms, clusters and molecules. On this road in particular a kinematically complete experiment on helium, the most simple two electron system, remains as an experimental challenge.

This work was supported by the Gesellschaft für Schwerionenforschung, the Max-Born-Institute, the Leibniz-program and the SFB 276 project B8 of the Deutsche Forschungsgemeinschaft DFG, and BMBF.

References

[1] R. Dörner et al., Phys. Rep. 330, 95 (2000)
[2] R. Moshammer et al., Phys. Rev. Lett. 83, 4721 (1999)
[3] M. Inokuti, Rev. Mod. Phys. 43, 297 (1971)
[4] R. Moshammer et al., Phys. Rev. Lett. 79, 3621 (1997)
[5] E.C. Montenegro et al., Adv. At. Mol. Opt. Phys. 34, 249 (1994)
[6] R. Dörner et al., Phys. Rev. Lett. 72, 3166 (1994)
[7] A. L'Huiller et al., Phys. Rev A 27, 2503 (1983)
[8] M. Protopapas et al., Rep. Prog. Phys. 60, 389 (1997)
[9] P. Corkum, Phys. Rev. Lett. 71, 1994 (1993)
[10] Th. Weber et al., Phys. Rev. Lett. 84, 443 (2000)
[11] R. Moshammer et al., Phys. Rev. Lett. 84, 447 (2000)

Three body fragmentation of CO_2 in collisions with 5.9 MeV/u Xe^{18+} and Xe^{43+} ions

B. Siegmann, I. Küster, U. Brinkmann, U. Werner, H.O. Lutz, University of Bielefeld
R. Mann, GSI Darmstadt

The multiple ionization and fragmentation of CO_2 by fast Xe^{18+} and Xe^{43+} ions was studied utilizing a position- and time-sensitive multi-particle detector which allows the coincident measurement of the momenta of correlated fragment ions. The experiment has been performed using the highly charged ion beam of the UNILAC at the GSI Darmstadt. The slow fragment ions and electrons generated in the collision process are separated by a weak electric field. Electrons were detected by a channeltron at one side of the interaction region; positive ions were accelerated towards the time- and position-sensitive multi-particle detector at the other side [1,2]. For each positive fragment ion the position and the time-of-flight relative to the electron signal were recorded. Of special interest are the Coulomb explosion processes where all fragments are positively charged. For these reaction channels the coincident measurement of the momenta of correlated fragment ions yields a kinematically complete image of the molecular break-up process, and the kinetic energy release as well as angular correlations can be derived for each individual event. In collisions of fast highly charged Xe-ions with CO_2 coincidences with a total charge of at least 6 are clearly separated. Among the various observed reaction channels the reactions $C^{q+} + O^{p+} + O^{r+}$ fulfill the conditions for a kinematically complete description of the fragmentation process. For these reactions the fragmentation dynamics may be analyzed in terms of three independent parameters. A practical choice of the characteristic variables consists of the kinetic energy release and the angles χ and θ_v in velocity space [3].

Fig. 1 shows the kinetic energy release spectrum and the measured distribution of the angles χ and θ_v observed in C^++O^++O^+ fragmentation in collisions with 5.9MeV/u Xe^{18+} and Xe^{43+}. All three characteristic parameters are independent of the projectile charge measured here. The maximum of the measured kinetic energy distribution is in good agreement with the prediction of the point charge Coulomb explosion model.

The angle χ, defined by the relative velocity of the O^+-ions $\vec{v}_{OO}$ and $\vec{v}_C$, is an indicator whether the molecular bonds break simultaneously or in a stepwise fashion [4]. The χ distribution shows a peak around 90 degrees which is consistent with a simultaneous break up of the molecular bonds. A break-up of the molecular bonds in a time short on a time scale defined by rotational and vibrational periods of the system leads to a strong angular correlation between the corresponding velocities which shows up as a narrow peak in the χ-distribution. In case of a two-step process the correlation would be lost resulting in a uniform χ-distribution.

The angle θ_v, defined by the two relative $\vec{v}_{CO}$ velocities, is closely connected with the O-C-O bond angle. For Carbon-dioxide as a linear molecule the maximum of the O-C-O bond angle would be expected around 180 degrees. The θ_v-distribution observed in collisions with fast highly charged ions is clearly shifted to smaller angles with a broad maximum around 120 degrees. This can be qualitatively understood taking into account the vibration modes of CO_2. Using a harmonic oscillator potential to describe the bending-mode groundstate ($\nu_2 = 0$) leads to a most probable "bond angle" of $\beta \approx 172.5$ degree. In the Coulomb explosion model this angle corresponds to an angle $\theta_v \approx 142°$ in velocity space which is in good qualitative agreement with the experimental results.

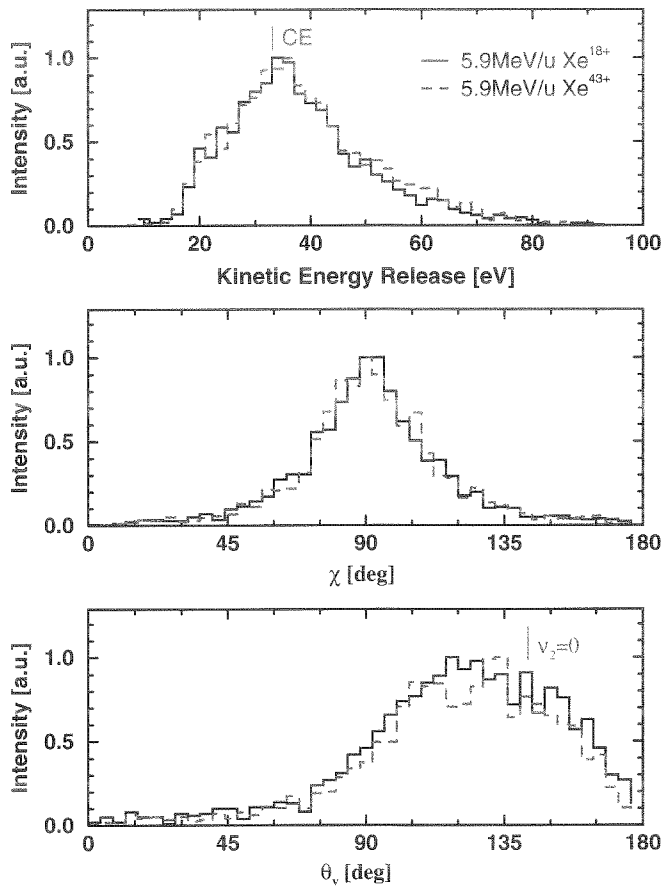

Figure 1: Kinetic energy release and angles χ and θ_v derived from coincident C^++O^++O^+ fragments in collisions with 5.9 MeV/u Xe^{q+}. The energy release predicted by the Coulomb explosion model (CE) and the most probable angle θ_v expected for the bending mode $v_2 = 0$ are marked in the figure.

References

[1] J. Becker et al., Nucl. Instrum. Methods **A337**, 409 (1994)
[2] U. Werner et al., Nucl. Instrum. Methods **B124**, 298 (1997)
[3] B. Siegmann et al., Aust. J. Phys. **52**, 545 (1999)
[4] U. Werner et al., Phys. Rev. Lett. **74**, 1962 (1995)

Experiments with Heavy Ions in Traps

Caen[1], CERN[2], GSI[3], Jyväskylä[4], Leuven[5], Mainz[6], Michigan[7], Montreal[8], München[9], Orsay[10]
and the SHIPTRAP Collaboration

HITRAP: A Facility for Experiments with Trapped Highly Charged Ions

W. Quint[3], J. Dilling[3], S. Djekic[6], H. Häffner[3], H.-J. Kluge[3], G. Marx[3], D. Rodríguez[3], J. Schönfelder[3], G. Sikler[3], T. Valenzuela[6], J. Verdú[3], C. Weber[3] and G. Werth[6]

The GSI midterm project HITRAP is a planned ion trap facility for capturing and cooling of highly charged ions (HCI) produced at GSI in the heavy-ion complex of the UNILAC-SIS accelerators and the ESR storage ring. In this facility heavy highly-charged ions up to uranium will be available as bare nuclei, hydrogen-like ions or few-electron systems at low temperatures. The trap for receiving and studying these ions is designed for operation at extremely high vacuum by cooling to cryogenic temperatures. The stored highly charged ions can be investigated in the trap itself or can be extracted from the trap at energies up to about 30 keV/q.

The basic components constituting the HITRAP facility are outlined in Fig. 1. Highly charged ions are accelerated in the heavy-ion synchrotron SIS, stripped in a foil to the desired charge state and injected into the Experimental Storage Ring (ESR). For bare or hydrogen-like ions, energies of a few hundred MeV/u are required. In the ESR the ions will be decelerated to an energy of 3 MeV/u. It is planned to demonstrate this low-energy operation mode of the ESR during 2001. They will then be extracted in a fast-extraction mode as short ion bunches.

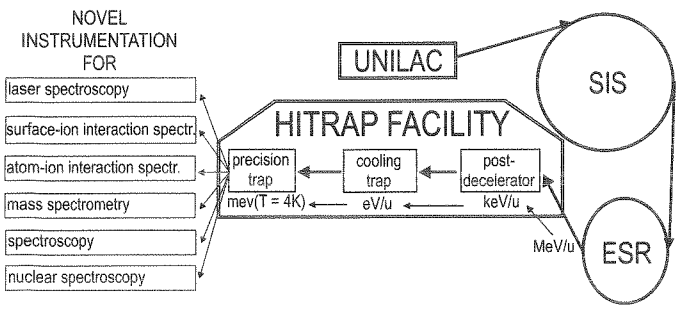

Figure 1: Schematic of the GSI accelerator complex and the planned HITRAP facility. Highly charged ions are extracted from the ESR storage ring at 3 MeV/u, decelerated in a post-decelerator to some keV/u, and then transferred into a Penning trap system.

The extracted ion bunches will be post-decelerated to a final energy of the order of 30 keV/q in a radiofrequency quadrupole structure (RFQ) or a linear interdigital H-mode (IH) drift tube structure. Recently, a RFQ decelerator has been successfully commissioned at the Antiproton Decelerator (AD) at CERN to allow antiprotons to be decelerated from an energy of 5.3 MeV down to below 100 keV. After post-deceleration the ions will be captured into a first Penning trap (Fig. 1) and cooled to a temperature of T = 4 K with a combination of electron or positron cooling and resistive cooling. The cooled highly charged ions can be extracted and transferred to physics experiments. The HITRAP facility will provide about 10^6 charges per second, i.e. about 10^4 ions/s in the case of U^{92+}.

The HITRAP physics programme includes collision studies with highly charged ions at well-defined low energies (eV/u), laser spectroscopy of hyperfine structure transitions in HCI, X-ray spectroscopy on HCI, and high-accuracy measurements to determine the magnetic moment anomaly (or *g-factor*) of the electron bound in hydrogen-like heavy ions and the atomic binding energies of few-electron systems.

For the determination of the g-factor of the bound electron in highly charged ions as a stringent test of Quantum Electrodynamics (QED) [1] a precision Penning trap has been developed in a joint effort of the University of Mainz and GSI. The g-factor of the bound electron is determined from the Larmor precession frequency ω_L of its magnetic moment in the magnetic field B, $\omega_L = g(e/2m_e)B$, and the cyclotron frequency of the hydrogen-like ion, $\omega_c = (Q/M)B$.

$$g = 2 \cdot \frac{\omega_L}{\omega_c} \cdot \frac{Q/M}{e/m_e}. \qquad (1)$$

Our measurement of the g-factor of the electron in hydrogen-like carbon ($^{12}C^{5+}$) yielded a value of $g_e^{exp}(C^{5+}) = 2.001\,041\,596(5)$, in excellent agreement with the theoretical value of $g_e^{th}(C^{5+}) = 2.001\,041\,591(7)$ [2]. Further improvement of the theoretical [3] as well as the experimental accuracy will make it possible to determine the atomic mass of the electron with an unprecedented precision of a few parts in 10^{-10}. In 2000 we performed a g-factor measurement on hydrogen-like oxygen ($^{16}O^{7+}$). The preliminary experimental value of $g_e^{exp}(O^{7+}) = 2.000047017(8)$ is in excellent agreement with the theoretical prediction of $g_e^{th}(O^{7+}) = 2.000\,047\,022(5)$. This is our second high-accuracy test of bound-state QED. At the HITRAP facility, the g-factor measurements will be performed up to the heaviest hydrogen-like ions, where the product of proton number and fine-structure constant ($Z\alpha$) approaches unity. This will provide a crucial test of QED calculations in extreme electromagnetic fields.

High Accuracy Mass Determination of unstable Nuclei with the Penning Trap Mass Spectrometer ISOLTRAP

F. Ames[2], G. Audi[10], D. Beck[3], K. Blaum[3], G. Bollen[7], J. Dilling[3], O. Engels[9], F. Herfurth[3,9], A. Kellerbauer[2], H.-J. Kluge[3], D. Lunney[10], R.B. Moore[8], M. Oinonen[2], C. Scheidenberger[3], S. Schwarz[5], G. Sikler[3], E. Sauvan[2], J. Szerypo[4] and C. Weber[3]

The Penning trap mass spectrometer ISOLTRAP is installed at ISOLDE/CERN. It provides mass measurements of short-lived nuclides with very high accuracy. Accurate experimental mass values serve for testing nuclear models, help to increase their predictive power for nuclides far from stability and can reveal nuclear structure. Additionally, some mass values represent important input parameters for Standard Model tests and astrophysical calculations.

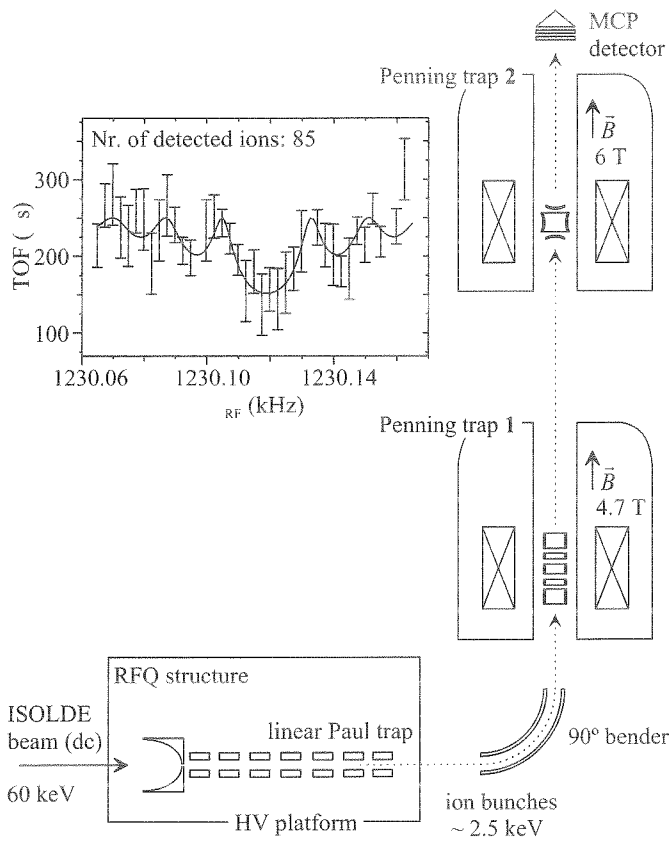

Figure 2: Experimental setup of the ISOLTRAP spectrometer. The inset shows the cyclotron resonance curve for ^{74}Rb. Plotted is the time of flight (TOF) of the ions from the trap to the ion detector as a function of the applied radiofrequency with the theoretical line shape fitted. This spectrum contains roughly one fourth of all ^{74}Rb data obtained during a recent run.

The ISOLTRAP Penning trap mass spectrometer (Fig. 2) consists of three main parts: a) a linear gas-filled radiofrequency quadrupole (RFQ) trap for retardation, accumulation, cooling and bunched ejection at low energy [4], b) a gas-filled cylindrical Penning trap for further cooling and isobaric separation [5], and c) an ultra-high vacuum hyperbolic Penning trap for isomeric separation and the mass measurement [6]. The mass measurement is performed via the determination of the cyclotron frequency $\omega_c = q/m \cdot B$ of the ion with mass m and charge q revolving in the magnetic field of strength B. The accuracy of the measured mass values is typically $\delta m/m = 1 \cdot 10^{-7}$.

Six radioactive beam times were carried out in 2000. In the first beam time, an uranium carbide target was used in conjunction with the resonant ionisation laser ion source (RILIS) to measure the mass of neutron-rich tin isotopes. The isotopes ^{128,129,130,132}Sn were investigated. Particularly, the mass of the doubly magic ^{132}Sn is of interest for astrophysical calculations along the r-process path.

The second beam time was dedicated to neutron-deficient Sr isotopes. The mass of ^{76}Sr and ^{77}Sr could be measured by determining the mass of SrF_2 molecules. ^{76}Sr is a possible waiting point on the astrophysical rp-process path.

One major project in 2000 was the measurement of the Q-value of the superallowed β-decay of ^{74}Rb. Two beam times were performed to measure the mass of ^{74}Rb (Fig. 2) and its daugther nucleus ^{74}Kr. ^{74}Rb is the shortest-lived nuclide ever investigated in a Penning trap ($T_{1/2} = 65$ ms). The accuracy of its mass value is governed by statistics and resolving power, which are limited by production rate and half-life. The relative accuracy reached for the mass of ^{74}Rb is about $3.4 \cdot 10^{-7}$ (i.e. ≈ 25 keV). The measurement of ^{74}Kr was performed with an unprecedented relative accuracy of only $3 \cdot 10^{-8}$. Additionally, the masses of the krypton isotopes with $A = 73$ and 75 were measured.

One beam time was performed using a molten lead target to complete the picture of binding energies for the neutron-deficient mercury isotopes. The isotopes ^{179,180,181}Hg were measured for the first time closing the gap in the binding energy sytematics.

The last beam time in 2000 was used to measure the mass of ^{34}Ar produced in a CaO target. This value is needed with very high accuracy in the context of the FT-value systematics for superallowed Fermi β decays. ISOLTRAP succeeded in measuring this mass with an uncertainty below 1 keV.

Future mass measurements will be performed in astrophysically interesting regions like the neutron-rich Cd and Sn isotopes, the neutron-deficient Y isotopes and around the rp-process waiting points ^{68}Se and ^{72}Kr. Additionally, the measurements in the context of fundamental tests will be continued measuring ^{32}Ar. Future technical developments focus on the improvement of the overall efficiency by improving the detector setup as well as different parts of the ion transfer.

Status of the SHIPTRAP project: A capture and storage facility for heavy radionuclides from SHIP

G. Marx[3], D. Ackermann[3], J. Dilling[3], F.P. Heßberger[3], S. Hoffmann[3], H.-J. Kluge[3], R. Mann[3], G. Münzenberg[3], Z. Qamhieh[3], W. Quint[3], D. Rodríguez[3], M. Schädel[3], J. Schönfelder[3], G. Sikler[3], C. Toader[3] and C. Weber[3]

The ion trap facility SHIPTRAP is being set up to deliver very clean and cool beams of singly-charged recoil ions produced at SHIP at GSI [7]. SHIPTRAP consists of a gas cell for stopping and thermalizing high-energy recoil ions from SHIP, an rf ion guide for extraction of the ions from the gas cell, a linear rf trap for accumulation and bunching of the ions, and a Penning trap for isobaric purification. The recent development for the SHIPTRAP stopping chamber and the extraction system is described in a separate section later in this report.

The Buncher

The ion bunching system is a 1 m long Radio Frequency Quadrupole (RFQ) immersed in a low-pressure buffer gas. The four rods have a diameter of 9 mm at a distance between two opposite rods of 7.86 mm. The rods are divided into 34 segments. With proper choice of applied voltages, one creates a potential slope with a harmonic potential well at the end of the quadrupole structure. When the ions lose energy in collisions with the buffer gas, they accumulate in this trap and can be extracted as a short bunch of cool ions. The radial motion in the RFQ is described by the Mathieu equations, where the solutions are characterized by the two dimensionless parameters a and q, but only $q = \frac{2eV_{rf}}{m\omega_{rf}^2 r_0^2}$ depends on the rf-amplitude. Presently we use the RFQ in a rf-only mode with no additional bias ($a = 0$). The ion motion is stable only in a certain range of q, for other values the amplitudes of the motion grow infinitely. For a certain rf amplitude V all ions of different masses whose q is below the stability limit of $q = 0.908$ pass through the buncher.

In first tests (no axial trapping) in the rf-only mode with a calibrated ion source a transmission of about 95% was achieved. Figure 3 shows a transmission plot for Ar^+ ions. The driving field frequency was set to $\nu_{rf} = 600$ kHz.

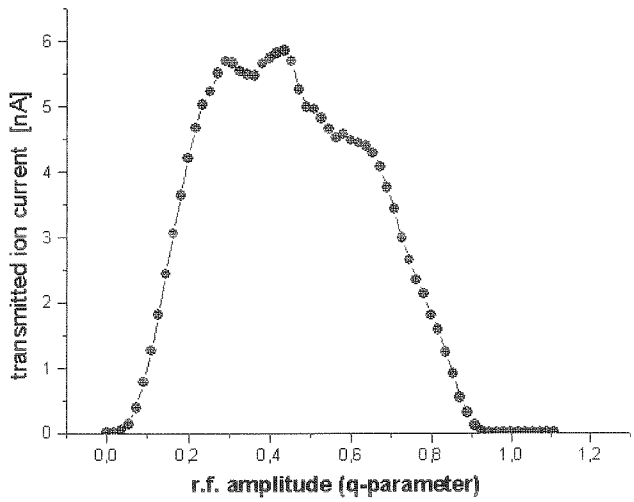

Figure 3: Transmission plot in rf-only mode for Ar^+ ions.

The basic task of the buncher at SHIPTRAP is to cool the ions from the stopping chamber and to collect them. Since the buncher will therefore be operated under buffer gas it is necessary to investigate the influence of gas on the ion motion. The average effect of ion collisions with buffer gas molecules can be approximated by a frictional drag force. This leads to the usual form of the Mathieu equation but with an added velocity dependent term. Figure 4 shows three measured transmission curves at different pressures. One can see a tendency that the right edge of the stability diagram is shifted to higher q-values. Due to the damping of the ion motion one can apply higher quadrupole field strength until the ion motion becomes unstable. The information how much the stability region is increased under buffer gas operation is important since one tries to use the limited mass resolution of the RFQ

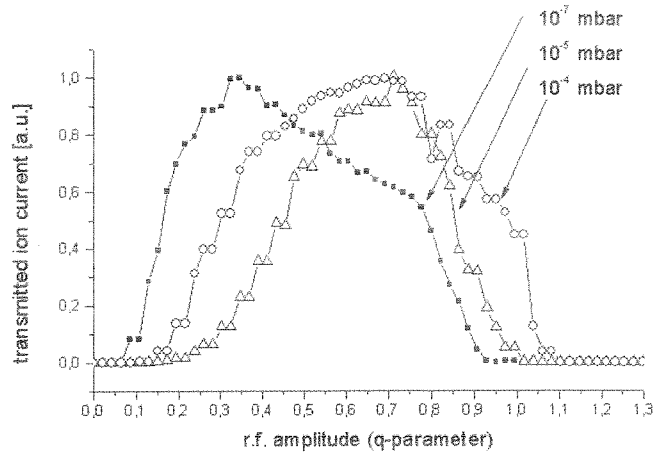

Figure 4: Influence of buffer gas on the transmission curve

in rf-only mode to suppress contamination of lighter ion species.

The Penning Trap System

Two Penning traps will be installed at SHIPTRAP, which are both housed in one superconducting magnet. The first Penning trap, a 207.5 mm long cylindrical trap with 32 mm open diameter, captures the ions from the buncher, cools and isobarically purifies them. The design is based on the one used for this purpose at the ISOLTRAP facility at ISOLDE [6]. In such a system the contaminating isotopes are very effectively suppressed due to the high mass resolving power of the cooling process. The second Penning trap, also cylindrical but shorter and with higher homogeneity in the electric and magnetic fields, will serve for precision mass measurements. The traps have been constructed, built and assembled in 2000. They are now ready for the first tests.

Summary

After an intense simulation and construction phase all components are set up and under test. SHIPTRAP will start operation in autumn 2001. The experimental programme which is envisaged by the SHIPTRAP user community promises to give new insights into the nuclear, atomic and chemical properties of the elements heavier than einsteinium.

The gas cell and extraction RFQ for SHIPTRAP

L. Beck[9], O. Engels[9], D. Habs[9], J. Neumayr[9], V. Varentsov[9], F. Voit[9] and A. Wilfart[9]

Set-up

The prototype of the gas cell for SHIPTRAP follows the concept of extracting the ions via the gas flow and guiding electrostatic fields. These two mechanisms can be simulated separately in first order due to the special feature of a high transmission grid in front of the nozzle. This grid prevents a loss of ions in the defocusing field inside the nozzle and improves the focusing inside the cell due to a spherical shape. The extraction RFQ separates the ions from the neutral gas. The prototype gas cell has a length and a diameter of 100 mm. The guiding field inside the

cell is created by three electrodes and a spherical grid covering the supersonic nozzle with an inner diameter of 0.6 mm. The subsonic part of the nozzle has a conical shape to achieve gas velocities high enough to drag the ions through the nozzle [8].

The design of the extraction RFQ and the electronics profits from the work done at ISOLTRAP and GSI in the past three years [4]. Compared to the structures used there the extraction RFQ of SHIPTRAP is a short structure with 12 segments and a total length of 120 mm. The diameter of the rods is 11 mm with an aperture (diameter) of 10 mm. The ions are mass selective detected in a QMS followed by a MSP (Micro Sphere Plate) [9]. The test set-up is shown schematically in Fig. 5.

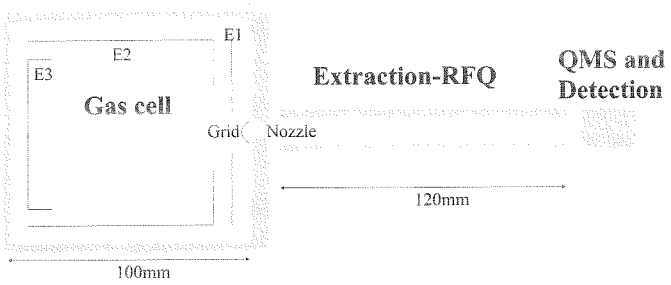

Figure 5: Test set-up for the SHIPTRAP gas cell. It consists of three electrodes (E1, E2, E3) and a nozzle covered by a high transmission grid, the extraction RFQ as a differential pumping section and the QMS and Detection section for a mass selective ion detection.

Simulations

The simulations covered the following topics: stopping of the ions in the gas (SRIM); drag of the ions via the electrical field in the cell towards a supersonic nozzle (SIMION); drag of the ions through the nozzle via the gas flow (VARJET, solving the full system of time dependent Navier-Stokes equations [10]).

First stopping simulations indicate that, whatever gas is used, a majority (50 to 90%) of most radionuclides of interest could be stopped within a spheroid of 40 mm diameter and 70 mm length (for ^{232}Th at 100 keV/u in He at 50 mbar). To these values one has to add the horizontal and vertical SHIP-beam dimensions of 50 mm and 30 mm. These simulations imply the minimum dimensions for the innermost electrode of the final gas cell for SHIPTRAP.

Measurements

First measurements with laser ionized Ni and Er in the gas cell were performed to optimize the voltages in the cell and the RFQ. Based on this the extraction times in dependence of the gas pressure and the voltage inside the cell were studied. A voltage difference of 10 V was applied between the first and last segment of the extraction RFQ together with an rf-voltage of 200V_{pp} at 1.2 MHz to guide the ions to the mass selective ion detection system. Figure 6 shows the measured time of flight (TOF) of Ni and Er ions at different pressures and voltages in the cell.

Furthermore, the measurements showed a clear dependence of the ion focusing towards the nozzle and the grid in front of the nozzle. The grid allows to achieve faster extraction times due to higher voltages applicable in the

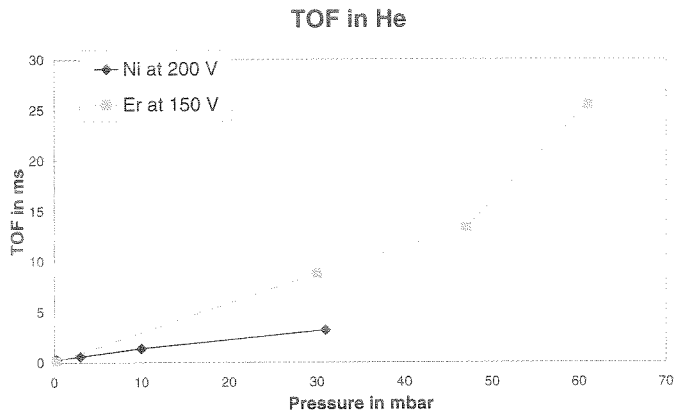

Figure 6: Measurement of the TOF of Ni and Er ions in dependence of gas pressure and voltage inside the cell (electrode E2).

cell. These higher voltages lead to a stronger defocusing of the ions. However, this drawback can be compensated by the better focusing properties of the grid.

An improved gas cell, based on these experiences is under construction. The new cell will allow higher voltages in the cell and is designed to stop and extract 90% of the ion cloud.

Optical Spectroscopy and Ion Chemistry of Trans-Fermium Elements at SHIPTRAP

H. Backe[6], A. Dretzke[6], G. Kube[6], W. Lauth[6], W. Ludolphs[6], A. Morbach[6] and M. Sewtz[6]

An ultra-sensitive laser spectroscopic method is being developed for the investigation of the completely unknown atomic structure of the elements No and Lr. First experiments will be performed on No which will be produced via the reaction ^{208}Pb(^{48}Ca,2n)^{254}No. The reaction products, separated by SHIP, will be stopped in a buffer gas cell in which Resonance Ionization Spectroscopy (RIS) is performed with detection of the ionization process by the α-decay of ^{254}No. The technique is similar to that developed for RIS on fission isomers [11]. To determine the stopping distribution of the 40 MeV No recoils, a 40 MeV $^{238}U^{8+}$ beam from the tandem van-de-Graaff accelerator at the MP-Tandem accelerator facility in Heidelberg was implanted in a buffer gas cell. The range distribution and the lateral straggling of the ions in the gas was measured for different gas pressures. The normalized count rate of the movable semiconductor detector is shown in Fig. 7 as a function of the distance from the entrance foil.

The code SRIM2000 predicts a 30% shorter range which might originate from assuming a too high effective charge state of the ions during the slowing-down process. Similar derivations between measurements and calculations have been found for the straggling. These results have been taken into account for the design of the buffer gas cell. The cell has been constructed, and first vacuum and high voltage tests have been carried out successfully [12].

Furthermore, we plan to study ion chemical reactions of heavy elements such as ^{254}No and ^{256}Lr in a buffer gas cell with well-defined admixtures, e.g. O_2, H_2O, CH_4, CO_2.

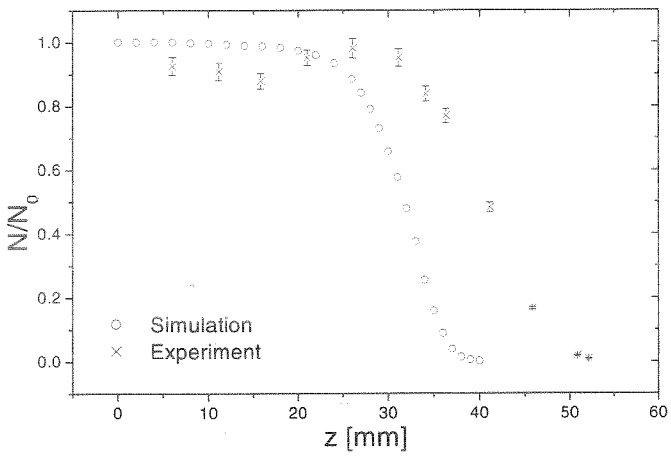

Figure 7: Range distribution of the U ions in Ar at a gas pressure of 250 mbar (×). The calculation (○) is based on the code SRIM2000 [13].

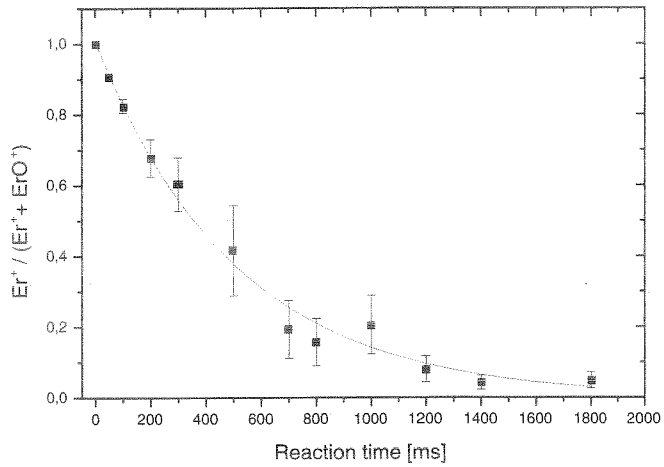

Figure 9: Intensity ratio of Er^+ to (Er^++ ErO^+) as function of the reaction time.

The reaction products will be identified mass selectively by the Ion Guide Quadrupole Mass Separation (IGQMS) technique [14, 15]. Presently, we are working on establishing the method on chemically homologue elements.

In a first step, ion-molecule reactions will be studied with a Fourier Transform Mass Spectrometer (FT/MS) under well-defined experimental conditions [16]. In first experiments erbium reactions with O_2 have been investigated. The ions are created by laser ablation from a solid target using a pulsed CO_2 laser, cooled by an argon buffer gas push and stored in a FT-ICR cell at constant O_2 gas pressure. An ejection sweep cleans the cell from all ions with the exception of erbium ions which react with oxygen. The results are shown in Fig. 8. The ratio of Er^+ to ErO^+ intensity, as obtained after various reaction times, is shown in Fig. 9. From the exponential decay of the Er^+ signal a reaction constant can be deduced.

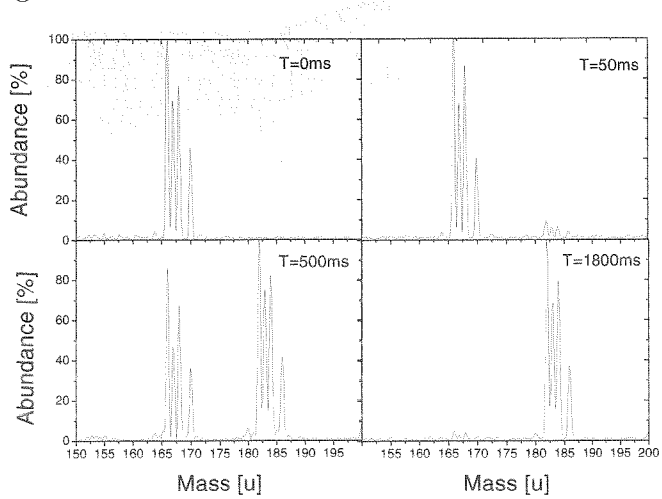

Figure 8: Er^+ and ErO^+ mass spectra at reaction time T as indicated. The groups around mass number 167 and 183 belong to Er^+ and ErO^+, respectively.

In a second step the results from these FT-ICR experiments which are obtained under clean experimental conditions will be compared with results obtained in the inert buffer gas cell to which the reaction gas is admixed. Energetic erbium ions from a Tandem van-de-Graaff accelerator will be implanted into the buffer gas cell. Ion-chemical reactions will be investigated in 'hot' and 'cold' surroundings. 'Hot' surrounding is expected if erbium thermalizes directly as an ion. If it thermalizes as an atom, which subsequently is resonantly ionized by the laser, the surrounding is 'cold'.

Acknowledgement

We acknowledge financial support by the European Union (Networks EXOTRAPS and EUROTRAPS) and by BMBF under contract number 06 LM 973.

References

[1] N. Hermanspahn et al., Phys. Rev. Lett. **84** (2000) 427.
[2] H. Häffner et al., Phys. Rev. Lett. **85** (2000), 5308.
[3] Thomas Beier, this annual report
[4] F. Herfurth et al., 2001, Nucl. Instr. Meth. **A** (in print), available as GSI preprint 2000-14
[5] H. Raimbault-Hartmann et al., Nucl. Instr. Meth. **B126** (1997), 378.
[6] G. Bollen et al., Nucl. Instr. Meth. **A368** (1996), 675.
[7] G. Münzenberg et al., Nucl.Instr.Meth.**161** (1979), 65.
[8] O. Engels et al., Annual Report, GSI (1999)
[9] R. Naaman et al., Rev. Sci. Instrum. **67** (1996), 3332.
[10] V.L. Varentsov et al., Nucl. Instr. Meth. **A 413** (1998) 447.
[11] H. Backe et al., Phys. Rev. Lett. **B 80** (1998), 920.
[12] W. Ludolphs, Diploma Thesis, Inst. f. Kernphysik, Universität Mainz, (2001).
[13] J.F. Ziegler et al., The Stopping and Range of Ions in Solids, Pergamon Press, New York, (1985), 488.
[14] H. Backe et al., Nucl. Instr. Meth. **B 126** (1997), 406.
[15] A. Iivonen et al., Phys. Scripta **42**, (1990), 133.
[16] A.G. Marshall, L. Schweikhard, Int. J. Mass Spectrom. Ion Proc. **118/119** (1992), 37.

Mean-Field Instability of Trapped Ultracold Fermi Gases

R. Roth and H. Feldmeier (GSI)

The success in cooling a cloud of fermionic ^{40}K atoms, kept in a magnetic trap, to temperatures significantly below the Fermi energy [1,2] opened a unique possibility to study the properties of dilute degenerate Fermi gases experimentally. One long-term goal is the observation of a BCS phase transition in these systems. The mechanism to create Copper pairs relies on an attractive interaction between the particles. At the same time these attractive interactions can cause a mean-field collapse of the metastable dilute Fermi gas towards high densities. Obviously a necessary prerequisite to reach the BCS transition is the stability of the normal Fermi gas.

We investigate the mean-field instability of the trapped Fermi gas in the framework of density functional theory. The energy density of the interacting multi-component Fermi gas is constructed in a mean-field picture using the Thomas-Fermi approximation. The interaction between the atoms is described by the s- and p-wave terms of the Effective Contact Interaction (ECI) [3,4], which depends on the s- and p-wave scattering length, a_0 and a_1, resp., as well as on the s-wave effective volume b_0. The ECI is constructed such that the exact two-body energy spectrum is reproduced by the expectation values of the ECI in mean-field type states.

The energy density of a single-component Fermi gas trapped in an external potential $U(\vec{x})$ reads

$$\mathcal{E}_1[\kappa(\vec{x})] = \frac{U(\vec{x})}{6\pi^2}\,\kappa^3(\vec{x}) + \frac{1}{20\pi^2 m}\,\kappa^5(\vec{x}) + \frac{a_1^3}{30\pi^3 m}\,\kappa^8(\vec{x}),$$

where $\kappa(\vec{x}) = \sqrt[3]{6\pi^2\rho(\vec{x})}$ denotes the local Fermi momentum and a_1 the p-wave scattering length. The first term originates from the external potential, the second one from the kinetic energy, and the third term from the p-wave interaction. The s-wave part of the interaction does not contribute in a system of identical fermions due to the Pauli principle.

For attractive p-wave interactions, i.e., negative p-wave scattering length $a_1 < 0$, the highest power of $\kappa(\vec{x})$ in the energy density has a negative coefficient. This implies that there is a maximum density up to which the system is stable. Beyond this density the energy decreases for growing density and the system collapses towards a high density configuration. For fixed particle number N we obtain the following local condition for the stability of the single-component Fermi gas [3,4]

$$-a_1\kappa(\vec{x}) \le \sqrt[3]{3\pi}/2.$$

If this stability condition is violated anywhere in the trap then the system will collapse.

The energy density of a two-component Fermi gas, where we assume equal local Fermi momenta $\kappa(\vec{x}) = \kappa_1(\vec{x}) = \kappa_2(\vec{x})$ for both components, reads

$$\mathcal{E}_2[\kappa(\vec{x})] = \frac{U(\vec{x})}{3\pi^2}\,\kappa^3(\vec{x}) + \frac{1}{10\pi^2 m}\,\kappa^5(\vec{x}) + \frac{a_0}{9\pi^3 m}\,\kappa^6(\vec{x}) + \frac{\tilde{a}_1^3}{10\pi^3 m}\,\kappa^8(\vec{x})$$

with $\tilde{a}_1^3 = a_1^3 + b_0/3$. In this case both, s- and p-wave interactions contribute and influence the stability of the system. We obtain the following stability condition for the two-component Fermi gas [3,4]

$$-a_0\kappa(\vec{x}) - 2\,[\tilde{a}_1\kappa(\vec{x})]^3 \le \pi/2.$$

For practical purposes this stability condition can be rephrased in terms of an upper limit in the number of particles $N = N_1 = N_2$ assuming a parabolic trapping potential with mean oscillator length $\ell = 1/\sqrt{m\omega}$ [3,4]. Figure 1 shows the logarithm of the maximum particle number of each component as a function of the s- and p-wave scattering length in units of the mean oscillator length.

Attractive s-wave as well as attractive p-wave interactions can cause a mean-field collapse. If both components are attractive then their combined action decreases the maximum allowed density or particle number for the stable configuration. If one component is attractive and the other repulsive then the repulsive one stabilizes the system, i.e., increases $N_{\max}$. New phenomena appear in the case of attractive s-wave and repulsive p-wave interactions. If the p-wave scattering length exceeds about $1/3$ of the s-wave scattering length (compare Fig. 1) the p-wave repulsion prevents a collapse completely, i.e., $N_{\max} \to \infty$. For p-wave repulsions slightly too weak to cause this absolute stabilization a novel high-density phase appears in the center of the trap if $N_{\max}$ is exceeded.

We conclude that p-wave interactions have an important influence on the stability and may thus be helpful on the way to Cooper pairing in trapped ultracold Fermi gases.

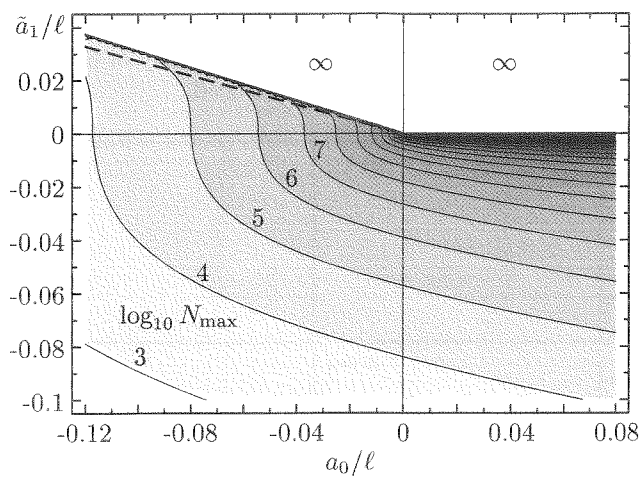

Fig. 1: Contour plot of the logarithm of the maximum particle number $N_{\max}$ in a two-component Fermi gas as function of the s- and p-wave scattering lengths, a_0/ℓ and $\tilde{a}_1/\ell$, where ℓ is the mean oscillator length of the trap.

[1] B. DeMarco, D.S. Jin; Science 285 (1999) 1703.
[2] B. DeMarco, S.B. Papp, D.S. Jin; e-print: cond-mat/0101445.
[3] R. Roth, H. Feldmeier; e-print: cond-mat/0102416.
[4] R. Roth, H. Feldmeier; J. Phys. B 33 (2000) 787.

see also: http://theory.gsi.de/~trap/

Parity Violation effects in highly-charged ions

I. Bednyakov, G. Plunien, G. Soff, Technische Universität Dresden
L.N. Labzowsky, St. Petersburg State University,
A.V. Nefiodov, St.Petersburg Nuclear Physics Institute,

Parity-nonconserving (PNC) atomic effects originate from the electroweak interaction of atomic electrons with the nucleus via Z-boson exchange. Comparing experimental results with theoretical predictions of the standard model allows to search for "new physics" beyond the standard model (e.g., a second Z-boson or new fermions) [1].

In the case of neutral atoms here is the discrepancy between theoretical and experimental results for PNC effects in the case of neutral atoms that might be explained by the uncertainties in the calculations caused by the inter-electronic interactions, correlation effects etc.

In highly-charged ions (HCI), on the other hand, the binding to the nucleus dominates by far the electron-electron interaction. The spin-independent part of an effective weak interaction Hamiltonian mediated by a Z-boson exchange is given by

$$\hat{H}_{\rm W}(\mathbf{r}) = -\frac{G_F}{2\sqrt{2}} Q_W \, \rho_N(\mathbf{r}) \gamma_5, \qquad (1)$$

where G_F is the Fermi constant, $\rho_N(r)$ is the nuclear density and γ_5 is the Dirac matrix. Due to this effective Hamiltonian states with opposite parity will be admixed. The transition amplitudes of a given atomic processes can be expressed as:

$$A = A_0 + i\eta A_1, \qquad (2)$$

where A_0 denotes the amplitude of the basic process and A_1 is the amplitude being related to parity violation.

Electroweak-radiative corrections were considered both for neutral atoms (e.g. see Ref. [2] and also for hydrogen-like ions [3]. The consideration of these radiative corrections becomes necessary because they can contribute up to 10% of the total magnitude of PNC effects.

For experiments, a promising situation occurs in He-like ions due to the near-degeneracy of two levels with opposite parities, 2^1S_0 and 2^3P_0 near $Z = 64$ (Gd^{62+}) as well as close to $Z = 92$ (U^{90+}). The situation has been analized in Gd^{62+} and Eu^{61+}. In particular we propose a quenching-type experiment with an interference of hyperfine- and weak-quenched transitions [4].

A typical situation for parity violation in atoms concerns the $M1$ transition with an admixture of the $E1$ transition. The one-photon hyperfine-quenched transition $2^1S_0 \to 1^1S_0$, via emission of a magnetic photon (M1), is due to the hyperfine mixing of the 2^1S_0 and 2^3S_1 levels. The weak interaction of electrons opens another one-photon decay channel $2^1S_0 \to 1^1S_0$, via the E1 emission through the mixing of the 2^1S_0 and 2^3P_1 levels by the operator $\hat{H}_W$. As a result, the total amplitude A in Eq. (2) appears as a mixture of the basic $M1$ amplitude $A_0 \equiv A_s$ and of the additional $E1$ amplitude $A_1 \equiv A_p$. The corresponding transitions rates are W_s and W_p, respectively. The weak mixing coefficient η is determined by

$$i\eta\triangle_0 = \langle 2^3P_0|\hat{H}_W|2^1S_0\rangle \, , \qquad (3)$$

where $\triangle_0 = E_{2^1S_0} - E_{2^3P_0}$. The theoretical predictions

Nucl.	$W_s(\mathrm{s}^{-1})$	$W_p(\mathrm{s}^{-1})$	η
$^{151}_{63}$Eu	0.68×10^8	0.11×10^{14}	0.33×10^{-6}
$^{155}_{64}$Gd	0.58×10^6	0.75×10^{11}	0.91×10^{-6}

for these quantities in europium and gadolinium are listed in the Table. Due to the admixture of states of opposite parity, in a polarized-beam experiment a small asymmetry in the number of emitted photons per direction should become visible, expressed by

$$dW(\boldsymbol{n}) = \frac{W_s}{4\pi}\left[1 + \varepsilon\,(\boldsymbol{\zeta}\cdot\boldsymbol{n})\right] d\Omega \qquad (4)$$

where $\boldsymbol{n}$ indicates the direction of the photon emission and $\boldsymbol{\zeta}$ is the unit vector in direction of the polarization of the ion. The coefficient of asymmetry is given by $\varepsilon = 3\lambda_0\eta R/(I+1)$ with $R = \sqrt{W_p/W_s}$. Here $\lambda_0 \le 1$ denotes the degree of polarization.

The total asymmetry effect turns out to be $\varepsilon \simeq 0.37\lambda_0 \times 10^{-3}$ for Gd^{62+}, which is unusually large for parity-violation effects, but the lifetime of the 2^1S_0 level is about one order of magnitude smaller than the hyperfine-quenched 2^3P_0 lifetime. This implies a strong background in experiments with Gd^{62+}.

In Eu^{61+} the weak asymmetry effect reduces to $\varepsilon \simeq 0.11\lambda_0 \times 10^{-3}$, but the 2^1S_0 level lives significantly longer than the hyperfine-quenched 2^3P_0 level.

Since photons being observed in this experiment originate from single-photon decays of the hyperfine- and weak-quenched $F = I$ state, the success of the experiment will depend crucially on the production of a significant degree of polarization for this state of the He-ion. This is a task to be achieved experimentally in order to exploit the advantages of highly-charged ion investigations for parity-violation effects.

References

[1] G. Soff, I. Bednyakov, T. Beier, F. Erler, I. Goidenko, U. Jentschura, L. N. Labzowsky, A. Nefiodov, G. Plunien, R. Schützhold, and S. Zschocke. *"Effects of QED and beyond from the atomic binding energy"* (APAC2000 Conference), "Hyperfine Interactions"

[2] B. W. Lynn and P. G. H. Sandars, J. Phys. B **27**, 1469 (1994).

[3] I. Bednyakov, L. Labzowsky, G. Plunien, G. Soff, and V. Karasiev, Phys. Rev. A **61**, 012103 (1999).

[4] L. N. Labzowsky, A. V. Nefiodov, G. Plunien, G. Soff, R. Marrus, and D. Liesen. *preprint 2000* "Parity-violation effect in heliumlike gadolinium and europium"

Divergence of Perturbation Theory and Resummation

Ulrich Jentschura and Gerhard Soff
Technische Universität Dresden, 01062 Dresden

Current determinations of fundamental constants [1] and the comparison of theory and expriment in high-precision experiments are based on perturbative expansions which can at best be regarded as divergent, asymptotic series in the coupling constant [2]. The first terms of the series decrease in absolute magnitude, before the factorial growth of the perturbative coefficients overcompensates the additional coupling factors of higher orders in perturbation theory, and the perturbation series ultimately diverges. Dyson's related argument [3] has given rise to much discussion and confusion, until recent explicit 30–loop calculations of perturbation series pertaining to ϕ^3 and Yukawa theories have firmly established the factorially divergent character of the perturbative expansion [4]. These considerations naturally lead to the question of how complete, nonperturbative results can be obtained from a finite number of perturbative coefficients, and how the nonperturbative result is related to the partial sums of the perturbation series.

We have investigated this problem [5] in connection to the Euler-Heisenberg-Schwinger effective Lagrangian which describes the quantum electrodynamic corrections to Maxwell's equations. The forward scattering amplitude of the vacuum ground state is described by a factorially divergent asymptotic series, $S_{\rm B} \propto \text{const.} \times g_{\rm B} \sum_{n=0}^{\infty} c_n\, g_{\rm B}^n$. The expansion coefficients

$$c_n = \frac{(-1)^{n+1}\, 4^n\, |\mathcal{B}_{2n+4}|}{(2n+4)(2n+3)(2n+2)}\,,$$

where $\mathcal{B}_{2n+4}$ is a Bernoulli number and $g_{\rm B}$ is the coupling, display an alternating sign pattern and grow factorially in absolute magnitude. The process by which a finite, nonperturbative result is ascribed to a divergent perturbation series is known as *resummation*. The resummation to the complete nonperturbative result for $S_{\rm B}$ is accomplished by employing the delta transformation,

$$\delta_n^{(0)}(\beta, s_0) = \frac{\displaystyle\sum_{j=0}^{n} (-1)^j \binom{n}{j} \frac{(\beta+j)_{n-1}}{(\beta+n)_{n-1}} \frac{s_j}{a_{j+1}}}{\displaystyle\sum_{j=0}^{n} (-1)^j \binom{n}{j} \frac{(\beta+j)_{n-1}}{(\beta+n)_{n-1}} \frac{1}{a_{j+1}}}\,,$$

where $s_n = \sum_{k=0}^{n} a_k$ is the partial sum of the input series and $a_j = c_j\, g^j$ is the jth term in the perturbation series; $(a)_m = \Gamma(a+m)/\Gamma(a)$ is a Pochhammer symbol. It has been observed that the delta transformation can be used under rather general assumptions for the extrapolation of the perturbation series, i.e. the prediction of unknown perturbative coefficients, and various applications to phenomenologically important quantum field theoretic perturbation series have been presented in [5,6]. In many cases, the delta transformation leads to better results than Padé approximants which have been discussed abundantly in the literature (see e.g. [7]).

A perturbation series often misses physically important physical effects when interpreted "at face value". For example, the perturbative expansion describing the energy shift of hydrogenic levels in an electric field (known as the Stark effect) has purely real coefficients, whereas the complete energy eigenvalue (more precisely, pseudoeigenvalue or resonance) also has an imaginary component. The imaginary part of the resonance, which describes the autoionization width, can be obtained from the purely real perturbation series by a transformation which can be characterized as a generalized Borel summation [8,9]. First, the factorial growth of the perturbation series is divided out by calculating the Borel transform, and the perturbation series $f(g) = \sum_n c_n g^n$ is replaced by its Borel transform $\mathcal{B}(g) = \sum_n c_n g^n/n!$. Then, the autoionization width is obtained by integrating the Borel transform in the complex plane along integration contours specified in [9,10]. The same resummation procedure can be used to obtain the quantum electrodynamic pair production amplitude for the case of an electric field background; the pair-production amplitude is related to the imaginary part of the effective action [10].

Recently, techniques have been investigated to acclerate the convergence of resummation procedures in order to obtain results even at large coupling, which are paradoxically based on the weak-coupling perturbative expansions [11]. The extrapolation from the weak-coupling limit to the regime of strongly coupled systems by analytic continuation of the perturbation series via Borel or delta transformations has wide applicability.

References

[1] P. J. Mohr and B. N. Taylor, Rev. Mod. Phys. **72**, 351 (2000).
[2] J. Zinn-Justin, *Quantum Field Theory and Critical Phenomena*, 3rd ed. (Clarendon Press, Oxford, 1996).
[3] F. J. Dyson, Phys. Rev. **85**, 631 (1952).
[4] D. Broadhurst and D. Kreimer, Phys. Lett. B **475**, 63 (2000).
[5] U. D. Jentschura, J. Becher, E. J. Weniger, and G. Soff, Phys. Rev. Lett. **85**, 2446 (2000).
[6] U. D. Jentschura, E. J. Weniger, and G. Soff, J. Phys. G **26**, 1545 (2000).
[7] M. A. Samuel, J. Ellis, and M. Karliner, Phys. Rev. Lett. **74**, 4380 (1995).
[8] V. Franceschini, V. Grecchi, and H. J. Silverstone, Phys. Rev. A **32**, 1338 (1985).
[9] U. D. Jentschura, e-print physics/0010038 (Phys. Rev. A, in press).
[10] U. D. Jentschura, Phys. Rev. D **62**, 076001 (2000).
[11] U. D. Jentschura and G. Soff, J. Phys. A **34**, 1451 (2001).

The g factor of an electron bound in hydrogenlike ions - status of the theoretical predictions

Thomas Beier, *Gesellschaft für Schwerionenforschung, Darmstadt, Germany*

For only few fundamental physical quantities experiment [1] and theory [2] agree that well as for the g factor of the free electron. It can therefore be considered as a precision test of quantum electrodynamics (QED) for free particles. To test QED also in the presence of strong electric fields, measurements on the g factor of an electron bound in a hydrogenlike system are one possible way. In $^{12}C^{5+}$, a value of $g = 2.001\,041\,596(5)$ was measured [3] which has to be compared to the theoretical prediction of $g = 2.001\,041\,591(7)$ [4]. This measurement is therefore the most stringent comparison of QED theory and experiment in any system heavier than hydrogen up to now. The major uncertainty of the experimental value results from the mass ratio $m_e/m_{^{12}C^{5+}}$, taken from [5], and an only slight improvement in the theoretical precision would allow to determine the electron mass more accurately. Here, the current limits to theory are presented and discussed.

The value given in [4] includes the g factor of the free electron including all QED corrections to that value, and in addition the corrections due to the binding to a heavy nucleus:

1. the binding correction itself which can be characterized as a transition from the spin quantum number to the total angular-momentum quantum number that is the only observable in a central field. It describes the deviation of g from the Dirac value of 2 for the free electron and is given by $g_j = (2/3)[1 + 2\sqrt{1-(Z\alpha)^2}]$ for the 1s state. This applies only to point-like nuclei. For extended nuclei, the wave function of the electron is slightly modified.
2. The finite nuclear-size correction which takes into account the extension of the nucleus is about 4×10^{-10} for carbon but amounts up to 1×10^{-3} for uranium where the uncertainty of the nuclear radius itself affects the prediction already on the 10^{-7} level.
3. The not-infinite nuclear mass causes the nucleus to move itself when orbited by the electron. A correct relativistic treatment has to consider nuclear recoil to all orders in the coupling constant $Z\alpha$ where Z is the charge of the nucleus. The exact form of this correction is not yet known and an existing expansion in $Z\alpha$ [6,7] yields reliable results only for light systems. For carbon it amounts to 87.5×10^{-9} with an estimated uncertainty of 1 % because of the expansion. This uncertainty should be considered to be 10 % of the value already for calcium. The complete relativistic recoil correction was calculated only for the Lamb shift up to now [8] and it seems to be much more complex for the g factor and the hyperfine structure splitting.
4. Another quantity connected with nuclear properties is that of nuclear polarization, i.e, the virtual excitation of nuclear degrees of freedom by exchange of at least two virtual photons with the electron. For the g factor, no investigations were carried out up to now. The works of G. Plunien and G. Soff [9] deal with the influence on the Lamb shift in the approximation of Coulomb-photon exchange, and only recently the problem of transverse-photon exchange which is crucial for magnetic interactions was considered at least for the Lamb shift case [10]. However, we expect this effect to be even weaker than for the Lamb shift because the typical matrix element for g factor measurements is $\langle r \rangle$, compared to $\langle 1/r \rangle$ for the Lamb shift, and therefore the inner parts of the electronic wave function that contribute most to the nuclear polarization are less pronounced. It should be mentioned that this is *not* the case for the hyperfine structure splitting where the typical matrix element is given by $\langle 1/r^2 \rangle$. In that case, however, the effect is screened by other nuclear uncertainties (for a recent overview see [11]).
5. The most interesting quantities related to the g factor are the bound-state QED corrections. Those of first order in (α/π) (i.e. one virtual photon line in the corresponding Feynman diagram) are depicted in Fig. 1. They were eval-

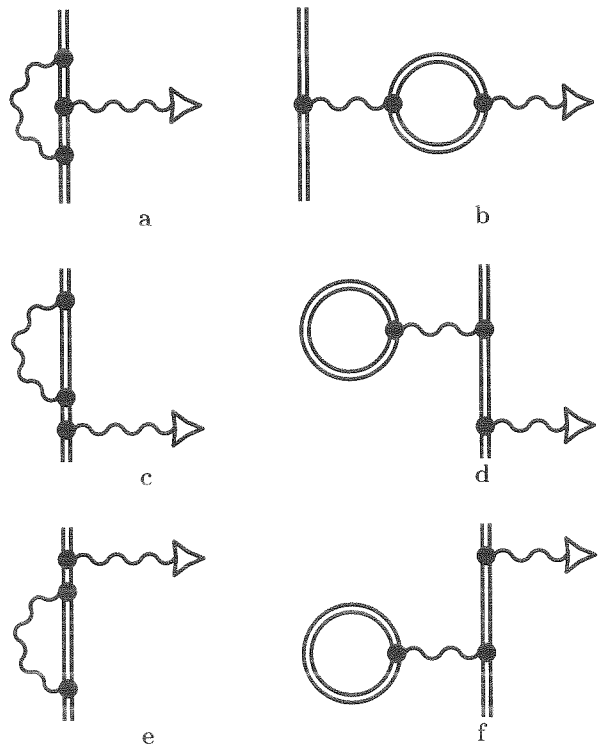

Fig. 1. Feynman diagrams representing the QED contributions of order (α/π) to the g factor of a bound electron. The wavy lines denote photons, which mediate the interaction with the external magnetic field represented by a triangle. In each diagram there is also one virtual photon. The solid double line indicates the electron and on the right side also virtual leptons in the electron-positron loops. The diagrams on the left are the self-energy-like corrections, those on the right the vacuum-polarization-like corrections. For the free electron, only the diagram similar to diagram a contributes.

uated in detail to all orders in $Z\alpha$ in [4]. They contain also the contribution to the g factor of the free electron of the same order, given by $\alpha/\pi \approx 2.323 \times 10^{-3}$. For comparison, the effect of binding in C^{5+} amounts only to 8.442×10^{-7}. In uranium the binding effect is 3×10^{-3} and therefore in particular heavy systems form an excellent base for investigations of bound-state QED.

The QED corrections of second order in (α/π) were never investigated beyond the first term in the $Z\alpha$ expansion. It can be shown for *all* orders of (α/π) that the leading term of the corresponding $Z\alpha$ expansion is given by $2 \times A^{(n)} \times (Z\alpha)^2/6$ where $A^{(n)}$ is the expansion coefficient for the nth power of (α/π) in the series for $g_{\rm free}/2$ [12], i.e., $A^{(1)} = 1/2$. The next term in the $Z\alpha$ expansion is at least of the order $(Z\alpha)^4$, and therefore the $Z\alpha$ expansion allows to estimate the bound-state $(\alpha/\pi)^2$ contributions with an uncertainty of about 50 % for the case of carbon. This uncertainty increases rapidly for increasing Z, and we expect the error to be at least 100 % in the case of calcium already, where the leading term of the expansion for the first order in (α/π) already deviates for about 70 % from the non-perturbative value. The whole set of 50 diagrams for the order $(\alpha/\pi)^2$ is shown in Fig. 2. For the order $(\alpha/\pi)^3$, the number of diagrams exceeds 500. The 50 diagrams shown in Fig. 2 can be obtained by fixing the magnetic interaction to each point of the 10 diagams contributing to the Lamb shift of order α^2 in hydrogenlike atoms (e.g., [13]). The calculation is slightly more complex because for each diagram the magnetic interaction and one additional electron propagator with the corresponding integration has to be considered. As there are problems already for some of the Lamb-shift diagrams, an evaluation of the set shown in Fig. 2 can not be expected without considerable effort. In particular, the diagrams that contribute most to the g factor in lighter systems are those with two self-energy loops in the upper rows of Fig. 2, and unfortunately exactly their counterpart, the so-called two-loop self-energy graphs, cause the major problems in the recent calculations for the Lamb shift (e.g., [14] and references therein). The situation would be different in muonic atoms where the vacuum-polarization contributions are strongly enhanced compared to those from self-energy-like graphs. An additional experiment on a muonic system therefore could provide valuable additional information. However, in muonic systems the nuclear polarization can expected to be as large as the QED corrections of order (α/π).

All theoretical contributions to the g factor of the electron bound in hydrogenlike carbon are given in Table 1. Together with the experimental value, this leads to an independent new value for the electron mass [15], $m_e = 5.485\,799\,092 \times 10^{-3}$ u. A detailed discussion about the corresponding measurement and evaluation procedure is to be found elsewhere in this report [16].

We want to thank S. G. Karshenboim, K. Pachucki, V. M. Shabaev, and V. A. Yerokhin for valuable discussions.

[1] R. S. Van Dyck Jr. *et al.*, PRL 59 (1987) 26.
[2] A. Czarnecki and W. J. Marciano, Nuc. Phys. B (Proc. Suppl.) 76 (1999), 245.
[3] H. Häffner *et al.*, PRL 85 (2000) 5308.
[4] T. Beier *et al.*, PRA 62 (2000) 032510.
[5] D. L. Farnham *et al.* PRL 75 (1995) 3598.
[6] R. Faustov, Nuovo Cimento LXIX A, No. 1 (1970) 37; Phys. Lett. 33B (1970), 422.
[7] H. Grotch, PRA 2 (1970) 1605; H. Grotch and R. A. Hegstrom, PRA 4 (1971) 59.
[8] V. M. Shabaev, PRA 57 (1998) 59; V. M. Shabaev *et al.*, PRA 57 (1998) 4235.
[9] G. Plunien and G. Soff, PRA 51 (1995) 1119; PRA 53 (1996) 4614, and references therein.
[10] N. Yamanaka *et al.*, Hyp. Int. 127 (2000) 297.
[11] T. Beier, Phys. Rep. 339 (2000) 79.
[12] A. Czarnecki *et al.*, Phys. Rev. A 63 (2001) 012509.
[13] P. Mohr *et al.*, Phys. Rep. 293 (1998) 227.
[14] V. A. Yerokhin, PRL 86 (2001) 1990, and refs. therein.
[15] G. Werth *et al.*, Hyp. Int., in print.
[16] W. Quint *et al.*, Contribution to this annual report.

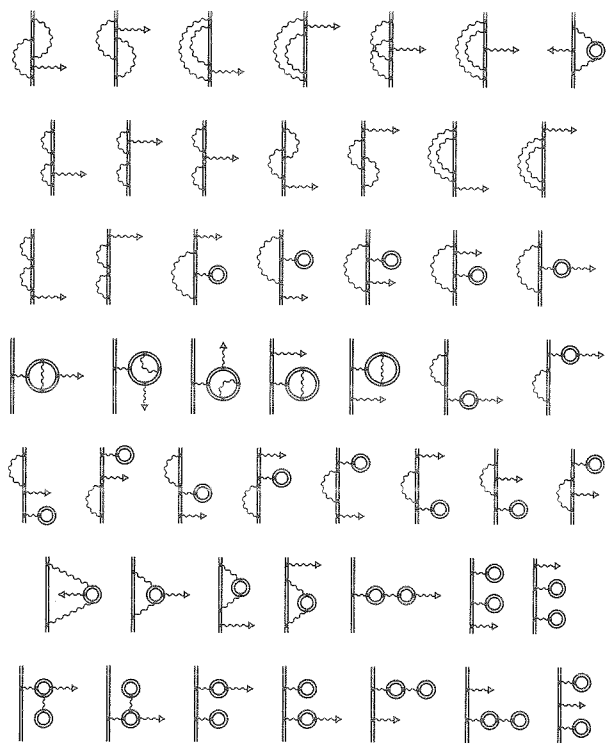

Fig. 2. Diagrams contributing to order $(\alpha/\pi)^2$ to the g factor of a bound electron. Only seven diagrams of this order have to be considered for the g factor of a free electron, similar to these of the first row.

Table 1. Known theoretical contributions to the g factor of an electron bound in the ground state of $^{12}C^{5+}$. All values are given in units of 10^{-9}. If no error is given, it is less than 0.5×10^{-10}. The error for the "total" value is a linear addition of the three errors given in order not to underestimate any systematic effect.

Contribution	numerical value (in 10^{-9})
binding	1 998 721 354.2
fin. nuc. size	0.4
recoil	87.5(9)
free QED, order (α/π):	2 322 819.6
bound QED, order (α/π):	844.3(12)
free QED, $(\alpha/\pi)^2$ to $(\alpha/\pi)^4$	−3 515.1
bound QED, $(\alpha/\pi)^2\,(Z\alpha)^2$	−1.1(5)
total:	2 001 041 589.8(26)

Interelectronic-interaction effect on the radiative recombination of an electron with a heavy He-like ion

V.A. Yerokhin [a,b,c], V.M. Shabaev [a,b,c], T. Beier [b], and J. Eichler [c]
[a] St.Petersburg State University, St.Petersburg, Russia
[b] Gesellschaft für Schwerionenforschung (GSI), Darmstadt, Germany
[c] Hahn-Meitner Institut Berlin, Germany

In energetic atomic collisions between highly charged high-Z ions and low-Z target atoms, radiative electron capture (REC) is one of the most important reaction channels. In the limit of a loosely bound target electron, REC is identical with radiative recombination (RR). Reactions of this type have been extensively studied in recent years for heavy highly charged projectiles up to bare uranium. The relativistic theory of REC in the one-electron approximation is well established at present ([1] and references therein), and results of numerical calculations are in excellent agreement with experiment [2]. While radiative recombination of an electron with a bare nucleus is well understood theoretically, the process involving an ion with several electrons is complicated by the interelectronic interaction. The REC process into the L-shell of He-like uranium was measured in [3].

We systematically investigated the interelectronic-interaction effect on radiative recombination of an electron with a heavy He-like ion. Here, the number of electrons (N=3) is much smaller than the nuclear charge number Z and therefore their mutual interaction is by a factor $1/Z$ smaller than that with the Coulomb field of the nucleus. To zeroth approximation, the interelectronic-interaction can be neglected and thus the process is equivalent to RR of an electron with a bare nucleus, studied thoroughly in [1]. Here, we investigated the correction of first order in $1/Z$ due to the interelectronic interaction.

We consider RR of an electron with a definite momentum and polarization with a heavy He-like atom in the ground state located at the origin of the coordinate frame. The final state of the system is a Li-like ion in the state $(1s)^2 v$, where v denotes a valence electron. The first-order (in $1/Z$) interelectronic-interaction correction to the process under consideration can be represented by a set of Feynman diagrams shown in Fig. 1. Here, the operator

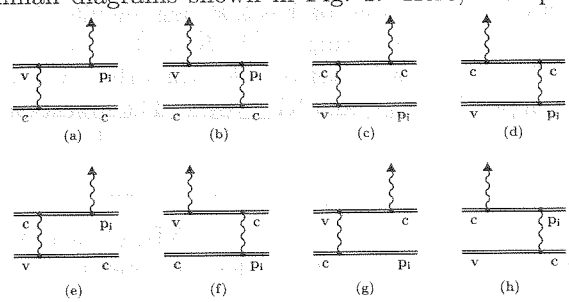

Fig. 1. Feynman diagrams representing the interelectronic-interaction corrections of first order in $1/Z$ to radiative recombination of an electron with a He-like atom. $\mathbf{p}_i$ denotes the incoming electron in the continuum spectrum, $\mathbf{v}$ and $\mathbf{c}$ indicate the valence and the core electrons, respectively. The line terminated by a triangle represents the emitted photon.

Table 1. Zeroth-order total cross section $\sigma^{(0)}$ and the first-order interelectronic-interaction correction in different evaluations, in barns. $\sigma^{(1)}_{\rm zeff}$ denotes the interelectronic-interaction correction calculated in the effective-nuclear-charge approximation with parameter $Z_{\rm eff} = 90.3$, $\sigma^{(1)}_{\rm scr}$ corresponds to the screening-potential approximation, $\sigma^{(1)}_{\rm int}$ indicates the results of the rigorous relativistic treatment.

E [Mev/u]		$\sigma^{(0)}$	$\sigma^{(1)}_{\rm zeff}$	$\sigma^{(1)}_{\rm scr}$	$\sigma^{(1)}_{\rm int}$
$2s_{1/2}$	10	504.65	−17.390	−19.635	−21.392
	100	41.203	−1.880	−1.393	−2.055
	700	2.457	−0.1768	−0.0979	−0.1051
$2p_{1/2}$	10	656.95	−38.523	−34.978	−35.396
	100	33.041	−2.975	−2.535	−3.088
	700	1.065	−0.1336	−0.1022	−0.0861
$2p_{3/2}$	10	854.82	−38.620	−39.671	−40.008
	100	31.489	−2.259	−2.275	−2.896
	700	0.622	−0.0600	−0.0568	−0.0489

of the photon emission and the operator of the electron-electron interaction are combined in all possible ways. We evaluate these diagrams directly, including the summation over the whole spectrum of the Dirac equation and the full electron-electron interaction that consists of the Coulomb, Breit and retarded parts. The details of the derivation are given in [4]. Here, we present the results of the evaluation.

The numerical results for the interelectronic-interaction correction to the total RR cross section of an electron with He-like uranium are presented in Table 1. The calculation is carried out for projectile energies of 10-700 MeV per nuclear mass unit. The results of the rigorous relativistic treatment are compared with the calculations based on an effective-nuclear-charge approximation and on the screening-potential approximation (for a discussion cf. [5]). The comparison shows a decreasing accuracy of the approximate methods for increasing projectile energy. On average, the screening-potential approximation is found to be more reliable than the effective-nuclear-charge approximation. Its typical deviation from the rigorous treatment is about 10 – 20 % of the interelectronic-interaction correction, i.e., about 1 – 2 % of the cross section of the process. Therefore, fully relativistic calculations are needed to obtain an accuracy better than a few percent of the cross section of the process.

We want to thank Th. Stöhlker for valuable discussions. Financial support by DFG and RFBR is gratefully acknowledged.

[1] J. Eichler and W. Meyerhof, *Relativistic Atomic Collisions*, Academic Press, San Diego, 1995.
[2] Th. Stöhlker *et al.*, Phys. Rev. Lett. 82 (1999) 3232.
[3] Th. Stöhlker *et al.*, Phys. Rev. Lett. 73 (1994) 3520.
[4] V. A. Yerokhin *et al.*, Phys. Rev. A 62 (2000) 042712.
[5] V. A. Yerokhin *et al.*, Hyp. Int, in print.

Resonant Transfer and Excitation for H- and He-like U-Ions

Zoltán Harman, Stephan Zakowicz, Matthias Gail, Norbert Grün, Werner Scheid
Institut für Theoretische Physik, Justus-Liebig-Universität Giessen

We present calculations for the angular distribution of photons emitted after KLL-RTE (Resonant Transfer and Excitation) in collisions of U^{91+}- and U^{90+}-ions with hydrogen atoms. Measurements with H-like projectiles were recently performed by Ma et al. at GSI and are currently being evaluated [1]. In the past, a similar process has been studied both experimentally [2] and theoretically [3], in which graphite was used as target. However, the width of the Compton profile of the electron bound in the H-atom is smaller than in graphite, resulting in a better resolution of the resonance groups in the cross sections.

The electron bound in the hydrogen atom can be regarded as quasifree. Therefore, the RTE cross section can be calculated by using the cross section of dielectronic recombination (DR). In DR, a free electron is captured by the projectile with the simultaneous excitation of a bound electron, followed by the emission of a photon. Doubly-excited states embedded in the one electron continuum give rise to resonances in the cross sections. With perturbation theory we obtain the following expression for the differential cross section in the rest frame of the projectile ion:

$$\frac{d\sigma^{DR}_{i\to d\to f}}{d\Omega_k} = \frac{2\pi}{F_i}\frac{1}{2(2J_i+1)}\sum_{M_f\lambda}\sum_{M_d}\sum_{M_i m_s} |\langle\Psi_d; J_d M_d|V_{capt.}|\Psi_i; J_i M_i, p_e m_s\rangle|^2 \times\frac{|\langle\Psi_f; J_f M_f, \mathbf{k}\lambda|H_{er}|\Psi_d; J_d M_d\rangle|^2}{(E-E_d)^2+\Gamma_d^2/4}\rho_f .$$

This formula makes use of the isolated resonance approximation, in which interference effects between the intermediate states are neglected. The first matrix element describes the resonant capture of the free electron, where the operator $V_{capt.}$ is the sum of the Coulomb- and Breit-interaction operators. The second matrix element describes the radiative transition. The differential cross section can be expressed by means of the total cross section:

$$\frac{d\sigma^{DR}_{i\to d\to f}}{d\Omega_k} = \frac{\sigma^{DR}_{i\to d\to f}}{4\pi}\left(1+\beta P_2(\cos\theta)\right),$$

where θ denotes the angle of emission of the photon with respect to the direction of the incoming electron. The anisotropy parameter β depends on the matrix elements for resonant capture and on the total angular momenta of the intermediate and final states.

In order to obtain the cross section for RTE in the impulse approximation, the cross section for DR is convoluted with the probability density of the target electron in momentum space:

$$\frac{d^2\sigma_{RTE}}{d\Omega d\omega} = \int d^3q' \frac{d\sigma_{DR}(\mathbf{q})}{d\Omega}|\phi_i(\mathbf{q}')|^2\delta(\omega+E_f-e_i-E_i).$$

Here, $\phi_i(\mathbf{q}')$ denotes the Fourier transform of the wave function of the target electron in the target frame. The δ-function ensures the conservation of energy.

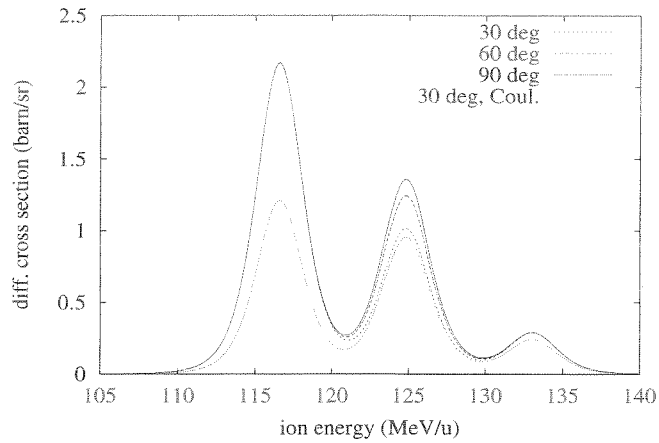

Figure 1: Differential cross sections for KLL-RTE in U^{91+} in the projectile frame at the angles $\theta = 30°$, 60° and 90°.

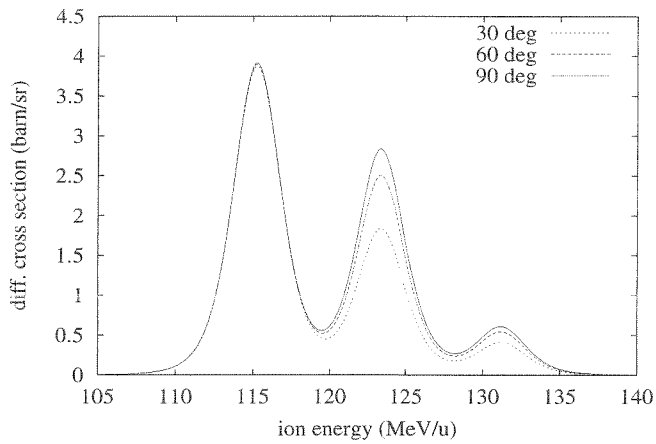

Figure 2: Differential cross sections for KLL-RTE in U^{90+} at the same angles.

Fig. 1 shows differential cross sections in the projectile system at different angles for U^{91+}-ions scattered on hydrogen atoms. The radiation has a strong angular dependence for energies in the range of the $KL_{1/2}L_{3/2}$ resonance group, while it is nearly isotropic for the other two resonance groups $KL_{1/2}L_{1/2}$ and $KL_{3/2}L_{3/2}$. The lowest curve was obtained by neglecting the effects of the Breit interaction.

The case of U^{90+}-ions is shown in Fig. 2. The cross section is anisotropic in the $KL_{1/2}L_{3/2}$ and $KL_{3/2}L_{3/2}$ groups. Also the cross sections are larger than the ones for the H-like projectile ions.

References

[1] X. Ma et al., this report (2001)
[2] T. Kandler et al., *Phys. Lett.* A **204** 274 (1995)
[3] M. Gail et al., *J. Phys.* B **31** 4645 (1998)

Hyperfine Splitting of Hydrogenlike Thallium

M. Tomaselli [a,b], T. Kühl [b], W. Nörtershäuser [b], D. Marx [b], S. Borneis [b], A. Dax [b], H. Wang [b], and S. Fritzsche [c]

[a] University of Darmstadt, [b] GSI Darmstadt, [c] University of Kassel

The investigation of hydrogenlike highly-charged ions is of interest for nuclear as well as for atomic physics. Measuring the ground-state hyperfine structure (HFS) splittings of these ions is a sensitive method to explore QED in extremely strong electric and magnetic fields and nuclear contributions to the electron energy. However, for a theoretical interpretation of the results it is necessary to separate the different contributions. Nuclear models have to provide charge and magnetization distributions of nuclei, which lead to the Breit-Rabi and the Bohr-Weisskopf effect, respectively, and corrections to the electron energy have to be calculated with QED. Interest was first focussed on the isotopes $^{207}Pb^{81+}$ and $^{205}Bi^{82+}$, where the theoretical description is simplified since they differ only by one nucleon from doubly-magic ^{208}Pb. The hyperfine structure of these isotopes was measured at GSI with laser spectroscopy at the ESR [1]. More recently, the hyperfine structure of $^{165}Ho^{66+}$, $^{185}Re^{74+}$, and $^{187}Re^{74+}$ was obtained by passive photon-emission spectroscopy in a high-energy electron-beam ion trap (SuperEBIT) at Livermore [2]. Similar experiments are presently under preparation to determine the HFS of thallium isotopes [3].

Previously, we applied the Dynamic Correlation Model (DCM) [4] to the hydrogenlike ions $^{207}Pb^{81+}$, $^{205}Bi^{82+}$, $^{165}Ho^{66+}$, and $^{185,187}Re^{74+}$ to derive the nuclear part in the HFS and combined the results with QED corrections [5]. The calculated hyperfine splittings are summarized in Table 1 and compared with other theoretical expectations [6, 7, 8] and experimental data. It turned out that the pure DCM results agree well with the experimental data, while adding the QED corrections led to a systematic deviation between theory and experiment. This is in contrast to the good description of nuclear properties by the dynamic correlation model and has motivated the application of the DCM to predict the HFS of the hydrogenlike thallium isotopes $^{203,205,207}Tl^{80+}$. The results are also included in Table 1. Besides, these calculations may guide future experiments at the GSI storage ring since an accurate *a priori* knowledge of the HFS transition frequency is required to avoid prohibitive large scan ranges.

In the DCM three terms contribute to the HFS: The first term is due to the single-hole magnetization, the second term was introduced in perturbative theory and describes spin-flip excitations [9], and the third term allows for collective correlation effects in the nucleus [5], it corresponds to higher-order perturbation diagrams. Taking these three terms into account the calculations accurately reproduce the experimental HFS. The systematic discrepancy to experimental data, which is observed after adding the QED corrections, might be the result of a double counting effect: The DCM calculations include "de facto" virtual mesons, which can decay into e^+e^- pairs, and these might be considered in radiative corrections as well. Another possibility is that the nuclear correlations, which are not taken into account in QED calculations, have a distinct influence on the radiative corrections. Hence, the central question is how to compare the DCM terms and the radiative corrections of Refs. [10, 11]. The importance of this problem is evident: In the extreme single-particle model, QED and nuclear-magnetization corrections for high-Z atoms are of the same order of magnitude. Thus, the feasibility of testing the QED corrections depends strongly on the accuracy of the model used to evaluate the nuclear magnetization.

Table 1: Wavelengths of transitions between the ground state HFS components in hydrogenlike ions as calculated in the DCM and after combination with QED corrections taken from [11]. For comparison other theoretical and experimental data is given. All values in nm.

Ion	Theory			Exp.
	DCM	+QED	Other	
$^{165}Ho^{66+}$	572.71	575.44	572.5 [7]	572.79(15)[2]
			563.9 [8]	
$^{185}Re^{74+}$	455.96	458.36	451.0 [7]	456.05(30)[2]
			448.6 [8]	
$^{187}Re^{74+}$	451.69	454.06	-	451.69(30)[2]
$^{207}Pb^{81+}$	1019.1	1024.76	1020.5 [7]	1019.7(2) [1]
			1017.0 [8]	
$^{209}Bi^{82+}$	243.91	245.26	243.0 [7]	243.87(2) [1]
			241.2 [8]	
$^{203}Tl^{80+}$	385.89	388.01	383.98[6]	
			384.0 [7]	
			382.2 [8]	
$^{205}Tl^{80+}$	382.79	384.89	380.22[6]	-
			380.2 [7]	
			378.6 [8]	
$^{207}Tl^{80+}$	377.68	379.74	-	-

References

[1] I. Klaft *et al.*, Phys. Rev. Lett. **73**, 2425 (1993); P. Seelig *et al.*, Phys. Rev. Lett. **81**, 4824 (1998).

[2] J. R. Crespo Lopez-Urrutia *et al.*, Phys. Rev. Lett. **77**, 826 (1996); Phys. Rev. A **57**, 879 (1998).

[3] P. Beiersdorfer, private communication (2000).

[4] M. Tomaselli, Ann. Phys. **205**, 362 (1991).

[5] M. Tomaselli *et al.*, Phys. Rev. C **51** 2989 (1995); Phys. Rev. C **58**, 1524 (1998).

[6] M.G.H. Gustavsson *et al.*, Hyperfine Interactions **127**, 437 (2000).

[7] V.M. Shabaev et al., Phys. Rev. A **56**, 252 (1997).

[8] V.M. Shabaev, J. Phys. B **27**, 5825 (1994).

[9] M. LeBellac, Nucl. Phys. **40**, 645 (1963).

[10] S.M. Schneider *et al.*, Phys. Rev. A **50**, 118 (1994); H. Person *et al.*, Phys. Rev. Lett. **76**, 1433 (1996).

[11] P. Sunergren *et al.* Phys. Rev. A **58**, 1055 (1998).

Asymptotic energy dependence of projectile inner-shell excitation cross sections in relativistic ion-atom collisions

Dorin Cezar Ionescu[1,3] and Thomas Stöhlker[1,2]

[1] Atomic Physics Division, Gesellschaft für Schwerionenforschung, D-64291 Darmstadt

[2] Institut für Kernphysik, J.W. Goethe Universität Frankfurt, D-60486 Frankfurt am Main

[3] Institut für Theoretische Physik, Technische Universität Dresden, D-01062 Dresden

In recent years atomic collisions with ions moving with velocities close to the velocity of light have become experimentally feasible. While in the first place we are interested in a basic understanding of atomic phenomena for their own sake, a precise knowledge of the cross sections for collision processes is needed for certain aspects of the design and operation of accelerators. As an example, Coulomb excitation of electrons which is essential for stopping power investigations, is also an important production process for characteristic projectile photons in ion-atom encounters.

In particular, Coulomb excitation of heavy projectile ions enable the investigation of the influence of relativistic bound state wave functions on the dynamics in relativistic ion-atom collisions. In addition, such studies provide detailed information on the effects associated with the Liénard-Wiechert interaction between the active electron and the target nucleus [1]. Thus, with increasing energy spin-flip mediated transitions where shown to become quite important above roughly 100 MeV/u such that contributions associated with the velocity dependent (magnetic) part of the time dependent interaction are quite relevant. In contrast to ionization where measured total cross sections are available for highly-charged ions up to uranium for more than one decade, it was only recently that detailed experimental data on the K-shell excitation of high-Z projectile ions were reported [1, 2].

In the present investigation we elucidate further details of the mechanisms associated with the Coulomb excitation of high-Z_P projectiles by considering the asymptotic energy dependence of the relevant cross sections. Specifically, we extend our previous results into the extreme relativistic energy domain with energies of hundreds of GeV/u. The numerical calculations are complemented by an analytic representation of the asymptotic energy dependence of cross sections which brings additional insight. The projectile ion is chosen as the origin of the coordinate system such that the target provides the time dependent perturbation mediating the transition.

In Figure 1 we show the energy dependence of reduced cross sections σ/Z_T^2 for exciting a K-shell electron in hydrogen-like gold colliding with an atomic target with charge number Z_T. The cross sections are divided by Z_T^2 which is the scaling behavior in lowest-order perturbation theory. We consider the (Ly-α_1) transition of a $1s_{1/2}$ spin-up electron ($\mu_i = 1/2$) to the $2p_{3/2}(\mu_f = \pm 1/2, \pm 3/2)$ states of the projectile ion (Au^{78+}). The upper curve (Σ) is associated with the total Ly-α_1 cross section, the dashed (short-dashed) curve corresponds to the transition with $\Delta\mu = \mu_f - \mu_i = +1(-1$, splin-flip), and the dotted (dott-dashed) curve is related to $\Delta\mu = +2(0)$.

The present numerical results demonstrate that cross

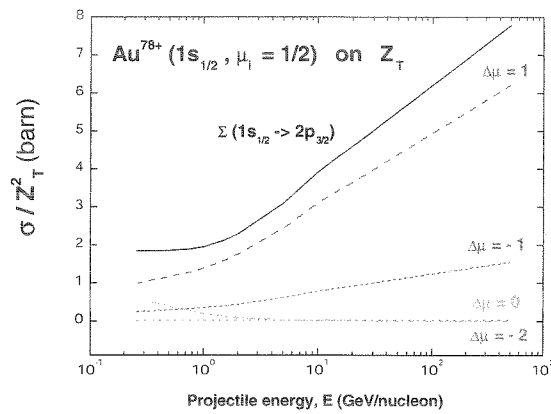

Figure 1: Reduced cross sections σ/Z_T^2 for projectile excitation as functions of the laboratory energy.

sections associated with transitions where the magnetic quantum number changes by one unit ($\Delta\mu = \pm 1$) *increase* with increasing energy roughly as $\ln E$ in the region above 1 GeV/u. In contrast, the cross sections associated with the other types of transitions ($\Delta\mu = 0, 2$) *decrease* with increasing collision energy, and approach zero in the asymptotic energy region. Note that the inclusion of screening would lead to different energy dependence [3]. As a result, the cross section for the unscreend Ly-α_1 transition is provided solely by the $\Delta\mu = \pm 1$ transitions for collision energies in the GeV/u region and higher.

An interesting parallel can be made with a computationally simple treatment of the excitation process in the Fermi-Weizsäcker-Williams (FWW) approximation. There the actual electromagnetic field created by the moving ions is approximated by the field associated with a swarm of real photons. In addition, a free parameter which is related to the maximum photon energy is to be fixed (in some sense arbitrary), such that the domain of applicability of the method is often not clear. From Figure 1 one can see that above roughly 3 GeV/u only transitions with $\Delta\mu = \pm 1$ provide a nonzero contribution to the cross section. Thus, the present investigation provides a quantitative measure of the range that can be treated safely in a computationally simple FWW scheme.

References

[1] Th. Stöhlker et al., Phys. Rev. A **57**, 845 (1998); Phys. Lett. A **238**, 43 (1998).

[2] T. Ludziejewski et al., Phys. Rev. A **61**, 052706-1 (2000).

[3] A.H. Sorensen, Phys. Rev. A**58**, 2895 (1999).

Stripping of Fast Heavy Low-Charged Ions in Gases

V. Shevelko (GSI and P.N. Lebedev Institute, Moscow),
T. Stöhlker (GSI)

Electron loss and capture processes arising in collisions of heavy low-charged ions with atoms and ions are the main charge-changing reactions in heavy-ion driven inertial fusion (HIDIF) [1]. However, at present time, virtually no experimental and theoretical data are available for removal processes involving fast heavy low-charged ions.

In this work, the projectile-ionization (stripping) cross sections and beam lifetimes in reactions

$$X^{z+} + A \rightarrow X^{(z+1)+} + e^- + ...$$

have been calculated for ions X = Xe, Pb, Bi, U ($z < 10$) colliding with neutral atoms A =H, He, Be, C, F, N, Ar, Xe in the $E = 1-100$ MeV/u energy range. Calculations have been performed for *single*-electron stripping in the first-order perturbation theory using the LOSS computer code. The atomic structure of the target was taken into account in the form of its atomic form-factor $F(q)$ depending on the momentum transfer q.

For the case of ionization of Pb-like ions (Xe^{0+}, Bi^{1+}, ..., U^{10+}) and the energy range considered, a scaling law for stripping cross sections was obtained in the form:

$$\tilde{\sigma} = \sigma \cdot (I_P/Z_T)^{1.4}, \quad \tilde{E} = E/I_P, \qquad (1)$$

where I_P is the *first* ionization potential of the projectile in eV, E is the beam energy in eV/u, and Z_T denotes the target nuclear charge. The scaled cross sections for Pb-like ions are displayed in Fig. 1 in comparison with available experimental data and other calculations (see [2] in detail); 1 Ry = 13.606 eV.

Ion-beam lifetimes τ have been calculated with account for electron capture processes using the CAPTURE computer code. The values of τ are shown in Fig. 2. A small minimum for U^{28+} ions around 2 MeV/u is related to the influence of electron capture which for these ions prevails at energies $E < 10$ MeV/u.

A comparison of the present calculations with experimental data [3]–[5], classical-trajectory Monte-Carlo (CTMC) calculations [6] and $Z_T^2 + Z_T$ scaling [7] shows the following peculiarities for the stripping processes of heavy low-charged ions in neutral targets:

1) the contribution from ionization of the projectile inner-shell electrons is very significant, and, in calculations, one has to account for 6–8 inner subshells,

2) at high energies, the stripping cross sections fall off approximately as $\sigma \sim E^{-1}$,

3) multiple-ionization processes seem to play a very important role and, according to [6], their contribution can reach up to 50 % to the total stripping cross section.

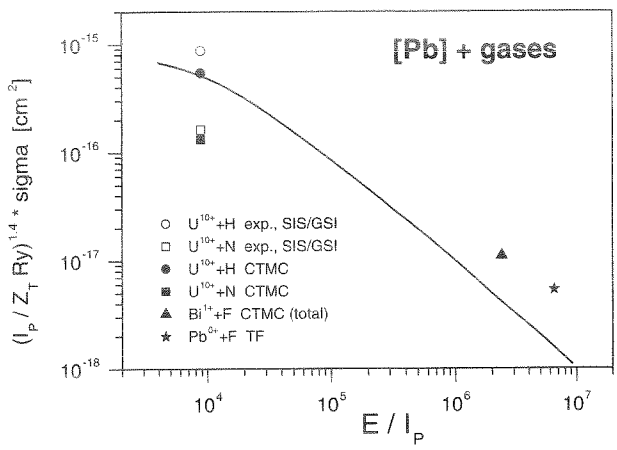

Figure 1: Scaled ionization cross sections of Pb-like ions colliding with neutral atoms, eq. (1). Solid curve – present result, symbols – experimental and theoretical data (see [2] in detail).

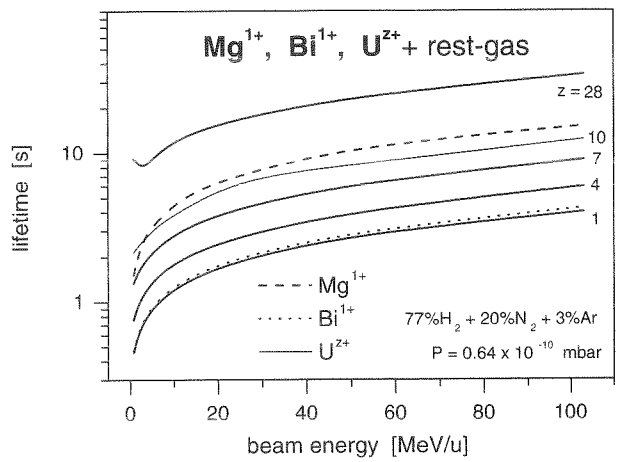

Figure 2: Beam lifetimes of ions colliding with a residual gas mixture and a gas pressure indicated in the figure – present result.

References

[1] I. Hofmann, G. Plass (eds.): *The HIDIF-Study*, Report GSI-98-06, Darmstadt (1998)

[2] I.Yu. Tolstikhina, V.P. Shevelko, Th. Stöhlker: Preprint GSI-2000-54, Darmstadt (2000)

[3] W. Erb: Report GSI-P-78, Darmstadt (1978)

[4] B. Franzke: IEEE, NS-**28**, 2116 (1981)

[5] K. Blasche et al.: GSI Scientific Report 1996, Darmstadt (1997), p. 159

[6] R. Olson: Proc. HIF-2000, San Diego (Febr. 2000) (in press)

[7] V.P. Shevelko et al.: Hyp. Int. **114**, 289 (1998); V.P. Shevelko et al.: NIM A **415**, 609 (1998)

HEAVY ION RESEARCH IN OTHER FIELDS

Plasma Physics

Heavy Ion Induced Effects in Solids

Biophysics With Highly Ionizing Beams

Chemistry

Relativistic Laser Plasmas Generating Intense, Collimated Ion Beams

M. Roth[1], T.E. Cowan[2], J. C. Gauthier[3], J. Meyer-ter Vehn[4], M. Allen[5], P. Audebert[3], A. Blazevic[6], J. Fuchs[3], M. Geissel[6], M. Hegelich[7], S. Karsch[7], A. Pukhov[4], T. Schlegel[6]

[1]Gesellschaft für Schwerionenforschung mbH, Planckstr.1, 64291 Darmstadt, Germany
[2]General Atomics, P.O. Box 85608, San Diego, California 92186-5608
[3]Laboratoire pour l'Utilization des Laser Intense, Palaiseau, France
[4]Max-Planck-Institut für Quantenoptik, Garching, Germany
[5]University of California, Berkeley, USA
[6] Technische Universität Darmstadt, Germany
[7]Ludwigs-Maximilian Universität, München, Germany

The exploration of new regimes in plasma physics has been enabled recently by the advent of ultra-intense short pulse lasers [1] with intensities exceeding 10^{19} W/cm^2. The interaction of these laser beams with solid targets can produce gamma rays of tens of MeV, fast electrons of greater than 100 MeV and energetic ions with up to tens of MeV [2] in energy. The generation of fast protons from laser irradiated solid surfaces is attributed to electrostatic fields produced by hot electrons [3,4]. Relativistic electrons generated from the laser-plasma interaction, having an average temperature of several MeV, envelope the target foil and form an electron plasma sheath on the rear, non-irradiated surface. The electric field in the sheath can reach $>10^{12}$ V/m, which field-ionizes atoms on the surface and accelerates the ions very rapidly normal to the rear surface. Protons, having the largest charge-to-mass ratio, are preferentially accelerated in favor of heavier ions over a distance of a few microns, and up to tens of MeV. This forms a collimated beam with an approximately Maxwellian energy distribution at kT = 5-6 MeV. This acceleration mechanism makes these intense ion beams highly interesting for many applications, especially if one can collimate or focus the beam by shaping the target, as suggested by numerical calculations [5,6,7]. Therefore we carried out experiments to investigate in detail the influence of the target parameters on the ion beam production.

The experiments were performed with the 100 TW laser at Laboratoire pour l'Utilization des Laser Intense (LULI). Pulses of up to 30 J at 300 fs pulse duration at λ=1.05 µm were focused with an f/3 off-axis parabolic mirror onto free standing target foils at normal incidence, at intensity up to 5×10^{19} W/cm^2. The $1/e^2$ focal spot radius measured in vacuum was about 5µm. Amplified spontaneous emission (ASE) occurred 2ns before the main pulse at a level of 10^{-7} of the main pulse energy and preformed a plasma.

A stack of radiochromic film (RCF) was positioned a few cm behind the target to measure the spatial beam profile. Two absolutely calibrated, permanent magnetic ion spectrometers were mounted at a distance of about 1m from the target covering a solid angle of $5\text{x}10^{-6}$ sr. The energy of the protons emitted normal to the target rear surface extended up to 25 MeV. The maximum energy of the protons dropped to about 13 MeV at an angle of 13°. The spectral shape of each proton energy distribution is generally continuous up to the cut-off energy, in agreement with the electrostatic sheath acceleration mechanism and as well as previously observed in experiments with the LLNL PETAWATT laser [2].

To investigate the influence of such target conditions on the creation of a collimated ion beam, we varied the target composition and structure of the rear surface.

We used thin (48 µm) targets of gold with either a flat or structured rear surface. The proton beam ejected from the rear surface is shown in Fig.1. The results showed a clear dependence of the spatial uniformity of the proton beam on the structure of the back surface. In contrast to the homogenous, collimated beam from the gold target, protons emitted from the structured gold rear surface showed filaments. To discriminate between conductivity and surface quality effects, we next used ~100 micron plastic and glass targets. The results of the glass and plastic targets were even more pronounced. While the flat surfaces of glass and plastic yielded a strong, but filamented proton beam, there were no protons detected above 1 MeV from the roughened targets. Using a Rasterscan-Electron-Microscope (REM) we examined the structure of the target surfaces (lower insets in Fig.1). Structuring the gold surface maintained a smooth surface with hills and valleys, visible as bright shadows on the lower right inset of Fig.1. The surface of the plastic and glass targets was largely destroyed by numerous cracks. The different behavior of the structured gold, glass and plastic targets can be understood within the context of the Target Normal Sheath Acceleration (TNSA) model [5]. When the material on the rear surface is exposed to the strong electric field generated by the electron plasma sheath, it is field ionized instantaneously.

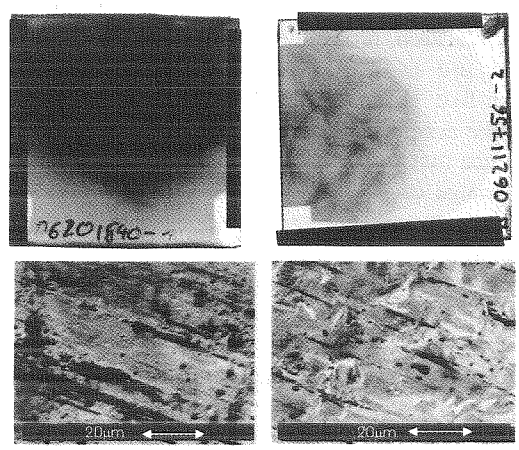

Fig. 1: Proton emission from smooth and roughened rear surfaces of a Au target. The roughened surface leads to the onset of filamentation. The REM images show the structure of the surface.

A shallow, wavelike surface, such as for the roughened gold targets, is expected to lead to a microlensing phenomenon, consistent with the observed filamentation or spatial modulation of the accelerated protons. Such effects have been calculated for the case of a single concave depression of the

surface [5]. In the case of a destroyed surface, the cracks and defects on the plastic and glass create many sharp excursions, very different from the rather smooth undulating surface of the gold targets. The ion plasma created by the field is therefore extended over a much larger scale length normal to the (average) surface. We expect this to partially compensate the charge separation sheath, and therefore suppress the ion acceleration.

An important question to be addressed for any future application of laser-accelerated protons and ions is the possibility of tailoring the proton beam, either collimating or focusing it, by changing the geometry of the target surface. We first attempted to defocus the beam in one dimension by using a convex target. A 60 μm diameter Au wire as a target basically constituted such a one-dimensional defocusing lens, and we observed a line as shown in Fig. 2. Tilting the wire also changed the orientation of the line, which results from the radial, fan-shaped expansion of the protons normal to the wire.

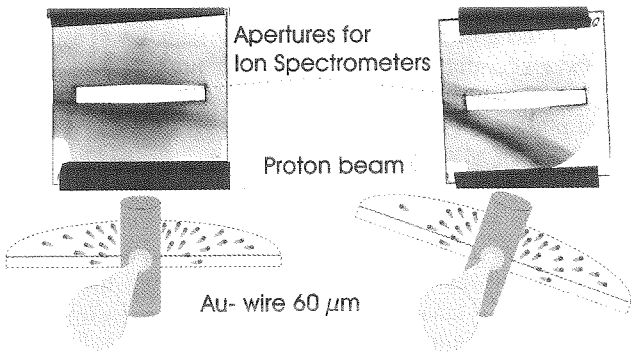

Fig. 2: Experimental setup and RCF images of experiments with 60 μm diameter gold wires. The convex rear surface constitutes a decollimating cylinder-lens. Accordingly the proton beam was formed into a line.

We then attempted to focus the protons by modifying the curvature of the target foil. Focusing of laser generated protons is essential for applications like ion-induced material damage research, proton fast ignition [8], proton radiography, and the use as next generation ion sources. Due to the gaussian-like shape of the hot electron debye sheath that causes the acceleration, there is an energy dependent angle of divergence that has to be compensated to focus the ions in the energy range of interest. Thus the effective focal length of a curved target rear surface is longer and dependent of the proton energy.

The curvature of the target surface used in these experiments was changed from a flat target to concave shaped targets with radii of curvature between 10 and 2.5 mm.

Fig.3 shows the experimental setup and the corresponding RCF images for a flat target and a target having a 2.5 mm radius of curvature. The RCF detector was mounted 9 mm behind the laser irradiated foil and protected from plasma blowoff by 10 μm of aluminum and 100 μm of titanium.

The respective ion energy in the layers of RCF corresponds to 5 MeV for the first layer and 7.5 MeV for the second. The results show a strong reduction in the divergence of the central core of the proton beam representing ballistic collimating of laser produced proton beams. For most of the future applications of laser generated ion beams the beam quality is the most important characteristic. As is apparent from the radiochromic film data, the angular divergence of the proton jet is rather well defined and decreases with increasing proton energy. This suggests that protons or other light ions accelerated by this mechanism may have a usefully small emittance in the sense of an actual ion beam.

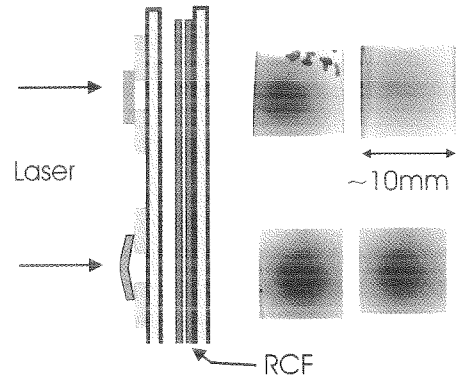

Fig.3: Focusing of laser generated proton beams. left: experimental setup. The RCF detector is shielded by 10 μm of aluminum and 100 μm of titanium. right: images of successive layers in RCF for a flat target and a target with 2.5 mm radius of curvature

To estimate our emittance, we used penumbral imaging of edges at different distances from the target with the magnetic spectrometers, to directly measure the core emittance of the proton beam. This technique is related to the conventional slit-emittance measurements made with apertures and screens at conventional accelerators. We determine the normalized emittance of protons from flat gold foils to be ~0.2 π mm-mrad, and a factor of at least two smaller than the resolution limited measurements we performed on the PETAWATT.

We have presented a detailed investigation of the target conditions on the proton and ion beam production from intense laser solid interactions. The observed strong dependence on the rear surface conditions is in agreement with the target normal sheath acceleration mechanism. The target conductivity appears to have a major influence on the quality of the ion beam, and the quality of the surface finish of the target is very important for maintaining a high gradient sheath and a laminar beam. It has been shown that tailoring the ion beam (yield, shape, homogeneity) by means of target shape and composition is possible, and we present first observations of laser-accelerated ion beam focusing.

The authors would like to thank the GSI target laboratory for the help designing the targets and for the REM measurements. This work was supported by the EU "Large Scale Facility Access Program"

References

1 M. Perry and G. Mourou, Science **264**, 917 (1994)

2 R.A. Snavely, et at., Phys. Rev. Lett. **14**, Vol 85, 2945 (2000)

3 S.J. Gitomer, Phys. Fluids **29**, 2679 (1986)

4 Y. Kishimoto, et al., Phys. Fluids **26**, 2308 (1983)

5 S.C. Wilks, et al., Phys. Plasmas, Vol. 8, 542 (2001)

6 H. Ruhl, et al., Plasma Physics Reports, in press, (2001)

7 A. Pukhov, accepted for publ. In Phys. Rev. Lett. (2001)

8 M. Roth, et al., Phys. Rev. Lett. **3**, Vol. 86, 436 (2001)

Spectroscopy of laser-generated ions and neutrons

S. Karsch[1,2], M. Hegelich[1,2], G. Pretzler[1,2], M. Roth[3], M. Geissel[3], A. Blaszevic[3], T. Schlegel[3], T. Cowan[4], M. Allen[4], P. Audebert[5], J. Fuchs[5], J.C. Gauthier[5], D. Habs[1] K.J. Witte[2], A. Pukhov[2], J. Meyer-ter-Vehn[2]
[1]LMU München, [2]MPQ Garching, [3]GSI Darmstadt, [4]General Atomics San Diego, [5]LULI Palaiseau

In recent laser plasma experiments, an intense and collimated beam of highly energetic protons was found to be emitted from the rear side of foil targets [1, 2, 3]. For example, using the Petawatt laser in Livermore, up to several percent of the laser energy was transferred into 2×10^{13} protons of energies > 10 MeV, with maximum energies above 58 MeV [4]. This effect is explained by an ultra-strong space charge field due to a relativistic electron cloud created by the laser pulse and located the backside of the target (TNSA mechanism [5]).

In previous experiments protons from surface contamination were found to be the dominant species to be accelerated independent of the target material.

In this experiment we tried to accelerate other ions as well by removing the contaminating layer. This was done embedded in a large experimental campaign at the 100-TW single shot laser at the Laboratoire pour l'Utilisation des Lasers Intenses (LULI) in Paris. The setup of our special experiment is shown in Fig. 1. Two Thomson parabola spectrometers distribute ions of one charge-to-mass ratio (q/m) on a parabolic trace according to their energy in the detector plane. CR39 nuclear track detectors recorded the traces.

We used 50μm aluminum targets with a rear-side 1μm carbon layer. Resistive heating led to a strong reduction of protons and an enhancement of carbon ions as obvious from Fig. 2. For quantitative analysis, single ion tracks on the CR39 films were counted by a scanning optical microscope [6]. First results suggest that C^4+ ions are dominantly accelerated with higher temperature and maximum energy than expected from linear interpolation. The full evaluation is under way and is expected to yield rich information on the dynamics of the ion acceleration mechanism.

In another experiment, targets with an amorphous CD-layer on the backside were used to produce a beam of accelerated deuterons. A CD_2 catcher target was positioned in this beam and $\sim 3 \times 10^7$ neutrons were generated, mainly by deuterium fusion.

At the MPQ ATLAS-10 laser facility, an adaptive optics system has been installed which consists of two deformable mirrors, wavefront and beam-profile diagnostics,

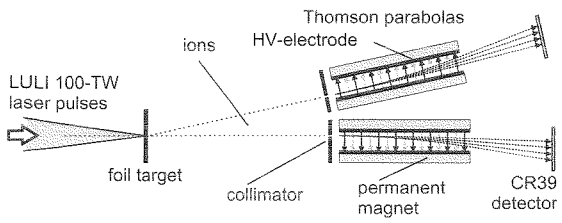

Figure 1: Setup for accelerating and diagnosing fast ions from the rear side of solid foils. Two Thomson parabolas were used at angles of 0° and 13° to the target normal.

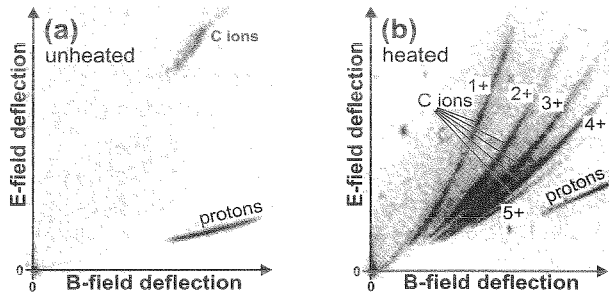

Figure 2: Thomson parabola spectra of laser accelerated ions. **(a)** Unheated target of 50 μm Al with a 1-μm layer of carbon at the rear surface. **(b)** Same target, but resistively heated for removing contaminating layers from the surface. The electric field in the Thomson parabola was different for the two shots.

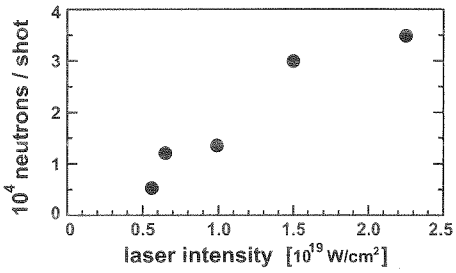

Figure 3: Dependence of the fusion neutron yield on laser intensity with solid CD_2 targets.

and automatic closed-loop alignment. The modifications now allow for reproducible high-intensity experiments up to $I > 2 \times 10^{19}$ W/cm^2. In ongoing fusion neutron generation experiments with solid CD_2-targets, a clear dependence of neutron yield on laser intensity has been found (Fig. 3). TOF spectroscopy of these neutrons allows to deduce the directional characteristics of the deuterons accelerated in the laser plasma, and a few different regimes were identified, with different angular deuteron distribution and probably with different acceleration mechanisms.

(sup. by DFG Ha 1101/7-1, GSI F/E LM/HABP and EU Large Scale Facility Access Program)

References

[1] S.P. Hatchett et al., Phys. Plasmas **7**, 2076 (2000).
[2] E.L. Clark et al., Phys. Rev. Lett. **84**, 670 (2000).
[3] A. Maksimchuk et al., Phys. Rev. Lett. **84**, 4108 (2000).
[4] R.A. Snavely et al., Phys. Rev. Lett. **85**, 2945 (2000).
[5] S.C. Wilks et al., Phys. Plasmas **8**, 542 (2001).
[6] W. Rusch et al., Nucl. Tracks Radiat. Meas. 19, 261 266 (1991).

Characterization of Laser Heated Targets for UNILAC Beams

M. Geißel[1], E. Brambrink[1], A.Ya. Faenov[3], D.H.H. Hoffmann[1], T. Pikuz[3], P. Pirzadeh,[2], F.B. Rosmej[1], O. Rosmej[2], M. Roth[2], W. Seelig[1], J. Wieser[2]

[1] *TU Darmstadt,* [2] *GSI Darmstadt,* [3] *VNIIFTRI Mendeleevo, Russia*

An enhanced energy loss of heavy ions in laser produced plasmas compared with cold gas targets has been observed and studied at GSI for several years [1]. A thorough spectroscopic investigation of the properties of these plasmas was essential and first experiments have been carried out during the last two years [2]. The use of CF_2 targets instead of carbon enabled the application of spherically bent mica crystal spectrometers, which provide spatial and high spectral resolution [3], but an additional measurement of energy losses for carbon and CF_2 was pending to compare the behavior of the two materials.

Previous measurements used foils of 2 μm thickness or less. As CF_2 is available with a minimum thickness of 5 μm only, comparable shots with carbon and CF_2 could only be performed after an upgrade of the nhelix laser, which was completed during the year 2000. Table 1 shows the current performance of the upgraded laser.

Table 1: Data of the upgraded nhelix laser system

front end	Continuum Powerlite 8000 200 mJ @ 10 Hz
pulse width	12 ns
wavelength	1064 nm
number of amplifiers	5
number of spatial filters	4
energy	50 J
repetition rate	1-2 shots/hour
I_{max}	10^{12} W/cm^2

The comparison of CF_2 targets with 5 μm thickness and carbon targets with 1 mg/cm^2 ($\approx 4.5\,\mu$m) showed an almost identical values of carbon and CF_2. Although the measurements have an error level of about 10% both temporal evolution and signal amplitude show the same behaviour (Fig. 1).

The X-ray spectra show a high abundance of He-like and H-like Ions. While the H-like ions are concentrated in the hot region of interaction, the He-like ions can be observed throughout the jet-like expanding plasma [2]. The simultaneous observation of the X-ray emission from both front and rear surface by two seperate spectrometers enabled a further distinction of the homogeneity of the target plasma. It was shown, that similar properties are generated on both sides of the plasma (Fig. 2).

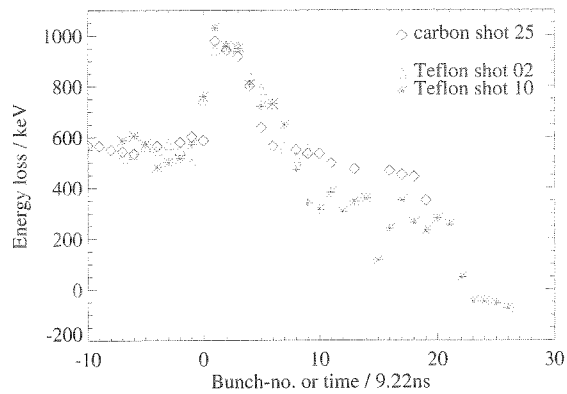

Figure 1: Comparison of different shots with carbon and CF_2 (Teflon) foil targets.

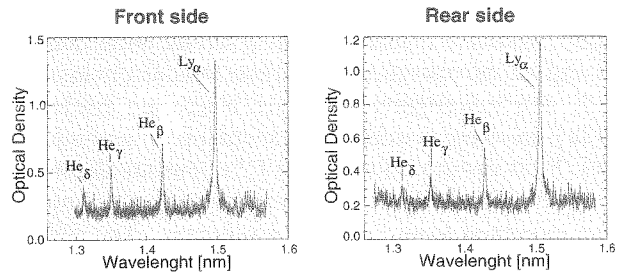

Figure 2: The comparison of X-ray spectra achieved on the front and rear surface shows similar conditions throughout the target.

References

[1] M. Roth, C. Stöckl, W. Süß, O. Iwase, D.O. Gericke, R. Bock, D.H.H. Hoffmann, M. Geißel, W. Seelig; Energy loss of heavy ions in laser-produced plasmas, Europhys. Lett., **50** (1), pp. 28–34 (2000)

[2] M. Geißel, R. Bock, A.Ya. Faenov, D.H.H. Hoffmann, T. Pikuz, P. Pirzadeh, F.B. Rosmej O. Rosmej, M. Roth; W. Süß, W. Seelig; GSI Scientific Report 1999, GSI-2000-1, p. 136

[3] I. Yu. Skobelev, A. Ya. Faenov, B. A. Bryunetkin, V. M. Dyakin, T. A. Pikuz, S. A. Pikuz, T. A. Shelkovenko, V. M. Romanova, A. R. Mingaleev; JETP **81**, 692ff (1995)

This work is supported by the BMBF of the Federal Republic of Germany, INTAS and WTZ

Advanced X-ray Diagnostics for Large Scale Dense Plasmas

F.B. Rosmej[1], D.H.H. Hoffmann[2,3], W. Süß[2,3], M. Geißel[2,3], A.Ya. Faenov[4], T.A. Pikuz[4]
[1]Université de Provence, Marseille, France, [2]GSI-Darmstadt, Germany
[3]TU-Darmstadt, Institut für Kernphysik, Germany, [4]VNIIFTRI MCISDC, Mendeleevo, Russia

Future GSI-experiments with intense heavy ion beams and the kilo-joule PHELIX-laser necessarily deal with large scale dense plasma objects. These plasmas might be either created by lasers to serve as a target for advanced studies of heavy ion beams interacting with matter or as intense back-lighter sources or may be created by intense heavy ion beams for, e.g., studies of strongly coupled plasmas.

The key issue and the request in common for the success of these experiments is a detailed characterization of large scale dense plasmas. Standard methods obviously fail due to the large optical thickness even for x-ray transitions. We therefore have undertaken an extended research program on this issue.

The novel aspect in this research is to base plasma diagnostic methods on forbidden line transitions with low transition probability A. This circumvents photo-absorption because the line center optical thickness τ_0 is proportional to A:

$$\tau_{0,ij} = \frac{1}{4}\lambda_{ji}^2 \frac{g_j}{g_i} A_{ji}\, n_i \left\{1 - \frac{g_i n_j}{g_j n_i}\right\} \varphi_{ij}(\omega = \omega_{ji})\, L_{eff}$$

This approach, however, is highly non-trivial because transitions with low radiative decay values A are, first, difficult to observe and, second, they are highly dependent on density variations (because in dense plasmas collisional rates easily approach the radiative decay rate even for highly charged ions) and this denies their diagnostic use.

Despite these obstacles we have successfully developed a new concept for large scale dense plasma diagnostics introducing intercombination and two-electron transitions from autoionizing states as diagnostic and as reference lines [1,2]. We also performed atomic structure calculations to establish the required data [1].

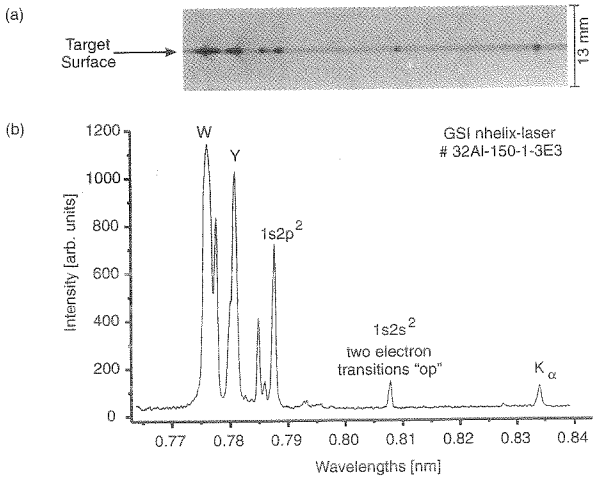

Figure 1: X-ray image of Al and spectrum near the target surface. Two-electron transitions have large intensity.

T

energies between 17 – 60 Joules, varying spot sizes from about 200 µm until 2 mm and laser pulse duration of 15 ns. Space resolved high resolution Argon K-shell X-ray radiation near λ = 0.8 nm has been obtained with spherically bent mica crystals [3] and Kodak DEF X-ray film in the 2nd reflection order. X-ray images were digitized with a 10.000 dpi EUROCORE drum scanner. Spectra have been corrected for filter transmission, crystal reflectivity, film response and non-linear dispersion using SCALE.

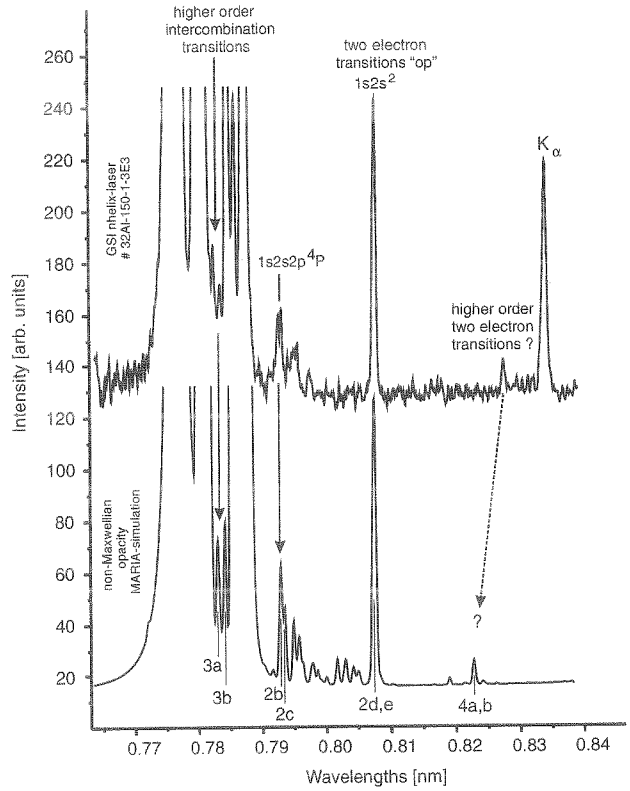

Figure 2: Large scale dense plasma diagnostic based on forbidden satellite transitions. Two-electron transitions serve as reference lines. Excellent agreement between the simulations and the experiment is obtained.

Figure 1 shows the plasma image and the corresponding spectrum near the target surface. Figure 2a demonstrates the intense observation of the requested forbidden satellite transitions. Fig. 2b shows the non-Maxwellian simulation which compares well with the experiment. The excellent agreement demonstrates the success of the present approach for the complicated case of large scale dense and non-Mawellian plasmas. The developed methods are therefore of general use and may readily be applied to PHELIX plasmas.

References

[1] F.B. Rosmej et al., Phys. Rev. A **63**, p032716 (2001).

[2] F.B. Rosmej et al., JQSRT, in print.

[3] I.Yu. Skobelev et al., JETP **81**, 692 (1985).

Projectile Spectroscopy: Space Resolved Registration of Projectile X-Rays Inside Matter

O.N. Rosmej[1], F.B. Rosmej[2], J. Wieser[1,3], M. Geißel[1,3], E. Brambrink[1,3], C. Niemann[1,3], A. Blazevic[1,3], K. Penache[1], D. Penache[1], J. Jacoby[1], E. Dewald[1], K. Weyrich[1], D.H.H. Hoffmann[1,3], A. Golubev[4], A. Borisenko[4]

[1]GSI-Darmstadt, Germany, [2]Université de Provence, Marseille, France, [3]TU-Darmstadt, Institut für Kernphysik, Germany, [4]ITEP, Moscow, Russia

We report about the first successful observation of highly charged projectile radiation inside extended solid and gaseous matter at GSI. These investigations are of extraordinary interest for the physics of heavy ion beams interacting with matter because the x-ray spectra contain the information of the effective projectile charge state inside matter.

5.9 MeV/u Ni^{7+} with I = 100 pnA are interacting with Ar gas (p = 600-800 mbar). Figure 1 shows the X-ray emission of the K-shell spectra near λ = 0.16 nm of the multi charged Ni ions recorded in the 10^{th} reflection order as well as the argon K_α transition in the 4^{th} reflection order of spherically bent mica crystals [1]. Spectra emitted from different distances clearly show a variation of the nickel charge states.

Similar type of experiments were conducted with 5.9 MeV/u Ar^{7+} projectiles with I = 100 pnA interacting with massive aerogel targets (SiO_2, ρ = 0.1 g/cm^{-3}, crystal lengths about 2 mm). The argon projectiles are stopped inside the crystal after about 1.3 mm. Space resolved high resolution Argon K-shell X-ray radiation near λ = 0.4 nm have been obtained in the 4^{th} reflection order.

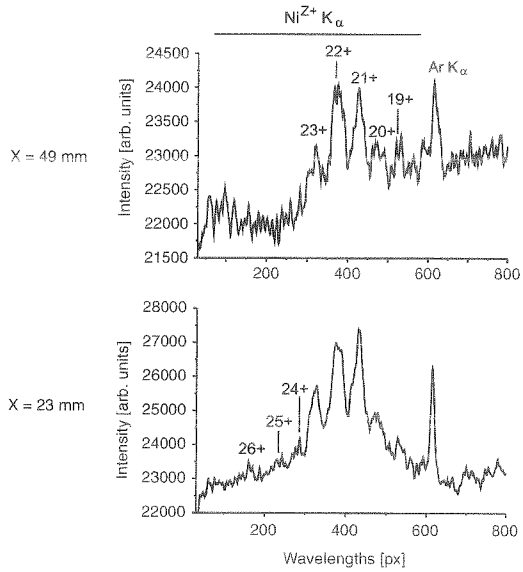

Figure 1: Space resolved X-ray spectra of Ni-projectiles

Figure 2 shows the characteristic K-shell emission of argon. The prominent spectral features are the H-like Ly_α lines $1s\ ^2S$ – $2p\ ^2P_{1/2,3/2}$, the He-like resonance line He_α = $1s2p\ ^1P_1$ – $1s^2\ ^1S_0$ and Al K_α (used as a reference line). The high quality of the space resolved spectra is easily demonstrated by the resolved Ly_α doublet (Fig. 2b). The set of figures (a-c) demonstrates the simultaneously achieved space resolution, however, due to the partial destruction of the SiO_2-target the definite relation to the target locations is not possible. The spectral features on the red wings of the H- and He-like resonance lines are identified as dielectronic satellite transitions, 2l2l' – 1s2l'' and 1s2l2l' – $1s^22l''$ respectively. Detailed investigation of the satellite group formation shows asymmetries to the red wavelengths side for both, the He-like and Li-like (see, e.g., the arrow in Fig. 2a) transitions. The origin of these kind of asymmetries has recently been explored for dense hot plasmas [2], [3]: hot electrons preferentially increase the inner-shell excitation channel. In the present experiments, this channel is driven by the fast argon ions colliding with the target molecules $T=SiO_2$.

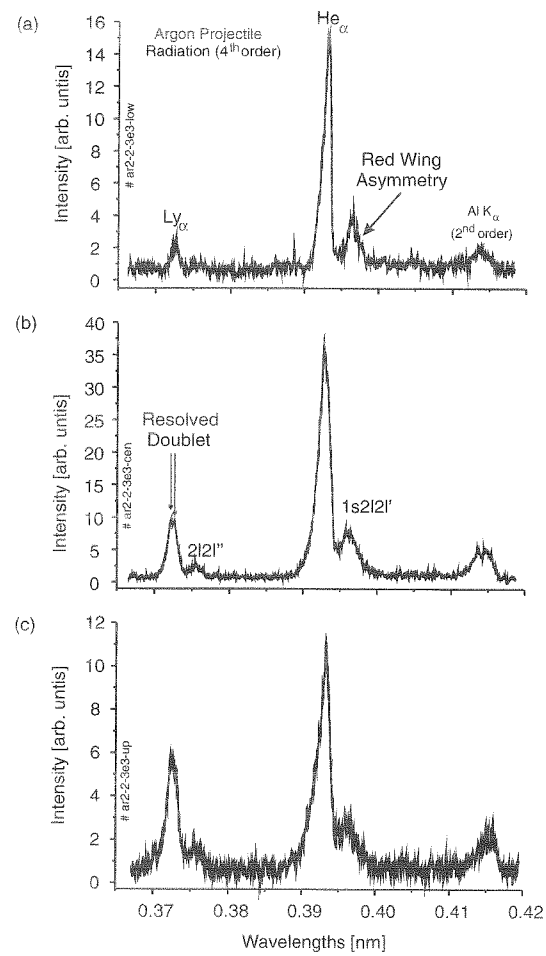

Figure 2: Space resolved X-ray spectra of H-, He- and Li-like argon projectiles emitted from the inner volume of an extended aerogel target

References

[1] I.Yu. Skobelev et al., JETP **81**, 692 (1985).

[2] O.N. Rosmej, F.B. Rosmej, 21st EPS Conference Proceedings on Controlled Fusion and Plasma Physics, Montpellier, France, Vol. III, p. 1292 (1994)

[3] F.B. Rosmej 1997, J. Phys. B Lett. **30**, L819.

This work is supported by the BMBF.

Optical Beam Diagnostics

J. Wieser[1], C. Constantin[2], E. Dewald[1], J. Jacoby[1], S. Udrea[2], D. Varentsov[2]
[1]*GSI-Darmstadt*, [2]*TU-Darmstadt*

The plasma-lens used at the HHT cave has been demonstrated to be a unique tool for shaping high energy ion beams into hollow beam spots [1] and achieving focal diameters, that are not accessible with regular magnets. However, electric currents on the order of 400kA within 9μs are necessary to achieve 10cm focal length. These currents, and the preionization pulses necessary for stable plasma formation, induce strong floating of the nearby ground-potentials, thus hindering low level electric measurements. In particular time resolved measurements of ion beam pulse intensities are strongly influenced by the plasma lens firing, as shown in Fig. 1.

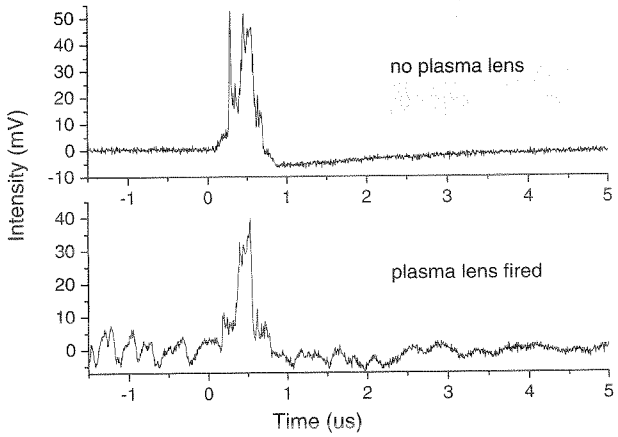

Figure 1: Fast current transformer signals of two different SIS pulses, without (upper) and with plasma lens fired (lower curve).

A first setup to circumvent this electric noise problem was installed, measuring the light emission from ion beam excited neon gas with a Si-PIN diode. Due to the optical measurement of the beam current, the system is rather insensitive to potential fluctuations and electric noise. A CF-100 double-cross was filled with 1bar neon, and the optical detector was placed in a distance of 0.5m. A D=2.5 neutral density filter had to be used for not overexposing the detector with an ion beam current of 2×10^9 Au particles per pulse. The signal to noise ratio increased by about one order of magnitude, without any additional means of shielding the signal lines (Fig.2).

Without plasma lens firing, the fast current transformer reflects well the temporal beam structure, except a negative overshoot after fast intensity drops. In order to simulate the optical signal, direct beam excitation of the light emitting species (neon 3p levels) is assumed, which then are supposed to decay within their natural lifetime of about 10ns. However, a 100ns decay time has to be used in order to coincide simulated and measured pulses, as shown in Fig. 3. This means that the 3p levels in neon, although no resonance transitions, are optically not thin and a linear response is not inherently given with the experimental conditions, used.

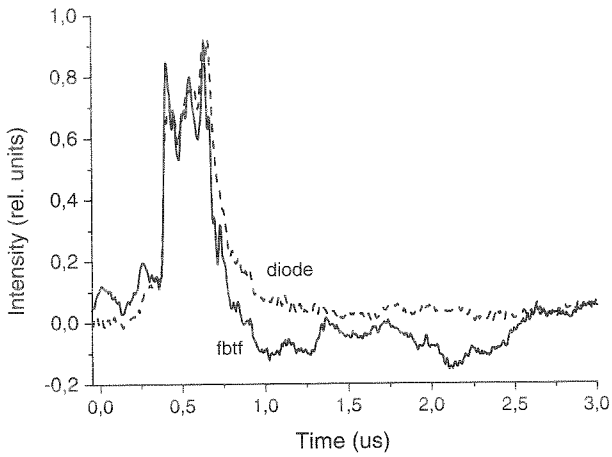

Figure 2: Comparison of the fast current transformer signal (fbtf, solid) and the optical signal (diode, dashed), with plasma lens fired. The entire pulse duration is 1μs.

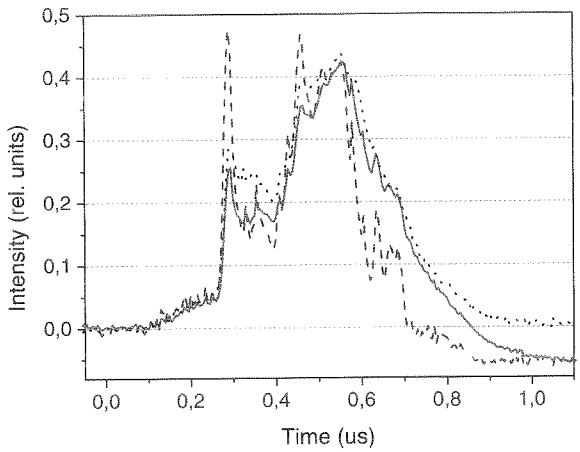

Figure 3: Without plasma lens fired, the signals of the fast beam transformer (dashed), the simulated optical signal (solid) and the measured diode signal (dotted) are given.

In a next set up, xenon will be used as a target gas, with a detector only sensitive to the molecular ion continuum radiation, not observing the 6p-6s transitions. In this way, a linear response over several orders of magnitude in ion beam intensities will be possible to be detected, with a linear response on a 5ns time scale, up to excitation densities of 10^{17}cm^{-3}.

work funded by BMBF

References

[1] U.Neuner et al., Phys. Rev. Lett. 85, 4518, (2000)

Diagnostics of Laser Initiated Plasma Channels for Ion Beam Transport

C. Niemann[1], D. Penache[2], A. Tauschwitz[2], F.B. Rosmej[2], S. Neff[1], R. Knobloch[1], D.M. Ponce[3]
R. Presura[1], H. Wahl[1], S.S. Yu[3], W.M. Sharp[3], D.H.H. Hoffmann[2]
[1] *GSI Darmstadt,* [2] *TU-Darmstadt,* [3] *Lawrence Berkeley National Laboratory (USA)*

Laser initiated, free standing discharge channels offer many attractive advantages for the transport and focusing of intense ion beams [1, 2]. Discharge plasmas can neutralize both current and space charge of such beams, while the azimuthal magnetic field provides strong focusing all the way through the channel. Experiments at GSI have produced 50 cm long stable plasma channels with peak currents in excess of 40 kA in 2 to 20 mbar NH_3 gas fill. The discharges are initiated by a CO_2 laser pulse, fired into the chamber along the chamber axis. Absorption of the laser causes strong gas heating. Subsequent expansion and rarefaction of the gas prepare the right conditions for a stable, reproducible discharge, suitable for ion beam transport. First experiments to study the ion optical properties of such channels were already reported in [3, 4]. During the last year the channel stability was considerably improved by a new CO_2 laser with an option for wavelength tuning. The wavelength can be adjusted to the P(32) transition for peak absorption, matching the $\nu = 950\ cm^{-1}$ vibrational mode in NH_3 [5]. In this way a large fraction of the laser energy is absorbed as the beam passes through the 50 cm long gas filled chamber, down to pressures of a few mbar (figure 1).

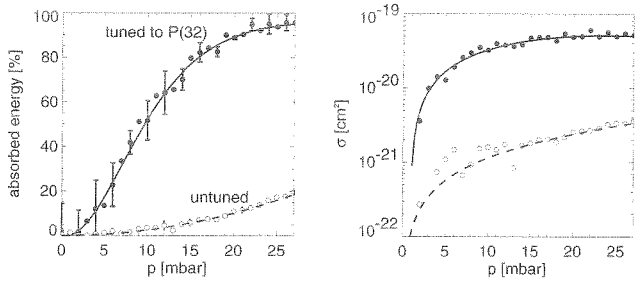

Figure 1: Improved laser gas heating due to laser wavelength tuning.

A set of plasma diagnostics was developed to gain a better understanding of the channel dynamics and the underlying physics. Schlieren measurements of neutral gas density gradients show a gas shock expanding radially with a velocity of a few $mm/\mu s$ while the discharge deposits its energy into the gas (figure 2). According to [6] this gas wall reduces the MHD instability growth rate and thus contributes to the stability of the channels. The plasma self emission was investigated by spectroscopy in the visible range. Electron densities around $10^{17} cm^{-3}$ can be estimated from Stark broadening of the observed hydrogen Balmer lines. Intensities of NII and NIII lines will be used to determine also the electron temperature. For more precise space resolved electron density measurements a Michelson imaging interferometer was set up. A pulsed Nd:YAG laser beam at 1064 and 532 nm with a diameter of several cm probes the plasma twice from a side and is then recombined with an undisturbed reference beam. The observed fringe shift (figure 2) yields the line integrated refractive index. The space resolved radial refractive index

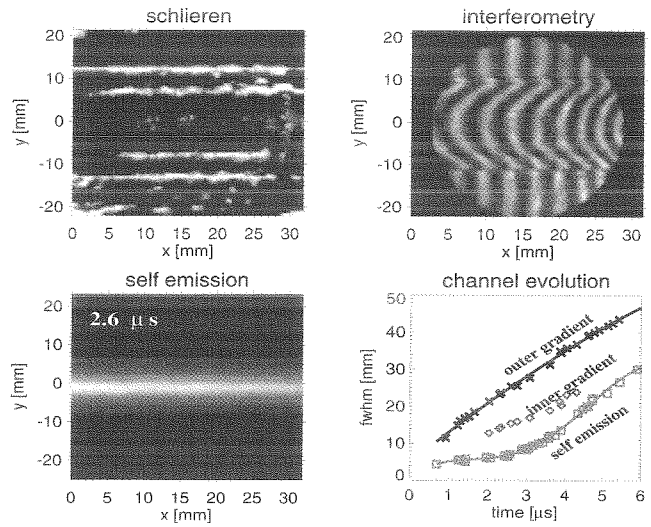

Figure 2: The channel as seen by different diagnostics.

profile follows from an Abel inversion. To distinguish between contributions from the electrons and the neutral gas to the refractive index the measurements were performed at both wavelength in subsequent discharges. A maximum fringe shift around 6 was observed at 1064 nm. A computer aided fringe counting method yields the fringeshift with a precision of around 0.2 fringes. Preliminary results are in agreement with spectroscopic density measurements.
These measurements in combindation with the ion optical investigations [7] will ultimately lead to a comprehensive understanding of the channel stability and dynamics. The results can then be used to engineer channels most suited for ion beam transport.

References

[1] A. Tauschwitz et al., Fus. Eng. Des. **32-33**, 493-502 (1996)
[2] S.S. Yu et al., Nucl. Instr. and Meth. A **415**, 174-181 (1998)
[3] D. Penache et al., GSI Report 1999(00), GSI-2000-1, p.125
[4] A. Tauschwitz et al., Proceedings: IFSA 1999, Elsevier, p. 521-526
[5] J.N. Olsen, J. Appl. Phys. **52**(5), 3279 (1981)
[6] W.M. Mannheimer et al., Phys. Fluids **16**, 7, 1126 (1973)
[7] A. Tauschwitz et al, this annual report

This work is supported by the BMBF

Ion Beam Transport in Discharge Channels: Interpretation of Experimental Results*

A. Tauschwitz, C. Niemann, D. Penache, S. Neff, R. Knobloch, H. Wahl, D.H.H. Hoffmann
GSI Darmstadt and TU Darmstadt

Discharge plasma channels are of interest for the current and space charge neutralized transport of intense ion beams for various applications. The channel transport in laser initiated discharges is currently studied at GSI [1]. In a series of experiments an uranium beam from the UNILAC with 11.4 MeV/u was transported through the 50 cm channel and was stopped in a fast scintillator behind the discharge. The picture at the left hand side of fig. 1 shows the force free drifting beamlets that are formed by a mask in front of the channel before the discharge is ignited. The mask consists of two perpendicular lines of 1-mm diameter holes with a distance of 2 mm between holes, forming a cross with the central hole missing. Three holes are drilled on each side, only two are visible, the last hole is clipped by the aperture in the cathode in front of the scintillator. An additional beamlet in the lower left sector serves to identify the orientation of the mask. The other seven pictures are taken at different times during the discharge with an exposure time of 100 ns. The exposure time, total

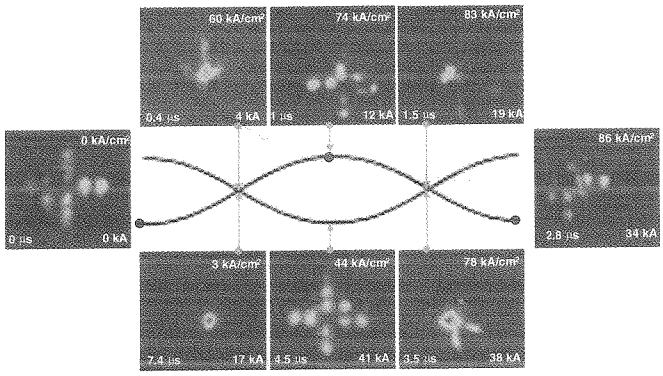

Figure 1: Image of the pepper-pot mask on the scintillator at different times during the first half wave of the current pulse

discharge current, and current density at exposure time are marked on the pictures. A representation of the betatron oscillation of the beamlets in the channel is shown in the center of fig. 1. The position of the asymmetric beamlet is marked by a dot. Arrows show at what phase of the oscillation the beamlets were intersected by the scintillator at the end of the discharge channel depending on the sinusoidal discharge current waveform. From the distortion of the image at 0.4 µs where a focal spot is expected, and at 1 µs where an inverted image is expected, it is obvious that the focusing field is nonlinear. At 1.5 µs the focusing is more linear and due to the expanding radius of the discharge channel the outermost beamlets become now visible as blurred spots below and right of the central spot. At a radius of 6 mm these beamlets were focused mainly in the decaying nonlinear magnetic field surrounding the discharge channel. At 2.8 µs the beamlets have performed a full betatron oscillation and the image of the mask is inverted twice. The outermost beamlets appear again as two blurred lines in the lower right sector of the cross. Although the total current is still increasing the current density and bending power of the channel is decreasing at 3.5 µs. The second focus is visible, the outermost beamlets show up more clearly now because the channel has expanded further and these beamlets were only for a short distance focused in the nonlinear field surrounding the channel. The peak current of 41 kA is reached at 4.5 µs, but due to the rapid expansion of the discharge channel the bending power is further decreasing so that the inverted image of the mask becomes visible again. At 7.4 µs the first focal spot appears again on the scintillator. By that time the channel has expanded to a diameter of more than 2 cm and the small size of the focus indicates a very linear field in the channel.

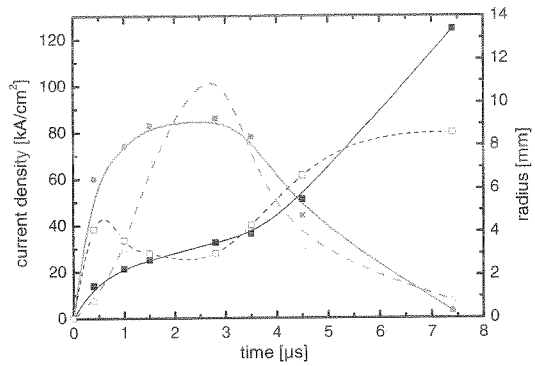

Figure 2: Development of current density and channel radius for a discharge in 17 mbar NH_3. Dashed lines are inferred from the beam transport assuming a homogeneous current distribution, solid lines from direct measurements.

An interpretation of the transport results is given in fig. 2. Measurements of the discharge current were evaluated together with framing pictures of the discharge channel to determine the discharge radius and the current density. For a first simple modelling the FWHM value of the light emission from the channel was assumed as the width of a homogeneous current distribution. The resulting radius and current density are plotted as solid lines in fig. 2.

$$J = \frac{2\pi\Re}{\mu_0}\left(\frac{kL}{L}\right)^2 \qquad (1)$$

Assuming again a homogeneous current flow in the discharge a current density J was determined according to equ. 1 from the phase of the beam betatron motion of the beamlets from fig. 1 with the beam rigidity $\Re$ and a phase kL of the betatron oscillation at the end of a channel with length L. For the first focal point, the inverted image, the second focus, and for the twice inverted image the phases of the oscillation are $\pi/2$, π, $3\pi/2$, and 2π respectively. The current density from equ. 1 and the resulting discharge radius are plotted in fig. 2 with dashed lines. Deviations during the first microsecond can be explained by the skin effect in the discharge, deviations at the end of the current half wave are probably due to the inverse skin effect [2].

References

[1] A. Tauschwitz et al. Proc. Int. Conf. on Inertial Fusion Sciences and Applications (IFSA), Bordeaux, 521 – 526 (1999)

[2] M.G. Haines, Proc. Phys. Soc. **74**, 576-586 (1959)

* work supported by BMBF

Electrical Conductivity Changes Induced by High Intensity Heavy Ion Beams in Metallic Targets

S. Udrea[1], E. Dewald[2], C. Constantin[1], D. Varentsov[1], J. Jacoby[2], U. Neuner[2], A. Tauschwitz[1], P. Spiller[2], D.H.H. Hoffmann[1,2]
TU-Darmstadt[1], GSI-Darmstadt[2]

The electrical conductivity of matter under extreme pressure and/or temperature conditions is of fundamental as well as practical interest [1]. The availability of high intensity heavy ion beams at GSI makes it possible to drive matter to extreme conditions, either through direct interaction or shock wave compression. As previously reported [2], we developed a method for measuring the mean electrical conductivity of plasmas created by direct interaction. During the last year this method was applied to obtain first experimental results on electrical conductivity changes induced by the interaction of high intensity heavy ion beams with solid (metallic) targets.

For the experiments Pb, Cu, Ag and Al were used as target materials. All the targets consisted of a 0.25mm diameter and 10mm long wire fixed on an insulating support and connected to the diagnostics device through a 50Ω coaxial cable. Measurements were done using two different positions of the target, namely, perpendicular to the focused ion beam due to an easier mechanical adjustment of the wire related to the beam, and along the focused ion beam which is demanding in terms of alignment but should give better measurement precision. During the different beamtimes ion beams with the following characteristics were used: ^{83}Kr, 300MeV/u, $1\div2\cdot10^{10}$ ions/bunch; ^{197}Au, 300MeV/u, $1\div2\cdot10^{9}$ ions/bunch; ^{18}O, 200MeV/u, $1\div2\cdot10^{10}$ ions/bunch; ^{40}Ar, 300MeV/u, $5\div8\cdot10^{10}$ ions/bunch.

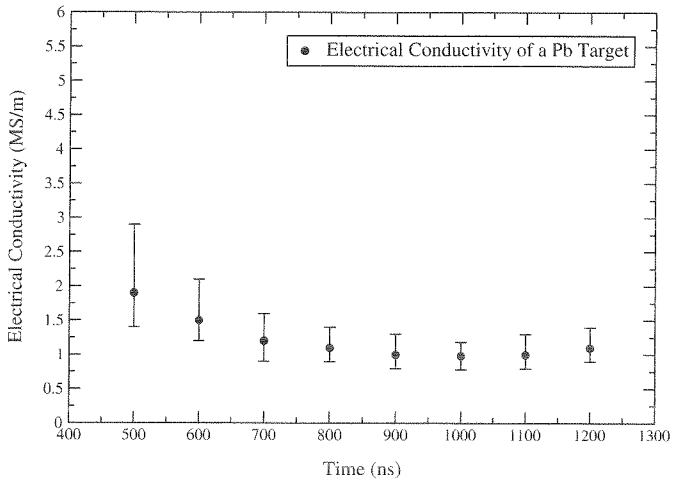

Figure 1: Mean electrical conductivity of a Pb target heated by a ^{18}O beam, with an intensity of $2\cdot10^{10}$ions/bunch, and focused to 0.7mm FWHM. The time is given with respect to the beginning of the irradiation.

The electrical signal obtained from the target is proportional to the changes of its resistance and thus to the changes in the mean electrical conductivity. Figure 1 shows the time evolution of the electrical conductivity of a Pb target irradiated by an ^{18}O beam.

The measurements show that at the end of the beam irradiation, the conductivity of the target corresponds to that of metals at temperatures of about 10^{-1}eV, and solid state density [3]. Due to the hydrodynamic expansion of the target, the conductivity drops in time, thus the electrical resistance grows. The rate at which this conductivity drop takes place depends strongly on the energy deposited in the target by the ion beam (i.e. on ion species and energy, beam intensity and focusing, and target material) and the thermodynamic properties of the target. This differences are shown in Figure 2.

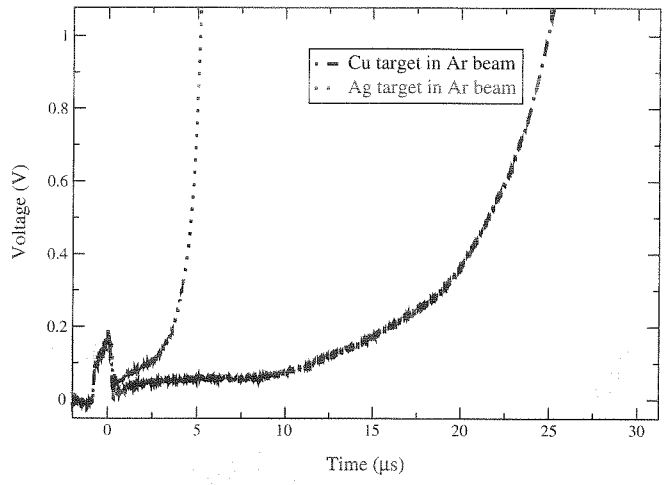

Figure 2: Electrical signals from Cu and Ag target heated by a ^{40}Ar beam, with an intensity of $7\cdot10^{10}$ions/bunch, and focused to 1.0mm FWHM. The beam bunch is visible arround t=0.

Acknowledgements: The authors acknowledge the help of Dr. N.A. Tahir and A. Kozyreva in understanding the theoretical aspects of these experiments and the numerical simulations of the hydrodynamics of the target. This work is supported by the BMBF.

References

[1] G.W. Collins et al., Science 281 (1998) 1178
[2] S. Udrea et al., GSI Scientific Report 1999
[3] Gmelins Handbuch der Anorganischen Chemie, Verlag Chemie GmbH, 1972

Schlieren investigations on pressure waves induced by the heavy ion beams in solid targets

C. Constantin[1], E. Dewald[2], C. Niemann[2], S. Udrea[1], D. Varentsov[1], U.N. Funk[1], D.H.Hoffmann[1]
J. Jacoby[2], U. Neuner[2], P. Spiller[2], A. Tauschwitz[1]
TU-Darmstadt[1], *GSI-Darmstadt* [2]

The intense relativistic heavy ion beams generated in the heavy ion synchrotron (SIS) of GSI offer the possibility to study the matter under extreme conditions. This is a subject of many on-going experiments at HHT area of GSI, such as investigations on the hydrodynamical evolution and cold compression of the matter supressed to the high energies delivered by the ion beam. The adiabatical cold compression of solid state matter is relevant for equation of state (EOS) studies including phase transitions to metallic state [1]. In one of these experiments a $^{83}Kr^{36+}$ ion beam with $2 \cdot 10^{10}$ particles/pulse, 300 MeV/u energy and 700 ns pulse duration was stopped in a solid layered target which is described in the graphic below (fig.1).

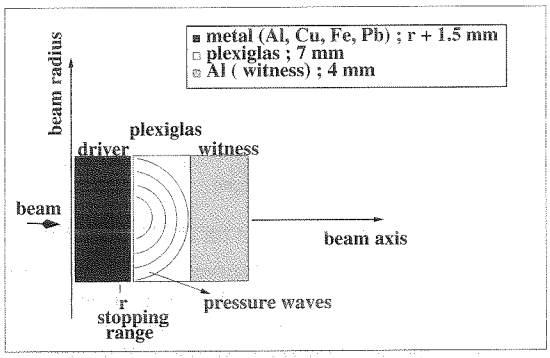

Figure 1: The target design: metal driver, 7 mm plexiglas window, 4 mm Al witness for observing the reflexions on interfaces between different materials.

After the beam is stopped in the driver pressure waves are launched and propagate in the plexiglas. To visualise and characterise them a schlieren technique was employed. Schlieren method is based on the bending of light rays when passing through refractive index gradients perpendicular to the optical path. The perturbances induced by the pressure waves in the target create regions of density gradients which will deflect some rays of the initially parallel laser beam towards the higher densities; these rays will no longer follow the parallel beam which is blocked by a beam stop put in the focus of the laser beam. They will pass near by and will be recorded on the detectors.The time resolved detection in this case was done by a streak camera working in a 10 μs streak time mode. The time resolution given by the streak slit width was of 180 ns and a very strict focusing on the target insured the space resolution. A framing camera was mounted together with the streak camera for two dimensional visualisation of the shock front. The 2D pictures so obtained showed a spherical wave expanding in time. From the streak pictures it was possible to determine the propagation velocity, which was found to be slightly higher than the speed of sound in plexiglas (2.6 km/s). The velocity and the consequently determined pressure values [2] depend on the heavy ion beam energy deposition in the driver material. For the Kr ion beam and all four materials this values are tabulated below (table 2).

species	driver	velocity [km/s]	pressure [Gpa]
$^{83}Kr^{36+}$	*Al*	2.82	0.26
	Fe	2.74	0.21
	Cu	2.70	0.16
	Pb	2.92	0.40

A typical behaviour for shock waves is to split whenever an interface between two materials with different acoustic impendences is encountered [3]. Due to this fact multiple pressure waves could be seen in the experimental pictures together with their reflections on the plexiglas boundaries (fig.2). Future experiments will consist in several optimiza-

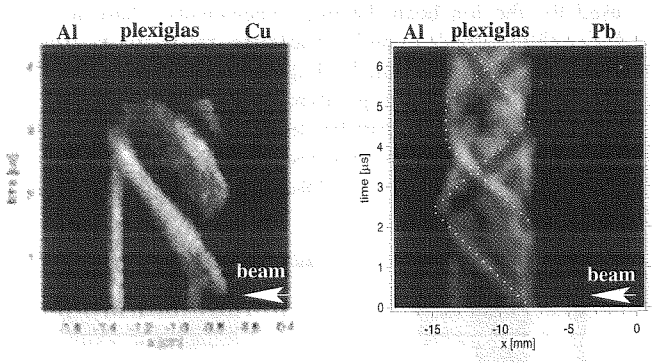

Figure 2: Experimental picture of a Pb-plexiglas-Al and Cu-plexiglas-Al target shooted with a Kr ion beam.

tions regarding the target geometry and moddeling of the shock front, i.e. to obtain planar shock waves, much more effective also from the investigation point of view. As a result, also an increase in the compression factor (around 0.04 in the actual conditions) is expected. The experimental set-up will be oriented towards absolute measurements of three main parameters: velocities of the shock wave propagation, pressures behind the shock waves and densities in the sample material. These results would constitute reliable benchmarks for the theoretical simulations and EOS studies.

Acknowledgments: We thank BMBF for supporting this work.

References

[1] N.A. Tahir, D.H.H. Hoffmann et al.: Phys.Rev.E, vol.16, no.2 (2000) 1975-1980

[2] Bao-Ping Zhang, F. Mueller: High Temperatures-High Pressures, volume 16 (1984) 475-483

[3] K. Baumung, H.J. Bluhm et al.: Laser and Particle Beams, vol. 14, no.2 (1996) 181-209

Shadowgraphy measurements on the heavy ion beam interaction with solid targets

E. Dewald[1], C. Constantin[2], S. Udrea[2], D. Varentsov[2], D.H.H. Hoffmann[2,1], J. Jacoby[1], U. Neuner[2], A. Tauschwitz[2], J. Wieser[1], N.A. Tahir[2], A Kozyreva[2], U. Geißler[2], M. Roth[1], P. Spiller[1] and R. Bock[1]
[1]GSI Darmstadt, [2]TU-Darmstadt

At the HHT experimental area, strongly coupled plasmas are created by the interaction of the SIS heavy ion beams with solid targets. To obtain a high energy deposition in the target, the ion beam is focused by the plasma lens [1] to diameters smaller than 1 mm in the focus. The generated plasmas have densities close to the solid state density, volumes of several mm^3 and temperatures up to 1 eV. The characterization of the matter under such extreme temperatures and pressures is of relevance for equation of state (EOS) studies, in astrophysics for understanding the formation of heavy elements in supernovae, for designs of future heavy ion driven Inertial Fusion Experiments (IFE) and others.

A wide range of optical diagnostics, such as shadowgraphy, time resolved spectroscopy in visible and VUV ranges, and schlieren techniques were recently developed to study the target behavior at the interaction with the ion beam.

Up to now, metallic and cryogenic gas crystal targets [2] were used for the ion beam heating experiments, characterized by backlighting shadowgraphy and time resolved spectroscopy. For these experiments the backlighter was a high energy (250 J) Xe flashlamp and the target dynamics was detected with a fast multiframing camera, capable to acquire simultaneously eight frames with an exposure time above 10 ns.

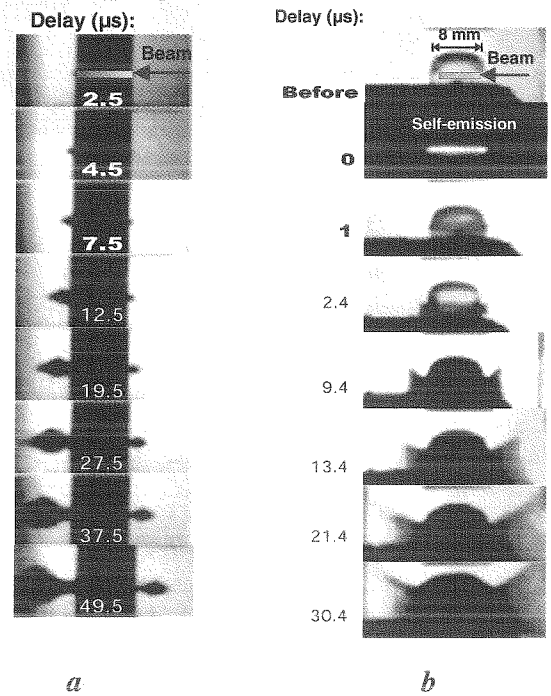

a *b*

Figure 1: Superrange target dynamics in beam-target interaction experiments for 1 μs beam duration (50-200 ns exposure):
(a) 6 mm thick Pb plate, Kr beam, 300 MeV/u, $N=10^{10}$ ions,
(b) 8 mm Ne crystal, U beam, 200 MeV/u, $N=10^9$ ions

Figure 1 shows typical hydrodynamics of targets larger than the ion beam range, for metallic plates and cryogenic gas crystals. Due to the non-uniform energy deposition, for the Pb plate (Fig. 1a) the matter expansion in the Bragg peak region is clearly more pronounced than in the direction opposite to the beam as it can be seen also in Figure 2. Moreover, due to a strong radial temperature decrease from the axis, the heated expanding matter has a droplet shape. For EOS studies the experiments are simulated by the BIG2 two-dimensional hydrodynamic code. According to the simulation, a maximum temperature of 0.3 eV is reached in the plate by ion beam heating. The matter expansion velocity is used to benchmark the simulation.

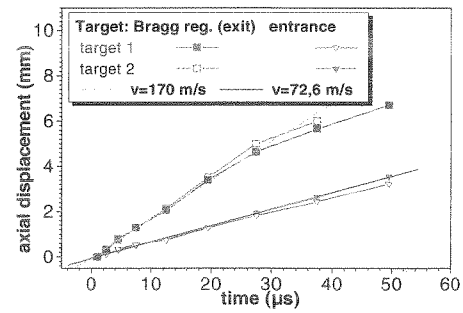

Figure 2: Axial matter expansion for the Pb plate (Fig. 1a)

Quite a different behavior was observed for the cryogenic gas targets, i.e. for most of the crystals there is a symmetric matter expansion even for targets thicker than the ion beam range (Fig.1b). This is mainly explained by the drilling effect of the beam which shifts the range during the beam pulse beyond the target thickness. This can be experimentally observed from the target self-emission and 1 μs after the beam (Fig 1b). For a specific energy deposition of 6.8 kJ/g, a maximum temperature of 0.48 eV is reached in the Bragg peak region according to the BIG 2 simulation. Furthermore, the Bragg peak in the crystals is less pronounced than in the metal plates which results in a more uniform energy deposition. A high expansion velocity (470 m/s) was observed in the first 5 μs, after which it decreases in 10 μs to a constant velocity of 140 m/s. For cryogenic crystals this behavior was already predicted in [3].

Another interesting feature is that the radial shockwave generated by the heated matter destroyes the crystal structure and consequently its transparence as it can be observed in Fig. 1b for the pictures taken 1, 2.4 and 9 μs after the beam.

Several experiments were performed using different ion beams, cryogenic crystals (H, D, Ne, Ar, Kr, Xe) and metallic plates.

The shadowgraphy measurements give an insight into the beam-target interaction and into the generated plasmas. Furthermore, the matter dynamics can be used to benchmark the simulation code as well as the used EOS data.

Acnowledgement: This work was supported by BMBF.

References

[1] M.Stetter et al., Fus. Eng. Des. 32-33(1996) 503
[2] U.N.Funk et al., Nucl. Inst. And Meth.A 415 (1998) 68
[3] M. Dornik, Ph.D. Thesis, TU Darmstadt, 1997

Necessity for Strong Bunch Compression for the SIS-200 Beam for FRS and Plasma Physic Experiments

N. A. Tahir[1], A. Kozyreva[1], D. H. H. Hoffmann[1,2], P. Spiller[2], A. Shutov[3]
[1]TU Darmstadt, [2]GSI Darmstadt, [3]ICPR Chernogolovka

GSI is planning to build a new synchrotron, SIS-200, that will have a magnetic rigidity of 200 Tm. It will be designed to accelerate 10^{12} uranium particles with energy ranging from 200 MeV/u to 1 GeV/u. The plasma physics experiments will require a lower energy of 200-400 MeV/u while the fragment separator (FRS) experiments would be carried out using 1 GeV/u.

The temporal profile of the beam is very important for these experiments. To demonstrate this we simulated hydrodynamic and thermodynamic response of a "sub-range" solid lead cylindrical target that is irradiated with the future SIS-beam with parameters given above. These simulations have been done using a two-dimensional computer code, BIG-2 [1]. The beam-target geometry is shown in Fig. 1.

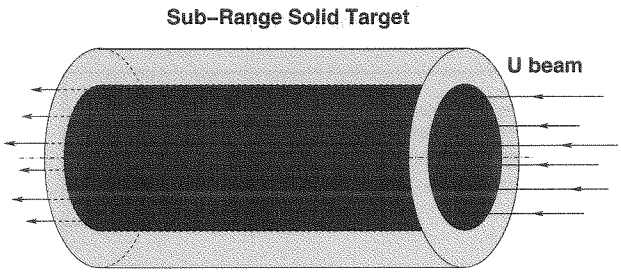

Figure 1: A "sub-range" lead target irradiated by 1 GeV/u uranium beam.

We considered two beam power profile configurations. First we assumed five identical parabolic bunches as showm in Fig.2. Each bunch is 140 ns long and every bunch contains 2×10^{11} particles. Bunch separation is also 140 ns so that the duration of the pulse is 1260 ns.

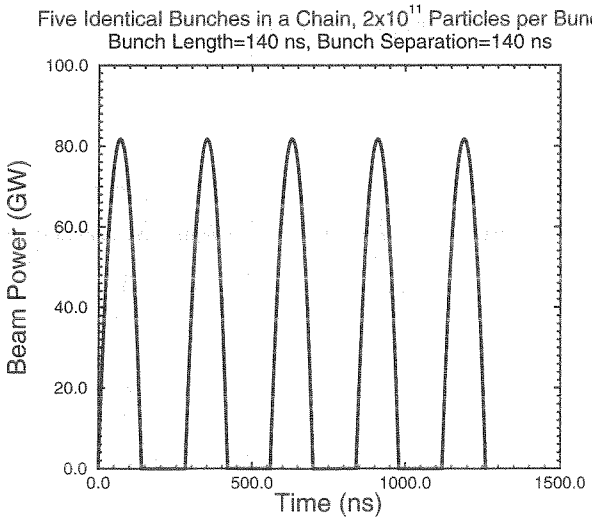

Figure 2: Beam Power vs Time.

In Fig. 3 we plot the energy of the ions escaping the target as a function of time along the axis for two values of the beam radius (FWHM), 0.5 mm and 1.0 mm respectively. It is seen that innitially, 75 % of the energy escapes the target. However at t = 140 ns, that is at the end of the first bunch, the fraction of the energy escaping the target increases considerably due to the hydrodynamic expansion of the target material caused by beam heating. The target continues to expand for the next 140 ns until the second bunch starts at t = 280 ns. Figure 3 shows that almost the total ion energy escapes the target. It is therefore clear that due to the target distortion caused by the first bunch, the ions that are delivered in the remainig four bunches pass through the target without interaction. Bulk of the beam energy is therefore wasted. In case of plasma physics experiments, such a reduction in beam-target coupling would lead to a strong reduction in temperature and pressure that could be achieved. For the FRS experiments, the production of fragments will decrease drastically. Also the fragment separator can accept only a few percent change in the energy of the escaping ions, otherwise most of the secondary beam will be lost.

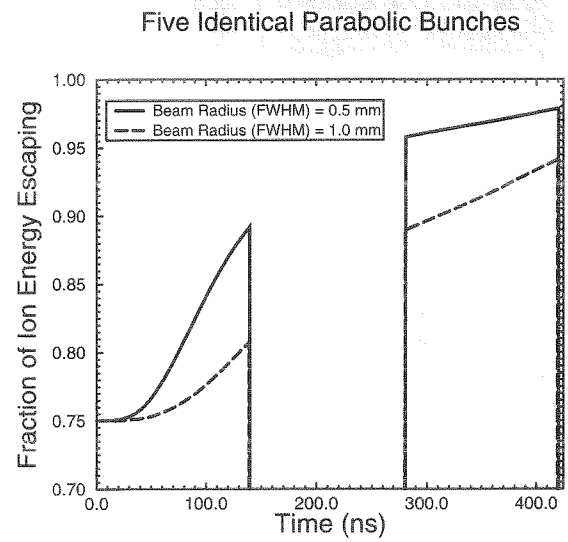

Figure 3: Energy of Ions Escaping the Target vs Time.

These diffuculties may be overcome by using a highly compressed single bunch with a length = 50 ns. For further details see Reference [2].

References

[1] V. E. Fortov et al., Nucl. Sci. Eng. 123 (1996) 169.
[2] N. A. Tahir, A. Kozyreva, P. Spiller, D. H. H. Hoffmann and A. Shutov, Phys. Rev. E (2001) 036407.

Supported by the German ministry for education and science (BMBF)

Simulation of Hydrogen Metallization Experiment Using the SIS-200

N. A. Tahir[1], A. Kozyreva[1], D. H. H. Hoffmann[1,2], A. Shutov[3], J. A. Maruhn[4], P. Spiller[2], U. Neuner[2], A. Tauschwitz[2], J. Jacoby[2], M. Roth[2], R. Bock[2], H. Juranek[5], R. Redmer[5]

[1]TU Darmstadt, [2]GSI Darmstadt, [3]ICPR Chernogolovka, [4]Universität Frankfurt, [5]Universität Rostock

This contribution presents two-dimensional hydrodynamic simulations of a cylindrical multi-layered target that contains a layer of frozen hydrogen and is irradiated by a uranium beam. These simulations have been done using the BIG-2 [1] computer code. The beam-target arrangement is shown in Fig. 1. The target is 3.0 mm long and the radius of the hydrogen layer is 0.5 mm whereas the outer target radius is 3.0 mm. The right face of the cylinder is irradiated with the SIS-200 beam. The beam consists of 10^{12} particles of U 400 MeV/u and the pulse length = 50 ns. The beam spot has an annular shape (ring shape). The inner radius of the focal spot ring is also 0.5 mm while the outer radius is 2.0 mm. This avoids direct heating of the hydrogen region. The range of 400 MeV/u uranium ions in solid cold lead is 4.25 mm. The energy deposition is therefore approximately uniform in the lead shell because the Bragg peak lies outside the target.

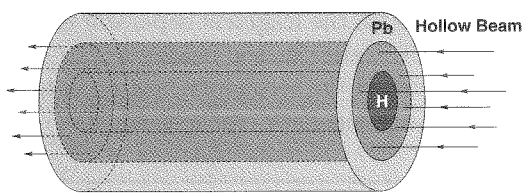

Figure 1: A Multi-Layered Cylindrical Target Driven by 400 MeV/u Uranium Beam

Figure 2 shows the density vs radius at L = 1.5 mm (middle of the cylinder) in the hydrogen region at different times during the implosion. It is seen that at t = 100 ns, a shock has entered into the hydrogen region and the shock front is at r = 150 μm. Moreover the hydrogen-lead boundary has moved from an initial position of 500 μm to about 350 μm. The shock converges at the cylinder axis at t = 115 ns and a return shock developes that is seen moving outwards at t = 120 ns. The return shock is again reflected at the hydrogen-lead boundary that continues to move inwards slowly. As a result of this multiple shock reflection and slow adiabatic compression, the hydrogen layer is compressed to physical conditions predicted for hydrogen metallization. These include a density of about 1 g/cm^3, a pressure of above 3 Mbar and a temperature of a few 0.1 eV. The SESAME equation-of-state data is used for hydrogen.

In Fig. 3 we plot the density, pressure and temperature vs radius in the hydrogen region at L = 1.5 mm at t = 170 ns. It is seen that the density is about 1 g/cm^3, the average temperature is about 0.2 eV while the pressure is above 5 Mbar. These conditions exist between t = 160 ns - 200ns which provides with enough time for experimental investigations. For details see Refs. [2,3].

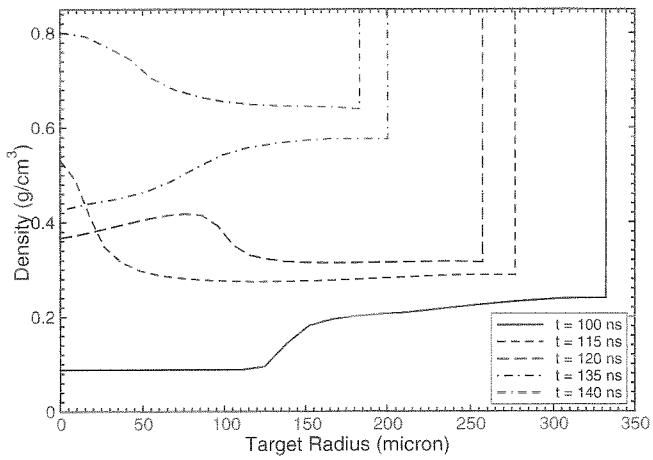

Figure 2: Density vs Target Radius at L = 1.5 mm

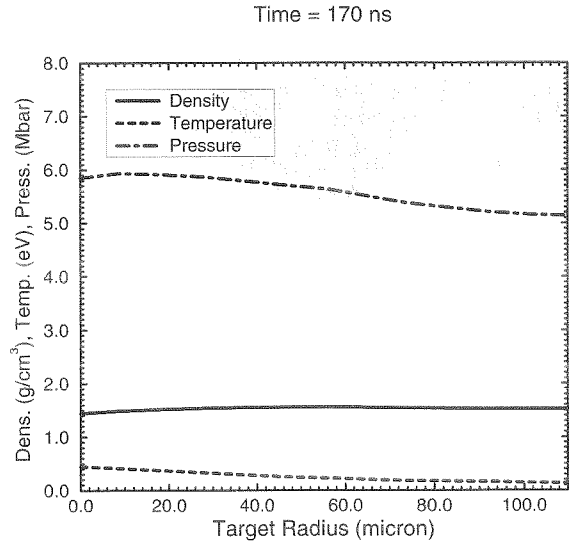

Figure 3: Density, Temperature and Pressure vs Target Radius at $L = 1.5$ mm and at $t = 170$ ns.

References

[1] V. E. Fortov et al., Nucl. Sci. Eng. 123 (1996) 169.

[2] N. A. Tahir, D. H. H. Hoffmann, A. Kozyreva, A. Tauschwitz, A. Shutov, J. A. Maruhn, P.Spiller, U. Neuner, J.Jacoby, M.Roth,R. Bock, H. Juranek and R. Redmer, Phys. Rev. E 63 (2001) 016402.

[3] N. A. Tahir, D. H. H. Hoffmann, A. Kozyreva, A. Tauschwitz, A. Shutov, J. A. Maruhn, P.Spiller, U. Neuner, J.Jacoby, M.Roth,R. Bock, H. Juranek and R. Redmer, Contrbu. Plasma Phys. (2001) In Print.

Supported by the German ministry for education and science (BMBF)

Calculation of the Current Density Distribution in a Plasma Lens to Produce Ring-like Ion Beam Profiles

S. Hakuli, U. Neuner
GSI Darmstadt and Institut für Kernphysik, TU Darmstadt

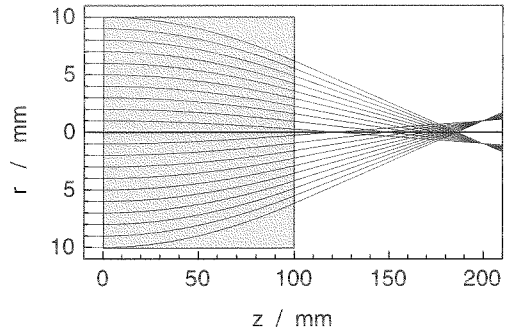

Figure 1: Schematic of focusing a 10 mm radius parallel ion beam into a 1 mm radius ring with a 100 mm long plasma lens with a negative radial gradient of the current density and a 100 mm long drift length.

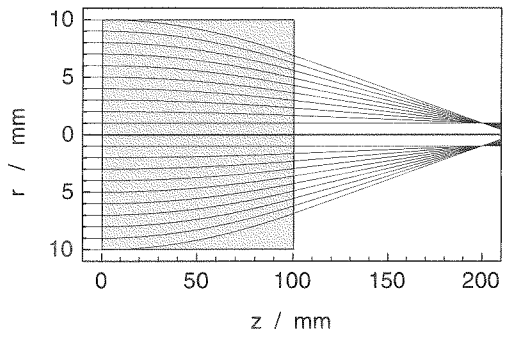

Figure 2: Same as Fig. 1 with a positive radial gradient of the current density.

A good understanding of the shaping of intense ion beams into hollow cylindrical form [1] was achieved by interpreting the experimental data [2] with numerical calculations.

The ion beam is shaped in a plasma lens, where an axially directed current produces an azimuthally directed magnetic field. In this field the ion trajectories of an initially parallel beam are bent towards the axis. This allows for the two focusing schemes plotted in Figs. 1 and 2, where all ion trajectories between 1 and 10 mm initial radius converge into a ring in the focal plane 100 mm after they exit from the plasma lens.

We simulated this focusing for a zero emittance beam in paraxial approximation. Since ions pass through radial regions of different focusing strength inside the plasma lens, the calculations were performed as follows: We divided the plasma lens into 100 thin slices, in which the radial variation of the trajectory is so small, that the focal strength can be approximated to be constant. The shape of the trajectories results from a calculation of the Lorentz force inside the plasma lens' slices. The radial current density distribution is discretized into shells of constant values. Increasing in radius one-dimensional nonlinear optimizations

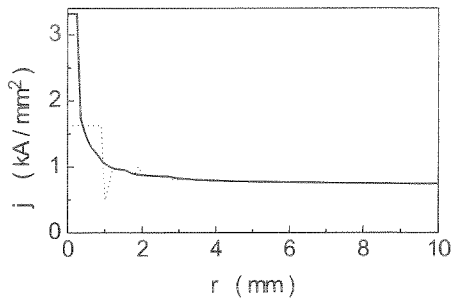

Figure 3: Current density distribution in the pinch mode.

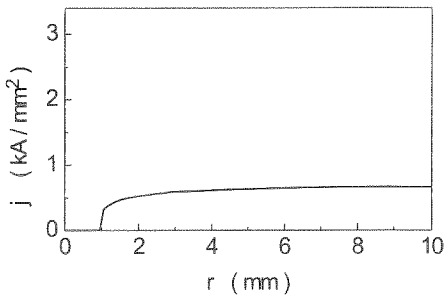

Figure 4: Current density distribution in the skin mode.

yield these values for the two focusing modes as mentioned above.

The solid curve in Fig. 3 shows the calculated current density in the plasma lens as a function of radius, that leads to focusing into a ring as shown in Fig. 1. Such a negative radial gradient can be realized in a pinch-like discharge. The dotted curve is also a valid solution for this focusing, however it seems unlikely to be realized in any known discharge. The current density in Fig. 4 corresponds to the focusing mode shown in Fig. 2. Positive radial gradients like this can be realized in skin effect dominated discharges.

With these results we now can experimentally optimize the plasma lens to produce ideal hollow cylinder shaped beams. They are required by the future experiments [3, 4, 5, 6].

References

[1] U. Neuner *et al.*, Phys. Ref. Lett. **85**, 4518 (2000).
[2] U. Neuner *et al.*, GSI-2000-1, 127 (2000) and GSI-2000-2, 3 (2000).
[3] D. A. Callahan-Miller and M. Tabak, Nucl. Fusion **39**, 1547 (1999).
[4] D. A. Callahan-Miller and M. Tabak, Phys. Plasmas **7**, 2083 (2000).
[5] N. A. Tahir *et al.*, Phys. Rev. E **62**, 1224 (2000).
[6] N. A. Tahir *et al.*, Phys. Rev. E **63**, 016402 (2001).

Investigation of heavy ion tracks in polymers by transmission electron microscopy

A. Adla[1], V. Buschmann[1], H. Fuess[1], C. Trautmann[2]
[1] TU Darmstadt, [2] GSI Darmstadt

Bulk samples and thin sections of polyethylene terephthalate (PET) and polyimide (PI) were irradiated with Se and Pb ions of 11.4 MeV/u at the UNILAC. The creation of latent tracks and related structural changes were studied by means of transmission electron microscopy (TEM) using a 200 kV Philips CM200-UTW microscope (point resolution 0.17 nm). Due to relatively similar electron densities within organic polymers, staining helps to increase the imaging contrast and improve the radiation resistivity under the electron beam.

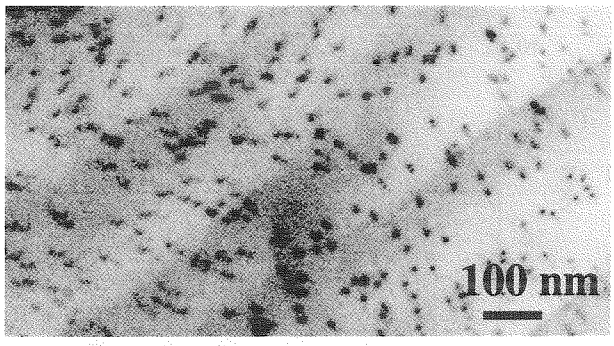

Fig. 1. TEM image of an originally 50 μm thick PET foil irradiated with Se-ions (6×10^{10} cm^{-2}, 900 MeV). The dark spots are the ion tracks decorated after irradiation by OsO_4.

Typical stains such as OsO_4 or RuO_4 contain elements with high atomic number and diffuse preferably into the amorphous regions of the polymer thus enhancing the contrast of different structural regions. We investigated several sample preparation techniques, e.g. staining in vapor phase or aqueous solution, applied at different stages before and/or after ultra-microtomy and ion irradiation.

Fig. 1 shows the TEM micrograph of a PET sample irradiated as an initially 50-μm thick foil. Subsequently, the film was stained (aq. OsO_4, 7 days) and cryo-sectioned perpendicular to the ion trajectories. The resulting ultrathin sections were stained again (2 h, OsO_4 vapor). The tracks are visible as dark spots indicating that the stain is preferentially accumulated in the amorphous track regions. The mean diameter is 12±3 nm. The areal density is in good agreement with the ion fluence.

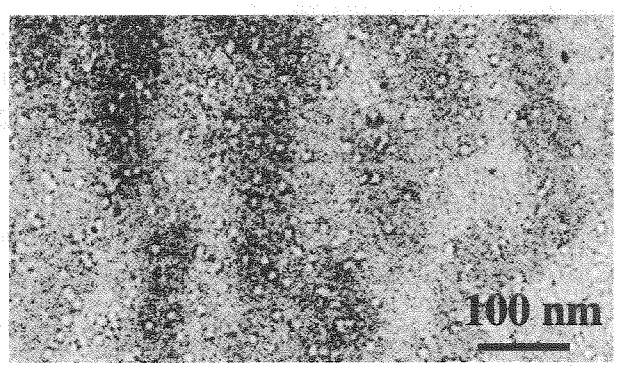

Fig. 2. TEM image of ultrathin section of PET, pre-stained (30 min, aqueous RuO_4) prior to irradiation with Pb-ions (5×10^{10} cm^{-2}, 2370 MeV).

The situation is quite different if pre-stained polymer samples are irradiated as thin sections (fig. 2). Tracks appear as light features of reduced contrast with a mean diameter of 9 ± 1 nm. The stain and probably even the polymer material are expelled from the track region by sputtering and outgassing. Under a tilted angle, the number of tracks is twice as large as expected because we image two spots per track, namely the impact region on the front and back side of the sample. The track cylinders in the bulk are visible, but the contrast fades rapidly during observation.

Compared to PET, the electron-beam resistance of PI is better, allowing imaging at even higher magnifications. Fig. 3 presents a single track in a pre-stained (aq. RuO_4, 2 h) and then irradiated 50-μm thick PI film. After ultramicrotomy, the thin section was stained again (OsO_4 vapor, 2 h). Note that in this case, tracks are imaged as bright regions although staining was performed after ion irradiation (cf. PET, Fig. 1). Since both, matrix and track regions, are amorphous, the selectivity of the post-staining process is apparently not high enough for preferential track decoration. In the matrix around the track, but not inside, the phase contrast of small crystalline areas of Ru or Os compounds can be recognized.

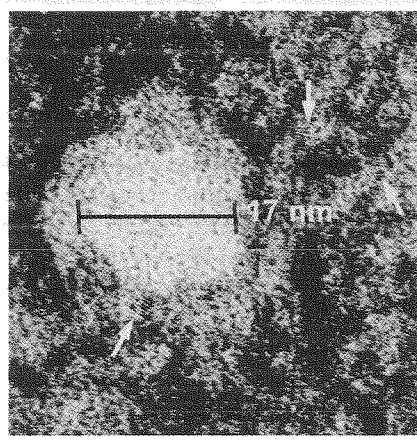

Fig. 3. High resolution TEM image of a single Pb-ion track in PI. The arrows indicate small crystalline areas in the track-surrounding matrix.

The track size observed here is in reasonable agreement however, slightly larger than diameters deduced earlier using other techniques such as small-angle x-ray scattering or IR-spectroscopy [1]. Also similar TEM studies on polyethylene [2] and on PI without staining [3] reported about 30% smaller track diameters. Finally, it should be mentioned that the precise determination of the track size in polymers using TEM is difficult due to the damage induced by the electron beam. The tracks may shrink or increase during imaging, making a direct comparison of different observations rather problematic.

[1] C. Trautmann, K. Schwartz, T. Steckenreiter, Nucl. Instr. Meth. B156 (1999) 162.
[2] J. Vetter, G. H. Michler, I. Naumann, Radiat. Eff. Def. Sol. 143 (1998) 273.
[3] Y. Eyal, K. Gassan, Nucl. Instr. Meth. B156 (1999) 183.

Tracks of swift heavy ions in graphite studied by STM

J. Liu [1,2], R. Neumann[1], C. Trautmann[1], C. Müller[1]
[1] GSI Darmstadt, [2] Institute of Modern Physics, Lanzhou, China

Cleaved samples of highly oriented pyrolytic graphite (HOPG) were exposed to various beams of Ni, Zn, Xe, and U ions (11.4 MeV/u) with a fluence up to maximally 2×10^{12} ions/cm^2. To vary the kinetic energy and thereby the energy loss (dE/dx) of the ions, aluminum degraders of different thickness were placed in front of the crystals. The topography of the irradiated samples was investigated by scanning tunneling microscopy (STM) with constant current mode and with mechanically prepared Pt-Ir tips.

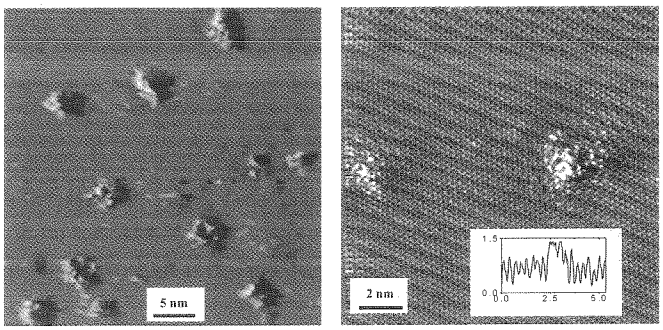

Fig. 1. STM images of original graphite surface bombarded under normal incidence with (left) 8×10^{11} U ions/cm^2 of 1.2 GeV and (right) 6×10^{11} Xe ions of 1.5 GeV. The inset shows a height profile across the hillock (scale in nm).

On the original surface, the tracks show extremely small hillock-like damage zones of mean diameters between 2 and 3.5 nm and heights of 0.3-0.9 nm (Fig. 1). Each protrusion is surrounded by the undisturbed crystal with lattice constant 0.246 nm. Fig. 2. presents the mean track diameter as a function of energy loss as calculated with the TRIM code.

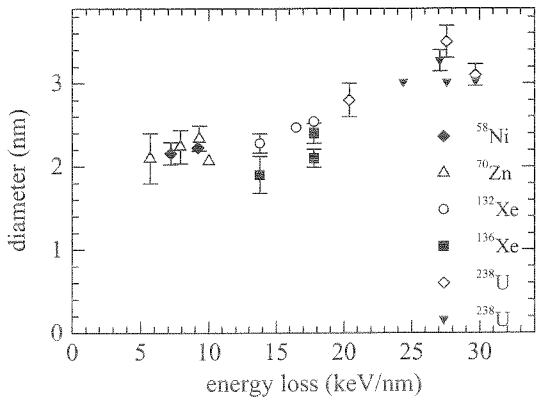

Fig. 2. Track diameter versus electronic energy loss. Tracks below 9 keV/nm are ascribed to nuclear collision processes.

In the dE/dx regime between 9-18 keV/nm, the areal density of observed protrusions is always smaller than the applied ion fluence. The creation yield as a function of the electronic energy loss varies over several orders of magnitude (Fig. 3). A one-to-one relation was found only for ions above about 18 keV/nm. From a linear fit of the yield data for 9≤dE/dx≤18 keV/nm, a threshold of 7.3±1.5 keV/nm is deduced. Above this value, track formation on the crystal surface is unambiguously ascribed to electronic energy loss processes.

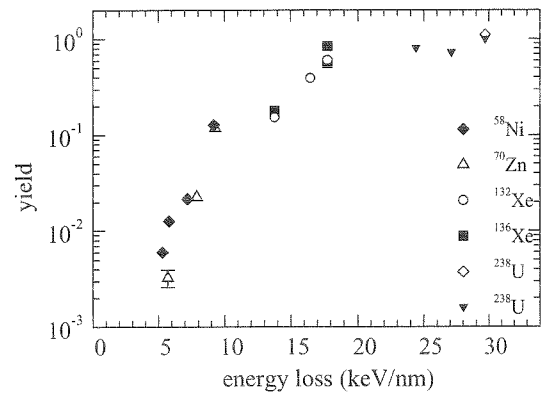

Fig. 3. Track creation yield defined as areal density of observed protrusions compared to the applied ion fluence on the original HOPG surface versus electronic energy loss.

We also recorded images from deeper bulk layers exposed by cleaving off thin slices from the crystal with an adhesive tape. On both adjacent lattice planes, hillocks are found, indicating that stress is relaxed towards the surface area around the impact site. The tracks are very similar to the features found on the original surface, however they are slightly (15-25%) reduced in size. Compared to the original surface, the probability for damage creation in the bulk is always significantly smaller. This phenomenon together with the dE/dx dependence of the yield observed on the surface can be understood, if we assume that the tracks consist of a discontinuous sequence of defect segments instead of a homogeneous damage cylinder.

Discussing track formation in graphite, the partly metallic character due to the lamellar structure has to be taken into account. The high thermal and electrical conductivity parallel to the layers allows efficient dissipation of the projectile energy radially from the ion path. Since graphite is a monoatomic crystal, we certainly have to consider that the disordering of the lattice is followed in time by a rapid recrystallisation occurring in particular in the bulk [1].

[1] L.T. Chadderton, D. Fink, Radiat. Eff. Def. Sol. 152 (2000) 87.

Charge collection with a Microbeam : Prospect for determination of ion track profile

T. Colladant[1,2], [1]GPS Université Paris 6 – 7 (France), [2]CEA-DIF (France)
O. Musseau, V. Ferlet-Cavrois, CEA-DIF (France)
A. B. Campbell, NRL (USA)
B. Fischer, M. Schlögl, GSI (Germany)

Introduction

Single event effects (SEE's) induced by heavy-ions from cosmic-rays are a major problem for the reliability of microelectronic devices in space environment. The energy deposited by a heavy-ion through the sensitive structure of a device produces, in a very short time, a dense concentration of electron-hole pairs along the ion trajectory. Generated carriers are collected by drift (if there is a local electric field) or by diffusion over hundreds of picoseconds. Previous works showed that differences in charge collection depend on the initial ion track structure [1][2].

Codes proposed by atomic physicists for ion tracks as TRKRAD [3] or TRIPOS [4] calculate a track profile which does not take into account the carrier thermalization and the recombination in the core of the track. For actual and future device generations, the knowledge of the ion track structure becomes necessary to correctly simulate the interaction within a device which has dimensions smaller than the ion track radius.

Test structures were fabricated in order to determine experimentally the effective size of an ion track and the carrier density profile [5][6]. They consist either of Schottky-barrier junctions or PN junctions on a silicon line.

Experiments

Following this way, Schottky-barrier junction microstrips are investigated here. They are made up of three lines (0.5 µm width with a 1.5 µm pitch) connected together. Schottky-barrier junctions were processed on a Silicon On Insulator (SOI) substrate to avoid long-distance charge collection, with a 0.6 µm thick silicon film (figure 1-a).

The devices were irradiated using the GSI scanning ion microprobe with 99.6 MeV carbon ions (LET=1.44 MeV.cm^2.mg^{-1} [7]). The microbeam spot diameter was 0.5 µm. All the electrodes were grounded during experiments including the metal lines via the charge preamplifier input impedance. When an ion strikes one of the lines, a charge is generated and detected by the amplifier chain. This collected charge and the coordinate of the ion strike are recorded by a multiparameter data taking system. The resulting charge collection image is shown (figure 1-b) after correction by an offset angle with respect to X and Y axis.

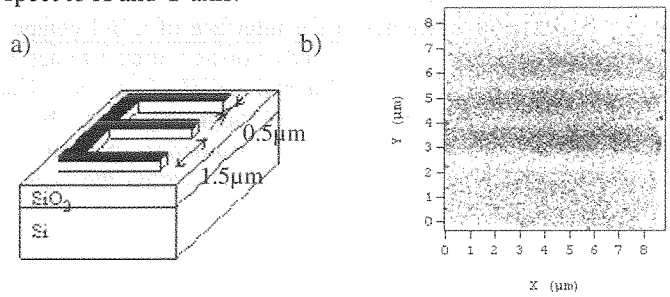

Figure 1: (a) Cross section of the tested devices, (b) charge collection image from experimental data (the dark area correspond to large collected charges).

Charges are collected in the Schottky-barrier junctions by drift due to the local electric field in the depletion region (thickness of about 0.13 µm) and by funneling effect. Charges collected from ion strikes outside the lines could be due to a capacitive coupling between silicon film and the substrate, and to a local electric field in the silicon near the oxide interface caused by trapped charge in the oxide from previous scanning.

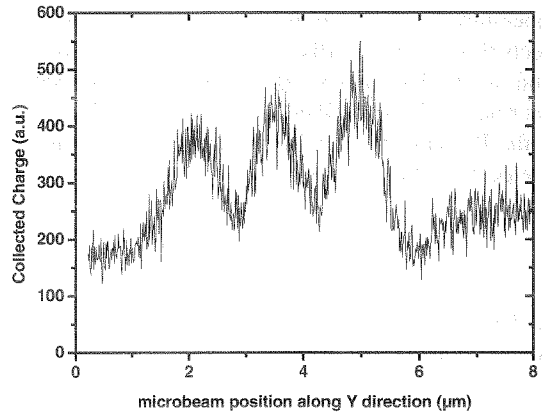

Figure 2: collected charge profile along Y direction.

An experimental charge collection profile is extracted from the charge collection image by integrating data over the X direction (figure 2).

Note that the ratio between the charge collected when the ion strikes a line and the bare SOI substrate is only 2. Thus, only the microbeam allows to extract the charge collected by lines, by rejecting the SOI substrate signal thanks to its small probing surface. This would indeed not be possible with a standard heavy ion beam.

Conclusion

The ion microbeam is the only technique which allows us to spatially measure the collected charge on Schottky-barrier junctions with a good signal to noise ratio.

With a complete understanding of the charge collection mechanisms by drift-diffusion simulations, it may be possible to correlate the charge collection on the strip with the ion track profile.

References

[1] H. Dussault et al., IEEE Trans. Nucl. Sci. NS-40, pp. 1926-1933 (1993)
[2] W. J. Stapor et al., IEEE Trans. Nucl. Sci. NS-35, 1585-1590 (1988).
[3] W. J. Stapor et al., J. Appl. Phys. 64, pp. 4430-4434 (1988).
[4] R. C. Martin et al., Physica Status Solidi A 104, pp. 743-754 (1987).
[5] J. W. Howard et al., IEEE Trans. Nucl. Sci. NS-41, pp. 2077-2084 (1994).
[6] O. Musseau et al., IEEE Trans. Nucl. Sci. NS-45, pp. 2563-2570 (1998).
[7] J.F. Ziegler et al, SRIM-2000.10, 1999 IBM Co.

Influence of Heavy Ion Induced Columnar Defects on the Vortex Dynamics of High-Temperature Superconductors

M. Basset[1], G. Jakob[1], G. Wirth[2], B. E. Fischer[2], P. Voss-de Haan[1], E. Jäger[2], and H. Adrian[1]
[1] Institut für Physik, Johannes Gutenberg-Universität, D-55099 Mainz
[2] Gesellschaft für Schwerionenforschung, D-64291 Darmstadt

The investigation of vortex dynamics in high-temperature superconductors (HTSC) is always related to the question of defects. In the presence of random disorder the long range order of the magnetic flux line lattice is destroyed and a vortex glass (VG) phase [1] is established below a characteristic glass temperature T_G. In the presence of heavy ion induced columnar defects this correlated disorder leads to a transition from vortex liquid to a Bose-glass (BG) phase [2]. In both cases this transition can be described with the appropriate scaling theory. For the BG case the scaling relation between current density J and electric field E is described by

$$\ell_{\perp}^{z'-1} E \approx \varepsilon_{\pm}\left(\ell_{\parallel}\ell_{\perp} J\right) \qquad (1)$$

with length scales $\ell_{\parallel}$ and $\ell_{\perp}$ parallel and perpendicular to the columnar defects that diverge as

$$\ell_{\perp} \propto \left(T_{BG} - T\right)^{\nu_{\perp}} \qquad (2)$$

where $\nu_{\perp}$ and z' are the static and dynamic exponents.

We performed electrical transport measurements on epitaxial $YBa_2Cu_3O_{7-x}$ thin films. Due to their extremely long measurement bridges l=10.9 cm that were patterned photolithographically we were able to measure current-voltage characteristics with an electric field resolution of 10^{-8} V/m and recent results have shown that the dynamic exponent of the VG transition in unirradiated thin films strongly depends on the experimentally accessible range of the electric field [3] which is in contrast to the theory. In order to study the dependence of the critical exponents from the electric field range we have irradiated the samples subsequently with 0.752 GeV ^{209}Bi, B_{ϕ} = 0.6 T and 0.749 GeV ^{208}Pb, B_{ϕ} = 1.0 T, ΣB_{ϕ} = 1.6 T. For this energy both ions have nearly the same electronic energy loss S_e which is responsible for the creation of columnar defects. We performed the same measurements as for the unirradiated case and the obtained data can be scaled well within the framework of the BG model for different magnetic fields. In accordance with the unirradiated case we could show that the dynamic critical exponent z' in the BG case also depends strongly on the electrical field range.

Another consequence of the irradiation is that the number of pinning centers for the vortex system is increased and the glass temperature T_G is shifted . Figure 1 shows the (H,T_G)-irreversibility line for the different irradiation doses and the unirradiated case respectively. For a magnetic field $\mu_0 H$ = 1 T the glass temperature is increased linearly with the irradiation dose as shown in the insert of Fig. 1.

We additionally take advantage of the different vortex dynamics in irradiated and unirradiated parts of HTSC thin films to study the effects at the interfaces between these regions. Different methods can be applied to prepare such a

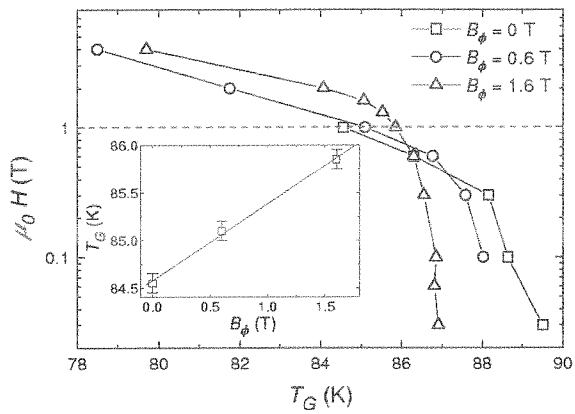

Figure 1: Irreversibility line before and after heavy ion irradiation. For B_{ϕ} = 0 T the glass temperature is determined using VG scaling, whereas the BG model is used for the irradiated sample. The number of coherent pinning centers is increased and the (H,T_G)-line is shifted. The insert shows the linear dependence between B_{ϕ} and T_G for a magnetic field $\mu_0 H$ = 1 T.

Bose-glass contact. In a first experiment we created a periodic array of strong and weak pinning channels using metal masks or the GSI-microprobe. These channels of width between 10 µm and 800 µm lead to a guided vortex motion (GVM) that can be detected by measuring in a Hall geometry [4]. We have shown that the characteristic fields and temperatures of this GVM are correlated to the BG phase. The second experiment currently is focussed on the electric field profile of a BG contact. Several equidistant (20 µm) voltage probes allow to measure the electric field across the interface between irradiated and unirradiated regions. The measured electric field profile of the weak pinning channel contains information about the characteristic length scales of the interaction between pinned and free vortices.

Thus vortex dynamics at the interface of a BG contact is a new field of investigation to study vortex-vortex interactions in HTSC thin films. Two experimental techniques are necessary to obtain more information: nanolithography and the GSI-microprobe in order to create irradiation patterns on a microscopic scale. This will be realized within the framework of the collaboration.

References

[1] D. S. Fisher *et al.*, Phys. Rev. B **43**, 130 (1991).
[2] D. R. Nelson *et al.*, Phys. Rev. B **48**, 13060 (1993).
[3] P. Voss-de Haan *et al.*, Phys. Rev. B **60**, 12443, (1999).
[4] M. Basset *et al.*, submitted to Phys. Rev. B

On the low temperature mixing processes in metal/ceramic interfaces

R. Nagel and A.G. Balogh
Institute for Materials Science, Darmstadt University of Technology, Petersenstrasse 43, 63741 Darmstadt

Heavy ions in materials science can be used for many applications concerning changes in composition, structure and physical properties. The modification of interfaces in bi-layer samples is frequently performed by ion beam mixing experiments [1-4]. However, the mixing behaviour of the components is much more complicated than in the earlier studied metal/metal systems, because of the more complex structure of the ceramic materials.

Samples with different composition (Fe, Cu, Ni, Pt, Zr, Ti and TiO_2 on Al_2O_3, SiO_2, MgO and SiC-substrates) were prepared by molecular-beam-epitaxy. The samples were irradiated at the GSI 300kV implantation facility with 150 keV Ar^+ ions at different temperatures. Rutherford backscattering spectroscopy (RBS) was used to obtain the element depth profiles. The surface topography and the surface roughness was studied with a high resolution scanning electron microscope (Philips XL 30 FEG) and with atomic force microscopy (AFM) .

The RBS spectra were converted to depth profiles by using the computer code *ndf* [5]. The width (σ_f) and the position of the interface was calculated using an error function. The measured and calculated mixing rates are shown in figure 1. In many systems (Cu/Al_2O_3, Cu/SiC, Fe/Al_2O_3, Fe/SiO_2, Fe/SiC, Ni/Al_2O_3, Ni/SiO_2, Ni/MgO, Ni/SiC, Pt/Al_2O_3, Pt/SiC, Zr/Al_2O_3, Zr/SiO_2, Ti/SiO_2 and TiO_2/SiO_2) the low temperature data can be interpreted using the binary collision model (BCS) [6] alone (fitted line in the upper part of fig.1). For the systems Cu/Al_2O_3, Fe/MgO, Cu/SiO_2, Ni/SiO_2, Pt/SiO_2 and Cu/MgO the measured values exceed the predictions of the BCS model. Therefore the model was expanded following the approach of Refs. [7-8]. The ion beam mixing rates will be enhanced in this compound model by a factor, which is the ratio between the atomic densities of the mixing species. Using the expanded c-BCS model all data points could be fitted correctly as it is shown at the lower part of fig.1. However, the difference between the predictions of the BCS model and the measured values can be also explained assuming the formation of local thermal spikes. After Cheng [9] the space filling character of the collision cascade, as primary condition for the formation of thermal spikes, is only possible, if the energy transferred to the recoils (E_R) is lower than the spike initiation threshold energy $E_{TS}=0.039eV*Z^{2.23}$, but higher than the displacement energy (E_d). Taking the Ni/Al_2O_3 system as an example, this means, that the formation of local thermal spikes will be allowed, if the recoil energy falls between 16 and 28 eV.

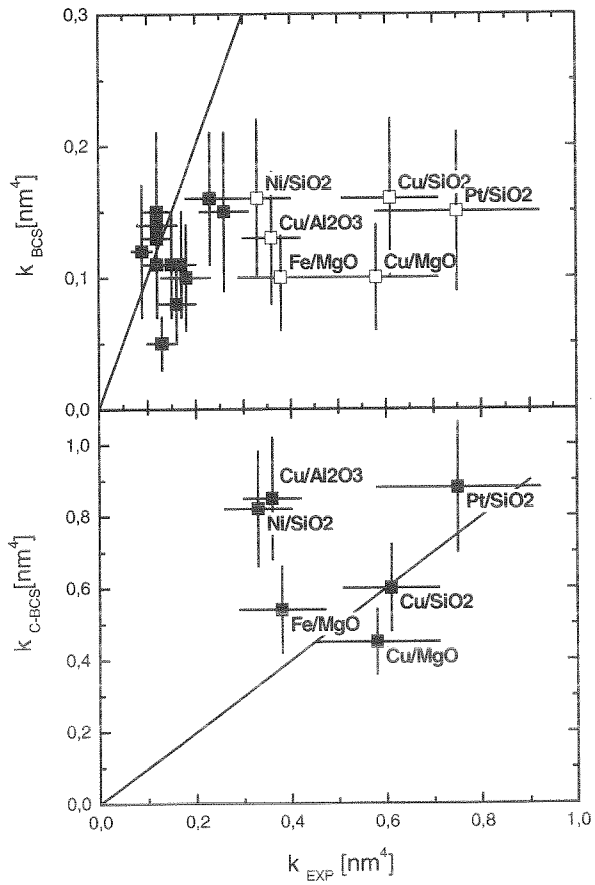

Fig. 1.: Measured and calculated mixing rates for different systems. At the top: fitted by the BCS model, at the bottom: fitted by the compound-BCS model.

References

[1] K.Neubeck, C.E.Lefaucheur, H.Hahn, A.G.Balogh, H.Baumann, K.Bethge, D.M.Rück, NIM B, 106 (1995) 58

[2] K.Neubeck, H.Hahn, A.G.Balogh, R.Hausner, H.Baumann, K.Bethge, D.M.Rück, NIM B, 113 (1996) 186

[3] R.Nagel, H.Hahn, A.G.Balogh, NIM B, 148 (1999) 930

[4] R.Nagel, A.G.Balogh, NIM B, 156 (1999) 135

[5] N.P.Barradas, C.Jeynes, R.P.Webb, Appl. Phys. Lett., 71 (1997) 291

[6] P.Sigmund, A.Gras-Marti, Nucl.Instr.Meth., 25 (1981) 182

[7] J.Desimoni, A.Traverse, Phys.Rev.B, 48 (1993) 13266

[8] S.Dhar, Y.N.Mohapatra, V.N.Kulkarni, Phys.Rev.B, 54 (1996) 5769

[9] Y.T.Cheng, Mat.Sci.Rep., 5 (1990) 45

Conducting ion tracks in diamond-like carbon films

A. Weidinger[1], C. Trautmann[2], J. Krauser[1], V. Hoffmann[1], N. Stolterfoht[1], H. Hofsäss[3], B. Schultrich[4], H. Sturm[5],
[1]HMI Berlin, [2]GSI Darmstadt, [3]Univ. Göttingen, [4]FhG Dresden, [5]BAM Berlin

The formation of ion tracks in diamond-like carbon (DLC) films on conducting Si substrates is studied. The films were produced by either conventional ion beam techniques (Univ. Göttingen) or by plasma deposition with magnetic filtering (filtered arc method, FhG Dresden). In both cases, the ions were implanted into the growing film with an energy in the order of 100 eV, thus creating by "subplantation" the conditions required for diamond formation. Such films are amorphous, contain 70-80% sp^3 bonds, and in the present case, have a thickness 40 and 100 nm, respectively.

The ion irradiation of the DLC films was performed at the UNILAC with Uranium projectiles of ~1GeV (moderated down from 2.7 GeV by Al foils). Due to the high energy deposition of the ions along their trajectories, the material is transformed from insulating diamond-like to conducting graphite-like carbon leading to thin electrically conducting channels embedded in an insulating matrix [1]. The properties of these channels were studied by means of scanning probe microscopy (AFM) using a conducting tip.

Figure 1 shows a three-dimensional AFM image of the surface topography of the irradiated DLC film. Hillocks with a few nm in height and ~20 nm in diameter are seen at the ion impact sites. The number of hillocks corresponds to the applied ion fluence.

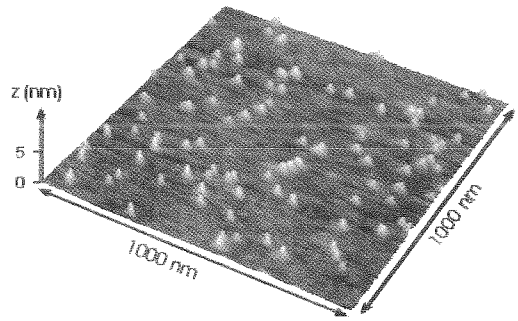

Fig.1 Topographical AFM image of a DLC film (FhG Dresden, 40 nm thick) irradiated with 10^{10} uranium ions per cm^2 of 1 GeV. The hillocks are due to the outflow of material at the ion impact site.

Figure 2 shows a three-dimensional plot of the current flowing between the AFM tip and the Si substrate through the DLC film. Each of the spikes corresponds to an ion track. Outside of the tracks the current is practically zero. Note, the current image originates from a different sample than the topographic image in figure 1.

The current between the substrate and the AFM tip as a function of voltage is presented in figure 3 for a spot on an ion-track and a spot outside of the track, indicating the overall noise level of the non-irradiated sample.

Assuming a track cross section of 100 nm^2, the measured current at 5 V gives a current density of 10^4 A/cm^2 and a electrical resistivity of ρ = 50 Ωcm. The conductance of the tracks is four orders of magnitude smaller than that of crystalline graphite, thus a very defective graphite filament is formed.

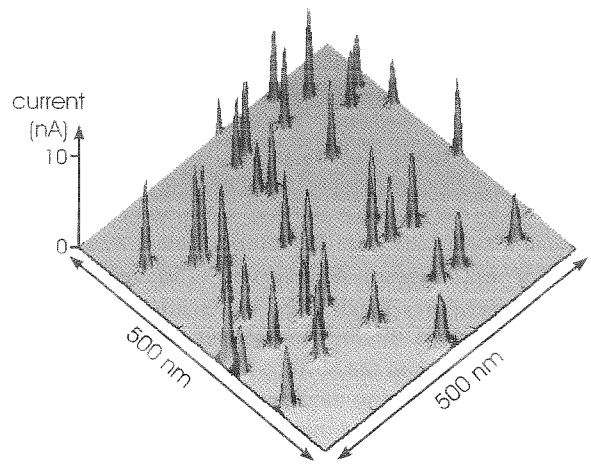

Fig.2 Current image of a DLC film (Univ. Göttingen, 100 nm thick) identically irradiated as sample of fig. 1. The current measurements were performed with a conducting AFM tip.

The general perspective of this kind of research is seen in the possibility to create nanostructures of materials which have properties distinctly different from the surrounding. In the present case, thin conducting filaments of graphite are embedded in an insulating diamond-like matrix. Such filaments may be useful in future mechanical or electrical nano-devices. A more immediate application is seen in the use of these tracks as electron field emitters in displays or other vacuum electronic devices (to replace hot filaments).

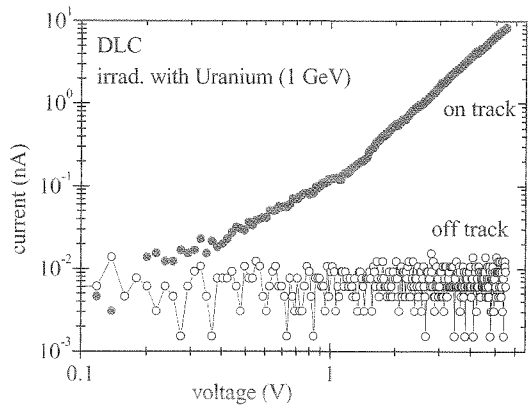

Fig.3 Current/voltage curve for a single ion track (AFM tip on top of a track). For comparison, the corresponding curve for the off track position is shown. DLC film from Univ. Göttingen, 100 nm thick.

[1] M. Waiblinger, Ch. Sommerhalter, B. Pietzak, J. Krauser, B. Mertesacker, M.Ch. Lux-Steiner, S. Klaumünzer, A. Weidinger, C. Ronning, H. Hofsäß, Appl. Phys. **A69** (1999) 239.

Visualization of latent alpha-recoil tracks in dark mica by scanning force microscopy

[1]Glasmacher, U.A., [2]von Grabczewski, N., [2]Heiß, M., [2]Neumann, R. & [1]Wagner, G.A.
[1]Forschungsstelle Archäometrie der Heidelberger Akademie der Wissenschaften am Max-Planck-Institut für Kernphysik, P.O. Box 103980, D-69029 Heidelberg, Germany, ua.glasmacher@mpi-hd.mpg.de;
[2]Gesellschaft für Schwerionenforschung (GSI), Planckstrasse 1, D-64291 Darmstadt, Germany,

As a natural mineral, dark mica contains α-emitters such as uranium and thorium. During their α-decay, part of the recoil energy is transferred to the daughter nuclei. These interact with the surrounding crystal lattice where they create 'nest-shaped' radiation damage, so-called alpha-recoil tracks (ART). If the volume density of such ART as well as the concentration of the α-emitters is known, one can evaluate the age of the sample [1]. For the registration of the ART volume density via optical phase contrast microscopy, the tracks have to be etched to a certain size. The etch pits are triangular in shape. If the track density is too high, the pits cannot be enlarged above the optical resolution of the microscope without overlapping. Therefore, up to now ART dating is restricted to dark micas of ages not exceeding 10^6 a.
To overcome this age limit, scanning force microscopy (SFM) was applied to visualize latent ART. Natural biotite from the Altai Mountains, China, was used to test whether SFM is able to image latent ART and, thus, suitable for the dating of older dark micas. Scanning the surface of freshly cleaved biotite did not reveal any tracks. Subsequently, this surface was kept in ambient conditions over a certain time period. Within several hours, small hillocks developed with an initial size as expected for latent ART in dark mica (see Figure 1).

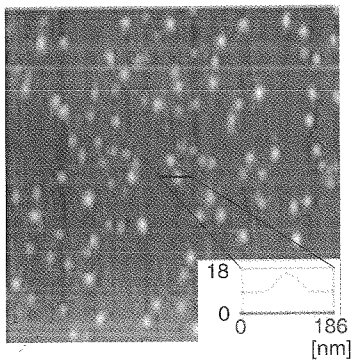

Figure 1: Topographic SFM image (2.4 µm x 2.5 µm) of a biotite cleavage plane kept in ambient conditions for several hours. Light areas represent hillocks. Both inset scales are in nm.

Diameter and topographic height increased with time, reaching a saturation limit several days after cleavage. The damaged material has a lower hardness than the intact surroundings. The areal density of tracks is similar to that of ART revealed by etching and phase contrast microscopy. After very short etching of the surface, the SFM image indicated triangular etch pits rather than the previously occurring hillocks (see Figure 2). These pits look similar to the etched ART in lower resolution (phase contrast microscopy).

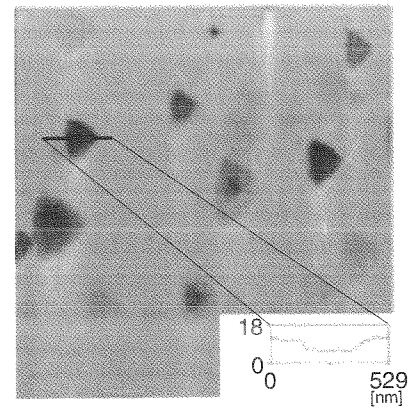

Figure 2: Topographic SFM micrograph (2.9 µm x 3.0 µm) of biotite after short etching, showing triangular etch pits.

Heating the biotite at 500 °C for 30 min annealed the latent ART. The annealed material was irradiated at the UNILAC of GSI with $^{136}Xe^{18+}$ and $^{238}U^{28+}$ ions at E_{kin} = 11.4 MeV/u and fluences of $5x10^{10}$ and $1x10^{10}$ ions/cm², respectively. Scanning these samples revealed hillocks. Etching develops the artificially created hillocks into circular rather than triangular etch pits (see Fig. 3), in contrast to the behaviour of the hillocks displayed in Fig. 1, which are attributed to alpha-recoil tracks.

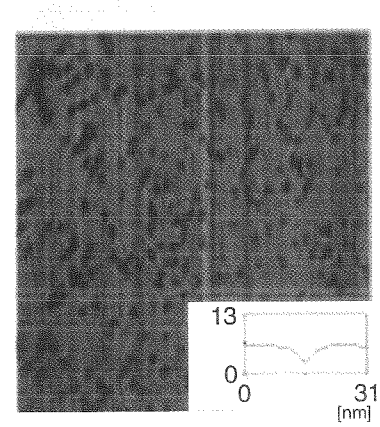

Figure 3: Topographic SFM image of irradiated ($^{136}Xe^{18+}$, fluence: $5x10^{10}$ ions/cm²) biotite after short etching (size: 830 nm x 860 nm).

In conclusion, visualization of latent ART by SFM enables us to reveal track densities beyond 10^8 cm^{-2} and thus extend the new ART dating technique to an age range > 10^6 a.

[1] Gögen, K., Wagner, G.A., 2000. Alpha-recoil track dating of Quaternary volcanics. Chemical Geology 166, 127-137.

Investigation of X-ray and ion irradiated DNA using scanning force microscopy

M. Heiß, G. Taucher-Scholz, N. von Grabczewski, R. Neumann
GSI Darmstadt

It is well known that the biological effectiveness for cell inactivation of radiation with high linear energy transfer (LET) around 100 keV/µm is higher than the one of low-LET radiation [1]. The reason for that may rely on the fact that double-strand breaks (DSB) of DNA-molecules induced by high-LET-radiation are repaired less efficiently than those, which are induced by low-LET-radiation [2]. This could be caused by a different spatial distribution of DSB, in connection with the inhomogeneous distribution of dose. To verify this hypothesis it is desirable to directly investigate the condition of DNA after irradiation.
In our work we did these investigations on plasmid DNA irradiated with X-rays and ions using scanning force microscopy (SFM). Therefore we developed a preparation method which allowed us to determine the fractions of the different plasmid conformations and additionally measure the length of DNA fragments in the pictures produced by the SFM (see Figure 1)

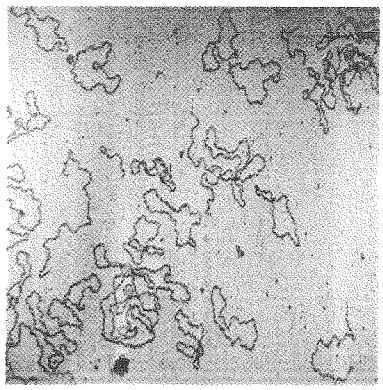

Figure 1: Typical SFM picture of DNA (size: 3µm x 3 µm)

Using this preparation method we studied ΦX174 plasmid DNA that was irradiated in 20 mM HEPES buffer in a supercoiled compact conformation with different doses of X-rays and Zn-ions.
As a result we obtained for every sample the fraction of each different plasmid conformation (see Figure 2) and the fragment distributions. From this we were in addition able to determine the mean fragment-lengths as well as the number of DSB per broken plasmid (see Figure 3).
In figure 2 the difference between high- and low-LET radiation in the production of DNA-DSB can be seen. For X-rays the linearised fraction increases quadratically with dose while for ions in the lower dose region this fraction increases linearly.

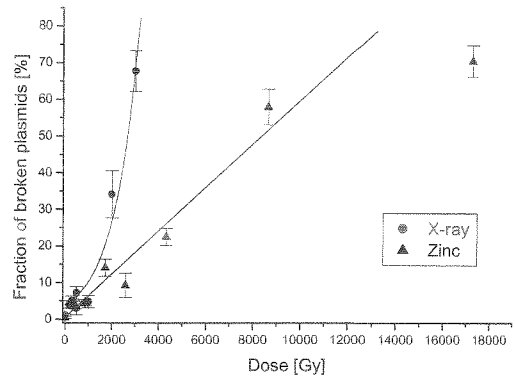

Figure 2: Fraction of broken plasmids

Figure 3 shows that the number of DSB per broken plasmid after high-LET irradiation with low doses is significantly higher than 1. After low doses of X-ray irradiation this number appears to be smaller than that after ion irradiation but it increases steeper with dose.

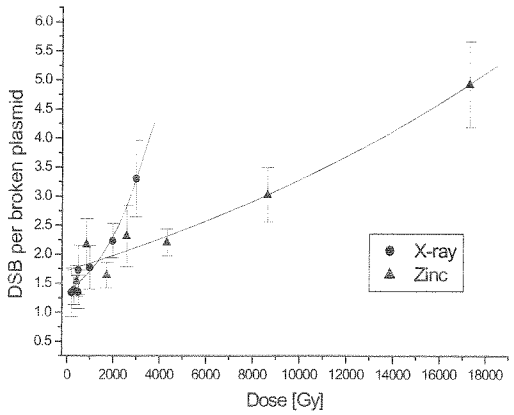

Figure 3: Number of DSB per broken plasmid

These results point to a spatial correlation of the induction of DSB's by densly ionising particles.
Yields of DSB per broken plasmid need to be further investigated at low fluences.

[1] W. K. Weyrather et al.; Int. J. Radiat. Biol. 75, 11, 1357-1364 (1999)

[2] G. Taucher-Scholz et al.; Radiat. Environ. Biophys. 34, 101-106 (1995)

Preparation of diode-like single-ion track-etch membrane using combination of chemical and electro-stopping

Apel P.Yu. [1], Korchev Yu.E. [2], Siwy Z. [3], Spohr R. [4], Yoshida, M. [5]
Flerov Laboratory of Nuclear Reactions, JINR, 141980 Dubna, Moscow Region, Russia
[2]Imperial College London, London W12 0NN, England
[3]Silesian University of Technology, 44100 Gliwice, Poland
[4]GSI Darmstadt, Planckstr. 1, D-64291 Darmstadt, Germany
[5]JAERI, Takasaki, Watanuki 1233, Takasaki, Gunma-Ken, 37012, Japan

Particle track etching has found diverse uses in science and technology [1]. Production of porous membranes stands out among other applications of the track-etch technique. In the past decade special attention was paid to the study of track-etch nanopores in poly (ethylene terephthalate) (PET) with respect to their ability to mimic biological ion channels (e.g. [2, 3]). Artificial cylindrical channels of few nanometers diameter and 5 or 10 micrometer length exhibited electrical and electro-kinetic properties similar to those observed earlier for biological membranes. One should realize however that the dimensions of artificial nanopores prepared by the track-etch method differ strongly from typical dimensions of biological ion channels e.g. the length of a pore in a PET membrane is app. 10 000 larger than biological channel length. We have aimed therefore at preparing a track-etch pore with dimensions closer to biological ion channels. One way to do that is based on preparation of a strongly asymmetric track-etch whereby the short and narrow part at the tip of the etch pit determines the electric properties of the whole channel.

For this purpose, a single-ion irradiated PET film is inserted into an electrolytic cell (see Fig. 1) and etched from one side in 9 M Na OH while bathing the other side in a mixture of 2M KCl and 2M HCOOH (1:1 by volume), electrically retracting the OH^- ions from the tip of the etch pit during pore break-through.

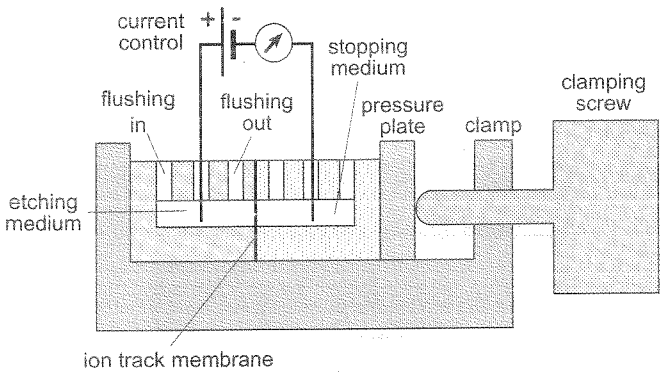

Fig. 1 Cross section of the electrolytic cell used for one-sided etching of ion track membranes. The clamping mechanism ensures a reliable seal (>10^{12} Ohm) between the chamber halves and the membrane.

The process results in the conically shaped pore having wider entrance of app. 800 nm in diameter (measured by SEM) while the diameter of limiting the transport tip is app. 2 nm (on the basis of PEG permeation). The structure and nature of the tip will be the subject of further investigation.

The electrical properties of the membrane were determined under symmetric bathing conditions of pH and KCl concentration. The current-voltage (I-V) characteristic was measured by stepping the voltage between –5 and +5 V. Each measured point corresponds to the current averaged over the dwell time (5 to 10 seconds). An example of observed asymmetric diode-like current-voltage characteristic has been shown in Fig. 2.

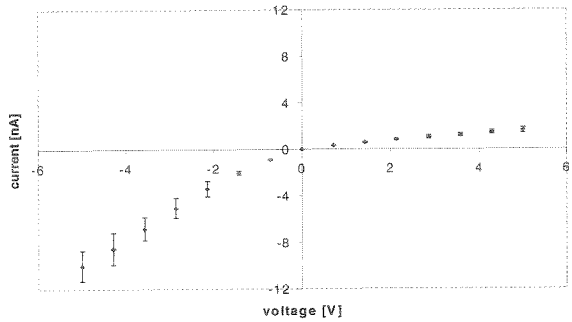

Fig. 2 Intrinsic asymmetry of voltage-gradient stopped single pore membrane. Current – voltage characteristic in symmetric concentration and pH conditions at 0.1 M KCl and pH = 7.

The observed diode-like behavior can be controlled by pH, electrolyte concentration and the pore dimensions. The phenomenon is reproducible and very stable: the same membrane can be studied for many days.

The obtained results have suggested that the one-sided etched pore in a PET membrane can serve as a model of a biological channel. Additionally the diode-like behavior of the membrane enables to use it as an electrical valve.

[1] Fleischer R.L., Price P.B., and Walker R.M.; Nuclear tracks in solids; Principles and Applications; Univ. of California Press, Berkeley, California, 1975.

[2] Pasternak C.A., Bashford C.L., Korchev Y.E., Rostovtseva T.K., Lev A.A. *Colloid Surfaces A*, **77** (1993) 119.

[3] Wolf, A., Siwy, Z., Korchev, Y.,E., Reber, N., Spohr,R. *Cell. Mol. Biol. Lett.* **4** (1999) 553.

Heavy Ion Induced Micropores in Glass as Nucleation Centers of Crystalline Silicon

P.-M. Wilde[1], K. Schmidt[1], P. Schramm[1], J. Vetter[2], and T. Boeck[1]
[1] Institut für Kristallzüchtung im Forschungsverbund Berlin e.V., D-12489 Berlin
[2] Gesellschaft für Schwerionenforschung mbH, D-64291 Darmstadt

The generation of crystalline structures on amorphous substrates (glass) is of interest in several application fields, as in photovoltaic cells and micro system technique. Glass is useful because it is an electronic insulator, has a high transparency and low thermal conductivity and can be produced in large panes at a low-cost level. However, an epitactical growth of perfect crystals or crystalline films is not possible due to the lack of lattice structure of this non-crystalline material. A novel method of selective nucleation has been developed to achieve crystalline structures on glass substrate using metallic droplets on the surface acting as nucleation centers [1]. These droplets can be deposited in micropores which are produced by irradiation of the glass samples with heavy ions. At this process ion tracks are created where the network structure of the glass is locally destroyed.

We used a borosilicate glass (T_G < 600° C) as substrate material. For irradiation $^{208}Pb^{n+}$ (n=28) ions with energies of 11.4 MeV/nucleon were used applying a dose of D = $3.3*10^5$ ions cm^{-2}.

In a subsequent chemical etch treatment of the material the ion traces are enlarged. As etching acid a mixture of HF (40 vol.%), HNO_3 (65 vol.%) and H_2O dest. in a 1:1:1 ratio was used. The etching time of irradiated samples was varied in four steps: 5 s, 20 s, 50 s and 80 s, respectively.

In this way, fields of micropores were generated in the glass surface. Scanning electron microscopy investigations (ZEISS DSM 962) reveal that the pores have a regular conical shape with smooth edges and walls. Depending on the etch time, pore diameters in the range 1,8 - 12 µm can be achieved (fig. 1). The aspect ratio of the pores was found to be 1.4 ± 0.2 (fig. 2). Microdroplets of low melting metals (gallium or indium) were deposited in these cavities by evaporation using the effect of coalescence due to the surface tension of liquid metal (fig. 3). In the next step, evaporated silicon is solved in the metal until droplets are saturated. Under the influence of a temperature gradient, nucleation occurs at the pits of the cavities. Solving additional vaporized silicon in the droplets, the growth of silicon crystallites inside of the cavities is continued. Thus, in each of the pores one silicon crystal is grown which can be observed when the solution is removed (fig. 4). Using this method, glass substrates with areas of more than 15 cm^2 can be covered regularly with silicon crytallites of about 1 µm size and mean distances of 20 µm.

[1] T. Boeck, Th. Teubner, K. Schmidt, P.-M. Wilde: J. Crystal Growth 198/199 (1999) 420-424.

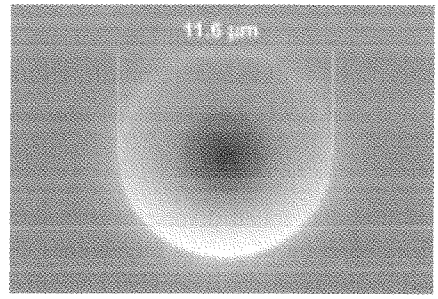

Fig. 1: SEM image of an etched ion track in the glass surface. The pore has a smooth wall and regular edge structure.

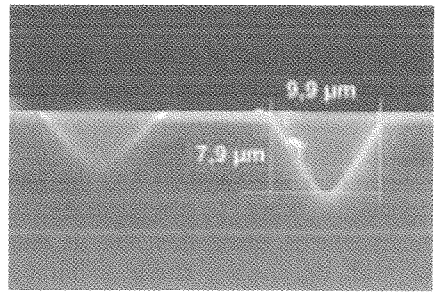

Fig. 2: Cross section of pores in glass with regular cone geometry. The measured aspect ratio is 1.25.

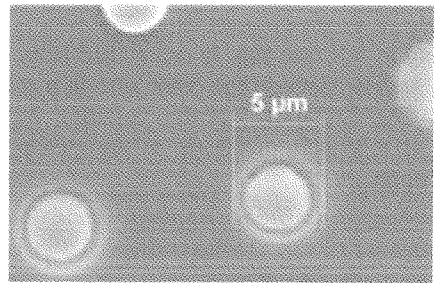

Fig. 3: SEM image of metallic microdroplets which are deposited in the pores.

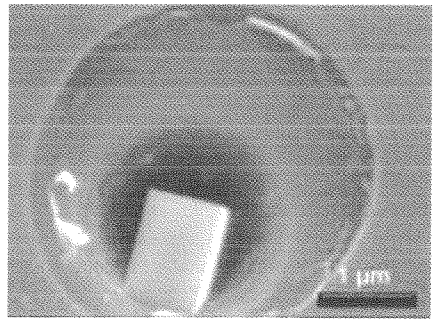

Fig. 4: A silicon single crystal is grown in the microcavity. The circular contour arises from the removed amorphous silicon.

Analysing the electrochemical process of copper deposition in etched ion track membranes

I.U. Schuchert*, D. Dobrev*, M. Martin#, M.E. Toimil Molares*, J. Vetter*
*GSI, D-Darmstadt, # RWTH Aachen, Inst. Phys. Chem., D-Aachen

Electrochemical techniques are widely used in many different fields. One example is the electrodeposition of copper for the production of printed circuits boards in microelectronics industry [1]. Compared to other methods like chemical and physical vapour deposition, electrochemical techniques have several advantages including avoidance of vacuum systems, high flexibility and low costs. Many investigations are being performed for the creation of novel micro- and nanostructures with high aspect ratios. One method widely used for this purpose is the electrochemical deposition of a metal into the pores of a template, e.g., etched ion track membranes or anodically oxidised aluminium. Nevertheless, up to now very little is known about the mechanism of this process itself [2], for which some similarities to the behaviour of microelectrode ensembles can be expected [3]. Therefore, the potentiostatic electrochemical process of filling etched ion track membranes with copper is studied in detail.

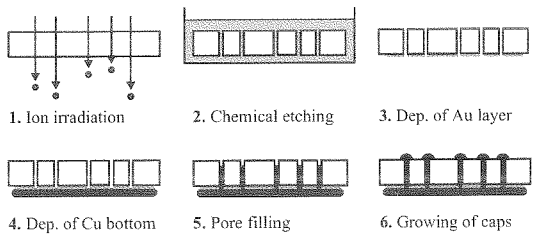

Fig. 1 Template method

Following the template method illustrated in fig. 1 polycarbonate foils with a thickness of 30 µm and a diameter of 5 cm are irradiated at the GSI UNILAC accelerator with Bi ions (11.3 MeV/u) up to a fluence of $1.25 \cdot 10^7$ ions cm^{-2}. Through a chemical etching process the latent ion tracks develop into cylindrical pores with diameters between 400 and 450 nm. A thin gold layer is then sputtered onto one side of the membrane and subsequently reinforced galvanically with copper. This conductive side acts as cathode during pore filling in a specially designed three-electrode cell. A simple salt electrolyte is used containing 2 mol/l H_2SO_4 but only 0.25 mol/l $CuSO_4$ to neglect mass transport due to migration.

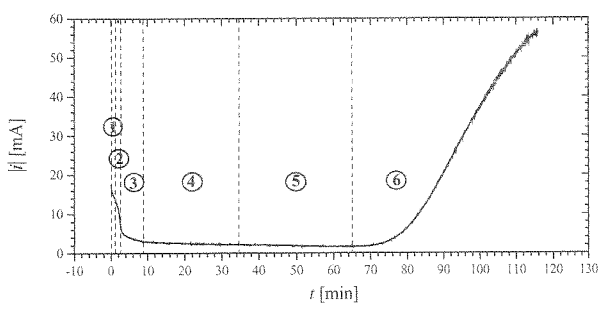

Fig. 2 Current-time-curve for $|\eta| = 120$ mV

In order to analyse the deposition process, current versus time curves are recorded for different applied overvoltages $|\eta|$ (difference between applied and open-circuit potential), namely between 80 and 440 mV. Fig. 2 shows the curve for $|\eta| = 120$ mV. Six different time periods are indicated corresponding to different events determining the overall reaction [4].

As soon as the potential is applied between cathode and reference electrode, copper is deposited and the electrolyte adjacent to the cathode depletes from copper ions – a concentration gradient starts to develop. For very short times (region 1) this gradient is nearly zero so that the charge transfer reaction $Cu^{2+} + e^- \rightarrow Cu^+$ determines the deposition process. Within region 2, the transition from charge transfer to diffusion control takes place - both overvoltages are of comparable size. With increasing time the depletion zone in front of the cathode (Nernst layer) is growing into the electrolyte - the concentration gradient is increasing and the over all reaction starts to be diffusion controlled. First, the thickness of the Nernst layer is smaller than the remaining pore length and the diffusion is linear inside the pores (region 3), compare fig. 3A. After some time the depletion zone exceeds the pore length, and a radial diffusion field establishes around each pore (region 4). The ions are diffusing radially towards the pore openings (fig. 3B). For long times (region 5) the radial diffusion fields start to overlap with their neighbours. The diffusion is again linear but now towards the whole membrane surface (fig. 3C). The increase of current in region 6 indicates that caps start to overgrow the membrane surface.

This model describes the deposition process qualitatively and can help to understand the mechanism for different metals in pores with various diameters and aspect ratios. For a quantitative analysis new suitable theories are needed.

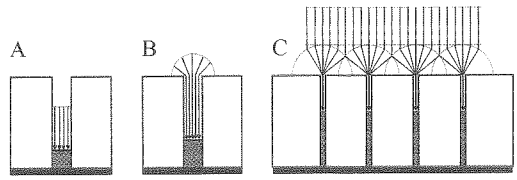

Fig. 3 Diffusion processes during pore filling

References

[1] J. W. Schultze, V. Tsakova, *Electrochim. Acta* **44** (1999) 3605.

[2] C. Schönenberger et al., J. Phys. Chem. B **101** (1997) 5497.

[3] K. Aoki, *Electroanalysis* **5** (1993) 627.

[4] I. U. Schuchert, Doctoral Thesis, TU Darmstadt 2000.

CDKN1A focus formation in mammalian cell nuclei at sites of particle traversal and association with repair or signaling proteins

G. Taucher-Scholz, G. Becker, S. Brons, B. Jakob, M. Scholz and G. Kraft (GSI, Biophysik)

In order to assess the biological endpoints of late radiation effects like genomic instability and transformation it is crucial to understand the signal transduction mechanisms that connect initial DNA lesions with the overall DNA damage response. At the molecular level, high ionization densities result in an increased complexity of DNA lesions leading to an impaired repair ability and extreme cell cycle delays. To gain insight to repair and signaling induced by high-LET radiation, we started monitoring the cellular response within defined subnuclear regions of human cells by examination of immunofluorescence-stained proteins using confocal scanning microscopy. The first protein we studied was CDKN1A (p21), one of the key signaling proteins, known to be induced in an irradiation (x or γ-ray) dependent manner and involved in the arrest of the cell cycle at the G1/S-phase checkpoint [1]. After particle irradiation, CDKN1A showed a rapid formation of localized foci within minutes which are correlated to the sites of ion traversal (Fig.1 left). This correlation was first established on the basis of the Poissonian distribution considering the particle fluence and the individual nuclear area (Fig.1 right) [2].

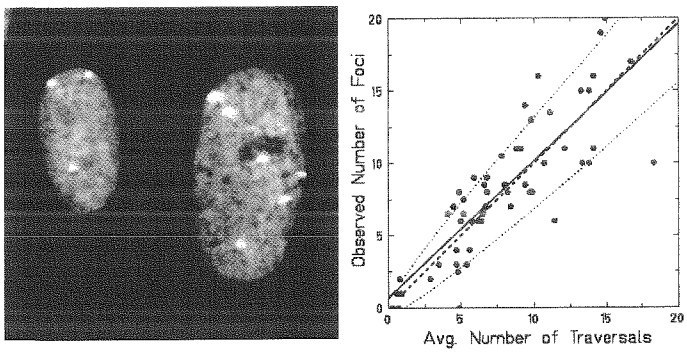

Fig.1 left: Local CDKN1A response (white spots, originally green fluorescence) of human fibroblast nuclei (counterstained with PI, originally red) traversed by uranium ions (9.1 MeV/u) at a fluence of $2.2 \bullet 10^6$ P•cm^{-2}. Size of image: 48 µm. **right:** Correlation between average number of particle traversals of the nucleus and observed number of CDKN1A foci from an experiment with lead ions. Solid line: linear fit to the data; dashed line expected correlation for the ideal case. Dotted lines indicate width of the Poisson distribution around the mean value.

Meanwhile we have obtained direct evidence for the spatial correlation of the nuclear CDKN1A response to particle tracks using broad field particle irradiation in conjunction with the retrospective determination of actual ion traversals through individual cells by track etching [3,4].
The observation that CDKN1A accumulation at sites of damaged DNA persisted for several hours (depending on the LET of the applied particles) before vanishing, indicated a possible function in the processing of radiation induced lesions. The fast translocation of CDKN1A into radiation dependent foci, together with evidence showing that foci are disrupted upon treatment of nuclei with DNAse, point to a new, yet unknown role of CDKN1A in the sensing or processing of DNA lesions generated by high LET particle irradiation. To address this role and to confirm the association to damaged DNA, we studied the response of proteins, known to be involved in different pathways of DNA-repair [5]. The hMre11-protein for example showed a strict correlation of the spatial accumulation to sites of observed CDKN1A foci as detected in differential immunostaining experiments (Fig. 2).

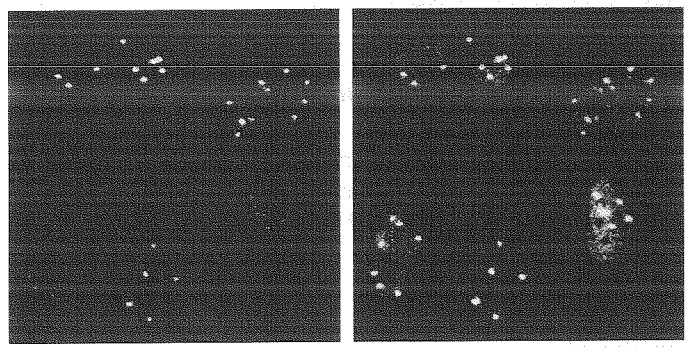

Fig.2 Spatial and temporal colocalization of radiation induced repair foci and CDKN1A in cell nuclei after traversal of gold ions (3.4 MeV/u) at a fluence of $1.9 \bullet 10^6$ P•cm^{-2}. Images were taken from a double immunostained sample and the recording channels were split. **left,** green channel: Immunofluorescence signal of CDKN1A. **right,** red channel: Localization of hMre11 indicating sites of DNA double strand break repair. Notice the identical pattern of bright spots on both images. Size of image: 160 µm.

hMre11 was shown to associate to damaged DNA (especially DSBs) in an heteromeric complex together with Rad50 and the protein mutated in the human autosomal disorder named Nijmegen Breakage Syndrome (NBS1) [6]. Nevertheless, differences in time course of radiation induced protein responses and studies utilizing mutant cell lines lacking functional components of the DNA damage sensing and signaling pathway revealed no direct interaction between examined proteins and CDKN1A foci formed after particle traversal up to now. The proposed new role of CDKN1A in the sensing or processing of radiation induced DNA lesions has therefore to be elucidated in further studies.

References

[1] Elledge S.J., Science 274, 1664-1672 (1996)

[2] Jakob B., Scholz M. and Taucher-Scholz G., Radiat. Res. 154, 398-405 (2000)

[3] Soyland C. and Hassfjell S.P., Radiat. Environ. Biophys. 39, 125-130 (2000)

[4] Scholz et al., Radiat. Res. submitted

[5] manuscript in preparation

[6] Maser R.S. et al. Mol. Cell. Biol. 17, 6087-6096 (1997)

Is the In-Vitro Production of Fibrosis-Associated Signal Protein TGFβ Radiation-Induced?

C. Fournier, P. Sander, G. Taucher-Scholz, G. Kraft (GSI, Darmstadt)

We have investigated whether irradiation of human fibroblasts leads to an enhanced synthesis and secretion of the cytokine TGFβ. Fibrotic in vitro-parameters known to be TGFβ mediated are the accelerated terminal differentiation of fibroblasts and the concomitant enhanced production of proteins [2] both shown to change dose- and LET-dependently [3]. Earlier studies on tissue and animal models reported in literature, revealed a key role of TGFβ in the signal transduction after irradiation resulting in the fibrotic phenotype [reviewed in 1]. Accordingly, the TGFβ-mediated in vitro effects can be suppressed by immuno-neutralisation at non-lethal doses [4,5], but the influence of dose and LET on the expression of TGFβ protein is less pronounced than expected [5,6].

In order to determine the influence of radiation quality on TGFβ synthesis, we irradiated semi-confluent human fibroblasts originating from different tissues (foreskin, skin and lung) with 250 kV x-rays and 11 MeV/u carbon ions (LET 153,5 keV/μm). The total TGFβ content (latent plus activated form) in the cell culture supernatant was measured up to 48 hours after irradiation using an immunoabsorbent assay (ELISA) under serum free conditions or in the presence of 10% fetal calf serum (fcs) containing appr. 8 ng TGFβ per ml. In unirradiated cells the TGFβ amount released into the cell culture medium increases proportionally to cell density, but the calculated production per cell decreases with increasing cell density. This effect is more drastic in the presence of 10% fcs than under serum free conditions (not shown). Under serum-free conditions the cells are arrested in G_1-phase and the cell density remains constant in each flask. After irradiation, the amount of TGFβ per flask increases in controls as well as in irradiated probes independently from dose (not shown). In the presence of 10% fcs the control cells continue to proliferate (1-2 population doublings within 48 hours), whereas the irradiated cells undergo a cell cycle delay, whose duration is dependent on the applied dose, resulting in significantly different cell densities. As shown in figure 1 (top) after 11 MeV/u carbon irradiation, the amount of TGFβ per flask in the presence of 10% fcs increases with time, but independently from dose, leading to an increment of TGFβ per cell (already shown in [5,6]). The observed correlations appear more clearly by directly comparing TGFβ production and cell density (figure 1, bottom): The control cells proliferate and the released TGFβ amount per flask increases proportionally. In contrast, the irradiated cells do not increase in cell density, but attain a comparable level of TGFβ within the same period of time. We could demonstrate this for the three fibroblast cell lines after X-irradiation and for foreskin fibroblasts (AG) after carbon irradiation.

These data confirm our preliminary results after X-irradiation [5] and are in line with data from literature [7]. We could show that the effects are not linked to radiation quality. The data presented sustain our hypothesis, that a fast regulatory step could be the crucial event leading to dose- and LET-dependent changes in fibrosis-related parameters after irradiation [2,5]. The measured changes in TGFβ production after irradiation could be regulated in a subsequent step in a way to assure a constant TGFβ level in the microenvironment of the cells. Such a regulation could normally depend on cell density and become independent from it after irradiation.

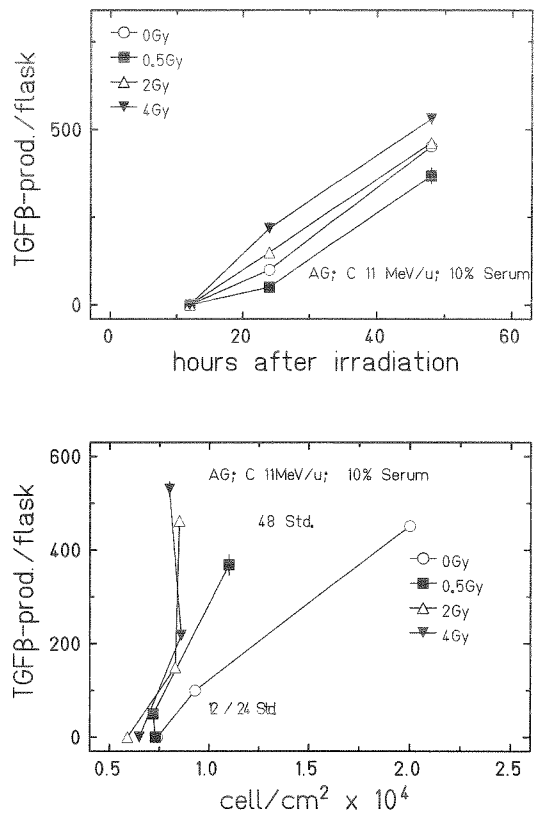

Figure 1: Time-course (top) and influence of cell density (bottom) on TGFβ production in human foreskin fibroblasts after exposure to carbon ions (153,5 keV/μm). Comparable and time-dependent levels of TGFβ are obtained independently of irradiation and concomittant growth inhibition. The increase is measured on top of a basal TGFβ level.

References

[1] Martin, M. *et al.*, Int. J. Radiation Oncology Biol.Phys. 47, 277-290 (2000)

[2] Burger, A. *et al.*, Int. J. Radiat. Biol. 73, 401-408 (1998)

[3] Fournier, C. *et al.*, Int. J. Radiat. Biol. ,in press (2001)

[4] Hakenjos, L. *et al.*, Int. J. Radiat. Biol. 76/4, 503-509 (2000)

[5] Fournier, C. PhD-Thesis (1999)

[6] Fournier, C. *et al.*, GSI-Scientific report 1999, p.156 (2000)

[7] Herskind, C. and Rodemann, H.P., Exp. Gerontol. 35, 747-755 (2000)

Cell and molecular biological analyses of the induction of fibrotic changes in human skin and lung fibroblasts exposed to heavy ion irradiation

H. Peter Rodemann, Oliver Haase,
Section of Radiobiology and Molecular Environmental Research,
Dept. of Radiooncology, Univ. of Tuebingen

As compared to conventional photon radiation heavy ions may offer specific therapeutic advantages in radiation oncology with respect to the higher relative biological effectiveness (RBE) at beam terminus. It has been demonstrated for heavy ion irradiation that the RBE in irradiated normal tissue, especially for acute effects is only slightly increased. However, since normal tissue reactivity, i.e. acute and late effects, is dose limiting in radiation therapy the proposed research project is concerned with the underlying cellular and molecular processes of normal tissue reactivity induced by heavy ions in comparison to photon irradiation. A prominent and clinically highly relevant radiation therapy-induced late reaction of normal tissue is fibrosis [1,2]. Fibrosis can occur especially in skin and lung and is characterized by remodelling of connective tissue resulting in enhanced collagen production and deposition. Although fibrosis is the result of a multicellular process involving endothelial cells smooth muscle cells, immunocompetent cells and fibroblasts within the irradiated tissue, the fibroblast cell system is the cell type responsible for the expression of the fibrotic tissue phenotype. Over the recent years our laboratory could demonstrate that the radiation-induced terminal differentiation of the fibroblast cell system, i.e. the induced differentiation of progenitor fibroblasts to postmitotic highly collagen synthesizing fibrocytes, is the key event in the induction and manifestation of the fibrotic tissue remodelling [3-8]. Molecular biological studies into the basic mechanisms of radiation-induced terminal fibroblast differentiation revealed that the cytokine TGF-β1 is the key factor which mediates the radiation-induced differentiation of progenitor fibroblasts to fibrocytes at the level of signal transduction in an autocrine as well as paracrine fashion. This has been demonstrated in a number of experiments analysing the cellular responses of both normal human or rat skin and lung fibroblasts to ionizing radiation (photons and heavy ions) with and without concomitant treatment with TGFß1-neutralizing antibodies [4-6,9]. Finally, by the use of lung fibroblast cultures from homozygous TGFß1-knock out mice, it could be demonstrated that TGFß1 is the main determinator of fibroblast radiation sensitivity [10].

On the basis of these molecular studies into the cellular mechanism of radiation-induced fibrosis it can be concluded and hypothesized that fibroblasts are stimulated to produce enhanced levels of activated TGFß1 in response to radiation exposure. Activated TGFß1 then binds to the TGFß1 receptor II. In a cascade of phosphorylation reactions several members, i.e. Smad proteins (esp. Smad 4), of the TGFß1-receptor-dependent signal transduction are activated and the TGFß1-signal is transduced to the nucleus. Consequently, the expression of TGFß1-target genes is upregulated resulting in an enhanced expression and activity of the cyclin-dependent kinase inhibitors (cdk-inh.) p21, p27, p15, and p16. Most likely these inhibitors are responsible for the induction of radiation-induced terminal fibroblast differentiation (Rodemann et al. 2001, in prep.). This assumption is based on the observation that TGFß1-neutralizing antibodies can block the long lasting or permanent (>6-8 hrs, TP53 independent) upregulation of p21 expression in response to both radiation and TGFß1-treatment, but not the transient, TP53-dependent p21 expression (< 6 hrs).

The results of the ongoing project will give detailed insights into the regulatory mechanisms of radiation-induced terminal fibroblast differentiation by heavy ions. Together with the results to be established by the Biophysics group at the GSI [11], which investigates the molecular mechanisms and processes of the radiation-dependent activation of the latent inactive form of newly synthesized and secreted LTGFß1, the data will help to describe the specific molecular and cellular pathways, which lead the development of fibrosis in response to radiation exposure. Consequently, these data will not only allow a specific estimation of the risk of fibrosis in radiation therapy applying heavy ions, but also lead to the development of new strategies to prevent or interfere with late normal tissue complications, like fibrosis in radiation oncology.

REFERENCES

[1] Martin M., Lefaix J-L., Pinton P., Crechet F., Daburon F.: Temporal modulation of TGF-ß1 and ß-actin gene expression in pig skin and muscular fibrosis after ionizing radiation. Radiat.Res., 134, 63-70, 1993.

[2] Martin, M., Lefaix, J.-L, Delanian S.: TGF-β1 and radiation fibrosis: a master switch and a specific therapeutic target? Int. J. Radiat. Oncol. Biol. Phys., 47, 277-290, 2000.

[3] Rodemann H.P., Bamberg M.: Cellular basis of radiation-induced fibrosis. Radiother.Oncol., 35, 83-90, 1995a.

[4] Rodemann H.P., Binder A., Burger A., Güven N., Löffler H., Bamberg M.: The underlying cellular mechanism of fibrosis, 1996, Kidney Int., 49, 32-36, 1996.

[5] Burger A., Löffler H., Bamberg M., Rodemann H.P.: Molecular and cellular basis of radiation fibrosis. Int. J. Radiat. Biol. 73:401-408, 1998

[6] Hakenjos L, Bamberg M., Rodemann H.P.: TGFß1-mediated alterations of rat lung fibroblast differentiation resulting in the radiation-induced fibrotic phenotype. Int. J. Radiat. Biol. 76:503-509, 2000a.

[7] Herskind C., Johansen J., Bentzen S. M.,Overgaard M., Overgaard, J., Bamberg M., Rodemann H.P.: Fibroblast differentiation in subcutaneous fibrosis after postmastectomy radiotherapy. Acta Oncologica, 39:383-388, 2000.

[8] Herskind C. and Rodemann H. P.: Spontaneous and radiation-induced differentiation of fibroblasts. Exp. Gerontol. 35:747-755 (2000).

[9] Haase O., Herskind C., Bamberg M., Rodemann H.P.: Can fibroblast cultures be used as a predictive system for radiation-induced fibrosis? Proceedings of Radiation Research 1999, Vol. 2:599-601, 2000a.

[10] von Pfeil A., Hakenjos L., Rodemann H.P.: Radiation sensitivity of mouse lung fibroblasts in vitro is determined by TGF-β1. Int. J. Radiat. Biol., 2001, submitted.

[11] Fournier C., Scholz M., Kraft-Weyrather W., Kraft G., Rodemann H. P.: Changes of fibrosis-related parameters after high and low LET irradiation of fibroblasts. Int. J. Radiat. Biol., 20001, submitted.

Short And Long Term Effects In Human Cells As A Consequence Of High LET Irradiation

J.Kool, B. Klein, M. van Eck-Smaling, A.J. van der Eb and C.Terleth.
Department of Radiation Genetics and Chemical Mutagenesis, Leiden University Medical Centre, Leiden, The Netherlands.

Introduction

In effort to mimick immortalization of human cells, a specific stage of the carcinogenic process *in vitro*, many experimental approaches have been used. Reproducible immortalization could be achieved by transforming human cells with DNA tumor viruses, such as for example SV40 and HPV. The oncogenes largeT and E6/E7 respectively, will modify the human fibroblast's regulatory systems in such a way that the cells will first bypass senescence. Subsequently, during the extended lifespan, the cells will accumulate chromosomal aberrations. Finally, genomic instability will be so massive that the transformed cells enter crisis, a stage defined by massive cell death. Occasionally, at a frequency of 10^{-7}, cells escape crisis and immortalize [1]. Alternatively, immortalization could be achieved by repeated treatments with DNA damaging agents such as 4-NQO and ^{60}Co rays. In these cases, cells would be treated 60-140 times at three day intervals [2]. Our initial interest in irradiating human cells with heavy ions originated from an observation by Dr. Laure Sabatier (CEA,F) that cells which had been exposed to a single high LET irradiation seemed to display an extended lifespan [3]. We wondered whether high LET would indeed lead to such an extension. The molecular basis for the processes discussed above is probably the length of the telomeres. Telomeres are specialized DNA structures at the end of the chromosomes which have a protective role. During the lifespan of the cell telomeres shorten until they reach a certain minimal size, which will trigger senescence. If the cells are forced past senescence, for example by viral oncogenes from DNA tumor viruses, the telomeres will shorten further. At this stage the telomeres become reactive leading to chromosomal instability. For a cell to escape the ensuing crisis, it is necessary to reactivate telomerase, a protein able to stabilize the ends of chromosomes. Indeed, in immortal tumor cells and in *in vitro* immortalized cells telomerase activity is commonly found (although alternative mechanisms of telomere lengthening (ALT) have also been described).

Long term effects

As extension of lifespan is an important step in tumorigenesis, we wanted to determine the effect of high LET irradiation on the lifespan of human cells. Thus we have irradiated normal fibroblasts as well as fibroblasts lacking key factors in installment of senescence (i.e. p16 and p53). In separate experiments, we have irradiated the cells with Ni or Ar, and with different fluences. Subsequently, the cell cultures were closely followed. Population doublings were calculated carefully, samples for RNA, DNA or protein isolations were taken at regular intervals, and chromosome analysis was performed. Results sofar show a gradual, and expected, decrease of telomeres in the cells as population doublings increase. No telomerase is activated and cells enter senescence eventually. In the irradiated cell cultures profound changes can be observed in the chromosomes as a consequence of irradiation, including a delayed genomic instability as has been described previously. The effect of high LET irradiation on lifespan is in this set of experiments very moderate, if significant, with an extension of 3 population doublings at most. However, in one experiment we included a fibroblast line derived from a patient with Nijmegen breakage syndrome (NBS). Interestingly, in these cells a single high LET irradiation has led to an extension of 10 population doublings, which is in the order of magnitude of the effects of the viral oncogenes E6 and E7 from HPV. Even more intriguing, the telomeres in the irradiated cells have increased in the absence of telomerase activity, suggesting activation of ALT. We have recently repeated this experiment including NBS cells from different patients, to see if this a reproducible phenomenon.

Short term effects

When human cells are exposed to irradiation many responses are induced. These responses include the induction of genes, which will eventually lead to processes such as cell cycle arrest, DNA repair or apoptosis. We have focussed in particular on the stress induced pathways involving the MAPkinases. Two kinases play an important role in these pathways; JNK which can activate transcription factors like c-Jun and ATF2, and p38 which can activate ATF-2 [4,5]. We examined activation of the kinases p38 and JNK after irradiation of human cells. Also activation of ATF2 and cJun was examined. In initial studies we have compared the effects of UV and X-rays. Whereas UV is a potent activator of both p38 and JNK, X-rays only weakly activate p38 but not JNK. We then decided to extend our studies to high LET as the RBE might be higher. Initial experiments were performed at GANIL (Caen, F) with Ar, and showed activation of p38 and ATF-2, but no JNK activation. However, our results at GSI for both Ar and C (UniLac and SIS) have been quite different. With Ar we did see clear activation of ATF2 and also cJun, but not of JNK and p38. With C irradiation with a high LET value (135keV/µm) minor activation of ATF2 and cJun was detected but no activation whatsoever could be observed in cells irradiated with C with a lower LET value (27.9keV/µm). Our hypothesis is that the differences seen in activation of the stress responses between irradiated cells are caused by the differences in LET values. It is known that cell survival after irradiation varies with different LET values. Our results suggest that the differences we find after irradiation with different LET values in short term responses, i.e. activation of stress-response pathways, could play a role in the differences seen on survival in the long term.

References

[1] Sedivy JM. (1998). *Proc. Natl. Acad. Sci.*, **95**, 9078-9081

[2] Tsuji T, Miyazaki M, Sakaguchi M, Inoue Y, Namba M. (2000) *Biochem. Biophys. Res. Commun.*, **268**, 20-24

[3] Martins MB, Sabatier L, Ricoul M, Pinton A, Dutrillaux B. (1993) *Mutat. Res.*, **285**, 229-23

[4] Tibbles LA, Woodgett JR. (1999) *Cell. Mol. Life. Sci.*, **55**, 1230-54

[5] Davis RJ. (2000) *Cell*, **103**, 239-252

Low dose hypersensitivity after high-LET irradiation

G. Böhrnsen[1,2], K.J. Weber[2], M. Scholz[1,2]
[1]GSI Darmstadt, [2]Radiologische Klinik Heidelberg

An unexpected hypersensitivity has been reported for several cell lines at low doses (<1Gy), which is not consistent with the linear-quadratic approach currently used in general for the description of survival curves [1,2,3,4]. The corresponding substructure of the survival curves has been attributed to induced radioresistance. There are indications, that high-LET irradiation with neutron or pion beams does not lead to low dose hypersensitivity [1,3], at least in single dose exposure experiments. But no systematic studies on the LET-dependence have yet been performed.

Measurements of low dose effects require high precision assays for the correspondingly high survival levels, where statistical errors represent a principal limit for the accuracy of the standard dilution assay. This problem can be bypassed by using absolute cell counting by means of either cell sorter assays [5] or automated video microscopy assays like e.g. the DMIPS assay [6].

With respect to application of high LET beams in tumor therapy, it is of particular interest, whether hypersensitivity is also observed in situations, which correspond to the radiation quality and dose levels occuring during therapy in the normal tissue in front of the target volume or in the region beyond the tumor. Both regions are characterized by low dose levels due to the inverted depth dose profile or due to beam fragmentation, which contributes to a small dose deposition beyond the tumor. If hypersensitivity is observed in these situations, this could have impact on the RBE values of the normal tissue surrounding the tumor.

In order to investigate the survival after low doses of high-LET radiation, an automated video microscopy system similar to the DMIPS system has thus been developed recently and used for first experiments. The system is able to automatically find the cells without staining using a phase contrast microscope. Cells can then by relocated by means of a computerized microscope stage at regular intervals to follow the fate and growth characteristics of individual cells. Inspection of a flask with approx. 100 cell positions lasts about 20 min; there will be, however, further improvements to accelerate the automatic cell finding and inspection procedures. The measurements include an automatic determination of the colony area, which is - within certain limits - a measure of the cell number per colony. This information can be used to determine growth curves for the individual cells.

The system has been used for experiments at the UNILAC and SIS. First, the agreement of survival curves obtained with the new technique with those obtained using the standard dilution assay has been investigated. No systematic deviations from the results using conventional techniques have been detected for doses higher than 1 Gy for the different radiation qualities.

The system was thus used to investigate in particular the effects of low doses after irradiation with 100 MeV/u carbon ions; the results are summarized in Fig. 1. Up to now, 8 independent experiments have been performed. A significant hypersensitivity at low doses (0.1 Gy) has been detected, whereas for higher doses (0.5 Gy) a transition to the linear-quadratic shape is observed. The general structure of the survival curves closely resembles those reported for low LET irradiation [3] and can be fitted well using a modified LQ-approach including a term for induced resistance [7]. This result is apparently in contrast to the results reported in the literature, where the effect of induced resistance has been reported to be largely reduced e.g. for peak pion irradiation at similar LET values.

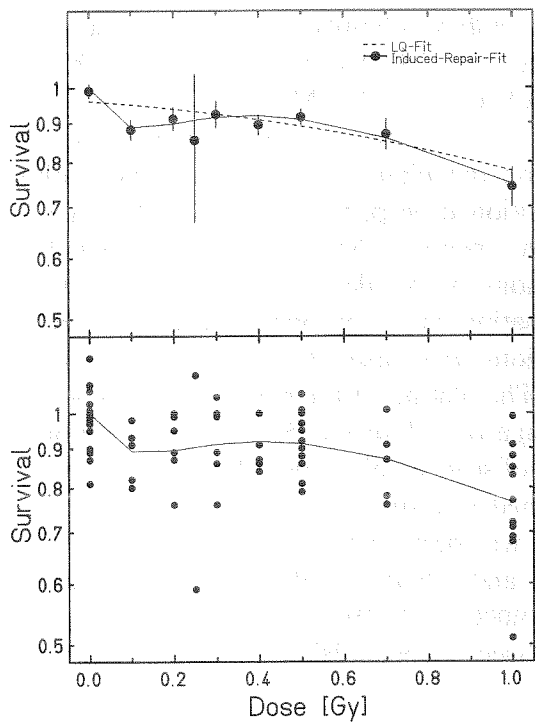

Figure 1: Survival of V79 cells after irradiation with low doses of 100 MeV/u carbon ions. Top: Average values from up to 8 independent experiments. Bottom: Distribution of survival for individual samples. Fits are performed according to an induced repair approach (full line) [7]. For comparison, the backextrapolation from a linear-quadratic fit to the high dose region is shown int the top panel.

References

[1] Lambin P. et al. (1993), Int. J. Radiat. Biol. 63, 639-650
[2] Marples B., Joiner M.C. (1993), Rad. Res. 133, 41-51
[3] Marples B. et al. (1994), Radiat. Res. 138, S81-S84
[4] Singh B. et al. (1994), Int. J. Radiat. Biol. 65, 457-464
[5] Freyer J.P. et al. (1984), Rad. Res. 97, 608-614
[6] Palcic B., Jaggi B. (1986), Int. J. Radiat. Biol. 50, 345-352
[7] Marples, B. Joiner, M.C. (1995), Rad. Res. 141, 160-169

Heavy Ion Irradiation of Human Colon Adenocarcinoma Cells in Multilayer Culture

S. Winhart, W. Müller-Klieser, University of Mainz

M. Scholz, G. Kraft, GSI Darmstadt

Introduction - The major goal of this project is to study the effect of heavy ion irradiation on radioresistant human tumour cells which are grown in a specific tissue-like culture model.

Materials and Methods - WiDr colon adenocarcinoma cells were cultured in either conventional monolayers or cellular multilayers in a specific culture chamber [1]. Cell cultures were irradiated with 250 kV X-rays, with a 100 MeV/u, 200 MeV/u or 400 MeV/u ^{12}C-beam (plateau region), or with an extended Bragg-peak. During irradiation the plane of the mono- and multilayers was positioned perpendicular to the direction of the radiation beam. After radiation, single cell suspensions were derived from the cultures by trypsinisation and appropriate dilution, and these suspensions were used for standardised clonogenic assays. The plating efficiency was determined as the percentage of colonies (>50 cells) in relation to the number of seeded cells, and relative cell survival was determined as a function of radiation dose. Cell cycle analysis was performed with standardised propidium iodide and BrdU labelling techniques and flowcytometry. Apoptoses were detected with a standardised TUNEL labelling using a commercial test kit.

Results - The fraction of apoptotic cells was very low, i. e., around 1 % in untreated cultures and could not be induced by heavy ion irradiation. There was a dose-dependent G_2/M-arrest which was more significant with heavy ions than with x-rays, and which resulted in a G_2-block in 91 % of the cells treated with 6 Gy in the extended Bragg peak. Cell survival rates were lower in monolayer than in multilayer cultures; this phenomenon was most pronounced in the Bragg peak compared to all other radiation conditions, as exemplified in Fig. 1.

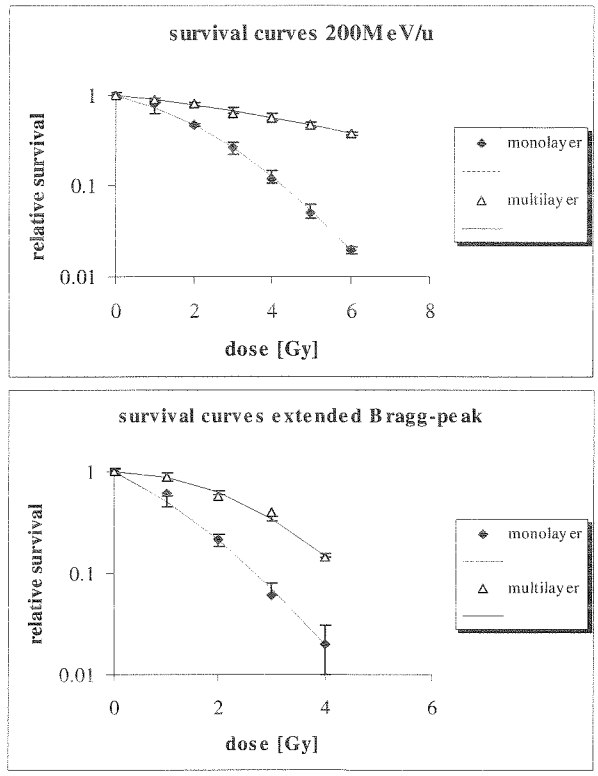

Fig. 1: Relative cell survival as a function of heavy Ion radiation dose in the plateau region (left panel) and in the extended Bragg peak (right panel) for monolayer (diamonds) and multilayer (triangles) cultures.

Discussion – The high radioresistance of WiDr cells compared to most other tumour cell lines can be partially explained by a pronounced G_2/M-arrest following irradiation. This intrinsic resistance is even enhanced by multicellular resistance when cells grow in a in a three-dimensional tissue-like arrangement. The molecular basis of these phenomena need to be investigated.

[1] Minchinton A. I., Wendt K. R. Clow K. A., and Fryer K. H., Acta Oncologica **36**, 13-16 (1997)

Biological effects of 12C - heavy ions on tumor cells

Hana Hofman-Hüther, Margret Rave-Fränk, Patricia Virsik-Köpp

Zentrum Radiologie, Universität Göttingen, Germany

We investigated the induction of chromosome aberrations by carbon ions of different energies in tumor cells of different intrinsic radiosensitivities: MCF-7, an extremely radiosensitive human breast adenocarcinoma cell line and WiDr, an extremely radioresistant colon carcinoma cell line. The aberration yields evaluated in cells in their first post-irradiation metaphase (BrdU-method) were constant independently on the culture time. Carbon ions were in general more efficient with respect to the aberration induction than 200 kV X-rays. The frequencies of dicentric chromosomes and excess acentric fragments were always higher for carbon ions as compared with X-rays in both tumor cell lines. However, in the radioresistant WiDr-cells, a pronounced yield of dicentric chromosomes (about 1 dicentric per cell) could be observed just after irradiation with D = 4 Gy in Bragg peak. Representative aberration data for carbon ions in comparison with X-rays, as observed after irradiation with a dose of 1 Gy are shown in fig. 1

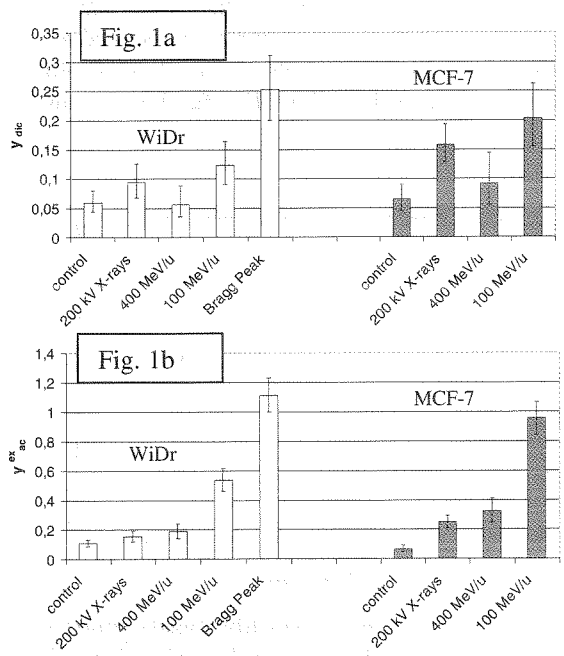

Figure 1: Frequency of dicentric chromosomes (a) and extra acentric fragments (b) per cell scored in first post-irradiation metaphases after irradiation with carbon ions (D=1 Gy) with energies of 400, 100 MeV/u and in Bragg peak, in comparison with 200 kV X-rays.

Using the FISH-method, we scored the radiation-induced simple reciprocal translocations as well as complex exchange aberrations. Since tumor cells are genomically unstable, we first analyzed various chromosomes in both cell lines with respect to their stability. Solely chromosomes No. 2, 4 and 5 were suitable for a FISH-analysis: these chromosomes showed in both unirradiated cell lines either no aberrations or one (or two) stable translocations. The translocation induction was strongly increased for carbon ions as compared with X-rays. Partial translocation yields in WiDr cells irradiated with carbon ions or 200 kV X-rays, as evaluated for chromosome No. 2, are shown as a representative example in fig. 2. Similar results were obtained for chromosomes No. 4 and 5, too. After irradiation with D = 4 Gy, a beginning saturation in the translocation yield could be observed; this is caused by a strong increase in the yield of complex exchanges, as shown in the next figure. Fig. 3 shows the relative proportions of cells containing complex exchanges after irradiation with two different doses of carbon ions or X-rays. Up to 50% of cells irradiated in Bragg peak contained different types of complex exchanges resulting mostly from interactions among 3 different chromosomes.

In summary, a strongly increased biological efficiency of heavy ions is thus confirmed in tumor cells of different intrinsic radiosensitivities with respect to the induction of unstable and stable chromosome aberrations. Moreover, carbon ions induce very efficiently complex exchange aberrations, especially in Bragg peak.

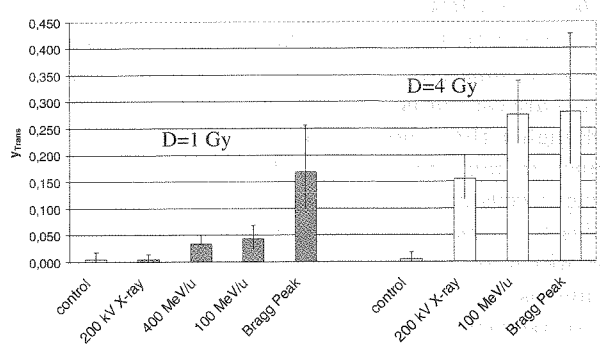

Figure 2: Partial reciprocal translocation yields in WiDr cells, evaluated for chromosome No. 2, irradiated with carbon ions of different energies or 200 kV X-rays.

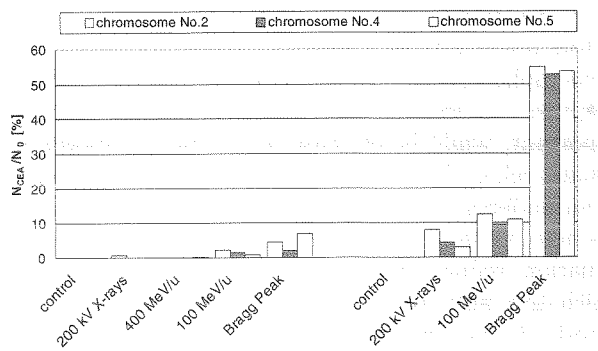

Figure 3: The relative proportions of WiDr cells containing complex exchanges after irradiation with two different doses D=1 Gy and D=4 Gy with carbon ions (100 MeV/u or Bragg peak) in comparison with 200 kV X-rays.

Quantification of High LET Induced Chromosome Aberrations

S. Ritter, S. Berger, T. Größer, P. Hessel G. Kraft (GSI, Darmstadt)
E. Nasonova (JINR, Dubna, Russia), K. Ando (NIRS, Chiba, Japan)
E. Gudowska-Novak (Institute of Physics, Krakow, Poland)

The classical cytogenetic assay relies on the scoring of chromosomal damage in cells at metaphase. According to the standard protocol the analysis is confined to cells at the 1st post-irradiation mitosis collected at one, early sampling time. For sparsely ionizing radiation this protocol allows a reasonable estimate of chromosomal damage, because in all commonly used cell system no or only a slight increase in the aberration yield with time has been observed [1,2 and references therein]. In contrast, as shown in our experiments with different Chinese hamster cell lines [e.g. 1-4] single fixation regimes do not necessarily allow a meaningful quantification of high LET induced cytogenetic damage. Following particle exposure a drastic increase in chromosomal damage with time has been observed. For example, in V79 cells exposed to X-rays the aberration frequency increased by a factor of 3 [1], but in Ar-irradiated samples by a factor of 20 (fig. 1). To account for the time-dependent expression of damage a mathematical approach was used [5], which allows to determine the total amount of aberrations induced within the whole cell population. Based on these total aberration yields RBE values have been calculated. For 10.4 MeV/u Ar (fig. 1) an RBE of 1.9 is obtained. Similarly, for V79 cells exposed to 10.6 MeV/u Ne ions (LET: 390 keV/μm) or 11.1 Kr ions (LET: 3980 keV/μm) RBE values of 3.2 and 1.3 are estimated. As expected, these RBE values are much higher than those reported in the literature [e.g. 6], because in our analysis also drastically delayed heavily damaged cells are included. Moreover, extension of these studies to human primary skin fibroblasts and lymphocytes which are usually used for radiation risk assessment in humans, have shown that the above described effects are not restricted to Chinese hamster cells. For example, in human lymphocytes exposed to 200 MeV/u Fe ions the aberration yield rises in 1st cycle cells by a factor of 7, while after X-irradiation only an increase by a factor of 1.2 is observed.

Furthermore, there is increasing evidence that besides the above described delay of heavily damaged cells additional factors might interfere with the expression of aberrations in metaphase cells. In the case of human lymphocytes apoptosis as well as interdonor variability seem to be important, while in the case of human fibroblasts a permanent cell cycle arrest in G_1 and/or G_2 might contribute to an underestimation of radiation induced damage. For example, as shown in figure 2, even low doses of low LET radiation reduce drastically the number of fibroblasts which are able to proceed to the 1st post-irradiation mitosis. In contrast, this effect is less pronounced for V79 cells which are "apoptosis-resistant" and do not undergo a permanent cell cycle arrest. Even after exposure to 6.5 Gy Kr ions (11.1 MeV/u, 3980 keV/μm) about 50% of V79 cells reach the 1st post-irradiation mitosis and thus can be analysed for chromosomal damage (see fig. 2).

Further experiments are in progress to examine the extent to which interdonor variability as well as high LET induced apoptosis or permanent cell cycle arrest affect the aberration yield detectable in metaphase cells.

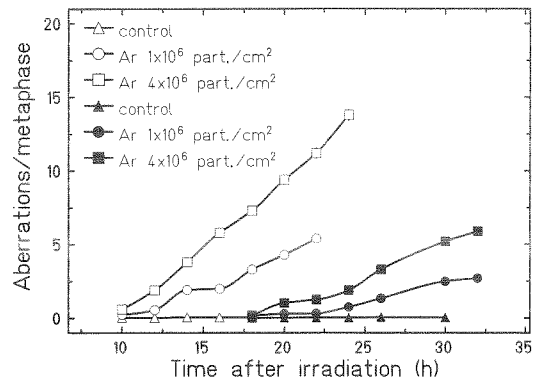

Figure 1: Time-course of aberrations in V79 cells after Ar-irradiation (10.4 MeV/u, 1226 keV/μm). Cells have been exposed in G_1 and chromosomal damage was scored at several sampling times (open symbols: 1st cycle metaphases; closed symbols: 2nd cycle cells). For further details see [3].

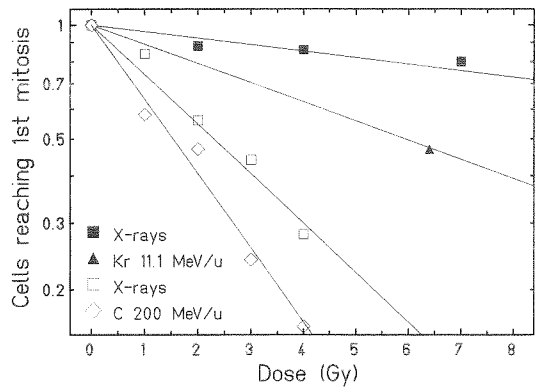

Figure 2: Fractions of human skin fibroblasts (open symbols) and V79 Chinese hamster cells (closed symbols) which reach the 1st post-irradiation mitosis. Human fibroblasts have been exposed to X-rays or 200 MeV/u C ions (LET: 16 keV/μm), V79 cells to X-rays or 11.1 MeV/u Kr ions (LET: 3980 keV/μm). Calculations were performed as described in reference [5].

References

[1] Ritter, S. *et al.*, Int. J. Radiat. Biol. 69, 155-166 (1996)
[2] Nasonova, E. *et al.*, Adv. Space Res. 22, 569-578 (1998)
[3] Ritter, S. *et al.*, Int. J. Radiat. Biol. 76, 149-161 (2000)
[4] Nasonova, E. *et al.*, Phys. Med., in press
[5] Scholz, M. *et al.*, Int. J. Radiat. Biol. 74, 325-331 (1998)
[6] Wu *et al.*, Radiat. Res. 148, S102-S107 (1997)

A comparison of relative biological effectiveness for DNA double strand and mutation induction

J. Kiefer, Strahlenzentrum der Justus-Liebig-Universität, Giessen

We have collected over the years a large date base for heavy ion induced DNA double strand breaks in yeast [1, 2] as well as for the formation of HPRT-mutants in Chinese hamster cells (summarised in [3]). Contrary to findings in mammalian cells [4] DSB induction in yeast cells shows an increase in RBE with LET, displaying a maximum around 100 – 300 keV/µm. Mutation induction is characterised by a qualitatively similar behaviour but with distinctly greater RBE values. In this report both dependencies are compared, results are shown in fig. 1. It is seen that RBE values for both experimental endpoints increase with LET but they are always lower for DSB than for mutation induction.

The broken curves are semi-empirical approximations to the experimental points which are based on the assumption that induction cross sections can be described by a linear-quadratic dependence of the following form

$$\sigma_i = \sigma_0 [1 - \exp - (\alpha L + \beta L^2)]$$

with σ_I induction cross section, σ_0 "saturation" cross section, L LET and α, β fitting parameters.

The best fit was obtained with the following values:
Mutation:

$$\sigma_i = 11 \times 10^{-7}\ \mu m^2$$
$$\alpha = 3{,}35 \times 10^{-4}\ \mu m/keV$$
$$\beta = 7 \times 10^{-5}\ (\mu m/keV)^2$$

DSB per base pair:

$$\sigma_i = 6 \times 10^{-7}\ \mu m^2$$
$$\alpha = 1{,}54 \times 10^{-3}\ \mu m/keV$$
$$\beta = 2{,}85 \times 10^{-5}\ (\mu m/keV)^2$$

References

[1] S. Ikpeme, M. Löbrich, T. Akpa, E. Schneider, J. Kiefer, Radiat. Env. Biophys. **34**, 95-99 (1995)
[2] J. Kiefer, R. Egenolf, S. E. Ikpeme, manuscript submitted to Radiat. Res. (2001)
[3] J. Kiefer, Radiat.. Res., in print (2001)
[4] Prise KM, Ahnstrom G, Belli M, Carlsson J, Frankenberg D, Kiefer J, Lobrich M, Michael BD, Nygren J, Simone G, Stenerlow B. Int J Radiat Biol. 74,:173-84 (1998)

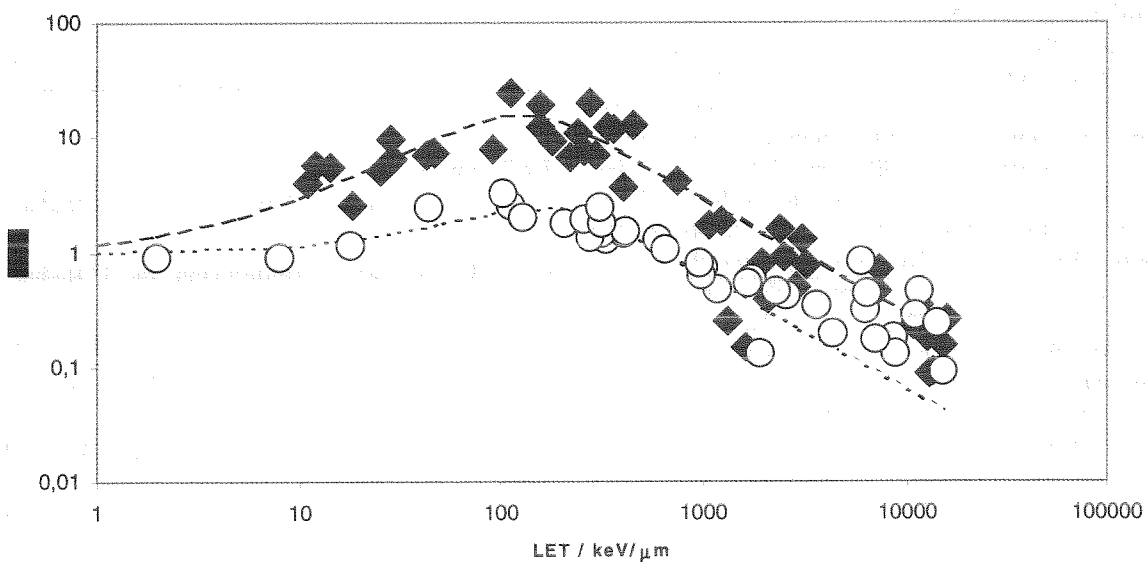

Fig.1: RBE in dependence of LET for DSB (open circles) and mutation induction (rhombi)

Molecular mechanisms of heavy-ion induced radiation damage: Free radicals and products from DNA and chromatin

Barbara Weiland, Anne-Kathrin Hoffmann, Heike Luxenburger and Jürgen Hüttermann, Fachrichtung Biophysik und Phys. Grundlagen der Medizin, Universität des Saarlandes, Klinikum Bau 76, D-66421 Homburg, Germany

Free radical formation in dry DNA and chromatin

A recent EPR analysis of spectra from X-irradiated freeze-dried DNA (77 K to 300°K, 10 kGy to 480 kGy) yielded ten assigned radicals: the oxidized guanine, the reduced thymine and cytosine (two protonation states), the thymine allyl radical, two deoxyribose radicals (C1' and C3'), the 5-thymyl radical, the deprotonated guanine cation and a radical at N7 of a purine [1]. Bombardment with heavy ions (^{50}Ti (11.4 MeV/u), ^{68}Zn (5 MeV/u), ^{197}Au (11.4 MeV/u) and ^{209}Bi (11.4 MeV/u)) at about 100 K confirmed the presence of most primary radicals. The spectra at 9.5 GHz were nearly identical to those after X-irradiation. Dose response curves gave G-values and saturation concentrations in the same order of magnitude [2]. At identical doses, a significant increase of the thymine allyl and the C1' radicals was detected after for heavy ions in aggreement with reports for oxygen impingement [3]. Radical formation in dry chromatin (calf thymus) gave again strong similarities in the EPR spectra after irradiation with either X-rays or heavy ions. Quantitative measurements of pure DNA and of chromatin after X-irradiation together with spectral analysis point at a spin transfer from protein to DNA as was suggested earlier in the literature but was proven only now [4]. The effect of the Bragg-peak was probed specifically by stacking pellets of dry DNA. Xe (11.4 MeV/u) and Ni (6.0 and 11.4 MeV/u) ions were used. For Ni and Xe at 11.4 MeV/u the fourth pellet contains the Bragg-maximum, with Ni at 6.0 MeV/u it is located in the second disk. Fig. 1 shows, that the LET has no effect on the total radical yield in each disk before and in the Bragg-maximum but the amount of thymine allyl radicals as well as C1'- and C3'-deoxyribose radicals increases with LET and dose. The sugar radicals are potential precursors of strand breaks, which in turn are connected with abasic sites.

Product formation in dry DNA

Solid DNA and DNA-nucleotides were used to study the products formed from direct radiation action at 300 K (X-rays and heavy ions in the beam vacuum, respectively). Polycrystalline pyrimidine nucleotides showed the release of unaltered bases as investigated by HPLC and NMR. [5] Further heavy ion experiments with pyrimidine as well as purine nucleotides showed for all these DNA model compounds the formation of the free bases [6]. Recently we found the release of the bases adenine, cytosine and thymine also for dry DNA after heavy ion bombardment. The modified base 8-hydroxy-adenine was identified as another product. X-irradiation and bombardment with Ti (11.4 MeV/u) led to a similar release of unaltered and modified bases, whereas bombardment with Bi (11.4 MeV/u) resulted in a decreasing release of bases. In contrast to the low-LET-irradiation, bombardment with heavy ions effected an increased formation of formate (Fig. 2). This is connected with oxidative sugar dammage and thus is a probe for strandbreaks. The release of bases is also connected with strand breaks in DNA.. If the induced single strand breaks (ssb) appear within few base pairs, a double strand break (dsb) is fromed. The maximum dsb/ssb ratios were calculated for neon and titanium ions. [7] With the assumption that the release of bases and the formation of formate can be connected with a ssb of DNA, we determined a maximum for titanium ions

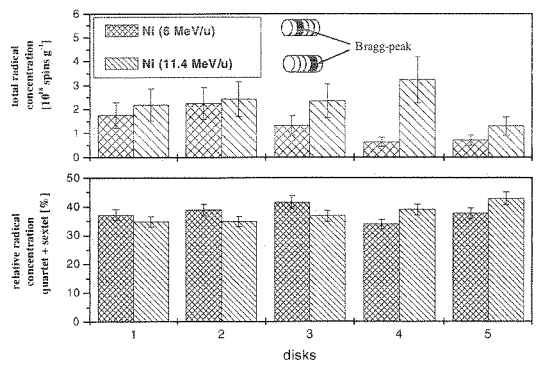

Fig.1 Total and relative radical yield vs. sample thickness

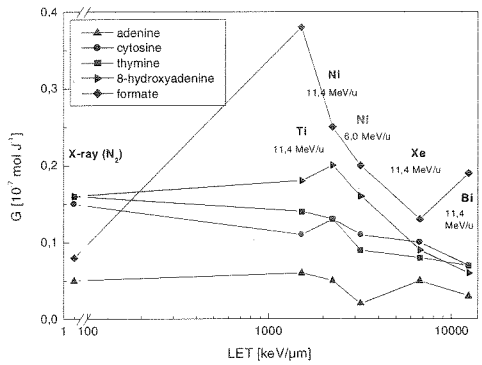

Fig.2 LET-dependence of product formation from DNA

References

[1] B. Weiland and J. Hüttermann, Int. J. Radiat. Biol., 1998, 74, 341-358.

[2] B. Weiland and J. Hüttermann, Int. J. Radiat. Biol., 1999, 1169-1175.

[3] D. Becker et al., Radiat. Res., 1996, 146, 361-368.

[4] B. Weiland and J. Hüttermann, Int. J. Radiat. Biol., 2000, 1075-1084.

[5] A.-K. Hoffmann and J. Hüttermann, Int. J. Radiat. Biol. 1997, 72, 735 - 744.

[6] A.-K. Hoffmann and J. Hüttermann, Int. J. Radiat. Biol. 2000, 76, 1167-1178

[7] [7] J. Heilmann et al., Radiat. Res. 1993, 135, 46-55.

Calculation of depth dose profiles with a track structure code

M. Krämer, GSI

A prerequisite for applying high-LET radiation like protons or carbon ions to patients is the precise knowledge of absorbed dose, specifically the depth dose distribution. The legal restraints imposed by the authorities requires the Bragg peak position to be reproduced within 0.5 mm and the calculated absorbed dose distribution to agree within 5% (on average) with the measurements. These conditions are usually met by our treatment planning code TRiP98 [1, 3] and its builtin beam model [4]. This code uses semi-empirical fragmentation cross sections and external energy loss tables to compute numerically the depth dose distributions. The question now arises whether microscopic Monte Carlo (MC) codes based on single interactions of ions and δ-electrons could reproduce depth dose distributions with similar accuracy. The answer is not obvious since ab-initio simulations would need very accurate primary interaction cross sections.

To address this question an established heavy ion track structure MC code [5] was reworked (TRAX, [6]). In particular, the restriction to track segment conditions has been removed so that ion depth dose profiles can easily be calculated. In addition, other therapy-relevant quantities like ionization yields in dosimetric setups and possibly even W-values could be simulated on a very basic level.

Total and differential elastic scattering cross sections for electrons were fitted to experimental data, as well as the excitation cross sections. Total electron ionization cross sections are calculated according to the relativistic model of Kim [7] with empirical corrections to match low-energy experimental data.

Ion cross sections are contructed semi-empirically as well. The relativistic Kim model was modified for ions to obtain the total ionization cross section, whereas the energy differential δ-electron cross section was evaluated with Rudd's formulae [8]. The angular distribution of δ-electrons was taken from the Binary Encounter Approximation. However, since depth dose distributions are one-dimensional projections and because the path of δ-electrons in water is short compared with the ion penetration depth, the accuracy of the angular distribution plays only a minor role. In contrast to track segment calculations where excitations by ions are usually neglected, these processes have to be included here to obtain reasonable agreement with the established energy loss tables. Since there are no experimental or theoretical data available an empirical approach was chosen by resorting to the electron excitation cross sections with the same velocity.

At first only exploratory calculations were performed, so nuclear fragmentation processes have not been considered, they will certainly be included in future simulations.

A first criterion is the correctness of the energy loss curve compared with the conventional approach. Figure 1 shows the ion energy loss obtained by integrating the δ-electron spectra and adding the binding energy as well as the energy loss from excitation. The agreement with the table used in our planning code is surprisingly good, with local deviations up to 4% in the therapy-relevant energy range from 1 MeV/u to 300 MeV/u. For very high and very low energies deviations are larger.

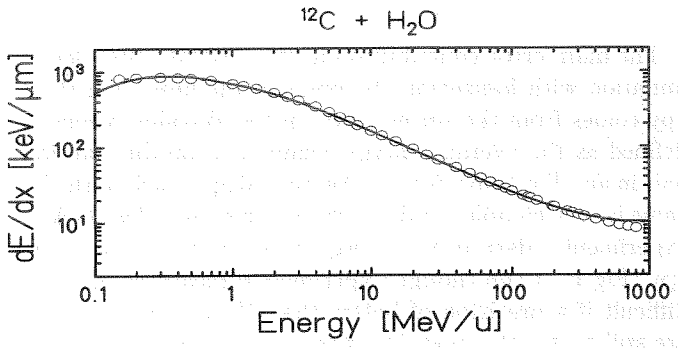

Figure 1: Energy loss for ^{12}C in H_2O. Symbols: from TRiP98, solid line: from TRAX

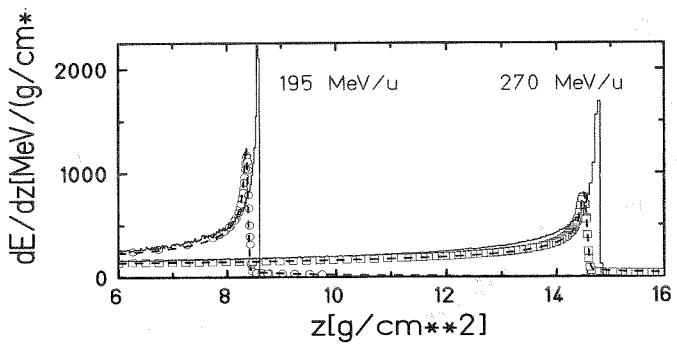

Figure 2: Depth dose profiles of ^{12}C in H_2O. Symbols: experimental data, dashed lines: TRiP98, solid lines: TRAX

Figure 2 compares the present MC results with depth dose calculations from treatment planning as well as experimental data. Bragg peak positions are overestimated by 1.5 to 2.5 mm, this corresponds to a systematic underestimation of the energy loss. Since nuclear fragmentation has not yet been included, the dose values around the Bragg peak are largely overestimated. To bring the MC results in sync with TRiP98 and experiments the ionization and excitation cross sections have to be ameliorated and nuclear fragmentation has to be accounted for.

References

[1] M. Krämer et al, Phys. Med. Biol., 45/11 (2000) 3299
[2] M. Krämer et al, this report
[3] T. Haberer, GSI-report 94-09
[4] M. Krämer, G. Kraft, Rad. Env. Bioph., 33 (1994) 91
[5] http://www.gsi.de/ bio/DOCS/TRAX/DOCS/traxinst.html
[6] Y.-K. Kim, et al., Phys. Rev. A 62 (2000), in press.
[7] M. E. Rudd et al., Rev. Mod. Phys., 64/2 (1992) 441

W-value measurements for carbon ions

J. Rodriguez-Cossio, D. Schardt, C. Brusasco, B. Voss, U. Weber
GSI, Darmstadt

The main error contribution in the absolute dose determination with ionization chambers in the heavy ion therapy comes from the uncertainty on the W-value, which is defined as the average energy required to produce an ion pair in air. For heavy ions, a theoretical approach to the W value is very complex and, moreover, there is a clear lack of experimental data in the energy range of interest in therapy (Fig 1). Even though experimental measurements are difficult if a precision of better than 5% is required, they are still by far the most important and accurate source of W-values.

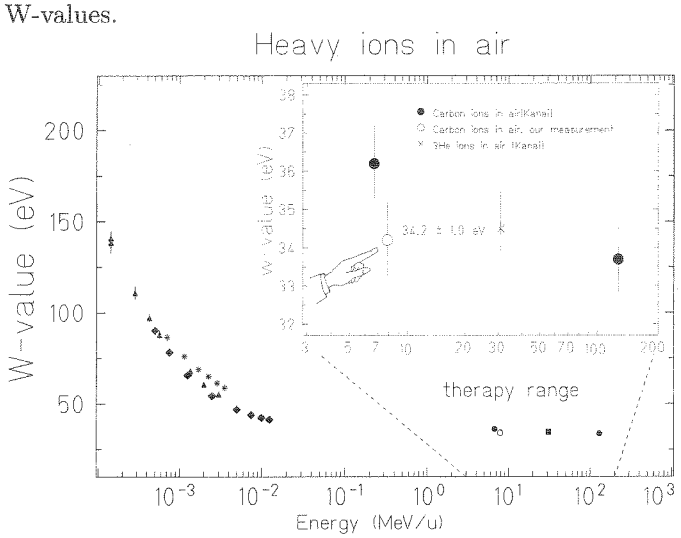

Figure 1: Compilation of the so far available W-value data for heavy ions in air.

In a measurement of the differential W value, three quantities have to be determined independently: the energy E of the incident ions, the mean energy ΔE deposited by one ion when traversing the gas gap and the mean number of ion pairs produced in the gas gap by one ion when dissipating ΔE. This last quantity can be obtained as the ratio of the number of primary ions N_{ions} and the chamber charge output Q, integrated during a certain interval. According to this, the differential W value can be expressed as:

$$w_E = \Delta E \cdot (N_{ions}/Q)$$

The measurements were carried out at the UNILAC target station X6. The beam passed through two double-slit collimators and a thin vacuum window (19 μm Hostaphan) in front of a parallel-plate ionisation chamber (IC) with 14 mm air gap and very thin entrance and exit foils (3,5 μm Mylar each). The energy lost in the vacuum window and in the air gap in front of the IC was calculated using the stopping power code ATIMA. Behind the IC the carbon ions were stopped in a 500 μm thick silicon detector. The energy loss in the air gap of the IC which enters into the w-value was determined as the energy difference observed in the silicon detector spectrum when moving it upstream by the IC gap distance using a precision linear drive.

In a second measurement, the ratio N_{ions}/Q was determined from the charge output of the IC, integrated by an electrometer with high accuracy, and the corresponding number of ions traversing the IC counted simultaneously in a fast scintillator. (Fig.2).

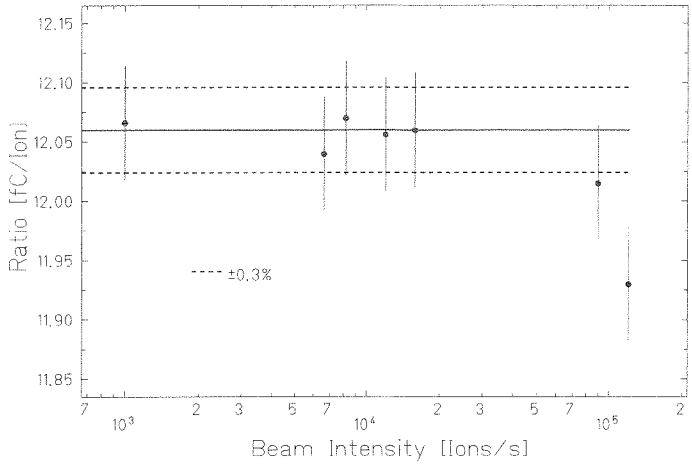

Figure 2: This plot shows the stability of the measured ratio charge per ion counted up to about 10^5 ions/s at the energy of 8 MeV/u. The decrease at higher intensities comes from the increasing relevance of the recombination effect in the chamber.

With this set-up we got the preliminary result :

$$w^{air}_{(7.6\pm0.3)MeV/u\ ^{12}C^{6+}ions} = (34.2 \pm 1.0)\,eV$$

In comparison with the result of Kanai et al.[1], our value is 6% lower but still in agreement within the given uncertainties as can be seen from Fig.1. The only other data points in the energy range relevant for tumor therapy are those for ^3He at 30 and ^{12}C at 129.4 MeV/u.

For future measurements, an optimised experimental set-up including an ionisation chamber with variable gap length is presently being constructed. The use of a CR39 plastics or diamond detector for the counting of the ions is also being studied for future measurements.

First tests were made at the SIS energy of 200 MeV/u in Cave A. The main findings are the strong build-up effect of the dose (about 5%) and the much weaker initial recombination, as expected, amounting only to a few per mille. The energy loss in the IC for these beam energies is only calculated, becoming a critical point, however, due to the discrepancy between tables when high precision is required.

[1] Kanai et al, Rad. Res. 135 (239), 1993

Fragmentation of High-Energy ^{12}C Ions in Tissue-Equivalent Targets

K.Gunzert, D.Schardt, R.S.Simon and M.Krämer, GSI Darmstadt

A detailed knowledge of the fragmentation properties of primary beam particles penetrating tissue is a major prerequisite for treatment planning in heavy-ion therapy. Projectile fragments are abundantly produced in peripheral nuclear collisions and have in general longer penetration ranges than the primary ions. This leads to a characteristic dose tail beyond the Bragg maximum. Furthermore, the lower-Z fragments have a different relative biological effectiveness as compared to the primary ions. Therefore, the composition of the particle field as a function of depth has to be included into the calculation of the biological effect.

Our earlier fragmentation studies concentrated on the measurement of production rates and angular and momentum distributions of charged particles produced by light ion beams (in particular ^{12}C) penetrating water and other tissue-equivalent targets [1,2,3]. These experiments were continued last year with the investigation of the fast neutron component.

A detector telescope consisting of a 15 cm long, 9 cm in diameter BaF_2 crystal and a 9 mm thin NE102 plastic scintillator in front of it was set up to measure yields, angular distributions and energy spectra of fast neutrons and of charged fragments generated by 100 to 400 MeV ^{12}C ions stopped in thick water, iron and lead targets. The thickness of the targets corresponded to 1.3 times the primary ion range. Operating the NE102 as a veto detector, neutrons can be discriminated from charged particles (mainly protons and α-particles). The neutron energies were measured by time-of-flight (3 m flight path) using a thin start detector (1 mm NE102) in front of the target. The neutron efficiency of the BaF_2 scintillator increases with neutron energy and is nearly constant (about 15%) in the range of 100 to 400 MeV. In collaboration with PTB Braunschweig (V. Dangendorf) the response of the BaF_2 detector was measured in the neutron beams available at Louvain-la-Neuve (Belgium) and Faure (South Africa) with energies of 45 MeV and 100 and 150 MeV respectively.

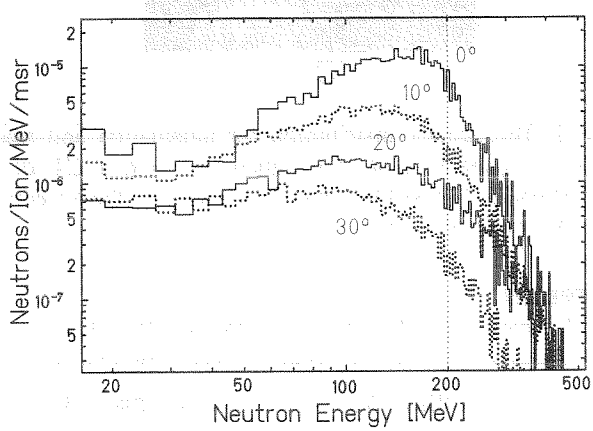

Figure 1: Neutron energy spectra from 200 AMeV ^{12}C ions in a 12.78 g/cm^2 thick water target at different angles.

The neutron energy spectra (Fig.1) show a broad peak at approximately 60% of the initial primary ion energy. This peak becomes more prominent in forward direction and signifies the production of fast neutrons in a break-up process while slower neutrons coming from evaporation processes are isotropically emitted. The fact that neutron energies up to about twice the energy of the incident particle are observed is due to the Fermi energy. These results were found to be in qualitative agreement with similar studies using ^4He ions stopped in various thick targets [4]. More recent results with heavier ions were reported in [5,6]. The angular distributions of energy-integrated spectra shown in figure 2 are forward peaked and gaussian shaped. The distributions of the neutrons and hydrogen (inclusive p, d, t) fragments are much broader than that for helium fragments.

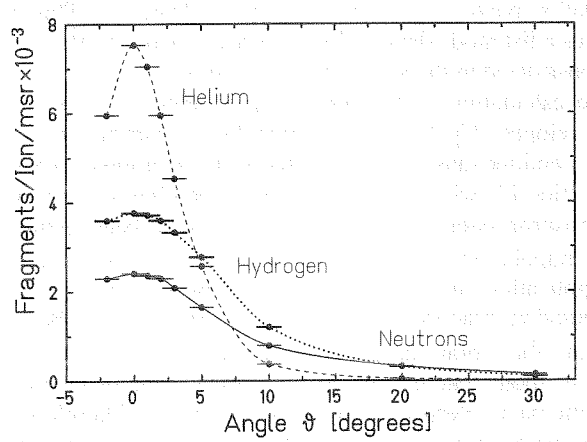

Figure 2: Angular distribution of neutrons, hydrogen and helium fragments produced by a 200 AMeV ^{12}C ion beam in a 12.78 g/cm^2 thick water target.

Besides these studies with phantom targets the characteristic of light particle production in actual patient treatments in Cave M was investigated. The telescope detector was placed 3 m downstream from the patient under polar angles of -5° to +90° degrees. Details of the observed spectra and fragment yields depend on the individual treatment plan, the location of the tumor and the patients anatomy. The aim of these studies is to compare the measured yields of light particles (n, H, He, Li) with those assumed by the physical model which was used for treatment planning.

References

[1] Schardt, D. *et al.*, Adv. Space Res. Vol.17, N° 2, 87(1996)

[2] Schall, I. *et al.*, NIM B 117,221(1996)

[3] Golovkov, M. *et al.*, Adv. in Hadrontherapy, Elsevier 1997, 316-324

[4] Cecil, R.A. *et al.*, Phys. Rev. C 21, 6, 2471-2484(1980)

[5] Kurosawa, T. *et al.*, Nucl. Sci. Eng. 132, 30-57(1999)

[6] Heilbronn, L. *et al.*, Nucl. Sci. Eng. 132, 2-15(1999)

Corrections of PET Data for Photon Attenuation, Scatter and Positron Range

F. Pönisch, W. Enghardt, B. Naumann; FZ Rossendorf
K. Lauckner; GSI Darmstadt

The evaluation of PET data acquired during ^{12}C therapeutic irradiations initiated a modification of the treatment planning data base improving the precision of the particle range in-vivo [1]. Thus, to an increasing extent delicate therapeutic situations characterized by high dose in close vicinity of organs at risk are treated. The validation of the correctness of such irradiations by means of PET requires precise and reliable methods of data processing. Since the PET control of therapy is based on the comparison of the β^+-activity distributions predicted from the treatment plan with those reconstructed from the data acquired during the patient treatment, both data sets have to be processed the same way. Therefore, the first step of the prediction is a Monte Carlo calculation [2] that describes the stopping of the therapeutic ion beam in tissue, the nuclear fragmentation, the decay of the β^+-emitters, the propagation of positrons and the annihilation photons and finally the γ-ray detection. This code produces a list mode data set like a measurement and thus it can be reconstructed in the same way as measured data.

For the calculation of the positron propagation a new model was developed. Up to now the probability distribution of the positron emitter range was supposed to be a bilinear exponential function [3] with three parameters depending on the maximum positron energy. These parameters have been estimated for β^+-endpoint energies up to 3.5 MeV, which is sufficient for PET applications in nuclear medicine. However, in the nuclear fragmentation reactions between the therapeutic carbon ion beam and the atomic nuclei of the tissue β^+-emitters of much higher endpoint energy (up to 16.7 MeV) are produced for which the parameterization of [3] is not proved. Therefore, the positron range distributions have been calculated by means of GEANT [4] simulations for all positron emitting isotopes that may be produced by the fragmentation of ^{12}C ions in tissue. In Fig. 1 the projection of the 3D spatial distribution on an arbitrary oriented axis (denoted with x) obtained by GEANT is compared with those of Hasch [2] and Derenzo [3]. A look-up table was generated on the basis of the GEANT results. This database is used for the sampling of positron ranges by means of choosing equally distributed random numbers within the interval [0,1].

In the original Monte Carlo code photon scattering was processed in a simplified way by assuming a homogeneous scatter volume (ρ = 1.18 g/cm^3) centred in the field of view (FOV) of the positron camera. Thus, the simulated data had to be reconstructed without attenuation correction. Obviously this approach is quantitatively incorrect and neglects the large tissue inhomogeneities of the head and neck region, as the typical target for carbon ion therapy at GSI. Therefore, a more comprehensive scatter description has been developed. It requires an attenuation map containing the information on the tissue composition and densities within and nearby the camera FOV. These information are derived from the X-ray computed tomograms (CT) of the patient and the head rest CT [5]. The two data sets (Fig. 2) are automatically merged. The created data set is also the basis for the calculation of the attenuation correction factors which are used in the reconstruction. The Fig. 2 shows that there is a significant influence of absorption by the head rest on the detector response leading, if not corrected, to image artefacts in the reconstruction. The dashed lines denote the acceptance cone of the tomograph. Several approaches are applied to the modified code that do not influence the accuracy but reduce the computing time by a factor of 4 in comparison with the original method. The CT based photon scatter estimation allows the reconstruction algorithm to be applied to the measured and simulated PET list mode data in the same way. This is, furthermore, the condition for including a scatter correction algorithm in the reconstruction in order to evaluate both simulated and measured data quantitatively.

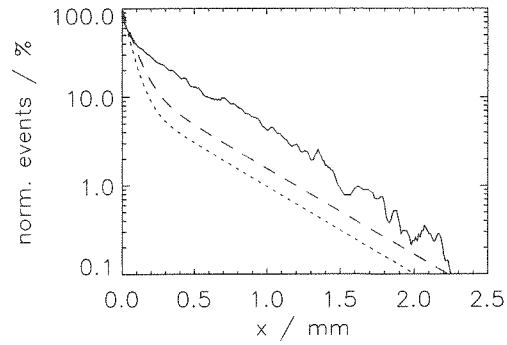

Figure 1: Projections of the positron range distributions for ^{11}C of this work (solid), Derenzo (dashed) and Hasch (dotted)

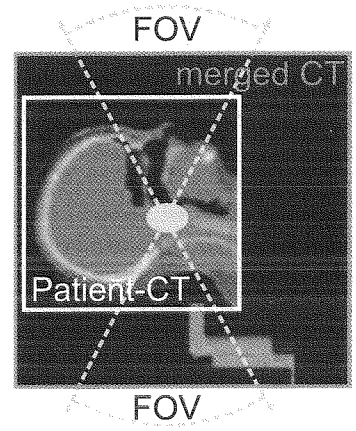

Figure 2: The density distribution for attenuation and scatter correction compared from the patient CT and a CT of the patient support. A possible tumour location and the acceptance cone of the positron camera are displayed.

References

[1] W. Enghardt et al., GSI Scientific Report 1999, 164

[2] B. G. Hasch et al., Annual Report 1996, FZR-179 , 87

[3] S. E. Derenzo, IEEE Trans. Nucl. Sci., 33 (1986), 565

[4] GEANT-Det. Descript., CERN Prog. Lib. W5013, (1994)

[5] F. Pönisch et al., FZR, Annual Report 2000 "An X-ray CT based attenuation correction ...", in press

Positron Emission Tomography (PET) for Ion Therapy Quality Assurance

W. Enghardt, K. Parodi, J. Pawelke, F. Pönisch, M. Sobiella; FZ Rossendorf
P. Crespo, T. Haberer, C. Kausch, K. Lauckner, D. Schardt; GSI Darmstadt

The therapeutic irradiations of 30 patients in 2000 have been observed by PET. The data verified that the modifications of the treatment planning data base [1] considerably improved the precision of dose localization even in delicate situations of very deep-seated and inhomogeneous target volumes (Fig. 1). However, still unpredictable dose deviations may occur because of

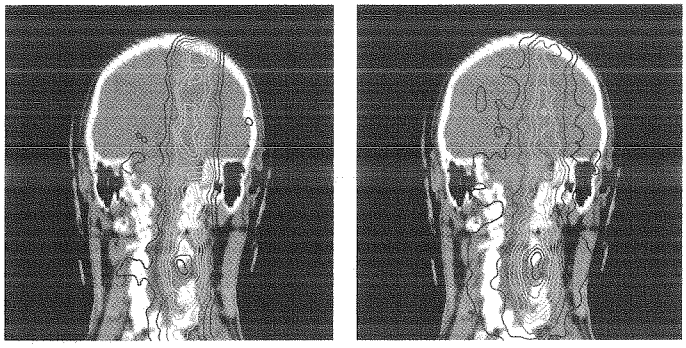

Figure 1: β^+-activity distributions for an irradiation of a tumour in the neck region from cranial, left: prediction from the treatment plan, right: measurement.

minor repositioning errors in connection with sharp density gradients in the beam path or changes in the physical condition of the patient. To quantify such deviations from PET data, improved attenuation, scatter [2] and random [3] correction methods for the measured data as well as refined models (positron range, photon scattering) for predicting the β^+-activity distribution from the treatment plan [2] are introduced. Furthermore, to compensate for the metabolic washout of the positron emitters, which is correlated to the local blood flow [4], the tissue dependent biological half-lives of the β^+-activity have to be known. It is expected that this information can be extracted from the more than 2600 list mode PET data sets measured during patient irradiations so far. An appropriate code that allows the data to be analyzed simultaneously in ordinary space and in the time domain has been developed.

To increase the flexibility in treatment planning the therapy facility will be equipped with a chair [5] for irradiating patients in a sitting position. This required to build a completely new PET gantry (Fig. 2), which allows the detector heads to be rotated around the beam axis [3].

Combining an in-beam PET scanner with an ion beam gantry, as it is planned for the Heidelberg clinical facility, requires new technical solutions, namely new scanner configurations. To predict their imaging properties a versatile PET simulation and reconstruction tool has been developed [3]. Gantry-delivered multi-field irradiations are expected to result in PET scans of low counting statistics, and thus, an optimization of the signal-to-noise ratio is required. For this we studied [6] the possibility of using the new scintillator material lutetium orthosilicate (LSO), which is superior to the currently used bismuth germanate (BGO). This feasibility study was addressed to the influence of background coincidences arising from the β^--decay of ^{176}Lu. Natural Lu contains 2.59 % of this isotope leading to

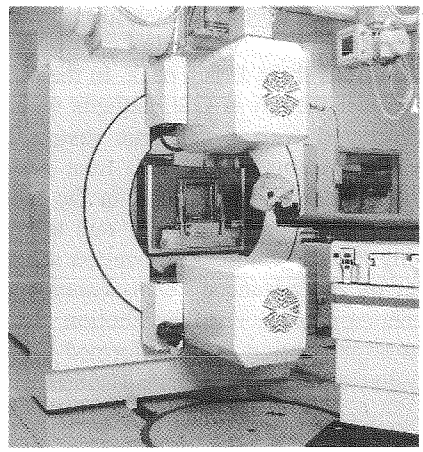

Figure 2: The new PET gantry. (Photo: A. Zschau, GSI).

an activity of 280 Bq per cm^3 of LSO. However, by means of a correct energy discrimination the influence of the natural activity to the images is eliminated and LSO seems to be a suitable scintillator material for in-beam PET.

In [7] we investigated an extension of the in-beam PET technique to proton therapy monitoring. During accelerator experiments in December 2000 proton beams of 110, 140 and 175 MeV have been delivered to cave M. They have been completely stopped in lucite phantoms positioned in the field of view of the positron camera. Depth distributions of β^+-activity have been measured with good statistics (Fig. 3) and the activity produced by protons has been found to be 3.2 ± 0.9 as high as that of carbon ions of equal dose and range.

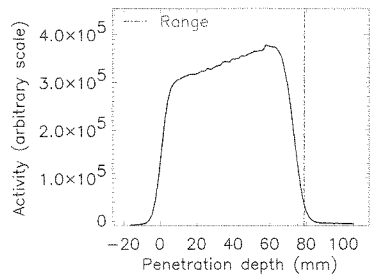

Figure 3: Depth distribution of β^+-activity produced by a proton beam of 110 MeV (range marked by a dashed-dotted line).

References

[1] E. Rietzel et al., Scientific Report 2000, GSI 2000-1, p. 166

[2] F. Pönisch et al., This Report

[3] Annual Report 2000, Institute of Nuclear and Hadron Physics, FZ Rossendorf, Part: Biomedical Research (in press)

[4] R. Hinz, Thesis, Dresden University of Technology, 2000

[5] P. Heeg et al., Scientific Report 2000, GSI 2000-1, p. 167

[6] K. Lauckner et al., IEEE Nucl. Sci. Symp. and Med. Imag. Conf. 2000, Lyon, France, Conference Records

[7] K. Parodi, W. Enghardt, Phys. Med. Biol. 45 (2000) N151

Computer simulations concerning influence of target motion on dose distribution delivered by the GSI raster scanner

Q.Li[1,2] S.Groezinger[1] T.Haberer[1] U.Weber[1] G.Kraft[1]
[1)]GSI Darmstadt, [2)]IMP-CAS Lanzhou

Target motion is a very big problem in conformal radiotherapy (CRT), especiallly for a charged particle beam because of its less lateral scattering and sharp Bragg peak. In the pilot project of the heavy-ion cancer therapy at GSI, patients with head and neck tumors are treated with a magnetic raster scanner[1]. However, if the raster scanner is used to treat patients with body tumors, motion of tumors is present in the lung, breast, liver, kidney and other disease sites, e.g. due to respiration. Therefore, applying the static dose optimization schemes[2] to the moving target by the advanced beam scanning technique could lead to a inhomogeneous dose distribution. So computer simulations about target motion were performed and Gaussian beam profile and sinusoidal movement are assumed as follows,

$$I(x,y) \sim e^{-\frac{x^2+y^2}{2\sigma^2}}, FWHM = \sqrt{8\ln 2}\sigma \quad (1)$$

$$\vec{r}(t) = A_r \sin(2\pi \frac{t}{T_r} + \Phi_0) \cdot \vec{r}_0 \quad (2)$$

here A_r, T_r and Φ_0 are the amplitude, period and initial phase of the movement, respectively. In clinical situation, the average amplitudes of respiration in cranio-caudal and lateral directions are 15mm and 5mm, respectively[3][4]. So maximum displacements of 15mm and 5mm of target volume with 40x40cm^2 in area under beam's eye view along the two different sides were assumed. Realistic raster scanning parameters for the irradiation of the rectangle were supposed, that is, scan stepsizes in x and y directions are 2mm, respectively, and the raster scanner keeps waiting till the prescribed particles have been deposited at a raster point and then moves to next one with a maximum speed of 10m/s.

The computer simulations were carried out with an experimentally measured beam-spill profile. Fig.1(a) and (b) show the dose distributions for static and moving targets delivered by the raster scanner. It is obvious that the dose homogeneity in the target volume decreases considerably in the case of target motion. In order to assess the inherent variability of dose homogeneity resulting from randomly initial phases, all the calculations repeated 10 times with randomly initial phases and the average values were regarded as the results.

Fig.2(a) shows the relationship between dose homogeneity and rescan at different prescribed particles per raster position. The dose fall-off width through the center of the target volume from the edge to 10% average dose level were also caculated. The dose homogeneity would be improved as the rescan time increases at the expense of the dose fall-off width. Moreover, the increment of dose homogeneity is small and the average dose fall-off widths increase by factors of 2.9 and 1.4 in x and y directions respectively when the rescan exceeds 5 times. In fact, the dose homogeneity will not be better than 82% only by means of rescan for a moving target.

The influence of moving period from 2s to 8s on the dose homogeneity was investigated. The results shows the medial respiratory cycle, for example 4s to 6s, would increase the dose homogeneity when the particle number per raster point is less than 4×10^5. Usually the displacements of target volume due to respiration in different directions are not the same, and the raster scanner has different scanning speeds in horizontal and vertical directions. So the influence of scanning direction along different movement amplitude on dose homogeneity was also evaluated. The result shows if the fast scanning direction (x axis in the simulations) of the raster scanner coincides with that of target movement with large amplitude, for instance the cranio-caudal direction, the dose homogeneity would be improved for prescribed particles per raster point less than 8×10^5 in comparison with the contrary case. When the particle number exceeds this limit, the situation is just contrarious.

Different ratios of raster spacing(δ) to FWHM would result in variable dose homogeneity in the static target volume with the raster scanner[1] as shown in the upper part of Fig.2(b). The computer simulations of moving target were made for raster scanning parameter with different δ/FWHM ratios from 0.25 to 0.5. As shown in the lower part of Fig.2(b), it is apparent that the dose homogeneity for raster scanning parameter with large δ/FWHM ratio would be better than that with small one for same specified particles at each raster position

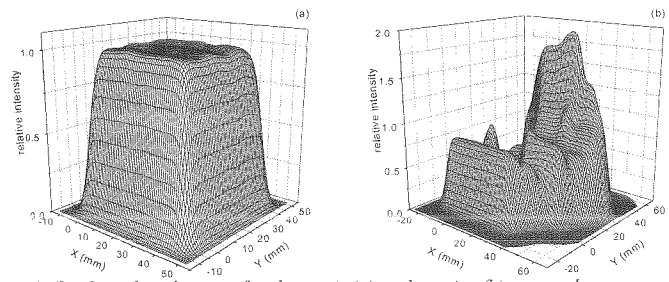

Fig.1 The dose distributions for the static(a) and moving(b) rectangle targets at the particle number per raster position of 5×10^5.

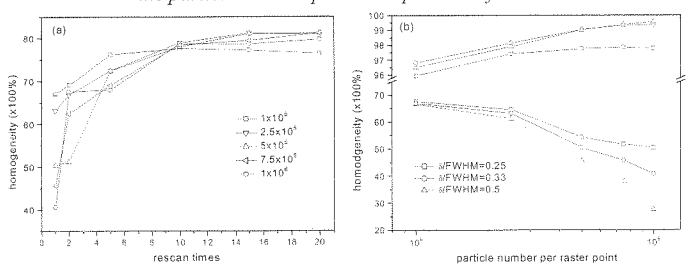

Fig.2 The relationships between dose homogeneity and rescan(a)and ratio of FWHM to raster spacing(b) at differing prescribed particles each raster point.

The simulations here provide a means for evaluating the dose distribution, and the results and implications of this work are being incorporated into the design of a method to compensate for the target motion with the raster scanner at GSI.

References

[1] T.Haberer, et al. Nucl Instrum Meth. A330, 1993:296.
[2] M.Kraemer, et al. Phys Med Biol. 45, 2000:3299.
[3] C.X.Yu, et al. Phys Med Biol. 43, 1998:91.
[4] S.Shimizu, et al. Int J Radiat Oncol Biol Phy. 48, 2000:471.

Treatment planning for the GSI radiotherapy

M. Krämer, C. Brusasco, C. Kausch, E. Rietzel, U. Weber, GSI; O. Jäkel, DKFZ

Throughout the year 2000 our standard treatment planning software TRiP98 [1, 2] which went into production last year [3] was used in combination with the Voxelplan environment for the planning of all 32 patients [4]. Specific improvements on the software side were the introduction of inhomogeneous dose prescriptions, extensions of the beam model and addition of auxiliary functions.

Inhomogeneous dose prescriptions

One major user requirement was the possibility of prescribing partial fields with individually inhomogeneous dose distributions across the target volumes instead of a constant overall weighting of the single fields. The superposition of the partial fields should yield again a homogeneous biologically effective dose distribution. This task was basically solved by allowing to specify 3D dose weighting information. In a first step a weighting cube with a ramp-like dose gradient across the target volume is generated. The gradient should, but need not, be along the beam's eye-view of the irradiation field. Since we have to account for biologically effective dose the initial weighting prescription has to be modified in a second step according to the rules of nonlinear effective dose addition [5] thus yielding two complementary biologically effective 3D weighting distributions. Finally, these distributions are fed into our established single-field optimization procedures, which have been modified to cope with inhomogeneous dose prescriptions instead of a single value. Dose superposition, assessment and verification proceed as usual.

Extensions of the beam model

Our treatment planning code includes a refined and streamlined version of the YIELD beam model [6]. It has been further improved for ^{12}C primary particles by adapting the projectile fragmentation cross sections. It was found that in the vicinity of the Bragg peak heavy fragments were overestimated whereas light fragments were underestimated. This caused a slight overestimation of absorbed and of biologically effective dose beyond the Bragg peak. The improved beam model will be verified and included into the production version in 2001.

Although not verified for primary particles other than ^{12}C our beam model can preliminary be used for treatment planning of lighter projectiles - in view of the upcoming clinic facility. Exploratory calculations showed that there is probably no significant benefit in terms of the ratio of target to entrance (exit) dose for projectiles lighter than carbon, in contrast to other predictions [7].

Miscellaneous improvements

A raster scan path algorithm was introduced which handles irregular patterns of scanner positions - a prerequisite for scanner optimization for moving targets [8].

Another add-on is the evaluation of dose-volume histograms (DVHs) as "figures of merit". Traditionally they are calculated and assessed within the Voxelplan environment. However, with the future multi-field optimization

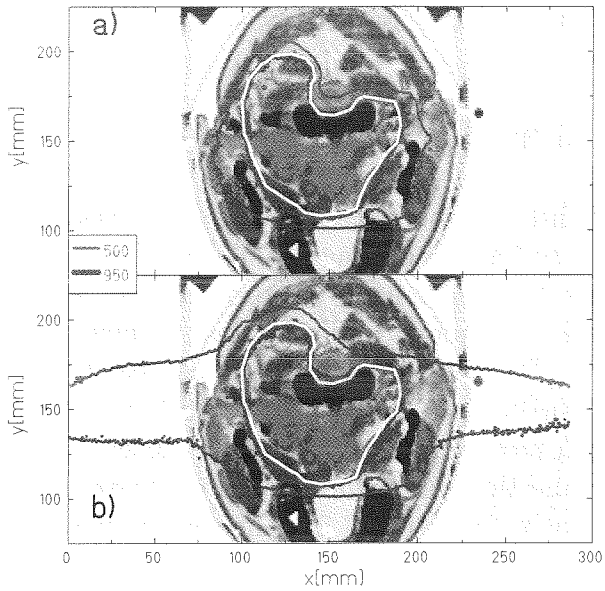

Figure 1: Patient plan with (a) 3 partial dose ramps and with (b) conventional opposing fields. Target as well as 50 and 95% isodoses are shown.

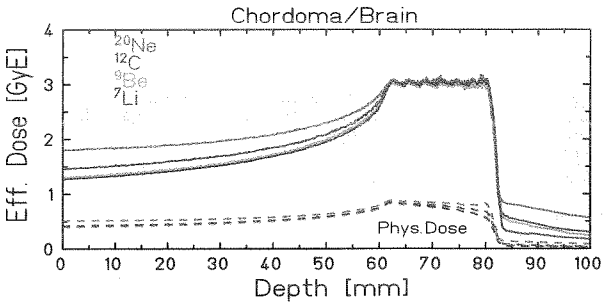

Figure 2: Biological dose profiles for various projectiles

in mind, DVH constraints will be necessary as objective functions for optimization already at the TRiP98 level.

Since the DKFZ CT scanner used since 1997 was replaced by a new one the Hounsfield calibration table had to be revised. Extensive measurements showed that reusing the old table would not lead to significant misalignments.

References

[1] M. Krämer et al, Phys. Med. Biol., 45/11 (2000) 3299
[2] M. Krämer et al, Phys. Med. Biol., 45/11 (2000) 3319
[3] M. Krämer et al, GSI Scientific Report 1999
[4] O. Jäkel et al., Phys. Med. Biol., 46 (2001), in press
[5] M. Krämer, J. Radiat. Res. 41/4 (2000), in press
[6] T. Haberer, GSI-report 94-09
[7] A. Brahme, GSI-report 2000-04
[8] Q. Li et al, this report

Heavy-Ion Therapy at GSI: Progress Report

Th. Haberer, J. Debus, H. Eickhoff, W. Enghardt, P. Heeg, G. Kraft, D. Schardt

GSI Darmstadt, Radiologische Klinik Heidelberg, FZ Rossendorf, DKFZ Heidelberg

Clinical Trials

In 2000 three Carbon beam blocks were used to treat 32 patients suffering from skull base tumors such as chordomas, chondrosarcomas, adenoid cystic carcinomas and other less frequent indications. Partially these ongoing clinical trials have reached phase II level. In total 73 patients have been treated within this experimental programme and the overwhelming part of treatments had a curative intention [1,2]. The very promising local control rate as well as the low treatment related toxicity rate kick off new clinical goals like a dose escalation or the treatment of extracranial locations. In preparation of treatments in the pelvic region a dedicated immobilization device was tested at GSI (see figure 1) and the mandatory approval is under way.

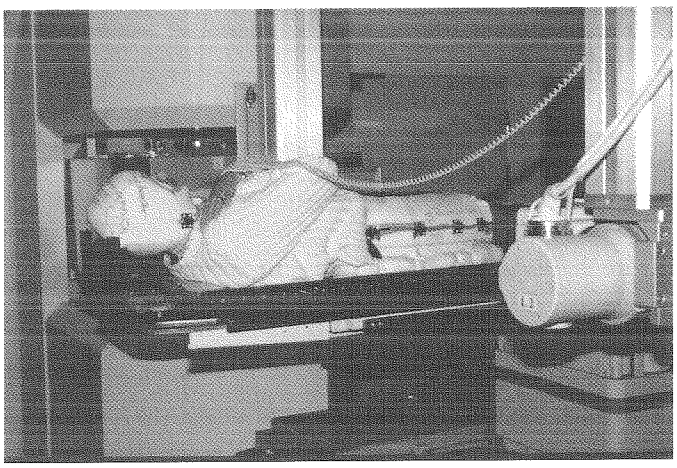

Figure 1: Patient in a rigid immobilization device adapted for the patient couch of GSI's medical cave.

Physical-technical Aspects

In the third year of routine operation $\approx$ 20% of the SIS-beamtime were used to operate the medical cave for 13 weeks in a time-sharing mode with physics experiments. The performance of the GSI accelerators reached an excellent level of more than 95% beam availability.
The limited angle positron camera BASTEI [3] installed at our treatment facility was upgraded to be rotatable (see figure 2). This feature will allow the use of the PET-method in combination with the patient chair which presently is under commissioning and should be operational by the end of 2001 [4]. This additional functionality will extend the variety of entrance channels thus offering the possibility of treating more patients and further reduce the unavoidable dose to the organs at risk.

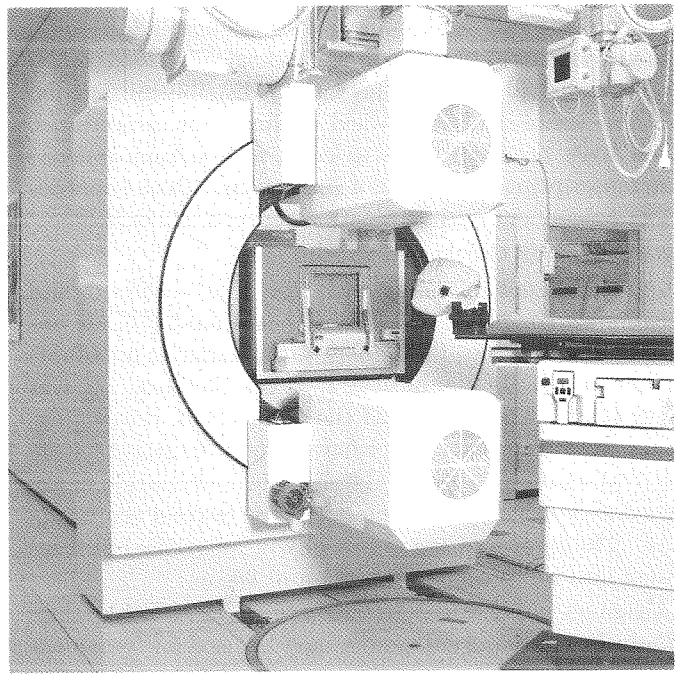

Figure 2: The nozzle of the treatment facility with the rotatable head of the PET camera.

References

[1] J. Debus et al., Strahlentherapie und Onkologie, 2000, 176(5): 211–216
[2] D. Schulz-Ertner et al., this report
[3] R. Hinz et al., Physica Medica **XIII/1**,1997, p. 61
[4] P. Heeg at al., GSI annual report 1999

Patient irradiations at GSI

D. Schulz-Ertner, C. Thilmann, M. Wannenmacher, J. Debus

Before patient irradiations started in 1997, a radiation unit was built at the heavy ion synchrotron of the GSI and major future directed technical and radiobiological innovations have been implemented. For the first time, tumor conform application of carbon beams was realized by intensity-controlled rasterscanning with pulse-to-pulse energy variation [1]. All patients had 3D treatment planning including a biological plan optimization using the treatment planning program TRIP developed at GSI [2]. A PET camera is used for online beam verification [3].

Up to now, 73 patients with tumors of the skull base and the brain have been treated with carbon ions. The study mainly contained patients with chordomas (33) and low grade chondrosarcomas (16) of the skull base, adenoid cystic carcinomas (8) and malignant meningiomas (8). These tumors are known to be relatively radioresistant against conventional photon irradiation. Proton radiotherapy has been shown to improve outcome in chordomas and low grade chondrosarcomas [4] but its availability is limited. In adenoid cystic carcinomas radiation therapy with heavy particles as neutrons results in improved local control rates compared to photon irradiation but causes severe side effects [5]. Malignant meningeomas commonly recur within the former irradiated fields even after high tumor doses. Carbon ion therapy presents a promising therapy option in the management of these tumors.

Within the feasibility study, median tumor dose was 60 GyE in chordomas and chondrosarcomas. Patients with adenoid cystic carcinomas and malignant meningiomas received fractionated stereotactic photon irradiation at Heidelberg University with a median dose of 50.4 Gy and a carbon ion boost with 18 GyE (6 x 3.0 GyE) to the gross tumor. Feasibility of this new therapy approach has been shown. First results are very promising with a local control rate of 94% at 1 year [6]. We observed a partial tumor regression in 7 of 33 patients treated for chordoma indicating that carbon ion therapy is effective in these tumors (figure 1+2). Tumor regression in chordomas is a finding which is rarely reported in literature after any kind of radiation therapy. Besides, active beam delivery using raster scanning allows for highly conformal dose distributions and therefore results in an optimal sparing of neighbouring normal tissue. The low toxicity rate allows further dose escalation. As a consequence the total tumor dose has been escalated from 60 GyE to 70 GyE for chordomas and chondrosarcomas in the following phase II study which has been activated in November 2000. A rigid immobilization device developed by Lohr et al.at DKFZ [7] has been tested at GSI and will guarantee the safe irradiation of extracranial tumors. In 2001 a phase I/II study for the treatment of sacral / spinal chordomas and low grade chondrosarcomas will be activated. Furthermore, photon irradiation with a carbon ion boost will be available within a clinical phase I/II study for adenoid cystic carcinomas in 2001.

Figure 1+2. Chordoma of the skull base a) prior to RT, b) 3 months after RT with carbon ions.

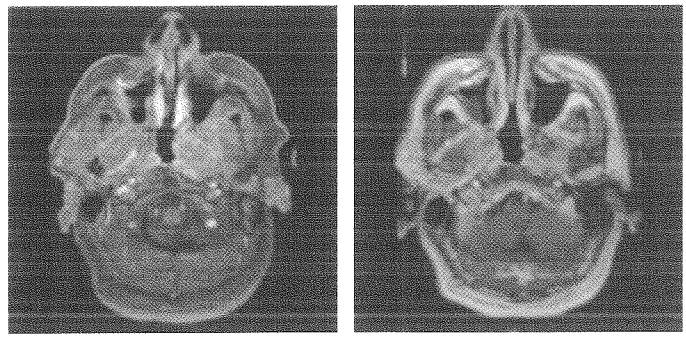

References

[1] Haberer T et al. Magnetic scanning system for heavy ion thrapy. Nucl Inst Phys Res 1993; 330:296-305.

[2] Scholz M et al. Cell cycle delays induced by heavy ion irradiation of synchronous mammilian cells. Int J Radiat Oncol Biol Phys 1994; 66:59-75.

[3] Enghardt W et al. The application of PET to quality assurance of heavy ion tumor therapy. Strahlenther Onkol 1999; 175:Suppl II:33-36.

[4] Munzenrider JE et al. Proton therapy for tumors of the skull base. Strahlenther Onkol 1999; 175:Suppl II:57-63.

[5] Krull A et al. Neutron therapy in malignant salivary gland tumors: results at European centers. Recent Res Cancer Res 1998; 150:88-99.

[6] Debus J et al. Carbon ion irradiation of skull base tumors at GSI. First clinical results and future perspectives. Strahlenther Onkol 2000; 176(5):211-216.

[7] Lohr et al. Noninvasive patient fixation for extracranial stereotactic radiotherapy. Int J Radiat Oncol Biol Phys 1999; 45(2):521-527.

K_d-Value Determination for ^{261}Rf (Element 104) with the Multi-Column Technique

A. Kronenberg[1], J.V. Kratz[1], P.K. Mohapatra[1], W. Brüchle[2], M. Schädel[2], B. Eichler[3], H.W. Gäggeler[3], A. Türler[3]
[1]Institut für Kernchemie, Universität Mainz, [2]GSI Darmstadt, [3]PSI Villingen (Switzerland)

After online experiments with ^{165}Hf ($t_{1/2}$ = 76 s, decaying into ^{165}Lu) at GSI [1] we performed two experiments with the multi-column-technique [2] with Rutherfordium.
^{261}Rf was produced in the ^{248}Cm(^{18}O, 5n) reaction at the PSI Philips Cyclotron. A 730 µg/cm^2 ^{248}Cm target was bombarded with a 0.5 μA_{part} $^{18}O^{5+}$ beam. The KCl aerosols transporting the activities was continuously dissolved in a degasser with a yield > 80% at a tolerable pressure in the target chamber of 1.7 bar at a gas-flow rate of 1.6 – 1.7 L/min and a distance between the target chamber and the degasser of approximately 50 m. The hold-up time of the activity in the degasser was about 2 s. A solution-level of 50 to 150 µL was kept at the bottom of the degasser through control by a light barrier which caused, if activated, an adjustment of the flow rate from the HPLC pump that pumped the solution into the degasser. The active solution leaving the degasser was pumped by a double-piston HPLC pump at a flow rate of 1 mL/min through a capillary of 0.3 mm inner diameter to three columns connected sequentially: A cation filter followed by the true chromatographic column filled with an anion-exchange resin, the latter followed by another cation filter.
Two experiments were performed, one using 0.5 M HF/0.1 M HNO_3 as the mobile phase, another one using 0.01 M HF (without any HNO_3). The running time was 24 hours in both cases. In the first case, the cation-exchange columns were filled with 330 mg of DOWEX 50WX8, minus 400 mesh. These filters were used for 3 hours and were then replaced by new ones. This ensured that there was no break-through by any of the descendants of ^{261}Rf, i.e. ^{257}No, ^{253}Fm, and ^{253}Es. The anion-exchange column was filled with 50 mg of DOWEX 1X8, minus 400 mesh in the nitrate form.
17 mg of DOWEX 1X8 in the fluoride form was used in the experiment with 0.01 M HF. In this experiment, 68 mg of DOWEX50WX8 were used as cation filters for running times of 4 hours. The effluent from the final cation filter was collected in a reservoir (activity AE).
After the end of the experiment, the final cation filter was stripped with 5 M HNO_3 (activity AD). The solutions AE and AD were spiked with ^{241}Am. After adjusting its pH to 2, the solution containing AE was passed over a cation-exchange column where ^{253}Fm and ^{253}Es were sorbed. This column and the cation-exchange columns containing AD were stripped with 5 M HNO_3 and the solutions were evaporated to dryness. The residues were dissolved in 8 M HCl and iron (from the steel capillary of the gas jet) was extracted into Aliquat 336 in chloroform. After evaporation to dryness of the aqueous phases, the residues were dissolved in 10 µl of 0.1 M HNO_3 and transferred into isopropanol for molecular plating. The latter was performed with 1200 V onto thin Ti foils of 430 µg/cm^2 thickness. These were subject to α spectroscopy in 4-π-geometry for more than 60 days, three half-lives of ^{253}Es. Overall chemical yields determined via the ^{241}Am activity (E_α=5.5 MeV) were 65% on the average. The background in the relevant energy window near 6.6 MeV was 1.5 α events per week.

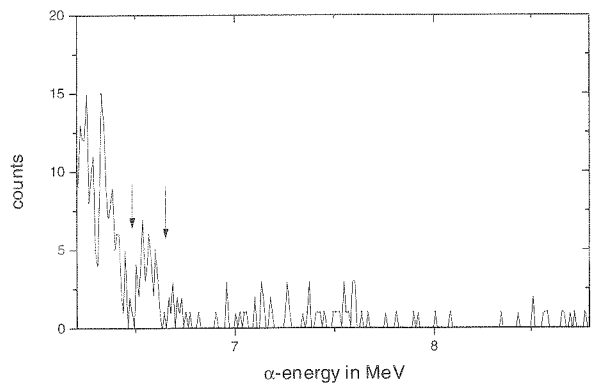

Fig 1: α–energy spectrum of sample AD in experiment 2 with the ^{253}Es energy window indicated by arrows.

In the first experiment using 0.5 M HF/ 0.1 M HNO_3, the entire ^{253}Es activity (80 events) was found in AE and no activity above background in AD indicating that the retention time of rutherfordium on the anion-exchange column must have been very short. From the activities, a **$K_d = 0^{+3}_{-0}$ mL/g** results in **0,5 M HF / 0,1 M HNO_3**. This is lower than the K_d value of ~5 determined with ARCA [3]. This is no major problem as it is known that K_d values < 10 are difficult to determine with ARCA and tend to be systematically high.
In the second experiment using 0.01 M HF (without HNO_3), we observed 90 events attributable to ^{253}Es in AD while no events above background were detected in AE. This leads within 1 standard deviation to a K_d value of **$394^{+\infty}_{-100}$ mL/g** in good agreement with data taken off-line by ARCA [4]. The error limits on the K_d values were determined by a Monte-Carlo simulation assuming a half life of ^{261}Rf of 78^{+11}_{-6} s [5] and a background due to electronic noise of 1.5 events per week in the interesting energy region (E_α=6.6 MeV).
These on-line experiments with ^{261}Rf corroborate the interesting finding [3,4] that the sensitivity of Rf fluoride complexes to the presence of the counter ion NO_3^- is much more pronounced than for the fluoride complexes of the lighter homologs Zr and Hf.

References

[1] A. Kronenberg et al.: GSI annual report 1998, 171
[2] A. Kronenberg et al.: Mainzer Jahresbericht 1999, 10
[3] E. Strub, J.V. Kratz, A. Kronenberg et al.: Radiochim. Acta 88(2000)265-271
[4] E. Strub, et al.:Mainzer Jahresbericht 2000
[5] B. Kadkhodayan et al.: Radiochim. Acta 72(1996) 169

Fluoride Complexation of Rutherfordium (Rf, Element 104)

E. Strub, J.V. Kratz, A. Kronenberg, A. Nähler, P. Thörle (Universität Mainz), W. Brüchle, E. Jäger, Z. Li, M. Schädel, B. Schausten, E. Schimpf (GSI Darmstadt),D. Jost, A. Türler (PSI), H.W. Gäggeler (Univ. Bern & PSI), J.P. Glatz (ITU Karlsruhe)

The distribution coefficient (K_d) of ^{261}Rf on ion exchange resins at various HNO_3/HF concentrations had been studied [1]. Rf was eluted at higher HF concentrations from CIX than Zr and Hf and rather resembled Th. Up to 1 M HF, Rf was not retained on the AIX also resembling its pseudo-homolog Th.

Th is known to form no anionic fluoride complexes, while Zr and Hf are forming complexes of the type $[MF_6]^{2-}$ in HF solutions and therefore can be resorbed on AIX resins.

We have continued these studiesNow of Rf and on-line produced Hf by systemetically varying both the HNO_3 and the HF concentration. If Rf is resembling Th, there should exist no concentration range in which Rf is adsorbed on the AIX.

^{261}Rf was produced in the ^{248}Cm(^{18}O,5n) reaction at the PSI Philips Cyclotron. A 730 µg/cm^2 ^{248}Cm target was bombarded with a 0.5 μA_{part} $^{18}O^{5+}$ beam. The target contained 10% Gd thus producing simultaneously short-lived Hf isotopes. Rf and Hf were transported by a He(KCl) gas jet and collected for 90 s by impaction on a slider in the Automatic Rapid Chemistry Apparatus ARCA II. The residue was dissolved in 200 µl 0.1 M HNO_3/x M HF (x variable) and fed onto the AIX. The effluent was evaporated to dryness as sample 1. In order to elute remaining Rf from the column, a second fraction (200 µl) was collected which is known to elute group 4 elements from the column (2 M HCl/0.01 M HF). This fraction was prepared as sample 2. 78-s ^{261}Rf was detected by α-spectroscopy. The counting time was 12 min. Every 8th pair of samples was monitored by additional γ-spectroscopy to determine the distribution of Hf. From the ratio of the counting rates, the K_d values were calculated.

The results are shown in in the table and are also plotted in the 3D graphs below (some values in the plot are interpolated).

It is obvious that the behavior of Rf and Hf in the examined system are remarkably different. While the K_d values of Rf are varying strongly with both HF and HNO_3 concentration, the dependence of the Hf K_d values on the acid concentrations is rather weak.

[HNO_3]	[HF]	log K_d (Hf)	log K_d (Rf)
0.1	0.01	2.1	0.8
0.1	0.03	2.1	0.9
0.1	0.05	2.0	0.8
0.1	0.5	2.1	0.9
0.1	1	2.2	0.7
0.03	0.5	2.2	1.7
0.01	0.01	2.1	1.0
0.01	0.05	2.3	1.6
0.01	0.5	2.5	1.6
0.003	0.5	2.7	1.7
0	0.01	2.5	2.7
0	0.1	2.7	2.4
0	0.5	2.8	1.8

Table: log K_d values of Hf and Rf in different media

Strong adsorption of both elements onto AIX can only be observed in pure HF solutions with concentrations [HF] > 0.01 M. This indicates the presence of anionic complexes under this condition which is in agreement with [3].

On the other hand, the sorption of the complexes on AIX seems to be influenced by the presence of other anions acting as counter ions on the exchanger resin (NO_3^- and/or HF_2^-, see [2]).

Thus, Rf shows the typical behavior of group 4 (formation of anionic fluoride complexes), but the interaction of these complexes with different counter ions is enhanced with respect to Zr and Hf.

References

[1] E. Strub et al., Radiochimica Acta 88, 265 (2000)
[2] E. Strub, Dissertation Universität Mainz (2000)
[3] Szeglowski et al., Radiochim. Acta 51, 71 (1990)

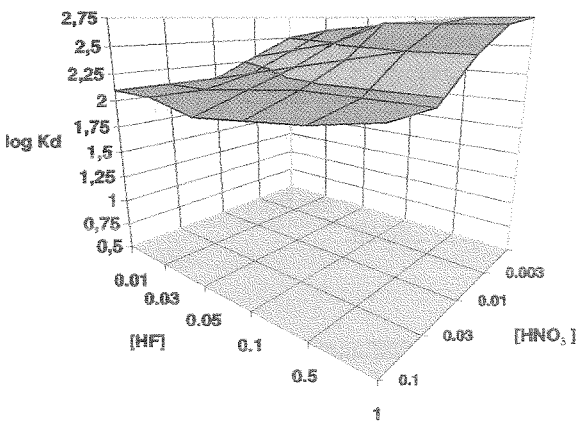

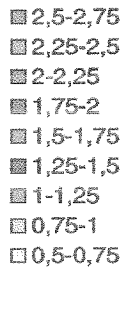

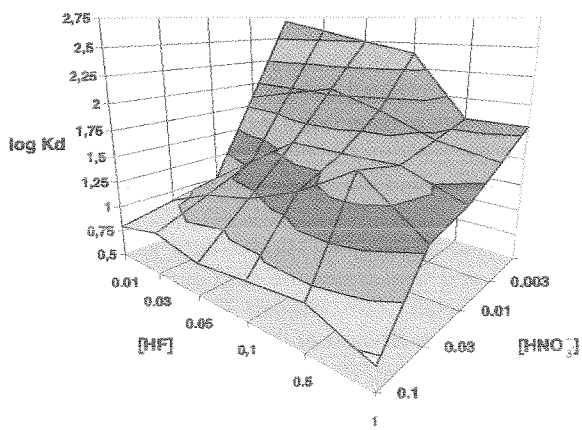

Fig.1: Sorption of Hf in HNO_3/HF solutions on a AIX resin (Aminex A27 or Riedel de Haën).

Fig.2: Sorption of Rf in HNO_3/HF solutions on a AIX resin (Aminex A27 or Riedel de Haën).

Theoretical Treatment of Fluoride Complexation of Element 104 in HF Solutions

V. Pershina[1,2] and J. V. Kratz[2]
[1]GSI, Darmstadt;
[2]Institut für Kernchemie, Universität Mainz, Mainz

Recent experiments on fluoride complexation of element 104, Rf, in aqueous HF/HNO_3 solutions [1,2] have demonstrated an unexpected behaviour of Rf in comparison with that of Zr and Hf: Whereas all the elements are retained as cations on cation exchange resins (CIX) below 10^{-3} HF, no rise of the K_d value of Rf is observed up to 1M HF in contrast to Zr and Hf when sorbed by anion exchange resins (AIX). This observation was tentatively interpreted as a difference in the competition between NO_3^- with respect to $RfF_x^{(x-4)-}$ on the one hand, and to $ZrF_x^{(x-4)-}$ and $HfF_x^{(x-4)-}$ on the other hand, for the binding sites on the AIX.

To interpret the unexpected behaviour of Rf in HF/HNO_3 solutions, we have studied the complex formation of Zr, Hf, and Rf theoretically using the model applied by us for prediction of complexation of element 105, Db, and element 106, Sg, in aqueous solutions [3,4].

In HF/HNO_3 solutions at HF between 10^{-3} M and 10^{-2} M HF/0.1 M HNO_3, at pH≅1, the complex formation can be described by the following equilibria

$$M(H_2O)_8^{4+} \Leftrightarrow MF(H_2O)_7^{3+} \;..\; \Leftrightarrow \;..\; MF_5(H_2O)^- \Leftrightarrow MF_6^{2-} \quad (1)$$

where M = Zr, Hf, and Rf. To predict the complex formation, the free energy change ΔG^r of equilibria (1) should be calculated. As an initial step, the following equilibrium was considered

$$M(H_2O)_8^{4+} + 6HF \Leftrightarrow MF_6^{2-} \quad (2)$$

According to our model, ΔG^r of a reaction can be expressed as

$$-\Delta G^r / 2.3RT = \Delta\sum a_i + \Delta\sum a_{ij} - \Delta S, \quad (3)$$

where $\sum a_i = OP$ (overlap population) is a non-electrostatic metal-ligand contribution to molecular bonding, and $\sum a_{ij} = \sum BQ_iQ_j / d_{ij}\varepsilon$ is a sum of each pairwise electrostatic interaction. Here, d_{ij} is the distance between moieties i and j; Q_i and Q_j are their effective charges; ε is a dielectric constant, and B is an independent constant. ΔS of eq. (3) is a change in the entropy term. Q_i and OP are obtained as a result of the Mulliken population analysis of the electronic structures of the complexes on the right- and left-hand side of reaction (2) calculated using the fully relativistic Density Functional Method (DFT) [5].

Geometry and bond lengths (R_e) of $M(H_2O)_8^{4+}$ (D_{2d}-symmetry) and MF_6^{2-} (M = Zr, Hf, and Rf) were assumed on the basis of analysis of the structural data for Zr and Hf and from calculated R_e for some simpler Rf gas-phase compounds [6].

As a result of the calculations, energetic, as well as electronic density distribution parameters were obtained. The Q_M and OP values (Table 1) show an increase in covalence of each type of complexes from Zr to Rf.

Table 1. E^C, ΔE^C (in eV) and ΔOP for the complexation reaction $M(H_2O)_8^{4+} \Leftrightarrow MF_6^{2-}$

E^C	Zr	Hf	Rf
Q_M: $M(H_2O)_8^{4+}$	1.97	1.89	1.85
Q_M: MF_6^{2-}	0.94	0.85	0.75
E^C: $M(H_2O)_8^{4+}$	-53.34	-52.07	-50.92
E^C : MF_6^{2-}	-2.60	-1.18	0.23
ΔE^C	50.75	50.88	51.15
OP: $M(H_2O)_8^{4+}$	8.93	9.03	9.11
OP: MF_6^{2-}	2.11	2.38	2.49
ΔOP	-6.82	-6.65	-6.62

The calculated E^C, ΔE^C and ΔOP, are also shown in Table 1. ΔE^C being the predominant type of the metal-ligand interaction shows that Rf should form complexes similarly to those of Zr and Hf only at slightly higher HF concentrations, so that the sequence in the complex formation is Zr > Hf > Rf. Thus, Rf is expected to be extracted by AIX shortly after Hf, with the differences between the three elements being very small.

The theoretically obtained sequence for Zr and Hf is in agreement with the experimental sequence for the descending K_d values in the sorption by CIX and the rising K_d values in the sorption by AIX. It is also in agreement with the descending K_d values for Rf in relation to those of Zr and Hf in the CIX sorption. Taking into account the very small difference in ΔG^r for the complexes of Rf as compared to those of Zr and Hf, the absence of a rising K_d curve on AIX for Rf at higher HF concentrations cannot be explained by the complexation step, provided the same types of complexes are formed. It can, at best, be accounted for by the formation of different types of complexes and their different partition. As a plausible explanation, formation of the neutral H_2RfF_6 in HF/0.1 M HNO_3 could be suggested due to a probable preference of the RfF_6^{2-} complex for the protonation. Nevertheless, from the point of view of the electronic structure of the Rf complexes, it is hard to foresee a large difference between Zr and Hf on the one hand, and Rf on the other hand, whatever is the process. The hypothesis suggested here, as well as those discussed in ref. [2], will be considered in our further theoretical research.

References

[1] E. Strub, *et al.*, *Radiochim. Acta* **88**, 265 (2000)
[2] E. Strub, *Zu den chemischen Eigenschaften von Rutherfordium, Dubnium und Seaborgium*, Thesis, Mainz 2000.
[3] V. Pershina, *Radiochim. Acta* **80**, 75 (1998)
[4] V. Pershina and J. V. Kratz, *Inorg. Chem.* **40**, 776 (2001)
[5] T. Bastug, *et al.*, *Chem. Phys. Lett.* **211**, 119 (1993)
[6] S. Varga *et al.*, *J. Phys. Chem.* **104**, 6495 (2000)

GAS CHEMICAL INVESTIGATION OF BOHRIUM (Bh, ELEMENT 107)

R. Eichler, Ch. Düllmann, H.W. Gäggeler (Univ. Bern & PSI), B. Eichler, D.T. Jost, D. Piquet, L. Tobler, A. Türler, P. Zimmermann (PSI), T. Häfeli, V.M. Lavanchy (Univ. Bern)
K.E. Gregorich, D.C. Hoffman, U. Kirbach, C.A. Laue, H. Nitsche, J. Patin, D.A. Shaughnessy, D. Strellis, P. Wilk (UCB&LBNL)
R. Dressler (TU Dresden), S. Hübener, S. Taut, A. Vahle (FZR)
W. Brüchle, M. Schädel (GSI)
Y. Tsyganov, A.B. Yakushev (JINR)

Neutron-rich isotopes of Bh can be produced in the nuclear fusion reaction ^{249}Bk(^{22}Ne;4n)^{267}Bh. The half-life of ~17 s and the production cross section of about 50 pb, which have been determined during the discovery experiment in Berkeley [1], make ^{267}Bh an ideal candidate to be used for gas phase chemical studies.

Assuming Bh to be a member of group 7 in the periodic table, a suitable chemical isolation procedure was developed in several model experiments using various nuclides of Tc and Re [2,3,4]. The gas chemical separation of MO_3Cl (M = Tc, Re) was shown to be suitable for the study of short-lived isotopes of group 7 elements.

A 670 µg/cm^2 ^{249}Bk target, prepared by LBNL, was irradiated at the PSI Philips cyclotron with a total beam dose of 3.02*10^{18} ^{22}Ne^{6+} particles at a beam energy of 119±1 MeV in the target and an average intensity of about 250 pnA for about 4 weeks. The nuclear reaction products were transported to the reaction oven of a low temperature OLGA III set-up using a carbon aerosol gas-jet. Shortly before the reaction oven a reactive gas mixture of HCl and O_2 was added to the gas-jet. At 1000°C the aerosol particles were burned in the reaction oven and the nuclear reaction products were converted to a large variety of oxides, chlorides, and oxychlorides. Subsequently this mixture of chemical products was separated according their adsorption interaction with the stationary quartz phase in the isothermal part of the chromatography set-up. This part was held at three different isothermal temperatures (T_{iso}). Only the most volatile compounds, able to pass the chromatography, were attached to another gas-jet of CsCl aerosol particles suspended in Ar to transport them to the detection system ROMA. For more details regarding the experimental set-up see [4,6].

6 correlated decay chains, attributed to the decay of ^{267}Bh have been observed. At 180°C and 150°C isothermal temperature (T_{iso}) 4 respectively 2 chains were detected. No Bh was registered at the same experimental sensitivity at 75°C.

The unambiguous identification of Bh after chemical separation allows to conclude that Bh forms a volatile oxychloride compound, presumably BhO_3Cl, and behaves like a typical member of group 7 of the periodic table. In order to evaluate first thermochemical data of bohrium, the relative yields of Bh at the adjusted isothermal temperatures have been calculated applying a careful statistical analysis of the data. The results are shown in Fig. 1 (squares) together with the yield vs. isothermal temperature curves of the corresponding compounds of Tc and Re (circles). Assuming the Bh compound to be BhO_3Cl, and applying a microscopic model of the adsorption process [5], we evaluated the standard adsorption enthalpy of BhO_3Cl on the quartz surface, $\Delta H_{ads}(BhO_3Cl) = -75^{+9}_{-6}$ kJ/mol (68%c.i.) [6]. Applying a well established empirical correlation between the single atom property ΔH_{ads} and the property of the macroscopic solid state, sublimation enthalpy ΔH_{subl} [7], from the result of our experiment it was possible to evaluate the first thermochemical measure of volatility of a Bh compound ΔH_{subl} (BhO_3Cl) = 89^{+21}_{-18} kJ/mol. Thus, the series of the volatility of group 7 oxychlorides MO_3Cl (M=Tc, Re, Bh) on quartz yields the sequence Tc>Re>Bh. This sequence can also be expected from thermochemical stability trends in the periodic table [8] and from an empirical physisorption model [9]. Experimentally this sequence is supported by the fact, that BhO_3Cl was reclustered with CsCl. This is an additional indication that BhO_3Cl is more similar to ReO_3Cl than to TcO_3Cl, since TcO_3Cl could only be reclustered with $FeCl_2$-aerosol particles [4].

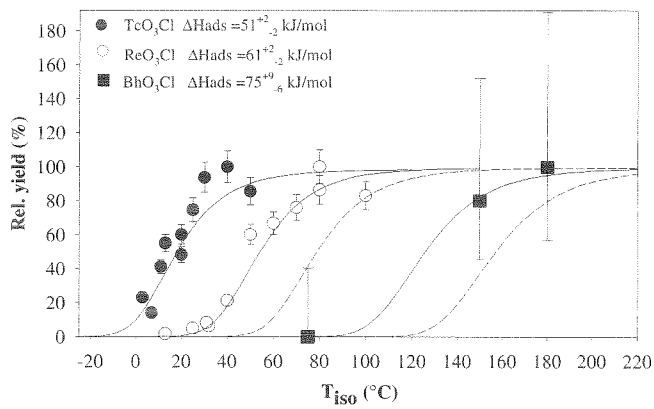

Fig. 1 Yield vs. isothermal temperature curves for the oxychlorides of ^{108}Tc ($t_{½}$=5.2 s), ^{169}Re ($t_{½}$=16 s), and ^{267}Bh ($t_{½}$=17 s). Symbols → Experimental data with 1σ–error bars; Lines → Monte Carlo model; thin lines → 1σ–error range for BhO_3Cl.

Acknowledgments

We are indebted to the US DOE for making the ^{249}Bk target material available through the transplutonium element program at Oak Ridge National Laboratory. We thank the staff of the PSI Philips cyclotron for providing intense beams of ^{22}Ne. This work was supported by the Swiss National Science Foundation.

References

1 Wilk, P.A. *et al.*, *Phys. Rev. Lett.* **85,** 2697 (2000).
2 Eichler, R. *et al.*, *Radiochim. Acta* **87**, 87 (1999).
3 Häfeli, T., *Diploma thesis* University of Bern (1999).
4 Eichler, R. *et al.*, *Radiochim. Acta* **88**, 151 (2000).
5 Zvara, I., *Radiochim. Acta* **38**, 95 (1985).
6 Eichler, R. *et al.*, *Nature* **407,** 63 (2000).
7 Eichler, B. *et al.*, *J. Phys. Chem. A* **103,** 9296-9306 (1999).
8 For more detailed information see: www1.psi.ch/www_lch_hn/Bh_chemistry_prediction.pdf.
9 Pershina, V., *et al.*, *J. Chem. Phys.* **113,** 1441 (2000).

DEPOSITION AND DETECTION OF VOLATILE OXIDES ON METALLIC SURFACES WITH CALLISTO

A. von Zweidorf[1], R. Angert[2], W. Brüchle[2], E. Jäger[2], J.V. Kratz[1], G. Langrock[1], M. Mendel[1], A. Nähler[1], M. Schädel[2], B. Schausten[2], E. Schimpf[2], E. Stiel[2], N. Trautmann[1], G. Wirth[2]

[1]Institut für Kernchemie, Johannes Gutenberg-Universität Mainz, [2]Gesellschaft für Schwerionenforschung Darmstadt

So far, no chemical properties of element 108, Hassium, are known. It can be assumed, that Hs has similar properties like the homologous elements ruthenium and osmium, i.e., that Hs forms a volatile tetroxide.

To form volatile oxides in-situ, nuclear reaction products are slowed down in oxygen containing gas mixtures, which transport these products. They are deposited and detected with **CALLISTO** (***C***ontinuously Working ***A***rrangement For ***Cl***uster***l***ess Transport Of ***I***n-***si***tu Produced Volatile ***O***xides) [1].

For the detection of α-active nuclides, a detector phalanx, as shown in Fig. 1, was developed. On one side, ten (10x10) mm^2 PIN diodes are linearly arranged. On the opposite side, a stripe of metallic Na was placed at a small distance. The carrier gas flows above the Na surface, where volatile oxides deposit and their α-decay can be detected.

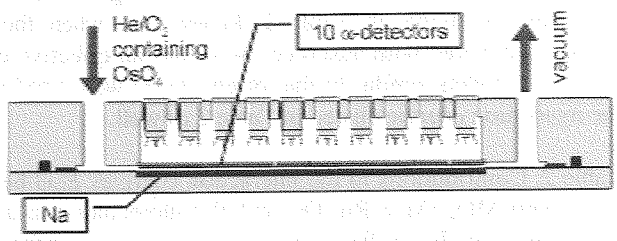

Fig. 1

The deposition efficiency of the volatile oxides depends on various factors, e.g., the deposition of OsO_4 on Na decreases considerably with increasing gas flow and it increases with decreasing humidity of the gases, see Fig. 2.

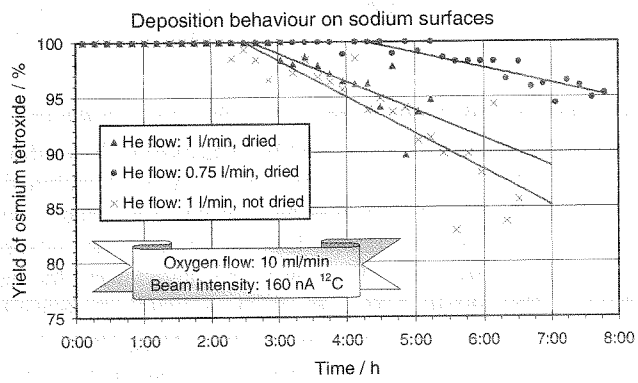

Fig. 2

^{172,173}Os, formed in a ^{26}Mg + ^{152}Gd test-reaction, are unambiguously identified in the α-spectrum, see Fig. 3. Additional smaller peaks can be assigned to other Os-isotopes.

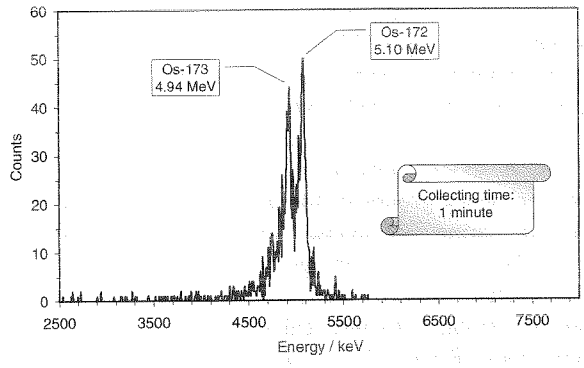

Fig. 3

In a test experiment, a good Po separation was achieved. After 50 min measuring time, no polonium, formed with a U-target, could be detected in the α-spectrum. With a He/KCl-cluster jet, however, Po was transported and measured in the detection system ROMA [2].

OsO_4, as a volatile compound, can be deposited at low temperatures on quartz surfaces. This technique requires much less humid gases than normally supplied, which contain approximately 100-500 ppm water.

Our recently developed gas-drying unit allows reducing the humidity to about 2 ppm. However, still a "collar" of ice deposits inside the cooled quartz spiral beginning at -70 °C. Presently, it is not clear, whether in our experiments OsO_4 was deposited on quartz or on ice. The experimentally observed absolute yield of OsO_4 as a function of temperature is shown in Fig. 4.

Further investigations will require humidity levels below 2 ppm H_2O, which can be obtained from a more efficient gas drying-unit.

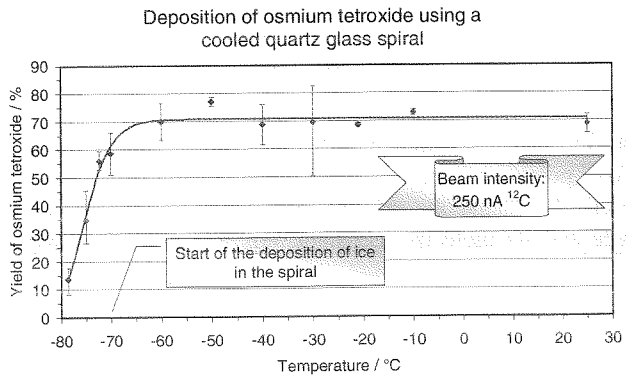

Fig. 4

Literature:

[1] A. von Zweidorf et al., GSI Scientific Report 1999, 236

[2] M. Schädel et al., GSI Scientific Report 1995, 10 ff.

Electronic Structure and Volatility of Group-8 Oxides MO_4, where M = Ru, Os, and Element 108, Hs

V. Pershina,[1,3] T. Bastug,[2] B. Fricke,[2] S. Varga[3]
[1]GSI, Darmstadt; [2]Universität Kassel, Kassel;
[3]Institut für Kernchemie, Universität Mainz, Mainz

The discovery [1] of a relatively long-lived isotope of element 108, Hs, makes it now possible to design chemical experiments studying its chemical properties. Hs is expected to be a member of group 8 of the Periodic Table and, thus, a homolog of Ru and Os. If the chemical properties of Hs are comparable to those of Ru and Os, it should form a very volatile tetroxide, HsO_4. Several experimental groups including one from Mainz/GSI are, therefore, preparing gas-phase experiments on studying volatility of OsO_4 and its holomogs, RuO_4 and OsO_4.

In the current report, we present results of the fully relativistic electronic structure calculations for group 8 gas-phase tetroxides, RuO_4, OsO_4, and HsO_4, and predict their volatility as an adsorption enthalpy with respect to the particular experimental conditions. The electronic structure calculations of MO_4 (M = Ru, Os, and Hs) including the geometry optimization were performed using the fully relativistic *ab initio* Density-Functional method in the GGA approximation for the exchange-correlation potential [2]. The calculated bond lengths, bond strengths, effective charges and covalence effects (OP) of these molecules are shown in Table 1. They indicate that HsO_4 is the most stable and the most covalent compound in the row.

The adsorption enthalpy of MO_4 on the quartz surface of the chromatography column was calculated using the following model of a molecule-slab interaction

$$E(x)_{\text{molecule-slab}} = -(\pi/6)NC_1/x^3, \qquad (1)$$

where N is the number of atoms per cm^3 and x is the molecule-surface interaction distance. In the case of the dispersion interaction of a polarizable molecule with an inert surface consisting of molecular units

$$C_1 = \frac{3}{2}\frac{\alpha_1\alpha_2}{\left(\frac{1}{h\nu_1}+\frac{1}{h\nu_2}\right)} \qquad (2)$$

where $h\nu_1$ and $h\nu_2$ denote roughly ionization energies, and α_1 and α_2 - polarizabilities of the molecule (1) and the surface (2), respectively. Using the relation between polarizability of the surface and its dielectric constant, eqs. (1) and (2) transform into

$$E(x) = -\frac{3}{16}\left(\frac{\varepsilon-1}{\varepsilon+2}\right)\frac{\alpha_{mol}}{\left(\frac{1}{h\nu_{slab}}+\frac{1}{h\nu_{mol}}\right)x^3} \qquad (3)$$

where ε = 3.81 is taken for the highest quartz modification - glass.

Table 1. Calculated bond lengths R_e (in Å), bond strengths D_e (in eV), ionization potentials IP (in eV), polarizabilities α (in a.u.), effective charges Q_M and overlap populations (OP) of MO_4 (M = Ru, Os, and Hs)

Property	RuO_4	OsO_4	HsO_4
R_e (calc.)	1.73	1.75	1.81
R_e (exp.) [3]	1.706	1.711	-
D_e (calc.)	27.48	27.71	28.44
α (calc.)	43.73	40.22	42.24
IP (calc.)	12.25	12.35	12.28
IP (exp.) [4]	12.19	12.35	-
Q_M	1.45	1.46	1.39
OP	1.92	1.94	2.17

By putting the experimental, when available, or calculated parameters into eq. (3), interaction energies $E(x)$ were calculated as shown in Table 2. In the case when the SiO_2 surface is covered with adsorbed O_2, or has an effective charge (Q=-0.4), models similar to that of eqs. (1-3) were used giving the interaction energies listed in Table 2 as well.

Table 2. Contributions to the interaction energies $E(x)$ between the neutral MO_4 (M = Ru, Os, and Hs) molecules and a) pure quartz surface; b) surface covered with O_2; c) surface with effective charge Qe (Q = -0.4)

Molecule	α-$\alpha(SiO_2)$ $E10^{24}\,x^3$ (eV cm^3)	α-$\alpha(O_2)$ $E10^{24}\,x^3$ (eV cm^3)	α-Qe $E10^{32}\,x^4$ (eV cm^4)
RuO_4	4.73	6.28	10.01
OsO_4	4.48	6.01	9.41
HsO_4	4.64	6.16	9.73

The unknown distance x (of 2.25 Å for OsO_4 in the case "a") was deduced from the experimental $\Delta H_{ads}(OsO_4)$ by setting $E(x)$ equal to -38 ± 1.5 kJ/mol. Taking x=2.25 Å as a benchmark and assuming that the molecule-surface distance is directly related to the size of the interacting molecules, the adsorption enthalpies for RuO_4 and HsO_4 were calculated using the data of Table 2. The obtained ΔH_{ads} for RuO_4 and HsO_4 (independently of the model) are larger and smaller than $\Delta H_{ads}(OsO_4)$ by about 2 kJ/mol, respectively. Thus, the volatility has the trend RuO_4 < OsO_4 < HsO_4, with the differences between the species being almost within the experimental uncertainties.

References

[1] S. Hofmann *Z. Phys.* **A 354**, 229 (1996)
[2] T. Bastug *et al. Chem. Phys. Lett.* **211**, 119 (1993)
[3] B. Krebs *et al. Acta Crystallogr.* **B 32**, 1334 (1976)
[4] P. Burroughs *et al. J. Chem. Soc.* **70**, 1985 (1974)

Ionization potentials of neutral and ionized species of elements 107 and 108 from extended MCDF calculations

T. Jacob[1], T. Inghoff[1], B. Fricke[1], S. Fritzsche[1], E. Johnson[2], V. Pershina[3]
[1]Fachbereich Physik, Universität Kassel, 34109 Kassel;
[2]Environmental Science Institute, Florida A&M University, Tallahassee, FL 32307, USA;
[3]GSI, Darmstadt

Theoretical predictions of the chemical behaviour of superheavy elements are very important for extensive and sophisticated "one-atom-at-a-time" chemical experiments. A number of experiments have been performed so far up to element 106 and recently a first experiment has been done for element 107. An important first step is the knowledge of the atomic data for each of these elements. (A review on this subject is given in Ref. [1] and [2])

Here we report on the very first large scale Multiconfiguration Dirac–Fock (MCDF) calculations on the elements 107 and 108 in neutral as well as ionized states up to 8+.

The actual calculations which we have performed here are extended relativistic Multiconfiguration Dirac–Fock calculations [3] using up to 650 configuration state functions. The method itself is best described by Grant [4] and Grant and Quiney [5].

Our calculations include all possible configurations which can be constructed from the relativistic ns, $np_{1/2}$, $np_{3/2}$, $(n-1)d_{3/2}$, and $(n-1)d_{5/2}$ single particle wavefunctions for a specific total angular momentum, parity, and charge state. Our assumption is that the core of each element is kept complete and the remaining electrons are distributed in all possible ways in the single particle wavefunctions given above.

Transition	Mn		Tc	
	MCDF	Exp.	MCDF	Exp.
0+→1+	6.84	7.43	6.33	7.28
0+→2+	21.7	23.1	20.6	22.54
0+→3+	54.2	56.8	49.3	52.08
0+→4+	104.4	108	90.9	
0+→5+	175.8	180	147.3	
0+→6+	270.5	275	219.5	
0+→7+	388.7	394	307.4	

Transition	Re		Bh	
	MCDF	Exp.	MCDF	Extrap.
0+→1+	6.84	7.46	6.82	7.5
0+→2+	22.4	25.53	23.4	25.5
0+→3+	48.9	56.58	49.0	53.4
0+→4+	87.9		85.3	89.0
0+→5+	140.4		133.3	137.5
0+→6+	207.6		194.5	199.0
0+→7+	289.1		268.4	273.7

Table 1: Multiple ionization potentials for group 7 elements in eV.

Due to some differences between the calculated (for the elements 104 to 106 see Ref. [6–8]) and experimental values of the ionization potentials, we have to "correct" the former for the elements 107 and 108 using an extrapolation procedure described in Ref. [6]. In this report we use in addition a double difference extrapolation scheme within the chemical rows 4 to 6 in order to get reliable values for the row 7 elements.

Our final results are summarized in the two Tables. For each element and all ionization states the theoretical MCDF results from these calculations are presented as well as the experimental values as far as they are known [9]. As can be seen easily the differences per ionization stage are in the order of 1 eV. This fact was used in the extrapolation schemes in the earlier publications of the analogue result for the elements 104 to 106. Using the extrapolation schemes which are discussed in Ref. [6] in detail we arrive at the values which are listed in both Tables for the elements Bh and Hs.

Transition	Fe		Ru	
	MCDF	Exp.	MCDF	Exp.
0+→1+	7.20	7.90	6.36	7.36
0+→2+	23.6	24.1	20.9	24.1
0+→3+	50.8	54.7	47.5	52.6
0+→4+	104.5	109.5	92.3	
0+→5+	178.7	184.5	151.6	
0+→6+	276.9	283.6	227.3	
0+→7+	401	409	320	
0+→8+			430	

Transition	Os		Hs	
	MCDF	Exp.	MCDF	Extrap.
0+→1+	7.45	8.43	6.69	7.7
0+→2+	23.2		23.3	26
0+→3+	48.7		50.4	54
0+→4+	89.7		87.0	92
0+→5+	144.5		137.4	142
0+→6+	214.2		200.5	206
0+→7+	300		278	
0+→8+	400		369	

Table 2: Multiple ionization potentials for group 8 elements in eV.

References

[1] V. Pershina and B. Fricke in Heavy Elements and Related New Phenomena, World Scientific 1999 (Ed. W. Greiner et al.) page 194
[2] J. V. Kratz, ibid., page 129
[3] J. P. Desclaux, Comp. Phys. Com., **9**, 31 (1975)
[4] I. P. Grant, Adv. Phys., **19**, 747 (1970)
[5] I. P. Grant and H. M. Quiney, Adv. Atom. Mol. Phys., **23**, 37 (1988)
[6] E. Johnson et al., J. Chem. Phys., **93**, 8041 (1990)
[7] B. Fricke et. al., Radiochim. Acta, **62**, 17 (1993)
[8] E. Johnson et al., J. Phys. Chem., **103**, 8458 (1999)
[9] CRC Handbook of Chem. and Phys. (Ed. David R. Lide), 78^{th} edition, New York (1997), page 10-214

Adsorption Studies with Homologs of Superheavy Elements

A. Vahle[1], S. Hübener[1], S. Taut[1], E. Jäger[2], M. Schädel[2], B. Schausten[2], B. Eichler[3]
[1]Forschungszentrum Rossendorf, [2]GSI Darmstadt, [3]PSI Villigen

Introduction

In preparation of chemical studies with superheavy elements around Z = 114, the adsorption behavior of these elements and their lighter homologs on different metals has been predicted based on (semi-)empirical models and extrapolations (see e.g. [1, 2]).
Adsorption studies with SHE homologs were performed on various metals, especially metals of group 10 and 11 (see e.g. [3]). The experimental results mainly confirmed the calculated data, but in a few cases great differences between predicted and experimental data were observed. Therefore, the adsorption behavior of SHE homologs on further metals is of great interest to prove the validity of the predictions.
In the present work the adsorption of Tl, Pb, Bi, and Po on the group 5 metals V, Nb, Ta as well as on Mo, Ni, Ti has been studied by thermochromatography. Experimental data have been compared to predictions.

Experimental

Bi, Pb, and Tl isotopes were produced by bombarding an ^{nat}Ir target (0.3 mg/cm^2) with a ^{12}C beam (90 MeV on target) at the GSI UNILAC. The recoil nuclei of the nuclear reactions were caught in catcher foils made of 9 µm Cu. These foils were preconditioned by heating them up to 800°C for 15 min in a 100 mL/min gas flow of N_2/H_2 (ratio 90:10). Hydrogen was used to reduce the surface layer of Cu oxide to Cu. The catcher foils served as the thermochromatographic samples without further preparation.
^{210}Po was obtained by neutron activation of ^{nat}Bi at the TRIGA Mainz reactor and subsequent decay of the produced ^{210}Bi. Po was separated from Bi by thermochromatography according to [4] and deposited on a Ta column. One cm pieces of the Ta column with the adsorbed Po were used as samples for the thermochromatography experiments.
The experimental setup was similar to that described in detail in [5]. Thermochromatographic columns were made from 20 - 25 µm thick Ti, V, Nb, Ta, Mo, and Ni foils. Quartz glass columns served as support tubes. The inside of these tubes was lined with thin Ta foils in order to adsorb the oxygen emitted from the quartz glass at high temperatures. A carrier gas flow of 25 or 50 mL/min He was established. The starting temperature was varied between 700 and 950°C. After 15 or 30 min thermochromatography time the nuclide distribution along the column was determined by γ- or α-spectroscopy of 1 cm column pieces.

Results

Po was nearly completely (> 98 %) volatilized from the Ta foils. Tl, Pb, and Bi partly remained in the catcher foils.
Thermochemical data were determined by two methods:
(1) Adsorption entropy and enthalpy were calculated according to [6] with $\tau_0 = 10^{-12}$ s.
(2) ΔS°_{ads} and ΔH°_{ads} were determined according to [7] using an individual τ_0 for each adsorpt-adsorbent combination.

As an example, predicted and experimentally determined adsorption enthalpies for Tl on several adsorbent metals are depicted in Fig. 1.

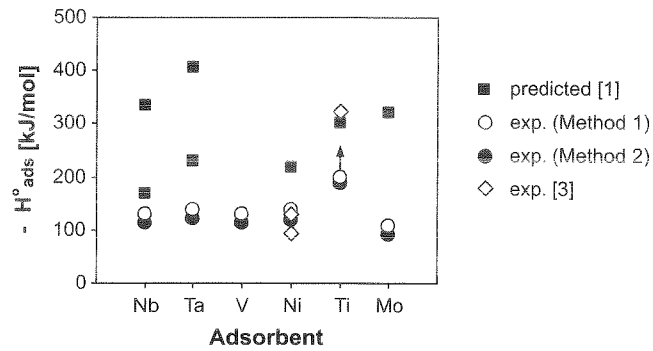

Fig. 1: Adsorption enthalpies of Tl on several metals
The two different values on Nb and Ta were obtained by different models.

The main results of our adsorption studies can be summarized as follows:

- Irrespective of the used method, significantly less negative adsorption enthalpies were obtained than predicted by [1].
- Our results correspond quite well with the experimental data given in [3].
- As predicted, less negative or similar adsorption enthalpies were found for all studied elements on Nb compared to Ni, Ta, and Ti. However, the least negative adsorption enthalpies of all studied elements were surprisingly obtained on Mo. This might be an erroneous result caused by an oxide layer on the column surface which could not be removed by heating in a He flow.
- On titanium, Tl and Pb were deposited in the starting position and only an upper limit of ΔH°_{ads} can be given. On all other adsorbent metals, less negative adsorption enthalpies were obtained for Tl than for Pb.

Acknowledgments

This work was performed in cooperation with the GSI. The preparation of the Ir target by the "Targetlabor" of GSI is gratefully acknowledged. We thank the staff of the TRIGA Mainz reactor for the irradiation of Bi.

References

[1] Roßbach, H. et al., Report ZfK-527 (1984)
[2] Eichler, B., PSI Bericht 00-09 (2000)
[3] Eichler, B. et al., Dubna Report P12-81-717 (1981)
[4] Hübener, S. et al., Annual Report 1982, ZfK-510 (1983), p. 123
[5] Taut, S. et al., Radiochim. Acta 78, 33 (1997)
[6] Eichler, B. et al., Radiochim. Acta 30, 233 (1982)
[7] Taut, S. et al., submitted to J. Chem. Phys.

A Geometric Model for Direct Condensation

A. Vahle, R. Dressler
Forschungszentrum Rossendorf

Direct condensation has been established as a well-suited deposition mode for high temperature gas chromatography experiments. Unfortunately, there is no simple model of this process in the literature until now. The model proposed here neglects the exact flow pattern near the deposition foil as well as diffusion processes which might influence the yield. A flow pattern of an underexpanded supersonic jet is formed during the efflux of the reaction gas into a low pressure region, e.g. the ROMA device. Such jets are characterized by a shock cell, the so-called zone of silence, in which the flow velocity is much greater than the local speed of sound and a boundary region between the jet and the ambient gas, in which the gas moves slightly faster than at the exit [1, 2]. The zone of silence consists of a barrel-shaped shock surrounding the jet and a nearly planar normal shock, or Mach disk, downstream. Pressure and temperature decrease dramatically in the zone of silence, whereas the mass flow rate is nearly unchanged. Behind the Mach disk the flow velocity drops down to a subsonic flow. Good conditions for direct condensation of chemical compounds exist within the zone of silence.

The radius of the Mach disk is $r_{mach} = \frac{0.67\ \text{bar} \cdot r_{in}}{\sqrt{P_0\ P_{ROMA}}}$

and its distance from the outlet is $d_{mach} = 4\, r_{mach}$

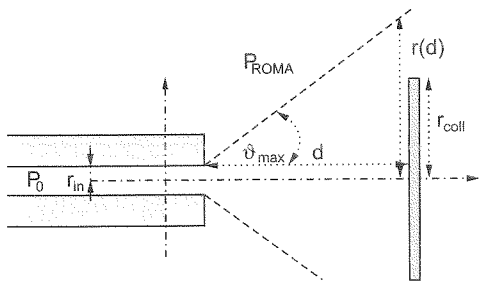

Fig. 1: Geometric model for the evaluation of the deposition yield (symbols are explained below)

A simple geometrical model (Fig. 1) is used to estimate the deposition yield. This model is based on four assumptions:
1) The gas velocity $v_\parallel$ in the direction of the axis of the chromatography column after passing the end of the column is constant. 2) The flow pattern is a sharp cone. The axis of the cone has the same direction as the axis of the chromatography column; the cone has an opening angle of $2\vartheta_{max}$. 3) The gas density in a disk perpendicular to the axis of the flow cone is constant. 4) The gas flow perpendicular to the axis of the cone has a constant velocity.

The yield ε is defined by $\varepsilon = \frac{\dot{m}_{coll}}{\dot{m}_{out}}$. The mass flow rates $\dot{m}_{coll}$ and $\dot{m}_{out}$ can be calculated by integrating the local gas density $\rho(d)$ over the collection and the outlet cross section, respectively.

This leads to $\dot{m}_{out} = \pi\ r_{in}^2\ v_\parallel\ \rho_L$

$$\dot{m}_{coll} = \int_0^{r_{coll}} 2\pi\ r\ v_\parallel\ \rho(d)\ dr$$

The mass flow rate is constant. $\rho(d)$ can be calculated by

$$\rho(d) = \left(\frac{r_{out}}{r(d)}\right)^2 \rho_L$$

The exit velocity $v_\parallel$ of the gas for $P_{ROMA} < P_0$ is given by

$$v_\parallel = \sqrt{\kappa \frac{P_L}{\rho_L}}$$

and the velocity component $v_\perp$ perpendicular to the direction of the out flow can be calculated by

$$v_\perp = \sqrt{\frac{2\kappa}{\kappa - 1} \cdot \frac{P_L}{\rho_L} \cdot \left[1 - \left(\frac{P_{ROMA}}{P_L}\right)^{\frac{\kappa-1}{\kappa}}\right]}$$

The opening angle ϑ_{max} of the flow cone can be calculated by

$$\tan(\vartheta_{max}) = \frac{v_\perp}{v_\parallel}$$

Combining these formulas yields

$$\dot{m}_{coll} = \begin{cases} \pi\ r_{in}^2\ v_\parallel\ \rho_L & \text{for} \quad r(d) < r_{coll} \\ \pi \left(\frac{r_{coll}}{r(d)}\right)^2 r_{in}^2\ v_\parallel\ \rho_L & \text{for} \quad r(d) > r_{coll} \end{cases}$$

for the collected mass flow.
Finally, the yield ε can be obtained by

$$\varepsilon = \begin{cases} \frac{\kappa - 1}{2} \cdot \left(\frac{r_{coll}}{d}\right)^2 \cdot \left[1 - \left(\frac{P_{ROMA}}{P_L}\right)^{\frac{\kappa-1}{\kappa}}\right]^{-1} & \text{for} \quad r(d) > r_{coll} \\ 1 & \text{for} \quad r(d) < r_{coll} \end{cases}$$

Experimental data (ε, optimum d, spot diameter) could be reproduced well with the proposed geometrical model [3]. For instance, the spots observed experimentally at the pressure optimum can be explained by the zone of silence. The Mach disk has a diameter of 3.3 mm close to the observed diameter of about 3 mm.

Acknowledgments

This work was performed in cooperation with the GSI.

References

[1] Trigg, G., L. (ed.): Encyclopedia of Applied Physics, Vol. 4, VCH, Weinheim 1992, pp. 43
[2] Tejeda, G. et al., Phys. Rev. Lett. 76, 34 (1996)
[3] Vahle, A. et al., submitted to Nucl. Instr. Meth.

Symbols: m_{coll} = mass collected on the catcher foil, m_{out} = mass flowing out of the tip of the chromatography column (cc), r_{in} = inner radius at the end of the cc, $\rho(d)$ = density at the distance d from the outlet, r_{coll} = radius of the catcher foil, d = distance between cc and catcher foil, r(d) = radius of the cone = d tan(ϑ_{max}), κ = POISSON coefficient = C_p / C_v, P_0 = back pressure in the cc, P_{ROMA} = ambient pressure in the ROMA device, ρ_0 = gas density at P_0, P_L = Laval pressure = $P_0 \left(\frac{2}{\kappa+1}\right)^{\frac{\kappa}{\kappa-1}}$, ρ_L = Laval density = $\rho_0 \left(\frac{2}{\kappa+1}\right)^{\frac{1}{\kappa-1}}$

ACCELERATOR-EXPERIMENTS AND -DEVELOPMENT

Accelerator-Development and Experiments

Operation Report of UNILAC and SIS

U. Scheeler, D. Wilms GSI

The statistics of the accelerator operation in 2000 were collected with the help of the program **PROST** [1]. The topics of accelerator development and experiments are described in separate contributions [2], [3] and [4] to this annual report.

1. General overview

In 2000 the new operation capabilities of the High Current Injector (HSI) determined the accelerator operation. After its start of operation in November 1999 a lot of experiences have been made concerning the pulse to pulse operation with up to three ion sources (see Figure 1 for the multiplicity of accelerated isotopes). The new operation possibilities allow to satisfy better the growing demands of the experiments concerning time sharing operation and beam intensity, but to satisfy them a careful scheduling of the beam time becomes more and more essential.
There was three longer beam periods in this year of over 2 month length and a shorter one (the second) of one and half month length. A four week shut down in September were used for maintenance of the Alvarez I cavity and the vacuum system behind the SIS.

Table 1: Overall beam time of the accelerator facility

	Total beam time '00 (h)	Target time '00 (h)	Target time '99 (h)
UNILAC experiments	6013	4854	3806
SIS experiments	8166	5118	4255
ESR experiments		1031	1081

The total beam time in comparison with the achieved target time is given in table 1 for the different experimental areas. The operation time of the accelerator facility (number of working hours), 6088 h in 2000, were two shifts shorter than in the last year. The main reason for the higher values of target time at the UNILAC and the SIS experimental area is due to the more extensive use of the time sharing operation. The value for the ESR accelerator remains nearly constant.
As shown in Figure 1 beams of 25 different isotopes (twice as much as in the last year) were accelerated. They were delivered to 20 low energy experiments at the UNILAC and to 29 high energy experiments behind the SIS. Ion beams from the Penning terminal with a mass to charge ratio below 20 (high duty cycle) were due to the low terminal voltage difficult to handle. This led sometimes to unstable beam parameters at the experiments. The planed installation of a new power supply for the preacceleration gap should solve this problem in 2001.

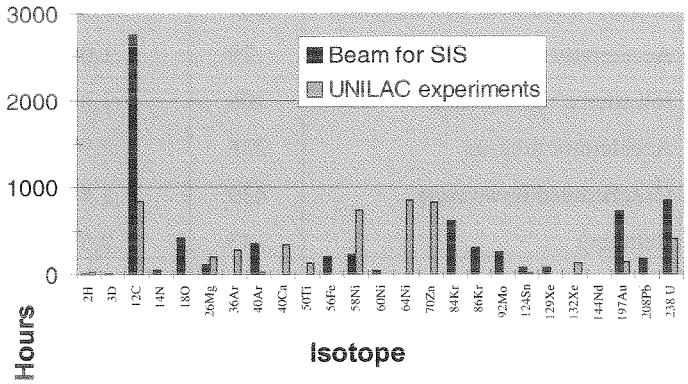

Figure 1: Accelerated isotopes in 2000

2. UNILAC Operation

The beam time for the UNILAC experiments is summarized in table 2. The column „performance" indicates the efficiency of the accelerator operation. It contains the ratio (in percent) between the corresponding number of hours and the total beam time. The difference between operation time and total beam time is due to the time sharing operation of the accelerator.

Table 2: Beam delivered to UNILAC experiments in 2000

	(h)	Performance
Target time for experiment runs	4854	80,8%
Beam for experiment tests	33	0,5%
Accelerator development	108	1,8%
Accelerator tune-up	496	8,2%
Ion source replacement	103	1,7%
Unscheduled down time	311	5,2%
Retuning	52	0,9%
Stand-by	56	0,9%
Total beam time	6013	

The sum of beam time for experiment (including tests) is higher as in 1999. The 108 hours for accelerator development result to a large fraction from the commissioning of the new High Current Injector.
The unscheduled down time was due to failures of injectors (36h), rf-amplifiers (78h), magnet power supplies (48h), beam diagnostics (3h), vacuum system (38h), computer control (12h) and others (96h).

Table 3 displays the provided beam time of the UNILAC for SIS injection. The operation of the new stripper section in the

Table 3: UNILAC beam delivered to SIS in 2000

	(h)	Performance
Beam available for SIS injection	7261	88,9%
Accelerator development	79	1,0%
Ion source replacement	106	1,3%
Accelerator tune-up	238	2,9%
Unscheduled down time	439	5,4%
Retuning	43	0,5%
Total beam time	8166	

beam transfer line to SIS allows the injection of stripped and unstripped ions into the SIS in the time sharing mode. Technical problems due to different field values of the dipole magnets in this operation mode made a permanent correction of the settings necessary. By installation of Hall probes in the corresponding magnets (scheduled in 2001) this problem should be solved.

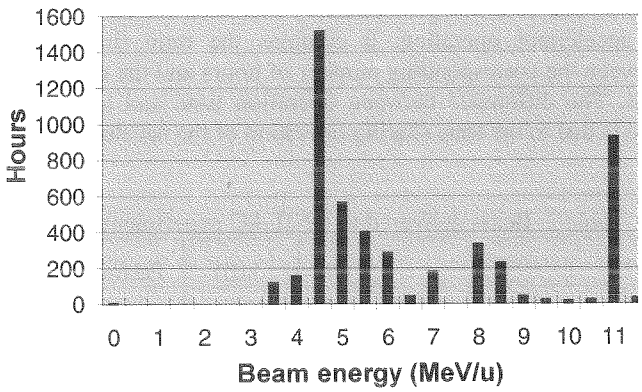

Figure 2: Beam energies of the UNILAC experiments

In Figure 2 the target time of the UNILAC experiments (without beam injected into SIS) is displayed versus energy. The upgrading of the phase control unit reduced the number of the available single gap resonators, so the energy range was restricted. The beam energies in the range from 4 to 6 MeV/u mainly result from the experiments for superheavy element synthesis and nuclear physics. Energies around 8 MeV/u were used for nuclear chemistry experiments and above 10 MeV/u for material science and for the plasmaphysics experiments.

3. SIS Operation

In table 4 the operating statistics for the SIS is given. The total target time is about 400 h higher compared to last year.
The loss in beam time due to technical failures distributes to power supplies (43h), rf-amplifiers (20h), beam diagnostics (5h), computer control (23h), vacuum system (149h) and others

Table 4: SIS operation time in 2000

	(h)	Performance
Beam for target area	3681	54,8%
Therapy	1437	21,4%
Beam delivered to ESR	1031	15,3%
Beam for experiment tests	6	0,1%
Total target time	6155	91,6%
Accelerator development	141	2,1%
Accelerator tune-up	70	1,0%
Unscheduled down time	354	5,3%
Total beam time	6720	

(114h). A leak caused by a broken vacuum window in an experimental setup is mainly responsible for the high number of vacuum loss hours.

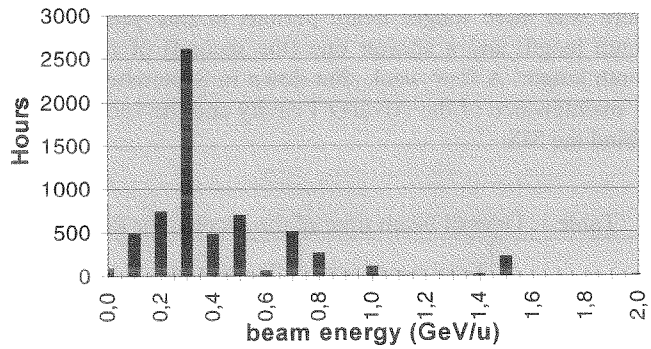

Figure 3: Beam energies delivered to the SIS experiments

Figure 3 shows the beam time versus energy for the SIS experiments. The high fraction of target time at about 400 MeV/u results as well as in the last year from the acceleration of ^{12}C beam for the cancer therapy. The lower range of energy was also used (Figure 3) to provide beam for the ESR and for plasma physics experiments.

References

[1] **PR**ogramm für **O**perating und **ST**atistik

[2] J. Klabunde et. al. UNILAC Status and Developments

[3] K. Blasche et. al. SIS Status Report

[4] M. Steck et. al. ESR Operation and Development

Ion Source Development and Operation

P. Spädtke, F. Heymach, R. Hollinger, R. Iannucci, R. Lang, H. Reich, H. Schulte, K. Tinschert

The past year was characterized by a a reliable ion source operation serving the accelerator and the beam time schedule. Ion source development took place mainly to produce the desired beams, in addition, collaborations have been established and continued to improve the different ion source types.

Operation

ECR Ion Source

The ECR ion source (ECRIS) at the High Charge State Injector (HLI) delivered ion beam to the accelerator facilities without interruption during all beam time blocks in 2000. Most of the time was dedicated to the cancer therapy. The production of C^{2+} beams for this purpose has become routine operation and worked without any problems. Besides therapy the HLI predominantly had to provide beams for the production of Super Heavy Elements (SHE) and for nuclear chemistry experiments.

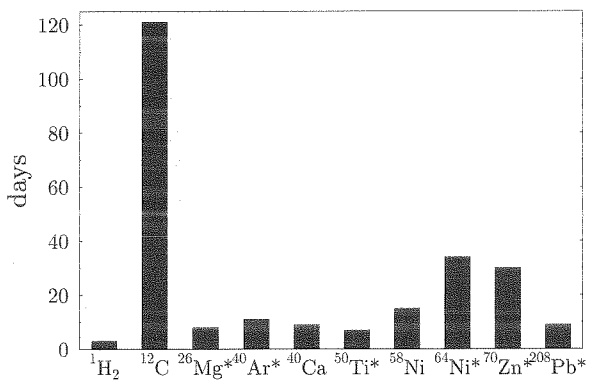

Figure 1: Element statistics of the ECRIS in 2000. An asterisk indicates the use of enriched isotope material.

Long periods were covered by $^{58}Ni^{9+}$ (natural) and $^{64}Ni^{9+}$ (enriched material) beams which could be performed with high reliability getting intensities of several tens of eμA. The usual material consumption of typically 5...6 mg/h for Ni could be considerably reduced for ^{64}Ni to ≤ 3 mg/h by carefully recycling condensated sample material from the orifice of the oven.

Another long time run for the production of SHE was $^{70}Zn^{10+}$. It was routinely produced from ^{70}ZnO pellets. A very constant beam of 70 eμA was obtained.

^{50}Ti was also requested for the production of SHE. Following the experience obtained from former experiments isotopic material of very high purity was used. However, the need for a high operating temperature of 1700 °C again showed that this is almost beyond the limit of the standard oven.

A solution of this problem appears to be a new type of high temperature oven which is being developed [1]. Its main features are an operating temperature of up to 2000 °C and a heating process by thermal radiation from a heater spiral of 10 mm diameter without any mechanical support. Thus any ceramics in the hot parts of the oven is avoided.

Tests was performed which proved the principal function of this oven. Nevertheless further modifications are necessary to improve its technical reliability in order to achieve satisfying long time operation. A 70 hours run could be performed at the test bench using natural Ti contained in a tungsten crucible. The achieved stability and intensity were comparable to the operation of Ni.

$^{208}Pb^{27+}$ was delivered to the SIS operating the ECRIS in afterglow mode. It was possible to reproduce the intensity and beam quality of a long beam time in the preceding year. However, the long time for preparation and optimization until sufficient stability is obtained demonstrates that it is not useful to schedule short beam time periods for the afterglow mode.

Two experiments at the UNILAC requested the alkaline earth ions ^{40}Ca and ^{26}Mg, respectively. The $^{40}Ca^{7+}$ ion beam could be reproduced under the same good conditions as it was done once before in 1999. A $^{26}Mg^{4+}$ ion beam was produced for the first time. Previous tests with natural Mg sample material had been encouraging. As for Ca the hot screen inset inside the plasma chamber is used for Mg, too. 60 eμA of $^{26}Mg^{4+}$ were achieved, but an increase of the intensity upon request by the experiment led to instable operating conditions caused by uncontrollable passive heating of the oven by the ECR plasma. This behaviour showed that further development work is necessary to improve the reliability of operation.

For ^{40}Ca as well as for ^{26}Mg the efficiency of ion beam production turned out to be very good compared to other metal ion operation. For ^{40}Ca 18 % of the sample material is transformed into ion beam distributed in the charge states 1+ ... 12+. 1.8 % of the material can be analyzed in the requested charge state 7+. For ^{26}Mg the corresponding values are 11.8 % in all charge states including 1+ ... 9+ and 2.5 % in the requested charge state 4+.

As further experiments are planned for the future which require beams of alkaline earth metals investigations were continued at the test bench. A common problem of these elements is the low operating temperature causing big difficulties to control the evaporation. Therefore, several modifications of the standard oven were applied in order to decrease the influence of passive external heating of the oven.

Experiments at the test bench (EIS) had shown that H_2^+ ions can be extracted from the ECRIS with 5 kV. This low extraction voltage is suitable for injection into the RFQ. An accelerator experiment at the HLI proved that a H_2^+ ion beam of good stability can be accepted and transported by the accelerator.

Penning Ion Source

The PIG source was used for standard beams as shown in Fig. 2. The particle current for several elements could be increased by the lower charge state required by the new prestripper accelerator. For the heaviest elements we are able to use charge state 6+ instead of 10+, nearly doubling the particle current in front of the accelerator.

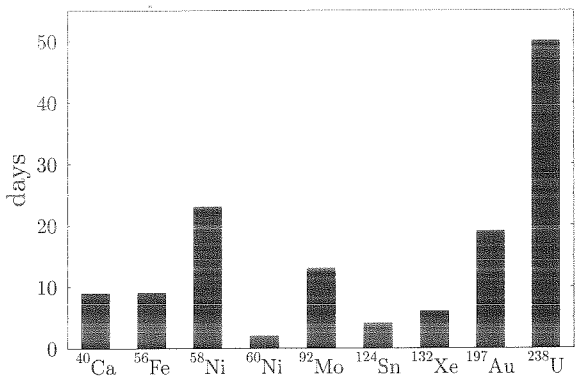

Figure 2: Element statistics of the PIG ion source in 2000.

High Current Ion Sources

For the commissioning of the high current injector up to 18 mA $^{40}Ar^{1+}$ have been produced by the MUCIS and transported to the RFQ. This beam is very reproducible and stable. For an experiment a $^{92}Mo^{2+}$ (15% isotope) was required. We checked three different ion sources for that purpose. It turned out, that the MEVVA delivered the highest ion currents in front of the RFQ (see table 1 and fig. 4.). Note, that all sources were operated with natural Mo. For a $^{197}Au^{4+}$-beam we found a different classification, showing that each source might have different capabilities for different elements.

Tab. 1: Comparison of different ion sources (regular PIG source, Half PIG type [2], MEVVA) for different elements. The current in front of the RFQ are given in emA.

	PIG	H-PIG	MEVVA
$^{92}Mo^{2+}$	0.1	0.2	1.0
$^{197}Au^{4+}$	0.3	$\leq$0.1	$\leq$0.1

The motorized remote cathode changer was taken into operation to prolong the operating time of the MEVVA ion source.

Ion Source Development

Several collaborations to improve our ion sources and to investigate the applicability of new types of ion sources are in progress:

- A new development for ECR sources with 28 GHz micro wave heating promises higher particle currents and is investigated in a European collaboration[3].

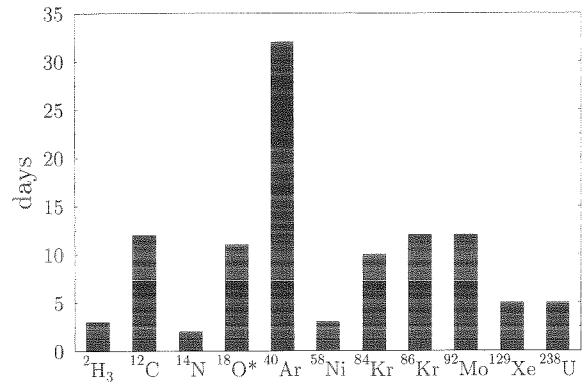

Figure 3: Element statistics of the high current ion sources. All gases have been provided by the MUCIS, whereas for all metals the MEVVA was used. For ^{18}O enriched material has been used.

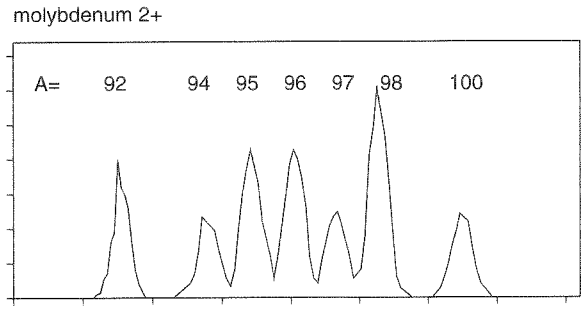

Figure 4: Isotope separation for Mo^{2+}. Note, that not a single pulse was missing during the measurement and the detected pulse currents reflect the natural isotope distribution, showing the good shot-to-shot reproduceability.

- A laser ion source [4] was investigated to demonstrate high particle currents with a charge state distribution suitable at the high current injector. In this experiment with a 100 J laser up to 20 emA Pb^{4+} with a pulse duration of 80 μs was a remarkable result.
- The subject of further improvement of the MEVVA ion source was a better noise reduction even for the high B field operation necessary for the production of U^{4+} [5]. This item is still to be improved.

References

[1] R. Lang, J. Bossler, H. Schulte, and K. Tinschert, RSI **71**, 651 (2000).
[2] M. Müller, Dual HCD Ion Source, this report.
[3] Research collaboration agreement K598/PS, CERN, CEA, ISN, GSI.
[4] K.N. Makarov, et. al., Feasibility study of U^{4+} pulsed ion beam generation in Laser Ion source. Internal report, ITEP, TRINITI.
[5] E. Oks, MEVVA ion source in the space charge limited operation mode. Internal report.

Dual HCD Ion Source

for high current metal ion beams

Michael Müller, GSI Darmstadt

From the plasma of a **H**ollow **C**athode **D**ischarge high current beams of positively charged metal ions have been extracted . Up to mass 100 ion beams with currents beyond 10 mA have been delivered in long time operation (50 to 100 hours). Ion source economy with respect to sputter material consumption is at least one order of magnitude better compared to conventional sputter PIG ion sources [1].

Ion sources for low charged Ions (Z/A) = 0.017 became interesting for the GSI Intensity Enhancement Project since the UNILAC Prestripper accepts now for example 4+ Uranium ions from the injector. This gave reason to think about ion generators covering well this (Z/A) range. The suitably modified hollow cathode discharge was found as a device fulfilling some of the demands at least for metal ions below Mass 100. The mechanical set up was derived from existing GSI PIG Ion Source structures [2] to fit advantageously the necessary infrastructure as were magnets, vacuum chambers and manifolds. Ions from PIG discharge are usually extracted out of the hollow anode. This ion source geometry is modified by introducing an additional coaxial electrode. The electrode sequence: "heated Cathode - Anode – SE – Anode – cold Cathode" can be seen as a symmetrical or **D**ual **H**ollow **C**athode **D**ischarge geometry. Ions are extracted in the same manner as formerly from the PIG Source but now out of the hollow cathode sputter electrode SE.

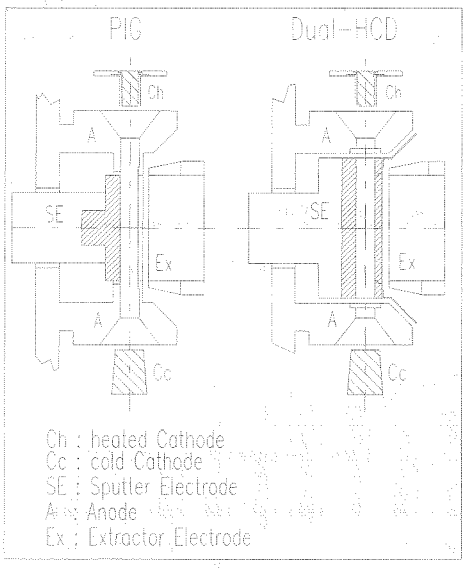

Fig.1: **Dual HCD and PIG Ion Source**

Sputtered particles from the inner wall of the hollow cathode, mostly of atomic nature, travel through the plasma column to become ionised in collision processes or to leave the plasma again hitting the cathode-wall . Ionised particles may contribute to the Sputtering by Self-Sputtering and / or being re-implanted into the surface, anyway staying available for further ion beam production.

Ions in the vicinity of the slit window going to leave the plasma are accelerated in the cathode fall before entering the strong electric extraction field of the outer ion beam forming area. The acceleration of the positive ions in the steep cathode fall prior to extraction is perhaps the reason for the surprisingly good beam quality.

Up to now most work was directed on the production of high current ion beams from lighter ions up to mass 100 . The **Dual HCD** was operated in the non-homogenous "magnetic bottle" field of the Compact - PIG - Ion Source [3] as well as in the homogenous magnetic field of the GSI PIG Ion source magnet . Results for selected ion species are shown in Table 1. Enhanced ion beam yields from the Compact Ion Source Set up are due to the higher extraction Voltages available in this arrangement.

Element		**Discharge**				**Ion Beam**	
Ion	Mass	U	I	B-Field		Curr	Extr
	amu	**V**	**A**	**Tesla**	**Form**	**mA**	**kV**
Mg1+	24	500	16	0.54	H	**20**	14
Al 1+	27	500	12	0.5	B	**20**	16
Al 1+	27	750	16	0.15	B	**45**	23
Ti 1+	48	500	6	0.77	H	**6**	13
Ti 1+	48	1000	22	0.15	B	**24**	25
Ti 2+	48	2400	6	0.53	H	**8**	13
Ti 2+	48	600	23	0.15	B	**15**	24
V 2+	51	750	8	0.55	H	**4**	14
V 1+	51	1100	13	0.15	B	**13**	21
Fe 1+	56	1650	18	0.8	H	**5**	12
Ni 1+	58	2000	15	0.84	H	**11**	13
Cu 1+	63	1000	4	0.14	B	**16**	18
Mo 2+	98	500	15	0.15	B	**10**	22
Zr 2+	90	400	18	0.75	H	**3**	13
Ta 3+	181	500	7	0.86	H	**1.5**	13
Ta 4+	181	500	6	0.86	H	**2**	17
Pb 1+	208	200	4	0.14	B	**1**	6
Pb 2+	208	200	4	0.15	B	**2**	12
U 1+	238	550	16	0.84	H	**0.4**	3.2
U 2+					H	**1.2**	6.4
U 3+					H	**2.5**	9.6
U 4+					H	**1.6**	12.8

Table 1: **Ion Yields from Dual HCD Ion source**
Values for 1% duty cycle operation (10/s;1 ms)
H : homogenous magnetic. Field (PIG)
B : magnetic bottle field (CPIG)

Ref :
[1] P.M. Morozow , B.N. Makov and M. S. Joffe, Atomnaya Energiya 3, 272, (1957)
[2] "Handbook of Ion Sources" by B. Wolf, GSI Darmstadt, Germany, Crc Press Boca Raton New York London Tokyo, 1995, P 69).
[3] M. Müller, IEEE Trans. Nucl. Sci. NS-30 (1983) 1499

UNILAC Status and Developments

J. Klabunde, W. Barth, L. Dahl, J. Glatz, GSI

Status of Operation

In 2000 both injectors – the new high current injector HSI and the high charge state injector HLI – were used for routine operation. The UNILAC was mainly operated in the time – sharing mode, for some fractions of beam time the three-beam operation was practiced. The scheduling of beam time and operation statistics in 2000 are reported in ref.[1].
As in the last year, long periods of beam time were used for the acceleration of carbon for the cancer therapy from the HLI with very high efficiency. For UNILAC experiments rare isotopes were accelerated by the HLI to take advantage of the low consumption rate of the ECR source (^{26}Mg, ^{60}Ni, ^{64}Ni, ^{36}Ar, ^{58}Fe, ^{70}Zn). ^{70}Zn and ^{64}Ni ions were used successfully for the search for super heavy elements. Over 60 days for each ion the availability was above 90%, interruptions occurred only for refilling of the ECR source with material every 5-6 days. For SIS injection the beam was mainly accelerated by the new injector linac HSI. PIG, MUCIS and MEVVA sources were in operation. The highest particle intensities were reached for argon from the MUCIS. More details on the status of high current acceleration are given in the following paragraph.

High Current Operation and Developments

Besides the routine operation of the linac, the commissioning of the HSI was continued. The scheme of the HSI is shown in Fig. 1.

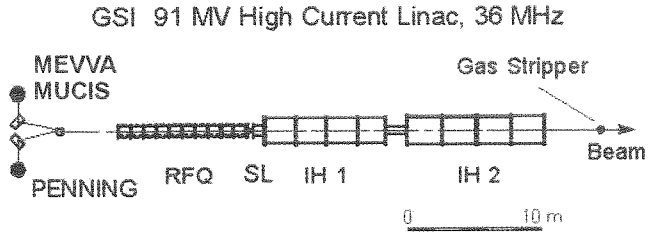

Fig. 1 Scheme of the new high current injector (HSI)

The aspects and status of the high current operation are reported in several contributions to the international linear accelerator conference 2000 (refs. 2-8). In table 1 the achieved beam intensities are listed. The design intensities at the end of the LEBT could be attained only for gaseous light ions up to argon from the MUCIS. Beam experiments indicated limitations of the beam transport of high current from the ion source through the dc pre-acceleration gap. Furthermore, the stability of the MEVVA ion source has to be improved at high intensities. As shown in table 1 the transmission of the whole HSI decreases to about 50% at high intensities. The RFQ is the bottleneck as emerged from many measurements. The transmission of the IH drift tube linac is better than 90% over a wide range of beam intensities and ion species. The beam loss within the RFQ can not be explained completely by large transversal input emittances; measurements of the emittances resulted in normalized 90%-values from 0.25 up to 0.45 π·mm·mrad without any significant influence to the RFQ transmission. Mismatch problems due to space charge effects or misalignment inside the RFQ are not excluded. Computer simulations and beam measurements are underway for better understanding of the RFQ behavior.

Table 1 Achieved beam intensities and comparison with design

		LEBT (Achieved)	LEBT (Design)	HSI-Transmission
MUCIS	H_3^+	3.5 mA	0.8 mA	-
	D_3^+	3.5 mA	1.6 mA	-
	N^+	4 mA	3.8 mA	-
	$^{18}O^+$	5 mA	4.8 mA	45 %
	CO^+	6 mA	7.5 mA	45 %
	$^{40}Ar^{1+}$	18 mA	10 mA	45 %
	$^{86}Kr^{2+}$	3 mA	11.5 mA	50 %
	$^{129}Xe^{2+}$	0.75 mA	17.5 mA	-
MEVVA	C^+	5.5 mA	3.2 mA	-
	$^{92}Mo^{2+}$	0.65 mA	12.4 mA	67 %
	$^{52}Cr^{1+}$	5.5 mA	14 mA	40 %
	$^{58}Ni^{1+}$	10 mA	15.5 mA	50 %
	$^{238}U^{4+}$	4-6 mA	16 mA	50 %

The argon intensity at the RFQ entrance could be increased above the design level (see table 1). By that the theoretical current limit of 10 emA Ar^{1+} was reached. In Fig. 2 the transmission of a high intensity argon beam from the LEBT to the end of the UNILAC is shown. The measurements are compared with the design values of current and transmission.

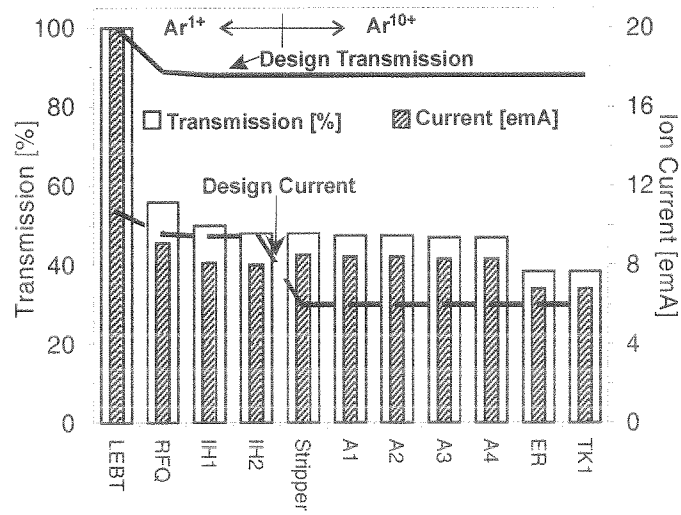

Fig. 2 Measured argon beam intensities along the UNILAC

In February 2000, a U^{4+} beam from the MEVVA source was accelerated for the first time. As listed in table 1, the design goals for the intensity of uranium could not be attained. A maximum intensity of 10 emA was measured at the end of the LEBT, but the fluctuations of ion source current - up to 25% - prevented a successful tuning and stable operation of the

accelerator facility. At the lower level of 4 emA a better reproducibility of the beam pulses could be achieved by optimization of source parameters. If the reduced transmission of the HSI by a factor of two is taken into account, the gap between present performance and design goal is a factor 6 to 8. Subject of improvements of the MEVVA source is the reduction of noise at the required intensity level [9]. Higher intensity and brilliance of the beam are expected by optimizing the transport from the ion source through the gap with solenoid focusing.

Fig. 3 summarizes the emittance measurement data at several energy stages of the HSI (120 keV/u, 750 keV/u and 1.4 MeV/u) and after the Alvarez linac at 11.4 MeV/u. The measurements were taken at 6.5 emA of Ar^{1+} at the HSI exit. The Ar^{10+} current came up to 7 emA after stripping and charge state analysis. The emittance growth agreed to the computer simulations.

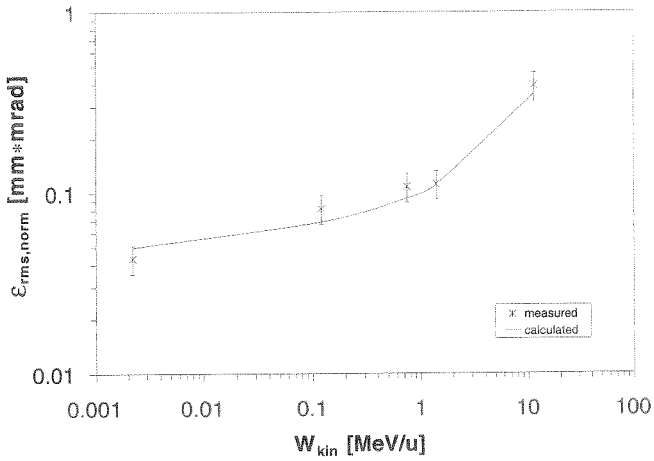

Fig. 3 Transversal emittance for several energy stages of the HSI and at 11.4 MeV/u; beam intensities: 6.5 emA Ar^{1+} at the HSI exit, 7 emA Ar^{10+} after the Alvarez

The RFQ and the superlens SL of the HSI (see fig. 1) still show pronounced dark current contributions at voltage amplitudes above 75% of the design level. There was no essential improvement after a long operation time at the U^{4+} rf voltage level (91% of the maximum design level). Further conditioning tests are planned in the year 2001. Both IH tanks, IH1 and IH2, show modest dark current contributions. In 2000 all rf structures of the HSI were conditioned up to the voltage level for $^{238}U^{4+}$.

Proton and Deuteron Acceleration at the UNILAC

After the replacement of the Wideröe prestripper accelerator by the HSI, the performance for light ions has been changed. With the Wideröe injector maximum intensities of protons and deuterons were attained by injection of H_3^+ and D_3^+ molecules resp. It was shown that the molecules – without gas stripping at 1.4 MeV/u – could be accelerated without loss up to 11.4 MeV/u. When the molecules pass the carbon foil stripper before injection into the synchrotron SIS, they break up into protons or deuterons. 280 µA deuterium D_3^+ were measured before the carbon foil and then transferred to 840 µA deuterons. $2 \cdot 10^{11}$ particles per pulse were accelerated in the synchrotron.

The new injector linac is optimized for maximum particle intensities of heavy ions (Kr to U). The maximum mass to charge ratio A/q is 65, the intensity limit is calculated by 0.25·A/q emA (electrical current). For singly charged ions the intensity limit is even lower (60%) compared to the Wideröe linac, but with better ion source performance and with the new LEBT, the previous maximum intensity should be surpassed.

The adjustment of the low rf power level is not a trivial task. The rf power needed for D_3^+ is by a factor 98 lower compared to the power of $^{238}U^{4+}$, for H_3^+ it is a factor 393. After an elaborate tuning of the rf transmitters and the control electronics, stable conditions for the rf phase and amplitude control could be adjusted only for D_3^+. At this low power level multipactoring did not occur.

Therefore, beam tests were performed with D_3^+ from the HSI, protons were injected from the ECR source into the high charge state injector HLI. During the first run an intensity of 600 µA deuterons were attained at SIS injection starting with an intensity of 1 mA D_3^+ at the RFQ entrance. By further improvement of ion source performance, HSI and poststripper transmission, an intensity of 3 mA D^+ should be feasible to fill the synchrotron to the space charge limit of 10^{12} particles per pulse.

From the ECR source H_2^+ molecules were extracted with an intensity of 100 µA. Due to the overall transmission of 50%, at least 100 µA protons can be expected at SIS injection at present, up to $5 \cdot 10^{10}$ protons per pulse can be accumulated in the SIS.

REFERENCES

[1] U. Scheeler, D. Wilms, Operating Report of UNILAC and SIS, This Scientific Report

[2] W. Barth, Commissioning of the 1.4 MeV/u High Current Heavy Ion Linac at GSI, Proc. of LINAC2000, Monterey, 2000, p. 1033

[3] H. Reich, F. Heymach, P. Spädtke, Commissioning of the High Current Ion Sources at the New GSI Injector (HSI), Proc. of LINAC2000, Monterey, 2000, p. 238

[4] L. Dahl, P. Spädtke, The Low Energy Beam Transport System of the New High Current Injector, Proc. of LINAC2000, Monterey, 2000, p. 241

[5] W. Barth, P. Forck, J. Glatz, W. Gutowski, G. Hutter, J. Klabunde, U. Ratzinger, R. Schwedhelm, P. Strehl, W. Vinzenz, D. Wilms, Commissioning of IH-RFQ and IH-DTL for the GSI High Current Linac, Proc. of LINAC2000, Monterey, 2000, p. 229

[6] W. Barth, P. Forck, The New Gas Stripper and Charge State Separator of the GSI High Current Injector, Proc. of LINAC2000, Monterey, 2000, p. 235

[7] G Hutter, W. Gutowski, W. Hartmann, G. Kube, M. Pilz, W. Vinzenz, The Rf-System of the New GSI High Current Linac HSI, Proc. of LINAC2000, Monterey, 2000, p. 977

[8] J. Glatz, J. Klabunde, U. Scheeler, D. Wilms, Operational Aspects of the High Current Upgrade at the UNILAC, Proc. of LINAC2000, Monterey, 2000, p. 233

[9], P. Spädtke, F. Heymach, R. Hollinger, R. Iannucci, R. Lang, H. Reich, H. Schulte, K. Tinschert, Ion Source Development and Operation, This Scientific Report

SIS Status Report

K.Blasche, U.Blell, O.Boine-Frankenheim, H.Eickhoff, M.Emmerling, P. Forck, B.Franczak, G.Hutter, K.Kaspar, H.G.König, B.Langenbeck, Y.Liu, G.Moritz, P.Moritz, C.Mühle, A.Peters, P.Spiller, W.Vinzenz
GSI – Darmstadt

1. Status of Operation

In 2000 sixteen different ion species – ^{1}H, ^{2}D, ^{12}C, ^{14}N, ^{18}O, ^{26}Mg, ^{40}Ar, ^{56}Fe, $^{58,60}Ni$, $^{84,86}Kr$, ^{92}Mo, ^{124}Sn, $^{129,132}Xe$, ^{197}Au, ^{208}Pb, and ^{238}U – were accelerated in the SIS. Altogether 6155 h of beam time were provided for experiments, often with one or more high-energy target experiments and the ESR running in a pulse-to-pulse timesharing operation mode. Another 211 h were used for accelerator tune-up and development. The total down-time of 354 h (5,3 % of the total operation time) was to a large part caused by a vacuum break-down in one of the experiment set-ups.

The total user time of 6155 h was distributed to radiotherapy with carbon ions (1437 h or 23 %), to production runs for target experiments (3681 h or 66%), and to the ESR (1031 h or 17 %).

SIS intensities for very heavy ions like U^{73+}-ions were still restricted, since the new high current injector HSI at the front-end of the Unilac has not yet reached the design injection current of 2 to 4 mA. With the available current of 150 µA the SIS provided about $2{\cdot}10^{9}$ U^{73+}-ions per machine cycle instead of $2{\cdot}10^{10}$. A comparable beam intensity has been achieved with much lower injection currents using beam accumulation with a series of multiturn-injections based on electron cooling. In this scheme the intensity was limited to about $2{\cdot}10^{9}$ U^{73+}-ions due to the onset of coherent transverse beam instabilities, which are typical for cooled low-emittance beams.

A new record beam intensity of $1.2{\cdot}10^{11}$ Ar^{11+}-ions was delivered for a FRS experiment. In this machine run the Unilac provided an injection current of about 3 mA, since no additional stripping of Ar^{11+} was necessary for the low energy of 500 MeV/u used in the experiment. The available beam intensity was close to the space-charge limit of $1.6{\cdot}10^{11}$ Ar^{11+}-ions.

The new HSI has been designed for low-charge-state heavy ions with A/q = 65. However, it could be shown that the Unilac can still provide light ions like ^{2}D-beams of about 1 mA for injection into the SIS, which will give about 2 to $3{\cdot}10^{11}$ ^{2}D-ions per machine cycle.

SIS operation with high intensity ion beams demands a careful control of beam losses. The efficiency of the multiturn injection will be controlled by a new interlock system, which was ordered in 2000. Beam losses during resonance extraction and along the beam transport system especially from the SIS to the FRS will be studied carefully using additional beam loss monitors in the extraction channel (diamond detectors) and along the beam-line (plastic scintillators).

The usual slow-extraction scheme is third-order resonance extraction with two fast extraction quadrupoles, which gradually shift Q_h towards 4 1/3 driving the coasting ions into a betatron resonance. Meanwhile an alternate scheme with operation at a constant Q_h close to the resonance was tested. A transverse rf noise voltage is used to knock out ions by excitation of large radial oscillations, which lead into resonance [1]. The new scheme provides excellent position stability for the extracted beam and an easy way to interrupt the spill and to proceed with slow extraction after a short pause. Both features are useful for the radiotherapy program. Further studies will show if the efficiency of the slow extraction process and the spill-structure can be improved, too. The complete device with an rf-noise-synthesizer locking onto the revolution frequency, newly developed power amplifiers and integration in the SIS control system is almost ready for routine operation.

2. SIS Machine Development

In 2000, a new device for precise dynamic tune measurement has been tested. Fig. 1 shows the measured horizontal and vertical tunes recorded in one machine cycle. It can be seen that the variation of both tunes is about 0.02 during acceleration, whereas on the flat top the vertical tune is constant and the horizontal tune increases slightly. The new Q-meter will be used for further precise tuning of the Q-values along the acceleration ramp, where the focusing scheme is shifted from triplet focusing at injection to almost duplet focusing at high energy.

Acceleration of protons to the maximum energy of 4.7 GeV requires a dynamic shift of the transition energy on the ramp, which is realised by a gradual change-over from 12 to 6 superperiod focusing. This scheme was successfully tested. Protons could be accelerated to 4.7 GeV without any beam losses on the acceleration ramp, since passing of the transition energy was avoided. On the flat-top the focusing scheme was reversed tuning 6 superperiod focusing back to the standard scheme with 12 superperiods, which is required for slow extraction. It could be shown that the coasting beam passes the transition energy without losses and phase-space degradation.

In 1999, it has been shown that transverse phase-space is kept constant during acceleration. However, in the longitudinal phase-space a blow-up by a factor of 3 is observed mainly during the rf-capture process (Fig. 2). Therefore the capture process has to be improved during the next time. At present the reduction of momentum spread due to the new debuncher system (36 MHz) in the SIS injector line does not yield the expected small momentum spread of the accelerated beam.

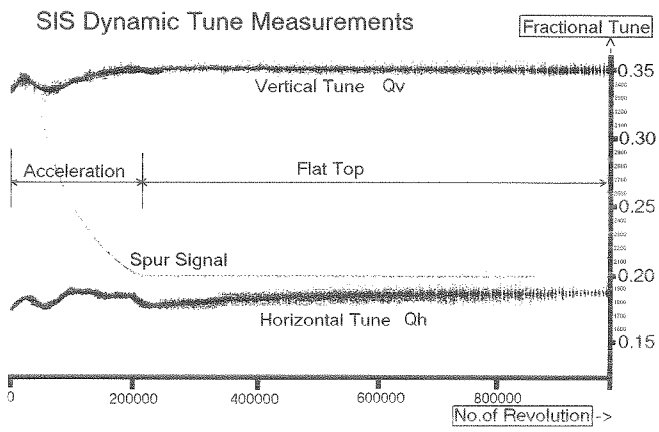

Fig. 1: Dynamic tune measurement for a SIS machine cycle.

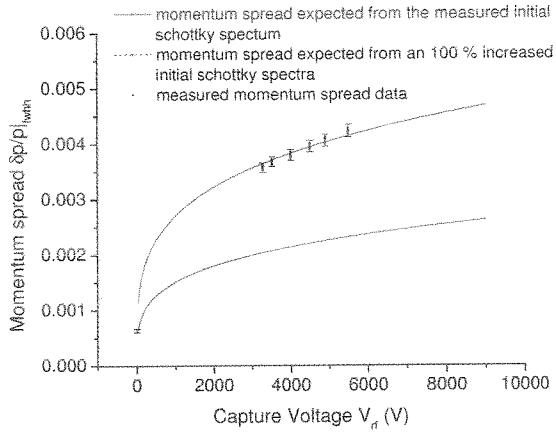

Fig. 2: Longitudinal phase space during RF-capture in the SIS. The measured momentum spread exceeds the calculated values by a factor of 2.

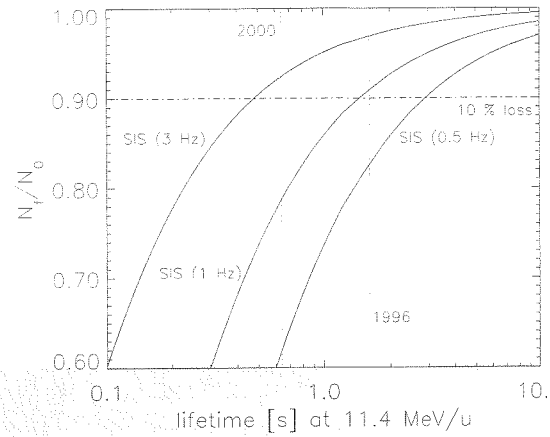

Fig. 3: Fraction of injected ions after acceleration versus beam life time at injection energy for three SIS operating modes.

It is very important to maintain the small phase space volume of the injected ion beam during RF-capture, acceleration, and debunching in the SIS, since a very low momentum spread is necessary for an effective use of the new bunch compressor system.
The acceleration of low charge-state ions e.g. Ar^{11+}-ions and especially U^{28+}-ions is used to provide very high beam intensities. Table 1 shows the 1/e beam life time for U^{28+}-ions at low energies and at 150 MeV/u as measured in 1996 and 2000. In 1996 the life-time was considerably larger than in 2000, although the measured average pressures $<p_{tot}>$ did not differ very much. It is assumed that the content of heavy molecules in the rest gas mass spectrum has increased since 1996.

Table 1: Beam life time (1/e) for U^{28+} ions at low energy and at 150 MeV/u as measured in 1996 and 2000.

Energy (MeV/u)	τ (sec)	$<p_{tot}>$ (mbar)	N_0	Date (year)
6	1.2	$5 \cdot 10^{-11}$	?	1996
8.7	0.56	$5.6 \cdot 10^{-11}$	$3 \cdot 10^{8}$	2000
150	1.6	$5.6 \cdot 10^{-11}$	$1.5 \cdot 10^{8}$	2000

Fig. 3 shows the resulting beam losses during acceleration, which amount to about 40 % with the present rather slow ramp rate of dB/dt = 1,5 T/s. However, with the vacuum of 1996 these losses can be reduced to 3 to 10 % for the SIS12 and SIS18 operation mode, if the design ramp rates of 10 and 4 T/s would be used. In any case, further improvements of the SIS vacuum system are planned for the future.

3. SIS Component Replacement and Development Program

In 2000 a complete set of new vacuum-chambers for the 24 dipole-magnets has been ordered. The 14 years old original chambers made from 0.3 mm thick stainless steel sheet reinforced with stiffening ribs have approached the fatigue limit. As a consequence of 5-10 bake out procedures they are all compressed by 5 to 10 mm and the vertical aperture is reduced from 70 to 60 mm.

In addition, three or four vacuum-chambers developed leaks during the bake out. The design of the new vacuum chamber removes the deficiencies of the original chambers, e.g. a long tube is used instead of three short welded sections and the stiffening ribs are strengthened. The installation of the new dipole chambers will be part of an extensive program that shall lead to a lower average vacuum pressure of about $1 \cdot 10^{-11}$mbar and to a reduction of heavy molecules in the residual gas.
In addition to the vacuum improvement program the following projects are under way:

1. a transverse feedback system,
2. a feedback system around the power amplifiers of the accelerating cavities,
3. a set of new correction coils, and
4. four bunch-compressor cavities.

The transverse feedback system shall be used to damp coherent transverse instabilities observed during operation with cooled ion beams e.g. with $2 \cdot 10^{9}$ U^{73+}-ions. It is planned to extend the range for stable operation with cooled beams to about $5 \cdot 10^{9}$ ions. The feedback-system includes two of the existing position monitor probes as pickup-system, a new feedback kicker, a new DSP processing stage (100 MHz, 12 bit), new power amplifiers, and a closed orbit suppressor system (CERN). All components are ready for tests of the complete system in March/April 2001.
The feedback systems around the power amplifier are developed to reduce the impedance of the two installed cavities from $R_p \simeq 3$ kΩ to below 1 kΩ. A complete SIS accelerating station has been built up for this development. Many components of the power amplifier stage were redesigned and adapted to the new requirements.
The set of new correction coils was designed to compensate and control the resonances $Q_V = 3\ 1/3$, $Q_V = 3\ 1/2$ and Q_h-$Q_V = 1$ to prepare SIS operation at a new high current working point ($Q_V = 4.2$, $Q_h = 3.6$), which allows operation with $2 \cdot 10^{11}$ Ne^{10+}-ions and $4 \cdot 10^{10}$ U^{73+}. The control of the difference resonance Q_h-$Q_V = 1$ will be used to optimise multiturn-injection and rf-capture and to manipulate the horizontal and vertical beam emittances. The correction coils are in production and the necessary power supplies will be ordered soon. It is planned to commission the complete system in the first quarter of 2002.
The four bunch compressor cavities will be installed to produce a short high intensity bunch before fast extraction e.g. a bunch

with $2 \cdot 10^{11}$ U^{28+}-ions of 50 ns or 10 m pulse width [2,3]. Fig. 4 shows the design of the new bunch-compressor cavities.
Each compressor cavity has an inductive load of twelve cores made of amorphous metallic alloy (MA core). VITROVAC 6030F from Vakuumschmelze (Hanau) is an appropriate material and two prototype cores will be delivered soon. The submission for the complete set of 48 cores is underway. The cavities are inductively coupled to the power amplifier stage by the anode cable led around the MA cores. For the low duty cycle operation the Thomson RS2054 is an adequate RF-tube. The components of the power amplifier stage were ordered and a prototype stage will be built soon.

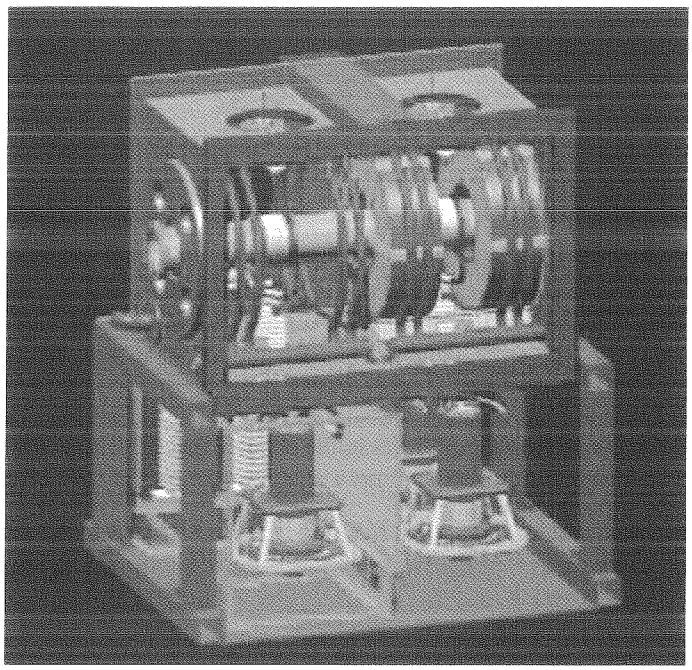

Fig. 4: Design of the SIS bunch compressor cavity based on magnetic alloy cores. Two out of four cavities are shown. Each cavity (top) is driven by a final amplifier stage in push-pull operation (bottom).

4. High Energy Beam Transport System

In 1998 a pion production target with a new beam line to the target area and the new HADES set-up have become part of the high energy facilities. At that time power supplies of the existing beam lines had to be used for sixteen additional beam line magnets to keep investment costs low. Meanwhile first experiments with the new pion beam line and with HADES have shown that power supply switching and the resulting strong restrictions for time sharing operation are a strong disadvantage for an efficient use of the high energy facility. Therefore it was decided to order all necessary power supplies. Installation was realised during the winter shut down 2000/2001. Now time sharing operation is available and with polarity switching different secondary beams like π^+, π^- or $\bar{p}$ can be provided easily.
In the beam line from the ESR to Cave A five new scintillator screens were installed.
In the SIS extraction beam line two prototype diamond detectors were installed. The first one is a square (30 × 30 mm) carrying nine parallel strips to show the horizontal beam profile and the second one is a smaller square (20 × 20 mm) with 16 pixels in a 4 × 4 array arrangement to monitor the (x,y) distribution of the beam intensity. At present both detectors are only 30 mm apart. Fig. 5. shows the pulse signals from a single uranium ion at an energy of 200 MeV/u passing the two CVD-diamond detectors [4]. The signal in the second detector is delayed by 200 ps according to the 30 mm distance showing the excellent time resolution of diamond detectors. As soon as both detectors will be fully equipped with 2 GHz broadband amplifiers, pulse shaping and pulse frequency dividers, the new diamond detectors will be used to monitor the beam intensity with high precision, and at the same time transverse beam-profiles as well as the time resolution of the spill-structure.

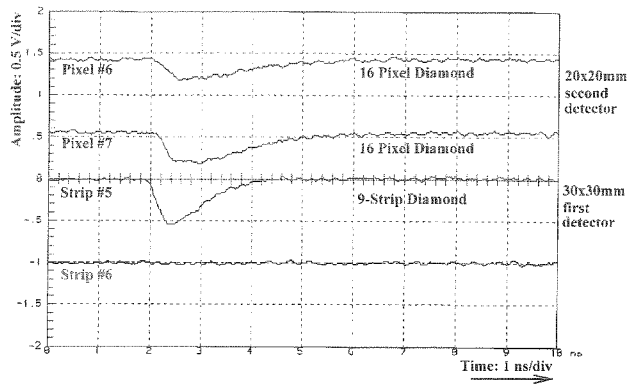

Fig. 5: Diamond counter signals from a single uranium ion at 200 MeV/u (v = 0.57 c) passing through two detectors. The first detector (lower two traces) is passed first at one strip, the second detector (upper two traces) is passed last. The ion trajectory in the second detector lay between two pixels and the signal was recorded coincidentally on two pixels of the same detector.

References:

[1] K.Hiramoto and M.Nishi; Resonant beam extraction scheme with constant separatrix; NIM A, 1992, pp. 154-160
[2] K.Blasche et al., Proceedings of the 6th EPAC, (1998) 1347
[3] P.Spiller et al., Generation of High Power Heavy Ion Beams at GSI, Proceedings of the 1999 PAC, New York (1999) 1788
[4] P.Moritz et al., Broadband electronics for CVD-diamond detectors, Diamond and Related Materials, 00(2001) in print

Simulation of Multibunch Instability

Y. Liu, O. Boine-Frankenheim, I. Hofmann, GSI Darmstadt

Longitudinal multibunch instability is a potential source of longitudinal beam quality reduction and beam loss in high intensity synchrotrons [1]. For the SIS high current design parameters of $2 \times 10^{11} U_{238}^{28+}$ ions at injection energy of 11.4Mev/u, with momentum spread $\Delta p/p_0 = \pm 3.5 \times 10^{-4}$ (coasting beam), a coupled bunch instability can be driven by the ring impedances after rf capture.

We use a self-consistent particle-in-cell (PIC) code to simulate the longitudinal motion of the beam under the presence of the rf field and the induced field. All electromagnetic characteristics of the beam environment and space charge are modeled as impedance. For each time step we fast Fourier transform the beam signal and couple it with impedance in order to get the induced field. Each particle is pushed using the local field quantities. Up to 500K macro-particles are usually used in the simulation to reduce the space charge induced simulation noise.

We set rf voltage $V_{rf} = 10kV$, and make the capture slow enough (140ms, due to low initial momentum spread) to be adiabatic. There is an initial rise due to coasting beam instability. In our case space charge impedance $Z_{SC}(p\omega_0)/p$ is $-3.36k\Omega$. Resistive impedance is assumed at h=1(around 215 kHz), and $\frac{Z_R(p\omega_0)}{p}|_{p=1} = 1.5k\Omega$, which is a possible value for SIS whole ring resistive impedance because of some special structures and resistivity between welded chambers in SIS. The simulation results are shown in Fig.1 and Fig.2. A cavity offset can also generate resistive impedance. The shunt impedance (10kΩ) of the bunch compressor cavity [3] operating around 1 MHz is another possible source of coupled bunch instability in the SIS.

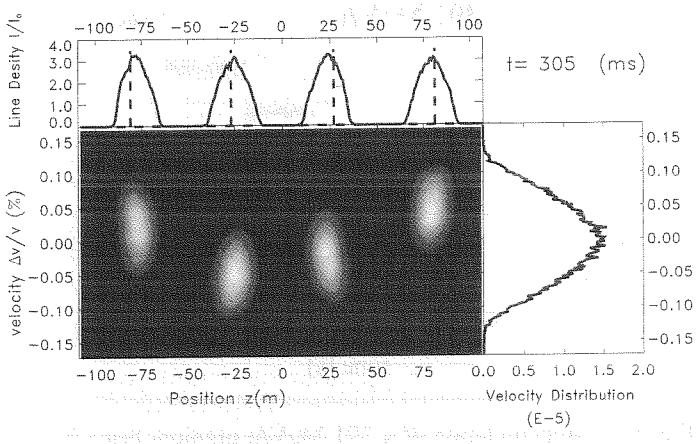

Figure 1: Evolution of the coupled bunch instability for the captured four bunches (total $2 \times 10^{11} U_{238}^{28+}$ ions) at injection energy of 11.4Mev/u in SIS, with momentum spread $\delta p/p|_{FWHM}$ increasing from 1.4×10^{-3} to 2.3×10^{-3}.

Multibunch instability can be damped by the synchrotron frequency spread created by nonlinearity of rf bucket. There is a boundary in the impedance plane, inside which bunches are stable. Fig.3 shows the result

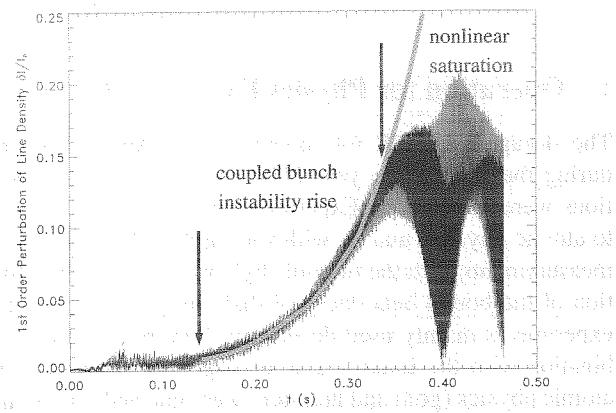

Figure 2: Evaluation of the instability rise time. Time evolution of first order Fourier component of line density.

from simulation and analysis. The stable boundary is obtained from a series of simulation runs. The rise curve is calculated by solving Sacherer's integral problem for the linearized problem.

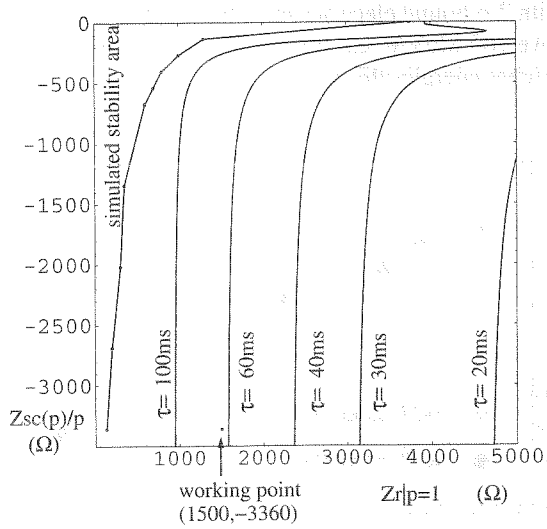

Figure 3: Stability graph in $Z_{SC}(p)/p, Z_r|_{p=1}$ plane.

We plan an experiment in SIS for the coming beam time using one cavity working at h=4 for capturing, and a second cavity with RF off and frequency tuned at h=5 or 7 to create a resistive impedance The coupled bunch mode can be measured and compared with calculations.

References

[1] F.Sacherer.Trans.IEEE BS-20, p.825 (1973)
[2] O.Boine-Frankenheim, I.Hofmann and G.Rumolo, Phys. Rev. Lett.82, 3256(1999)
[3] K.Blasche et al., Proceedings of the EPAC 98, p. 1347

ESR Operation and Development

M. Steck, K. Beckert, P. Beller, W. Bourgeois, B. Franzke, F. Nolden,
U. Popp, A. Schwinn, GSI Darmstadt

1 Operation for Physics Experiments

The storage ring ESR was operated until August with beam, during the rest of the year 2000 several technical modifications were performed. Experiments in the ESR were devoted to atomic physics, mainly with very highly charged ions, mass measurements with the time-of-flight method, and the observation of the bound beta decay of thallium [1]. Atomic physics experiments mainly used decelerated bare heavy ions in combination with the internal gas jet target. The heavy ions for atomic physics (gold and uranium) were injected after stripping at around 300 MeV/u and decelerated to various energies between 120 and 30 MeV/u. The typical intensities for the decelerated beam were a few times 10^7 ions. The efficiency for deceleration to these energies was 30 - 50 %, typically.

2 Machine Development

A new set of stripper foils was installed in front of the ESR. Additional carbon foils with thicknesses between 10 and 30 mg/cm^2 allow to inject for heavy ions ($A \geq 200$) charge states with 2-6 bound electrons in sufficient abundance at energies above 200 MeV/u, e.g lithium-like systems will be available at higher energies this way.

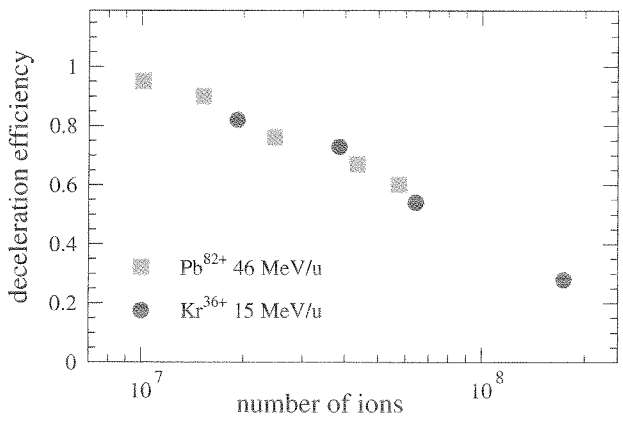

Figure 1: Efficiency for deceleration from 300 MeV/u injection energy to the energy indicated in the legend.

Experiments to decelerate heavy ion beams to even lower energies were continued. For energies below 12 MeV/u the rf frequency has to be changed from harmonic h=2 to h=4. The debunching and rebunching has been successfully tested at energies between 12 and 30 MeV/u. Supported by continuous electron cooling the de- and rebunching process proved to be free of significant loss. With the beam bunched at harmonic h=4 the lowest energy achieved was 9 MeV/u, but still large losses were observed. The intensity of the beam at 9 MeV/u was on the order of a few times 10^5 ions. The ramping speed at the low energy part of the deceleration procedure (below 15 MeV/u) had to be reduced to 0.01 T/s in order to minimize adverse hysteresis effects. Measurements of tune and of beam position during ramping showed moderate variations, which cannot account for the large losses. The main reason for the losses has not been spotted, but it is likely a combination of the unavoidable adiabatic emittance growth and closed orbit distortions. This is in agreement with measurements of the efficiency for deceleration (Fig. 1). The relative losses increase with beam intensity. It is well known that the emittance of the cooled ion beam, which is always the starting point for deceleration, increases with intensity due to intrabeam scattering [2]. Therefore for higher beam intensity the larger emittance beam is subject to larger losses at aperture limitations.

A first attempt to use the drag force of the electron cooler for deceleration was successful. The rf amplitude was set to zero during deceleration, whereas the accelerating voltage of the electron beam and the magnetic field of the ring magnets were ramped synchronously with a constant electron beam of 0.25 A [3]. The energy of the ion beam was reduced from 15 to 11 MeV/u within 6.7 s, corresponding to a ramp rate of 0.005 T/s, which is only a factor of two slower than what has been achieved with the rf system. However, further studies have to show whether this deceleration mode can provide favorable conditions for routine deceleration to lowest energies.

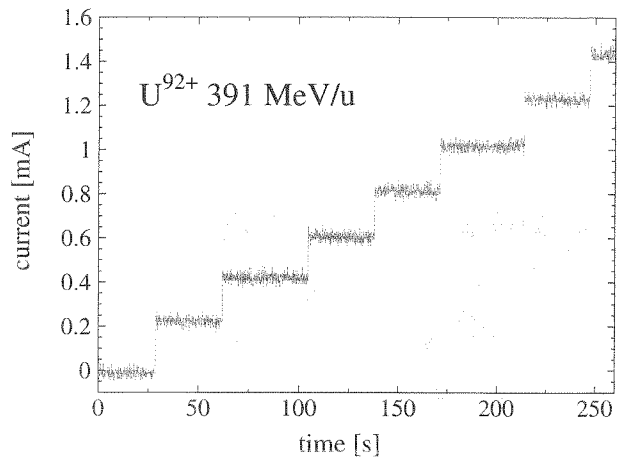

Figure 2: Accumulation of a 391 MeV/u uranium beam by a combination of stochastic precooling, rf stacking and electron cooling of the beam stack.

Stochastic cooling of heavy ions was demonstrated for the first time with a beam of bare uranium ions at an energy of 391 MeV/u [4]. The stochastic cooling system is presently tuned to the corresponding beam velocity ($\beta = 0.71$). Cooling times of about 0.5 s were measured for the longitudinal and vertical cooling. Horizontal cooling was a factor of five slower. The stochastically precooled beam was subsequently stacked by a momentum reduction of 1.8 % with the rf system and contin-

uous electron cooling of the stacked beam at the lower momentum. Figure 2 shows the circulating ion current increase with time. The low and irregular repetition rate of the injections is caused by the availability of the synchrotron SIS for injection into the ESR, as this machine development was performed parasitically to physics experiments served by the synchrotron. The first experience promises that this mode will also be available after some further improvements for fast accumulation of radioactive beams.

The observation of the strong reduction of the momentum spread for electron cooled heavy ion beams of a few thousand ions or less has been explained by an ordered structure of the ions which are confined by their nearest neighbors to their longitudinal position [5]. New experiments have shown that the existence of such an ordered structure can also be indicated by the temporal evolution of the momentum spread after an interruption of cooling. By a fast high voltage switch which stops or starts the extraction of electrons from the cathode within less than 1 ms the cooling was switched on and off alternatingly for time intervals of 6.8 s. The evolution of the momentum spread was monitored by fast Fourier analysis of the longitudinal Schottky noise (Fig. 3).

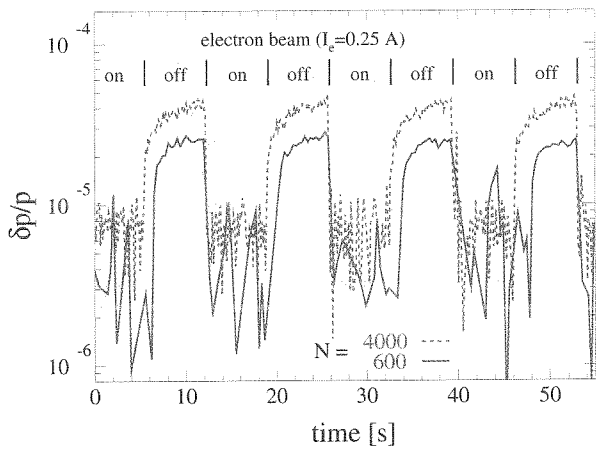

Figure 3: Momentum spread of a U^{92+}beam at 390 MeV/u above (dashed) and below (full line) the transition point to small momentum spread as a function of time. The electron beam is switched on and off for time intervals of 6.8 s. The low intensity cold beam heats up with a delay of about 1 s.

The high intensity beam (particle number $N \simeq 4000$) shows an instantaneous longitudinal heating due to intrabeam scattering. The beam with an intensity below the transition point to small momentum spread ($N \simeq 600$), which is supposed to be in an ordered state, remains in the cold state for nearly 1 s (more than 10^6 revolutions in the storage ring) before the momentum spread starts growing in a manner similar to the higher intensity beam. The ordered structure is obviously not immediately destroyed by intrabeam scattering.

3 Technical Developments

The long shutdown starting in September 2000 was used for several new installations in the ESR. The ramping range of the dipole magnets was hitherto limited by the power supplies for the correction coils sitting in the main dipoles to improve the flatness of the radial field distribution. Replacement by more powerful and bipolar power supplies will allow ramped operation over the full magnetic rigidity range of the ESR. This will be particularly valuable for bare decelerated heavy ions. They can be injected at higher energy with a higher stripping efficiency and then be decelerated to the required energy. It will also ease ESR operation in general.

The internal gas jet target section was completely disassembled. The reconstruction of this area will make room for the installation of new experimental equipment, such as a zero degree electron spectrometer downstream the target, Helmholtz coils to guide electrons produced in the interaction of the beam with target atoms, or a cryogenic bolometer for X-ray detection. The modification of the target section is a prerequisite for a large variety of new experiments which are planned with the internal gas target.

The stepping motors driving the detector pockets for the installation of particle detectors behind the gas target and the electron cooler were replaced by pressurized air actuators. The new actuators can be positioned within 1 s with an accuracy of 0.1 mm for particle detection, compared to times of the order of minutes which were needed to position the detectors with stepping motors. The thickness of the stainless steel entrance windows to the detector volume has been reduced from 50 to 25 μm in order to detect decelerated heavy ions with energies down to 7 MeV/u.

References

[1] T. Ohtsubo et al., this report.

[2] M. Steck et al., GSI Scientific Report 1999, GSI 00-1.

[3] M. Steck et al., Proc. of the 7^{th} Europ. Part. Acc. Conf., Vienna, 587 (2000).

[4] F. Nolden et al., Proc. of the 7^{th} Europ. Part. Acc. Conf., Vienna, 1262 (2000).

[5] R.W. Hasse, M. Steck, Proc. of the 7^{th} Europ. Part. Acc. Conf., Vienna, 274 (2000).

Multiple Coulomb Ordered Strings of Ions in the ESR

Rainer W. Hasse, GSI

In a recent paper, Radon *et al.* [1] reported on high precision mass measurements with Schottky mass spectrometry of about 100 new isotopes with a high resolving power. In that experiment fully stripped isotopes were produced by fragmentation of a $^{209}Bi^{67+}$ beam at 930 MeV/u, separated in the fragment separator, and stored and cooled in the ESR. For fixed magnetic rigidity each species of the beam has its own frequency $f_i = v/C_i$, where C_i is the length of its trajectory close to the circumference of the ESR, C=108.4 m. Neighboring masses Δm run on slightly different trajectories due to their different rigidities and, thus, have different frequencies. Typical deviations were found from the measured frequencies of known isotopes as compared to the known calibration curve. If there are at least two masses so close to each other that their difference in frequencies is smaller than about 80...90 Hz on the average, the lower (higher) one is shifted characteristically to a higher (lower) value. This anomalous effect limits the mass resolution to about 20 μu and such masses then have to be discarded from the results.

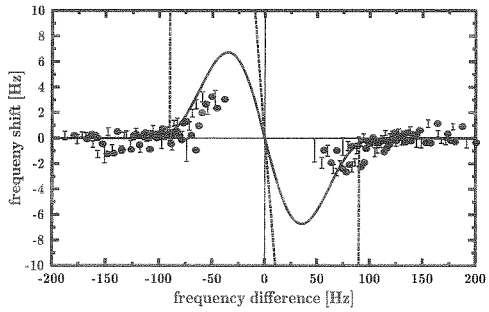

Figure 1: Average anomalous frequency shifts of neighboring isotopes *vs.* difference between their measured frequencies. (after Ref.[1]) with the result of the model calculation included (full line). The dashed sawtooth curve would result without folding over their thermal overlap volume.

In the present work we explain and make a model for the origin of these anomalous frequency shifts on the basis of the anticipation that the ions run on strongly correlated trajectories. The parameters here are of the same order of magnitude as the ones of the machine experiments on the anomalous jump to very low momentum spreads in the ESR [2] and in the SIS [3]. There it has been shown [4] that under the experimental conditions intra-beam scattering is strongly suppressed and that the ions cannot pass each other any more and, thus, run on strings.

Nuclides with different masses but with the same velocity run on different trajectories which are horizontally displaced so that, apart fom thermal fluctuations, $v = Cf$ remains constant, thus $\Delta C/C = -\Delta f/f$. This difference in length of trajectory transforms into the horizontal displacement $-\Delta x = (C/2\pi)\Delta f/f = 17\ \mathrm{m} \times \Delta f/f$. This fact leads to the model that if the displacement is larger than the thermal diameter, the two (or more) strings run on well separated trajectories yielding two (or more) distinct peaks in the Schottky spectrum which lie at the correct positions. The result of Fig. 1 is obtained assuming that this locking is not instantaneous if the clouds start to overlap, but that there is a smooth transition with a probability proportional to the overlap region of the clouds due to the averaging procedure over the experimental data, and folding this probability together with the experimental resolution of 15 Hz into the sawtooth curve of shifts (the dashed lines in Fig. 1). The dashed sawtooth line would result if the strings were always captured if their thermal radii start to overlap. Note that apart from the uncertainty coming from the assumed capture probability this model has no free parameters and that the result agrees nicely with the experiment.

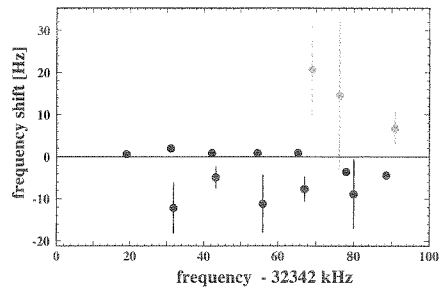

Figure 2: Measured anomalous frequency shifts in a relatively warm beam. The dots with nearly zero shifts belong to isotopes of the primary beam, others are nearby fragment nuclides. The gray dots are questionable by the lack of intensity (after Ref.[5]).

There is indication that the effect of locking or capture is not restricted to the existence of ultra-cold chains. During the preparation of the precision mass experiments similar anomalous frequency shifts have been observed in Ref. [5] in an experiment with a bare gold beam at 295 MeV/u. Its isotopes and other strongly populated fragments had velocity spreads of about 10^{-5} and thermal widths of about 4 mm. By cooling and scraping the beam radius the velocity spread decreased by one order of magnitude. Nearby fragment nuclides with slightly larger masses then acquired anomalous negative frequency shifts of the order of a few Hz, see Fig. 2.

Evidently, the low intensity fragment isotopes (with negative shifts and error bars) and masses slightly larger than the mass of the primary beam (with nearly zero shifts and no error bars) have been absorbed into the cloud of the primary beam itself, thereby reducing their frequencies slightly. The observed positive frequency shifts are statistically irrelevant.

References

[1] T. Radon et al., Nucl. Phys. A **677**, 75 (2000)
[2] M. Steck, *et al.*, Phys. Rev. Lett. **77**, 3803 (1996)
[3] R.W. Hasse, M. Steck, Proc. EPAC 2000, Vienna (2000) p. 274
[4] R.W. Hasse, Phys. Rev. Lett. **83**, 3430 (1999)
[5] B. Schlitt, *PhD. thesis Univ. Heidelberg*, GSI report DISS. 97-01, GSI Darmstadt (1997)

Design of a 7 MeV/u, 217 MHz Injector Linac for Therapy Facilities

B. Schlitt[1], A. Bechtold[2], U. Ratzinger[2], A. Schempp[2]
[1] GSI, [2] Institut für Angewandte Physik (IAP), Frankfurt am Main

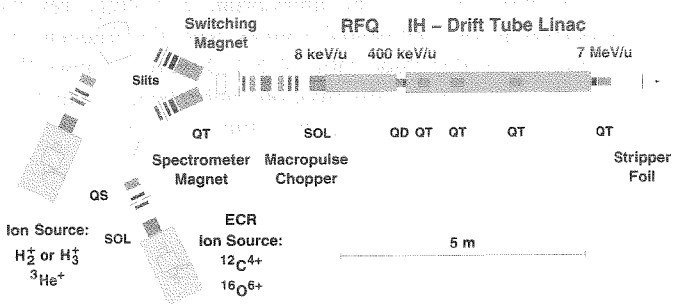

Figure 1: Schematic drawing of the injector linac. SOL ≡ solenoid magnet, QS, QD, QT ≡ magnetic quadrupole singlet, doublet, triplet.

Table 1: Major parameters of the injector linac.

Design ion	$^{12}C^{4+}$	$(A/q = 3)$
Operating frequency	216.816	MHz
Final beam energy	7	MeV/u
Pulse currents after stripper	≈ 100	eμA C^{6+}
	≈ 0.7	mA protons
Beam pulse length	≤ 200	μs @ ≤ 5 Hz
Duty cycle	≤ 0.1	%
Norm. transverse exit beam emittances (95%) [1]	≈ 0.8	π mm mrad
Exit momentum spread [1]	±0.15	%
Total injector length [2]	≈ 13	m

[1] Not including emittance growth effects in the stripper foil.
[2] Including the ion sources and up to the foil stripper.

A dedicated clinical synchrotron facility for cancer therapy using energetic proton and ion beams (carbon, helium and oxygen) has been designed at GSI for the Radiologische Universitätsklinik in Heidelberg [1]. A compact injector design is proposed (Fig. 1 and Table 1) [2, 3]. The LEBT allows for switching between two ion sources as well as for beam chopping and for controlled beam current variation. A 4-rod type RFQ of about 1.5 m in length accelerates the ions from 8 keV/u to 400 keV/u. A very compact intertank section has been proposed for matching the beam parameters at the exit of the RFQ to the ones required at the entrance of the subsequent IH-type drift tube linac (Fig. 2). It consists of a two-gap rebuncher integrated into the RFQ tank [3], a pair of steerer magnets, a magnetic quadrupole doublet and a diagnostic box comprising a beam transformer and a phase probe. The total length between the RFQ and IH tanks is about 20 cm only. The IH-DTL for the acceleration to 7 MeV/u has a length of roughly 3.8 m and an expected rf power consumption around 1 MW. It consists of three integrated magnetic quadrupole triplets and 56 accelerating gaps grouped in four KONUS sections. Finally, the beam is focused by another quadrupole triplet following the DTL onto a stripper foil located about 1 m behind of the linac.

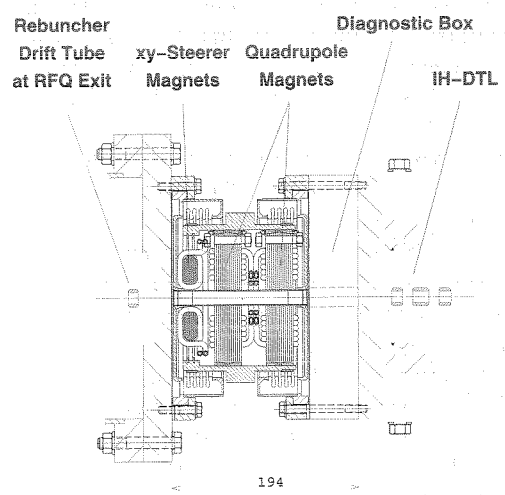

Figure 2: Design of the intertank matching section.

In the last year we focused on the optimization of several details and proceeded in the design of the most challenging critical parts. The integration of two drift tubes into the RFQ tank has been further investigated at the IAP by detailed measurements using rf models and by MAFIA simulations [3, 4]. Realistic field configurations of the transition from the RFQ electrodes to the drift tube geometry have been calculated by 3D simulations and have been integrated into the particle dynamics simulations using a modified PARMTEQ version.

The DTL design has been optimized and a 1:2 scaled rf model is under construction. Due to the comparatively high frequency of 217 MHz the diameter of the IH tank amounts to roughly 30 cm only, requiring very small triplet lenses of around 25 cm in length and about 16 cm in diameter. First 3D design studies of these small quadrupole magnets using the TOSCA code have been performed by B. Langenbeck and C. Mühle, GSI.

To enhance the efficiency of synchrotron injection the momentum spread of the ion beam can be reduced to $\Delta p/p \leq \pm 0.1\,\%$ by an additional debunching cavity installed in the synchrotron injection line. Detailed particle dynamics simulations and a first cavity design study have been performed [5].

References

[1] H. Eickhoff et al., in: *Proc. EPAC 2000, Vienna, 2000*, p. 2512, and in: *GSI Scientific Report 1999*, p. 196.
[2] B. Schlitt, A. Bechtold, U. Ratzinger and A. Schempp, in: *Proc. LINAC 2000, Monterey, 2000*, p. 226.
[3] A. Bechtold, A. Schempp, U. Ratzinger and B. Schlitt, in: *Proc. EPAC 2000, Vienna, 2000*, p. 2500, and in: *GSI Scientific Report 1999*, p. 198.
[4] A. Bechtold, PhD Thesis, in preparation.
[5] M. Crescenti, GSI Arbeitsnotiz KLB22110.SI, 2000.

An RF Chopped Electron Beam Driver for H-Type Cavities

S. Setzer*[1], T. Weiland[1], U.Ratzinger[2], S. Minaev[3]; [1]TU-Darmstadt, [2]Universität Frankfurt, [3]MEPI, Moscow

During the last three years a high power rf generator design capable of providing several MW rf power at frequencies between 200 and 300 MHz has been investigated. Instead of using conventional techniques for bunch formation in electron beam based generators like grids or longitudinal velocity modulation it is based on an innovative scheme which was first proposed in 1986 [1]. It allows to directly drive the resonant mode of an H-type cavity by the electron beam resulting in a much simplified rf driver system. The basic concept is to use a continuous electron beam produced by a thermionic gun. The time structure of the electron beam is achieved by a rf driven chopping system using the E×B drift which deflects about 80% of the beam to a suppressed collector where the main part of the beam energy is recovered. The remaining bunched electron beam is injected into the IH tank where the beam energy will drive the IH_{110} mode. To increase the efficiency of the beam deflection a second deflector stage working on dc potential may be added [2]. The setup of the total system is shown in Fig. 1. To prove the feasibility of the proposed rf generator the individual components were simulated with the three dimensional particle in cell code TS3 which is part of the simulation package MAFIA. It is capable of solving Maxwell´s equations including the self fields of charged particles in motion. Starting with the high perveance electron gun the simulations resulted in a reasonable geometry which delivers a 100 A, 100 keV beam with a radius of 5 mm which is injected into a confining magnetic field with a flux density of 100 mT.

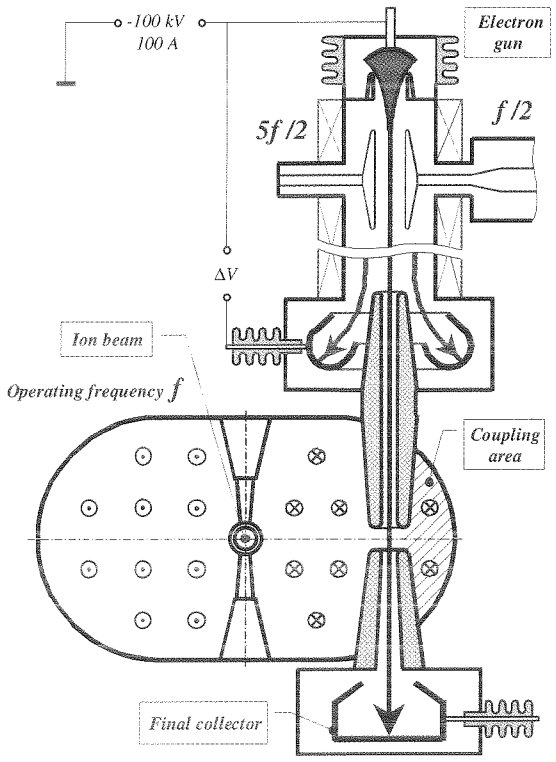

Figure 1: Setup of the total rf system

The chopper stage is directly connected to the gun exit and driven by an rf of about 50 kV while the dc stage needs a potential of about 60 kV. The appropriate rf voltage results from superposing two sinusoidal signals with the frequencies f/2 and 5f/2 at an amplitude ratio of 5:1. Figure 2 shows the resulting electron density distribution right behind the two deflecting stages predicted by the simulations.

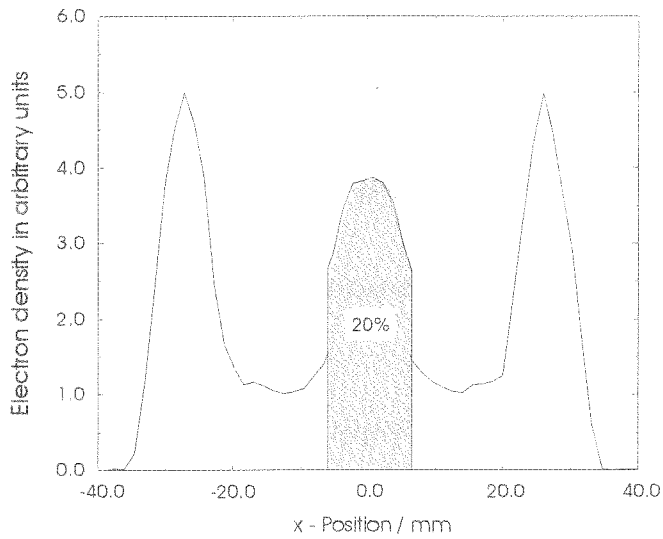

Figure 2: Electron density distribution behind the deflector

The hatched area corresponds to a transverse beam width of ±6.3 mm. Longitudinally the beam has a rectangular profile with a length of about 96 degree in units of the operating frequency of 200 MHz [3].

A 200 MHz prototype of the deflector is under construction at the IAP, University of Frankfurt. Its purpose is to demonstrate the chopper principle and to compare the results with the predictions of the simulations.

References

[1] U. Ratzinger, Doctoral thesis, TU München, 1986, p.53

[2] S. Minaev, U. Ratzinger, GSI Arbeitsnotiz ALG16129HF

[3] S. Setzer, T.Weiland, U.Ratzinger, S.Minaev ,"A Chopped Beam Driver for H-Type Cavities", Proc. of Linac 2000, pp. 1001

* Member of the Graduiertenkolleg (DFG GK-GRK 410/1)

TECHNICAL DEVELOPMENTS

Detector Developments

Computing and Electronics

Proton Scattering of Neutron-Rich He-Isotopes in Inverse Kinematics A New Setup for the High Momentum Transfer Measurements

F. Aksouh[1], O.A. Kisselev[1,2], A. Bleile[1], O.V. Bochkarev[3], L.V. Chulkov[3], D. Cortina-Gil[1], A.V. Dobrovolsky[1,2], P. Egelhof[1], H. Geissel[1], M. Hellström[1], N.B. Isaev[2], B.G. Komkov[2], M. Màtos[1], F.V. Moroz[2], G. Münzenberg[1], M. Mutterer[4], V.A. Mylnikov[2], S.R. Neumaier[1], V.N. Pribora[3], D.M. Seliverstov[2], L.O. Sergueev[2], A. Shrivastava[1], K. Sümmerer[1], H. Weick[1], M. Winkler[1] and V.I. Yatsoura[2]

[1] *GSI,* [2] *PNPI Gatchina,* [3] *Kurchatov Institute Moscow,* [4] *TU Darmstadt*

Proton elastic scattering at intermediate energies of around 700 MeV/u is well suited for determining radii and nuclear matter distributions of halo nuclei such as ^{6,8}He [1] and ^{11}Li [2]. The first measurement on the ^{6,8}He nuclei in inverse kinematics has been performed at low momentum transfer up to $|t| = 0.05$ (GeV/c)^2 using gaseous hydrogen as proton target. From theoretical investigations [3] a high sensitivity on the inner part of the nuclear matter distributions is predicted when extending the p^{6}He and p^{8}He elastic cross section measurement to the higher momentum transfer region ($|t| = 0.1$ - 0.4 (GeV/c)^2). Calculations based on Glauber theory show that the position of the first diffraction minimum depends on the shape of the density distribution, and is within the model strongly correlated to the core radius of the halo nucleus . We conclude, that a measurement of the angular distribution at higher momentum transfer should yield unambiguous information about the intrinsic structure of these nuclei. In addition, also inelastic reaction channels may be investigated.

A recent experiment has been carried out at GSI in October 2000. The ^{6,8}He beams were obtained via fragmentation of an ^{18}O primary beam of about 10^{10} ions/spill. The projectile fragments were separated by the FRS yielding secondary beam intensities of 5×10^3-10^5 ions/s with an energy of about 700 MeV/u. The experimental setup installed in cave B is shown in fig.1. A forward spectrometer has been used for tracking and identifying the projectile nuclei and for separating the elastic events from the inelastic and break-up channels. It also provided the signal for the first level trigger. This spectrometer consisted of four X-Y position sensitive multiwire proportional chambers (MWPC) P1-P4 with cathode strip channel-by-channel readout, several beam scintillators (S1-S3, Veto), the ALADIN magnet and a position sensitive scintillator wall behind. The proportional chambers had rather high position resolution of 100-150 μm and an efficiency close to 100%. A second position sensitive scintillator wall was used to measure ΔE and time-of-flight of the recoil protons. The second level trigger used the signals from two proportional chambers (P5, P6) detecting and tracking the recoil protons. The essential difference with respect to the previous ^{6,8}He experiment [1] was, that the high recoil proton energies up to $E_p = 160$ MeV allowed to replace the gaseous H_2 target by a 600 mg/cm^2 liquid H_2 target. This target and the cryogenic device used for the experiment were constructed at CEA, Saclay. The cylindrical target had a total length of 120 mm and an inner diameter of 30 mm. The use of a liquid hydrogen target allows to decrease significantly the background as compared to similar experiments with CH_2 targets.

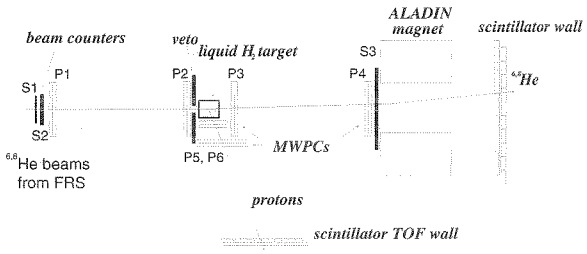

Figure 1: Schematic drawing of the S174 experimental setup.

The data analysis is still in progress. To illustrate the quality of the acquired data, X-position spectra obtained with the MWPC P4 in the field free region before the ALADIN magnet for two different experimental conditions are displayed in fig.2. The spectrum on the left side was taken for the case the second level trigger (that demands recoil protons) being switched on. The one shown on the right side was obtained for the case the second level trigger was switched off, thus displaying the profile of the unscattered beam. The dominant peak in the spectrum on the left side clearly reflects the distribution of elastically and inelastically scattered ^{6}He projectiles, whereas the peak around X=0 is due to the unscattered beam particles contributing to the background. From these online raw spectra we conclude that practically background free data on elastic and inelastic p^{6,8}He scattering will be available after the final analysis taking into account all measured parameters.

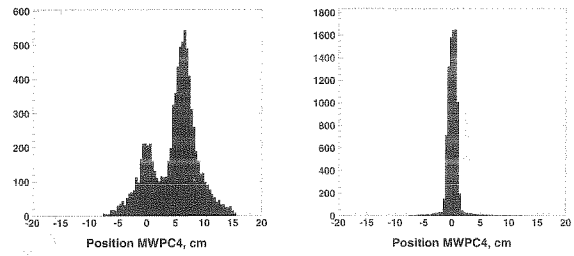

Figure 2: X position spectra from the MWPC P4 obtained for p^{6}He scattering for two different experimental conditions (see text).

References

[1] G.D. Alkhazov *et al.*, Phys. Rev. Lett. 78 (1997) 2313.
[2] S.F. Neumaier *et al.*, to be published in Nucl. Phys. A, A.V. Dobrovolsky *et al.*, this report.
[3] L.V. Chulkov et al., Nucl. Phys. A 587 (1995) 291.

Progress in the Optimization of the FOCAL Crystal Spectrometer

H.F. Beyer[9], J. Bojowald[4], G. Borchert[4], F. Bosch[9], W. Brüchle[9], M. Czanta[9], R.D. Deslattes[1], E. Förster[3], A. Freund[2], A. Gumberidze[9], A. Hamacher[4], J. Hoszowska[2], P. Indelicato[6], H.-J. Kluge[9], Chr. Kozhuharov[9], D. Liesen[9], B. Lommel[9], T. Ludziejewski[8], X. Ma[9], B. Manil[6], I. Mohos[4], D. Protić[4], A. Simionovici[2], Th. Stöhlker[9], C. Striezel[7] S. Toleikis[9], N. Trautmann[5], J. Tschischgale[3], A.H. Walenta[7], O. Wehrhan[3]

[1]National Institute of Standards and Technology, Gaithersburg, Maryland 20899, USA
[2]European Synchrotron Radiation Facility (ESRF), F-38043 Grenoble, France
[3]Institut für Optik und Quantenelektronik, Friedrich Schiller-Universität, D-07743 Jena, Germany
[4]FZ Jülich, Institut für Kernphysik, Germany
[5]Institut für Kernchemie, Universität Mainz, D-55128 Mainz, Germany
[6]Université P. et M. Curie, Lab. Kastler Brossel, F-75252 Paris Cédex, 05 France
[7]Universität Siegen, Fachbereich 7 Physik, D-57068 Siegen, Germany
[8]The Andrzej Soltan Institute for Nuclear Studies, 05-400 Swierk, Poland
[9]GSI Darmstadt

The FOCAL x-ray spectrometer is being developed for the accurate measurement of the 1s Lamb shift in one-electron heavy ions. In the **FO**cussing **C**ompensated **A**symmetric **L**aue geometry part of the possible wavelength resolution is traded off in favor of an increased sensitivity through a broadening of the crystal rocking curve [1].

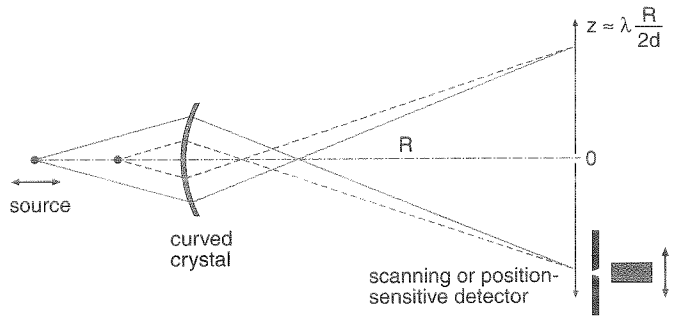

Figure 1: Principle of the x-ray optical arrangement used for systematic tests of the FOCAL spectrometer. The x-ray path is shown for one wavelength at two different locations of the gamma-ray source.

The spectrometer has been set up on a test bench where several systematic investigations were performed during the past year. Figure 1 schematically shows the x-ray optical arrangement with a movable x-ray source parked at two different positions. The x rays are dispersed along the positive and negative z axis in a symmetric way where the displacement is approximately proportional to the wavelength. Spectra obtained from a ^{169}Yb source were recorded either with a scanner equipped with a narrow slit and a conventional Ge(i) detector or with the new micro-strip germanium detector under development [2]. Recording the x-ray spectra for a couple of different gamma-ray lines and for a range of source-to-crystal distances, it is possible to map out the x-ray optics and the performance and possible deviations of the crystal from it's ideal cylindrical shape. Up to now such tests have solely been made with the scanner. A first test of the spectrometer in combination with the new micro-strip detector was made for a fixed source-to-crystal separation amounting to 300 mm compared to 2 m as the nominal radius of curvature of the crystal.

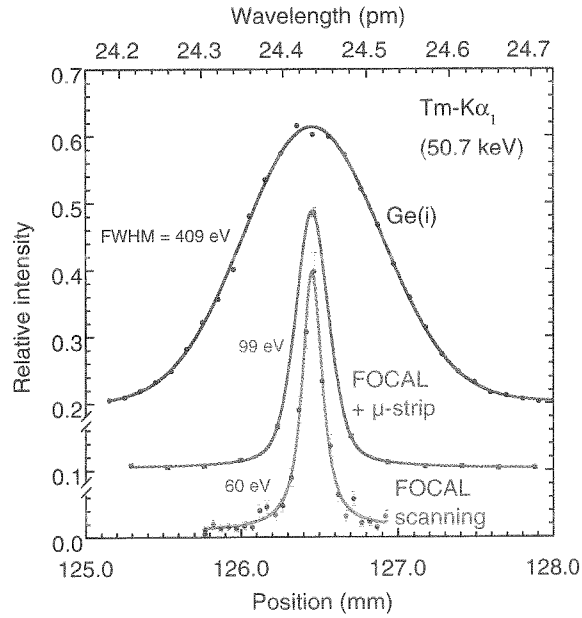

Figure 2: The wavelength profile of the Tm-Kα_1 line measured as the pulse-height spectrum of a conventional solid-state Ge(i) detector or measured with the FOCAL spectrometer equipped either with a position-sensitive micro-strip detector or in scanning mode.

Figure 2 compares measurements of the Tm-Kα_1 line near 50.7 keV from the decay of ^{169}Yb with FOCAL operated in scanning mode or with the micro-strip detector attached. For reference the pulse-height spectrum of the conventional Ge(i) is also included. The line widths of 150 μm (60 eV) and 250 μm (99 eV) for the scanner and for the micro-strip detector, respectively, are consistent with the expectations taking into account the slit width of 50 μm and the 235 μm combined stripe and gap width. Additionally the natural line width of 30 eV and the

contribution from the rocking curve amounting to 40 eV have to be considered.

The present position sensitive detector has an area of 47 × 23.4 mm^2 and is structured with 200 stripes, each 200 μm wide, which are separated by grooves of 35 μm width. This prototype will soon be replaced by an upgraded version optimized in order to cover a substantial fraction of the astigmatic height of the spectral lines and to be position sensitive in *two* dimensions. This will be realized by etching grooves into both the front and rear surface of the germanium crystal.

For characterizing the silicon crystal, the source-to-crystal separation was varied between 260 and 550 mm. Gamma-rays near 50, 63 and 110 keV were reflected from different spots on the crystal that are offset by a distance ranging from ±8 to ±28 mm from the centre of the crystal. The results from these measurements revealed deviations of the curvature from the ideal cylindrical shape. In figure 3 the observed line widths are plotted as a function of the calculated position on the crystal. Going from the centre towards the edges of the crystal the width strongly increases. Presumably this is caused by the mechanical stress introduced in the bending device. We will try to reduce this effect by using only the inner region of a larger crystal and by a change of the design of the crystal bender.

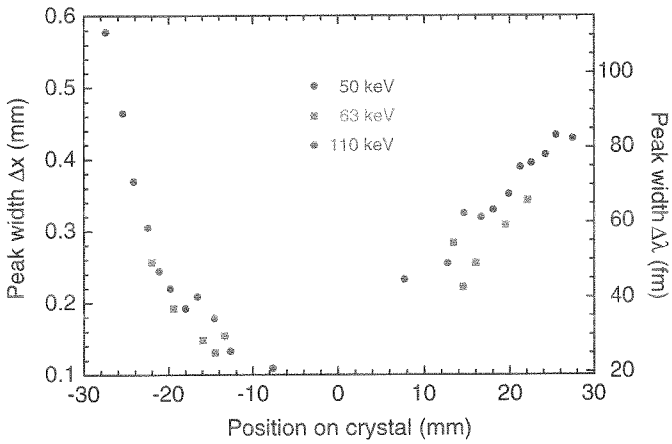

Figure 3: Observed line width for three different x-ray energies and for reflections occurring at different locations on the crystal.

For a more stringent test the crystal curvature was measured with synchrotron radiation at the optics beamline of the ESRF in Grenoble. There the white synchrotron beam was collimated down to a width of 0.5 mm with the secondary slits located at some 40 m downstream the bending magnet. The measurement setup is schematically illustrated in figure 4.

In a first step two *flat* silicon crystals having the same dimensions as the curved one, namely 80 × 40 × 1.5 mm^3, were prepared for the 220 reflection in the Laue case with an asymmetry angle of $\chi = 2°$. The crystals were aligned using a scintillator detector and reflections were found in the non-dispersive (+1,-1) and dispersive (+1,+1) geometry by rotating the second crystal relative to the first one. The setup was tuned to a Bragg angle of 3.034° corresponding to approximately 61 kev x-ray energy. The first crystal, serving as a monochromator, was not touched anymore throughout the rest of the experiment.

In a second step the second crystal of the arrangement was replaced by the curved crystal to be tested and subsequently the (+1,-1) reflection was found. The x-ray beam incident on the curved crystal was shifted horizontally, in an approximately parallel way, in steps of 2 mm by means of an according movement of the secondary collimating slits in front of the experimental setup. For each translation Δx of the incident beam the Bragg reflection on the curved crystal was found by rotating the curved crystal.

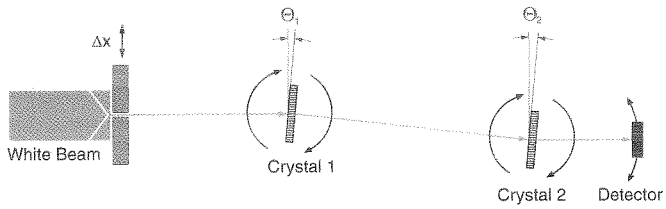

Figure 4: The two-crystal set up used at the optics beamline at the ESRF.

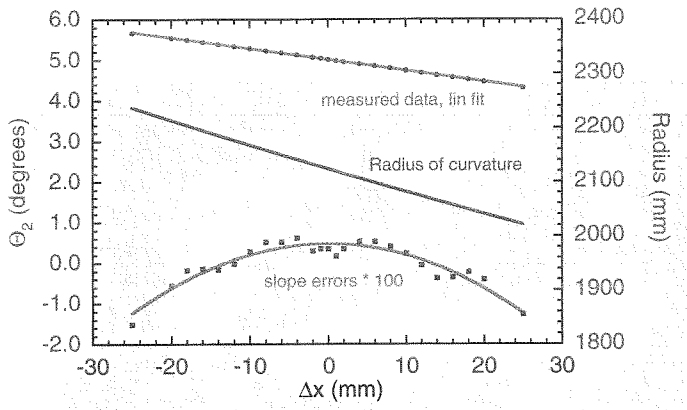

Figure 5: Curvature results obtained with the measurement illustrated in figure 4. From the deviations of the angular positions from a strict linear behavior the variation of the bending radius across the crystals long dimension is obtained.

The relation between the angular position θ_2 of the reflection maximum and the translation Δx is plotted in figure 5. For an ideal cylinder a straight line is expected. Small deviations from the linear fit are shown in the figure as *slope errors*, i.e. as the differences between the angular data measured and the linear fit. For better visibility the slope errors were multiplied by a factor of 100. From the smooth curve through the slope errors the variation of the radius of curvature across the crystals long dimension has been derived which is also plotted in figure 5. The ±5% variation of the radius for a ±25-mm excursion on the crystal is consistent with optical measurements using the crystals reflecting surfaces.

The present results were obtained for a trace centered on the crystal. As soon as an improved version of the bent crystal is assembled we will complement the curvature measurements tracing the crystal also in the anticlastic direction.

References

[1] H.F. Beyer, Nucl. Instrum. Methods. A **400** (1997) 137; H.F. Beyer et al., GSI Scientific Report 1999, p. 209.

[2] Th. Stöhlker et al., GSI Scientific Report 1999, p. 206. D. Protić et al., IEEE Trans. Nucl. Sci. to be published.

PHELIX, a Petawatt High Energy Laser for Heavy-Ion Experiments

Th. Kühl[1], J. Alvarez[1], B. Becker-de Mos[1], R. Bock[1], S. Borneis[1], H. Brand[1], D. Browning[4], C. Bruske[1], K. Brück[3], J. Caird[4], E. Dewald[2], C. Haefner[1], D.H.H. Hoffmann[2], H.-J. Kluge[1], D. Marx[1], P. Neumayer[1], M. Perry[5], H. Powell[4], I. Reinhard[1], M. Roth[1], W. Seelig[2], A. Tauschwitz[2], R. Wilcox[4]

[1]Gesellschaft für Schwerionenforschung mbH, Planckstr.1, 64291 Darmstadt, Germany
[2]TU Darmstadt, Schlossgartenstr. 7, 64283 Darmstadt, Germany
[3]Universität Mainz, Staudingerweg 7, 55099 Mainz
[4]Lawrence Livermore National Laboratory, 7000 East Ave., Livermore, CA 94550
[5]General Atomics, P.O. Box 85608, San Diego, CA 92186
http://www.gsi.de/phelix

The laser building for PHELIX [1], started with the ground-breaking in December 1999, was finished in August. It was inaugurated as part of the celebration of 30 years of GSI by the German Federal Minister für Bildung und Forschung, E. Buhlman and the Hessian State Minister für Wissenschaft und Kunst, R. Wagner (Fig.1)

Fig. 1.: Inauguration of the laser building August 25th 2000 by the German Bundesminister für Bildung und Forschung, E. Buhlman (with scissors) and the Hessian Staatsminister für Wissenschaft und Kunst, R. Wagner

On the ground floor the building houses the 500 m^2 laser hall for the main amplifier and the laser front-ends and an additional preparation space of 60 m^2. These rooms are equipped as class-10000 clean rooms. A mirror tower, solidly anchored to the 90 cm-thickness foundation plate, will lead the beam up to the beam switchyard on the second floor. Here also the pulsed power bay, the control-room, and a 60 m^2 class-100 clean room for the assembly of laser optics are situated. The building was engineered to allow operation and target delivering of the laser at the typical level of ground vibrations found under operation of the accelerator and the installations in the accelerator halls.
In parallel to the construction, preparations of the laser installations were made. The design parameters of the main amplifier [2][3] were verified by calculations performed at the Lawrence Livermore National Laboratory in Livermore, California, and at the CEA laboratory in Le Barp, near Bordeaux. The conclusion was to foresee 5 amplifier heads within the 2-pass amplifier. This will allow to create pulses with up to 1 Kilojoule in this first part of the amplifier, and to reach values necessary for Petawatt operation with only this section. In the booster amplifier, isolated by a Faraday isolator, 5 more amplifiers are planned to increase the energy level to 5 Kilojoules for 5 ns to 10 ns pulses. The floor plan of the laser installation is shown in Fig. 2.
This makes it possible to send pulses up to the 1-Kilojoule level directly to the experiments, and to inject into the booster amplifier section only for the high-energy option.

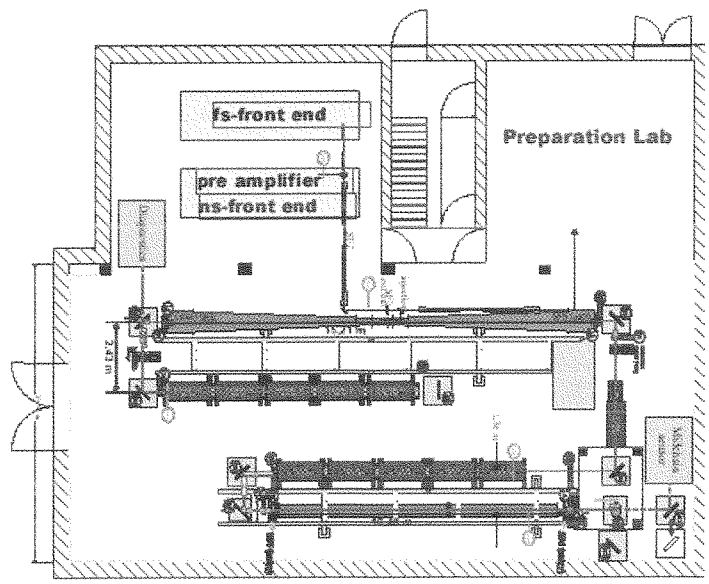

Fig. 2.: Modified lay-out of the PHELIX chain.

Shortly after the laser building became utilizable the fs-front-end components were shipped and installed. This system consists of a commercial femto-second oscillator, pumped by a diode-pumped Nd:YVO_4 laser, and two custom-built regenerative amplifiers. The first parts of the PHELIX nanosecond front-end have been assembled and tested. The ns-frontend basically consists of seven individual parts, the fiber-oscillator, a fiber-based double pass amplifier, an amplitude modulator to tailor the temporal pulse shape, a phase modulator to provide additional bandwidth, a fail safe system to protect the bigger laser components, a ring regenerative amplifier and a beam shaping section to modulate the spatial laser beam profile. Within 2000 the first three parts have been built and

tested in close collaboration with the Lawrence Livermore National Laboratory. The PHELIX design is based on a modified prototype which is to be used for the National Ignition Facility and similar to the Z-beamlet laser system at Sandia. Except for the the ring regenerative amplifier and the beam shaping section the PHELIX ns-frontend is based on fiber technology. This provides stable and robust operation without much further alignment and maintenance. The fiber components are housed in 19" racks that can be placed anywhere inside the laser building.

The oscillator module provides a stable, continuous laser beam of 15 mW, single mode, at 1053 nm delivered by a laser diode pumped Y-doped fiber laser. It is injected into a double pass fiber amplifier, which is shown in Fig. 3.

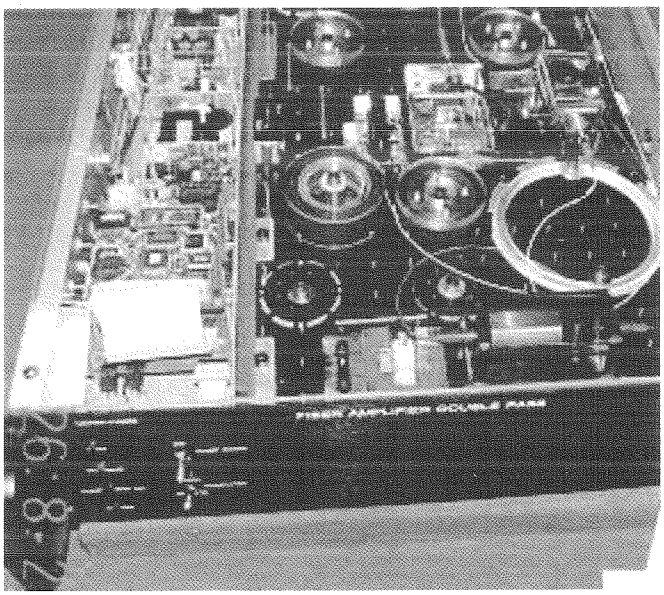

Fig. 3.: The 19" fiber-optics double-pass amplifier of the ns-frontend.

The laser beam is chopped by an acousto-optic modulator into individual pulses of 100 ns length and amplified to several nanojoules (corresponding to a few Watts peak power) with the aid of a laser diode pumped Y-doped fiber and a Bragg grating used as a fiber end-mirror.

These pulses are then sent to the amplitude modulator section. The modulator consists of two fiber based Mach-Zehnder interferometers made of Li-Niobate. If a low voltage electrical signal is applied to one arm of each of the interferometers, it changes the refractive index of the material and therefore causes a modulation of the exiting laser radiation. The electrical input signal is converted into temporal shaping of the laser pulse. The temporal resolution of the modulator is better than 100 picoseconds, mainly limited by the driving electrical circuit.

For most of the future experiments planned for PHELIX, nanosecond temporal resolution is required. Thus, and due to the varying experimental conditions, a highly versatile electrical pulse generator (arbitrary waveform generator, AWG) is used. Individually designed electrical pulses can be generated in the computer control system and will be transformed into PHELIX laser pulses using the AWG. Fig. 4. shows long term stability test results for the system (oscillator, double pass and modulator). An excellent energy stability was found even though the whole system was housed not in a temperature controlled environment like it will be in the PHELIX building. Furthermore the performance of the modulator section was tested as seen in Fig. 5. The electrical input signal from the

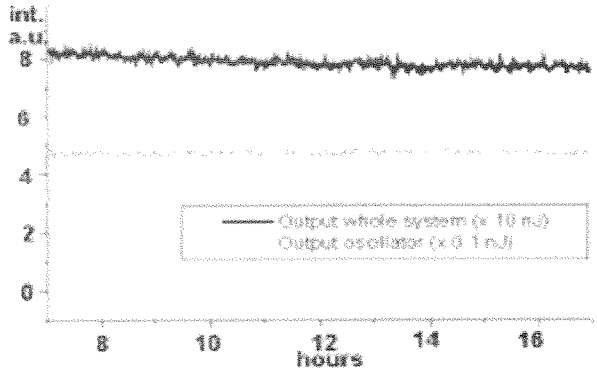

Fig. 4.: PHELIX ns-frontend long term energy stability.

AWG is shown together with the optical output of the laser beam measured by a fast photodiode. The chosen pulse shape was similar to a 'Haan' type pulse that is used in laser fusion experiments. The test results show a excellent response of the electro-optical system to the input signals. A total contrast ratio of 60 dB has been obtained, which is sufficient for further amplification up to the kilojoule level.

The components have been shipped to GSI and were re-activated successfully. The remaining parts, namely the phase

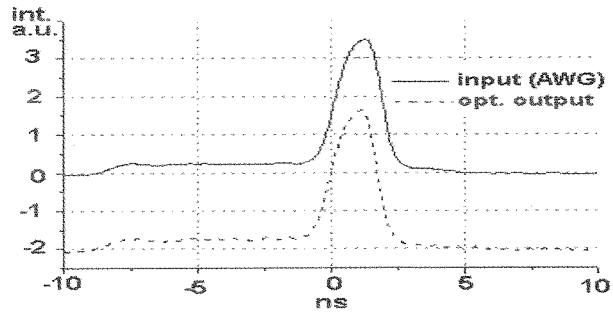

Fig. 5.: Performance test of the modulator section.

modulator and the fail safe system are currently under construction at Livermore and will become operational within the year 2001. The regenerative amplifier is operational at GSI and will be placed into the PHELIX building for detailed performance tests.

Parts for the preamplifier section which will amplify these pulses up to the 10 Joule level are under preparation together with the Lawrence Livermore Laboratory.

In conclusion, the first parts of the PHELIX front-ends are operational with excellent performance and will be coupled to the following amplifier sections early in the year 2001.

References

[1] PHELIX Project, GSI-98-10 Report, December 1998

[2] PHELIX - A Petawatt High-Energy Laser for Heavy-Ion Experiments, R. Bock et al., Inertial Fusion Sciences and Applications 99, C. Labaune, W.J. Hogan, K.A. Tanaka Eds., Elsevier Publishing, Paris, Amsterdam, Lausanne, New York, Oxford, Shannon, Tokyo (2000) 703

[3] PHELIX – ein Petawatt-Hoch-Energie-Laser, Th. Kühl, Phys. Bl. 5 (2000) 49

A Zero-Degree Electron Spectrometer for (e,2e) Spectroscopy at the ESR

S. Hagmann[1,2,3], R. Moshammer[3,4], J. Ullrich[3,4], Th. Stöhlker[2], H.Kollmus[2,3,4], R.Mann[2]

[1]J.R.Macdonald Lab., Dept. of Physics, KSU, Manhattan, KS,USA; [2]GSI-Darmstadt;
[3]Fakultät für Physik, Universität Freiburg; [4]MPI- Heidelberg

The jet target of the ESR provides unprecedented conditions to study atomic collision dynamics in the realm of relativistic ion beams. A complete rebuild of the target environment has broadened the range of possible experiments considerably. Besides x-ray spectroscopy, now recoil-ion momentum and electron spectroscopy experiments can be conducted.

Presently we are implementing a magnetic electron spectrometer at the ESR storage ring dedicated to 0^0-electron spectroscopy in collisions of stored ions with gaseous and cluster targets at the gasjet target region: we will focus on high resolution electron spectroscopy of Rydberg states of the projectile and on electrons in the projectile continuum, emphasizing electron impact ionization (e,2e) of the projectile. The spectrometer expands the possibilities of the new longitudinal reaction microscope (RM)[1] for kinematically complete experiments with relativistic ions in the ESR.

In recent experiments the fundamental process of Coulomb ionization of atoms and ions has been investigated in kinematical complete experiments using the reaction microscope[1,2]. The break-up of atoms, i.e. Single and Multiple Ionization (SI, MI) for weak and strong perturbing fields and perturbation times down to 10^{-18} sec have been studied[2] with respect to the dependence of the emission characteristics of electrons on the momentum transfer **k** from the dipolar (small **k**) to the binary regime (large **k**).

Applying the reaction microscope we have begun, first at low collision energies, to investigate for the first time kinematically complete electron impact ionization (e,2e) of ions[2] which is inaccessible to standard crossed beam techniques due to insufficient luminosity.

(e,2e) collision channels in ion-atom collisions are characterized by simultaneous correlated emission of a fast electron with $v_e \cong v_{Projectile}$ in a narrow cone around the projectile direction and a slow electron, mostly in the forward hemisphere. In the reaction microscope all collision products are detected with near 4π efficiency; for collision energies well below 4AMeV mapping both, the fast and the slow electron onto one multihit capable detector still results in an acceptable momentum resolution. The collision plane of the ionizing collisions is then event-wise reconstructed.

This technique gains orders of magnitude in luminosity over standard crossed beam techniques which are restricted to one collision plane predefined by detector geometry with correspondingly low efficiency. This way one opens up the avenue to electron impact ionization of few-electron highly charged ions over the entire Z range.

However, for collision energies above ≈ 4AMeV, it is not acceptable to map the fast and the slow electron onto one multihit capable detector. For this reason an independent magnetic spectrometer is necessary at ESR energies which guides electrons emitted into a narrow cone around the beam direction onto a position sensitive detector and which allows to reconstruct the initial momentum of the fast electron. The design criteria for construction of the instrument are a) separate electrons from the flood of secondary products with minimum interference with the ESR beam, b) analyze electrons emitted in a direction near 0^0 close to the beam over a wide range of momenta including $v_e \cong v_{Projectile}$ up to specific projectile energies of 560AMeV; in non-position sensitive mode a momentum resolution $\Delta p/p = 10^{-3}$ is desired, c) in position sensitive mode, reconstruct the emission direction of the electron in the target zone after transport from the jet-target in the ESR to the detector.

ESR-Jet target and
Reaction- Microscope

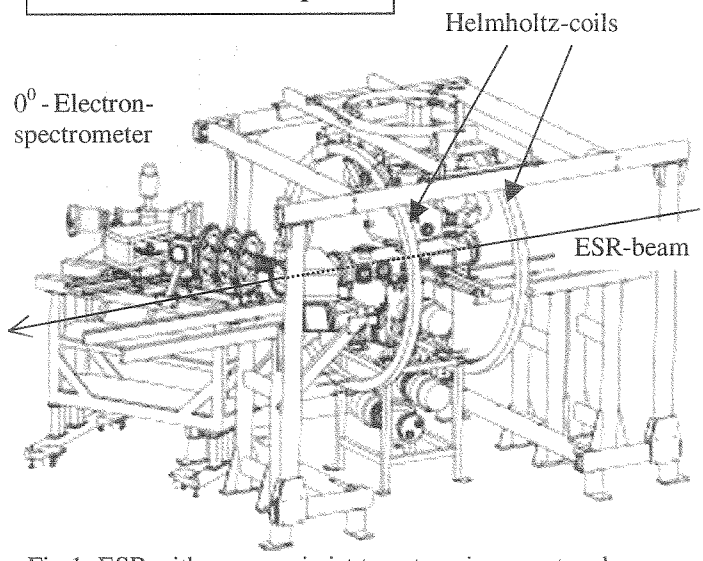

Fig.1: ESR with supersonic jet target environment and downstream 0^0 magnetic electron spectrometer

The design chosen using beam trajectory calculations with the Mirko code is of D-T-D type and covers a solid angle of $4\ 10^{-4}$ sr. A 60^0 magnetic dipol of bending radius 200mm, with an aperture of vertically 100mm and horizontally 250mm as required by the ESR, 940mm from the target zone and just downstream of the target chamber is followed by a magnetic quadrupole triplett of 80mm aperture and a second dipole, identical to the first one. This is followed by a pair of horizontal slits and 2D position sensitive electron detector. As an option an open hyperpure Ge detector for independent analysis of the energy of electrons and identification of other particles potentially transmitted through the spectrometer will be installed during commisioning of the spectrometer as the low energy spectrum of secondary particles produced in the ESR target zone is currently not known.

[1] J. Ullrich et al., J.Phys.B30(1997)2917
[2] R.Moshammer et al, this Annual Report

LabVIEW@GSI

D. Beck, H.Brand, Poppensieker, K. Wunderle, DVEE, GSI Darmstadt

DVEE started the evaluation of LabVIEW (National Instruments, NI[1]) as a tool for the development of slow control systems for experiments of small and medium size in 1999. During the past years the use of LabVIEW in research and industry has strongly increased. For GSI, the main advantages of using NI software are the following: First, NI provides both hard- and software. By this, the time consuming development of low level drivers is not an issue any more. Second, it provides efficient tools for the development of graphical user interfaces (GUIs). Finally, LabVIEW, being a graphical programming language, eases the software development even for inexperienced programmers. As a result, software development with LabVIEW becomes more efficient and less time consuming for many cases. The maintenance and further development of existing LabVIEW based systems is rather easy.

LabVIEW is the method of choice for software development when PC hardware with Microsoft operating systems can be used. Even real time applications can be implemented using embedded systems from NI. Interfaces to access VXI/VME and CAMAC hardware from a PC based system is made possible by hardware provided by NI. This gives access to legacy hardware that is widely used in research.
LabVIEW is also available for Linux and the number of supported hardware interfaces is continuously growing. However, porting the LabVIEW applications itself to other operating systems like LynxOS, which are not supported by NI, is almost excluded.

At GSI, DV&EE is involved in several LabVIEW projects required for physics experiments:

- TargetScanner[2], Target Laboratrory [1].
- SHIPTRAP[3], Atomic Physics
- Life time measurements in Cave A, Atomic Physics
- PHELIX[4], Atomic Physics
- Detector test, Detector Laboratory

For these projects different hardware and field-busses are supported.

- NI Flex- and Value-Motion, with a MOVTEC power amplifier for stepper motors
- NI IMAQ[5] to acquire images from different analog and digital cameras
- CAN bus to control high voltage modules (iseg)
- GPIB to control local and remote GPIB devices
- NI FieldPoint to control digital and analog I/O via Ethernet
- Profibus via an interface from COMSOFT
- CAMAC and VME

All this hardware can easily be accessed via LabVIEW, which is an integrated development environment. LabVIEW also includes powerful libraries and add-on toolkits that help to efficiently set-up control systems:

- SQL- and Internet-Toolkit to access data bases and networks.
- Statistical Process Control for quality assurance of continuous processes
- PID and Fuzzy-Toolkit for closed loop control
- Advanced IMAQ Vision library for image processing and analysis
- Data Logging and Supervisory Control (former BridgeVIEW) for alarm and event handling, online and historical trending and security

We use these tools to develop prototype applications and instrument drivers in LabVIEW. Most of these projects are maintained using a build-in Source Code Control System that is part of the LabVIEW environment. More detailed information can be found on the web, http://www-wnt.gsi.de/LabVIEW.
The EPICS ActiveX Channel Access Server library [2] for LabVIEW was successfully evaluated for HADES[6].
The Data Logging and Supervisory Control Module (former Bridgeview) for LabVIEW provides OPC client and server functionality that can be used to set-up communication with commercial OPC servers like the one from COMSOFT for a Profibus controller.

There are two more NI software packages to mention. LabWindows/CVI is the C based analogue to LabVIEW and ComponentWorks++ provides C++ libraries and GUI elements which can be used with other C/C++ development environments like Microsoft Visual Studio.
To provide CAMAC access over the network we used those packages to implement the ESONE client library on Windows via a C/C++ DLL. The MBS[7] [3] provides the ESONE server. For this purpose the ONC RPC software package was used. It implements SUN Remote Procedure Calls for Windows using the XDR format (External Data Representation. Microsoft RPC uses NDR format, Network Data Representation, which is not compatible with XDR). A wrapper library for LabVIEW is supported too. VME is also easily accessible via a VME-MXI-2 Controller from NI.

To summarize, LabVIEW from NI provides powerful software tools for the implementation of PC based control systems. At GSI it is currently mainly used for small and medium sized experiments.

References

[1] H.Brand et. al., "Project Targetscanner – A Status Report", GSI Annual Report 2000

[2] Kai-Uwe Kasemir, http://mesa53.lanl.gov/lansce8/epics/PC/

[3] H.G. Essel und N. Kurz, „The General Purpose Data Acquisition System MBS", IEEE TRANSACTION ON NUCLEAR SCIENCE, VOL. 47, NO. 2, APRIL 2000

[1] http://www.ni.com
[2] http://www-wnt.gsi.de/TargetScanner
[3] http://www-aix.gsi.de/~shiptrap
[4] http://www-aix.gsi.de/~phelix
[5] IMageAcQuisition

[6] http://www-hades.gsi.de
[7] Multi Branch System

On-line Analysis in MBS 3.0

H. G. Essel, N. Kurz
DVEE, GSI Darmstadt

Current Status

Since there are powerful VME processor boards on the market and MBS [1] event builders may run also on standard PCs under LynxOS, analyzing events on-line becomes a reasonable option. This on-line analysis may be useful for several tasks:

1. *Software filter*: Analysis decides which events to store.
2. *Monitoring*: Analysis controls if the experiment equipment works correctly.
3. *Histogramming*: Sometimes it may not be necessary to store the event data, if histograms can be accumulated on-line.

In all cases the data need not to be transferred over networks and the analysis processes all events. MBS 3.0 has integrated the full **L^{e}A** [2] histogram package except the IDL graphics part. Visualization can be done by any GSI histogram client (**L^{e}A**, Origin, Go4viewer, MBS GUI), as shown in figures 1 and 2.

Developing an On-line Analysis

An MBS on-line analysis can be completely developed on Linux, AIX, or VMS using the **L^{e}A** tools. With the GUI one can set up the histograms. Then **L^{e}A** generates all necessary include files, templates, startup procedures and makefiles for LynxOS. After copying these files to an MBS node, the makefile generates a user specific MBS collector program.

With the identical sources the **L^{e}A** user program can be made on the other platforms. The analysis can be tested off-line or on-line. If it runs correctly it can again be distributed to the MBS node, remade, and run inside the collector.

Differences to L^{e}A

Because the event loop in the MBS collector is different from **L^{e}A**, the event analysis function in MBS (f_mbs_anal) has different arguments than the **L^{e}A** function (f_anal). One can, however, use the MBS function also in **L^{e}A**.

Data bases are transient in **L^{e}A** but persistent in MBS. In both cases bases can be dumped, exchanged, and restored. In the startup procedures of MBS the base might be attached if it already exists or restored, if not.

In MBS there is another task, the Histogram Manager, to control the data bases, i.e. manage histograms and conditions. This task also runs a histogram server thread providing remote access to the histograms.

In MBS, the analysis function f_mbs_anal is called event by event in the collector after the acquisition has been started. This calling can be switched on or off by commands.

Compatibility to L^{e}A

Data bases containing histograms and conditions can be exchanged between all platforms. All commands managing histograms or conditions are the same. Therefore command procedures can be exchanged.

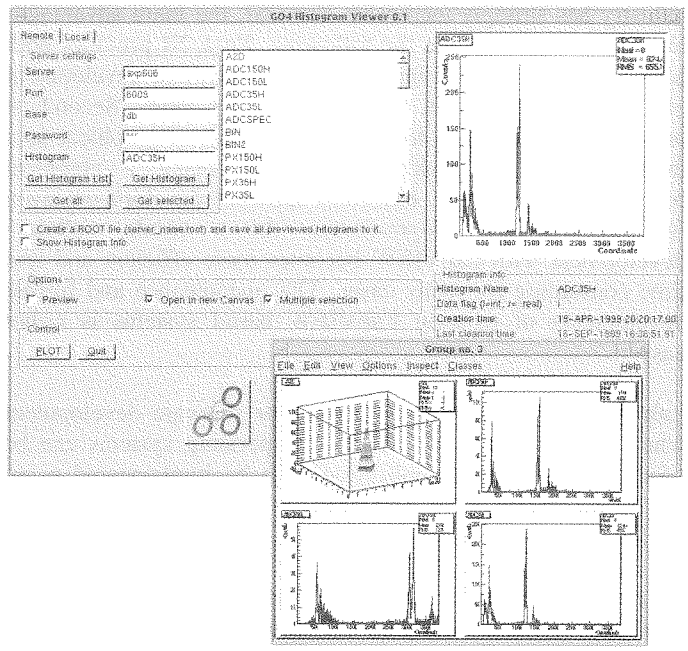

Figure 1: Go4viewer based on ROOT.

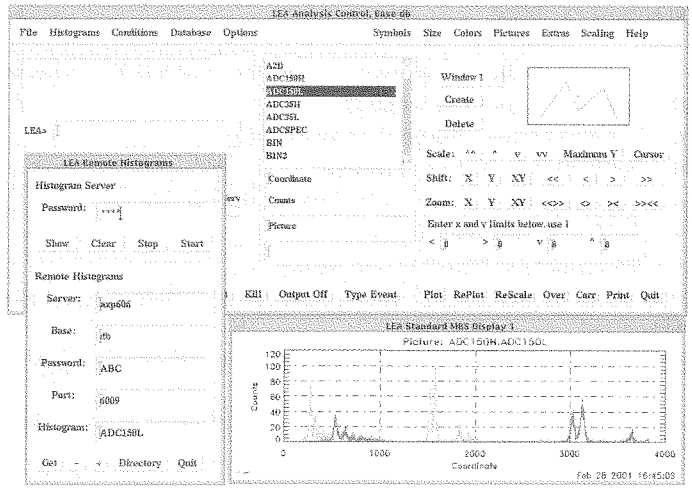

Figure 2: **L^{e}A** as histogram client.

Actual information on further developments can be found on http://daq.gsi.de or http://lea.gsi.de .

References

[1] H.G.Essel and N.Kurz, "The General Purpose Data Acquisition System MBS", IEEE Trans. NS, Vol. 47, No. 2, (April 2000), pp. 337

[2] H.G.Essel; "Lean Analysis with **L^{e}A**", GSI Report 1999 (2000), p 233

Go4: Multitasking Multithreaded Class Library

J. Adamczewski, M. Al-Turany, H. G. Essel, H. Göringer
DVEE, GSI Darmstadt

At the beginning of the GSI Online-Offline-Object-Oriented analysis project GO4, the principle of a multi threaded analysis based on the ROOT framework [1] had already been demonstrated by a first prototype [2]. In the following phase, the software has been redesigned completely using UML tools such as *RationalRose 2000* [3] and, more recently, *Together 4.2* [4], in connection with the *Sniff++* development environment [5].

Go4 Thread Manager

The *Go4ThreadManager* package provides foundation and service classes to launch any number of named threads within a ROOT application. It is based on the ROOT TThread library which had been updated in the course of the first Go4 prototype. The *Go4ThreadManager* implements the concept of runnable classes (like JAVA) which the user may specialize by inheritance for any job without changing the Go4 thread classes themselves.

Go4 Task Handler

The first goal of the Go4 kernel was to control several independent, distributed analysis clients (slaves) from one user interface server task (master). Therefore, the *Go4TaskHandler* package and the related service packages (*Go4Socket*, *Go4Queue*, *Go4CommandsBase*, and *Go4StatusBase*) were designed for such inter task connections.

The client communicates with the server via three sockets (data, command, and status channel). Each of these channels is processed by a dedicated thread and is buffered against the user's application by means of a thread safe template queue. The entire communication setup is encapsulated within the *Go4TaskHandler* class.

Exchange of information between server and clients is done by command objects and by status objects. Here we use a command design pattern [6] with an invoker singleton, and a modified memento pattern, respectively. Commands created by the server may be either sent to one of the remote clients, or added to a local command queue to be executed in a local thread preventing the blocking of the GUI.

Status objects are created by the clients and are sent to the server which may e.g. display the current analysis status. Additionally, any named ROOT object created by an analysis client (e.g. a histogram) can be sent to the GUI via the task handler data channel.

A new client process may either be launched from an existing GUI server process and can be added to the list of clients; or the client may be started independently and may request a new connection to the server process at any time.

Test of Go4 Multitasking

As a first test of the *Go4TaskHandler* package, we built an example client (subclass of TGo4ClientTask), and an example display (subclass of TGo4ServerTask). The client has two additional threads working on an example application (the actual analysis later on) . The client status information is sent to the server regularly by thread one, while thread two executes commands and processes the analysis (here a random histogram fill). The server has a simple GUI control panel, a ROOT canvas and a status window.

Two server threads wait to display any client objects appearing at the status and data queues, respectively. Pressing a GUI button, a histogram is requested from the currently selected client by command, sent to the server and drawn on the canvas. This example was running successfully over >24 hours with 1 server task connected to 7 client tasks on 4 different nodes, which promises a stable operation of the task handler system.

Go4 Viewer

In addition to the design of the Go4 framework, the *Go4Viewer* is being built as a first tool for visualization and interactive manipulation of histograms, ntuples and root TTrees. Based on native ROOT GUI classes it features access to data from different sources: from GSI histogram servers like LeA, GOOSY and MBS, from local root or paw files, and from the GSI mass storage system using the root TRFIO classes. Histograms and ntuples from any data sources are converted on the fly to ROOT file format and may be analyzed later by all means of the ROOT system.

Conclusions and Outlook

The Go4 Task handler package might be a flexible tool for any kind of distributed tasks using the ROOT environment. In contrast to the existing parallel root facility PROOF (which is specialized for parallel processing on the same dataset), the *Go4TaskHandler* is capable of controlling independent clients with threaded applications, required both for non blocking online analysis or slow control jobs.

The next step will be the implementation of the actual analysis framework, containing abstract interfaces for the event related classes, a dynamic list which will keep and process online generated histogram objects, and a system of analysis condition classes. Here we will still benefit from the first Go4 prototype experiences.

The *Go4Viewer* may be a test bed for the future GUI layout, until the first test analysis of the Go4 framework will produce viewable data.

Documentation of Go4 can be found at *http://go4.gsi.de.*

References

[1] http://root.cern.ch

[2] *Status of ROOT Based Analysis System Go4*, J.Adamczewski, H.G.Essel, H.Göringer, M. Hemberger, N. Kurz, M.Richter; GSI scientific report 1999, p.232

[3] http://www.rational-software.de

[4] http://www.togethersoft.com

[5] http://www.windriver.com/products/html/sniff.html

[6] *Design Patterns: Elements of Reusable Object-Oriented Software*, E.Gamma, R.Helm, R.Johnson, J.Vlissides ; Addison-Wesley 1999

Grid Tests and Developments

Ingo Giese, Peter Malzacher
GSI Darmstadt

The DataGrid project

The computing model for the storage, management, simulation, reconstruction, distribution, and analysis of the data of the four LHC experiments (ALICE, ATLAS, CMS, and LHCb) consists of two key elements[1]:

- A multi-tier hierarchical model of regional centres developed by the MONARC (Models of Networked Analysis at Regional Centres for LHC experiments) group [2].
- Grid[3] software will be used as flexible middleware for the secure, coordinated access to the resources distributed worldwide.

After an about one year preparation phase, the EU funded DataGrid project[4] started in January 2001: A three year development and test phase to demonstrate the feasibility of the grid approach to the LHC computing challenge. The major development projects are:

- Data grid services to provide workload management, scheduling, and data movement as well as monitoring services across institutional boundaries.
- Fabric management including network infrastructure, cluster and mass storage management.
- A production quality test bed using scientific applications from high energy physics, earth observation, and biology.

Globus Installation

To explore grid tools and to be ready to use the first test bed of the DataGrid project, release 1.1.3 of the Globus Toolkit[5] has been installed on the central Linux and AIX clusters of GSI. Globus offers the basic protocols, services, and APIs (application programmer interfaces) to use geographically and organizationally dispersed computing resources:

- GRAM: The Globus Resource Allocation Manager. It units grid machines, providing a common user interface to the different batch systems.
- GIS: The Grid Information Service. It provides a common interface to discover the properties of grid resources.
- GSI: The Grid Security Infrastructure, a library for providing generic security services for applications that will be run on the grid.

Users on all central Linux and AIX machines at GSI can use the Globus services to submit processes to other grid sites. The main advantage is a single worldwide Globus user id. A test machine has been configured as gatekeeper to our local batch system LSF.

A major computational challenge for the ALICE collaboration during 2001 will be the simulation for the physics performance report. After successful explorations between different centres, it is planed to use Globus tools for parts of these massive productions.

ROOT and Grid

AliRoot, the ALICE off-line framework for simulation, reconstruction, and analysis is built on ROOT[6], a set of OO frameworks widely used in high energy and nuclear physics to build data acquisition, simulation, and analysis systems. The main features of ROOT are:

- The ability to handle and analyse large amounts of data in an efficient way.
- The built-in CINT C++ interpreter, which allows for a fast prototyping, since the command language, scripting language, and the implementation language are all C++.
- A rich set of classes including histogramming, fitting, and visualization.

To build the basic infrastructure for one of the long term use cases of ALICE - interactive distributed analysis on the grid – we started to interface two Globus APIs to ROOT.

PROOF, the Parallel ROOT Facility, allows to send work via wide area networks to a master server which distributes it to slave servers, collects the results, and sends the results back to the client. A prototype of using the grid security infrastructure to authenticate the client to the servers has been developed. It will be put into the ROOT distribution soon. The same mechanism can be used for remote file access via TNetFile and rootd or for the coming TFtp class.

Wide area distributed analysis requires careful selection of the resources used, based on available CPUs, network bandwidth, and load as well as data location. Neither manual configuration nor defaults are acceptable. Manual configuration requires deep knowledge of the remote system that an average user does not posses. Even the best defaults cannot fit to the ever changing resources. Decisions should be made at run-time based on the structure and state of the computing environment as well as the needed resources. Therefore the second Globus API we want to use in ROOT is the grid information service. The basic protocol for this information service is LDAP (Lightweight Directory Access Protocol)[7]. We developed a small C++ layer on top of the LDAP C API. The next step is to integrate it in ROOT along the lines of the SQL interface classes.

References

[1] Report of the Steering Group of the LHC Computing Review, CERN/LHCC/2001-004.

[2] MONARC Phase 2 report, CERN/LCB/2000-001.

[3] Ian Forster, Carl Kesselman, Steven Tuecke: The Anatomy of the Grid, Enabling Scalable Virtual Organizations, to appear: Int. J. Supercomputer Applications, 2001.

[4] http://www.datagrid.cnr.it/.

[5] Ian Foster, Carl Kesselman, Globus: A Toolkit-Based Grid Architecture. In: Ian Forster, Carl Kesselman (Eds), The GRID: Blueprint for a new Computing Infrastructure, (1999) pages 259-278. See also http://www.globus.org.

[6] Rene Brun and Fons Rademakers, *ROOT - An Object Oriented Data Analysis Framework*, NIM A389 (1997) 81-86. See also http://root.cern.ch/.

[7] RFC 1823: The LDAP Application Programming Interface.

Project Targetscanner – A Status Report

Holger Brand, Klaus Poppensieker, Willi Hartmann, Birgit Kindler,
Josef Klemm, Bettina Lommel, Jutta Steiner

Introduction: With the Fragment Separator (FRS) at GSI radioactive-heavy-ion beams can be prepared to study properties of and reactions with relativistic exotic nuclei. The quality of this beam depends crucially on the perfection of the energy degraders which are necessary for slowing down the heavy ions according to their mass and charge, and therefore, act as variable ion-optical devices. The accuracy of the energy adjustment and the perfection of isotope separation depends on the thickness of the degrader parts as a lateral function.

The actual cause for the project Target Scanner was the plan to replace the degrader units of the FRS. In a first step S1 will be replaced, the other units will follow little by little. Among others the degraders at S1 consists in the moment of two aluminium wedges with ~230mmx500mm in dimension. Several years ago the thickness distribution of these parts was measured fully manual with about one measuring point every 5 mm. That meant positioning, measuring, reading and writing down the values for about 4000 times per wedge. Since the new degraders have to be made a lot more precisely also the thickness measurement has to be more precise. We have to measure at least once every mm that means at least a 100.000 data points per part.

That is the reason for setting up the Target Scanner, a device for measuring and evaluating the thickness of parts variable in geometry and size as a lateral function fully automatically via a PC. The target scanner works purely mechanically, which means that there are no special requirements concerning the properties of the surfaces to be measured. The only restrictions are for very ductile materials and extremely sensitive surfaces.

Set-up: The mechanical components of the Target Scanner are shown in Figure 1. The whole set-up is mounted on a vibration-

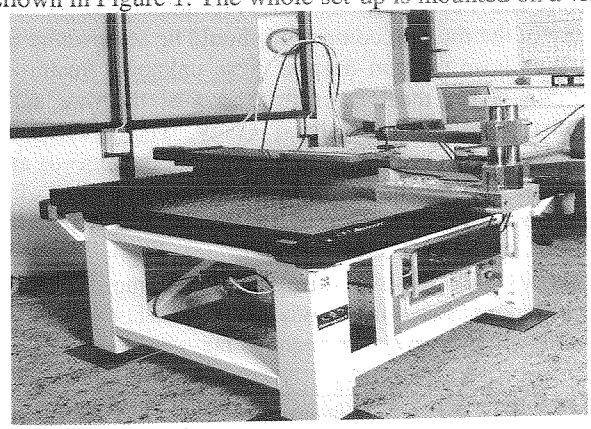

Figure 1: Set-up of the Target-Scanner

damped table from NEWPORT that guaranties a stable horizontal positioning of the table top. The positioning unit consists of two linear positioning stages from Schneeberger with a maximum travel of 300mm and 600mm respectively that are mounted perpendicular to each other and are driven by a 2-axes servo motor controller. At the front end of the upper stage the samples can be mounted with different self-constructed sample holders and can be moved relatively to the fixed thickness measuring unit. This thickness measuring unit consists of two digital length gauges from Heidenhain mounted in vertical position in such a way that the difference of the two length signals gives the thickness of the sample at the respective point, as one can see in Figure 1. Each length gauge has a travel of 60mm in maximum and an accuracy of ± 0.1µm.

Software: LabVIEW was a good candidate for GSI to support developments of small and medium sized control systems and test stands. This project seemed to be a good choice to evaluate LabVIEW. We could make use of the Graphical user interface, the 3D graphics, the advanced analysis, the SQL-Toolkit, the Internet-Toolkit, the VISA interface, the NI hardware, and guidelines of instrument driver developments.

Because no LabVIEW instrument drivers were available for ND231 and SM300 they were developed at GSI. Both instrument driver libraries were developed with respect to the NI recommendations. High level VI's are provided to access all parameters described in the manuals. The details of the communication protocol are not seen by the user.

All data, configuration, measurement and analysis data are stored in a relational database (Oracle). The database design is shown in figure 2. The data is required for experiment analysis. Oracle security is used to control access by the LabVIEW application before any movable devices are initialized.

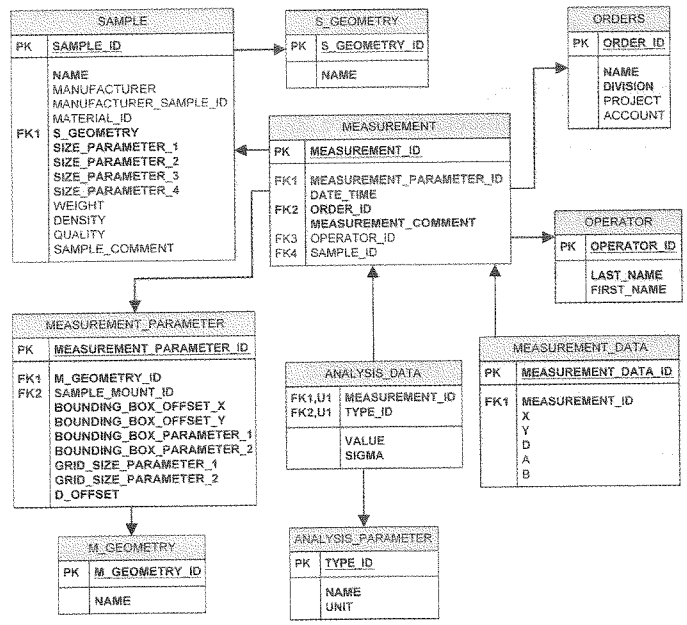

Figure 2: Oracle Database Design

Status: The mechanical components as well as the controlling components and software are ready and tested. The resolution of the thickness measurement is better than half a micrometer and the accuracy of the positioning is ± 2 µm, as expected. During the first measurements we found some critical points that could influence the results considerably, for instance, the exact mounting of the sample, the time-dependent deformation of the soft measuring tips and films or dirt on the surfaces of the sample or tips. These errors have to be eliminated or, at least, have to be taken in account. After the last debugging run in the next step the comfort in software handling will be proved and an automatic report and data evaluation will be implemented.

Improvement of the Target Durability for the Heavy Element Production

S. Antalic, H.-G. Burkhard, P. Cagarda, D. Gembalies-Datz, W. Hartmann, B. Kindler, J. Klemm, J. Kojouharova, B. Lommel, R. Mann, H.-J. Schött, J. Steiner, D. Ackermann, F.-P. Heßberger, S. Hofmann

Introduction

The search for new elements with low production cross sections makes it necessary to enhance the beam intensity on the target in order to keep the required beam time at a reasonable length. For element 112 for example the cross section for the synthesis was ~ 1 pb. This corresponds to one event per week on average [1]. A higher beam current, however, leads to severe problems concerning the targets. To synthesize heavy elements at the SHIP set-up lead and bismuth targets are used [2]. At present the maximum beam intensity is limited by the low melting temperatures of lead with 600 K and bismuth with 544 K, respectively. In this range the cooling via radiation is small. Since the target wheel rotates in vacuum there is also no heat conduction via surrounding gas. The third mechanism for temperature reduction is heat conduction along the target itself. But since the target layers are very thin and the amorphous carbon layers are poor thermal conductors, this process is not very effective. Therefore, technical improvements had to be developed in order to protect the targets from melting.

Implemented Improvements:

Several improvements to reduce the stress on the targets are already implemented [3]. After an increase of the active target area by nearly 60%, the Gaussian-like intensity profile of the heavy-ion beam was refined to illuminate the area as complete as possible. To optimise the intensity distribution, two octupole magnets will be installed in the beam line, allowing for a rectangular beam intensity profile across the size of the beam spot.

The background of scattered particles at the detector position has higher energies on the left hand side than on the right. A reduction of this background with a homogeneous degrader is not very effective since one has to take care not to absorb the reaction products. We therefore developed aluminium degraders with a wedge-shaped thickness profile. Depending on the projectile-target combination, degraders with a slope of up to 3 µm over 100 mm length are used. This results in a reasonable compromise between background reduction and slowing down of the evaporation residues, since too low kinetic energies of the latter lead to too low implantation depths and thus to losses of escaping alphas.

To further enhance the durability of the targets at high currents, we investigated different possibilities in parallel that could possibly be combined later on, as there are chemical compound targets, target cooling, and target monitoring [4].

Chemical Compound Targets

The first idea concerning the improvements for the target material itself was to find some chemical compound of lead and bismuth, which is suitable and has a higher melting temperature compared to that of the pure element. We decided to concentrate in the beginning on lead compounds since this is the target material that is needed more often. There exist significantly more binary phases for lead than for bismuth; with the help of the known phase diagrams and suitable vapour pressures several compounds are ruled out.

The compound in question should be non-toxic, the melting temperature being considerably higher than 700 K in order to profit from radiation cooling. On the other hand the evaporation temperature should not be too high because then the target material would have to be evaporated with an electron gun which involves a much higher material consumption than thermal evaporation. For highly enriched material that could be very cost-intensive.

Up to now we have already synthesized and evaporated two lead compounds, namely ^{208}PbS and Tm^{208}Pb$_3$. Leadsulfide has a melting temperature of about 1400 K but at approximately 1220 K it already has a vapour pressure of 10^{-3} bar. The evaporated targets look very homogeneous. They have a black colour which should be advantageous concerning the radiation cooling. The targets do not show any signs of aging, oxidization or other visible alterations, and they are mechanically stable. A disadvantage could be that the compound is non-metallic and therefore electrostatic charging could become a problem. With a scanning electron microscope one can see that the surface consists of very small needles and looks furry.

Tm^{208}Pb$_3$ is a metallic compound. Since there is no known binary phase diagram, we estimated the melting temperature from two neighbouring phase diagrams of rare earth elements with lead, namely DyPb$_3$ that has a melting temperature of T_M ~ 1170 K and YbPb$_3$, T_M ~ 1010 K. Presumably the melting temperature of the thulium compound should be somewhere in-between. We chose thulium despite these unknown quantities since thulium is the most insensitive one of the rare earth elements that usually are oxidized easily. The material as evaporated looks a bit brittle but in principle homogeneous and mattly metallic. But this material shows an obvious aging after one or two weeks. There is a sort of whisker growth of metallic lead on the surface. Besides, the surface begins to look inhomogeneous and starts to oxidize after some time.

Targets were produced from both compounds but they could not be tested with the heavy-ion beam so far.

Target Cooling

Another possibility to avoid the melting of the targets is an active cooling with a He-jet. A He-jet will be blown at the beam spot on the target thus transporting heat load away from the target surface. Additionally the He-jet will result in a low pressure He-atmosphere in the target chamber thus allowing for a cooling of the whole target wheel through convection and conduction. In order to avoid vacuum windows, the whole target chamber of SHIP will have to be reconstructed a differential pumping system has to be installed. To optimise the measures and distances for this new target chamber design, test experiments are inevitable.

Target Monitoring

Another item, we are working on, is a new target monitoring

system. On the one side we use an infrared camera to observe the thermal distribution across the target during irradiation. It is also helpful for the controlling of the experiments concerning new target materials and target cooling. On the other side we work on the implementation of an online thickness measurement of the targets by scanning them with an electron beam and analysing the energy loss behind the target with a position sensitive detector. This will be done in a position of the wheel opposite to the irradiation spot.

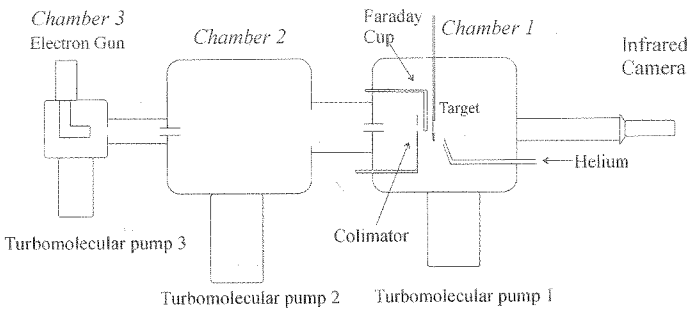

Figure 1: Test bench for high-current production target at SHIP. The target in Chamber 1 is heated by an electron beam. The electron beam can be measured by a movable Faraday cup. The target can be cooled with a He-jet guided through a Laval nozzle. The temperature distribution is measured via an infrared camera.

Test Bench for a high-current Production Target

Since beam time is rare, valuable and the most expensive part of heavy-ion experiments we had to create the possibility to test offline all the improvements described above. We therefore constructed a set-up where all the components developed can be built in to test and optimise the dimensions and the overall performance.

The test bench basically consists of three vacuum chambers arranged in a line, as is shown in Figure 1. Each chamber is connected with a high vacuum pumping system with turbomolecular pumps. The heavy-ion beam is simulated by an electron beam. The electron beam gun is mounted in chamber 3 and the electron beam is guided and focused by electromagnetic lenses on the target, which is placed in chamber 1. Behind chamber 1 an infrared camera is flanged to a long tube so that the target can be observed from the rear side. The temperature distribution of the beam spot on the target as well as melting of the target material can be recorded. By holding the power of the electron beam constant the durability of up to five different target materials mounted on one ladder can be compared directly with each other. Also depicted in Figure 1 is the first stage of the target cooling with a He-jet which is transported directly to the electron beam spot on the target via a Laval nozzle.

Recently the fixed target ladder was replaced by a target wheel that can be driven in the same way as in the SHIP set-up. In Figure 2 two infrared snapshots of a target mounted on a target wheel in the test bench are shown. In both cases the target wheel was rotating with 375 rpm. In the upper picture the wheel was rotating in vacuum and an energy of 1.3 W was deposited in the target with the electron beam. In the lower picture the chamber was filled with a low pressure atmosphere of 0.6 mbar He. To reach the same maximum temperature of 150°C as in vacuum an energy deposition of 2.7 W is needed. The energy increase of 1.4 W is a measure for the cooling efficiency of the additional atmosphere. In the same way the cooling efficiency of the He-jet or He-jets, blowing from both sides onto the target, will be tested and optimised. It is also noteworthy that minimum temperature of 85°C in vacuum (upper picture) is reduced to 35°C in He-atmosphere (lower picture).

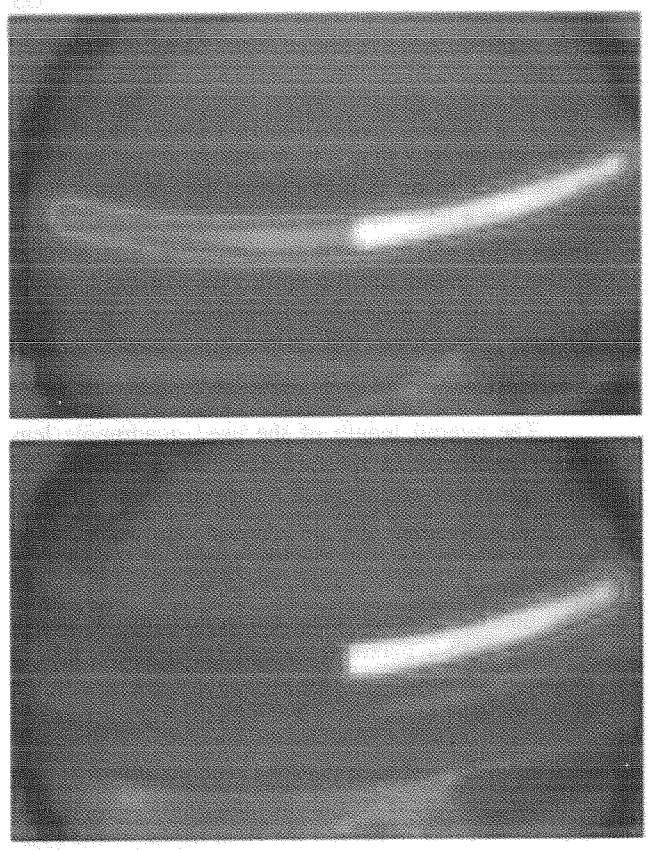

Figure 2: Infrared snapshot of 208Pb-targets mounted on a wheel rotating counter clockwise with 375 rpm. *Upper*: In vacuum, deposited energy 1.3 W; *Lower*: In 0.6 mbar He-atmosphere, deposited energy 2.7 W.

The test bench is also applied for the development and testing of the differential pumping system. Further on the online thickness monitor will be implemented in the test bench with a second smaller electron gun mounted in front of chamber 1.

We also try to reproduce the measured data by temperature calculations. These calculations are performed as function of the velocity of the target wheel, the backing material and backing thickness, the gas flow and the geometry of the target cooling.

References:

[1] S Hofmann. and G. Münzenberg., Rev. Mod. Phys. 72, 733–767 (2000).

[2] H. Folger et al., Nucl. Instr. and Meth. **A** 362, 64-69 (1995).

[3] B. Lommel et al., to be published in Nucl. Instr. and Meth. **A**

[4] B. Kindler et al., to be publ. in April 2001 in the *Proceedings of the 16th International Conference on the Application of Accelerators in Research and Industry*

Strong Pulsed Magnetic Quadrupole Lens

V. Chichkine[1], M. Winkler[3], K.-H. Behr[2], H. Geissel[2], A. Kalimov[1], G. Li[3],
G. Muenzenberg[2], C. Scheidenberger[2], H.Weick[2], H. Wollnik[3]

[1]St-Petersburg Technical University, Russia
[2]GSI Darmstadt
[3]2. Physikalisches Institut, Universität Giessen

In a recent test experiment we could successfully focus for the first time a high-energy heavy ion beam at the FRS using a high-current pulsed quadrupole lens. Such a lens, most frequently used in accelerator technology, can be built by arranging four electric conductors parallel to the optic axis. Pulsing a strong electric current through neighbouring conductors in opposite directions will produce a magnetic field distribution of fourfold symmetry.

The overall length of the used quadrupole lens was 97 mm with an aperture diameter of 20 mm. The pulse generator consisted of a capacitor bank of 1640 μF with a maximal charging voltage of 3.2 kV which corresponds to a stored electric energy of 8.4 kJ. The pulse period of the current oscillation was ≈500 μs [1]. The electric current was controlled by a power thyristor with a maximal current rating of 34 kA. In this case the achievable magnetic field gradient in the quadrupole is more than 1000 T/m [2].

In the experiment the FRS was mainly used as a transport system. The pulsed quadrupole was placed approximately 2 m behind the final triplet of the FRS. Another 300 mm downstream from the pulsed quadrupole a scincillator target was set and the beam profile was monitored by a CCD camera (Fig.1).

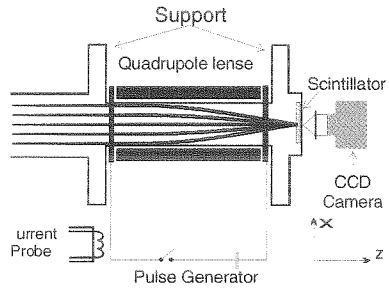

Fig. 1. Experimental setup to focus an initially parallel high-energy heavy ion beam with a pulsed quadrupole.

In the experiment a $^{197}Au^{79+}$ heavy ion beam was used with an energy of 650 MeV/amu which corresponds to a magnetic rigidity of the beam of about 10.5 Tm. The final quadrupol triplet of the FRS provided a parallel beam at the entrance of the pulsed quadrupole. The SIS was operated in the fast-extraction mode where 4 bunches per spill are extracted in ≈1μs. Since the flat-top of the current oscillation is about 10 μs a quasi constant magnetic field is put up during the beam extraction
To determine the focusing properties of the quadrupole the pulse generator was charged stepwise from 0 to ≈2.5 kA and for each step the resulting beam profile on the scintilator screen was measured. The smallest beam size was observed at a charging voltage of 1.4 kV. This corresponds to a peak current of about ≈11 kA and a magnetic flux density of ≈4.65 T respectively at the surface of the quadrupole wires. The beam, which was initially ±10 mm, was focused to approximately ±2.5 mm which is limited by the emittance of the beam. Applying higher charging voltages leaded to a defocusing of the beam.

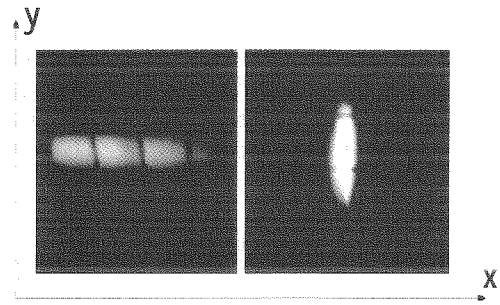

Fig.2. CCD snapshots: a beam with an initial size of ±10 mm (left) could be focused to ±2.5 mm (right). The grid size is 5 mm .

One of the feasible applications for pulsed quadrupole lenses is a short focal length condenser system (Fig.3.), with which it's possible to increase the transmission for nuclear reactions products [3]. Such condenser lenses must be arranged shortly behind a reaction target and have a focal lengths as short as possible. Corresponding quadrupole lenses thus should have small apertures and high field gradients. One such condenser system has been designed for the projectile fragment separator at GSI, Darmstadt [4].

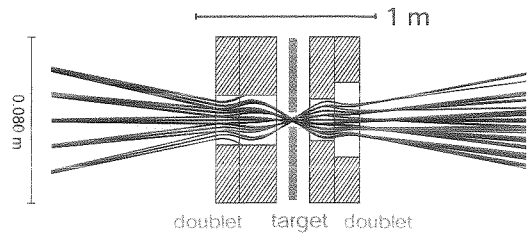

Fig. 3. A condenser system as a possible application for strong focusing lenses.

References

[1] G. Li et al., Rev. Science. Inst. 71 (2000) 376.
[2] V. Chichkine et al. NDTCS-2000, Vol 4, A 6.
[3] H. Wollnik, Nucl. Instr. And Meth. Vol 83, (1970), 229.
[4] H. Geissel et al., GSI Report 89, 30, (1989).

CVD-Diamond Detectors - Status Report 2000

E. Berdermann, H. W. Daues, P. Moritz, H. Stelzer, B. Voss

The excellent results obtained from CVD-diamond detectors in heavy-ion timing measurements with intense beams initiate applications in new fields [1]. A large area (6 x 4 cm²) diamond strip detector of 200 µm thickness containing 32 strips of a 1.8 mm pitch has been successfully used in the atomic physics Cave A at GSI as the focal plane detector of a magnetic spectrometer. Beam loss monitors are under consideration, enabling controlled beam transport in hot regions along the high-current injector beamlines. Very first results from the time resolution in measurements with minimum ionizing particles are encouraging. Polished CVD-diamond material with a collection distance > 200 µm is being used for. Because of the much better Signal-to-Noise ratio required, new timing amplifiers are currently under development [2].

The investigations of CVD-diamond detectors are continued with studies of the influence of the electric field and the bias polarity to the detector response. A variety of papers [3] is available in the literature discussing the origin and the nature of numerous trap levels detected in the range from 20 meV to 3.6 eV in CVD diamond. Due to the appearance of fixed space charge in the diamond bulk, the electric field inside the detector is not homogeneous. The mobility of carriers in the crystalline grains is orders of magnitude higher than in disordered grain boundaries. Conductivity models are discussed, where the average collected charge is affected by electron capture in grain boundaries (assumed as amorphous carbon) and hole capture in grain defects. Because of the columnar growth structure of the polycrystalline CVD diamond the electrical behaviour of material neighbouring nucleation side is quite different compared to the growth side. The influence of the detector thickness to this picture is obvious.

Three detectors made of unpolished CVD diamond grown with identical process parameters but different thicknesses were used to study the detector behaviour under different electric field conditions. The detectors of an 1 cm² area were mounted in a stack with increasing thickness in beam direction (d_{D1} = 93 µm, d_{D2} = 158 µm, d_{D3} = 246 µm). The beam test has been performed with ^{84}Kr projectiles of 650 MeV/amu.

The data obtained are limited by the bandwidth and the sensitivity of the available electronics. In order to avoid saturation of the pulse heights as observed for D2 and D3 in some cases (see Fig. 2, Fig. 3) a new amplifier DBAIII (3 GHz) with variable gain 1:100 has been developed. Low sensitivity QDC's and TDC's of higher resolution than the currently used (25 ps/ch) are urgently required for future measurements.

Characterisation data of the D1 sample (d = 93 µm, C = 37 pF) are shown in Fig.1. The pulses (a) demonstrate the limitation of the measurement system to determine the signal rise time. Commonly, a higher amount of charge is collected for positive bias on the growth side whereas a shorter carrier drifttime is observed for negative polarity (b).

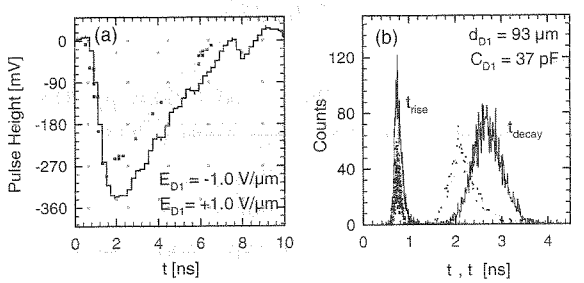

Fig 1: (a) Single-particle pulses at positive resp. negative bias. (b) The corresponding rise-time and decay-time distribution

Fig.2 shows the timing results obtained from each diamond detector versus a plastic scintillator used in coincidence. The σ–widths of the ToF spectra are plotted over the electric field applied in (a) and over the detector thickness in (b).

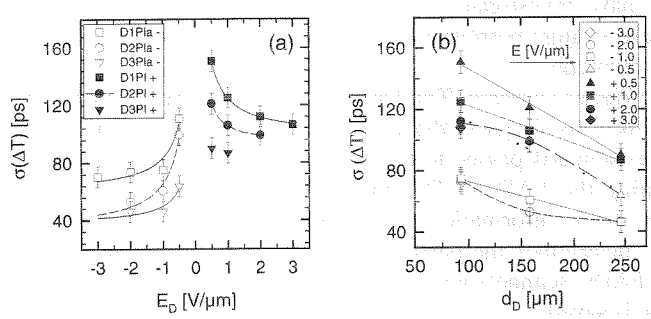

Fig. 2: ToF resolution measured with three diamond detectors of different thicknesses versus a scintillator detector. The σ-widths of the ToF spectra are plotted over the applied electric field E in (a) and over the detector thickness in (b).

The corresponding pulse-height results are shown in Fig. 3.

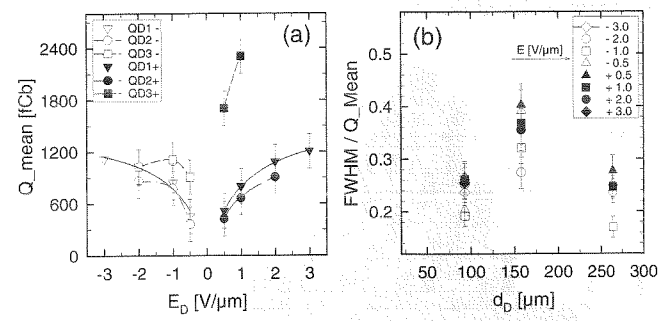

Fig. 3: The mean collected charge plotted over the applied electric field (a) and the pulse-height resolution under the same electric field conditions over the detector thickness (b).

Due to saturation effects of the D2 and D3 pulse heights no final conclusions concerning the thickness dependence of the collected charge signal can be extracted quantitatively. Nevertheless, the general trend is obvious. For both polarities the data indicate an erratic increase of the collected charge above a certain thickness. Although the charge collected with positive bias on the growth side is much higher, the best time resolution is obtained for thicker detectors at the highest negative electric field. These data have to be confirmed.

References

[1] E. Berdermann et al., "The Use of CVD Diamond for Heavy-Ion Detection", 7th Int. Conf. on New Diamond Science and Technology, Hong Kong 2000, to be publ. in Diamond and Related Materials (2001)

[2] M. Petrovici et al., "Preliminary Results on Timing Properties of CVD diamond Detectors for MIPs", GSI Internal Report 2000

[3] Diamond Data Base, "http://www.tribology.dti.dk/cgi-bin/DIA_database

FOPI Trigger: Improving Statistics on Strange Particles

O. Brosch, A. Kugel, R. Männer – Lehrstuhl für Informatik V,
Universität Mannheim, Germany (brosch@ti.uni-mannheim.de)

Introduction. FOPI experiments produce low statistics with respect to certain strange particles, especially negatively charged kaons [1]. The reasons are their rareness and the slow data read-out even with the updated FADC scanning system [2]. Thus, a trigger system is required to ensure that only events containing these particles are read by the FADC scanners [3]. We have investigated, how our trigger algorithm [4] can increase strange particle yield and how this affects hardware [5] requirements.

Trigger Concept. The trigger will be integrated into the experiment as follows: the central drift chamber's (CDC) sense wires signal is passed to the trigger via a discriminator, circumventing the FADCs. The trigger algorithm extracts the particles' track information, and together with the time-of-flight data determines the particles' species. If an anti-kaon is found the FADC scanners get a "start read-out" signal. If not, read-out time is saved.

Performance. The first version of the trigger algorithm [4] was designed to classify – under optimal conditions – every particle contained in the CDC data. While this is the best way to analyze a single event, the procedure does not significantly increase the number of kaons that can be recorded during an experiment of fixed duration.

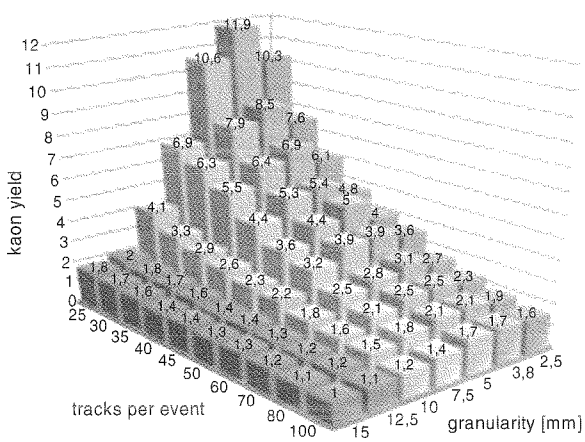

Fig. 1: kaon yield vs. granularity and occupancy.

Ghost Tracks. A simulation was elaborated that produces the number of kaons that can be found in a given period of time rather than the percentage of particle tracks that can be classified accurately. The result is that the number of detected kaons highly depends on the number of "ghost tracks" and only secondarily on the percentage of accurately classified particles. The number of ghost tracks in turn basically depends on the occupancy in the detector image, i.e. the number of particle tracks contained in the sense wires' signals. Ghost tracks emerge from sets of hits that incidentally form a track. Their number is significantly increased by the fact that – induced by the CDC design – 50 percent of the detector's signal lead to mirrored hits. To focus on suppressing ghost tracks turned out to be the proper strategy for increasing the yield of a certain particle species. Other parameters, like granularity of search patterns or filter operators, were used to fine-tune algorithm performance. Another interesting result is that kaon yield does not significantly depend on the algorithm's execution time.

Kaon Yield. Compared to kaon yield without a trigger our simulation suggests that the algorithm can increase the number of kaons by a factor of ~3 with approximately 50 particle tracks per event, and a factor of ~6 to 8, if only ~30 particle tracks occupy the detectors' data. Fig. 1 shows the dependence of the yield as a function of occupancy (number of tracks) and granularity (resolution of predefined tracks or number of search patterns).

Hardware Requirements. Hardware consumption of the FOPI trigger algorithm primarily depends on the granularity, i.e. how many predefined patterns have to be compared with the hits on the CDC wires (the detector image). A second important parameter is the occupancy and the size of the hit space, i.e. the number of tracks, detector pixels per track and thus of active pixels in the CDC. The latter determines the algorithm's execution speed. Fig. 2 shows hardware consumption as a function of granularity, occupancy, and kaon yield.

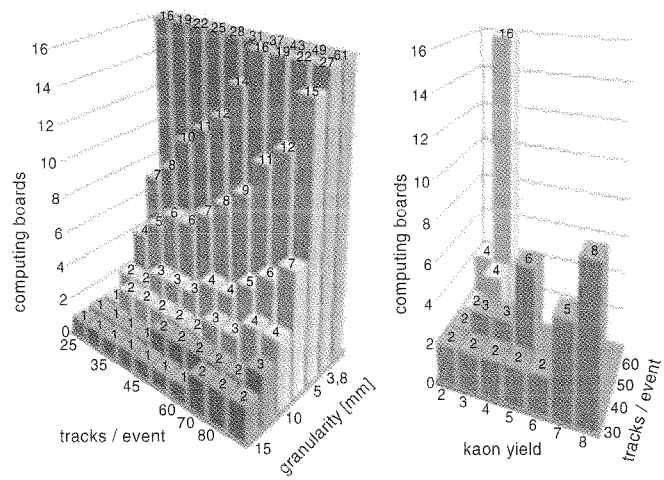

Fig. 2: hardware consumption vs. granularity, occupancy, and kaon yield.

Outlook. The physical interface between Atlantis and the CDC still has to be developed, the next step is the coding of time critical and computing intensive parts of the algorithm into a hardware description language (CHDL [6] or VHDL) and to test the result on the Atlantis [5] hardware.

References

[1] K. Wisniewski et al., Eur. Phys. J. A9 (2000), pp. 515-519

[2] FOPI Collaboration, GSI Sci. Rep. 1999, p. 215

[3] O. Brosch et al, GSI Sci. Rep. 1998, p. 176

[4] O. Brosch et al, GSI Sci. Rep. 1999, p. 218

[5] O. Brosch et al, Springer LNCS 1800 (2000), pp. 890-897

[6] K. Kornmesser et al, Proc. PACT'98 Workshop on Reconf. Comp. (1998), pp. 78-82

The New Readout Electronics for TAPS*

P.Drexler[2], U.Thöring[2], W.Bonn[2], H.A.P.van der Duin[3], R.Holzmann[1], G.van der Kruk[3], B.Krusche[4], H.Löhner[3], V.Metag[2], T.W.Nijboer[3], J.G.Messchendorp[2], R.Novotny[2], C.Salz[2], S.Schadmand[2], M.Steinacher[4], M.Thiel[2], H.Vorenholt[3],*for the TAPS collaboration*

[1] GSI, Darmstadt
[2] II. Physikalisches Institut, Universität Gießen
[3] KVI, Groningen, The Netherlands
[4] Department of Physics and Astronomy, University of Basel, Switzerland

The new readout electronics for the electromagnetic calorimeter TAPS is being built by the Gießen physics department in collaboration with KVI, Groningen (The Netherlands) and the University of Basel. It is planned to employ the new electronics in joint experiments with TAPS and the dilepton spectrometer HADES at GSI, Darmstadt. The concept is based on the VME-standard and accommodates modern expectations regarding data rate, resolution, flexibility and trigger selectivity. An additional requirement is compatibility with the HADES readout system [1].

An 8-channel prototype miniseries from the new VME-readout electronics for the electromagnetic calorimeter TAPS [2] has been employed during a first test beam time at the MAMI tagged photon beam facility. The analog functions for the TAPS telescopes (BaF_2 scintillators and TAPS Veto System) are implemented on a piggyback residing on HADES/TAPS ADC Motherboards [3]. The determination of time-of-flight information (time chain) as well as the separate charge integration of the two scintillator components with two dynamic ranges (energy chain) has been implemented for each BaF_2 detector. The piggyback board logic is derived from constant fraction discriminators. Additional leading edge discriminators allow fast, selective triggers. Programmable logic devices (PLD) are used bi-directionally for setting discriminator thresholds and, during data taking, for registering the discriminator signals. A prototype for a 64-channel multiplicity coincidence unit for the TAPS first level trigger has been completed and tested. Test results of the time chain using a time calibrator have been reported earlier [2].

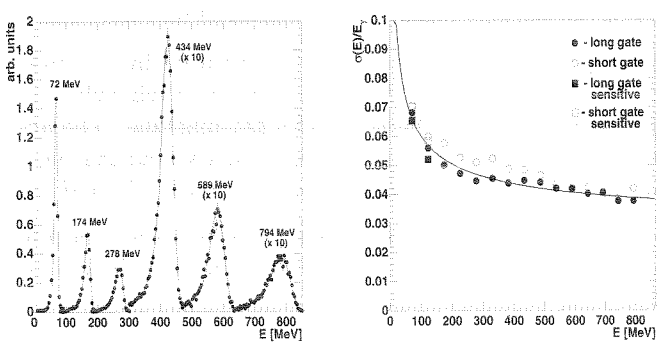

Figure 1: *Left: Shower line shapes for various incident photon energies from the first in-beam test measurement with 7 BaF_2 crystals. Right: Energy resolutions for the 4 integration gates as a function of incident photon energy.*

An in-beam test was performed to study the energy resolution and linearity. A detector array consisting of 7 BaF_2-crystals was placed in the tagged photon beam. Figure 1 presents the energy response to incident photon energies between 70 and 800 MeV. The analog signals have been integrated over $2\mu s$ with a full scale range of 1 GeV. The line shapes are fitted with the typical response of BaF_2 crystal arrays (solid lines). The corresponding resolutions (σ) as function of incident photon energy are also shown in Figure 1.

A second test measurement employing a mini-series of the new TAPS electronics is realized by participation in a current TAPS experiment at MAMI. The experimental setup includes the TAPS detector in a wall formation placed on one side of the beam covering ca. 30% of 4π. The small detector array (7 BaF_2 crystals) is placed on the other beam side at 100° and read out by a HADES-compatible acquisition. Figure 2 presents the $\pi^\circ \rightarrow \gamma\gamma$ invariant mass peak from the reaction $\gamma + {}^4He$ where one of the final state photons was detected in the small detector array read out by the new electronics. The figure demonstrates the clean observation of $\gamma\gamma$ invariant masses, being one of the key ingredients of a standard TAPS analysis.

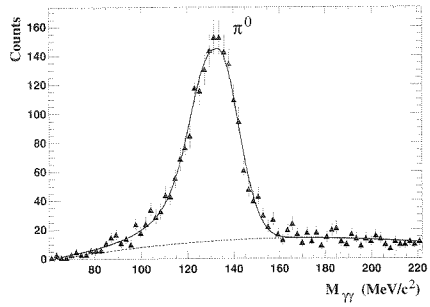

Figure 2: *The $\pi^\circ \rightarrow \gamma\gamma$ invariant mass peak from the reaction $\gamma + {}^4He$. One of the final state photons was detected in the small detector array read out by the new TAPS electronics prototypes. The solid line represents a fit with the known $\pi^\circ \rightarrow \gamma\gamma$ line shape plus background (dotted line).*

Milestones for the year 2001 include the final revision and mass production of the TAPS piggybacks. The readout of four channels per VME module is foreseen to be managed per motherboard. Accordingly, the BaF_2 calorimeter with a planned total of 9x64 detectors necessitates 144 VME-modules.

* supported by BMBF, GSI, SNF, and FOM

References

[1] http://www.physik.uni-giessen.de/hades/
[2] GSI Scientific Report 1999
[3] R.Bassini et al., A 32 Channel TDC on a VME-Board, IEEE Trans. on Nucl. Science, Vol. 45, 3, June 1998

New data acquisition system for CERES/NA45 at CERN

P. Braun-Munzinger, J. Holeczek, D. Miśkowiec, H. Sako, GSI
H. Tilsner, H. Wessels, University of Heidelberg

For the 2000 run of CERES a new TPC readout scheme was implemented [1]. The data acquisition system (DAQ) needed to be adapted to the new readout. Between March and September 2000 we designed and implemented a completely new DAQ. It was then successfully used to collect 30 millions central Pb+Au events in the 160 GeV/nucleon run. Below we briefly describe the DAQ scheme and performance. More details can be found in [2].

The new DAQ was to a large extent based on standard hardware components (20 personal computers under linux) and software tools. It was highly modular so we could optimize one part of the system without touching the others. Ten readout PCs were collecting events during the 5 s long SPS burst. In the 14 s long burst pause they were sending the collected data via ethernet to an event builder PC in the CERN Central Data Recording facility (CDR). There the ten data buffers were merged into one and saved on disk. The tape daemon, asynchronously running on this machine, copied the file to tape. The cleaner process was deleting the oldest files such that half of the disk space was always available. Below we go through the collecting, storing, sending, and event building stages in more detail.

Charges induced on the TPC readout pads were digitized in FEDC modules [3] sitting in VME crates in the experimental zone. Each VME crate was connected via a MXI interface and a 20 m cable to a readout PC, located in the counting room. Eight readout PCs were needed to read the 16 TPC chambers. Other CERES detectors, SDD, RICH1, and RICH2, sent their data via receivers to memory modules, then via optical links and O2PCI modules to the memory of an embedded PC. The beam detectors ADCs and TDCs in three daisy-chained VME crates were accessed by yet another readout PC via PVIC.

The readout was triggered by an external signal applied to an input channel of an I/O card (PC36C by Eagle Technology) plugged in each readout PC. The collector software was polling on the bit. Once a trigger has been seen, the PC would set a busy signal on an output line of the I/O card. A logic OR of all busy signals went to the trigger system and inhibited new triggers. The busy signal was removed only after the complete data had been in the memory of the PC (unless in the pipeline mode, see below).

The event size was 0.5 MB. The average busy duration, i.e. the average time needed to get the event into the memory of a readout PC, was 1.7 ms for the beam detector crates, 3.8 ms for SDD, 2.3 ms for RICH, and 5.7 ms for TPC. The largest fraction of the latter was spent in the data transfer from the FEDC to the readout PC via MXI (12 MB/s). With the beam intensity of 10^6 per burst, and with the centrality trigger of 8%, the rates of offered and accepted triggers per burst were 1000 and 300, respectively. In the middle of the run a pipeline readout was implemented for the TPC. The 5.7 ms were split in two parts: ~1 ms, needed for the data to get in the ALTRO chips of the FEDC, and ~5 ms for the transfer to the readout PC. The number of accepted triggers increased to 400 per burst.

On all readout PCs the data were collected in the upper most 64 MB of the total 128 MB physical memory. This memory was disabled for linux by an appropriate entry in `lilo.conf`. A memory device driver, similar to `mem.c`, was used to access this area via `/dev/daqmem`. From the system level the user could handle `/dev/daqmem` like an ordinary disk file, including dumping, editing, copying, etc.

The collecting was controlled by a set of parameters, residing in the kernel memory. After a trigger, the collector process would read them to know where to store the event. After storing it would update the appropriate numbers. Later, when the burst was finished and the data needed to be sent to CDR, the sending routine would read the parameters to figure out how many bytes to send. The access to the parameters was provided via a simple device driver. From the system level the user could access the parameters at any time via `/proc/daqctrl`.

In the burst pause the readout PCs sent the collected data to one event builder PC in CDR via sockets. The 10 receiver processes, running on the event builder machine, dumped the data into named pipes (FIFOs). The sending speed of each readout PC was limited to about 10 MB/s (fast ethernet). The Gigabit ethernet card on the CDR side, however, was limiting the total transfer rate to 30 MB/s. Furthermore, because of the run control overhead and because of activities on the event builder PCs, only 200-250 MB of burst data could be sent within the burst pause in a stable mode. This was the bottle neck of the DAQ. The resulting continuous data rate was 10 MB/s.

The event builder (evb) read the FIFOs, checked the consistency of event counters, merged the subevents, and saved the output, containing one complete burst, to a disk file. The processing speed was 15-17 MB/s and thus the data of the next burst had to be sent to a different CDR machine. In total seven event builder machines were used.

A tape control script sorted link files created by evb into tape job queues and submitted them on each evb machine. Typically there were 1-3 jobs per machine. The actual copying to tape was done using CERN `tpwrite` with 5 MB/s. The overal taping rate was limited to 20 MB/s.

The new DAQ, in spite of various problems, was working from the beginning of the heavy ion run and allowed to collect total of 30 millions events.

References

[1] H. Tilsner, GSI Annual report 2000.
[2] http://www.gsi.de/ misko/ceres/daq/note.html
[3] Design by Luciano Musa, CERN.

The New Readout Electronic for the CERES TPC

C. Engster[1], P. Glässel[2], J. Holeczek[2], M. Joos[1], D. Miśkowiec[3], L. Musa[1], M. Richter[2], H. Sako[3], W. Seipp[2], J. Stachel[2], G. Thomas[1], H. Tilsner[2], J. Wessels[2]

[1] CERN, [2] Universität Heidelberg, [3] GSI Darmstadt

For the CERES beam-time in 2000 the readout system of the TPC was completely changed. A modified version of the original front-end board (see fig. 1 and [1]) and the motherboards were still used. The electronics close to the DAQ (receivers, memory modules, Compact PCI system) was replaced by newly designed boards (**F**ront **E**nd **D**igitization **C**ards). The design of these cards is based on a development for the ALICE TPC readout system. In the new setup the motherboards were used for configuring the front-end electronics and for distributing the trigger and abort signals.

Immediately after receiving a trigger signal the SCA (Switched Capacitor Array) on the front-end board starts to sample the 16 outputs of the amplifier in parallel. Up to 250 individual time samples for each channel can be stored to allow three-dimensional reconstruction of the tracks. The sampling phase is followed by the readout phase in which the stored analog values are dumped in a time-wise order. During the readout phase the output signal of the SCA has a maximum swing (AC component) of 2 V and a baseline (DC component) that can be adjusted online via a DAC on the front-end board.

The digitization and further processing of the TPC signals is done on the FEDC-boards. These boards are realized as 9U VXI devices which can contain up to 48 readout channels. Each readout channel comprises a 10-bit ADC and a digital chip for signal processing (a modified version of the ALTRO chip for the ALICE TPC [2]) and processes the data from one front-end board. After converting the analog signal the data stream is demultiplexed according to the 16 channels of the preamplifier. The resulting 16 data streams are processed in parallel inside the ALTRO chip. The data is represented and processed only with the 9 MSB, resulting in a loss of 1 bit in resolution. Therefore, the signal is described by a 9 bit code (0 – 511).

In the following processing steps the polarity of the signal is changed and the baseline is subtracted. After this subtraction the signal should be contained in the first half of the 9 bit range. Therefore the most significant bit can be omitted reducing the signal representation to 8 bit codes. Finally the signal undergoes zero suppression. Samples with a value smaller than a constant threshold (8 bit) are rejected. When a sample is found to be above the threshold, it is considered as the start of a pulse (cluster) and stored in the central memory of the FEDC.

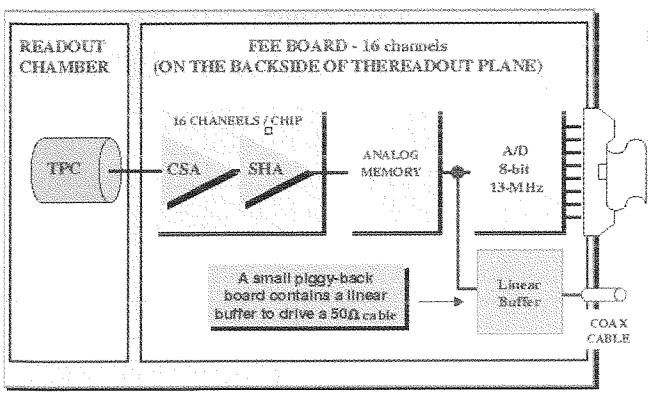

Figure 1: The modified FEE card.

Inside the FEDC an event is stored in memory as a back-linked structure. Due to reordering of samples between accepted clusters, the timing information is lost during the zero-suppression process. This requires the addition of two additional words – the time-stamp and the cluster-length. The cluster-length corresponds to the total number of samples plus the time-stamp and the cluster-length. The time-stamp gives the (sample-)position of the last sample in the cluster relative to the trigger signal. This cluster structure (sample values + time-stamp + cluster-length) is repeated for each accepted cluster in a specific channel. For each channel up to 250 time samples can be accepted.

Because each ALTRO chip processes data coming from 16 TPC-channels with a maximum of 250 time samples, it was not possible to provide enough memory inside the chips to hold pedestal values for all samples. Instead, a scheme using a look-up table was implemented. The look-up table contains 250 7 bit words. The index (the linenumber) of this table corresponds to the sample number. The entries are the addresses of the data-buffers which contain the pedestal values. This means, 128 pedestal values can be assigned to each channel.

Three FEDC boards are combined in one VME-crate. Each of these boards is connected to 40 front-end cards, i. e. processing the data from 640 TPC pads. In total, 24 FEDC boards are needed to read out the whole TPC. The connection between these crates and the readout PCs (cf. [3] for more details) are realized with National Instruments' MXI-bus. MXI-bus is a general purpose, 32-bit multi-master system bus on a cable. It provides a way of controlling VXI systems using commercially available desktop computers and workstations. In CERES a PCI-VME bridge is used. This configuration consists of a PCI card (plugged in the readout PCs), MXI-2 bus and a MXI-VME interface card which is plugged into the VME-crate for the FEDC cards. Data and control signals are converted on the PCI board and sent over the MXI bus, which is essentially the VME on a cable, into the MXI-VME interface board. The 6U MXI-VME interface board in conjunction with the MXI-2 cable enables data transfers up to 38 MBytes/s using D64 transfers.

References

[1] R. Baur *et al.*, GSI Scientific Report 1998 p. 190.

[2] ALICE Collaboration, Technical Design Report, CERN/LHCC 2000-001

[3] D. Miśkowiec *et al.*, this Report

Front-end electronics for ALICE TPC-Detector

H. K. Soltveit and J. Stachel

The front-end electronics for the ALICE TPC to read out the charge detected by 570132 pads located on the readout chamber end-caps is here presented. The read-out chambers are multiwire proportional chambers with cathode pad read-out. The pads receive as the image charge of the signal on the anode amplification wires a signal with a fast rise time (less than 1 ns), and a long tail due to the motion of the positive ions. The signal is delivered on the detector impedance which varies between 3 pF to 12 pF. Therefore the front-end electronics must cope with different pad capacities. The electronics will be located in an area with limited access. High reliability is thus a concern. The circuit was developed in 0.35 μm CMOS technology.

The front-end electronics consist of a charge sensitive preamplifier/shaper, a 10-bit 10 MHz low-power ADC and an ASIC which contains a shortening digital filter for the tail cancellation, the baseline subtraction and zero-suppression circuits, and a multiple-event buffer [3]. The image charge induced on the TPC pads is amplified and integrated by a low input-impedance amplifier. It is based on a continously sensitive charge sensitive amplifier followed by a semi-gaussian pulse shaper of second order. The amplitude, which is different for the 3 different pad sizes, has a typical value of 7μA.

The Preamplifier/shaper for the ALICE TPC (Fig.1) is based on the design of the preamplifier/shaper for the NA45/CERES TPC. The main modifications concern:

- migration from the technology AMS CMOS 0.8 μm to the AMS CMOS 0.35 μm;
- optimization of the design to better fulfil the ALICE requirements;
- removal of the tail cancellation circuit that, in the ALICE design, is implemented in the digital ASIC.

This continuously sensitive design is particularly suitable for a detector with high occupancy. A peaking time of $\tau_s = 120$ ns and noise consideration (< 1000 electrons) dictate a P-channel input transistor and a feedback resistance $R_F > 10$ MΩ. The feedback resistance R_F is realized by using a MOS transistor biased in subthreshold region. The MOS transistor MF establishes the DC path and continuously discharges C_F with a decay time $T_{decay} = C_F \times R_{ds}$ (MF).

The only practical way to realize such a high resistance in CMOS technology is by using the associated drain-source R_{ds}(MF) of a MOSFET transistor. A transistor operating in this area is very sensitive to process, temperature and supply voltage variations. To prevent or reduce these effects a Self-Adaptive scheme to bias the feedback transistor MF is used. The MOS-transistor Mzero is

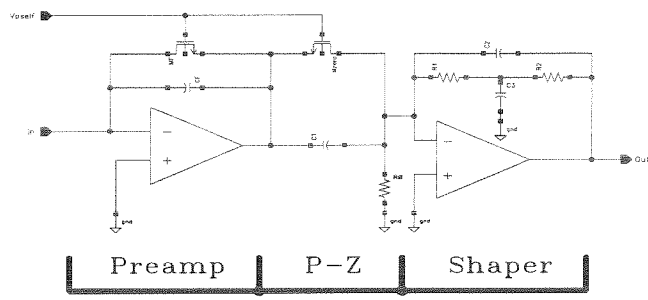

Figure 1: Schematic of the preamplifier/shaper chain.

biased the same way as MF during the discharge of C_F. The Zero associated to the network Mzero-C1, adapts itself dynamically to accurately cancel the pole associated to the network CF-MF. There is also a benefit from the reduction of R_{ds}(MF) at high Qin, i.e. faster return to the baseline of the output of the CSA-shaper, without worsening the linearity of its conversion gain. In terms of noise requirements, the ALICE preamplifier/shaper fulfills the requirement with an ENC of less than 500 electrons for input capacitances between 3 pF and 17 pF. The response is linear ($< 0.2\%$) up to an dynamic range of 1.3 V with a peaking time around 120 ns. The gain of the preamplifier/shaper is about 7.8mV/fC. The total power consumption is 7 mW/channel.

The front-end electronics for the read-out for the TPC has been designed and fabricated with the AMS 0.35 μm CMOS process. The first prototyp is received and a first testing shows promising results. A new version is under development. The main change is the inclusion of a fourth-order filter to obtain a more symmetrical response to increase the double track resolution. The gain of the circuit will also be distributed towards the input to decrease the noise even further.

References

[1] R.Baur. GSI Annual Report 1997.

[2] G.Gramegna, P. O'Connor, P. Rehak, S.Hart, Nucl. Instr. and Meth., **A390 (1997), 241-250.**

[3] ALICE Technical Design Report, Cern/LHCC, January 2000.

ALICE TPC Readout Chambers

P. Braun-Munzinger[1], J. Fiess[2], M. Ivanov[1], R. Renfordt[2], H. Sann[1], H.R. Schmidt[1], H. Stelzer[1], D. Vranic[1]

[1]GSI Darmstadt, [2]University of Frankfurt

A major component of the CERN-LHC ALICE detector is the central barrel, contained in the large L3 magnet and composed of detectors devoted mainly to the study of hadronic signals [1] and dielectrons [2]. The main tracking devices are the silicon based Inner Tracking System (ITS) and the Time Projection Chamber (TPC). Within their acceptance ($-1 \leq \eta \leq 1$) about 12000 tracks will be recorded, yielding information about particle type and momentum.

The readout planes at the two sides of the TPC field cage are subdivided into 18 segments each. The segments are split into an inner and an outer readout chamber (ROC). The ROCs will be conventional multiwire proportional chambers with cathode pad readout as used in many TPCs before. However, the high particle load puts severe constraints on the design parameters in terms of pad geometry and gas gain and leads to requirements that go beyond an optimization in terms of momentum and dE/dx resolution.

To both minimize the pad occupancy and to ensure a sensible pad response function, $4 \times 7.5mm^2$ pads were chosen for the inner chambers. The outer chambers have a pad size of $6 \times 10mm^2$ (inner half) and $6 \times 15mm^2$ (outer half). Altogether, the inner chamber has 5504 pads, while the outer one has 9984 pads. The wire spacing for both the anode and cathode wires is $2.5mm$, while the gating grid has a wire spacing of $1.25mm$. The distance from the pad plane to the anode wire is 2 and 3 mm for the inner and outer chambers, respectively.

A full size prototype of an inner readout-chamber has been built has GSI in order to verify the design parameters, such as gating efficiency, gas gain, signal-to-noise ratio, pad response function, cross talk, etc.

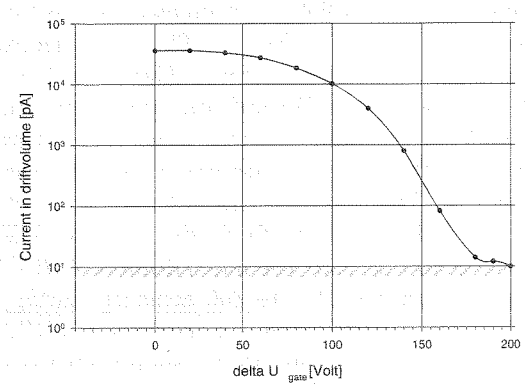

Figure 1: Measurement of ion feedback into the drift volume. The sensitivity limit is indicated by the hatched bar.

The measured gating efficiency against positive ion feedback from the amplification region into the drift region is shown in Fig. 1. The measured current at the drift electrode for gate closed ($\Delta U = 200V$) is $12 \pm 2pA$, which is comparable to the offset current from primary ionization in the drift volume. The total current at the anode is 115 nA, of which $\approx 30\%(= 34nA)$ are seen at the drift electrode. An upper 2σ-limit on the gating inefficiency is 0.5×10^{-4} fulfilling the design requirements.

256 out of 5504 channels have been equippd with CERES preamplifier-shapers. This chip, used in the CERES experiment, is the basis of the ALICE PASA chip and thus comparable in its properties. The RMS noise of the PASA with full capacitive load ($\approx 15pF/pad$) has been measured to be below 1000e, which projects to a signal-to-noise ratio for minimum ionizing tracks better than 20.

The gas gain of the chamber filled with 90% Ne, 10% CO_2 has been determined. The nominal gas gain of 2×10^4 is reached at a voltage of $\approx 1250V$. The chamber, irradiated with a strong ^{90}Sr-source, has be operated stablely for several weeks at this gain.

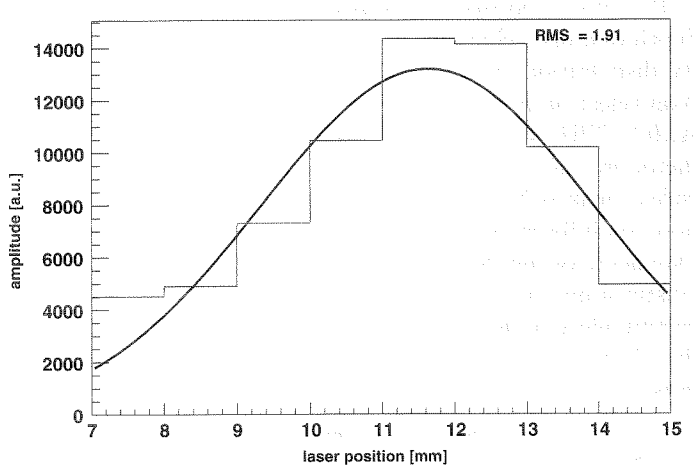

Figure 2: Signal induced by a laser beam.

Fig. 2 shows the response of the chamber to a Nd:YAG laser beam in terms of the pad response function (PRF). The histogramm represents the reponse of a given pad to a laser beam at different positions relative to the pad. From this data the pad response function is extracted to be $\sigma \approx 2mm$ in accordance with the expectations [3]. This number, together with the measured RMS noise figure, allows the conclusion tha the prototyp chambers works according to the specifications in terms of 2-track and position resolution.

References

[1] ALICE Collaboration, Technical Proposal, CERN/LHCC/95-71

[2] ALICE Collaboration, Technical Proposal, Addendum 2, CERN/LHCC/99-13

[3] ALICE Collaboration, Technical Design Report, CERN/LHCC/00-001

Prototype tests for the ALICE TRD

A. Andronic[1], H. Appelshäuser[2], C. Blume[1], P. Braun-Munzinger[1], D. Bucher[3], G. Cătănescu[4], M. Ciobanu[4], H. Daues[1], A. Devismes[1], Ch. Finck[1], N. Herrmann[2], T. Lister[3], T. Mahmoud[2], T. Peitzmann[3], M. Petrovici[4], K. Reygers[3], R. Santo[3], R. Schicker[2], S. Sedykh[1], R.S. Simon[1], J. Stachel[2], H. Stelzer[1], J. Wessels[2], O. Winkelmann[3], B. Windelband[2], C. Xu[2] (ALICE Collab.)
[1]GSI Darmstadt, [2]Universität Heidelberg, [3]Universität Münster, [4]NIPNE Bucharest

The ALICE Transition Radiation Detector (TRD) has been designed to improve the pion rejection capability of the ALICE detector by at least a factor of 100 for momenta above 2 GeV/c [1]. To demonstrate that this goal is achievable, during the last year we have conducted prototype tests at the pion (with natural electron content) beam facility at GSI Darmstadt. A complete description of the experimental setup and of the results (including references) can be found in [2]. Many types of radiators were tested, composed of foils, fibres and foams.Here we summarize the results concerning the pion rejection performance in case of a fibres (of 17 μm diameter) radiator, which was established to be the best candidate for the final radiator.

The measured distributions of energy deposit over the depth of a drift chamber have been employed as probability distributions in simulations aimed at determining the pion rejection factor for the proposed configuration of the ALICE TRD with 6 layers. To extract the pion rejection factor we have studied three different methods: i) truncated mean of integrated energy deposit, TMQ; ii) likelihood on integrated energy deposit, L-Q; iii) bidimensional likelihood on energy deposit and position of the largest cluster found in the drift region of the DC, L-QX. Cuts of certain electron efficiency were involved on the likelihood distributions and the pion efficiency is derived within these cuts.

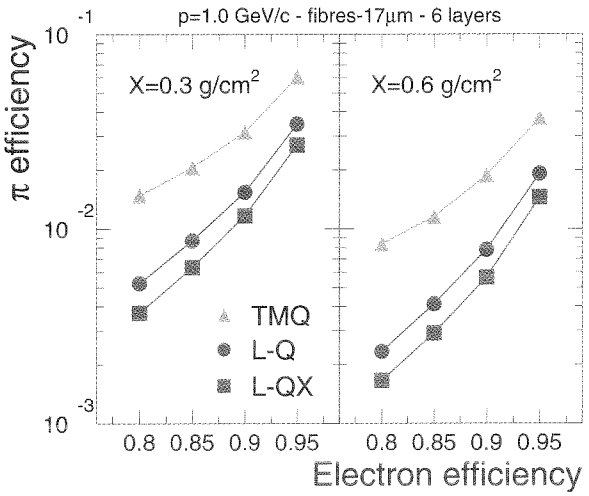

Figure 1: The pion efficiency as function of electron efficiency using the three methods discussed in the text.

In Fig. 1 we present the pion efficiency (the inverse of the rejection factor) as function of electron efficiency (90% electron efficiency is the commonly used value) in case of fibres radiators for the momentum of 1 GeV/c. The three methods introduced above are compared. The truncated mean method, although it delivers sizeably worse identification, has the advantage of being very easy to use, being advantageous especially for an on-line identification. The bidimensional likelihood delivers the best rejection factor. In general, the three methods employed here give results in good agreement with earlier studies.

By doubling the equivalent thickness of the radiator from X=0.3 g/cm^2 (left panel of Fig. 1) to X=0.6 g/cm^2 (right panel) one gains a factor of about 2 in pion rejection power. However, it remains to be seen how the additional material will influence (by producing secondary particles) the performance of the TRD itself and of other ALICE sub-detectors.

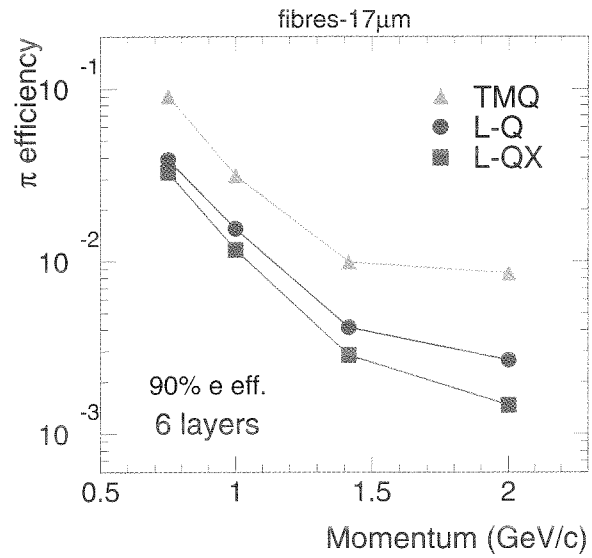

Figure 2: Pion efficiency as function of momentum for a radiator with 17 μm fibres.

The pion efficiency at 90% electron efficiency as function of momentum is shown in Fig. 2. The steep decrease of pion efficiency at momenta around 1 GeV/c is due to the onset of TR production. Towards our highest momentum value, 2 GeV/c, the pion efficiency reaches a saturation, determined by the TR yield saturation and by the pion relativistic rise. Due to these effects the pion rejection is expected to get slightly worse for momenta above 3 GeV/c. As one can see in Fig. 2, at the momentum of 2 GeV/c the pion rejection factor of 300 to 600 achieved during these tests is above the required value for the ALICE TRD. However, one has to bear in mind that a significant worsening of TRD performance has been registered when going from prototype tests to real detectors. This can be the effect of detector loads in a multiparticle environment. On the other hand, impressive pion rejection factors of 1000 and above have been achieved in full size TRDs, i.e. by the HERMES experiment.

References

[1] TRD Proposal, CERN/LHCC 99-13, available at *http://www.gsi.de/~alice*
[2] A. Andronic et al., nucl-ex/0102017 (accepted to IEEE Trans. Nucl. Sc.)

ANNEX

Availability of GSI-Publications

GSI Reports and Preprints

GSI reports and preprints are distributed, on exchange, to other libraries and institutions working in the field of heavy ion physics. Individual copies are made available free of charge, as long as stock lasts.

Written requests should be made to: GSI-Bibliothek, Planckstr. 1, D-64291 Darmstadt, Germany or e-mail can be send to U.Grundinger@gsi.de

Other Papers

For copies of papers published in periodicals, books or conference proceedings, please contact your local Library or one of the authors. **GSI provides no centralized distribution of reprints.**

Publications

Adam, W.; E. Berdermann, P. Bergonzo, G. Bertuccio, F. Bogani, E. Borchi, A. Brambilla, M. Bruzzi, C. Colledani, J. Conway, P. D'Angelo, W. Dabrowski, P. Delpierre, A. Deneuville, W. Dulinski, B. van Eijk, A. Fallou, F. Fizzotti, F. Foulon, M. Friedl, K.K. Gan, E. Gheeraert, G. Hallewell, S. Han, F. Hartjes, J. Hrubec, D. Husson, H. Kagan, D. Kania, J. Kaplon, R. Kass, T. Koeth, M. Krammer, A. Logiudice, R. Lu, L. mac Lynne, C. Manfredotti, D. Meier, M. Mishina, L. Moroni, A. Oh, L.S. Pan, M. Pernicka, A. Peitz, L. Perera, S. Pirollo, M. Procario, J.L. Riester, S. Roe, L. Rousseau, A. Rudge, J. Russ, S. Sala, M. Sampietro, S. Schnetzer, S. Sciortino, H. Stelzer, R. Stone, B. Suter, R.J. Tapper, R. Tesarek, W. Trischuk, D. Tromson, E. Vittone, A.M. Walsh, R. Wedenig, P. Weilhammer, M. Wetstein, C. White, W. Zeuner, M. Zoeller, RD42 Collaboration:
Micro-Strip Sensors Based on CVD Diamond
Nucl. Instr. and Meth. in Phys. Res.A453,141(2000)

Agakichiev, G.N. et al.:
Fast Method for Searching Tracks in Multilayer Drift Chambers of HADES Spectrometer
Phys. Part. & Nuclei Letters, Dubna, No. 4 (2000)

Aggarwal, M.M.; A. Agnihotri, Z. Ahammed, A.L.S. Angelis, V. Antonenko, V. Arefiev, V. Astakhov, V. Avdeitchikov, T.C. Awes, P.V.K.S. Baba, S.K. Badyal, A. Baldine, L. Barabach, C. Barlag, S. Bathe, B. Batiounia, T. Bernier, K.B. Bhalla, V.S. Bhatia, C. Blume, R. Bock, E.-M. Bohne, Z. Böröcz, D. Bucher, A. Buijs, H. Büsching, L. Carlen, V. Chalyshev, S. Chattopadhyay, R. Cherbatchev, T. Chujo, A. Claussen, A.C. Das, M.P. Decowski, H. Delagrange, V. Djordjadze, P. Donni, I. Doubovik, S. Dutt, M.R. Dutta Majumdar, K. El Chenawi, S. Eliseev, K. Enosawa, P. Foka, S. Fokin, V. Frolov, M.S. Ganti, S. Garpman, O. Gavrishchuk, F.J.M. Geurts, T.K. Ghosh, R. Glasow, S.K. Gupta, B. Guskov, H.Å. Gustafsson, H.H. Gutbrod, R. Higuchi, I. Hrivnacova, M. Ippolitov, H. Kalechofsky, R. Kamermans, K.-H. Kampert, K. Karadjev, K. Karpio, S. Kato, S. Kees, B.W. Kolb, I. Kosarev, I. Koutcheryaev, T. Krümpel, A. Kugler, P. Kulinich, M. Kurata, K. Kurita, N. Kuzmin, I. Langbein, A. Lebedev, Y.Y. Lee, H. Löhner, L. Luquin, D.P. Mahapatra, V. Manko, M. Martin, G. Martínez, A. Maximov, R. Mehdiyev, G. Mgebrichvili, Y. Miake, D. Mikhalev, Md. F. Mir, G.C. Mishra, Y. Miyamoto, B. Mohanty, D. Morrison, D.S. Mukhopadhyay, V. Myalkovski, H. Naef, B.K. Nandi, S.K. Nayak, T.K. Nayak, S. Neumaier, A. Nianine, V. Nikitine, S. Nikolaev, P. Nilsson, S. Nishimura, P. Nomokonov, J. Nystrand, F.E. Obenshain, A. Oskarsson, I. Otterlund, M. Pachr, A. Parfenov, S. Pavliouk, T.Peitzmann, V. Petracek, F. Plasil, W. Pinganaud, M.L. Purschke, J. Rak, R. Raniwala, S. Raniwala, V.S. Ramamurthy, N.K. Rao, F. Retiere, K.Reygers, G. Roland, L. Rosselet, I. Roufanov, C. Roy, J.M. Rubio, H. Sako, S.S. Sambyal, R. Santo, S. Sato, H. Schlagheck, H.-R. Schmidt, Y. Schutz, G. Shabratova, T.H. Shah, I. Sibiriak, T. Siemiarczuk, D. Silvermyr, B.C. Sinha, N. Slavine, K. Söderström, N. Solomey, S.P. Sørensen, P. Stankus, G. Stefanek, P. Steinberg, E. Stenlund, D. Stüken, M. Sumbera, T. Svensson, M.D. Trivedi, A. Tsvetkov, L. Tykarski, J. Urbahn, E.C. van der Pijll, N. van Eijndhoven, G.J. van Nieuwenhuizen, A. Vinogradov, Y.P. Viyogi, A. Vodopianov, S. Vörös, B. Wyslouch, K. Yagi, Y. Yokota, G.R. Young (WA98 Collaboration):
Delta (++) Production in 158 AGeV Pb^{208}+Pb^{208} Interactions at the CERN SPS
Phys. Lett. B477, 37 (2000)

Ahle, L.; Y. Akiba, K. Ashktorab, M.D. Baker, D. Beavis, B. Budick, J. Chang, C. Chasman, Z. Chen, Y.Y. Chu, T. Chujo, J. Cumming, R. Debbe, J.C. Dunlop, W. Eldredge, K. Fleming, S.-Y. Fung, E. Garcia, S. Gushue, H. Hamagaki, R. Hayano, G.H. Heintzelman, J.H. Kang, E.J. Kim, A. Kumagai, K. Kurita, J.H. Lee, Y.K. Lee, Y. Miake, A.C. Mignerey, M. Moulson, C. Muentz, K. Nagano, C. A. Ogilvie, J. Olness, K. Oyama, L. Remsberg, H. Sako, R. Seto, J. Shea, K. Shigaki, S.G. Steadman, G.S.F. Stephans, T. Tamagawa, M.J. Tannenbaum, S. Ueno-Hayashi, F. Videbaek, H. Xiang, F. Wang, K. Yagi and F. Zhu, B.B. Back, R.R. Betts, J. Chang, W. C. Chang, C.Y. Chi, Y.Y. Chu, J.B. Cumming, J.C. Dunlop, W. Eldredge, S.Y. Fung, R. Ganz, E. Garcia, A. Gillitzer, G.H. Heintzelman, W.F. Henning, D. Hofman, B. Holzman, J.H. Kang, E.J. Kim, S.Y. Kim, Y. Kwon, D. McLeod, A.C. Mignerey, M. Moulson, V. Nanal, C.A. Ogilvie, R. Pak, A. Ruangma, D. Russ, R. Seto, P.J. Stanskas, G.S.F. Stephans, H. Wang, F.L.H. Wolfs,

Publications

A.H. Wuosmaa, H. Xiang, G.H. Xu, H.B. Yao, C.M. Zou (E866/E917 Collaboration):
Excitation Function of K+ and pi+ Production in Au+Au Reactions at 2-10AGeV
Phys. Lett. B4765, 1 (2000)

Aleksandrov, D.; T. Aumann, L. Axelsson, T. Baumann, M.J.G. Borge, L.V. Chulkov, J. Cub, W. Dostal, B. Eberlein, Th. W. Elze, H. Emling, H. Geissel, V. Z. Goldberg, A. Grünschloß, MHellström, J. Holeczek, R. Holzmann, B. Jonson, J. V. Kratz, G. Kraus, R. Kulessa, Y. Leifels, A. Leistenschneider, T. Leth, K. Markenroth, M. Meister, I. Mukha, G. Münzenberg, F. Nickel, T. Nilsson, G. Nyman, B. Petersen, M. Pfützner, V. Pribora, A. Richter, K.Riisager, C. Scheidenberger, G. Schrieder, W. Schwab, H. Simon, M. H. Smedberg, J. Stroth, A. Surowiec, O. Tengblad, M. V. Zhukov:
Halo Excitations in Fragmentation of ^{6}He at 240 MeV/u on Carbon and Lead Targets
Nucl. Phys. A669, 51 (2000)

Alpat, B.; G. Ambrosi, C. Balboni, R. Battiston, A. Biland, M. Bourquin, W.J. Burger, Y.H. Chang, A. E. Chen, N. Dinu, P. Extermann, E. Fiandrini, S. R. Hou, M. Ionica, R. Ionica, W.T. Lin, W. Lustermann, G. Maehlum, M. Menichelli, M.Pauluzzi, N. Produit, D. Rapin, D. Ren, M. Ribordy, H. Sann, D. Schardt, K. Sümmerer, G. Viertel, D. Vité, W. Wallraff, S. X. Wu:
High-Precision Tracking and Charge Selection with Silicon Strip Detectors for Relativistic Ions
Nucl. Instr. and Meth. in Phys. Res.A446,522(2000)

Andreyev, A.N.; M. Huyse, P. van Duppen, L. Weissmann, D. Ackermann, J. Gerl, F.P. Heßberger, S. Hofmann, A. Kleinböhl, G. Münzenberg, S. Reshitko, C. Schlegel, H. Schaffner, P. Cagarda, M. Matos, S. Saro, A. Keenan, C. Moore, C.D. O'Leary, R.D. Page, M. Taylor, H. Kettunen, M. Leino, A. Lavrientiev, R. Wyss, K. Heyde:
A Triplet of Different Shaped Spin-Zero States in the Aromic Nucleus ^{186}Pb
Nature, 405, 430 (2000)

Armbruster, P.:
On the Quest of Production of Superheavy Nuclei in Reactions of ^{48}Ca with the Heaviest Actinide Targets
Eur. Phys. J. A7, 23 (2000)

Armbruster, P.:
On the Production of Superheavy Elements
Ann. Rev. Nucl. Part. Sci. 50, 411, 2000

Bapat, B., S. Keller, R .Moshammer, R. Mann, J. Ulrich:
Double Ionization of Helium in Fast Ion Collisions: The Role of the Correlated Initial State
J. Phys. B33, 1437 (2000)

Barrette, J.; R. Bellwied, S. Bennett, R. Bersch, P. Braun-Munzinger, W.C. Chang, W. E. Cleland, M. Clemen, J.D. Cole, T.M. Cormier, Y. Dai, G. David, J. Dee, O. Dietzsch, M.W. Drigert, K. Filimonov, J.R. Hall, T.K. Hemmick, N. Herrmann, B. Hong, C.L. Jiang, S.C. Johnson, Y. Kwon, R. Lacasse, Q. Li, T.W. Ludlam, S. McCorkle, S.K. Mark, R. Matheus, D. Mikowiec, E. O'Brien, S. Panitkin, T. Piazza, M. Pollack, C. Pruneau, Y.J. Qi, M.N. Rao, E.L. Reber, M. Rosati, N.C. daSilva, S. Sedykh, J. Sheen, U. Sonnadara, J. Stachel, H. Takai, E.M. Takagui, S. Voloshin, T. Vongpaseuth, J.P. Wessels, C.L. Woody, N. Xu, Y. Zhang, Z. Zhang, C. Zou(E877 Collaboration):
Light Fragment Yields from Central Au + Au Collisions at 11.5 AGeV
Phys. Rev. C61, 044906 (2000)

Barrette, J. R. Bellwied, S. Bennett, R. Bersch, P. Braun-Munzinger, W.C. Chang, W.E. Cleland, M. Clemen, J. Cole, T.M. Cormier, Y. Dai, G. David, J. Dee, O. Dietzsch, M. Drigert, K. Filimonov, S.C. Johnson, J.R. Hall, T.K. Hemmick, N. Herrmann, B. Hong, Y. Kwon, R. Lacasse, Q. Li, T.W. Ludlam, S.K. Mark, R. Matheus, S. McCorkle, J.T. Murgatroyd, D. Miskowiec, E. O'Brien, S. Panitkin, P. Paul, T.Piazza, M. Pollack, C. Pruneau, Y.J. Qi, M.N. Rao, E. Reber, M. Rosati, N.C. daSilva, S. Sedykh, U. Sonnadara, J. Stachel, E.M. Takagui, V. Topor Pop, S. Voloshin, T.B. Vongpaseuth, G. Wang, J.P. Wessels, C.L. Woody, N. Xu, Y. Zhang, C. Zou:
Proton and Pion Production in Au+Au Collisions at 10.8-GeV/c
Phys. Rev. C62, 024901 (2000)

Publications

Baumann, I., A. Breidenassel, C. Zühlke, A. Kasimov, G. zu Putlitz, I. Reinhard, K. Jungmann:
Pressure Dependance of the Mg3s4s^{3}S1 → 3s3p^{3}P$_{0,1,2}$ Transition in Superfluid ^{4}He
Eur. Phys. J. D12, 117 (2000)

Bechtold, A.; A. Schempp, U. Ratzinger, B. Schlitt:
Development of an RFQ-Injector for a Therapy Synchrotron
EPAC 2000, p. 2500, CERN, Geneva 2000 (eds.: J.-L. Laclare, W. Mitaroff, Ch. Petit-Jean-Genaz, J. Poole, M. Regler) '7th Europ. Part. Acc. Conf.', Vienna, Austria, June 26-30, 2000

Beck, D.; F. Ames, G. Audi, G. Bollen, F. Herfurth, H.-J. Kluge, A. Kohl, M. König, D. Lunney, I. Martel, R.B. Moore, H. Raimbault-Hartmann, E. Schark, S. Schwarz, M. de Saint Simon, J. Szerypo (ISOLDE Collaboration):
Accurate Masses of Unstable Rare-Earth Isotopes by ISOLTRAP
Eur. Phys. J. A8, 307 (2000)

Becker, F.; N. Amzal, P. Bringel, P.A. Butler, N. Buforn, C. Chandler, R.A. Cunningham, T. Czosnyka, G. de France, J. Gerl, A. Görgen, P. Greenlees, F. Hannachi, K. Hauschild, K. Helariutta, R.-D. Herzberg, M. Houry, H. Hübel, A. Hurstel, J. Iwanicki, A. Jansen, P. Jones, R. Julin, H. Kankaanpää, W. Korten, Y. Le Coz, C.F. Liang, A. Lopez-Martens, R. Lucas, E. Mergel, M. Muikku, P. Nieminen, P. Paris, P.H. Regan, Ch. Schlegel, G. Schönwasser, Ch. Theisen, H.-J. Wollersheim:
Shape Coexistence in the Kr Isotopes
LUIP 0003, Sweden, p. 82 (2000), ISSN 0348-9329
eds: D. Rudolph, M. Hellström
(Proc. of the 'Int. Workshop on N=Z Nuclei (PINGST 2000), Lund, Sweden, 06.-10.06.2000)

Beier, T., I. Lindgren, H. Persson, S. Salomonson, P. Sunnergren, H. Häffner, N. Hermanspahn:
The G_j Factor of an Electron Bound in a Hydrogenlike Ion
Phys. Rev. A62, 032510 (2000)

Bleile, A.; P. Egelhof, H.-J. Kluge, U. Liebisch, D. McCammon, H.J. Meier, O. Sebastián, C.K. Stahle, M. Weber:
Low Temperature X-Ray Detectors for Precise Lamb Shift Measurements on Hydrogen-Like Heavy Ions
Nucl. Instr. and Meth. in Phys. Res.A444,488(2000)

Bleile, A.; P. Egelhof, H.-J. Kluge, U. Liebisch, D. McCammon, H.J. Meier, O. Sebastián, C.K. Stahle, T. Stöhlker, M. Weber:
Calorimetric Low Temperature Detectors for for High Resolution X-ray Spectroscopy on Stored Highly Stripped Heavy Ions
AIP Conference Proc. 512, p. 259 (2000)
eds. H.-O. Meyer, P. Schwandt
(Proc. of the '4th Int. Conference on Nuclear Physics at Storage Rings, STORI, Bloomington, Indiana, USA, 1999)

Bock, R.; S. Borneis, Ch. Bruske, J. Caird, D. Habs, D. Hoffmann, H. Kluge, Th. Kühl, D. Marx, P. Nickles, M. Perry, M. Roth, W. Sandner, W. Seelig, A. Tauschwitz:
PHELIX – A Petawatt High-Energy Laser for Heavy-Ion Experiments
Inertial Fusion Sciences and Applications 99, eds.: C. Labaune, W.J. Hogan, K.A. Tanaka (Elsevier Publ., Paris, p. 703, 2000)

Boine-Frankenheim, O.; I. Hofmann:
Vlasov Simulation of the Microwave Instability in Space Charge Dominated Coasting Ion Beams
Phys. Rev. ST Accel. Beams 3, 104202 (2000)

Boine-Frankenheim, O.; I. Hofmann:
Simulation and Observation of Nonlinear Longitudinal Space-Charge Phenomena in Coasting Beams
Nucl. Instr. and Meth. in Phys. Res.A441,28 (2000)
(Proc. of the Workshop on 'Electron Cooling and Related Topics', Uppsala, Sweden, May 1999)

Borcea, R.; J. Äystö, P. Dendooven, M. Gierlik, M. Gorska, H. Grawe, M. Hellström, Z. Janas, A. Jokinen, M. Karny, R. Kirchner, M. La Commara, P. Mayet, A. Nieminen, H. Penttilä, A. Plochocki, M. Rejmund, E. Roeckl, C. Schlegel, K. Schmidt, R. Schwengner, M. Sawicka:
Beta Deacy of ^{56}Cu
LUIP 0003, Sweden, p.126 (2000),ISSN 0348-9329
eds: D. Rudolph, M. Hellström
(Proc. of the 'Int. Workshop on N=Z Nuclei (PINGST 2000), Lund, Sweden, 06.-10.06.2000)

Borneis, S.; B. Becker-de Mos, H.-J. Kluge, T. Kühl, D. Marx, P.V. Nickles, P. Neumayer, W. Sandner, W. Seelig:
X-Ray Laser Spectroscopy at the ESR: a Proposed Novel Tool for the Investigation of Exotic Isotopes
Hyperfine Interactions 127, 537 (2000)

Publications

Borneis, S.; A. Dax, T. Engel, C. Holbrow, G. Huber, T. Kühl, D. Marx, P. Merz, W. Quint, F. Schmitt, P. Seelig, M. Tomaselli, H. Winter, K. Beckert, B. Franzke, F. Nolden, H. Reich, M. Steck:
Ground State Hyperfine Structure of Heavy Hydrogen-Like Ions
Hyperfine Interactions 127, 305 (2000)

Braun-Munzinger, P.:
Towards the Quark-Gluon Plasma
Nucl. Phys. A663-664, 183 (2000)
(Proc. of the '15th Int. Conf. on Particle and Nuclei (PANIC '99)', Uppsala, Sweden, June 1999)

Braun-Munzinger, P.; J. Stachel:
(Non)Thermal Aspects of Charmonium Production and a New Look at J/PSI Suppression
Phys. Lett. B490, 196 (2000)

Brusasco, C.; B. Voss, D. Schardt, M. Krämer, G. Kraft:
A Dosimetry System for Fast Measurement of 3D Depth-Dose Profiles in Charged-Particle Tumor Therapy with Scanning Techniques
Nucl. Instr. and Meth. in Phys. Res.B168,578(2000)

Callegari, C.; A. Conjusteau, I. Reinhard, K.K. Lehmann, G. Scoles:
First Overtone Helium Nanodroplet Isolation Spectroscopy of Molecules Bearing the Acetylenic CH Chromophore
J. Chem. Phys. 113, 10535 (2000)

Callegari, C.; I. Reinhard, K.K. Lehmann, G. Scoles, K. Nauta, R.E. Miller:
Finite Size Effects and Rotational Relaxation in Superfluid Helium Nanodroplets: Microwave-Infrared Double-Resonance Spectroscopy of Cyanoacetylene
J. Chem. Phys. 113, 4636 (2000)

Cappi, R.; B. Autin, M. Chanel, J. Gareyte, R. Garoby, M. Giovannozzi, H. Haseroth, M. Martini, E. Metral, D. Möhl, K. Schindl, H. Schönauer, I. Hofmann, C. Prior, G. Rees, S. Koscielniak:
Design of a 2.2 GeV Accumulator and Compressor for a Neutrino Factory
EPAC 2000, p. 921, CERN, Geneva 2000
(eds.: J.-L. Laclare, W. Mitaroff, Ch. Petit-Jean-Genaz, J. Poole, M. Regler) '7th Europ. Part. Acc. Conf.', Vienna, Austria, June 26-30, 2000

Chulkov, L.V.; O.V. Bochkarev, D. Cortina-Gil, H. Geissel, M. Hellström, M. Ivanov, R. Janik, K. Kimura, T. Kobayashi, A.A. Korsheninnikov, G. Münzenberg, F. Nickel, A.A. Ogloblin, A. Ozawa, M. Pfützner, V.N. Pribora, M.V. Rozhkov, H. Simon, B. Sitár, P. Strmen, K. Sümmerer, T. Suzuki, I. Tanihata, M. Winkler, K. Yoshida:
Total Charge-Changing Cross Sections for Neutron-Rich Light Nuclei
Nucl. Phys. A674, 330 (2000)

Conjusteau, A. ; C. Callegari, I. Reinhard, K.K. Lehmann, G. Scoles :
Microwave Spectra of HCN and DCN in ^{4}He Nanodroplets: A Test of Adiabatic Following
J. Chem. Phys. 113, 4840 (2000)

Crochet, P.; N. Herrmann, K. Winiewski, Y. Leifels, A. Andronic, R. Averbeck, A. Devismes, C. Finck, A. Gobbi, O.Hartmann, K.D. Hildenbrand, P. Koczon, T. Kress, R. Kutsche, W. Reisdorf, D. Schüll, J.P. Alard, V. Barret, Z. Basrak, N. Bastid, I. Belyaev, A. Bendarag, G. Berek, R. Caplar, N. Cindro, P. Dupieux, M. Dzelalija, M. Eskef, Z. Fodor, Y. Grishkin, B. Hong, J. Kecskemeti, Y. J. Kim, M. Kirejczyk, M. Korolija, R. Kotte, M. Kowalczyk, A. Lebedev, K.S. Lee, V. Manko, H. Merlitz, S. Mohren, D. Moisa, W. Neubert, A. Nianine, D. Pelte, M. Petrovici, C. Plettner, F. Rami, B. de Schauenburg, Z. Seres, B. Sikora, K.S. Sim, V. Simion, K. Siwek-Wilczyska, V. Smolyankin, A. Somov, M. Stockmeier, G. Stoicea, M. Vasiliev, P. Wagner, D. Wohlfarth, J.T. Yang, I. Yushmanov, A. Zhilin (FOPI Collaboration):
Sideward Flow of K^+ Mesons in Ru+Ru and Ni+Ni Reactions near Threshold
Phys. Lett. B486, 6 (2000)

Cub, J.; C. Grund, D. Pansegrau, G. Schrieder, H. Stelzer:
A Position Sensitive Parallel Plate Avalanche Counter for Single Particle and Current Readout
Nucl. Instr. and Meth. in Phys. Res.A453,522(2000)

Daugas, J. M.; R. Grzywacz, M. Lewitowicz, L. Achouri, J.C. Angélique, D. Baiborodin, K. Bennaceur, R. Bentida, R. Béraud, C. Borcea, C. Bingham, W.N. Catford, A. Emsallem, G. de France, H. Grawe, K.L. Jones, R.C. Lemmon, M.J. Lopez Jimenez, F. Nowacki, F. de Oliveira Santos, M. Pfützner, P.H. Regan, K. Rykaczewski,

Publications

J.E. Sauvestre, M. Sawicka, G. Sletten, M. Stanoiu:
The 8^+ Isomer in ^{78}Zn and the Doubly Magic Character of ^{78}Ni
Phys. Lett. B476, 213 (2000)

Dauvergne, D.; M. Chevallier, C. Cohen, N. Cue, J. Dural, R. Kirsch, A. L'Hoir, D. Lelievre, P.H. Mokler, J.-C. Poizat, H.-T. Prinz, J.-M. Ramillon, J. Remillieux, P. Roussel-Chomaz, J.-P. Rozet, F. Sanuy, D. Schmaus, C. Stephan, M. Toulemonde, D. Vernhet, A. Warczak:
X-Rays and Inner-Shell Processes with Heavy Ions Channeled in Thin Crystals
X-Rays and Inner-Shell Processes, AIP-CP 506, 418 (2000)

Denisov, V.Y.:
Subbarrier Heavy Ion Fusion Enhanced by Nucleon Transfer
Eur. Phys. J. A7, 87 (2000)

Denisov, V.Yu.; S. Hofmann:
Production of Superheavy Elements in Cold Fusion Reactions
Acta Phys. Pol. B31, 479 (2000)

Denisov, V.Yu.; S. Hofmann:
Formation of Superheavy Elements in Cold Fusion Reactions
Phys. Rev. C61, 034606 (2000)

Deutsch, C.; I. Hofmann:
Intense Ion Beams for Inertial Fusion
C.R. Acad. Sci. Paris, 1, Serie IV, 751 (2000)

Devismes, A. (for the FOPI Collaboration):
Results from FOPI on Strangeness Production and Propagation in Hot and Dense Nuclear Matter
in: Hadrons in Dense Matter, p.104, GSI Darmstadt, ISSN 0720-8715
(Proc. of the 'Int. Workshop XXVIII on Gross Properties of Nuclei and Nuclear Excitations', Hirschegg, Austria, Jan. 2000) (eds.: M. Buballa, W. Nörenberg, B.-J. Schäfer, J. Wambach)

Dilling, J.; D. Ackermann, J. Bernard, F.P. Hessberger, S. Hofmann, W. Hornung, H.J. Kluge, E. Lamour, M. Maier, R. Mann, G. Marx, R.B. Moore, G. Münzenberg, W. Quint, D. Rodriguez, M. Schädel, J. Schönfelder, G. Sikler, C. Toader, L. Vermeeren, C. Weber, G. Bollen, O. Engels, D. Habs, P. Thirolf, H. Backe, A. Drezke, W. Lauth, W. Ludolphs, M.T.S.C. Sewtz:
The SHIPTRAP Project: A Capture and Storage Facility at GSI for Heavy Radionuclides from SHIP
Hyperfine Interactions 127, 491 (2000)

Dobrev, D.; Vetter, J.; Angert, N.; Neumann, R.:
Periodic Reverse Current Electrodeposition of Gold in an Ultrasonic Field Using Ion-Track Membranes as Templates: Growth of Gold Single-Crystals
Electrochimica Acta 45, 3117 (2000)

Döring, J.; Y.A. Akovali, C. Baktash, F.E. Durham, C.J. Gross, P.F. Hua, G.D. Johns, M. Korolija, D.R. LaFosse, I. Y. Lee, A.O. Macchiavelli, W. Rathbun, D.G. Sarantites, D.W. Stravener, G.Z. Solomon, S.L. Tabor, A. Vander Molen, A.V. Afanasjev, I. Ragnarsson:
Band Terminations in the Valence Space of ^{86}Zr
Phys. Rev. C61, 034310 (2000)

Döring, J.; C. Plettner, M. Axiotis, R Borcea, J. Eberth, A. Gadea, M. Gorska, H. Grawe, Z. Janas, R. Kirchner, M. La Commara, C. Mazzocchi, E. Nacher Gonzales, A. Plochocki, E. Roeckl, K. Schmidt, R. Schwengner, T. Steinhardt, J. Zylicz:
Beta-Decay Study of the N=Z Odd-Odd Nuclei ^{62}Ga and ^{70}Br
LUIP 0003, Sweden, p.131 (2000),ISSN 0348-9329
eds: D. Rudolph, M. Hellström
(Proc. of the 'Int. Workshop on N=Z Nuclei (PINGST 2000), Lund, Sweden, 06.-10.06.2000)

Dolinskii, A.; H. Eickhoff, B. Franczak:
The Synchrotron of the Dedicated Ion Beam Facility for Cancer Therapy, Proposed for the Clinic in Heidelberg
EPAC 2000, p. 2509, CERN, Geneva 2000
(eds.: J.-L. Laclare, W. Mitaroff, Ch. Petit-Jean-Genaz, J. Poole, M. Regler) '7th Europ. Part. Acc. Conf.', Vienna, Austria, June 26-30, 2000

Eichler, R.; W. Brüchle, R. Dressler, Ch.E. Düllmann, B. Eichler, H.W. Gäggeler, K.E. Gregorich, D.C. Hoffman, S: Hübener, D.T. Jost, U.W. Kirbach, C.A. Laue, V.M. Lavanchy, H. Nitsche, J.B. Patin, D. Piquet, M.M. Schädel, D.A. Shaughnessy, D.A. Strellis, S. Taut, L. Tobler, Y.S. Tsyganov, A. Türler, A. Vahle, P.A. Wilk, A.B. Yakushev:
Chemical Characterization of Bohrium (Element 107)
Nature 407, 63 (2000)

Publications

Eickhoff, H.; D. Böhne, Th. Haberer, B. Schlitt, P. Spiller, J. Debus, A. Dolinskii:
The Proposed Dedicated Ion Beam Facility for Cancer Therapy at the Clinic in Heidelberg
EPAC 2000, p. 25152, CERN, Geneva 2000 (eds.: J.-L. Laclare, W. Mitaroff, Ch. Petit-Jean-Genaz, J. Poole, M. Regler) '7th Europ. Part. Acc. Conf.', Vienna, Austria, June 26-30, 2000

Emling, H.:
Double Phonen Giant Resonances in Nuclei
in: Quasipart. and Photon Excit. in Nuclei, World Scie. Publ., 2000, eds. N. Dinh Dang, A. Arima)

Fahlander, C.; M. Palacz, D. Rudolph, D. Sohler, J. Blomqvist, J. Kownacki, L.O. Norlin, J. Nyberg, A. Algora, C. Andreoiu, G. deAngelis, A. Atac, D. Bazzacco, L. Berglund, T. Bäck, J. Cederkäll, B. Cederwall, Zs. Dombradi, B. Fant, E. Farnea, A. Gadea, M. Gorska, H. Grawe, N. Hashimoto-Saitoh, A. Johnson, A. Kerek, W. Klamra, K. Lagergren, S.M. Lenzi, A. Likar, M. Lipoglavsek, M. Moszynski, D. Napoli, C. Rossi-Alvarez, H. Roth, T. Saitoh, D. Seweryniak, Ö. Skeppstedt, M. Weiszflog, M. Wolinska :
The $g_{7/2}$ and $d_{5/2}$ Single-Particle Energies with Respect to ^{100}Sn Determined from Excited States in ^{103}Sn
LUIP 0003, Sweden, p. 34 (2000), ISSN 0348-9329
eds: D. Rudolph, M. Hellström
(Proc. of the 'Int. Workshop on N=Z Nuclei (PINGST 2000), Lund, Sweden, 06.-10.06.2000)

Falch, M.; K.E.G. Löbner, Th. Kerscher, F. Attallah, F. Bosch, B. Franzke, H. Geissel, M. Hausmann, O. Klepper, H.-J. Kluge, C. Kozhuharov, G. Münzenberg, F. Nolden, Y. Novikov, Z. Patyk, T. Radon, C. Scheindenberger, M. Steck, M. Winkler, H. Wollnik:
Schottky Mass Spectrometry at the ESR with a New Data Acquisition System
AIP Conference Proc. 512, p. 263 (2000)
eds.: H.-O. Meyer, P. Schwandt
(Proc. of the 4th Int. Conf. STORI99, Bloomington, USA, Sept. 12-16, 1999)

Feili, D.; Ph. Bosselmann, K.-H. Schartner, F. Folkmann, A.E. Livingston, E. Träbert, X. Ma, P. H. Mokler:
Measurements of the $2s^2S_{1/2} - 2p^2P_{1/2}$ Transition Energies in Lithium-Like Ions: III. Experimental Results for Sn^{47+} and Xe^{51+}
Phys. Rev. A64, 022501 (2000)

Fischer, B. ; S. Metzger:
Single-Ion Micromechanics
MRS Bulletin 25, 39 (2000)

Fornal, B.; R. Broda, W. Królas, T. Pawlat, J. Wrzesinski, D. Bazzacco, S. Lunardi, C. Rossi Alvarez, G. Viesti, G. de Angelis, M. Cinausero, D. Napoli, J. Gerl, E. Caurier, F. Nowacki:
New States in ^{44,46}Ar Isotopes from Deep-Inelastic Heavy Ion Reaction Studies
Eur. Phys. J. A7, 147 (2000)

Franchetti, G.; I. Hofmann, G. Rumolo:
Effect of Space Charge on Bunch Compression near the Transition
Phys. Rev. ST Accel. Beams, 3, 084201 (2000)

Franchetti, G.; I. Hofmann:
Optimizing Multiturn Injection with Space Charge and Linear Coupling
EPAC 2000, p. 1292, CERN, Geneva 2000 (eds.: J.-L. Laclare, W. Mitaroff, Ch. Petit-Jean-Genaz, J. Poole, M. Regler) '7th Europ. Part. Acc. Conf.', Vienna, Austria, June 26-30, 2000

Franzke, B.; K. Beckert, F. Nolden, P. Beller, M. Steck, A. Dolinskii:
Efficient Collection and Cooling of Radioactive Ion Beams in a Collector Ring (CR)
EPAC 2000, p. 536, CERN, Geneva 2000 (eds.: J.-L. Laclare, W. Mitaroff, Ch. Petit-Jean-Genaz, J. Poole, M. Regler) '7th Europ. Part. Acc. Conf.', Vienna, Austria, June 26-30, 2000

Friman, B.; M. Lutz, G. Wolf:
From Meson-Nucleon Scattering to Vector Mesons in Nuclear Matter
in: Hadrons in Dense Matter, p.161, GSI Darmstadt, ISSN 0720-8715
(Proc. of the 'Int. Workshop XXVIII on Gross Properties of Nuclei and Nuclear Excitations', Hirschegg, Austria, Jan. 2000) (eds.: M. Buballa, W. Nörenberg, B.-J. Schäfer, J. Wambach)

Publications

Fritzsche, S., Th. Stöhlker, O. Brinzanescu, B. Fricke:
Formation of Excited States in High-Z Helium-Like Systems
Hyperfine Interactions 127, 257 (2000)

Funk, U. N.; R. Bock, M. Geißel, D.H.H. Hoffmann, U. Neuner, F.B. Rosmej, M. Stetter, S. Stöwe, N.A. Tahir, A. Tauschwitz:
Interaction Experiments with Intense Heavy Ion Beams Using Solid State Targets
J. Phys. IV France 10, Pr5, 215 (2000)

Gadea, A.; S.M. Lenzi, D.R. Napoli, C.A. Ur, G. Martinez-Pinedo, M. Gorska, E. Caurier, M. Axiotis, G. de Angelis, F. Brandolini, D. Cano-Ott, E. Farnea, E. Nacher, B. Rubio, J. L. Tain, R. Borcea, J. Döring, H. Grawe, Z. Janas, R. Kirchner, M. La Commara, C. Mazzocchi, E. Roeckl, K. Schmidt, C. Fahlander, M. Hellström, L. Batist, A. Plochocki, J. Zylicz, C. Plettner, R. Schwengner:
γ and β Decay of the 12^+ Yrast Trap in ^{52}Fe
LUIP 0003, Sweden, p.118 (2000),ISSN 0348-9329
eds: D. Rudolph, M. Hellström
(Proc. of the 'Int. Workshop on N=Z Nuclei (PINGST 2000), Lund, Sweden, 06.-10.06.2000)

Gazdzicki, M.; C. Markert:
Production and Measurement of D-Mesons in Nucleus-Nucleus Collisions at the CERN SPS
Acta Phys. Pol. B31, 965 (2000)

Geissel, H.; H. Gilg, A. Gillitzer, R. S. Hayano, S. Hirenzaki, K. Itahashi, M. Iwasaki, P. Kienle, M. Münch, G. Münzenberg, W. Schott, K. Suzuki, D. Tomono, H. Weick, T. Yamazaki, T. Yoneyama:
Observation of Well-Resolved 1s and 2pπ States in Pb by High Resolution (d, ^{3}He) Spectroscopy
Nucl. Phys. A663-6643, 206 (2000)
(Proc. of the '15th Int. Conf. on Particle and Nuclei (PANIC '99)', Uppsala, Sweden)

Gerl, J.:
High-Resolution Detectors in Nuclear Spectroscopy
Nucl. Instr. and Meth. in Phys. Res.A442,238(2000)

Giardina, G.; S. Hofmann, A.I. Muminov, A.K. Nasirov:
Effect of the Entrance Channel on the Synthesis of Superheavy Elements
Eur. Phys. J. A8, 205,(2000)

Gillitzer, A.; H. Geissel, H. Gilg, R.S. Hayano, S. Hirenzaki, K. Itahashi, M. Iwasaki, P. Kienle, M. Münch, G. Münzenberg, W. Schott, K. Suzuki, D. Tomono, H. Weick, T. Yamazaki, T. Yoneyama:
Observation of Well Resolved 1s and 2p π^- States in Pb by High Resolution (d, ^{3}He) Spectroscopy
Nucl. Phys. A663-664, 206c (2000)
(Proc. of the '15th Int. Conf. on Particle and Nuclei (PANIC '99)', Uppsala, Sweden, June 1999)

Götte, S.; A. Goplan, J. Bömmels, M.-W. Ruf, R. Hotop:
A Triply Differentially Pumped Supersonic Beam Target for High-Resolution Collision Studies
Rev. Sci. Instr. 71, 4079 (2000)

Gourio, D.; D. Ardouin, M. Assenard, G. Auger, Ch.O. Bacri, N. Bellaize, A. Benkirane, J. Benlliure, B. Berthier, E. Bisquer, B. Borderie, R. Bougault, P. Box, R. Brou, J.L. Charvet, A. Chbihi, J. Colin, D. Cussol, R. Dayras, E. De Filippo, A. Demeyer, C. Donnet, D. Durand, P. Ecomard, P. Eudes, M. Germain, D. Guinet, L. Lakehal-Ayat, P. Lautesse, J.L. Laville, L. Lebreton, C. Le Brun, J.F. Lecolley, T. Lefort, A. Lefèvre, R. Legrain, N. Le Neindre, O. Lopez, M. Louvel, N. Marie, V. Métivier, L. Nalpas, A. Ouatizerga, M. Parlog, J. Péter, E. Plagnol, E. Pollaco, A. Rahmani, R. Régimbart, T. Reposeur, M.F. Rivet, E. Rosato, F. Saint-Laurent, S. Salou, M. Squalli, J.C. Steckmeyer, G. Tabacaru, B. Tamain, L. Tassan-Got, E. Vient, C. Volant, J.P. Wieleczko, A. Wieloch, K. Yuasa-Nakagawa:
Emission Time Scale of Light Particles in the System Xe+Sn at 50 AMeV. A Probe for Dynamical Emission
Eur. Phys. J. A7, 245 (2000)

Gudowska-Novak, E.; S. Ritter, G. Taucher-Scholz, G. Kraft:
Compound Poisson Processes and Clustered Damage of Radiation Induced DNA Double Strand Breaks
Acta Phys. Pol. B 31, 1109 (2000)

Häffner, H.; T. Beier, N. Hermanspahn, H.-J. Kluge, W. Quint, S. Stahl, J. Verdu, G. Werth:
High-Accuracy Measurement of the Magnetic Moment Anomaly of the Electron Bound in Hydrogenlike Carbon
Phys. Rev. Lett. 85, 5308 (2000)

Publications

Hasse, R.W.:
Coulomb Order in a Storage Ring
J. Phys. IV 19, Pr5-149 (2000)
(Proc. 1999 Int. Conf. on 'Strongly Coupled Coulomb Syst.', St. Malo, France, Sept. 4-10, 1999)

Hasse, R.W.; ; M. Steck:
Ordered Ion Beams
EPAC 2000, p. 274, CERN, Geneva 2000
(eds.: J.-L. Laclare, W. Mitaroff, Ch. Petit-Jean-Genaz, J. Poole, M. Regler) '7th Europ. Part. Acc. Conf.', Vienna, Austria, June 26-30, 2000

Hasse, R.W. :
Theoretical Verification of Coulomb Strings of Ions
EPAC 2000, p. 1241, CERN, Geneva 2000
(eds.: J.-L. Laclare, W. Mitaroff, Ch. Petit-Jean-Genaz, J. Poole, M. Regler) '7th Europ. Part. Acc. Conf.', Vienna, Austria, June 26-30, 2000

Hasse, R.W.:
Ordnung im Ionenstrahl
Physikal. Blätter 56, 73 (2000)

Hatchett, S.P.; C.G. Brown, T.E. Cowan, E.A. Henry, J.S. Johnson, M.H. Key, J.A. Koch, A.B. Langdon, B.F. Lasinski, R.W. Lee, A.J. Mackinnon, D.M. Pennington, M.D. Perry, T. W. Phillips, M. Roth, T.C. Sangster, M.S. Singh, R.A. Snavely, M.A. Stoyer, S.C. Wilks, K. Yasuike:
Electron, Photon, and Ion Beams from the Relativistic Interaction of Petawatt Laser Pulses with Solid Tragets
Phys. of Plasmas, 7/52, 2076 (2000)

Hausmann, M.; F. Attallah, K. Beckert, F. Bosch, A. Dolinskiy, H. Eickhoff, M. Falch, B. Franczak, B. Franzke, H. Geissel, Th. Kerscher, O. Klepper, H. -J. Kluge, C. Kozhuharov, K. E. G. Löbner, G. Münzenberg, F. Nolden, Yu. N. Novikov, T. Radon, H. Schatz, C. Scheidenberger, J. Stadlmann, M. Steck, T. Winkler, H. Wollnik:
First Isochronous Mass Spectrometry at the Experimental Storage Ring ESR
Nucl. Instr. and Meth. in Phys. Res.A446,569(2000)

Hees, H.van; J. Knoll:
Finite Pion Width Effects on the Rho-Meson and Di-Lepton Spectra
in: Hadrons in Dense Matter, p.177, GSI Darmstadt, ISSN 0720-8715
(Proc. of the 'Int. Workshop XXVIII on Gross Properties of Nuclei and Nuclear Excitations', Hirschegg, Austria, Jan. 2000) (eds.: M. Buballa, W. Nörenberg, B.-J. Schäfer, J. Wambach)

Heinz, A.; E. Berdermann, F. Heine, O. Joeres, P. Kienle, I. Koenig, W. Koenig, C. Kozhuharov, U. Leinberger, M. Rhein, A. Schröter, H. Tsertos, The ORANGE Collaboration at GSI:
Positron Spectra from Internal Pair Conversion Observed in ^{238}U + ^{181}Ta Collisions
Eur. Phys. J. A9, 55 (2000)

Henning, W.:
Conference Summary
Nucl. Instr. and Meth. in Phys. Res.B172,951(2000)
(Proc. of the 8th. Int. Conf. on Accelerator Mass Spectroscopy, Vienna, Austria, Sept. 6-10, 1999)

Hermanspahn, N.; H. Häffner, H.J. Kluge, W. Quint, S. Stahl, J. Verdu, G. Werth:
Observation of the Continuous Stern-Gerlach Effect on an Electron Bound in an Atomic Ion
Phys. Rev. Lett. 84, 427 (2000)

Heßberger, F.P.; S. Hofmann, D. Ackermann, V. Ninov, M. Leino, S. Saro, A. Andreyev, A. Lavrentev, A.G. Popeko, A.V. Yeremin.:
Decay Properties of Neutron-Deficient Nuclei in the Region Z=86-92
Eur. Phys. J. A8, 521 (2000)

Heßberger, F.P.; S. Hofmann, D. Ackermann, P. Armbruster, B. Kindler, B. Lommel, G. Münzenberg, A.Yu. Lavrentev, A.G. Popeko, A.V. Yeremin, M. Leino, S. Saro, P. Cagarda:
GSI Experiments on the Synthesis of Superheavy Elements – Results and Plans for the Future
Fission and Properties of Neutron-Rich Nuclei, World Scientific, Singapore, p. 293 (2000), eds.: J.H. Hamilton, W.R. Philips, H.K. Carter
(Proc. 2nd Int. Conf. on Fission and Neutron-rich Nuclei, St. Andrews, UK, 28.06.-02.07.1999)

Herzberg, R.-D.; P.A. Butler, A.J. Chewter, G.D. Jones, R.D. Page, J.F.C. Cocks, O. Dorvaux, K. Helariutta, P.M. Jones, R. Julin, S. Juutinen, H. Kankaanpää, H. Kettunen, P. Kuusiniemi, M. Leino, M. Muikku, P.Nieminen, P. Rahkila, P. Reiter, A. Savelius, W.H. Trzaska, J. Gerl, F.P. Heßberger, Ch. Schlegel, H.-J. Wollersheim, F. Becker, M. Houry, W. Korten, R. Lucas, Y. Le Coz, Ch. Theisen, P. Reiter, T.L. Khoo, C.J. Lister, K. Eskola:

Publications

Gamma Spectroscopy of the Tranfermium Nucleus ^{254}No
Fission and Properties of Neutron-Rich Nuclei, World Scientific, Singapore, p. 196 (2000), eds.: J.H. Hamilton, W.R. Philips, H.K. Carter (Proc. 2nd Int. Conf. on Fission and Neutron-Rich Nuclei, St. Andrews, UK, 28.06.-02.07.1999)

Hoefman, M.; H.W. Wilschut, L. Aphecetche, J. Bacelar, H. Delagrange, J. Diaz, D. d' Enterria, M.J.van Goethem, R. Holzmann, H. Huisman, N. Kalantar-Nayestanaki, A. Kugler, H. Loehner, F.M. Marques, G. Martinez, J.G. Messendorp, R.W. Ostendorf, S. Schamand, R.H. Siemssen, R.S. Simon, Y. Schutz, R. Turrisis, M. Volkerts, V. Wagner
Coherent Bremsstrahlung and radiative Capture in the α+p System
Phys. Rev. Lett. 85, 1404 (2000)

Hoffknecht, A.; C. Brandau, T. Bartsch, C. Böhme, H. Knopp, S. Schippers, A .Müller, C. Kozhuharov, K. Beckert, F. Bosch, B. Franzke, A. Krämer, P.H. Mokler, F. Nolden, M. Steck, Th. Stöhlker, Z. Stachura:
Recombination of Bare Bi^{83+} Ions with Electrons
Phys. Rev. A63, 012702 (2000)

Hoffmann, D.H.H.; R. Bock, A.Y. Faenov, U. Funk, M. Geissel, U. Neuner, T. A. Pikuz, F. Rosmej, M. Roth, W. Süß, N. Tahir, A. Tauschwitz:
Plasma Physics with Intense Laser and Ion Beams
Nucl. Instr.+Meth. in Phys. Res.B161-163, 9 (2000)

Hofmann, S.; G. Münzenberg:
The Discovery of Superheavy Elements in Cold Fusion Reactions
Rev. Mod. Phys. 72, 733 (2000)

Hu, Z.; L. Batist, J. Agrammunt, A. Algora, B.A. Brown, D. Cano-Ott, R. Collatz, A. Gadea, M. Gierlik, M. Gorska, H. Grawe, M. Hellström, Z. Janas, M. Karny, R. Kirchner, F. Moroz, A. Plochocki, M. Rejmund, E. Roeckl, B. Rubio, M. Shibata, J. Szerypo, J. L. Tain, V. Wittmann:
Beta Decay of ^{98}Ag: Evidence for the Gamov-Teller Resonance near ^{100}Sn
Phys. Rev. C62, 064315 (2000)

Ilievki, S.; O. Dersch, S. Kinkel, J. Maldener,A. Zouine, F. Rauch, R. Haspel, F.W. Kramer: :
Practical IR Extinction Coefficients for Water in Commercial Glasses Determined by Nuclear Reaction Analysis
Glass Science and Technology-73, 39 (2000)

Ivanov, Yu.B.; J. Knoll, D.N. Voskresensky:
Resonance Transport and Kinetic Entropy
Nucl. Phys. A672, 313 (2000)

Jäckel, O.; G.H. Hartmann, P. Heeg, D. Schardt:
Effective Point of Measurement of Cylindrical Ionization Chambers for Heavy Charged Particles
Phys. Med. Biol. 45, 599 (2000)

Janas, Z.; L. Batist, B.A. Brown, Z. Hu, M. Karny, E. Roeckl, TAS Collaboration et al.:
Gamow-Teller Decay of Neutron-Deficient Nuclei
LUIP 0003, Sweden, p. 99 (2000), ISSN 0348-9329 eds: D. Rudolph, M. Hellström (Proc. of the 'Int. Workshop on N=Z Nuclei (PINGST 2000), Lund, Sweden, 06.-10.06.2000)

Janik, R.A.; M.A. Nowak, G. Papp, I. Zahed:
Chiral Disorder in Two-Order QCD with Abelian External Fluxes
Nucl. Phys. - Proc. Suppl. B83, 977 (2000)

Jurado, B.; K.H. Schmidt, F. Farget, T. Enqvist, F. Ameil, P. Armbruster, J. Benlliure, M. Bernas, B. Mustapha, L. Tassan-Got, C. Stephan, A. Boudard, S. Leray, R. Legrain, C. Volant, S. Czajkowski, M. Pravikoff:
Projectile Fragmentation at Relativistic Energies: A Possibility to Determine the Viscosity of Nuclear Matter
Acta Phys. Pol. B31, 367 (2000)

Klepper, O.; Ch. Kozhuharov:
Particle Detectors for Beam Diagnostics and for Experiments with Stable and Radioactive Ions in the Storage Ring (ESR)
AIP Conf. Proc. 512, 269 (2000)
(Proc. of the 'Int. Conf. on Nucl. Physics at Storage Rings (STORI '99)', Bloomington, USA, 1999)

Knoll, J.:
Finite Pion Width Effects on the Rho Meson
Nucl. Phys. A683, 369 (2000)

Publications

Knoll, J.; H. van Hees:
Finite Pions Width Effects on the Rho Meson and Di-Lepton Spectra
in: Hadrons in Dense Matter, p. 177 (2000)
eds.: M. Buballa, W. Nörenberg, B.-J. Schäfer, J. Wambach,
(Proc. of the Int. Workshop XXVIII on Gross Properties of Nuclei and Nuclear Excitation, Hirschegg, Austria, Jan. 16-22, 2000)

Knoll, J.:
Soft Modes, Quantum Transport and Kinetic Antropy
in: Progress in Nonequillibrium Green's Funtions, World Scientific Publ. Co., p. 310 (2000)
(Kadanoff-Baym Workshop, Rostock, Germany, Oct. 20-24, 1999)

Knoll, J.:
Resonances Transport and Kinetic Entropy
Nucl. Phys. A672, 313 (2000)

Krämer, M.; O. Jäkel, T. Haberer, G. Kraft, D. Schardt, U. Weber:
Treatment Planning for Heavy-Ion Radiotherapy: Physical Beam Model and Dose Optimization
Phys. Med. Biol., 45/11, 3299 (2000)

Krämer, M.; M. Scholz:
Treatment Planning for Heavy-Ion Radiotherapy: Calculation and Optimization of Biologically Effective Dose
Phys. Med. Biol., 45/11, 3319 (2000)

Kraft, G.:
Tumortherapy with Ion Beams
Nucl. Instr. and Meth. in Phys. Res. A454, 1 (2000)

Kraft, G.:
Tumor Therapy with Heavy Charged Particles
Progr. in Part. and Nucl. Phys. 45, S473 (2000)

Kühl, T.:
PHELIX – ein Petawatt-Hoch-Energie-Laser
Phys. Bl. 5, 49 (2000)

Kühl, T.:
Positronen auf dem Labortisch
Phys. Bl. 12, 6 (2000)

Labzowsky, L.N.; A.V. Nefiodov, G. Plunien, G. Soff, D. Liesen:
Hyperfine Structure of Highly Charged $^{238}U_{92}$ Ions with Rotationally Excited Nuclei
Phys. Rev. Lett., 84, 851 (2000)

La Commara, M.; J. Gomez del Campo, A. D'Onofrio et al, A. Gadea, M. Glogowski, P. Jarillo-Herrero, N. Belcari, R. Borcea, G. de Angelis, C. Fahlander, M. Górska, H. Grawe, M. Hellström, R. Kirchner, M. Rejmund, V. Roca, E. Roeckl, M. Romano, K. Rykaczewski, K. Schmidt, F. Terrasi:
Production of Very Neutron-Deficient Isotopes near ^{100}Sn via Reactions Involving Light-Particle and Cluster Emission
Nucl. Phys. A6689, 43 (2000)

Laue, F.; C. Sturm, I. Böttcher, M. Debowski, A. Förster, E. Grosse, P. Koczon, B. Kohlmeyer, M. Mang, L. Naumann, H. Oeschler, F. Pühlhofer, E. Schwab, P. Senger, Y. Shin, J. Speer, H. Ströbele, G. Surowka, F. Uhlig, A. Wagner, W. Walus:
Production of Charged Pions, Kaons and Antikaons in Relativistic C+C and C+Au Collisions
Eur. Phys. J. A9, 397 (2000)

Lenzi, S.M.; N. Marginean, D.R. Napoli, C.A. Ur, D. Tonev, A. Poves, J. Sanchez-Solano, A.P. Zuker, A. Algora, M. Axiotis, D. Bazzacco, M.A. Bentley, P.G. Bizzeti, A. Bizzeti-Sona, F. Brandolini, J.A. Cameron, C. Chandler, G. deAngelis, M. De Poli, A. Dewals, E. Farnea, A. Gadea, J. Garces-Narro, W. Gelletley, H. Grawe, D.T. Joss, C. Kalfas, T. Lampman, S. Lunardi, T. Martinez, R. Menegazzo, P. Pavan, Zs. Podolyak, R.V. Ribas, C. Rossi Alvarez, B. Rubio, P. Spolaore, P. von Brentano, W. von Oertzen, N-Wall Collaboration:
Isobaric Analogue Rotational Bands in T=1, A=50 Mirror Nuclei
LUIP 0003, Sweden, p.240 (2000),ISSN 0348-9329
eds: D. Rudolph, M. Hellström
(Proc. of the 'Int. Workshop on N=Z Nuclei (PINGST 2000), Lund, Sweden, 06.-10.06.2000)

Ludziejewski, T.,; Th. Stöhlker, D.C. Ionescu, P. Rymuza, H. Beyer, F. Bosch, C. Kozhuharov, A. Krämer, D. Liesen, P.H. Mokler, Z. Stachura, P. Swiat, A. Warczak, R.W. Dunford:
Simultaneous Excitation and Ionization of He-Like Uranium Ions in Relativistic Collisions with Gaseous Targets
Phys. Rev. A61, 052706-1(2000)

Publications

Lutz, M.:
Chiral Dynamics of Nuclear Saturation
Nucl. Phys. A670, 214c (2000)
(Proc. of 'Int. Symp. on Physics of Hadrons and Nuclei', Tokyo, Japan, Dec. 1998)

Lutz, M; B. Friman, C. Appel:
Saturation from Nuclear Pion Dynamics
Phys. Lett. B474, 7 (2000)

Lutz, M.F.M.; E.E. Kolomeitsev:
Effective Chiral Theory of Kaon-Nucleon Scattering
in: Hadrons in Dense Matter, p.117, GSI Darmstadt, ISSN 0720-8715
(Proc. of the 'Int. Workshop XXVIII on Gross Properties of Nuclei and Nuclear Excitations', Hirschegg, Austria, Jan. 2000) (eds.: M. Buballa, W. Nörenberg, B.-J. Schäfer, J. Wambach)

Matulewicz, T.; L. Aphecetche, Y. Charbonnier, H. Delagrange, K.K. Gudima, G. Martinez, M. Ploszajcak, Y. Schutz, V.D. Toneev, M. Appenheimer, R. Averbeck, J. Diaz, A. Döppenschmidt, M.J. van Goethem, S. Hlavac, M. Hoefman, R. Holzmann, A. Kugler, H. Löhner, A. Martin, V. Metag, R. Novotny, R.W. Ostendorf, R.H. Siemssen, R.S. Somin, R. Stratmann, H. Ströher, P. Tlusty, P.H. Vogt, V. Wagner, J. Weiss, H.W. Wilschut, F. Wissmann, A. Wolf, M. Wolf:
Observation of $\Delta^+ \rightarrow p\,\pi^0$ Decay in Heavy-Ion Collisions
Eur. Phys. Lett. A9, 69 (2000)

Mazzocchi, C.; L. Batist, Y. Belleguic, C. Bingham, R. Borcea, J. Döring, S. Galanoupoulos, M. Gierlik, M. Gorska, H. Grawe, S. Harissopoulos, M. Hellström, Z. Janas, M. Karny, R. Kirchner, G. Kriembardis, M. La Commara, A. Ostrowski, G. Rainowski, E. Roeckl, K. Schmidt:
Decay Properties of N≅ Z Nuclei Below ^{100}Sn
LUIP 0003, Sweden, p. 29 (2000), ISSN 0348-9329
eds: D. Rudolph, M. Hellström
(Proc. of the 'Int. Workshop on N=Z Nuclei (PINGST 2000), Lund, Sweden, 06.-10.06.2000)

Menzel, M.; I. Böttcher, M. Debowski, A. Förster, E. Grosse, P. Koczon, B. Kohlmeyer, F. Laue, L. Naumann, H. Oeschler, F. Pühlhofer, E. Schwab, P. Senger, Y. Shin, H. Ströbele, C. Sturm, G. Surowka, F. Uhlig, A. Wagner, W. Walus:
First Measurement of Antikaon Phase-Space Distributions in Nucleus-Nucleus Collisions at Subthreshold Beam Energies
Phys. Lett. B495, 26 (2000)

Mergel, V.; R. Dörner, M. Achler, Kh. Khayyat, S. Lencinas, J. Euler, O. Jagutzki, S. Nüttgens, M. Unverzagt, L. Spielberger, W. Wu, R. Ali, J. Ullrich, H. Cederquist, A. Salin, C.J. Wood, R.E. Olson, Dz. Belkic, C.L. Cocke, H. Schmidt-Böcking:
Intra-Atomic Electron-Electron-Scattering in p-He Collisions (Thomas Process) Investigated by Cold Target Recoil Ion Momentum Spectroscopy
Phys. Rev. Lett. 79, 387 (2000)

Messchendorp, J.G.; J.C.S. Bacelar, M.J. van Goethem, M.N. Harakeh, M. Hoefman, H. Huisman, N. Kalantar-Nayestanaki, H. Löhner, R. W. Ostendorf, S. Schadmand, R. Turrisi, M. Volkerts, H. W. Wilschut, R. S. Simon:
Virtual Bremsstrahlung in Proton-Proton Scattering below the Pion-Production Threshold
Phys. Rev. C61, 064007 (2000)

Meyer, V., S.N. Bagayev, P.E.G. Baird, P. Bakule, M.G. Boshier, A. Breitrück, S.L. Cornish, S. Dychkov, G.H. Eaton, A. Grossmann, D. Hübl, V.W. Hughes, K. Jungmann, I.C. Lane, Yi-Wei Liu, D. Lucas, Y. Matyugifl, J. Merkel, G. zu Purlitz, I. Reinhard, P.G.H. Sandars, R. Santra, P.V. Schmidt, C.S. Scott, W.T. Toner, M. Towrie, K. Träger, L. Willmann, V. Yakhontov:
Measurement of the 1s-2s Energy Interval in Muonium
Phys. Rev. Lett. 84, 1136 (2000)

Mokler, P.H.; A. Wolf:
The Physics of Highly Charged Ions – A Report on the IX Int. Conference "HCI-98", Bensheim
Comments on Modern Physics 2, D83-88 (2000)

Mokler, P.H.:
Relativistic Effects in Collisions of High-Z Ions
in: The Physics of Electronic and Atomic Collisions, AIP 500, p.463 (2000)
(eds.: Y. Itikawa et al.)

Müller, A.; C. Müller, R. Neumann, F. Ohnesorge:
Scanning Force Microscopy of Heavy-Ion Induced Damage in Lithium Fluoride Single-Crystals
Nucl.Instr.+Meth. in Phys.Res.B166/167,581(2000)
(Proc. of the '10th Int. Conf. on Radiation Effects in Insulators', Jena, Germany, 1999)

Publications

Müller, W.F.; B. Bruyneel, S. Franchoo, M. Huyse, J. Kurpeta, K. Kruglov, Y. Kudryavtsev, N.V.S.V. Prasad, R. Raabe, I. Reusen, P. Van Duppen, J. Van Roosbueck, L. Vermeeren, L. Weissman, Z. Janas, M. Karny, T. Kszczot, A. Plochocki, K.L. Kratz, B. Pfeiffer, H. Grawe, U. Köster, P. Thirolf, W.B. Walters:
Beta Decay of ^{66}Co, ^{68}Co and ^{70}Co
Phys. Rev. Lett., C61, 054308 (2000)

Münzenberg, G.; G. Schrieder:
Reaction Studies with Exotic Nuclei in Storage Rings
in: Nuclear Physics at Storage Rings, AIP, 293 (2000) (Eds.: H.-O. Meyer, P. Schwandt)

Nagaraja, H.S.; F. Ohnesorge, D.K. Avasthi, R. Neumann, O. Mohan Rao:
Scanning Force Microscopy of Ion-Irradiated Organic Single Crystals of Benzoyl Glycine
Appl. Phys. A71, 337 (2000)

Nayak, T.K.; M.M. Aggarwal, A. Agnihotri, Z. Ahammed, A.L.S. Angelis, V. Antonenko, V. Arefiev, V. Astakhov, V. Avdeitchikov, T.C. Awes, P.V.K.S. Baba, S.K. Badyal, A. Baldine, L. Barabach, C. Barlag, S. Bathe, B. Batiounia, T. Bernier, K.B. Bhalla, V.S. Bhatia, C. Blume, R. Bock, E.-M. Bohne, D. Bucher, A. Buijs, E.-J. Buis, H. Büsching, L. Carlen, V. Chalyshev, S. Chattopadhyay, K.E. Chenawi, R. Cherbatchev, T. Chujo, A. Claussen, A.C. Das, M.P. Decowski, V. Djordjadze, P. Donni, I. Doubovik, M.R. Dutta Majumdar, S. Eliseev, K. Enosawa, H. Feldmann, P. Foka, S. Fokin, V. Frolov, M.S. Ganti, S. Garpman, O. Gavrishchuk, F.J.M. Geurts, T.K. Ghosh, R. Glasow, S.K. Gupta, B. Guskov, H.A. Gustafsson, H. H. Gutbrod, R. Higuchi, I. Hrivnacova, M. Ippolitov, H. Kalechofsky, R. Kamermans, K.-H. Kampert, K. Karadjev, K. Karpio, S. Kato, S. Kees, H. Kim, B. W. Kolb, I. Kosarev, I. Koutcheryaev, A. Kugler, P. Kulinich, V. Kumar, M. Kurata, K. Kurita, N. Kuzmin, I. Langbein, A. Lebedev, Y.Y. Lee, H. Löhner, D.P. Mahapatra, V. Manko, M. Martin, A. Maximov, R. Mehdiyev, G. Mgebrichvili, Y. Miake, D. Mikhalev, G.C. Mishra, Y. Miyamoto, B. Mohanty, D. Morrison, D.S. Mukhopadhyay, V. Myalkovski, H. Naef, B.K. Nandi, S.K. Nayak, S. Neumaier, A. Nianine, V. Nikitine, S. Nikolaev, S. Nishimura, P. Nomokov, J. Nystrand, F.E. Obenshain, A. Oskarsson, I. Otterlund, M. Pachr, A. Parfenov, S. Pavliouk, T. Peitzmann, V. Petracek, F. Plasil, M. L. Purschke, B. Raeven, J. Rak, S. Raniwala, V. S. Ramamurthy, N. K. Rao, F. Retiere, K. Reygers, G. Roland, L. Rosselet, I. Roufanov, J. M. Rubio, S.S. Sambyal, R. Santo, S. Sato, H. Schlagheck, H.-R. Schmidt, G. Shabratova, I. Sibiriak, T. Siemiarczuk, B.C. Sinha, N. Slavine, K. Söderström, N. Solomey, S.P. Sørensen, P. Stankus, G. Stefanek, P. Steinberg, E. Stenlund, D. Stüken, M. Sumbera, T. Svensson, M.D. Trivedi, A. Tsvetkov, C. Twenhöfel, L. Tykarski, J. Urbahn, N. v. Eijndhoven, W.H. v. Heeringen, G.J. v. Nieuwenhuizen, A. Vinogradov, Y.P. Viyogi, A. Vodopianov, S. Vörös, M.A. Vos, B. Wyslouch, K. Yagi, Y. Yokota, G.R. Young (WA98 Coll.):
Search for Disoriented Chiral Condensates in 158 AGeV Pb+Pb Collisions
Nucl. Phys. A663-664, 745c (2000)
(Proc. of the '15th Int. Conf. on Particle and Nuclei (PANIC '99)', Uppsala, Sweden, June 1999)

Neuner, U.; R. Bock, M. Roth, P. Spiller, C. Constantin, U.N. Funk, M. Geissel, S. Hakuli, D.H.H. Hoffmann, J. Jacoby, A. Kozyreva, N.A. Tahir, S. Udrea, D. Varentsov, A. Tauschwitz:
Shaping of Intense Ion Beams into Hollow Cylindrical Form
Phys. Rev. Lett. 85, 4518 (2000)

Nishimura, S.; M.M. Aggarwal, A. Agnihotri, Z. Ahammed, A.L.S. Angelis, V. Antonenko, V. Arefiev, V. Astakhov, V. Avdeitchikov, T.C. Awes, P.V.K. S. Baba, S.K. Badyal, A. Baldine, L. Barabach, C. Barlag, S. Bathe, B. Batiounia, T. Bernier, K.B. Bhalla, V.S. Bhatia, C. Blume, R. Bock, E.-M. Bohne, Z. Böröcz, D. Bucher, A. Buijs, H. Büsching, L. Carlen, V. Chalyshev, S. Chattopadhyay, R. Cherbatchev, T. Chujo, A. Claussen, A.C. Das, M.P. Decowski, V. Djordjadze, P. Donni, I. Doubovik, S. Dutt, M. R. Dutta Majumdar, K. El Chenawi, S. Eliseev, K. Enosawa, P. Foka, S. Fokin, V. Frolov, M.S. Ganti, S. Garpman, O. Gavrishchuk, F.J.M. Geurts, T.K. Ghosh, R. Glasow, S.K. Gupta, B. Guskov, H.Å. Gustafsson, H.H. Gutbrod, R. Higuchi, I. Hrivnacova, M. Ippolitov, H. Kalechofsky, R. Kamermans, K.-H. Kampert, K. Karadjev, K. Karpio, S. Kato, S. Kees, H. Kim, B.W. Kolb, I. Kosarev, I. Koutcheryaev, T. Krümpel, A. Kugler, P. Kulinich, M. Kurata, K. Kurita, N. Kuzmin, I. Langbein, A. Lebedev,

Publications

Y.Y. Lee, H. Löhner, L. Luquin, D.P. Mahapatra, V. Manko, M. Martin, A. Maximov, R. Mehdiyev, G. Mgebrichvili, Y. Miake, D. Mikhalev, Md. F. Mir, G.C. Mishra, Y. Miyamoto, D. Morrison, D.S. Mukhopadhyay, V. Myalkovski, H. Naef, B.K. Nandi, S.K. Nayak, T.K. Nayak, S. Neumaier, A. Nianine, V. Nikitine, S. Nikolaev, P. Nilsson, S. Nishimura, P. Nomokonov, J. Nystrand, F.E.Obenshain, A. Oskarsson, I. Otterlund, M. Pachr, A. Parfenov, S. Pavliouk, T. Peitzmann, V. Petracek, F. Plasil, W. Pinanaud, M.L. Purschke, B. Raeven, J. Rak, R. Raniwala, S. Raniwala, V.S. Ramamurthy, N.K. Rao, F. Retiere, K. Reygers, G. Roland, L. Rosselet, I. Roufanov, C. Roy, J.M. Rubio, H. Sako, S.S. Sambyal, R. Santo, S. Sato, H. Schlagheck, H.-R. Schmidt, G. Shabratova, T.H. Shah, I. Sibiriak, T. Siemiarczuk, D. Silvermyr, B.C. Sinha, N. Slavine, K. Söderström, N. Solomey, S.P. Sørensen, P. Stankus, G. Stefanek, P. Steinberg, E. Stenlund, D. Stüken, M. Sumbera, T. Svensson, M.D. Trivedi, A. Tsvetkov, L. Tykarski, J. Urbahn, E.C. v. d. Pijll, N. v. Eijndhoven, G.J. v. Nieuwenhuizen, A. Vinogradov, Y.P. Viyogi, A. Vodopianov, S. Vörös, B. Wyslouch, K. Yagi, Y. Yokota and G.R. Young (WA98 Collaboration):
Collective Flow and HBT in Pb+Pb Collisions at the CERN SPS
Nucl. Phys. A663-664, 729c (2000)
(Proc. of the '15th Int. Conf. on Particle and Nuclei (PANIC '99)', Uppsala, Sweden, June 1999)

Nörenberg, W.; G. Papp, P. Rozmej
Stability and Instability of a Hot and Dilute Nuclear Droplet
Eur. Phys. J. A9, 327 (2000)

Nolden, F.; K. Beckert, F. Caspers, B. Franczak: B. Franzke, R. Menges, A. Schwinn, M. Steck:
Stochastic Cooling in the ESR
Nucl. Instr. and Meth. in Phys. Res.A441,219(2000)
(Proc. of the Workshop on 'Electron Cooling and Related Topics', Uppsala, Sweden, May 1999)

Odeh, T.; R. Bassini, M. Begemann-Blaich, S. Fritz, S.J. Gaff-Ejakov, D. Gourio, C. Groß, G. Imme, I. Iori, U. Kleinevoß, G.J. Kunde, W.D. Kunze, U. Lynen, V. Maddalena, M. Mahi, T. Möhlenkamp, A. Moroni, W.F.J. Müller, C. Nociforo, B. Ocker, F. Petruzzelli, J. Pochodzalla, G. Raciti, G. Riccobene, F.P. Romano, A. Saija, M. Schnittker, A. Schüttauf, C. Schwarz, W. Seide, V. Serfling, C. Sfienti, W. Trautmann, A. Trzinski, G. Verde, A. Wörner, Hongfei XI, B. Zwieglinski:
Fragment Kinetic Energies and Modes of Fragment Formation
Phys. Rev. Lett. 84, 4557 (2000)

Nolden, F.; K. Beckert, P. Beller, B. Franczak, B. Franzke, A. Schwinn, M. Steck, F. Caspers:
Fast Stochastic Cooling of Heavy Ions at the ESR Storage Ring
EPAC 2000, p. 1262, CERN, Geneva 2000
(eds.: J.-L. Laclare, W. Mitaroff, Ch. Petit-Jean-Genaz, J. Poole, M. Regler) '7th Europ. Part. Acc. Conf.', Vienna, Austria, June 26-30, 2000

Ohnesorge, F.:
Intricate Stepline Artifact can Mimic True Atomic Resolution in Atomic Force Microscopy
Phys. Rev. B 61, 5121 (2000)

Ohnesorge, F.; R. Neumann:
Scanning Force Microscopy Corrected for nm-Scale Sample Elasticity on Single Latent Heavy-Ion Tracks in Polymers
Eur. Phys. Lett. 50, 742 (2000)

Ohnesorge, F.; A. Müller, R. Neumann:
Scanning Force Microscopy in a Liquid on Single Latent Ion Tracks: Towards Applications in Polymers and Atomic Resolution on Crystals
Nucl.Instr.+Meth. in Phys.Res.B166/167,938(2000)
(Proc. of the '10th Int. Conf. on Radiation Effects in Insulators', Jena, Germany, 1999)

Ozawa, A.; O. Bochkarev, L. Chulkov, D. Cortina, H. Geissel, M. Hellström, M. Ivanov, R. Janik, K. Kimura, T. Kobayashi, A.A. Korsheninnikov, G. Münzenberg, F. Nickel, A.A. Ogloblin, M. Pfützner, V. Pribora, H. Simon, B. Sitar, P. Strmen, K. Sümmerer, T. Suzuki, I. Tanihata, M. Winkler, K. Yoshida:
Production Cross- Sections of Light Neutron-Rich Nuclei from ^{40}Ar Fragmentation at about 1 GeV/Nucleon
Nucl. Phys. A673, 411 (2000)

Patra, S.K.; W. Greiner, R.K. Gupta:
Shell Structure of Superheavy Nuclei
J. of Phys. G26, L65 (2000)

Pausch, G.; H. Prade, M. Sobiella, H. Schnare, R. Schwengner, L. Käubler, C. Borcan, H.-G. Ortlepp, U. Oehmichen, H. Grawe, R. Schubart, J. Gerl, J. Cederkäll, A. Johnson, A. Kerek,

Publications

W. Klamra, M. Moszynski, D. Wolski, M. Kapusta, A. Axelsson, M. Weiszflog, T. Härtlein, D. Pansegrau, G. de Angelis, S. Ashrafi, A. Likar, M. Lipoglavsek:
RoSiB - a 4pi Silicon Ball for Charged Detection in EUROBALL
Nucl. Instr. and Meth. in Phys.Res.A443,304(2000)

Pershina, V.; T. Bastug:
The Electronic Structure and Properties of Group 7 Oxychlorides, Mo_3Cl, where M=Tc, Re, and Element 107, Bh
J. of Chemical Physics, 113, 1441 (2000)

Pestov, Yu.N.; H.R. Schmidt, B. Schreiber:
Timing Performance of Spark Counters and Photon Feedback
Nucl. Instr. + Meth. in Phys. Res. A456,11(2000)

Pfrepper, G.; A. Pfrepper, A. Kronenberg, J.V. Kratz, A. Näher, W. Brüchle, M. Schädel:
Continuous On-line Chromatography of Short Lived Isotopes of Tungsten as Homolog of Seaborgium (Element 106)
Radiochm. Acta 88, 273 (2000)

Podolyak, Zs.; P.H. Regan, M. Pfützner, J. Gerl, M. Hellström, M. Caamaño, P. Mayet, Ch. Schlegel, A. Aprahamian, J. Benlliure, A.M. Bruce, P.A. Butler, D. Cortina Gil, D.M. Cullen, J. Döring, T. Enqvist, F. Rejmund, C. Fox, J. Garcés Narro, H. Geissel, W. Gelletly, J. Giovinazzo, M. Górska, H. Grawe, R. Grzywacz, A. Kleinböhl, W. Korten, M. Lewitowicz, R. Lucas, H. Mach, M. Mineva, C.D. O'Leary, F. De Oliveira, C.J. Pearson, M. Rejmund, M. Sawicka, H. Schaffner, K. Schmidt, Ch. Theisen, P.M. Walker, D.D. Warner, C. Wheldon, H.J. Wollersheim, S.C. Wooding, F.R. Xu:
Isomer Spectroscopy of Neutron Rich $^{190}W_{116}$
Phys. Lett. B491, 225 (2000)

Quint, W.:
CPT-Test in der Garage
Phys. Bl. 56 Nr. 2, 14 (2000)

Radon, T.; H. Geissel, G. Münzenberg, T. Radon, H. Geissel, G. Münzenberg, B. Franzke, Th. Kerscher, F. Nolden, Yu. N. Novikov, Z. Patyk, C. Scheidenberger, F. Attallah, K. Beckert, T. Beha, F. Bosch, H. Eickhoff, M. Falch, Y. Fujita, M. Hausmann, F. Herfurth, H. Irnich, H.C. Jung, O. Klepper, C. Kozhuharov, Yu. A. Litvinov, K.E.G. Löbner, F. Nickel, H. Reich, W. Schwab, B. Schlitt, M. Steck, K. Sümmerer, T. Winkler,
H. Wollnik:
Schottky Mass Measurements of Stored and Cooled Neutron-Deficient Projectile Fragments in the Element Range of 57< Z< 84
Nucl. Phys. A677, 75 (2000)

Rami. F.; Y. Leifels, B. de Schauenburg, A. Gobbi, B. Hong, J.P. Alard, A. Andronic, R . Averbeck, V. Barret, Z. Basrak, N. Bastid, I. Belyaev, A. Bendarag, G. Berek, R. Caplar, N. Cindro, P. Crochet, A. Devismes, P. Dupieux, M. Dzelalija, M. Eskef, C. Finck, Z. Fodor, H. Folger, L. Fraysse, A. Geonoux-Lubain, Y. Grigorian, Y. Grishkin, B. Herrmann, K.D. Hildenbrand, J. Kecskemeti, Y.J. Kim, P. Koczon, M. Kirejczyk, M. Korolija, R. Kotte, M. Kowalczyk, T. Kress, R. Kutsche, A. Lebedev, K.S. Lee, V. Manko, H. Merlitz, S. Mohren, D. Moisa, J. Mösner, W. Neubert, A. Nianine, D. Pelte, M. Petrovici, C. Pinkenburg, C. Plettner, W. Reisdorf, J. Ritman, D. Schöll, Z. Seres, B. Sikora, K. S. Sim, V. Simion, K. Siwek-Wilczynska, A. Somov, M.R. Stockmeier, G. Stoicea, M. Vasiliev, P. Wagner, K. Wisniewski, D. Wolfarth, J.T. Yang, I. Yushmanov, A. Zhilin.:
Isospin Tracing: A Probe of Nonequilibrium in Central Heavy-Ion Collisions
Phys. Rev. Lett. 84, 1120 (2000)

Rehm, K.E.; F. Borasi, C.L. Jiang, D. Ackermann, I. Ahmad, F. Brumwell, C.N. Davids, P. Decrock, S.M. Fischer, J. Görres, J.P. Greene, G. Hackmann, B. Harss, D. Henderson, W. Henning, R.V.F. Janssens, G. McMichael, V. Nanal, D. Nisius, J. Nolen, R.C. Pardo, M. Paul, P. Reiter, J.P. Schiffer, D. Seweryniak, R.E. Segel, I. Wiedenhöver, M. Wiescher, A.H. Wuosmaa:
Experiments with Radioactive ^{56}Ni Beams
Nucl. Instr. and Meth. in Phys. Res.A449,208(2000)

Reiter, P.; T.L. Khoo, T. Lauritzen, C.J. Lister, D. Seweryniak, A.A. Sonzogni, I. Ahmad, N. Amzal, P. Bhattacharyya, P.A. Butler, M.P. Carpenter, A.J. Chewter, J.A. Cizewski, C.N. Davids, K.Y. Ding, N. Fotiades, J.P. Greene, P.T. Greenlees, A. Heinz, W.F. Henning, R.-D. Herzberg, R.V.F. Janssens, G.D. Jones, H. Kankaanpää, F.G. Kondev, W. Korten, M. Leino, S. Siem, J. Uusitalo, K. Vetter, I. Wiedenhöver:
Entry Distribution Fission Barrier and Formation Mechnaism of ^{254}No
Phys. Rev. Lett. 84, 3542 (2000)

Publications

Rejmund, F.; A.V. Ignatyuk, A.R. Junghans, K. H. Schmidt:
Pair Breaking and Even-Odd Structure in Fission-Fragment Yields
Nucl. Phys. A678, 215 (2000)

Rejmund, M.; K.H. Maier, R. Broda, B. Fornal, M. Lach, J. Wrzesinski, J. Blomqvist, A: Gadea, M. Gorksa, H. Grawe, M. Kaspar, H. Schaffner, Ch. Schlegel, R. Schubart, H.J. Wollersheim:
Particle Octupole-Vibration Coupling near ^{208}Pb
Eur. Phys. J. A8, 161 (2000)

Ritter, S.; E. Nasanova, E. Gudowska-Novak, M. Scholz, G. Kraft:
High LET Induced Chromosome Aberrations in V79 Cells Analysed in First and Second Post-Irradiation Metaphases
Int. J. Radiat. Biol. 76, 149 (2000)

Ritter, S.; E. Nasanova, G. Kraft:
Radiation Risk Based on Chromosome Data: which Factors should be Considered?
in: Exploring Future Research Strategies in Space Radiation Sciences, p. 115,
eds. H. Majima, K. Fujitaka, Iryokagakusha Co. Tokyo, Japan (2000)

Roth, M; C. Stöckl, W. Süss, O. Iwase, D.O. Gericke, R. Bock, D.H.H. Hoffmann, M. Geissel, W. Seelig:
Energy Loss of Heavy Ions in Laser-Produced Plasmas
Europhys. Lett. 50, 28 (2000)

Roth, M.; T. Cowan, A. Hunt, J. Johnson, C. Brown, W. Fountain, S. Hatchett, E. Henry, J. Johnson, M. Key, Th. Kühl, T. Parnell, D. Pennington, M. Perry, T. Sangster, M. Singh, R. Snavely, M. Stoyer, Y. Takahashi, S. Wilks:
Laser-Driven Nuclear Fusion, Positron Creation and Electron Acceleration in Ultra-Intense Laser-Solid Experiments on the Petawatt
in: Inertial Fusion Sciences and Applications 99, eds.: C. Labaune, W.J. Hogan, K.A. Tanaka, Elsevier Publishing, p. 1010 (2000)

Rück, D.M.:
Ion Induced Modification of Polymers at Energies between 100keV and 1GeV Applied for Optical Waveguides and Improved Metal Adhesion
Nucl.Instr.+Meth. in Phys.Res.B166/167,602(2000)
(Proc. of the '10th Int. Conf. on Radiation Effects in Insulators', Jena, Germany, 1999)

Rumolo, G.; O. Boine-Frankenheim, I. Hofmann, G. Miano:
Theory and Simulations of Intense Laser Cooled Coasting Beams
Nucl. Instr. and Meth. in Phys. Res.A441,191(2000)
(Proc. of the Workshop on 'Electron Cooling and Related Topics', Uppsala, Sweden, May 1999)

Saathoff, G.; G. Gwinner, T. Kühl, D. Schwalm, H. Winter, A. Wolf:
Rate Prediction for Two-Photon Spectroscopy of Highly Charged Ions through Laser-Induced Recombination
Hyperfine Interactions 127, 211 (2000)

Scheidenberger, C.; G. Bollen, F. Bosch, A. Casares, H. Geissel, A. Kholomeev, G. Münzenberg, H. Weick, H. Wollnik:
Gross Properties of Exotic Nuclei Investigated at Storage Rings and Ion Traps
AIP Conf. Proc. 512, 275 (2000),
ed. H.O.Meyer, P. Schwandt
(Proc. of the 4th Int. Conf. on Phys. at Storage Rings, Bloomington, IN, USA, Sept. 1999)

Scheidenberger, C.:
Precision Mass Measurements of Exotic Nuclei in the Experimental Storage Ring ESR
Czech. J. Phys. 50, 239 (2000)

Schlegel, Ch.; P.H. Regen, M. Pfützner, J. Gerl, M. Hellström, Zs. Podolyak, M. Caamano, P. Mayet, A. Aprahamian, J. Bennliure, A.M. Bruce, P.A. Butler, D. Cortina Gil, D.M. Cullen, J. Döring, T. Enqvist, F. Farget, C. Fox, J. Garces Narro, W. Gelletly, J. Giovinazzo, M. Gorska, H. Grawe, R. Grzywacz, A. Kleinböhl, W. Korten, M. Lewitowicz, R. Lucas, H. Mach, M. Mineva, C.D. O'Leary, F. DeOliveira, C.J. Pearson, M. Rejmund, M. Sawicka, H. Schaffner, K. Schmidt, Ch. Theisen, P.M. Walker, D.D. Warner, C. Wheldon, H.J. Wollersheim, S. Wooding, F. Xu:
K-Isomers in Very Neutron-Rich Nuclei around Mass 180
Phys. Scripta T88, 72 (2000)

Schlitt, B.; A. Bechtold, U. Ratzinger, A. Schempp:
Design of the 7 MeV/u, 217 MHz Injector Linac for the Proposed Ion Beam Facility for Cancer Therapy at the Clinic in Heidelberg
Proc. of the 'XX Int. Linac Conf. (LINAC 2000), Monterey, ed. A.W. Chao, p. 226 (2000)

Publications

Schlögl, M.; B.E. Fischer:
Investigation of the Detection Efficiency of Polycrystalline Diamond Detectors with a Heavy Ion Microprobe
IEEE, 132 (2000), ISBN 0-7803-5726-4
(Proc. of the '5th Eur. Conf. Radiat. and its Effects on Components and Systems, (RADECS '99), 13.-17. Sept. 1999, Fontevraud, France

Schmidt, K.; C. Mazzocchi, R. Borcea, J. Döring, S. Galanopoulos, M. Gorska, H. Grawe, S. Harissopulos, M. Hellström, Z. Janas, R. Kirchner, G. Kriembardis, M. La Commara, A.N. Ostrowski, G. Rainovski, E. Roeckl:
Beta Decay of ^{93}Pd
Eur. Phys. J. A8, 303 (2000)

Schmidt, K.-H.:
A New Test for Random Events of an Exponential Distribution
Eur. Phys. J. A8, 141 (2000)

Schmidt, K.-H.; S. Steinhäuser, C. Böckstiegel, A. Grewe, A. Heinz, A.R. Junghans, J. Benlliure, H.-G. Clerc, M. De Jong, J. Müller, M. Pfützner, B. Voss:
Relativistic Radioactive Beams: A New Access to Nuclear-Fission Studies
Nucl. Phys. A665, 221 (2000)

Schmitt, F.; A. Dax, R. Kirchner, H.-J. Kluge, T. Kühl, I. Tanihata, W. Wakasugi, H. Wang, C. Zimmermann:
Towards the Determination of the Charge Radius of ^{11}Li by Laser Spectroscopy
Hyperfine Interactions 127, 111 (2000)

Schönauer, H.; B. Autin, R. Cappi, J. Gareyte, R. Garoby, M. Giovannozzi. H. Haseroth, I. Hofmann, M. Martini, E. Metral, W. Pirkl, C.R. Prior, G.H. Rees, U. Senichev:
A Slow Cycling Proton Driver for a Neutrino Factory
EPAC 2000, p. 966, CERN, Geneva 2000
(eds.: J.-L. Laclare, W. Mitaroff, Ch. Petit-Jean-Genaz, J. Poole, M. Regler) '7th Europ. Part. Acc. Conf.', Vienna, Austria, June 26-30, 2000

Scholz, M.:
Heavy Ion Tumour Therapy
Nucl. Instr. and Meth. in Phys. Res.B161, 9(2000)

Schulz, M.; R. Moshammer, W. Schmitt, H. Kollmus, B. Feuerstein, R. Mann, S. Hagmann, J. Ullrich:
Electron Correlations Observed Through Intensity Interferometry
Phys. Rev. Lett. 84, 863 (2000)

Schulz, M.; R. Moshammer, W. Schmitt, H. Kollmus, R. Mann, S. Hagmann, R.E. Olson, J. Ullrich:
Correlated Three Electron Continuum States in Triple Ionization by Fast Heavy Ion Impact
Phys. Rev. A61, 022703 (2000)

Senger, P.: (for the KaoS Collaboration)
Strange Mesons in Dense Matter
in: Hadrons in Dense Matter, p. 96 GSI Darmstadt, ISSN 0720-8715
(Proc. of the 'Int. Workshop XXVIII on Gross Properties of Nuclei and Nuclear Excitations', Hirschegg, Austria, Jan. 2000) (eds.: M. Buballa, W. Nörenberg, B.-J. Schäfer, J. Wambach)

Sharma, A.:
3D Simulation of Charge Transfer in a Gas Electron Multiplier (GEM) and Comparison to Experiment
Nucl. Instr. and Meth. in Phys. Res.A454,267(2000)

Siegmann, B.; U. Werner, R. Mann, N.M. Kabachnik, H.O. Lutz:
Kinetic Energy Release Distributions in Coulomb Explosion of N2 Molecules Induced by Fast Highly Charged Ion Impact
Phys. Rev. A62, 022718 (2000)

Siwy, Z.; S. Mercik, K. Weron, R. Spohr, A. Wolf, Z. Grzywna:
Comparison of Single Channel Potassium Current in Biological and Synthetic Systems – Dependance on Voltage
Acta Phys. Pol. B31, 1125 (2000)

Soyeur, M.; M. Lutz, B. Friman:
Quantum Interference in the $e^+ e^-$ Decays of ρ^0 and ω -Mesons Produced in π^- p Reactions
in: Hadrons in Dense Matter, p.170, GSI Darmstadt, ISSN 0720-8715
(Proc. of the 'Int. Workshop XXVIII on Gross Properties of Nuclei and Nuclear Excitations', Hirschegg, Austria, Jan. 2000) (eds.: M. Buballa, W. Nörenberg, B.-J. Schäfer, J. Wambach)

Publications

Spädtke, P.; C. Mühle:
Simulation of Ion Extraction and Beam Transport
Rev. Scie. Instr. 71, 820 (2000)

Spielberger, L.; O. Jagutzki, R. Dörner, V. Mergel, U. Meyer, Kh. Khayyat, T. Vogt, M. Achler, H. Schmidt-Böcking, J. Ullrich, M. Unverzagt, B. Krässig, M. Jung, E.P. Kanter, D.S. Gemmell, M.H. Prior, H. Khemliche, C.L. Cocke:
Studies of Photoabsorption and Compton Scattering Using Cold Target Recoil Ion Momentum Spectroscopy
AIP Conf. Proc. 213, p. 392 (2000)

Spiller, P.; D. Böhne, A. Dolinskii, H. Eickhoff, B. Franczak, Th. Haberer, B. Langenbeck, E. Malwitz, M. Pavlovic:
Gantry Studies for the Proposed Heavy Ion Cancer Therapy Facility in Heidelberg
EPAC 2000, p. 2551, CERN, Geneva 2000 (eds.: J.-L. Laclare, W. Mitaroff, Ch. Petit-Jean-Genaz, J. Poole, M. Regler) '7th Europ. Part. Acc. Conf.', Vienna, Austria, June 26-30, 2000

Stadlmann, J. H. Geissel, M. Hausmann, F. Nolden, T. Radon, H. Schatz, C. Scheidenberger, F. Attallah, K. Beckert, F. Bosch, M. Falch, B. Franczak, B. Franzke, Th. Kerscher, O. Klepper, H.-J. Kluge, C. Kozhuharov, K.E.G. Löbner, G. Münzeneberg,, Yu.N. Novikov, M. Steck, Z. Sun, K. Sümmerer, H. Weick, H. Wollnik:
First Isochronous Time-of-Flight Mass Measurements of Short-Lived Projectile Fragments in the ESR
AIP Conf. Proc. 512, p. 305 (2000), eds.: H.O. Meyer, P. Schwandt

Steck, M.; L. Gröning, K. Blasche, B. Franczak, B. Franzke, T. Winkler, V. V. Parkhomchuk:
Beam Accumulation with the SIS Electron Cooler
Nucl. Instr. and Meth. in Phys. Res.A441,175(2000)
(Proc. of the Workshop on 'Electron Cooling and Related Topics', Uppsala, Sweden, May 1999)

Steck, M.; K. Beckert, H. Eickhoff et al.:
Cooling of Radioactive Isotopes for Schottky Mass Spectrometry
in: 'Trapped Charged Particles and Fundamental Physics', AIP, p. 87, 1999 (eds.: D.H.E. Dubin, D. Schneider)

Steck. M., K. Beckert, P. Beller, B. Franczak, B. Franzke, F. Nolden:
Decceleration of Highly Charged Heavy Ions in the ESR
EPAC 2000, p. 587, CERN, Geneva 2000 (eds.: J.-L. Laclare, W. Mitaroff, Ch. Petit-Jean-Genaz, J. Poole, M. Regler) '7th Europ. Part. Acc. Conf.', Vienna, Austria, June 26-30, 2000

Stiebing, K.E.; K. Müller, J. Baumann, K. Bethge, J. Bernhardt, H. Bokemeyer, H. Folger, O. Fröhlich, O. Hohn, G. Kavermann, G. Lambrinidis, A. Müller, J. Peter, S. Runkel, L. Schmidt, H. Schmidt-Böcking, P. Senger, P. Thee, J. Ullrich:
On the Spectroscopy of Atomic Electrons (Positrons) in the Range of 10 to 50 MeV from Heavy-Ion Collisions at Intermediate Energies
Eur. Phys. J. A8, 87 (2000)

Stöhlker, Th.; P.H. Mokler, F. Bosch, R.W. Dunford, F. Franzke, O. Klepper, C. Kozhuharov, T. Ludziejewski, F. Nolden, H. Reich, P. Rymuza, Z. Stachura, M. Steck, P. Swiat, A. Warczak:
1s Lamb Shift in Hydrogenlike Uranium Measured on Cooled, Decelerated Ion Beams
Phys. Rev. Lett. 85, 3109 (2000)

Stöhlker, Th.; O. Brinzanescu, A. Krämer, T. Ludziejewski, X. Ma:
Time-Reversed Photoionization Studied via Radiative Electron Capture in Heavy-Ion Atom Collisions
in: X-Ray and Inner Shell Processes, AIP Conf. Proc. 506, p. 389 (2000), eds.: D.S. Gemmel, E.P. Kanter, L. Young
(Proc. of the 18th Int. Conf., Chicago, USA,1999)

Stolz, A.; E. Wefers, T. Faestermann, R. Schneider, K. Sümmerer, J. Friese, H. Geissel, M. Hellström, P. Kienle, H.-J. Körner, M. Münch, G. Münzenberg, Ch. Schlegel, P. Thirolf, H. Weick:
Decay Studies of N≡Z Nuclei from ^{77}Y to ^{100}Sn
LUIP 0003, Sweden, p.113 (2000),ISSN 0348-9329
eds: D. Rudolph, M. Hellström
(Proc. of the 'Int. Workshop on N=Z Nuclei (PINGST 2000), Lund, Sweden, 06.-10.06.2000)

Strub, E.; J.V. Kratz, A. Kronenberg, A. Näher, P. Thörle, S. Zauner, W. Brüchle, E. Jäger, M.Schädel, E. Schmipf, Li Zongwei, U. Kirbach, D. Schumann, D. Jost, A. Türler, M. Asai, Y.Nagame, M. Sakama, K. Tsukada, H.W. Gäggeler, J.P. Glatz:

Publications

Fluoride Complexation of Rutherfordium, Rf (Element 104)
Radiochim. Acta 88, 265 (2000)

Struckmeier, J.; C. Riedel:
Exact Invariants for a Class of Three-Dimensional Time-Dependent Classical Hamiltonians
Phys. Rev. Lett. 85, 3830 (2000)

Struckmeier, J.; C. Riedel:
'A posteriori' Error Estimation for Simulations of Charged Particle Beams
EPAC 2000, p. 1405, CERN, Geneva 2000 (eds.: J.-L. Laclare, W. Mitaroff, Ch. Petit-Jean-Genaz, J. Poole, M. Regler) '7th Europ. Part. Acc. Conf.', Vienna, Austria, June 26-30, 2000

Sturm, C.; I. Böttcher, M. Debowski, A. Förster, E. Grosse, P. Koczon, B. Kohlmeyer, F. Laue, M. Mang, L. Naumann, H. Oeschler, F. Pühlhofer, E. Schwab, P. Senger, Y. Shin, J. Speer, H. Ströbele, G. Surowka, F. Uhlig, A. Wagner, W. Walus:
Strange Mesons in Dense Nuclear Matter
Acta Phys. Pol. B31, 2313 (2000)

Sturm, C.; I. Böttcher, M. Debowski, A. Förster, E. Grosse, P. Koczon, B. Kohlmeyer, F. Laue, M. Mang, L. Naumann, H. Oeschler, F. Pühlhofer, E. Schwab, P. Senger, Y. Shin, J. Speer, H. Ströbele, G. Surowka, F. Uhlig, A. Wagner, W. Walus:
Evidence for a Soft Nuclear Equation -of-State from Kaon Production in Heavy Ion Collisions
Phys. Rev. Lett. 86, 39 (2000)

Sümmerer, K.; B. Blank
Modified Empirical Parametrization of Fragmentation Cross Sections
Phys. Rev. C61, 034607 (2000)

Tahir, N.A.; D.H.H. Hoffmann, A. Kozyreva et al.:
Numerical Simulations of Heavy-Ion-Matter Interaction Experiments at the GSI Darmstadt
Elsevier, Paris p. 576 (2000), eds.: W. Hogan, C. Laubanne, K. Tanaka, (Proc. of the '1st Int. Conf. on Inertial Fusion Sciences and Applications (IFSA '99), Bordeaux, France, Sept. 1999)

Tahir N.A.; D.H.H. Hoffmann, A. Kozyreva, A. Tauschwitz, A. Shutov, J. A. Maruhn, P. Spiller, U. Neuner, J. Jacoby, M. Roth, R: Bock, H. Juranek, R. Redmer:
Hydrogen Metallization in Heavy-Ion Imploded Multi-Layered Targets
Phys. Rev. E63, 016402 (2000)
J. Phys. IV France 10, Pr5, 327 (2000), eds.: C. Deutsch, B. Jancovici, M.M.Gombert (Proc. of the 'Int. Conf. on Strongly Coupled Coulomb Systems', St. Malo, France, Sept. 1999)

Tahir, N.A.; A. Kozyreva, A. Shutov, P. Spiller, D.H.H. Hoffmann:
Creation of Strongly Coupled Plasmas Using Intense Beams of 400MeV/u Uranium Ions to be Generated at the GSI SIS-200
Phys. of Plasmas, 7, 4379 (2000)

Tahir, N.A.; D.H.H. Hoffmann, J.A. Maruhn, P. Spiller, R. Bock:
Heavy-Ion-Beam-Induced Hydrodynamic Effects in Solid Targets
Phys. Rev. E60, 4715 (2000)

Tahir, N.A.; D.H.H. Hoffmann, A. Kozyreva, A. Shutov, J. A. Maruhm U. Neuner, A. Tauschwitz, P. Spiller, R. Bock:
Schock Compression of Condensed Matter Using Intense Beams of Energetic Heavy Ions
Phys. Rev. E61, 1975 (2000)

Tahir, N.A.; D.H.H. Hoffmann, A. Kozyreva, A. Shutov, J. A. Maruhn, U. Neuner, A. Tauschwitz, P. Spiller, R. Bock:
Equation-of-State Properties of High-Energy-Density Matter Using Intense Heavy Ion Beams with an Annular Focal Spot
Phys. Rev. E62, 1224 (2000)

Tarbutt, M.R.; P.H. Mokler, E.G. Myers, J.D. Silver:
X-Ray Spectroscopic Intercomparison between Hydrogenic Ions of Different Z as a Method for Determining Lamb Shifts
Hyperfine Interactions 127, 333 (2000)

Tomaselli, M.; S. Fritzsche, T. Kühl, H. Winter:
Hyperfine Structure of Li-Like Bismuth
Hyperfine Interactions 127, 315 (2000)

Tomaselli, M.; M. Hjorth-Jensen, S. Fritzsche, P. Egelhof, S.R: Neumaier, M. Mutterer, T. Kühl, A. Dax, H. Wang:
Matter and Charge Distributions of ^{6}He and ^{5,6,7,9}Li within the Dynamic-Correlation Model
Phys. Rev. C62, 067305 (2000)

Publications

Tomaselli, M.; P. Egelhof, S.R. Neumaier, M. Mutterer, T. Kühl, A. Dax, F. Schmitt, S. Fritzsche:
Microscopic Calculations of Matter and Charge Distributions of Exotic Nuclei within the Dynamic-Correlation Model
Hyperfine Interactions 127, 95 (2000)

Trautmann, C.; M. Toulemonde, K. Schwartz, J.M. Costantini, A. Müller:
Damage Structure in the Ionic Crystal LiF Irradiated with Swift Heavy Ions
Nucl.Instr.+Meth. in Phys.Res.B164/165,365(2000)
(Proc. of the '8th Int. Conf. on Atomic Collisions in Solids', Odense, Denmark, 03.-08.08.1999)

Trautmann, C.; M. Toulemonde, J.M. Costantini, J.J. Grob, K. Schwartz:
Swelling Effects in Lithium Fluoride Induced by Swift Heavy Ions
Phys. Rev. B62, 13 (2000)

Trautmann, C.; S. Klaumünzer, H. Trinkaus:
Effects of Stress on Track Formation in Amorphous Ion Tracks as Elastic Inclusions
Phys. Rev. Lett. 85, 3648 (2000)

Varga, S.; B. Fricke, M. Hirata, T. Bastug, V. Pershina, S. Fritsche:
Total Energy Calculations of $RfCl_4$ and Homologous in the Framework of Relativistic Density-Functional Theory
J. Phys. Chem. 104, 6495 (2000)

Wagner, A.; C. Müntz, H. Oeschler, C. Sturm, R. Barth, M. Cieslak, M. Debowski, E. Grosse, P. Koczon, F. Laue, M. Mang, D. Miskowiec, E. Schwab, P. Senger, P. Beckerle, D. Brill, Y. Shin, H. Ströbele, W. Walus, B. Kohlmeyer, F. Pühlhofer, J. Speer, I.K. Yoo:
The Emission Pattern of High-Energy Pions: a New Probe for the Early Phase of Heavy-Ion Collisons
Phys. Rev. Lett. 85, 18 (2000)

Weick, H.; H. Geissel, C. Scheidenberger, F. Attallah, T. Baumann, D. Cortina, M. Hausmann, B. Lommel, G. Münzenberg, N. Nankov, F. Nickel, T. Radon, H. Schatz, K. Schmidt, J. Stadlmann, K. Sümmerer, M. Winkler, H. Wollnik:
Slowing Down of Relativistic Few-Electron Heavy Ions
Nucl.Instr.+Meth. in Phys.Res.B164/165,168(2000)
(Proc. of the '8th Int. Conf. on Atomic Collisions in Solids', Odense, Denmark, 03.-08.08.1999)

Wiedeking, M.; R.A. Kaye, G.Z. Solomon, S.L.Tabor, J. Döring, G.D. John, F. Cristancho, M.Devlin, F. Lerma, D.G. Sarantites, I.Y. Lee, A.O. Macchiavelli:
Transition Strengths in Odd-Odd ^{86}Nb
Phys. Rev. C62, 024316 (2000)

Wlazlo, W.; T. Enqvist, P. Armbruster, J. Benlliure, M. Bernas, A. Boudard, S. Czajkowski, R. Legrain, S. Leray, B. Mustapha, M. Pravikoff, F. Rejmund, K.- H. Schmidt, C. Stephan, J. Taieb, L. Tassan-Got, C. Volant:
Cross Sections of Spallation Residues Produced in 1A GeV ^{208}Pb on Proton
Phys. Rev. Lett. 84, 5736 (222)

Yang, Z.H.; X. Ma, Y.D. Wang, H.P. Liu, H. Su, D.Y. Yu:
Measuremen of Excitiation Spectra for Highly Ionized Sulphur
Science in China A43, 205 (2000)

Zeng, X.T.; S.B. Du, J.W. Li, L.Y. Jiang, S.D. Yao, H.Z. Chen, H.P. Liu, X.W. Ma, Y.D. Wang, C. Jupen, I. Martinson:
Spectrum and Energy Levels of Mg-Like Br XXIV
Physica Scripta 61, 464 (2000)

Zschiesche, D.; P. Papazoglou, C. Beckmann, S. Schramm, J. Schaffner-Bielich, H. Stöcker, W. Greiner:
Chiral Model for Dense, Hot and Strange Hadronic Matter
Nucl. Phys. A663-664, 737c (2000)
(Proc. of the '15th Int. Conf. on Particle and Nuclei (PANIC '99)', Uppsala, Sweden, June 1999)

GSI-Reports and Preprints

Reports

2000-01
Grundinger, U.(ed.):
Scientific Report 1999

2000-02
Bock, R.: (ed.)
High Energy Density in Matter Produced by Heavy Ion Beams
(Annual Report 1999)

2000-03
Kagarlis, M.A.:
PLUTO^{++} - A Monte Carlo Simulation Tool for Hadronic Physics

2000-04
Kraft, G.; K. Langbein:
7th Workshop on Heavy Charged Particles in Biology and Medicine
(Book of Abstract)

Preprints

2000-01
Weick, H.; H. Geissel, C. Schneidenberger, F. Attalah, T. Baumann, D. Cortina, M. Hausmann, B. Lommel, G. Münzenberg, N. Nankov, F. Nickel, T. Radon, H. Schatz, K. Schmidt, J. Stadlmann, K. Sümmerer, M. Winkler, H. Wollnik:
Slowing Down of Relativistic Few-Electron Heavy Ions
Nucl. Instr.+Meth. inPhys.Res.B164/165,168(2000)

2000-02
Hofmann, S.; G. Münzenberg:
The Discovery of the Heaviest Elements
Rev. on Mod. Phys. 72, 733 (2000)

2000-03
Feldmeier, H.; J. Schnack:
Molecular Dynamics for Fermions
Rev. on Mod. Phys. 72, 655 (2000)

2000-04
Wlazlo, W.; T. Enqvist,P. Armbruster, J. Benlliure, M. Bernas, A. Boudard, S. Czajkowski, R. Legrain, S. Leray, B. Mustapha, M. Pravikoff, F. Rejmund, K.-H. Schmidt, C. Stephan, J. Taieb, L. Tassan-Got, C. Volant:
Cross-Sections of Spallation Residues Produced in 1A GeV ^{208}Pb on Proton Reactions
Phys. Rev. Lett. 84, 5736 (2000)

2000-05
Benlliure, J.; P. Armbruster, M. Bernas, A. Boudard, J.P. Dufour, T. Enqvist, R. Legrain, S. Leray, B. Mustapha, F. Rejmund, K.-H. Schmidt, C. Stephan, L. Tassan-Got, C. Volant:
Isotopic Production Cross Sections of Fission Residues in ^{197}Au+p Collisions at 800 A MeV

2000-06
Rejmund, F.; B. Mustapha, P. Armbruster, J. Benlliure, M. Bernas, A. Boudard, J.P. Dufour, T. Enqvist, R. Legrain, S. Leray, K.-H. Schmidt, C. Stephan, J. Taieb, L. Tassan-Got, C. Volant:
Measurement of Isotopic Cross Sections of Spallation Residues in 800 A MeV ^{197}Au+p Collisions

2000-07
Chulkov, L.V.; O.V. Bochkarev, D. Cortina-Gil, H. Geissel, M. Hellström, M. Ivanov, R. Janik, K. Kimura, T. Kobayashi, A.A. Korscheninnikov, G. Münzenberg, F. Nickel, A.A. Ogloblin, A. Ozawa, M. Pfützner, V.N. Pribora, M.V. Rozhkov, H. Simon, B. Sitar, P. Strmen, K. Sümmerer, T. Suzuki, I. Tanihata, M. Winkler, K. Yoshida:
Total Charge-Changing Cross Sections for Neutron-Rich Light Nuclei
(Nucl. Phys. A674, 330 (2000)

2000-08
Pestov, Yu. N.; H.R. Schmidt, B. Schreiber:
Timing Performance of Spark Counters and Photon Feedback
Nucl. Instr. + Meth. in Phys. Res.A456,11(2000)

GSI-Reports and Preprints

2000-09
Berdermann, E.; B.E. Fischer, M. Schlögl, H. Stelzer, B. Voss:
Recent Results from CVD-Diamond Heavy-Ion Detectors

2000-10
Odeh, T.; R. Bassini, M. Begemann-Blaich, S. Fritz, S.J. Gaff-Ejakov, D. Gourio, C. Groß, G. Imme, I. Iori, U. Kleinevoß, G.J. Kunde, W.D. Kunze, U. Lynen, V. Maddalena, M. Mahi, T. Möhlenkamp, A. Moroni, W.F.J. Müller, C. Nociforo, B. Ocker, F. Petruzzelli, J. Pochodzalla, G. Raciti, G. Riccobene, F.P. Romano, A. Saija, M. Schnittker, A. Schüttauf, C. Schwarz, W. Seidel, V. Serfling, C. Sfienti, W. Trautmann, A. Trzcinski, G. Verde, A. Wörner, Hongfei Xi, B. Zwieglinski:
Fragment Kinetic Energies and Modes of Fragment Formation
Phys. Rev. Lett. 84, 4557 (2000)

2000-11
Schmidt, K.-H.:
A New Test for Random Events of an Exponential Distribution
Eur. Phys. J. A8, 141 (2000)

2000-12
Lutz, M.; W. Florkowski:
Non-Local Effects in Kaonic Atoms
Systematic Experimental Survey on Projectile Fragmentation and Fission Induced in Collisions of ^{238}U at 1 AGeV with Pb
Acta Phys. Pol. B31, 2567 (2000)

2000-13
Wagner, A.; C. Müntz, H. Oeschler, C. Sturm, R. Barth, M. Cieslak, M. Debowski, E. Grosse, P. Koczon, F. Laue, M. Mang, D. Miskowiec, E. Schwab, P. Senger, P. Beckerle, D. Brill, Y. Shin, H. Ströbele, W. Walus, B. Kohlmeyer, F. Pühlhofer, J. Speer, I.K. Yoo:
The Emission Pattern of High-Energy Pions: A New Probe for the Early Phase of Heavy Ion Collisions
Phys. Rev. Lett. 85, 18 (2000)

2000-14
Herfurth, F.; J. Dilling, A. Kellerbauer, G. Bollen, S. Henry, H.-J. Kluge, E. Lamour, D. Lunney, R.B. Moore, C. Scheidenberger, S. Schwarz, G. Sikler, J. Szerypo:
A Linear Radiofrequency Ion Trap for Accumulation, Bunching, and Emittance Improvement of Radioactive Ion Beams

2000-15
Beck, D.; F. Ames, G. Audi, G. Bollen, F. Herfurth, H.-J. Kluge, A. Kohl, M. König, D. Lunney, I. Martel, R.B. Moore, H. Raimbault-Hartmann, E. Schark, S. Schwarz, M. de Saint Simon, J. Szerypo (ISOLDE Collaboration):
Accurate Masses of Unstable Rare Earth Isotopes by ISOLTRAP
Eur. Phys. J. A8, 307 (2000)

2000-16
Schmidt, K.; C. Mazzocchi, R. Borcea, J. Döring, S. Galanopoulos, M. Gorska, H. Grawe, S. Harissopulos, M. Hellström, Z. Janas, R. Kirchner, G. Kriembardis, M. La Commara, A.N. Ostrowski, G. Rainowski, E. Roeck:
Beta Decay of ^{93}Pd
Eur. Phys. J. A8, 303 (2000)

2000-17
Grawe, H.; M. Gorska, C. Fahlander, M. Palacz, F. Nowacki, E. Caurier, J.M. Daugas, M. Lewitowicz, M. Sawicka, R. Grzywacz, K. Rykaczewski, O. Sorin, S. Leenhardt, F. Azaiez:
Experimental Approach towards Shell Structure at ^{100}Sn and ^{78}Ni

2000-18
Datta Pramanik, U.; T. Aumann, A. Leistenschneider, K. Boretzky, D. Cortina, J. Cub, W. Dostal, Th.W. Elze, H. Emling, H. Geissel, A. Grünschloß, M. Hellström, R. Holzmann, S. Ilievki, N. Iwasa, M. Kaspar, A. Kleinböhl, J.V. Kratz, R. Kulessa, Y. Leifels, E. Lubkiewicz, G. Münzenberg, P. Reiter, M. Rejmund, C. Scheidenberger, Ch. Schlegel, H. Simon, J. Stroth, K. Sümmerer, E. Wajda, W. Walus, S. Wan:
Measurement of the Dipole Response of Neutron-Rich Nuclei in the A~ 20 Region

GSI-Reports and Preprints

2000-19
Braun-Munzinger, P.; J. Stachel
(Non) Thermal Aspects of Charmonium Products and a New Look at J/ψ Suppression
Phys. Lett. B490, 196 (2000)

2000-20
Braun-Munzinger, P.:
Chemical Equilibration and the Hadron-QGP Phase Transition

2000-21
Sobiczewski, A.; I. Muntian, Z. Patyk:
Problem of "Deformed" Superheavy Nuclei

2000-22
Markenroth, K.; M. Meister, B. Eberlein, D. Aleksandrov, T. Aumann, L. Axelsson, T. Baumann, M.J.G. Borge, L.V. Chulkov, W. Dostal, Th.W. Elze, H. Emling, H. Geissel, A. Grünschloß, M. Hellström, J. Holeczek, B. Jonson, J.V. Kratz, R. Kulessa, A. Leistenschneider, I. Mukha, G. Münzenberg, F. Nickel, T. Nilsson, G. Nyman, M. Pfützner, V. Pribora, A. Richter, K. Riisager, C, Scheidenberger, G. Schrieder, H. Simon, J. Stroth, O. Tengblad, M.V. Zhukov:
^{8}He-^{6}He: A Comparative Study of Nuclear Fragmentation Reactions

2000-23
Gadea, A.; S.M. Lenzi, D.R. Napoli, C.A. Ur, G. Martinez-Pinedo, M. Gorska, E. Caurier, M. Axiotis, G. de Angelis, F. Brandolini, D. Cano-Ott, E. Farnea, E. Nacher, B. Rubio, J.L. Tain, R. Borcea, J. Döring, H. Grawe, Z. Janas, R. Kirchner, M. La Commara, C. Mazzocchi, E. Roeckl, K. Schmidt, C. Fahlander, M. Hellström, L. Batist, A. Plochocki, J. Zylicz, C. Plettner, R. Schwengner, J. Äystö, P. Dendooven, M. Gierlik, A. Jokinen, M. Karny, P. Mayet, A. Nieminen, H. Penttilä, M. Rejmund, C. Schlegel, M. Sawicka, J. Eberth, T. Steinhardt, B.A. Brown, Z. Hu, V. Belleguic, C. Bingham, S. Galanoupoulos, M. Gierlik, S. Harissopulos, G. Kriembardis, A. Ostrowski, G. Rainowski:
Recent Experiments on N=Z Nuclei, Performed at the GSI On-Line Mass Separator

2000-24
Krämer, M.; M. Scholz:
Treatment Planning for Heavy Ion Radiotherapy: Calculation and Optimization of Biologically Effective Dose
Phys. in Med. and Biol., 45, 3319 (2000)

2000-25
Krämer, M.; O. Jäkel, T. Haberer, G. Kraft, D. Schardt, U. Weber:
Treatment Planning for Heavy Ion Radiotherapy: Physical Beam Model and Dose Optimization
Phys. in Med. and Biol., 45, 3299 (2000)

2000-26
Grawe, H.; M. Gorska, J. Döring, C. Fahlander, M. Palacz, F. Nowacki, E. Caurier, J.M. Daugas, M. Lewitowicz, M. Sawicka, M. Pfützner, R. Grzywacz, K. Rykaczewski, O. Sorlin, S. Leenhardt, F. Azaiez, M. Rejmund, K. Hauschild, J. Uusitalo:
Nuclear Structure in the Vicinity of Shell Closures far from Stability

2000-27
Pochodzalla, J.; W. Trautmann:
Chemical Equilibrium and Isotope Temperatures

2000-28
Enqvist, T.; W. Wlazlo, P. Armbruster, J. Benlliure, M. Bernas, A. Boudard, S. Czajkowski, R. Legrain, S. Leray, B. Mustapha, M. Pravikoff, F. Rejmund, K.-H. Schmidt, C. Stephan, J. Taieb, L. Tassan-Got, C. Volant:
Isotopic Yields and Kinetic Energies of Primary Residues in 1 AGeV ^{208}Pb+p Reactions

2000-29
Ma, X.; Th. Stöhlker, F. Bosch, O. Brinzanescu, S. Fritzsche, C. Kozhuharov, P. Mokler, T. Ludziejewski, A. Warczak:
Subshell Differential Cross Sections for Electron Transfer in Collisions of U^{90+} Ions with Gaseous Targets

2000-30
Stöhlker, Th.; X. Ma, T. Ludziejewski, H.F. Beyer, F. Bosch, O. Brinzanescu, R.W. Dunford, J. Eichler, S. Hagmann, A. Ichihara, C. Kozhuharov, A. Krämer, D. Liesen, P.H. Mokler, Z. Stachura, P. Swiat, A. Warczak:

GSI-Reports and Preprints

Near-Threshold Photionization of Hydrogenlike Uranium Studied in Ion-Atom Collisions via the Time-Reversed Process

2000-31
Krämer, A.; A. Kritzer, H. Reich, Th. Stöhlker:
Commisioning of a Hydrogen Cluster Target at the Experimental Storage Ring

2000-32
Stöhlker, Th.; P.H. Mokler, F. Bosch, R.W. Dunford, B. Franzke, O. Klepper, C. Kozhuharov, T. Ludziewski, F. Nolden, H. Reich, P. Rymuza, Z. Stachura, M. Steck, P. Swiat, A. Warczak:
The 1s Lamb Shift in Hydrogenlike Uranium Measured on Cooled, Decelerated Ion Beams
Phys. Rev. Lett. 85, 3109 (2000)

2000-33
Brinzanescu, O.; Th. Stöhlker:
Radiative Recombination Rate Coefficients

2000-34
Hu, Z.; L. Batist, J. Agramunt, A. Algora, B.A. Brown, D. Cano-Ott, R. Collatz, A. Gadea, M. Gierlik, M. Gorska, H. Grawe, M. Hellström, Z. Janas, M. Karny, R. Kirchner, F. Moroz, A. Plochocki, M. Rejmund, E. Roeckl, B. Rubio, M. Shibata, J. Szerypo, J.L. Tain, V. Wittmann:
Beta Decay of ^{98}Ag: Evidence for the Gamow-Teller Resonance near ^{100}Sn
(Phys. Rev. C62, 064315 (2000)

2000-35
Senger, P.:
Strange Mesons in Dense Nuclear Matter
Workshop ‚Hirschegg' (2000)

2000-36
Menzel, M.; I. Böttcher, M. Debowski, F. Dohrmann, A. Förster, E. Grosse, P. Koczon, B. Kohlmeyer, F. Laue, L. Naumann, H. Oeschler, F. Pühlhofer, E. Schwab, P. Senger, Y. Shin, H. Ströbele, C. Sturm, G. Surowka, F. Uhlig, A. Wagner, W. Walus:

First Measurement of Antikaon Phase-Space Distributions in Nucleus-Nucleus Collisions at Subthreshold Beam Energies
Phys. Lett B495, 26 (2000)

2000-37
Benlliure, J.; J. Pereira-Conca, K.-H. Schmidt:
New Approach to Determine the Angular Transmission in Zero-Degree Magnetic Spectrometers

2000-38
Schmidt, K.-H.; J. Benlliure, A.R. Junghans:
Fission of Nuclei far from Stability

2000-39
Ivanov, Yu.B.; E.G. Nikonov, W. Nörenberg, A.A. Shanenko, V.D. Toneev:
Directed Flow of Baryons in Heavy-Ion Collisions

2000-40
Jacoby, J.:
Which-Path Information and Interference of Elastic Scattering

2000-41
Benlliure, J.; K. Helariutta, M.V. Ricciardi, K.-H. Schmidt:
Model Calculations of a Two-Step Reaction Scheme for the Production of Neutron-Rich Secondary Beams

2000-42
Sturm, C.; I. Böttcher, M. Debowski, A. Förster, E. Grosse, P. Koczon, B. Kohlmeyer, F. Laue, L. Naumann, H. Oeschler, F. Pühlhofer, E. Schwab, P. Senger, Y. Shin, J. Speer, H. Ströbele, G. Surowka, F. Uhlig, A. Wagner, W. Walus:
Evidence for a Soft Nuclear Equation-of-State from Kaon Production in Heavy-Ion Collisions
Phys. Rev. Lett. 86, 39 (2001)

2000-43
Schwarz, C.:
Proton Emission Times in Spectator Fragmentation

2000-44
Trautmann, W.:
Hot Fragmentation of Nuclei

2000-45
Ionescu, D.C.; A.H. Sorensen, A. Belkacem:
Photoionization at Relativistic Energies

GSI-Reports and Preprints

2000-46
Protic, D.; Th. Stöhlker, H.F. Beyer, J. Bojowald, G. Borchert, A. Gumberidze, A. Hamacher, C. Kozhuharov, X. Ma, I. Mohos:
A Micro-Strip Germanium Detector for Position Sensitive X-Ray Spectroscopy

2000-47
Ma, X; Th. Stöhlker, F. Bosch, O. Brinzanescu, S. Fritzsche, C. Kozhuharov, T. Ludziejewski, P.H. Mokler, Z. Stachura, A. Warczak:
State-Selective Electron Capture into He-Like U^{90+} Ions in Collisions with Gaseous Targets

2000-48
Herfurth, F.; J. Dilling, A. Kellerbauer, G. Audi, D. Beck, G. Bollen, S. Henry, H.-J. Kluge, D. Lunney, R.B. Moore, C. Scheidenberger, S. Schwarz, G. Sikler, J. Szerypo:
Breakdown of the Isobaric Multiplet Mass Equation (IMME) at a=33, T=3/2

2000-49
Vogt, R.:
Shadowing Effects on Vector Boson Production

2000-50
Botvina, A.S.; I.N. Mishustin:
Statistical Evolution of Isotope Composition of Nuclear Fragments

2000-51
Nörenberg, W.; G. Papp, P. Rozmej:
Stability and Instability of a Hot Dilute Nuclear Droplet
Eur. Phys. J. A9, 327 (2000)

2000-52
Hofmann, S.; F.P. Heßberger, D. Ackermann, S. Antalic, P. Cagarda, B. Cwiok, B. Kindler, J. Kojouharova, B. Lommel, R. Mann, G. Münzenberg, A.G. Popeko, S. Saro, H.J. Schött, A.V. Yeremin:
The new Isotope ^{270}110 and its Decay Products ^{266}Hs and ^{262}Sg

2000-53
Hofmann, S.:
Synthesis of Superheavy Elements Using Radioactive Beams and Targets

2000-54
Shevelko, V.P.; I.Yu. Tolstikhina, Th. Stöhlker:
Stripping of Fast Heavy Low-Charged Ions in Gaseous Targets

2000-55
Braun-Munzinger, P.; J. Stachel:
On Charm Production near the Phase Boundary

2000-56
Karny, M.; L. Batist, B.A. Brown, D. Cano-Ott, R. Collatz, A. Gadea, R. Grzywacz, A. Guglielmetti, M. Hellström, Z. Hu, Z. Janas, R. Kirchner, F. Moroz, A. Piechaczek, A.Plochocki, E. Roeckl, B. Rubio, K. Rykaczewski, M. Shibata, J. Szerypo, J.L. Tain, V. Wittmann, A. Wöhr:
Determination of the Gamow-Teller Strength Function for the Neutron-Deficient Isotopes $^{104\text{-}107}$In

Meetings, Workshops and Research Seminars at GSI

13./14.01.	Biophysics Meeting
24.25./01.	Research Board
28./29.01.	CERES Coll. Meeting
03./04.02.	FRS User Meeting
20.-23.02.	Workshop EOS 2000
25.02.	EUROBALL-Meeting
08./09.03.	PHELIX Workshop
03./04.04.	FOPI Coll. Meeting
10./11.04.	Coll. Meeting CIRIL/Caen - Material Res./GSI Darmstadt
11./12.04.	Adv. Board for the Therapy Project
19.04.	EXOGAM Meeting
02./03.05.	Shell-Model-Workshop
04.05.	Rhein-Neckar-Main(RNM) Meeting
15./16.05.	HGF Workshop, Datenacquisition, Analysis and Controls
26.05.	Nano-Pore Applications in Biophysics and Microtechnology
10./11.07.	Future Physics with Exotic Nuclei
07.08.-29.09.	Students Program
25.09.-28.09.	7th Workshop on Heavy Charged Particles in Biology and Medicine. RBE and Treatment Planing
18.-20.10.	GSI Workshop on its Future Facility
22.11.	IEEE-NPSS German Chapter Workshop "Pulsed Power in der Beschleuniger- und Lasertechnologie"
23./24.11.	Workshop "Physics with Euroball Detectors at GSI

Jointly organized Conferences, Workshops, Meetings,

10.-11.04.	Coll. Meeting CIRIL/Caen, France and Materials Research/GSI
08.-16.05.	RF and Microwave Measurements, Seeheim, Germany (Joint CERN Accelerator School)
26.05.	Granzer Workshop, Nano-Pore Applications in Biophysics and Microtechnology, University of Frankfurt, Germany
03.-07.07.	Nucleus-Nucleus 2000, Strasbourg, France (GSI/GANIL)
11.-14.09.	Int. Comp. Accelerator Physics Conf. (ICAP 2000), TU Darmstadt, Germany (GSI/TU/DESY/DPG u.a.)

Invited Talks at Conferences

Acicastello, Italy: 3rd Catania Relativistic Ion Studies, CRIS 2000, 22.-26.05.2000

C. Schwarz
Time Scales in Spectator Fragmentation

Amsterdam, The Netherlands: Research School "Fantom", 15.-19.05.2000

T. Kühl
The PHELIX Project

Arona, Italy: 1st Int. Workshop on Space Radiation Research, 27.-31.05.2000

G. Kraft
What can we Learn from Heavy-Ion Therapy for Radiation Protection in Space

Bad Honnef, Germany: Symp. on Fundamental Issues in Elementary Matter, 25.-29.09.2000

H. Emling
Two Phonon Giant Resonances

S. Hofmann
Advances in the Search for Superheavy Elements at GSI

P. Senger
Strange Mesons in Dense Nuclear Matter

Beijing, China: Xiangshan Meeting, Academia Sinologica, 14.09.2000

G. Kraft
Heavy-Ion Therapy – Basic Considerations, Technical Realization and Clinical Results

Berlin, Germany: Reise zum Urknall, Urania, 03.-09.94.2000

P. Armbruster
Expedition ins Reich der Atomkerne

Berlin, Germany: PTCOG 2000, Sept. 2000

M. Krämer
Treatment planning for scanned ion beams

Bologna, Italy: Int. Conf. on 'Structure of the Nucleus at the Dawn of the Century', 29.05.-03.06.2000

E. Roeckl
Decay Properties of N≡Z Nuclei below ^{100}Sn

C. Schwarz
Proton Emission Times in Spectator Fragmentation

Bonn, Germany: DPG, 03.-07.04.2000

P. Egelhof
Hochauflösende kalorimetrische Tieftemperaturdetektoren für massenspektrometrische Anwendungen in der Schwerionenphysik mit exotischen Kernen

C. Haumann, U. Brinkmann, B. Siegmann, U. Werner, H.O. Lutz, R. Mann
Vielfach-Ionisation und Fragmentation kleiner Moleküle in Stössen mit MeV/u Xe-Ionen

N. Kabachnik, B. Siegmann, U. Werner, H.O. Lutz, R. Mann
Kinetic Energy Release Distributions in Coulomb Explosion of N_2 Molecules Induced by Fast Heavy Ion Impact

W. Quint
Die Messung des magnetischen Moments des gebundenen Elektrons in hochgeladenen Ionen: Ein Präzisionstest der Theorie der Quantenelektrodynamik

Bormio, Italy: XXXVIII Int. Winter Meeting on Nuclear Physics, 24.-29.01.2000

W. Trautmann
Kinetic Energies in Multifragmentation

Brighton, UK : The Physics Congress, Europ. Women in Science, 27.-30.03.2000

C. Kausch
Women in Physics in Germany

Caen, France: Atelier INDRA V, 08.-10.03.2000

W. Trautmann
New Results on the Caloric Curve

Caen, France: CERN – GANIL Theory Workshop, 12./13.04.2000

J. Knoll
Hadronisation

Caen, France: 2nd Workshop on Traget and Ion-Source Technology (TWIST II), 14.-16.06.2000

K. Sümmerer
Cross Sections of Heavy-Ion Spallation Residues

Campinas, Brazil: I. Latin American Symposium on Nuclear Physics, 23.-27.12.2000

T. Aumann
Nuclear and Coulomb Breakup of Loosely Bound Neutron-Rich Nuclei

Invited Talks at Conferences

A. Leistenschneider
Electromagnetic Excitation of Neutron-Rich Oxygen-Nuclei 17-22

Cargèse, France: 2nd Euroconf. on 'Atomic Physics at Accelerators: Mass Spectroscopy (APAC2000)', 17.-22.09.2000

W. Quint
The HITRAP-Project at GSI

E. Roeckl
Recent Decay Experiments an N≡Z Nuclei: The Role of Masses, Q Values and Separation Energies

Castiglione della Pescaia, Italy: Simple Atomic Systems, May 2000

Th. Stöhlker
Experiments on High-Z One-Electron Systems

Chiba, Japan: 2nd Int. Space Workshop 2000, 16.-18.02.2000

S. Ritter
Radiation Risk Based on Chromosome Data: Which Factors Should be Considered?

Chicago, USA: Workshop on Low-Energy pbar Storage Ring, 03.-05.08.2000

W. Henning
GSI Plans for an Antiproton Facility

Cracow, Poland: Biophys. Modelling for Radiobiology, Radiotherapy and Radiation Protection, 22.-24.07.2000

C. Fournier
Accelerated Differentiation as Alternative Way for Fibroblasts to Survive Radiation Insult is Related to Fibrosis

S. Ritter
High and low LET Induced Chromosomal Changes: Insights from Interphase Cytogenetics

Cracow, Poland: Workshop on Semihard QCD, 29.04.2000

J. Knoll
Resonance Transport

Cracow, Poland: Meson 2000, 19.-23.05.2000

P. Senger
Strange Mesons in Dense Nuclear Matter

Darmstadt, Germany: Symp. on Future Physics with Exotic Nuclei, 10./11.07.2000

P. Armbruster
My Longstanding (30 years) of Collaboration with G. Münzenberg (1971-2000)

S. Hofmann
Superheavy Elements - Experiments

K.-H. Schmidt
Fission: Recent Research and New Applications

P. Senger
Experiments in Dense Nuclear Matter Research

Darmstadt, Germany: Int. Comp. Acc. Phys. Conf. (ICAP 2000), 11.-14.09.2000

O. Boine-Frankenheim
Phase Space Resolution Issues in Beam Instability Simulation

Darmstadt, Germany: 7th Workshop on Heavy Ion Charged Part. in Biol. and Medicine, 28.-30.09.2000

S. Ritter
RBEs for Chromosomal Damage: Are they reliable?

Debrecen, Hungary: Int. Symposium on Exotic Nucelar Structure ENS 2000, 15.-20.05.2000

T. Aumann
Nuclear Strucutre Studies with Radioactive Beams at GSI

Denton, USA: 16th Int. Conf. on the 'Application of Accelerators in Res. and Industry', 01.-05.11.2000

T. Haberer
Carbon Ion Therapy at GSI Using Scanning Beams

B. Kindler
Status of the Target Development for the Heavy Element Program

Divonne les Bains, France: 5th Int. Conf. on Radioact. Nuclear Beams (RNB-5), 03.-08.04. 2000

H.-J. Kluge
Nuclear Physics using Atomic Physics Techniques

E. Roeckl
Recent Developments at the GSI On-Line Mass Separator

K.-H. Schmidt, J. Benlliure, T. Enqvist et al.:
Future Prospects for Secondary-Beam Production

J. Taieb, P. Armbruster, J. Benlliure et al.:
Measurement of ^{238}U Spallation Product Cross Sections at 1 GeV per Nucleon

Invited Talks at Conferences

Dresden, Germany: Int. Workshop on Atomic Physics in Extreme Fields, 23.-25.03.2000

Th. Stöhlker
Strong Field Effects on the Structure and Dynamics of High-Z Systems

Dresden, Germany: School on the Physics and Chemistry of the Actinides, 02./03.05.2000

M. Schädel
Superheavy Elements Take a Seat at the (Periodic) Table

Dresden, Germany: DPG Spring Meeting, 20.-24.03.2000

M.A. Kargalis, V. Hejny, J. Ritman
PLUTO^{++}: A Monte Carlo Simulation / Analysis Tool for Hadron Physics

C. Kausch
Where have all the women gone…?

Ch. Müntz
HADES: Status Report

Dubna, Russia: Workshop on Fusion Dynamics at the Extremes, 25.-27.05.2000

S. Hofmann
Experiments on Synthesis of Heavy Elements at SHIP

Erice, Italy: Int. School of Nuclear Physics, Radioactive Beams for Nuclear and Astrophysics, 16.-24.09.2000

P. Egelhof
Nuclear Matter Distribution of Neutron-Rich Halo Nuclei from Intermediate Energy Elastic Proton Scattering in Inverse Kinematics

H. Emling
Nuclear Structure Experiments with Unstable Fragment Beams at GSI

W. Henning
Future Plans for the GSI Facilities

S. Hofmann
Synthesis of Superheavy Elements Using Radioactive Beams and Targets

Florence, Italy: ICAP, 04.-09.06.2000

W. Quint
The g-Factor of the Bound Electron in Hydrogen-like Ions. A High-accuracy Test of Bound-state QED

Hayama, Japan: Int. Symposium on Perspective in Physics with Radioactive Isotopes Beams 2000 (RIB00), 13.-16.11.2000

P. Egelhof
Nuclear Structure Studies on Halo Nuclei by Direct Reactions with Radioactive Beams

Heidelberg, Germany: Spring School on Stored Charged Particles and Fundamental Physics, 03./04.03.2000

T. Beier
QED – Theory and Tests

Hirschegg, Austria: Int. Workshop XXVIII on Gross Properties of Nuclei and Nuclear Excitations, 16.01.-22.01.2000

A. Devismes
Results from FOPI on Strangeness Production and Propagation in Hot and Dense Nuclear Matter

J. Knoll, H. van Hees
Finite Pion Width Effects on the Rho Meson and Di-Lepton Spectra

Hirschegg, Austria: Workshop on Physics of High Energy Density in Matter, 30.01.-05.02.2000

R.W. Hasse
Coulomb Strings at GSI

I. Hofmann
Progress on Inertial Fusion at GSI

P. Senger
Strange Mesons in Dense Matter

Hong Kong, China: 7th Int. Conf. on new Diamond Science & Technology ICNDST-7, 23.-28.07.2000

E. Berdermann
The Use of CVD Diamond for Heavy Ion Detection

Honolulu, USA: Pacifichem 2000, Symp. on Science with Radioactive Beams, 14.-19.12.2000

P. Egelhof
Nuclear Matter Distributions of Neutron-Rich Nuclei from Intermediate Energy Elastic Proton Scattering in Inverse Kinematics

Leuven, Belgium: Euro Summer School on Exotic Beams, 31.08.-08.09.2000

H. Grawe
High Spin Isomers Beyond ^{208}Pb – Empirical vs. Large Scale Shell Model

K.-H. Schmidt
Lectures on Production Mechanism of Exotic Nuclei

Invited Talks at Conferences

Les Houches, France: Int. School on "Trapped Particle and Fundamental Phys.", 23.05.-02.06.2000

H.-J. Kluge
Storing Charged Partcles for Fundamental Physics

H.-J. Kluge
Radioactive Ions for Fundamental Physics

H.-J. Kluge
Highly Charged Ions for Fundamental Physics

Lisbon, Portugal: Conf. on Advanced Monte Carlo for Radiation Physics, Particle Transport Simulation and Applications, 23.-26.10.2000

P. Armbruster
New Method and Data on Residue Production in Spallation of ^{197}Au, ^{208}Pb and ^{238}U on Protons Relevant for the Design of Spallation Sources and Accelerator-Driven Systems

Lorne, Australia : 9th Int. Conf. on Fission Track Dating and Thermochronology, 11.02.2000

R. Neumann
Characterization of Ion Tracks in Solids by Near-Field Microscopy and TEM

Lüderitz, Namibia : Fundamental and Applied Aspects of Modern Physics, 13.-17.11.2000

D. Schardt
Tumor Therapy with High-Energy Heavy-Ion Beams

Lund, Sweden: Int. Workshop on Selected Topics on N=Z Nuclei, (PINGST 2000), 06.-10.06.2000

R. Borcea
Beta Decay of ^{56}Cu

J. Döring
Beta-Decay Study of the N=Z Odd-Odd Nuclei ^{62}Ga and ^{70}Br

Z. Janas
Gamow-Teller Decay of Neutron-Deficient Nuclei

M. LaCommara
1s Cluster Emission: an Effective Mechanism to Produce Very Neutron-Deficient Isotopes Near ^{100}Sn?

C. Mazzocchi
Decay Properties of N≈Z Nuclei Below ^{100}Sn

Luso, Portugal: Int. Workshop on Fission Dynamics of Atomic Clusters and Nuclei, 15.-20.05.2000

K.-H. Schmidt
Puzzling Results on Nuclear Shells from the Properties of Fission Channels

Lyon, France: Symposium Lyon, Medical School, 08./09.03.2000

G. Kraft
The Darmstadt Experience with Carbon Ions

Lyon, France: IEEE Nucl. Science Symposium and Medical Image Conference, 15.-20.10.2000

A. Andronic
Prototype Tests for the ALICE TRD

Lissabon, Portugal: Monte Carlo 2000, Oct. 2000

M. Krämer
Treatment Planning for Radiotherapy with Scanned Ion Beams

M. Krämer
TRAX – Ion Track Structure Simulations

Mumbay, India: Int. Symposium on Nuclear Physics, 18.-22.02.2000

U. Datta Pramanik
The Structure of Light Neutron Rich Nuclei through Coulomp Dissociation

Munich, Germany: Deutsche Gesellschaft für Radioonkologie, 07.10.2000

G. Kraft
Physik und Biologie der Schwerionentherapie

Munich, Germany: DEGRO 2000, Oct. 2000

M. Krämer
Treatment planning for scanned ion beams

Orsay, France: Town Meeting, Europ. Isotope Separation On-Line Radioactive Nuclear Beam Facility (EURISOL), 6./7.11.2000

W. Henning
Future Plans at GSI with In-Flight RNBs

Osaka, Japan: Int. Conference on Giant Resonances, 12.-15.06.2000

T. Aumann
Measurements of the Dipole Response with Radioactive Beams

Paris, France: French Physics Society Meeting on Nuclear Physics, 13./14.01.2000

S. Hofmann
The GSI Program of Superheavy Element Research

Invited Talks at Conferences

Paris, France: OECD Global Science Forum Workshop on Strategic Policy Issues Concerning Future High-Intensity Proton Beam Facilities, 25.06.2000

W. Henning
Radioactive Ion and Hadron Beam Facilities for Nuclear Physics Research

Paris, France: Colloque 'Actualité de Frédéric Joliot-Curie', Collège de France, 09./10.10.2000

P. Armbruster
La Recherche de Nouveaux Noyaux et de Nouveau Elements

Paris, France: GEDEON Workshop for the Period 1996-2000, 15./16.11.2000

P. Armbruster
New Method and Data on Residue Production in Spallation of ^{197}Au, ^{208}Pb and ^{238}U on Protons Relevant for the Design of Spallation Sources and Accelerator-Driven Systems

Petersburg, Russia: Int. Conf. on 'Clustering Phenomena in Nuclear Physics', 14.-17.06.2000

E. Roeckl
Decay Properties of N≡Z Nuclei

Pontresina, Italy: 5th Int. Conf. on 'Nuclear and Radiochemistry', 03.-08.09.2000

M. Schädel
Aqueous Chemistry of Transactinides

Quebec, Canada: 7th Int. Conf. on the Intersections of Particle and Nuclear Physics, 22-28.05.2000

W. Henning
Physics of Rare Isotopes

Rossendorf, Germany: Workshop on 'Nuclear Spectroscopy and Nuclear Astrophysics (NSNA)', 27.-29.04.2000

H. Grawe
Nuclear Structure near the Doubly Magic ^{100}Sn and ^{78}Ni

E. Roeckl
Decay Properties of N=Z Nuclei and their Relevance in Astrophysics

K. Sümmerer
Generation of Medium-Mass Radioactive Beams

Rostock, Germany: 2nd Int. Konf. f. „Biosysteme und medizinische Technologie", 09.09.2000

G. Kraft
Heavy Ion Therapy – Clinical Motivation and the Biophysical Basis for a New Concept of a Local Tumor Therapy

San Diego, USA: 13th Int. Symp. on Heavy Ion Inertial Fusion, 13.-17.03.2000

O. Boine-Frankenheim
Simulation of High-Current Phenomena in Ring Machines

I. Hofmann
Heavy Ion Inertial Fusion in Europe

H. Trassl
Ion-Ion Charge Exchange Cross Sections for Heavy Ion Fusion

San Fransisco, USA: 219th ACS Award Meeting, Symp. for Nucl. Chemistry, 26.-30.03.2000

H.-J. Kluge:
Nuclear Physics with Cooled Particles stored in Ion Traps, Storage Rings and Laser Traps

M. Schädel
Superheavy Elements: A Nuclear and a Chemical Puzzle

Schleching, Germany: 31. Arbeitstreffen "Kernphysik", 08.-16.03..2000

P. Armbruster
"Was bringt's". Von Sternen und Kernen, von Beschleunigern und Reaktoren

Seeheim, Germany: CERN Accelerator School, RF Engineering, 08.-16.05.2000
F. Nolden
Stochastic Cooling and Related RF Components

Storrs, USA: DAMOP Meeting 14.-19.07.2000

Th. Stöhlker
Atomic Collision Processes Involving High-Z Ions Studies at the ESR Storage Ring

Strasbourg, France: 7th Int. Conf. on Nucleus-Nucleus Collisions 2000 (NN2000), 02.-07.07.2000

P. Egelhof
Nuclear Matter Distributions of Neutron-Rich Li-Isotopes from Elastic Proton Scattering in Inverse Kinematics

K.-H. Schmidt, J. Benlliure, C. Böckstiegel et al.:
New Results on Structure Effects in Nuclear Fission

Invited Talks at Conferences

P. Senger
Strange Mesons in Dense Nuclear Matter

W. Trautmann
Hot Fragmentation of Nuclei

Tokyo, Japan: Symp. on 'Shell Model 2000', 05.-08.03.2000

H. Grawe
Experimental approach towards shell structure at ^{100}Sn and ^{78}Ni

E. Roeckl
Recent Beta-Decay Experiments on N≅Z Nuclei

Tours, France: Symposium on Nuclear Physics IV, 04.-07.09.2000

H. Grawe
Nuclear Structure in the vicinity of shell closures far from stability

Trieste, Italy: QED2000, 05.-11.10.2000

W. Quint
The g-Factor of the Bound Electron in Hydrogen-like Ions. A High-accuracy Test of Bound-state QED

Uppsala, Sweden: The Svedberg Lab. Workshop on Physics at the CELSIUS Ring, 04.05.2000

W. Trautmann
Kinetic Energies in Multifragmentation

Utrecht, The Netherlands: PAC Symp. Element2000, 02./03.04.2000

M. Schädel
Heavy Element Synthesis

Vienna, Austria: 7th Europ. Part. Acc. Conf., 26.-30.06.2000

I. Hofmann
Optimizing Multiturn Injection with Space Charge and Linear Coupling

M. Steck
Ordered Ion Beams

Volga River, Russia: Joint Accelerator School (JAS2000), 01.-14.07.2000

J. Struckmeier
Intrabeam Scattering

Warsaw, Poland: 33rd COSPAR Scientific Assembly, 16.-23.07.2000

C. Fournier
In Vitro Investigation on Late Effects after Low and High LET Irradiation of Fibroblasts

S. Ritter
Use of Chromosome Aberrations for Radiation Risk Assessment : Possibility and Limitations

S. Ritter
Time Course Analysis of Chromosome Damage: An Instructive Approach

Washington, USA: 220th ACS National Meeting of the American Chemical Society, 20.-24.08.2000

V. Pershina
Theoretical Predictions of Chemical Properties of the Heaviest Elements

Williamsburg, USA: APS Annual Fall Meeting of the Division of Nuclear Physics, 04.-07.11.2000

W. Henning
Physics with Rare Isotopes

Zakopane, Poland: XXXV Zakopane School on Physics, 05.-13.09.2000

A. Leistenschneider
Electromagnetic Excitation of Neutron-Rich Oxygen Nuclei 17-22

Invited Talks at other Institutes

Armbruster, P.:
Atomkerne – 2000
University of Magdeburg, Germany, 13.06.2000

Aumann, T.:
Nuclear and Electromagnetic Induced Reactions of Exotic Nuclei
Universita di Milano, Italy, 21.01.2000

Aumann, T.:
Electromagnetic Excitation of Realtivistic Secondary Beams
IPCR RIKEN, Saitama, Japan, 19.06.2000

Aumann, T.:
Nuclear Structure Studies using High-Energy Secondary Beams
Inst. of Technology, Tokyo, Japan, 19.06.2000

Aumann, T.:
Untersuchung von exotischen Kernen mit hochenergetischen Sekundärstrahlen
University of Mainz, Germany, 06.06.2000

Beier. T.:
Wissenschaft enthüllt die Geheimnisse antiker Schönheit: Woher bezog Nofretete ihr Parfüm?
TU Bergakademie Freiberg, Germany, 08.02.2000,
University of Bochum, Germany, 30.06.2000

Devismes, A.:
Results from FOPI on Strangeness Production and Propagation
INPL, Lyon, France, 09.06.2000

Grawe, H.:
Nuclear Structure in the Vicinity of Shell Closures far from Stability
KU Leuven, Belgium, 04.10.2000

Haberer, T.:
The GSI Therapy Project – Gantry Study and Treatment Control
BNL Upton, USA, 28.08.2000

Haberer, T.:
Cabon Ion Radiotherapy at GSI with a Beam Scanning System
Massachusetts General Hospital, Boston, USA, 31.08.2000

Haberer, T.:
Ionenstrahlen gegen Krebs – eine neue Form der Tumortherapie
Radioaktivität – eine Facette der Natur, Wiesbaden, Germany, 23.11.2000

Hasse, R.W.:
Heavy Ion Research – Theory and Experiments
Jordan Univ. of Science and Techn., Irbid, Jordan, 28.05.2000

Hasse, R.W.:
Ordered Systems of Particles
Jordan Univ. of Science and Techn., Irbid, Jordan, 28.05.2000

Hasse, R.W.:
Structures of Ordered Particles
Yarmouk Univ., Ibid, Jordan, 30.05.2000

Helariutta, K.:
Cross Section Studies with the Fragment Separator
Univ. of Jyväskylä, Finland, 20.09.2000

Henning, W.:
Physik u. technische Herausforderung von Strahlen kurzlebiger Kerne
MPI f. Kernphys., Heidelberg, Germany,03.02.2000

Henning, W.:
Physik mit radioaktiven Strahlen u. allgemeine Zukunftsperspektiven der GSI zur Kern- u. Hadronenphysik mit Sekundärstrahlen
University of Giessen, Germany, 14.02.2000

Hennig, W.:
Schwerionenforschung an der GSI: Heute, morgen, übermorgen
University of Mainz, Germany, 15.02.2000

Henning, W.:
Navigating the Chart of Nuclei towards New Forms of Matter
Hebrew University of Jerusalem, Israel, 14.03.2000

Henning, W.:
Atomkerne: Herz der Materie, Brennstoff für Sterne
University of Tübingen, Germany, 12.07.2000

Invited Talks at other Institutes

Henning, W.:
GSI: Future Plans
KVI, Groningen, The Netherlands, 21.07.2000

Henning, W.:
Atomkerne: Forschung heute und morgen
FZ Karlsruhe, Germany, 16.10.2000

Henning, W.:
Research at GSI - Current Program and Future Plans
GANIL, Caen, France, 27.10.2000

Henning, W.:
Radioisotope - Detektive für Wissenschaft, Technik und Kunst
Radioaktivität - eine Facette der Natur, Wiesbaden, Germany, 21.11.2000

Henning; W.:
Future Plans at GSI
NuPECC-Meeting, CERN, Geneva, Switzerland, 15.12.2000

Heßberger, F.P.:
α- and α-γ-Decay Studies of Neutron Deficient Isotopes in the Region Z=88-92
LBNL Berkeley, USA, 15.03.2000

Heßberger, F.P.:
Experimente zur Synthese superschwerer Elemente
University of Bonn, Germany, 29.06.2000

Heßberger, F.P.
Experiments on the Synthesis of Superheavy Elements
IPN Orsay, France, 11.09.2000,
GANIL Caen, France, 12.09.2000

Heßberger, F.P.:
Experimente zur Synthese superschwerer Elemente
Klinikum Hof, Germany, 20.09.2000

Heßberger, F.P.:
Recent Result on the Investigation of Superheavy Nuclei (at SHIP)
University of Jyväskylä, Finnland, 12.12.2000

Hildenbrand, K.D.
Kaons, Chiral Symmetry, Semiconductive Glass
Warsaw University, Poland, 17.11.2000

Hofmann, I.:
Energieaustausch und Equipartitioning in Hochstromlinacs
University of Frankfurt, Germany, 01.12.2000

Hofmann, I.:
Space Charge Issues in Proton Drivers
ICFA Mini-Workshop, CERN, Geneva, Switzerland, 08.03.2000

Jurado, B.:
New Results on the Role of Dissipation in Nuclear Fission
IPN Orsay, France, 12.10.2000

Jurado, B.:
Fission: a Tool to Investigate Dissipation in Nuclei
Univ. of Santiago de Compostela, Spain, 26.04.2000

Kluge, H.-J.:
Durch Kühlung zur Präzision: Atom- und Kernphysik mit gespeicherten Teilchen
University of Göttingen, Germany, 26.06.2000,
TU Berlin, Germany, 30.11.2000

Kluge, H.-J.:
Lasers and Heavy Ions at GSI/Darmstadt
PALS, Prague, Czech Republic, 07.12.2000

Knoll, J.:
Resonance Transport
KVI Groningen, The Netherlands, 29.02.2000

Knoll, J.:
Resonance Transport and Kinetics Entropy
ETC Trento, Italy, 06.04.2000

Krämer, M.:
Treatment Planning for Radiotherapy with Scanned Ion Beams
Lyon, France, Dec. 2000

Invited Talks at other Institutes

Kraft, G.:
Tumortherapie mit schweren Ionen
DPG, Berlin, Germany, 18.01.2000

Kraft, G.:
Tumortherapie mit Ionenstrahlen
Univ. of Kaiserslauter, Germany, 31.01.2000

Kraft, G.:
Biologische Aspekte der Tumortherapie mit Schwerionen
TU Darmstadt, Germany, 15.02.2000

Kraft, G.:
Grundlegende Fragen zur Tumortherapie
Rhön-Kliniken, Wiesbaden, Germany, 27.03.2000

Kraft, G.:
Physical and Technical Aspects of Heavy Ion Therapy
Inst. of Modern Phys., Lanzhou, China, 18.09.2000

Kraft, G.:
Biomedical Aspects of Heavy-Ion Therapy
Inst. of Modern Phys., Lanzhou, China, 19.09.2000

Kraft, G.:
Ionenstrahlen gegen Krebs: Eine neue Form der Tumortherapie
Radioaktivität – eine Facette der Natur, Wiesbaden, Germany, 08.11.2000

Kraft, G.:
Active Beam Application and Verification for Ion Beam Therapy
MedAustron, Vienna, Austria, 01.12.2000

Kraft, G.:
Tumortherapie mit hochenergetischen schweren Ionen
University of Augsburg, Germany, 04.12.2000

Kühl, T.:
PHELIX – Ein Petawatt Hochenergier Laser für Schwerionenexperimente
University of Jena, Germany, 26.05.2000,
University of Siegen, Germany, 23.11.2000

Mokler, P.H.:
Atomphysik bei straken Zentralfeldern
TU Berlin, Germany, 10.02.2000

Mokler, P.H.:
Atomic Physics at Strong Central Fields
University of Cracow, Poland, 10.12.2000

Pershina, V.:
Relativistic Calculations of the Electronic Structure of the Heaviest Elements
University of Bern, Switzerland, February 2000

Quint, W.:
Grundlagenexperimente an einzelnen Teilchen in Ionenfallen
University of Tübingen, Germany, 31.01.2000

Quint, W.:
Grundlagenexperimente in Ionenfallen
University of Bonn, Germany, 18.04.2000

Quint, W.:
Grundlagenexperimente an gespeicherten Teilchen in Ionenfallen und Speicherringen
University of Giessen, Germany, 26.06.2000

Quint, W.:
Experiments with Exotic Particles in Ion Traps
KVI Groningen, The Netherlands, 05.06.2000

Quint, W.:
Astrids Quantensprünge im Ionenkäfig – oder: Kann man ein einzelnes Atom sehen?
Radioaktivität – eine Facette der Natur, Wiesbaden, Germany, 24.11.2000

Reinhard, I.:
Hochauflösende Molekularspektroskopie in superfluiden He-Clustern
University of Gießen, Germany, 13.07.2000

Reinhard, I.:
Mit Laserlicht zu Zuständen heißer als das Sonnenfeuer
Radioaktivität – eine Facette der Natur, Wiesbaden, Germany, 14.11.2000

Invited Talks at other Institutes

Ritter, S.:
Cell Inactivation and Induction of Chromosomal Damage in CHO-K1 and xrs5 Cells Following X-ray and Particle Exposure
NIRS, Chiba, Japan, 14.02.2000

Ritter, S. :
Chromosomal Damage Induced in Human Lymphocytes and Tumor Cells. Report on Experiments Performed at NIRS
NIRS, Chiba, Japan, 05.04.2000

Schädel, M.:
Kernchemie der Transactinoiden – chemische und nukleare Aspekte superschwerer Kerne
LMU und TU Munich, Germany, 18.02.2000

Schardt, D.:
The Heavy-Ion Therapy Program at GSI
NAC Faure, South Africa, 10.11.2000

Scheidenberger, C.:
Massenmessung exotischer Kerne am Experimentierspeicherring ESR
University of Freiburg, Germany, 21.06.2000

Schlitt, B.:
Patient Irradiation with Carbon Ion Beams at GSI and the Proposed Ion Beam Facility for Cancer Therapy at the Clinic in Heidelberg
Loma Linda Medical Center (LLUMC), Loma Linda, USA, 30.08.2000

Schmidt, K.-H.
Systematik der Struktureffekte in der Kernspaltung Neue experimentelle Erkenntnisse
University of Bale, Switzerland, 08.06.2000

Schmidt, K.-H.
Three Lectures on Residual Nuclide Production in Relativistic Nuclear Collisions
Univ. of Louvain-la-Neuve,Belgium,10.-12.04.2000

Schmidt, K.-H.
Zur Lösung des Problems radioaktiver Abfälle nit kernphysikalischen Methoden
University of Mainz, Germany, 17.-22.02.2000

Senger, P.:
Seltsame Teilchen in komprimierter Kernmaterie oder: Wie entsteht aus einem Neutronenstern ein Schwarzes Loch?
University of Frankfurt, Germany, 05.04.2000

Senger, P.:
Strange Mesons as a Probe for Dense Nuclear Matter
IPN Orsay, France, 27.11.2000

Senger, P.:
Seltsame Mesonen als Sonden komprimierter Kernmaterie
TU and LMU Munich, Germany, 31.11.2000

Senger, P.:
Strange Mesons as a Probe for Dense Nuclear Matter
University of Heidelberg, Germany, 05.12.2000

Stöhlker, Th.:
Test of QED in High-Z One- and Few-Electron Ions
NIST, Gaitherburg, USA, Nov. 2000

Stöhlker, Th.:
Präzise Erkenntnisse aus kalten Ionen – Atomphysik am Speicherring der GSI
Radioaktivität eine Facette der Natur, Wiesbaden, Germany, 24.11.2000

Stöhlker, Th.
Charge Exchange Processes and Beam Lifetimes for Heavy Few Electron Systems
Atomic Phys. Seminar, Lanzhou, China, Oct. 2000

Stöhlker, Th.:
1s-Lamb Shift Studied for H-Like High-Z Ions at the ESR Storage Ring
Atomic Phys. Seminar, Lanzhou, China, Oct. 2000

Taucher Scholz, G.:
Leben mit Strahlen – Chance oder Risiko? Zur Wirkung von Strahlen auf unseren Organismus
Deutsches Museum: Wissenschaft für Jedermann, München, Germany, 06.12.2001

Invited Talks at other Institutes

Trautmann, W.:
Multifragmentation mit ALADIN
LMU + TU Munich, Germany, 26.05.2000

Weyrather, W.K.:
Tumortherapie mit Ionenstrahlen – Grundlagen, Technik, erste Ergebnisse
DESY Hamburg, Germany, 08.03.2000

Weyrather, W.K.:
Tumortherapy with Relativistic Ion Beams
IPN Orsay, France, 18.09.2000

Weyrather, W.K.:
Die relative biologische Wirksamkeit für Hoch-LET-Strahlen
FZ-Rossendorf, Germany, 10.11.2000

Weyrather, W.K.:
Advantages of Heavy-Ion Therapy – Dose Distribution and High-LET Effects
Wien, Austria, 01.12.2000

Lectures and Courses

Berdermann, E.:
Strahlungsresistente, superschnelle Detektoren aus CVD Diamant
University of Giessen, Germany, 23.11.2000

Bokemeyer, H.:
WS1990/2000: Atomphysik II
(University of Frankfurt, Germany)

Bokemeyer, H.:
SS2000: Atomphysik IV
(University of Frankfurt, Germany)

Bokemeyer, H.:
WS2000/2001: Atomphysik III,
Beschreibung fundamentaler Wechselwirkungen
(University of Frankfurt, Germany)

Bosch, F.:
WS99/2000: Kern- und Elementarteilchenphys. I
(University of Kassel, Germany)

Bosch, F.:
SS2000: Kern- und Elementarteilchenphysik II
(University of Kassel, Germany)

Bosch, F.; B. Fricke:
WS2000/2002: Astrophysik Seminar
(University of Kassel, Germany)

Egelhof, P.:
WS99/2000: Seminar zum Praktikum für Fortgeschrittene
(University of Mainz, Germany)

Egelhof, P. (AG EXAKT):
WS99/2000: Seminar über „Experimentelle Atom- und Kernphysik"
(University of Mainz, Germany)

Egelhof, P., D. Ackermann, G. Huber, G. Münzenberg:
WS99/2000: Seminar über „Anwendungen der Atom- und Kernphysik in der Umwelt- und Medizinforschung"
(University of Mainz, Germany)

Egelhof, P. (AG EXAKT):
SS2000: Seminar über „Experimentelle Atom- und Kernphysik"
(University of Mainz, Germany)

Egelhof, P.:
WS2000/2001: Seminar zum Praktikum für Fortgeschrittene
(University of Mainz, Germany)

Egelhof, P. (AG EXAKT):
WS2000/2001: Seminar über „Experimentelle Atom- und Kernphysik"
(University of Mainz)

Egelhof, P., D. Ackermann, G. Huber, G. Münzenberg:
WS2000/2001: Seminar über „Interdisziplinäre Anwendungen der Atom- und Kernphysik"
(University of Mainz, Germany)

Emling, H.:
WS99/2000: Gruppenunterricht zur Vorlesung Physik III
(University of Heidelberg, Germany)

Emling, H.:
WS2000/2001: Gruppenunterricht zur Vorlesung Physik V
(University of Heidelberg, Germany)

Kluge, H.-J.; Liesen, D.:
Oberseminar über Atomphysik
(University of Heidelberg, Germany)

Kluge, H.-J.:
WS99/2000: Oberseminar über Atomphysik
(University of Heidelberg, Germany)

Kluge, H.-J.:
SS2000: Oberseminar über Atomphysik
(University of Heidelberg, Germany)

Kluge, H.-J.:
WS2000/20001: Doktorandenseminar über neuere Fragen der Physik
(University of Heidelberg, Germany)

Lectures and Courses

Knoll, J.:
SS2000: Introduction to the Physics of Hot and Dense Hadronic Matter I
(University of Heidelberg, Germany)

Knoll, J.:
WS99/2000: Introduction to the Physics of Hot and Dense Hadronic Matter II
(University of Heidelberg, Germany)

Kraft, G.:
WS99/2000: Heilen mit Hadronen
(Saturday Morning Phys., TU Darmstadt, Germany)

Kraft, G.:
WS99/2000: Energiedeposition und biologische Wirkungen von Ionen
(TU Darmstadt and GhK Kassel, Germany)

Kraft, G.:
13./14./16.11.: Strahlenschutzsonderkurs
(GhK Kassel, Germany)

Kraft, G.:
SS2000: Physik für Biologen
(TU Darmstadt, Germany)

Kraft, G., D. Schardt:
WS2000/2001: Strahlenbiophysik
(TU Darmstadt, Germany)

Kühl, T.:
SS2000: PHELIX – Ein Petawatt Hochenergie Laser für Schwerionenexperimente
(University of Jena, Heraeus Sommerschule, Germany)

Kühl, T.; J.A. Maruhn, P. Mulser:
WS99/2000: Seminar zur Physik dichter Plasmen mit Schwerionen- und Laserstrahlen
(TU Darmstadt, University of Frankfurt, University of Mainz, Germany)

Kühl, T.; J.A. Maruhn, P. Mulser:
SS2000: Seminar zur Physik dichter Plasmen mit Schwerionen- und Laserstrahlen
(TU Darmstadt, University of Frankfurt, University of Mainz, Germany)

Kühl, T.; J.A. Maruhn, P. Mulser:
WS2000/2001: Seminar zur Physik dichter Plasmen mit Schwerionen- und Laserstrahlen
(TU Darmstadt, University of Frankfurt, University of Mainz, Germany)

Kühl, T.:
WS2000/2001: Vorlesung Physik der Ultra-Hochintensitätslaser
(University of Mainz, Germany)

Liesen, D.:
SS2000: Gruppenunterricht zur Physik IV
(University of Heidelberg, Germany)

Liesen, D.:
WS2000/2001: Gruppenunterricht zur Physik III
(University of Heidelberg, Germany)

Mokler, P.H.; A. Müller
SS2000: Experimentelle Atomphysik
(Graduiertenkurs II)
(University of Giessen, Germany)

Mokler, P.H.; N. Grün, A. Müller, E. Salzborn, K. -H. Schartner, W. Scheid:
SS2000: Seminar über Atomphysik (Graduierte)
(University of Giessen, Germany)

Mokler, P.H.; N. Grün, A. Müller, E. Salzborn, K. -H. Schartner, W. Scheid:
WS2000/01: Sem. über Atomphysik(Graduierte)
(University of Giessen, Germany)

Neumann, R.:
SS2000: Hochauflösende Mikroskopie und Nanotechnologie I
(University of Heidelberg, Germany)

Neumann, R.:
WS2000/2001: **Hochauflösende Mikroskopie und Nanotechnologie II**
(University of Heidelberg, Germany)

Orth, H.:
WS99/2000: Phänomene aus der Quantenwelt, Grundlagen und Anwendungen
(University of Heidelberg, Germany)

Lectures and Courses

Orth, H.:
WS99/2000: Tutorium zur Physik II: Elektronmagnetismus, Wellen, Optik
(University of Heidelberg, Germany)

Orth, H.:
SS2000: Spezielle und Allgemeine Relativitätstheorie im Test von Experimenten
(University of Heidelberg, Germany)

Quint, W.:
WS99/2000: Experimentelle Atomphysik: Atome und Felder
(University of Heidelberg, Germany)

Quint, W.:
SS2000: Experimentelle Atomphysik: Atomare Mehrteilchensysteme
(University of Heidelberg, Germany)

Quint, W.:
WS2000/2001: Experimentelle Atomphysik: Atome und Felder
(University of Heidelberg, Germany)

Stroth, J.:
WS2000/2001: Ergänzungen zur Kernphysik I
(University of Frankfurt, Germany)

Inaugural Dissertation, Thesis, Diploma

Inaugural Dissertation

Beier, T.:
The g_j Factor of a Bound Electron and the Hyperfine Structure Splitting in Hydrogenlike Ions
(Techn. University of Dresden, Germany, 2000)

Thesis

Bär, R.C.:
Untersuchung der quadrupolaren BFT-Methode zur Diagnose intensiver Ionenstrahlen
(University of Frankfurt, Germany, 2000)

Bathelt, B.:
Filmdosimetrie in der Schwerionen-Tumortherapie: 3-dimensionale Dosisverifikation in gemischten Teilchenstrahlenfeldern
(Univ. Gesamthochschule Kassel, Germany, 2000)

Brinzanescu, O.:
X-Ray Emission of High-Z Projectiles in Collisions with Electrons and Atoms
(University of Heidelberg, Germany, 2000)

Brachmann, J.:
Kollektiver Fluß im Dreiflüssigkeitenmodell
(University of Frankfurt, Germany, 2000)

Grünschloß, A.
Coulombanregung von Dipolriesenresonanzen und Fragmentation von ^{136}Xe in peripheren relativistischen Schwerionenstößen
(University of Frankfurt, 2000)

Häffner, H.:
Präzisionsmessung des magnetischen Moments des Elektrons in wasserstoffähnlichem Kohlenstoff
(University of Mainz, Germany, 2000)

Hees, H. van:
Renormierung selbstkonsistenter Näherungen in der Quantenfeldtheorie bei endlichen Temperaturen
(Techn. University of Darmstadt, Germany, 2000)

Hermanspahn, N.
Das magnetische Moment des gebundenen Elektrons in wasserstoffartigem Kohlenstoff (C^{5+})
(University of Mainz, Germany, 2000)

Hollinger, R.:
Entwicklung und Untersuchung einer Hochstrom-Ionenquelle zur Erzeugung intensiver, hochbrillanter Protonenstrahlen
(University of Frankfurt, Germany)

Ilievski, S.:
Mehr-Phononen-Riesentesonanzen und Coulombspaltung von ^{238}U in relativistischen Schwerionenstößen
(University of Frankfurt, Germany, 2000)

Krämer, A.:
Untersuchungen zur Stoßdynamik von schweren, hochgeladenen Ionen am Tattarget des ESR Speicherringes - Die Entwicklung eines H_2-Cluster-Targets
(University of Frankfurt, Germany, 2000)

Kutsche, R.:
Untersuchung der In-Medium-Eigenschaften von K°_{s}-Mesonen und Λ-Hyperonen an der Produktionsschwelle
(Techn. University of Darmstadt, Germany, 2000)

Roland, Ch.:
Flavor Fluctuations in Central Pb-Pb Collisions at 158 GeV/Nucleon
(University of Frankfurt, Germany, 2000)

Inaugural Dissertation, Thesis, Diploma

Roth, R.:
Effektive Wechselwirkungen für Quantenflüssigkeiten und Quantengase
(Techn. University of Darmstadt, Germany, 2000)

Schmitt, F.:
Zweiphotonen- und Resonanzionisations-Laserspektroskopie an atomaren Lithium
(University of Heidelberg, Germany, 2000)

Schuchert, I.:
Elektrochemische Untersuchungen zur Abscheidung und zum Korrosionsverhalten von Kupfermikrostrukturen
(Techn. University of Darmstadt, Germany, 2000)

Seelig, P.:
Laserspektroskopie der 1s-Hyperfeinstrukturaufspaltung an wasserstoffähnlichem $^{207}Pb^{81+}$
(University of Mainz, Germany, 2000)

Wisniewski, K.:
Kaon and Antikaon Production in Heavy-Ion Collisions for the Reaction Ru+Ru and Ru+Zr at 1.69 AGeV Beam Kinetic Energy
(Warsaw University, Poland, 2000)

Diploma

Grabczewski, N. von:
Untersuchung von Alpha-Rückstoß-Spuren in Biotit mittels Rasterkraftmikroskopie
(University of Heidelberg, Germany, 2000)

Heiß, M.:
Untersuchung von Röntgen- und Ionenbestrahlter DNA mittels Rasterkraftmikroskopie
(University of Heidelberg, Germany, 2000)

Pirzadeh, P.:
Strahloptimierung am Hochenergielasersystem nhelix durch Raumfrequenzfilterung
(Techn. University of Darmstadt, Germany, 2000)

Seminars at GSI

11.01.
J. Schaffner-Bielich, Brookhaven Nat. Lab.
Strange Dibaryons, their Weak Decay and how to Detect them in Relativistic Heavy-Ion Collisions

11.01.
Ch. Stoeckl, University of Rochester
Laser-Experimente in Rochester

11.01.
K.-L. Kratz, Univ. of Mainz
Nuclear Physics Input for the Astrophysical Process: from B^2FH to Present

12.01.
R. Kutsche, GSI Darmstadt
Untersuchungen der In-Medium-Eigen-schaften von K^0_s-Mesonen und Λ-Hyperonen an der Produktionsschwelle

12.01.
R. Moshammer, Univ. of Freiburg
Ionisation in intensiven, ultrakurzen Laserpulsen

13.01.
A. Tauschwitz, TU Darmstadt
Erzeugung, Transport und Fokussierung intensiver Ionenstrahlen mit Methoden der Plasmaphysik

18.01.
S. Bernd, University of Frankfurt
Simulation schwerionenbestrahlter Targets mit gitterloser Teilchen-Hydrodynamik

18.01
J.P. Delahaye, CERN, Geneva
The CLIC Study of a Multi-TeV $e^{\pm}$ Linear Collider

19.01.
A.B. Voitkiv, University of Giessen
Projectile-Electron Excitation and Loss in Relativistic Collisions with Target Electrons

19.01.
W. Barth, GSI, Darmstadt
Anmerkungen zur Inbetriebnahme des Hochstrominjektors

25.01.
P.L. Biermann, MPI f. Radioastronomie, Bonn
The Sources of the Highest Energy Cosmic Rays Observed in the Universe

01.02.
H. Satz, University of Bielefeld
Phase Transitions in QCD

02.02.
V.P. Shevelko, Lebedev Inst., Moscow
Charge Exchange and Photoionization of Heavy Low-Charged Ions

02.02.
B. Blank, CEN Bordeaux-Gradignan
Discovery of Doubly Magic ^{48}Ni

08.02.
C. Schwarz, GSI Darmstadt
Hydrogen Burning: pp Chain

08.02.
Y. Maron, Weizmann Institute, Israel
Fast Magnetic Field Penetration and Particle Flow in Plasma

09.02.
Th. Steih, University of Giessen
Dielektronische Rekombination an hochgeladenen, schweren Ionen

09.02.
H. Oeschler, TU Darmstadt
Particle Production in Heavy Ion Collisions at SIS Energies - Thermal Equilibrium versus Dynamics

15.02.
R. Landau, CERN, Geneva
Antihydrogen Atoms - A Glimpse of the Anti-World?

15.02.
M. Basko, TU Darmstadt, ITEP Moscow
Physics of Magnetized Target Fusion and Possible Implosion Experiments with GSI and TWAC Beams

Seminars at GSI

16.02.
C. Toepffer, University of Erlangen
Radiative Recombination of Highly Charged Ions in Magnetized Electron Plasmas

17.02.
D.C. Ionescu, GSI Darmstadt
Dynamics of Atomic Processes in Strong Electromagnetic Fields

22.02.
S. Jacquemot, CEA, Bruyères-le-Chatel
Highlights on the Physics of Inertial Confinement Fusion and Diagnostics of Hot Dense Plasmas

23.02.
K. Blaum, University of Mainz
Resonanzionisations-Massenspektrometrie zur Ultraspurenanalyse von Gadolinium: Die Suche nach den Seltenen Erden

24.02.
R. Eichhorn
Entwicklung von supraleitenden H-Moden-Resonatoren

25.02.
Fan Wo, Suzhou Medical College, China
Nuclear Medicine and Radiopharmaceuticals in China

28.02.
F. Hammache, GSI Darmstadt
Current Models of the Sun

02.03.
I. Hofmann, GSI Darmstadt
Aussichten neuer Injektionsverfahren für höchste Intensitäten

03.03.
O. Scavenius, Copenhagen, Denmark
Strong Soft Pion Field in a First Order Chiral Phase Transition

10.03.
Prof. Dr. Thomas Holstein, TU Darmstadt
Funktion des ß-Catenin-Komplexes in der Zelladhäsion und Signalweiterleitung bei Hydra.

14.03.
Th. Schenkel, LLNL, Livermore
Wechselwirkung langsamer, hochgeladener Schwerionen mit Festkörpern: Grundlagen und Anwendungen

14.03.
M.B. Tsang, MSU, East Lansing
Scaling Behavior of Isotopes Produced in Nuclear Reactions

15.03.
G. Walter, IKF, Frankfurt
Ionenstrahlmodifikation von Ti und Fe-Legierungen - Untersuchungen mit nuklearen Methoden

27.03.
T. Aumann, GSI Darmstadt
Current Status of the Solar Neutrino Problem

28.03.
Dr. Romualdo de Souza, Indiana University, Bloomington
Investigating Heavy-Ion Reactions with Fragment-Fragment Correlations

05.04.
S.A. Fayans, Kurchatov Institute, Moscow
Local Energy-Density Functional Approach to Many-Body Nuclear Systems with S-Wave Pairing

05.04.
B. Franzke, GSI Darmstadt
Stand der Überlegungen für den Ausbau der GSI-Beschleuniger-Anlage

17.04.
F. Attallah, GSI Darmstadt
Helium Burning

18.04.
J. Ullrich, University of Freiburg
Atomare Dynamik in extremen Feldern: von Atto- zu Femtosekunden

26.04.
V.D. Toneev, GSI Darmstadt+ Dubna, Russia
A Mixed Phase Model: Observable Consequences of Cross-Over Type of Deconfinement Phase Transitions

Seminars at GSI

28.04.
G. Mourou, University of Michigan
Ultrahigh Intensity Lasers: Physics of the Extreme on a Tabletop

02.05.
M. Dreher, MPQ Garching
Superradiant Amplification of Ultra-Short Laser Pulses in Plasma: A New Scheme for Compression of Laser Energy

02.05.
P. Braun-Munzinger, GSI Darmstadt
Creation of Big Bang Matter in the Laboratory: Survey of Heavy Ion Experiments at the CERN SPS

03.05.
Th. Beier, GSI Darmstadt
Hochgeladene Ionen und QED: Prüfsteine für die beste Theorie in der Physik

04.05.
P. Spiller, GSI Darmstadt
Bunch Kompression im Schwerionensynchrotron SIS

09.05.
Th.E. Cowan, LLNL Livermore
Particle Acceleration and Nuclear Phenomena in Ultra-Intense Laser Experiments

10.05.
B. Nefkens, UCLA, USA
New Results with the Crystal Ball Multiphoton Spectrometer

16.05.
O. Willi, Oxford Imperial College, United Kingdom
Inertial Fusion Physics and Ultra Short Laser-Pulse Interaction

17.05.
K. Poppensieker, GSI Darmstadt
Sicherheit und Kontrolle bei der Schwerionentherapie

23.05.
M. Roth, GSI Darmstadt
Intense Ion Beams Accelerated by Petawatt-Class Lasers and the Concept of Proton Fast Ignition

23.05.
K. Kleinknecht, University of Mainz
Verletzung der Symmetrie zwischen Materie und Antimaterie in der schwachen Wechselwirkung

24.05.
H. Häffner, University of Mainz
High Accuracy Determination of the g-Factor of the Electron in $^{12}C^{5+}$: A Test of Bound-State QED

29.05.
Fr. N. Erdmann, Inst. f. Transuran. Elem., Karlsruhe
Charakterisierung von spaltstoffhaltigen Partikeln mitSpaltspuranalyse, Alpha-Autoradiographie, Rasterlektronenmikroskopie und Sekundärionen-massenspektrometrie

29.05.
H. Emling, GSI Darmstadt
General Characteristics of Reaction Rates

30.05.
H. Brand
Automatisierte Messung von Targetdicken

30.05.
K.D.A. Wendt, University of Mainz
Bestimmung seltenster Isotope mit der resonanten Laser-Massenspektroskopie

31.05.
M. Steck, GSI Darmstadt
Stand der Überlegungen zu einem neuen Speicherring ESR

31.05.
U. Meissner, Forschungszentrum Jülich
The Nucleon-Nucleon Interaction from Effective Field Theory

31.05.
J. Gerl, GSI Darmstadt
Status Report of the VEGA Project

05.06.
U.D. Pramanik, GSI Darmstadt
Explosive Burning, Supernovae

06.06.
P. Senger, GSI Darmstadt
Strange Mesons as a Probe for Dense Nuclear Matter

Seminars at GSI

06.06.
S. Pfalzner, University of Jena
Laserfusion als Laborastrophysik

07.06.
C. Elster, Jülich and Ohio
Towards Faddeev Calculations at Intermediate Energies

13.06.
S. Neff, TU Darmstadt
Hochenergie-Laser

14.06.
H.F. Beyer, GSI Darmstadt
Wege zur Präzisionsmessung der 1s-Lambverschiebung hochgeladener Ionen

14.06.
V. Duflot, GANIL, GANIL, Caen, France
Signals of Phase Transition in Finite Systems

15.06.
M. Crescenti, TERA
TERA Activities and the RF System of the CNAO Synchrotron

20.06.
S. Kuhlbrodt, University of Rostock
Transporteigenschaften dichter Plasmen

20.06.
M. Weidemüller, MPI f. Kernphysik, Heidelberg
Trapping Particles with Laser Light: from Ultracold Atoms to Ultracold Molecules

20.06.
S.L. Taylor, Florida State University, Tallahessee
Nuclear Physics in the Sunshine State

21.06.
C. Kozhuharov, GSI Darmstadt
Dielektronische Rekombination hochgeladener, schwerer Ionen

21.06.
J. Stroth, GSI Darmstadt and University of Frankfurt
Status of the HADES Project

26.06.
M. Hausmann, GSI Darmstadt
R-Process

27.06.
Th. Schlegel, GSI Darmstadt
Niederentropie-Targetkonpression mittels Ionenstrahlen für Messungen der Zustandsgleichung

27.06.
A.M. Kellerer, GSF Neuherberg
The Hiroshima Neutron Discrepancy A Central Issue in Risk Assessment

28.06.
E. Sauvan, LPC-ISMRA, Caen
Breaking the Halo: Experimental Probes for Light Neutron-Rich Nuclei

28.06.
M. Moshinsky, Mexico
On Canonical Transformations for Time Evolution and their Representation in Wigner Distribution Phase Space

03.07.
O. Klepper, GSI Darmstadt
Cosmic Ray Physics

05.07.
V.P. Shevelko, Lebedev Inst., Moscow
Stripping of Fast Heavy Low-Charged Ions in Gaseous Targets

05.07.
Th. Stöhlker, GSI Darmstadt
Experimente zur Lamb-Verschiebung in den schwersten Ein-Elektronensystemen

11.07.
I. Tanihata, RIKEN
Physics with Next Generation Exotic Nuclear Beam Facilities

14.07.
V. Saveliev, Moscow Eng.+Phys. Institute
Transition Radiation: Particle Identification and Beam Diagnostic

17.07.
A. Leistenschneider, GSI Darmstadt
Chronometers

Seminars at GSI

27.07.
K. Fong, TRIUMF, Vancouver
RF Systems and RF Control in the TRIUMF-ISAC Project

09.08.
Th. Schäfer, SUNY, Stony Brook
Kaon Condensation in High Density QCD

21.08.
Th. Elze, Rio de Janeiro
Collective Neutrino Interaction in Type II Supernovae

05.09.
K. Koch, GSI Darmstadt
Luminiszenz mit Cluster-Ionen im MeV-Bereich

06.09.
R. Thompson, Århus University
Cold Antiparticles: Their Creation and a few interesting Applications

07.09.
R.W. Hasse, GSI Darmstadt
Erklärung der geordneten Strahlen in ESR und SIS

19.09.
C.K. Rhodes, University of Illinois
Saturated Amplification of Xe(L) at 2.9Å from Hollow Atom States

27.09.
R. Roth, GSI Darmstadt
Structure and Stability of Trapped Ultracold Fermi Gases Using Effective s- and p-Wave Contact Interactions

28.09.
- J. Kewisch, Brookhaven National Laboratory
  RHIC Commissioning 2000

- S. Peggs, Brookhaven National Laboratory
  The Rapid Cycling Medical Synchrotron, RCMS

29.09.
R. Roth, GSI Darmstadt
The Unitary Correlation Operator Method for Dense Quantum Liquids

04.10.
J. Randrup, LBL Berkeley, USA / GSI Darmstadt
Quantum Field Effects in Disoriented Chiral Condensates

12.10.
L. Labzowsky, St. Petersburg
Parity Violation in He-like Highly Charged Ions

24.10.
R.P. Freifelder, Univ. of Pennsylvania, Philadelphia
New Developments in Positron Emission Tomography: Dedicated Brain and Breast Scanners

25.10.
J. Schnack, University of Osnabrück
Magnetic Molecules - A New Playground for the Heisenberg Model

25.10.
P.H. Mokler, GSI Darmstadt
Atomic Physics Experiments in Cave A - a Status Report

27.10.
R. Vogt, LBNL Berkeley+GSI Darmstadt
Heavy Quark Production Beyond Next to Leading Order

31.10.
G. Werth, University of Mainz
The g-Factor of the Bound Electron: New Possibilities for Precision Physics

01.11.
J. Connell, University of Chicago
Cosmic Ray Composition Studies: Nuclear Physics on a Galactic Scale

01.11.
A. Paul, PTB Braunschweig
Prompte (n,γ) Spektrometrie zur Präzisions-bestimmung von Massendifferenzen und Isotopenverhältnissen für das Avogadro-Projekt

01.11.
H. van Hees, GSI Darmstadt
Symmetries and Self-Consistency: Vector Mesons at Finite Temperature

Seminars at GSI

02.11.
S. Runkel, University of Frankfurt
Untersuchungen von grundlegenden physikalischen Prozessen in Elektron-Zyklotron-Resonanz-Ionenquellen

07.11.
P.-G. Reinhard, University of Erlangen-Nürnberg
Exotic Nuclei - A Challenge for Nuclear Models

07.11.
A. Iwase, JAERI/Tokai
Electronic Excitation and Atomic Displacements in Materials Irradiated with High-Energy Particles

07.11.
H. Hora, Univ. of New South Wales, Sydney
Acceleration of Electrons in Vacuum by Lasers at Relativistic Intensities

08.11.
M. Hausmann, GSI Darmstadt
Mass Measurements of Exotic Nuclides in the ESR

14.11.
D. Varentsov, TU Darmstadt
Time-Resolved Energy-Loss Spectroscopy of Energetic Heavy Ion Beams Generating a Dense Plasma

14.11.
C. Rolfs, University of Bochum
Schlüsselreaktionen der nuklearen Astrophysik: Neue experimentelle Möglichkeiten

15.11.
E. Gaul, University of Texas, Austin
Wave Guides for Laser Wakefield Acceleration

15.11.
P. Braun-Munzinger, GSI Darmstadt
Report on Status of HIGGS Searches at LEP

21.11.
E. Shuryak, SUNY Stony Brook
Flows and Fluctuations

22.11.
D. Beck, GSI Darmstadt
The WITCH Experiment

23.11.
I. Mishustin, Copenhagen, Denmark
Unusual Bound States of Quark Matter within the NJL Model

24.11.
L. Musa, CERN Geneva
ALICE (TPC-Electronic)

28.11.
K. Rohr, University of Kaiserslautern
Teilchenspektroskopie lasererzeugter Plasmen

28.11.
J. Jolie, University of Köln
Experimental Tests of Dynamical Symmetries in Atomic Nuclei

29.11.
V.A. Yerokhin, St. Petersburg State Univ., Russia
Two-Loop Self-Energy in Hydrogen for Pedestrians

29.11.
W. Florkowski, Cracow, Poland
Different Hagedorn Temperatures for Baryons and Mesons

30.11.
D. Varentsov, TU Darmstadt
Time-Resolved Energy Loss Spectroscopy of Energetic Heavy Ion Beams Generating a dense Plasma

05.12.
R. Genzel, MPI f. extraterrestr. Physik, Garching
Massive schwarze Löcher in Galaxienkernen

05.12.
B. Wattellier, LULI-Ecole Polytechnique Palaiseau
Focal Sport Optimization and Shaping of High Power CPA Lasers

06.12.
H. Satz, University of Bielefeld
The Search for the QGP - A Critical Appraisal

06.12.
W. Henning, GSI Darmstadt
Next Steps Towards the Future GSI Accelerators

Seminars at GSI

12.12.
P. van Duppen, KU Leuven
Decay Studies of Exotic Nuclei Produced at the LISOL Facility using a Laser Ion Source

13.12.
X. Ma, IMP Lanzhou, China
Electron Capture Processes Involving High-Z Ions Studies at the ESR Storage Ring

14.12.
O.B. Malyshev, CERN Geneva
Vacuum Problems in the LHC

18.12.
R. Nagel, FB Mat. u. Geowissensch., TU Darmstadt
Transportprozesse an Metall-Keramik-Grenzflächen unter Schwerionen-Bestrahlung

19.12.
J. Hein, T. Töpfer, FSU Jena
POLARIS - Ein diodengepumpter Laser der Ein-Petawatt-Klasse

19.12.
F. Antinori, CERN Geneva
Strange Baryon Signals of a New State of Matter in Pb-Pb Collisions at the CERN SPS

20.12.
R. Morgenstern, KVI Groningen
Hot Recoils from Cold Atoms

21.12.
S. Russenschuck, LHC/ICP/CERN Geneva
Design und Optimierung supraleitender Magnete für den Large Hadron Collider (LHC) am CERN

Repeated Seminars:

Knoll, J.:
GSI Theory Seminar: Lectures on Theory
(GSI Darmstadt, Germany)

Knoll, J.:
GSI Student Program
(GSI Darmstadt, Germany)

Experiments performed at the GSI Accelerators in 2000

P. Egelhof, beam time coordinator

1. SIS/ESR Experiments

exp. no.	spokesperson	affiliation	short title	beam	exp. area	shifts (8h)
E000	Blell, Franzke, Geissel, Steck	GSI	ESR commissioning	^{12}C, ^{84}Kr, ^{197}Au, ^{238}U	ESR, FRS + ESR	38
E013	Bosch	GSI	charge exchange cross sections	^{238}U	ESR	1
E017, E019	Scheidenberger, Bosch	GSI	EC and β-decay of highly charged ions	^{208}Pb	FRS + ESR	15
E018	Deslattes	Gaithersburg	angle-tuned spectroscopy	^{197}Au	ESR	29
E036	Wollnik	Giessen	isochronus mass measurements	^{84}Kr	FRS + ESR	15
E040	Schatz	MSU	nuclear astrophysics studies	^{238}U	FRS	13
E044	Ma	GSI	e-e interaction at strong fields	^{238}U	ESR	13
S000	Blasche, Fehrenbacher, Franzke, Spiller	GSI	SIS commissioning	^{1}H, ^{2}H, ^{12}C, ^{18}O, ^{197}Au, ^{238}U	SIS, HHT	23
F000	Blasche, Geissel	GSI	FRS commissioning	^{132}Xe, ^{197}Au, ^{238}U	FRS	10
M000	Fehrenbacher	GSI	therapy commissioning	^{12}C	M	1
M000	Debus	Heidelberg	tumor therapy	^{12}C	M	171
SBIO	Schardt, Scholz	GSI	SIS biology experiments	^{12}C	A, M	41
STHE	Haberer	GSI	therapy studies	^{12}C	A, M	4
S020	Scheidenberger	GSI	slowing-down of rel. heavy ions	^{58}Ni, ^{238}U	FRS	7
S146	Amaldi	CERN	3-D hadron dosimetry	^{12}C	M	2
S174	Egelhof	GSI	elastic proton scattering off n-rich nuclei	^{12}C, ^{18}O, ^{26}Mg	B, FRS + B	26
S183	Pelte	Heidelberg	central collisions	^{12}C	B	3
S198	Neuner	GSI	high energy density in matter	^{18}O, ^{40}Ar, ^{58}Ni, ^{86}Kr, ^{197}Au, ^{238}U	HHT	10
S200	Friese	München	HADES commissioning	^{12}C, ^{84}Kr	HADES	12
S220	Lemmon	Daresbury	study of N = Z nuclei	^{92}Mo	FRS	29
S221	Emling	GSI	isospin struct. of giant resonances	^{124}Sn, ^{238}U	B	2
S223	Sümmerer	GSI	astrophysical reaction rates	^{12}C	FRS + C	35
S225	Marrus	Berkeley	lifetimes of helium-like ions	^{197}Au	A	10
S228, S230	Connell, Armbruster	Chicago, GSI	fragmentation cross sections	^{56}Fe, ^{58}Ni, ^{60}Ni	FRS	32
S232	Scheit	Heidelberg	quadrupole collectivity of n-rich nuclei	^{86}Kr	FRS + B	24
S233	Aumann	GSI	dipole response of dripline nuclei	^{12}C, ^{40}Ar	B, FRS + B	34
S234	Gerl	GSI	hypernuclear γ-spectroscopy	^{12}C	C	5
S237	Schmidt, Simon	GSI	detector tests for the ALICE exp.	^{12}C, ^{84}Kr ^{197}Au	B, C, HHT	27
S240	Phlips	Washington	test of the "Glast calorimeter"	^{12}C, ^{58}Ni	HHT	2
S241	Bartalucci	Rom	radiation hardness of VLSI devices	^{208}Pb	A	3

exp. no.	spokesperson	affiliation	short title	beam	exp. area	shifts (8h)
S246	Hammache	GSI	Coulomb dissociation of ^{6}Li	^{12}C	FRS	3
S260	Ting	MIT	radiation hardness of AMS electronics	^{132}Xe, ^{197}Au, ^{238}U	A	27

total: 667 shifts

2. UNILAC Experiments

exp. no.	spokesperson	affiliation	short title	beam	exp. area	shifts (8h)
U000	Barth, Forck, Franzke	GSI	UNILAC commissioning	^{1}H, ^{2}H, ^{12}C, ^{40}Ar, ^{238}U	UNILAC, X2	65
UBIO	Scholz, Schardt	GSI	UNILAC biology experiments	^{12}C, ^{40}Ca, ^{58}Ni, ^{64}Ni, ^{70}Zn, ^{197}Au, ^{132}Xe, ^{238}U	X6	33
UMAT	Fischer , Neumann, Trautmann, Vetter, Wirth,	GSI	UNILAC material science	^{12}C, ^{58}Ni, ^{70}Zn, ^{132}Xe, ^{197}Au, ^{238}U	X0, Z5	38
U068	Egelhof	GSI	bolometric detectors	^{58}Ni	Y7	3
U074	Roth	GSI	high energy density in matter	^{64}Ni, ^{70}Zn	Z6	3
U089	Fischer	GSI	single event radiation	^{124}Sn, ^{132}Xe	X0	3
U124	Schädel	GSI	chemistry of heavy elements	^{12}C	X1	2
U129	Janas	GSI	decay studies near ^{100}Sn	^{58}Ni	Y5	15
U161	Hagmann	Kansas	electron ionization cross sections	^{70}Zn	X4	1
U164	Köster	CERN	release properties of ISOL-targets	^{12}C	X1	2
U173	Gadea	Legnaro	decay of the I = 12^{+} Yrast trap in ^{52}Fe	^{36}Ar	Y5	16
U176	Karny	Warsaw	GT β-decay in n-deficient nuclei	^{40}Ca, ^{58}Ni	Y5	45
U177	Tauschwitz	Darmstadt	properties of high current discharge channels	^{197}Au, ^{238}U	Z4	3
U178	Tauschwitz	Darmstadt	Coulomb stopping in ionized matter	^{40}Ca, ^{238}U	Z4, Z6	2
U179	Hessberger	GSI	structure of Z=103 – 105 nuclei	^{12}C	Y7	4
U180	Janas	GSI	decay studies of barium isotopes	^{58}Ni	Y5	5
U182	Kratz	Mainz	chem. properties of element 106	^{12}C, ^{26}Mg, ^{36}Ar, ^{70}Zn	X1	14
U183	Tabor	Tallahassee	isomer spectr. and β-decay of $^{77\text{-}79}$Y	^{36}Ar, ^{40}Ca	Y5	24
U184	Hofmann	GSI	synthesis of superheavy elements	^{26}Mg, ^{50}Ti, ^{58}Ni, ^{64}Ni, ^{70}Zn	Y7	171
U186	Grawe	GSI	β/EC-decay of ^{100}In	^{58}Ni	Y5	12
U189	Rosmej	GSI	x-ray spectroscopy from projectiles inside matter	^{36}Ar, ^{64}Ni	Z6	2

total: 463 shifts

ACCELERATOR FACILITIES AND EXPERIMENTAL AREAS

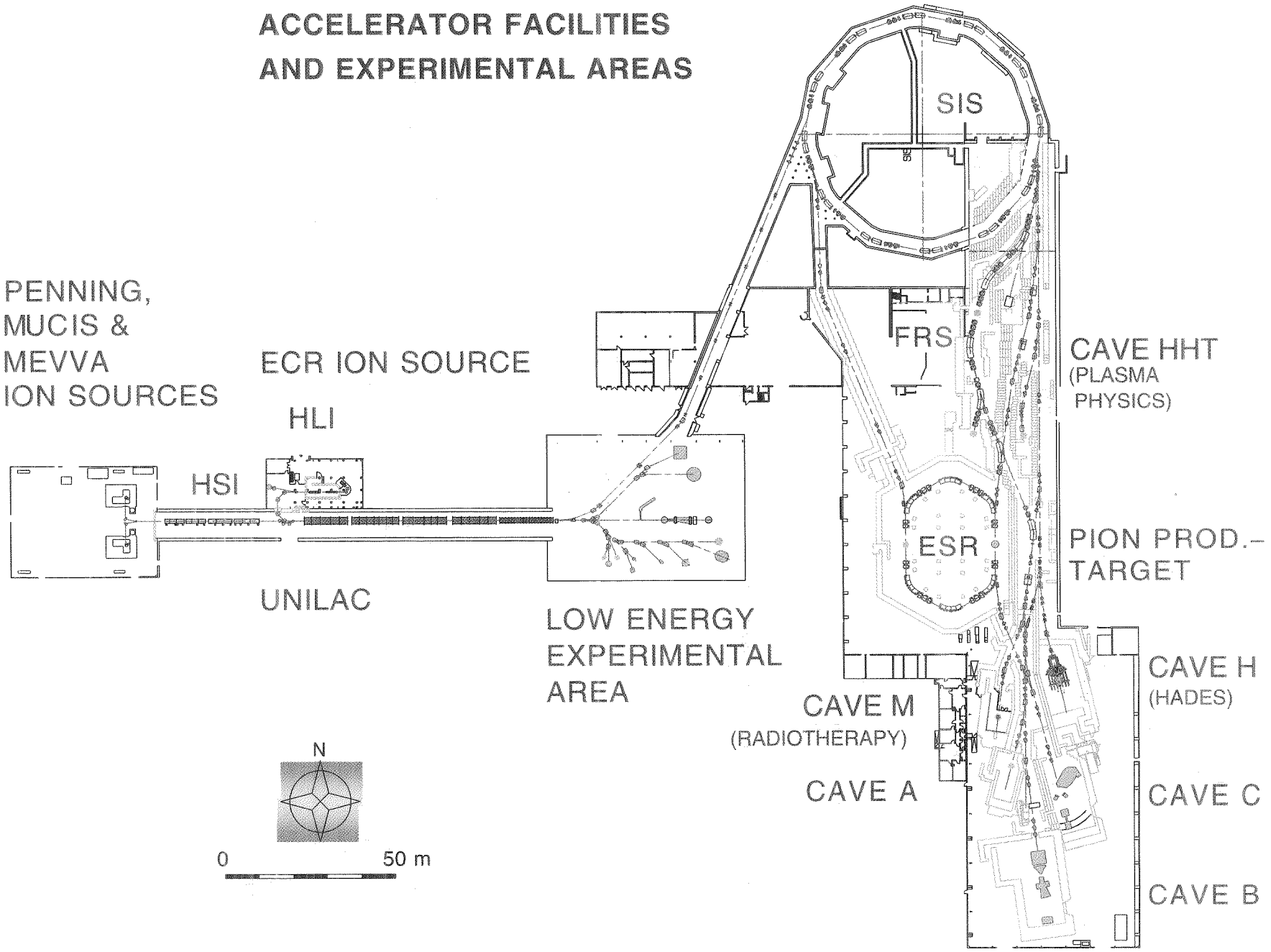

Collaborations

ALADIN Collaboration

R. Bassini[2], M. Begemann-Blaich[1], S. Fritz[1], S.J. Gaff[8], C. Gross[1], X. Hongfei[1], G. Imme[3], I. Iori[2], U. Kleinevoss[4], G.J. Kunde[8], W.D. Kunze[1], U. Lynen[1], V. Maddalena[3], M. Mahi[1], T. Möhlenkamp[5], A. Moroni[2], W.F.J. Mueller[1], C. Nociforo[3], B. Ocker[6], T. Odeh[1], F. Petruzzelli[2], J. Pochodzalla[9], G. Raciti[3], G. Riccobene[3], F.P. Romano[3], T. Rubehn[1], A. Saija[3], H. Sann[1], M. Schnittker[1], A. Schüttauf[6], C. Schwarz[1], W. Seidel[5], V. Serfling[1], C. Sfienti[3], W. Trautmann[1], A. Trczinski[7], G. Verde[3], A. Wörner[1], B. Zwieglinski[7]

[1]GSI Darmstadt, Germany,
[2]Univ. of Milano and I.N.F.N. Milano, Italy
[3]Univ. of Catania and I.N.F.N., Catania, Italy
[4]Fachber. Physik, Univ. of Münster, Germany
[5]FZ Rossendorf, Dresden, Germany
[6]Inst. f. Kernphys., Univ. of Frankfurt, Germany
[7]Soltan Inst. for Nuclear Studies, Warsaw, Poland
[8]NSCL, MSU, East Lansing, USA
[9]MPI f.Kernphysik Heidelberg, Germany

CERES Collaboration

D. Adamová[7], G. Agakichiev[3], H. Appelshäuser[6], V. Belaga[4], P. Braun-Munzinger[3], A. Cherlin[8], S. Damjanović[6], T. Dietel[6], L. Dietrich[6], A. Drees[9], S.I. Esumi[6], K. Filimonov[6], K. Fomenko[4], Z. Fraenkel[8], C. Garabatos[3], P. Glässel[6], A. Gnaenski[8], G. Hering[3], J. Holeczek[3], V. Kushpil[7], B. Lenkeit[2], W. Ludolphs[6], A. Maas[3], A. Marín[3], F. Messer[9], J. Milošević[6], A. Milov[8], D. Miśkowiec[3], Yu. Panebrattsev[4], O. Petchenova[4], V. Petráček[6], A. Pfeiffer[2], J. Rak[3], I. Ravinovich[8], P. Rehak[1], H. Sako[3], W. Schmitz[6], J. Schukraft[2], S. Sedykh[3], S. Shimansky[4], J. Slívová[6], H.J. Specht[6], J. Stachel[6], M. Šumbera[7], H. Tilsner[6], I. Tserruya[8], J.P. Wessels[6], T. Wienold[6], B. Windelband[6], J.P. Wurm[5], W. Xie[8], S. Yurevich[6], V. Yurevich[4]

[1]Brookhaven Nat. Lab. Upton, USA
[2]CERN, Geneva, Switzerland
[3]GSI Darmstadt, Germany
[4]JINR Dubna, Russia
[5]MPI f.Kernphysik Heidelberg, Germany
[6]Univ. of Heidelberg, Germany
[7]NPI/ASCR Řež, Czech Republic
[8]Weizmann Inst. Rehovot, Israel
[9] SUNY, Stony Brook, USA

FOPI Collaboration

A. Andronic[4], Z. Basrak[12], N. Bastid[3], A. Bendarag[3], G. Berek[2], V. Barret[3], R. Caplar[12], N. Cindro[12], P. Crochet[4], A. Devismes[4], P. Dupieux[3], M. Dzelalija[12], Ch. Finck[4], Z. Fodor[2], J. Gasparic[12], A. Gobbi[4], Y. Grishkin[7], O. Hartmann[4], N. Herrmann[6], K.D. Hildenbrand[4], B. Hong[9], D. Kang[9], J. Kecskemeti[2], Y.J. Kim[9], M. Kirejczyk[11], P. Koczon[4], 4M. Korolija[12], R. Kotte[5], M. Kowalczyk[11], T. Kress[4], R. Kutsche[4], A. Lebedev[7], Y. Leifels[6], V. Manko[8], D. Moisa[1], W. Neubert[5], D. Pelte[6], M. Petrovici[1], F Rami[10], W. Reisdorf[4], B. de Schauenburg[10], D. Schüll[4], Z. Seres[2], B. Sikora[11], K.S. Sim[9], V. Simion[1], K. Siwek-Wilczynska[11], M. Smolarkiewicz[11], V. Smolyankin[7], J. Soliwoda[11], A. Somov[7], M. Stockmeier[6], G. Stoicea[1], Z. Tyminski[11], P. Wagner[10], K. Wisniewski[11], D. Wohlfarth[5], I. Yushmanov[8], A. Zhilin[7]

[1]NIPNE Bucharest, Romania
[2]CRIP/KFKI Budapest, Hungary
[3]LPC Clermont-Ferrand, France
[4]GSI Darmstadt, Germany
[5]FZ Rossendorf/Dresden, Germany
[6]Univ. of Heidelberg, Germany
[7]ITEP Moscow, Russia
[8]Kurchatov Institute, Moscow, Russia
[9]Korea University Seoul, Korea
[10]IReS Strasbourg, France
[11]Univ. of Warsaw, Poland
[12]RBI Zagreb, Croatia

Collaborations

HADES Collaboration

H. Agakichiev[3], C. Agodi[7], H. Alvarez-Pol[15], E. Atkin[12], E. Badura[3], A. Balanda[8], F. Ballester[19], R. Bassini[16], G. Bellia[7], M. Bertini[3], J. Bielcik[3], M. Boehmer[14], C. Boiano[16], H. Bokemeyer[3], J. Boyard[4], S. Brambilla[16], P. Braun-Munzinger[3], S. Chernenko[10], R. Coniglione[7], M. Dahlinger[3], H. Daues[3], J. Diaz[19], R. Dressler[2], I. Duran[15], T. Eberl[14], A. Elhardt[14], W. Enghardt[2], L. Fabbietti[14], O. Fateev[10], C. Fernandez[15], P. Finocchiario[7], J. Friese[14], I. Fröhlich[11], B. Fuentes[15], J. Garzon[15], R. Gernhäuser[14], L.Glonti[10], O. Goepfert[3], M. Golubeva[5], E. Grosse[2], F. Gruber[5], H. Göringer[3], J. Hehner[3], T. Hennino[4], S. Hlavlac[13], J. Hoffmann[3], R. Holzmann[3], J. Homolka[14], I. Iori[16], M. Jaskula[8], J. Jourdain[4], M. Kajetanowicz[8], T. Karavicheva[5], M. Kargalis[3], A. Kastenmüller[14], L. Kidon[8], P. Kienle[14], I. Koenig[3], W. Koenig[3], H. Koerner[14], B.Kolb[3], U. Kopf[3], R. Kotte[2], A. Kugler[1], R. Kulessa[8], A. Kurepin[5], W. Kühn[11], J. Lehnert[11], E. Lins[11], C. Lippmann[9], R. Lorenzo[15], D. Magestro[3], P. Maier-Komor[14], C. Maiolino[7], J. Markert[9], V. Metag[11], H. Meunier[17], Y. Mishin[12], M. Münch[14], C. Müntz[9], L. Naumann[2], A. Nekhaev[6], W. Niebur[3], W. Ott[3], J. Otwinowski[8], Yu.Panebratsev[10], M. Pardo[19], V. Pechenov[10], M. Petri[11], P. Piattelli[7], J. Pietraszko[8], R. Pleskac[1], M. Ploskon[8], J. Pouthas[4], W. Prokopowicz[8], W. Przygoda[8], N. Rabin[6], B. Ramstein[4], A. Reshetin[5], J. Ritman[11], G. Roche[17], K. Rosenkranz[9], M. Roy-Stephan[4], B. Sailer[14], P. Salabura[8], C. Salz[11], M. Sanchez[15], P. Sapienza[7], R. Schicker[3], C. Schroeder[3], S.Schroeder[14], D. Schuell[3], W. Schön[14], P. Senger[3], R. Simon[3], V. Smoliankin[6], L. Smykov[10], J. Sowa[8], H. Stelzer[3], H. Stroebele[9], J. Stroth[9], A. Taranenko[1], V. Tiflov[5], A.Titov[10], P. Tlusty[1], M. Traxler[11], H. Tsertos[18], I. Turzo[13], A. Ulrich[14], D. Vassiliev[7], A. Vazques[15], Yu. Volkov[12], V. Wagner[1], E. Wajda[8], C. Wallner[14], W. Walus[8], Y. Wang[9], J. Wieser[14], S. Winkler[14], T. Wojcik[8], J. Wüstenfeld[9], N. Yahlali[19], Yu. Zanevsky[10], K. Zeitelhack[14], P. Zumbruch[3]

[1]Inst. of Nucl. Phy. INP, Řež, Czech. Rep.
[2]FZR Rossendorf, Germany
[3]GSI Darmstadt, Germany
[4]IPN Orsay, France
[5]Inst. for Nucl. Res., Moscow, Russia
[6]ITEP, Moscow, Russia
[7]INFN-LNS, Depart. di Fisica, Catania, Italy
[8]Jagellonian University Cracow, Poland
[9]Univ. of Frankfurt, Germany
[10]JINR Dubna, Russia
[11]Univ. of Giessen, II. Physik. Inst., Germany
[12]Moscow Eng. Physics Inst. Moscow, Russia
[13]Inst. of Physics IOP Bratislava, Slovakia
[14]TU Munich, Phys. Depart., Garching, Germany
[15]Univ. of Santiago de Compostela, Spain
[16]Dip. di Fisica, Univ. di Milano, Italy
[17]Univ. of Clermont-Ferrand, Aubiere, France
[18]University of Cyprus, Nicosia, Cyprus
[19]Univ. of Valencia, Burjasot, Spain

KaoS Collaboration

I. Böttcher[4], M. Debowski[5], A. Förster[2], E. Grosse[1,6], P. Koczon[1], B. Kohlmeyer[4], M. Menzel[4], L. Naumann[6], H. Oeschler[2], F. Pühlhofer[4],W. Scheinast[6], E. Schwab[1], C. Schneider[6], P. Senger[1], Y. Shin[3], H. Ströbele[3], C. Sturm[2], G. Surowka[1,5], F. Uhlig[2], A. Wagner[2], W. Walus[5]

[1]GSI Darmstadt, Germany
[2]TH Darmstadt, Germany,
[3]Univ. of Frankfurt, Germany
[4]Univ. of Marburg, Germany
[5]Jagellonian Univ., Cracow, Poland
[6]FZ Rossendorf, Germany

Collaborations

LAND Collaboration

T. Aumann[2], K. Boretzky[3], U. Datta Pramanik[2], Th.W.Elze[1], H.Emling[2], A. Grünschloß[1], G. Ickert[2], S. Ilievski[2], K. Jones[2], J.V. Kratz[3], R. Kulessa[5], Le Hong Khiem[3], A. Leistenschneider[1], E. Lubkiewicz[5], W. Prokopowicz[2,5], H. Simon[4], K. Sümmerer[2], T. Lange[1], E. Wajda[5], W. Walus[5]

[1]Univ. of Frankfurt, Germany
[2]GSI Darmstadt, Germany
[3]Univ. of Mainz, Germany
[4]TH Darmstadt, Germany,
[5]Jagellonian Univ., Cracow, Poland

NA49 Collaboration

S.V. Afanasiev[10], W. Amend[11], T. Anticic[20], J. Bächler[6,8], D. Barna[5], L.S. Barnby[3], J. Bartke[7], R.A. Barton[3], J. Bershin[11], L. Betev[14], H. Bialkowska[17], A. Billmeier[11], C. Blume[8], C.O. Blyth[3], R. Bock[8], B. Boimska[17], M. Botje[21], J. Bracinik[4], F.P. Brady[9], R. Bramm[11], R. Brun[6], P. Buncic[6,11], L. Carr[19], D. Cebra[9], V. Cerny[4], G.E. Cooper[2], J.G. Cramer[19], P. Csato[5], P. Dinkelaker[11], V. Eckardt[16], F. Eckhardt[15], D. Ferenc[9], P. Filip[16], H.G. Fischer[6], Z. Fodor[5], P. Foka[8], P. Freund[16], V. Friese[15], J. Gal[5], R. Ganz[16], M. Gazdzicki[11], G. Georgopoulos[1], E. Gladysz[7], S. Hegyi[5], C. Höhne[15], G. Igo[14], P. Jacobs[2], P.G. Jones[3], K. Kadija[16,20], V.I. Kolesnikov[10], T. Kollegger[11], M. Kowalski[7], I. Kraus[8], M. Kreps[4], M. van Leeuwen[21], P. Levai[5], U. Lynen[8], A.I. Malakhov[10], S. Margetis[13], C. Markert[8], B.W. Mayes[12], G.L. Melkumov[10], A. Mischke[8], J. Molnar[5], J.M. Nelson[3], G. Odyniec[2], G. Palla[5], A.D. Panagiotou[1], Y. Pestov[8], A. Petridis[1], M. Pikna[4], L. Pinsky[12], A.M. Poskanzer[2], D.J. Prindle[19], F. Pühlhofer[15], J.G. Reid[19], R. Renfordt[11], W. Retyk[18], H.G. Ritter[2], D. Röhrich[11], C. Roland[8], G. Roland[11], A. Rybicki[7], T. Sammer[16], A. Sandoval[8], H. Sann[8], E. Schäfer[16], N. Schmitz[16], P. Seyboth[16], F. Sikler[5,6], B. Sitar[4], E. Skrzypczak[18], R. Snellings[2], G.T.A. Squier[3], H. Stelzer[8], R. Stock[11], H. Ströbele[11], T. Susa[20], I. Szentpetery[5], J. Sziklai[5], M. Toy[2,14], T.A. Trainor[19], S. Trentalange[14], D. Varga[5], M. Vassiliou[1], G.I. Veres[5], G. Vesztergombi[5], S. Voloshin[2], D. Vranic[6], F. Wang[2], D.D. Weerasundara[19], S. Wenig[6], A. Wetzler[11], C. Whitten[14], N. Xu[2], T.A. Yates[3], I.K. Yoo[15], J. Zaranek[11]J. Zimanyi[5],

[1]Dep. of Physics, Univ. of Athens, Greece
[2]Lawrence Berkeley Laboratory, USA
[3]School of Physics, Univ. of Birmingham, UK
[4]University of Bratislava, Slovakia
[5]KFKI Budapest, Hungary
[6]CERN, Geneva, Switzerland
[7]Inst. of Nuclear Physics, Cracow, Poland
[8]GSI Darmstadt, Germany
[9]Univ. of California at Davis, USA
[10]JINR, Dubna, Russia
[11]Fachber. Phys., Univ. of Frankfurt, Germany
[12]Univ. of Houston, Houston, USA
[13]Kent State Univ. Kent, USA
[14]Univ. of California, Los Angeles, USA
[15]Fachber. Phys., Univ. of Marburg, Germany
[16]MPI für Physik, München, Germany
[17]Inst. for Nuclear Studies, Warsaw, Poland
[18]Inst. for Exp. Physics, Univ. of Warsaw, Poland
[19]University of Washington, Seattle, USA
[20]Rudjer Boskovic Inst., Zagreb, Croatia
[21]NIKHEF, Amsterdam, The Netherlands

PESTOV Collaboration

E. Badura[1], V. Dodokhov[4], J. Eschke[1], Z. Fodor[5], A. Frolov[2], U. Frankenfeld[1], V. Grigoriev[3], V. Kaplin[3], J. Lühning[1], U. Lynen[1], Ch. Neyer[1], Y. Pestof[1,2], F. Pühlhofe[6], H. Sann[1], H.R. Schmidt[1], B. Schreiber[1], R. Schulze[1], H. Stelzer[1], J. Sziklai[5], F. Sikler[5], S. Vodopianov[4]

[1]GSI Darmstadt, Germany
[2]BINP Novosibirsk, Russia
[3]MEPHI Moscow, Russia
[4]JINR Dubna, Russia
[5]RMKI Budapest, Hungary
[6]Univ. of Marburg, Germany

RD42 Collaboration

Collaborations

W. Adam[1], E. Berdermann[2], P. Bergonzo[3], F. Bogani[4], E. Borchi[5], A. Brambilla[3], M Bruzzi[5], C. Colledani[6], J. Conway[7], P. D'Angelo[8], W. Dabrowski[9], P. Delpierre[10], W. Dulinski[6], J. Doroshenko[7], M. Doucet[15], B. van Eijk[11], A. Fallou[10], F. Fizotti[12], F. Foulon[3], M Friedl[1], K.K. Gan[13], G. Hallewell[10], S. Han[13], F. Hartjes[11], J. Hrubec[1], D. Husson[6], H. Kagan[13]*, D. Kania[13], J. Kaplon[14], R. Kass[13], T. Koeth[7], M. Krammer[1], A. Logiudice[12], R. Lu[12], L. mac Lynne[7], C. Manfredotti[12], D. Meier[14], M. Mishina[16], L. Moroni[8], J. Noomen[11], A. Oh[15], L.S. Pan[13], M Pernicka[1], L. Perera[7], S. Pirollo[5], M. Procario[17], J. L. Riester[6], S. Roe[14], L. Rousseau[3], A. Rudge[14], J. Russ[17], S. Sala[8], M. Sampietro[18], S. Schnetzer[7], S. Sciortino[5], H. Stelzer[2], R. Stone[7], B. Suter[17], W. Trishuk[19], D. Tromson[3], E. Vittone[12], R. Wedenig[1], P. Weilhammer[14]*, M. Wetstein[7], W. Zeuner[15], M. Zoeller[13]

[1]HEPHY, Vienna, Austria
[2]GSI Darmstadt, Germany
[3]LETI-CEA Saclay, Paris, France
[4]LENS, Florence, Italy
[5]Univ. of Florence, Florence, Italy
[6]LEPSI, IN2P3/CNRS-ULP, Strassbourg, France
[7]Rutgers University, New York, USA
[8]INFN, Milano, Italy
[9]UMM, Cracow, Poland
[10]CPPM, Marseille, France
[11]NIKHEF, Amsterdam, Netherlands
[12]Univ. of Torino, Torino, Italy
[13]The Ohio State Univ., Columbus, USA
[14]CERN, Geneva, Switzerland
[15]II. Inst. f. Exp. Physik, Hamburg, Germany
[16]FNAL, Batavia, USA
[17]Carnegie-Mellon Univ. Pittsburgh, USA
[18]Polytechnico di Milano, Milano, Italy
[19]Univ. of Toronto, Toronto, Canada
*Spokespersons

S135 Collaboration

D. Aleksandrov[1], T. Aumann[2], L. Axelsson[3], T. Baumann[2], M.J.G. Borge[4], D. Cortina-Gil[2], L.V. Chulkov[1,2], W. Dostal[5], B. Eberlein[2,5], Th.W. Elze[6], H. Emling[2], C. Forssen[3], H. Geissel[2], A. Grünschloss[6], M. Hellström[2], B. Johnson[3], J.V. Kratz[5], R. Kulessa[7], Y. Leifels[2], A. Leistenschneider[6], K. Markenroth[3], M. Meister[3,8], I. Mukha[1,8], G. Münzenberg[2], T. Nilsson[3], G. Nyman[3], M. Pfützner[2], A. Richter[8], K. Riisager[9], C. Scheidenberger[2], G. Schrieder[8], H. Simon[8], O. Tengblad[4], M.V. Zukhov[3]

[1]Kurchatov Institute Moscow, Russia
[2]GSI Darmstadt, Germany
[3]University of Göteborg, Sweden
[4]CSIC Madrid, Spain
[5]University of Mainz, Germany
[6]Univ. of Frankfurt, Germany
[7]Jagellonski University, Krakow, Poland
[8]TU Darmstadt, Germany
[9]University of Aarhus, Denmark

SHIPTRAP

D. Ackermann[3], J. Äystö[1], H. Backe[2], G. Bollen[14], F. Bosch[3], J. Dilling[3], A. Dretzke[2], O. Engels[5], T. Faestermann[4], J. Friese[4], H. Geissel[3], A. Gillitzer[4], H. Grawe[3], D. Habs[5], F.P. Heßberger[3], S. Hofmann[3], M. Huyse[6], A.A. Ignatiev[7], A. Junghans[3], P. Kienle[4], H.-J. Kluge[3], H.J. Körner[4], Ch. Kozhuharov[3], J.V. Kratz[8], W. Lauth[2], M. Leino[1], W. Ludolphs[2], D. Lunney[9], R. Mann[3], G. Marx[3], R.B. Moore[10], G. Münzenberg[3], J. Neumayr[5], J.A. Pinston[11], W. Quint[3], D. Rodriguez[3], E. Roeckl[3], G. Savard[12], M. Schädel[3], K.-H. Schmidt[3], J. Schönfelder[3], R. Schneider[5], U. Schramm[5], S. Schwarz[14], M. Sewtz[2], G. Sikler[3], A. Steinhof[2], T. Stöhlker[13], P.G. Thirolf[5], C. Toader[3], N. Trautmann[8], P. Van Duppen[6], V.L. Varentsov[5], C. Weber[3]

Collaborations

[1]University of Jyväskylä, Finland
[2]University of Mainz, Germany
[3]GSI, Darmstadt, Germany
[4]TU München, Germany
[5]LMU München, Germany
[6]University of Leuven, Belgium
[7]Inst. for Inform. and Automation, St.Petersburg, Russian Federation
[8]Universität of Mainz, Germany
[9]CSNSM-IN2P3-CNRS, Orsay, France
[10]McGill University, Montreal, Canada
[11]ISN, Grenoble, France
[12]Argonne National Laboratory, Argonne, USA
[13]University of Frankfurt, Germany
[14]Michigan State University, USA

TAPS Collaboration

J. Ahrens[7], L. Aphecetche[3,10], R. Averbeck[1], J.C.S. Bacelar[6], F. Ballester[4], R. Beck[7], H. Delagrange[3,10], D. d'Enterria[3,10], J. Díaz[4], K. Föhl[7], V. Hejny[8], S. Hlavac[1], M. Hoek[2], R. Holzmann[1], S. Janssen[2], N. Kalantar-Nayestanaki[6], M. Kotulla[2], B. Krusche[11], A. Kugler[5], H. Löhner[6], G. Martínez[3,10], T. Matulewicz[9], J.G. Messchendorp[2], V. Metag[2], R. Novotny[2], V. Olmos de Leòn[7], R. Ortega[3,10], R.W. Ostendorf[6], M. Pfeiffer[2], R. Pleskac[5], K. Römer[2], S. Schadmand[2], Y. Schutz[3,10], R. Siemssen[6], R.S. Simon[1], H. Ströher[8], A. Taranenko[5], P. Tlusty[5], M. Volkerts[6], V. Wagner[5], H.W. Wilschut[5], N. Yahlali[4]

[1]GSI Darmstadt, Germany
[2]II. Phys. Inst., Univ. Giessen, Germany
[3]GANIL Caen, France
[4]IFIC Valencia, Spain
[5]NPI Rez u Prahy, Czech. Republic
[6]KVI Groningen, The Netherlands
[7]Inst. für Kernphysik, Univ. Mainz, Germany
[8]FZ Jülich, Germany
[9]Inst. of Exp. Physics, Warsaw Univ., Poland
[10]present addr.: SUBATECH Nantes, France
[11]University of Basel, Schwitzerland

VEGA-Collaboration

J. Döring[1], J. Gerl[1], M. Gorska[1,3], H. Grawe[1], M. Hellström[1], F. Hessberger[1], S. Hofmann[1], I. Kozhoukharov[1], E. Roeckl[1], C. Schlegel[1], H.J. Wollersheim[1],

[1]GSI Darmstadt, Germany
[2]University of Frankfurt, Germany
[3]University of Warsaw, Poland

WA98 Collaboration

M.M.Aggarwal[1], A.Agnihotri[2], Z.Ahammed[3], A.L.S.Angelis[4], V.Antonenko[5], V.Arefiev[6], V.Astakhov[6], V.Avdeitchikov[6], T.C.Awes[7], P.V.K.S.Baba[8], S.K.Badyal[8], A.Baldine[6], L.Barabach[6] C.Barlag[9], S.Bathe[9], B.Batiounia[6], T.Bernier[10], K.B.Bhalla[2], V.S.Bhatia[1], C.Blume[9], R.Bock[11], E. M.Bohne[9], D.Bucher[9], A.Buijs[12], E.-J.Buis[12], Z.Böröcz[9], H.Büsching[9], L.Carlen[13], V.Chalyshev[6], S.Chattopadhyay[3], R.Cherbatchev[5], T.Chujo[14], A.Claussen[9], A.C.Das[3], M.P.Decowski[12], H.Delagrange[10], V.Djordjadze[6], P.Donni[4], I.Doubovik[5], S.Dutt[8], M.R.Dutta Majumdar[3], K.El Chenawi[13], S.Eliseev[15], K.Enosawa[14], P.Foka[4], S.Fokin[5], V.Frolov[6], M.S.Ganti[3], S.Garpman[13], O.Gavrishchuk[6], F.J.M.Geurts[12], T.K.Ghosh[16], R.Glasow[9], S.K.Gupta[2], B.Guskov[6], H.Å.Gustafsson[13], H.H.Gutbrod[10], R.Higuchi[14], I.Hrivnacova[15], M.Ippolitov[5], H.Kalechofsky[4], R.Kamermans[12], K.-H.Kampert[9], K.Karadjev[5], K.Karpio[17], S.Kato[14], S.Kees[19], B.W.Kolb[11], I.Kosarev[6], I.Koutcheryaev[5], T.Krümpel[9], A.Kugler[15], P.Kulinich[18], M.Kurata[14], K.Kurita[14], N.Kuzmin[6], I.Langbein[11], A.Lebedev[5], Y.Y.Lee[11], H.Löhner[16], L.Luquin[10], D.P.Mahapatra[19], V.Manko[5], M.Martin[4], G.Martinez[10], A.Maximov[6], R.Mehdiyev[6], G.Mgebrichvili[5], Y.Miake[14], D.Mikhalev[6], Md.F.Mir[8], G.C.Mishra[19],

Collaborations

Y.Miyamoto[14], D.Morrison[20], D.S.Mukhopadhyay[3], V.Myalkovski[6], H.Naef[4], B.K.Nandi[19], S.K.Nayak[10], T.K.Nayak[3], S.Neumaier[11], A.Nianine[5], V.Nikitine[6], S.Nikolaev[5], P.Nilsson[13], S.Nishimura[14], P.Nomokonov[6], J.Nystrand[13], F.E.Obenshain[20], A.Oskarsson[13], I.Otterlund[13], M.Pachr[15], A.Parfenov[6], S.Pavliouk[6], T.Peitzmann[9], V.Petracek[15], F.Plasil[7], W.Pinganaud[10], M.L.Purschke[11], J.Rak[15], R.Raniwala[2], S.Raniwala[2], V.S.Ramamurthy[19], N.K.Rao[8], F.Retiere[10], K.Reygers[9], G.Roland[18], L.Rosselet[4], I.Roufanov[6], C.Roy[10], J.M. Rubio[4], H.Sako[14],S.S.Sambyal [8], R.Santo[9], S.Sato[14], H.Schlagheck[9], H.-R.Schmidt[11], Y.Schutz[10], G.Shabratova[6], T.H.Shah[8], I.Sibiriak[5], T.Siemiarczuk[17], D.Silvermyr[13], B.C.Sinha[3], N.Slavine[6], K.Söderström[13], N.Solomey[4], S.P.Sørensen[20], P.Stankus[7], G.Stefanek[17], P.Steinberg[18], E.Stenlund[13], D.Stüken[9], M.Sumbera[15], T.Svensson[13], M.D.Trivedi[3], A.Tsvetkov[5], L.Tykarski[17], J.Urbahn[11], E.C.v.d.Pijll[12], N.v.Eijndhoven[12], G.J.v.Nieuwenhuizen[18], A.Vinogradov[5], Y.P.Viyogi[3], A.Vodopianov[6], S.Vörös[4], M.A.Vos[12], B.Wyslouch[18], K.Yagi[14], Y.Yokota[14], G.R.Young[7]

[1]Univ. of Panjab, Chandigarh, India
[2]Univ. of Rajasthan, Jaipur, India
[3]VECC, Calcutta, India
[4]Univ. of Geneva, Switzerland
[5]Kurchatov Inst., Moscow, Russia
[6]JINR, Dubna, Russia
[7]ORNL, Oak Ridge National Laboratory, USA
[8]Univ. of Jammu, Jammu, India
[9]Univ. of Münster, Germany
[10]Subatech, Ecoles des Mines, Nantes, France
[11]GSI Darmstadt, Germany
[12]Univ. of Utrecht, The Netherlands
[13]Univ. of Lund, Lund, Sweden
[14]Univ. of Tsukuba, Ibaraki, Japan
[15]Nucl. Physics Inst., Rez, Czech Republic
[16]KVI, Univ. of Groningen, The Netherlands
[17]Inst. of Nucl. Studies, Warsaw, Poland
[18]MIT, Cambridge, USA
[19]IOP, Bhubaneswar, India
[20]Univ. of Tennessee, Knoxville, USA
[21]CERN, Geneva, Switzerland

Author Index

Author Index

Author Index

Author Index

Author Index

Author Index

Author Index

Author Index

Author Index

COLLABORATIONS

GSI - Organigramm
Gesellschaft für Schwerionenforschung mbH

Gesellschafterversammlung
Bund/Land Hessen

Wissenschaftlicher Rat
12 Mitglieder
Vorsitzender
R. Stock

Wiss. Ausschuß
18 Mitglieder
Vorsitzender
2652 P. Senger

Experiment Ausschuß
13 Mitglieder
Vorsitzender
D. Habs

Öffentlichkeitsarbeit
2598 G. Siegert

Wiss.-Koordination
2535 K.-D. Groß

Sicherheit und Strahlenschutz
2007 G. Fehrenbacher

Aufsichtsrat
Vorsitzender H. Schunck
Stellv. Vorsitzender H. Wolf

Geschäftsführung
W.F. Henning, H. Zeitträger
Wissenschaftliches Direktorium
W.F. Henning (Vors.), N. Angert, H.-J. Kluge,
P. Braun-Munzinger, H. Zeitträger

Innenrevision / Datenschutz
2636 F.-J. Pleser / S. Schulz 2855

Patente und Technologietransfer
2630 D. Rück

Controlling Betriebsabrechnung
2621 J. Heilmann

Betriebsrat
2503 A. Schlossarek / Vorsitz.

Frauenbeauftragte
2721 S. Lüttges / Vorsitz.

Schwerbehinderten
2524 W. Krall / Vertrauensm.

Forschung
2722 H.-J. Kluge

- **Atomphysik** 2722 H.-J. Kluge
- **Biophysik** 2607 G. Kraft
- **Kernphysik I** 2760 P. Braun-Munzinger
- **Kernphysik II** 2733 G. Münzenberg
- **Kernphysik III** 2763 U. Lynen
- **Materialforschung** 2172 R. Neumann
- **Plasmaphysik** 2790 R. Bock /D.Hoffmann 2723
- **Theorie** 2747 W. Nörenberg

Wiss.-Technische Infrastruktur
(1) (2) (3) (4) *

- **Gebäude und Anlagentechnik** 2526 H. Egger (4)
- **Bibliothek und Dokumentation** 2610 U. Grundinger (3)
- **Datenverarbeitung u. Exp.-Elektr.** (2) M. Richter 2394
- **Detektorlabor** 2273 H. Stelzer (2)
- **Targetlabor** 2691 B. Lommel (3)
- **Zentrale Technik** 2385 R. Fuchs (1)

*Zuständigkeiten:

N. Angert	(1)
P. Braun-Munzinger	(2)
H.-J. Kluge	(3)
H. Zeitträger	(4)

Beschleuniger
2397 N. Angert

- **Therapiebeschl. Heidelberg** 2395 H. Eickhoff
- **Beschleunigerphysik** 2366 B. Franzke
  - **Betrieb** 2316 D. Wilms
  - **Ionenquellen** 2320 P. Spädtke
  - **Injektoren** 2344 J. Klabunde
  - **Beschleuniger-Entwicklung** 2395 H. Eickhoff
  - **ESR** 2406 M. Steck
  - **Beschleuniger-Elektronik** 2392 R. Steiner
  - **UHV** 2404 W. Jacoby
- **Hochstrom-Strahlphysik** 2409 I. Hofmann
- **Beschleunigertechnik** 2383 K. Blasche
  - **Strahldiagnose** 2311 P. Strehl
  - **HF / Beschl. Strukturen** 2490 U. Ratzinger
  - **Elektrische Energietechnik** 2377 G. Breitenberger
  - **Magnettechnik** 2369 B. Langenbeck
  - **Beschl.-u.Experimentservice** 2327 R. Schwedhelm

Verwaltung
2646 H. Zeitträger

- **Personal- u. Sozialwesen** 2611 J. Größer
- **Finanzabteilung** 2597 A. Städter
- **Einkauf u. Materialwesen** 2577 M. Hener

Koordinierungsstelle KKS
2848 D. Müller

Postanschrift: Postfach 11 05 52 64220 Darmstadt
Telefon: 0 61 59/71-0 Telefax: 0 61 59/71-27 85

Stand: 13.02.2001
Organi.cht

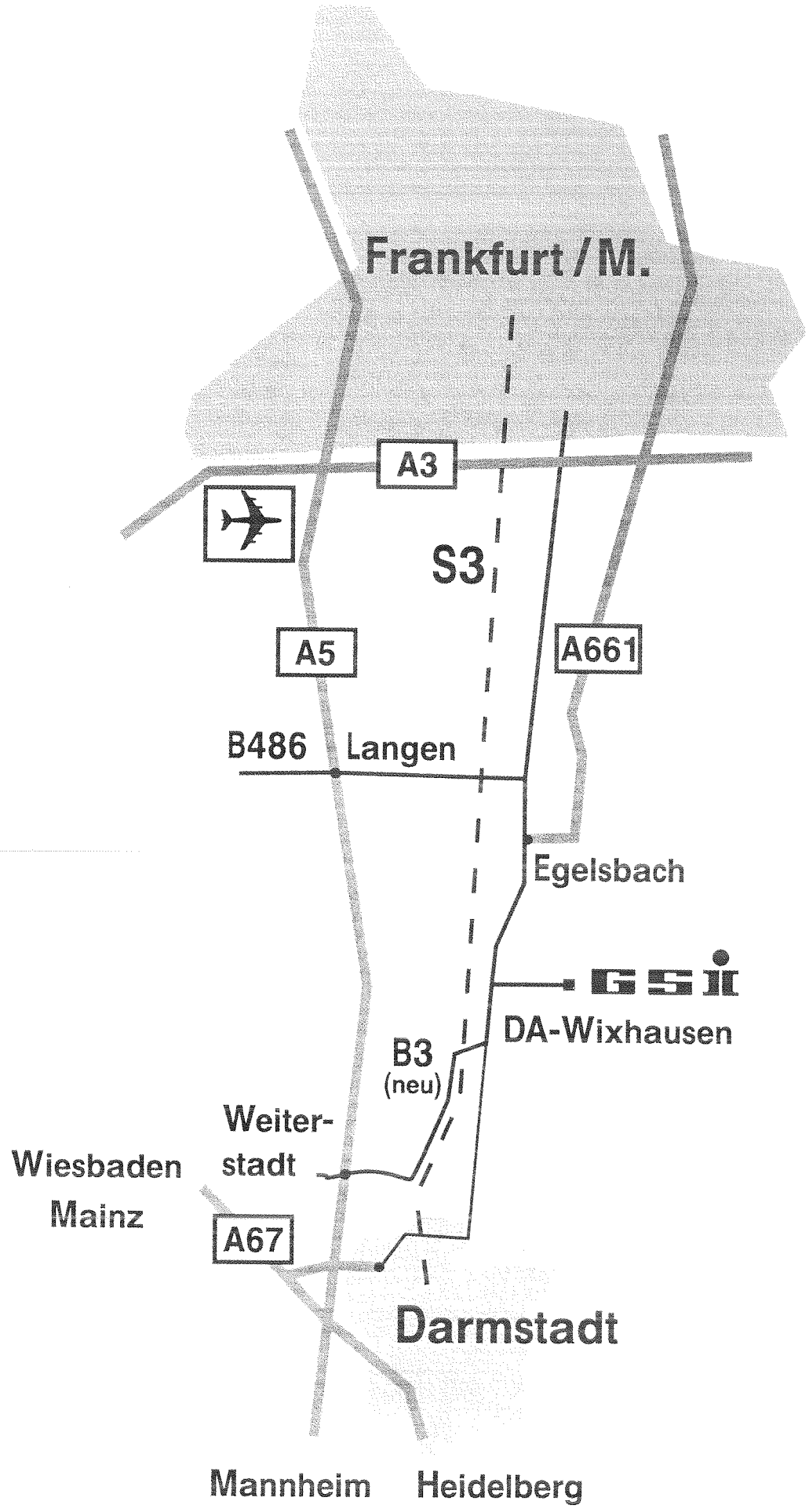
Frankfurt / M.
A3
S3
A5
A661
B486
Langen
Egelsbach
GSI
DA-Wixhausen
B3
(neu)
Weiter-
stadt
Wiesbaden
Mainz
A67
Darmstadt
Mannheim
Heidelberg